Lecture Notes in Electrical Engineering 389

Jiadong Sun
Jingnan Liu
Shiwei Fan
Feixue Wang
Editors

China Satellite Navigation Conference (CSNC) 2016 Proceedings: Volume II

Springer

Lecture Notes in Electrical Engineering

Volume 389

About this Series

"Lecture Notes in Electrical Engineering (LNEE)" is a book series which reports the latest research and developments in Electrical Engineering, namely:

- Communication, Networks, and Information Theory
- Computer Engineering
- Signal, Image, Speech and Information Processing
- Circuits and Systems
- Bioengineering

LNEE publishes authored monographs and contributed volumes which present cutting edge research information as well as new perspectives on classical fields, while maintaining Springer's high standards of academic excellence. Also considered for publication are lecture materials, proceedings, and other related materials of exceptionally high quality and interest. The subject matter should be original and timely, reporting the latest research and developments in all areas of electrical engineering.

The audience for the books in LNEE consists of advanced level students, researchers, and industry professionals working at the forefront of their fields. Much like Springer's other Lecture Notes series, LNEE will be distributed through Springer's print and electronic publishing channels.

More information about this series at http://www.springer.com/series/7818

Jiadong Sun · Jingnan Liu
Shiwei Fan · Feixue Wang
Editors

China Satellite Navigation Conference (CSNC) 2016 Proceedings: Volume II

Springer

Editors
Jiadong Sun
Chinese Academy of Sciences
China Aerospace Science and Technology Corporation
Beijing
China

Jingnan Liu
Wuhan University
Wuhan
China

Shiwei Fan
China Satellite Navigation Office
Beijing
China

Feixue Wang
National University of Defense Technology
Changsha
China

ISSN 1876-1100 ISSN 1876-1119 (electronic)
Lecture Notes in Electrical Engineering
ISBN 978-981-10-0936-5 ISBN 978-981-10-0937-2 (eBook)
DOI 10.1007/978-981-10-0937-2

Library of Congress Control Number: 2016937343

Printed on acid-free paper

This Springer imprint is published by Springer Nature
The registered company is Springer Science+Business Media Singapore Pte Ltd.

Preface

BeiDou Navigation Satellite System (BDS) is China's global navigation satellite system which has been developed independently. BDS is similar in principle to global positioning system (GPS) and compatible with other global satellite navigation systems (GNSS) worldwide. The BDS will provide highly reliable and precise positioning, navigation and timing (PNT) services as well as short-message communication for all users under all-weather, all-time, and worldwide conditions.

China Satellite Navigation Conference (CSNC) is an open platform for academic exchanges in the field of satellite navigation. It aims to encourage technological innovation, accelerate GNSS engineering, and boost the development of the satellite navigation industry in China and in the world.

The 7th China Satellite Navigation Conference (CSNC2016) is held during May 18–20, 2016, Changsha, China. The theme of CSNC2016 is Smart Sensing, Smart Perception, including technical seminars, academic exchanges, forums, exhibitions, and lectures. The main topics are as follows:

S1 BDS/GNSS Application Technology
S2 Navigation and Location-Based Services
S3 Satellite Navigation Signals
S4 Satellite Orbit and Clock Offset Determination
S5 BDS/GNSS Precise Positioning Technology
S6 Atomic Clock and Time-frequency Technology
S7 BDS/GNSS Augmentation Systems and Technology
S8 BDS/GNSS Test and Assessment Technology
S9 BDS/GNSS User Terminal Technology
S10 Multi-sensor Fusion Navigation
S11 PNT System and Emerging Navigation Technology
S12 Standardization, Intellectual Properties, Policies, and Regulations

The proceedings (Lecture Notes in Electrical Engineering) have 176 papers in ten topics of the conference, which were selected through a strict peer-review process from 440 papers presented at CSNC2016. In addition, another 193 papers

were selected as the electronic proceedings of CSNC2016, which are also indexed by "China Proceedings of Conferences Full-text Database (CPCD)" of CNKI and Wan Fang Data.

We thank the contribution of each author and extend our gratitude to 237 referees and 48 session chairmen who are listed as members of editorial board. The assistance of CNSC2016's organizing committees and the Springer editorial office is highly appreciated.

The 7th China Satellite Navigation Conference (CSNC 2016) Committees

Scientific Committee

Chairman
Jiadong Sun, China Aerospace Science and Technology Corporation

Vice-Chairman
Rongjun Shen, China
Jisheng Li, China
Qisheng Sui, China
Changfei Yang, China
Zuhong Li, China Academy of Space Technology
Shusen Tan, Beijing Satellite Navigation Center, China

Executive Chairman
Jingnan Liu, Wuhan University
Yuanxi Yang, China National Administration of GNSS and Applications
Shiwei Fan, China

Committee Members (By Surnames Stroke Order)
Xiancheng Ding, China Electronics Technology Group Corporation
Qingjun Bu, China
Liheng Wang, China Aerospace Science and Technology Corporation
Yuzhu Wang, Shanghai Institute of Optics and Fine Mechanics, Chinese Academy of Sciences
Guoxiang Ai, National Astronomical Observatories, Chinese Academy of Sciences
Shuhua Ye, Shanghai Astronomical Observatories, Chinese Academy of Sciences
Zhaowen Zhuang, National University of Defense Technology
Qifeng Xu, PLA Information Engineering University
Houze Xu, Institute of Geodesy and Geophysics, Chinese Academy of Sciences
Guirong Min, China Academy of Space Technology

Xixiang Zhang, China Electronics Technology Group Corporation
Lvqian Zhang, China Aerospace Science and Technology Corporation
Junyong Chen, National Administration of Surveying, Mapping and Geoinformation
Benyao Fan, China Academy of Space Technology
Dongjin Luo, China
Guohong Xia, China Aerospace Science and Industry Corporation
Chong Cao, China Research Institute of Radio Wave Propagation (CETC 22)
Faren Qi, China Academy of Space Technology
Sili Liang, China Aerospace Science and Technology Corporation
Shancheng Tu, China Academy of Space Technology
Rongsheng Su, China
Zhipeng Tong, China Electronics Technology Group Corporation
Ziqing Wei, Xi'an Institute of Surveying and Mapping

Organizing Committee

Secretary General
Haitao Wu, Navigation Headquarters, Chinese Academy of Sciences

Vice Secretary General
Wenhai Jiao, China Satellite Navigation Office Engineering Center
Jianjun Wu, National University of Defense Technology
Weina Hao, Navigation Headquarters, Chinese Academy of Sciences

Committee Members (By Surnames Stroke Order)
Qun Ding, The 20th Research Institute of China Electronics Technology Group Corporation
Miao Yu, China Academy of Space Technology
Li Wang, International Cooperation Research Center China Satellite Navigation Engineering Office
Ying Liu, China Satellite Navigation Office Engineering Center
Shuhua Zhang, National University of Defense Technology, Changsha
Xiuwan Chen, Peking University
Xiangan Zhao, China Defense Science and Technology Information Center
Ouyang Guangzhou, Academy of Opto-electronics, Chinese Academy of Sciences
Gang Hu, Beijing Unicore Communications, Inc.
Min Shui, National Remote Sensing Centre of China
Zhong Dou, National Time Service Center, Chinese Academy of Sciences

Editorial Board

Contents

Part I
Satellite Navigation Signals

The Application of Fountain Code in Satellite Navigation System

Qiao Liu, Wenjing Zhang, Yong Wang and Hui Li

Abstract The research on satellite navigation signal is one of the most essential topics in satellite navigation system. The enhancement of the signal will undoubtedly improve the service quality of navigation system. Dealing with this problem, applying latest emerging coding schemes have been proved to be efficient. Therefore, we analyze the application of fountain code into satellite navigation system in this paper. To achieve better transmission, we first propose a modified encoding algorithm to reduce the minimized transmission packets cost. Further, by introducing Low-Earth orbit satellite, we concatenate digital fountain code with traditional channel code. By doing so, we can optimize the utilization of fountain code in satellite channels. Finally, simulation results are conducted to valid our theoretical analysis.

Keywords Fountain code · Satellite navigation system · Concatenated code

1 Introduction

The satellite navigation signals are the direct factors to affect the quality of navigation service. However, the navigation signals suffer a bad signal-to-noise condition due to the satellite communication channel properties. Therefore, the instability of navigation signals is always the bottleneck for the navigation service. Abundant of solutions have been explored to improve the navigation signal transmitting. Among them, applying error correction code, including LDPC, Turbo, and RS code, has been proved to be an efficient way. Following such approach, this paper applies the latest emerging close Shannon limit code, i.e., fountain code, into the satellite navigation system.

The idea of fountain code is first proposed over binary erasure channel in 1998, and this idea is realized into practice by LT code in [4] and Raptor code in [5].

Q. Liu (✉) · W. Zhang · Y. Wang · H. Li
ISN, School of Cyber Engineering, Xidian University, Xi'an, China
e-mail: qiao.liu@uwaterloo.ca; windachilles@gmail.com

J. Sun et al. (eds.), *China Satellite Navigation Conference (CSNC) 2016 Proceedings: Volume II*, Lecture Notes in Electrical Engineering 389,
DOI 10.1007/978-981-10-0937-2_1

Following these two well-known fountain codes, the research has been divided into two directions. One is the code improvement and another is the code application. For the fountain code improvement, the degree distribution attracts most attentions [6]. Besides degree distribution, the encoding and decoding algorithms have also been analyzed, see [1]. For the application, the usage of fountain code has been extended into more channel models rather than binary erasure channel, like Block fading channels [2] and AWGN channels [3]. The fountain code also witnesses its application in different networks, like [7, 8]. In particular, the authors in [8] apply the LT code into satellite communication with an enhanced decoding algorithm. We hold an identical motivation with [8] to apply the fountain code into satellite communication, however, with a different approach.

Besides the error correction code, another technique is also attracted enough attention to be a promising method to improve satellite navigation, namely Low-Earth orbit (LEo) satellite. The LEo satellites have a better transmission channel than the Medium-Earth orbit (MEo) satellite for its low distance to the Earth surface, where the MEo contains most navigation satellites. Utilizing LEo satellite in communication becomes a hot topic in the last few years, however the recent connection between LEo satellites and navigation only lies in the locating of LEo satellites by the GPS. Thus, a novel scheme is desired to improve navigation signal with help of LEo satellites.

Following previous discussed motivations, we apply the fountain code into satellite navigation system. Rather than a naive transplanting, the encoding algorithm is modified to reduce the redundancy cost. Further, by involving the LEo satellites, the fountain code is concatenated with error correction code. These two approaches are also the main contributions of this work.

2 Fountain Code

2.1 Overview of the Fountain Code

The fountain code is name after a metaphorical sense in which considers the transmission as a process of filling water into a bucket. During the transmission, the transmitter encodes and sends its messages like a fountain, and the receiver, comparing to a bucket, will continually receive the water until correct decoding. Thus, one round of information transmitting is completed.

The encoder unit of fountain code is packet. It means that the encoder in the transmitter will first divides the source file into fixed length packets, and then encodes each packet. The receiver will continually collect these encoded packets and make an attempt to recovering all of them.

In practical, the number of the received packets is a little larger than the encoded packets number but uncertain. Therefor the rate of the fountain code is unfixed. This property is perfect suitable for the satellite channel. The satellite channel will

change rapidly with the time varying, so the traditional fixed code rate will either bring unnecessary overhead when the channel condition is good or suffer incorrect transmitting when the channel condition is bad. These two problems will be solved by the fountain code.

Another property belonging to fountain code is message recover inevitability. This property comes from that the transmitter can unstoppable encode until the receiver correctly recover the message. With this property, the navigation system will have no anxiety for the navigation signal missing problem.

2.2 LT Code

Following the concept of the rateless, Luby propose the first rateless code, namely Luby transform (LT) code. The encoding of LT code contains four steps as following:

- Step 1: The transmitter divide the original message into k packets with equal length: l bits each packet. Padding 0 if the last packet is not long enough.
- Step 2: The transmitter randomly picks degree d according to the degree distribution $\rho = (\rho_1, \rho_2, \ldots, \rho_k)$, which $p(d = i) = \rho_i$.
- Step 3: Random picking d packets from the divided k pickets.
- Step 4: Output a transmitting packet by doing XOr operation for the d picked packets.

The transmitter will continually generate encoded packets until all the transmitting packages are recovered. In theoretical, the transmitter can generate infinity encoding packets. However, the generated packets number is a little larger than k in practical, but this number is uncertain. Thus, the rate of the code is also an uncertain number, namely rateless.

Then we move on to introduce the decoding part of LT code. Belief propagation (BP) algorithm has been shown as an accepted efficient method to decode LT. The BP algorithm is based on the tanner graph of LT code, and we have given a sample example in Fig. 1. Recall the Step 4 in encoding algorithm, the tanner graph is defined by connecting the encoded packets with its constituted source packets.

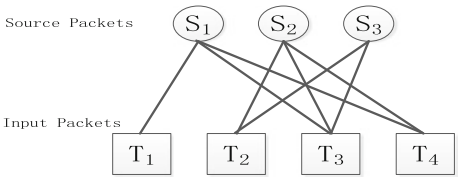

Fig. 1 Tanner graph for LT code

After transmission, the encoded packets will become the input packets of the decoder, so we rename such packets as input packets in the following discussion.

Based on this graph, we introduce the decoding algorithm as following steps:

- Step 1: Find the input packet with one-connected source packet. If there is no one-connected input packets, the decoder will wait for more input packets.
- Step 2: If one-connected packet exists, recovering the source packet as the input packet. In the previous example, T_1 is the one-connected input packet connecting to S_1, so the source packet S_1 will be decoded as T_1.
- Step 3: Delete the recovered source packet and reset the input packets by X or operation which connected to it.
- Step 4: Update the tanner graph.
- Step 5: Repeat Step 1 to Step 4 until all the source packets are recovered.

The one-connected input packet is come from the degree-one packet in encoding process. Consequently, the degree distribution will directly influence the tanner graph. That means the optimization of the degree distribution design will increase the decoding successful probability. For this reason, a lot of works have focused on to propose novel optimized degree distribution just as former mentioned. However, the research on degree distribution has met the bottleneck, in this paper we will give an optimal encoding algorithm rather than the degree distribution. We will leave the optimization of the degree distribution for satellite communication as the future work of this paper.

3 Modification for the LT Code Encoding Algorithm

We have briefly introduced the encoding and decoding algorithm of LT code in the previous section. With former discussion of the LT code, we can see that the transmission efficiency is mainly depended on the design of the degree distribution. However, the research on degree distribution has suffered bottleneck in the last few years. The new designed degree distribution cannot marginally increase the encoding efficiency. Consequently, other approaches must be raised to improve the LT code. Under such motivation, we first analyze the LT encoding algorithm in detail, and then propose a new algorithm to achieve better performance. Here we have a note that the encoding algorithm of the Raptor code is mainly based on LT encoding, hence the improvement of LT Encoding algorithm will undoubtedly increase the transmission efficiency.

3.1 Analysis for the LT Encoding Algorithm

In the previous section, we have introduced the encoding algorithm for LT code. From the discussion, we clearly see that different degree distribution function leads

to different performance. Focusing on Robust Soliton distribution, we first analyze the encoding and decoding performance.

The Robust Soliton distribution is shown as follows:

$$\mu(d) = \frac{\rho(d) + \tau(d)}{\sum_d (\rho(d) + \tau(d))}, \tag{1}$$

where $\rho(d)$ is the Ideal Soliton distribution as

$$\rho(d) = \begin{cases} 1/K & d = 1 \\ \frac{1}{d(d-1)} & d = 2, 3, \ldots, K \end{cases}, \tag{2}$$

and $\tau(d)$ is:

$$\tau(d) = \begin{cases} \frac{S}{K}\frac{1}{d}, & d = 1, 2, \cdots, \frac{K}{S} - 1 \\ \frac{S}{K}\log\left(\frac{S}{\delta}\right), & d = \frac{K}{S} \\ 0, & d > \frac{K}{S} \end{cases}. \tag{3}$$

In Eq. (3), δ is the allowed decoding failure possibility, which is a forecasting number. Usually, δ is a very small number for satellite communication, like $\delta = 0.01$. S is defined as: $S \triangleq c\sqrt{K}\ln(K/\delta)$, where c is a constant. In theoretical, c can be chosen as any real number, but we usually choose $c < 1$ in practical. Actually, choosing of c determines the performance of LT code crucially. However, theoretical analysis of determining c is still a hard problem, therefore we demonstrate the choosing of factor c with fixed δ by following simulation result in Fig. 2.

We simulate the decoding successful probability with receive packets under different c. The original packet is set as 1000. With the simulation results as shown

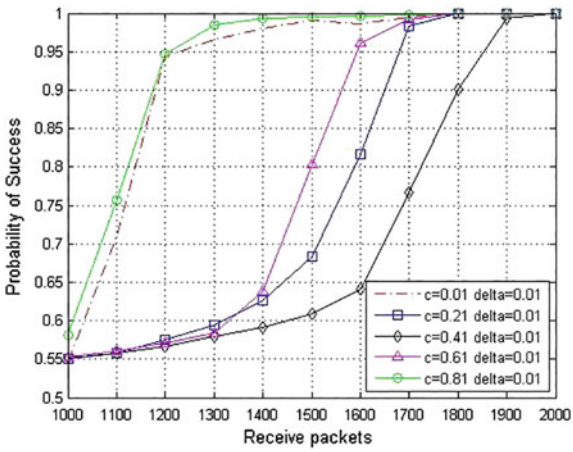

Fig. 2 Successful probability comparison with different c

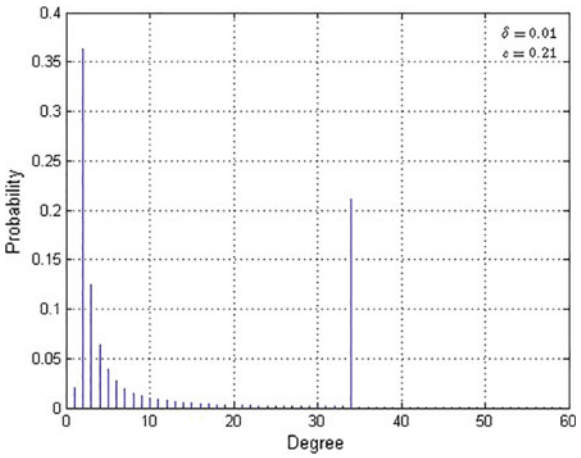

Fig. 3 Robust soliton distribution with $\delta = 0.01$ and $c = 0.21$

in Fig. 2, we can see that for Robust Soliton distribution, an optimal performance can be achieved as c = 0.81. Although this result cannot be proved by theoretical analysis yet, this simulation is be of great value as a guide to implementation.

Following the simulation instruction, we draw the Robust Soliton distribution with $\delta = 0.01$ and c = 0.81 in Fig. 3. With that we can clearly see that degree = 2 is the most frequently chosen degree; therefore, the modification of the encoding algorithm under degree 2 case will be of great value. Then we move on to propose a novel algorithm aiming at improving LT encoding performance under degree 2 case.

3.2 Modified Algorithm for LT Code Encoding

With the analysis in the last subsection, we show that the degree 2 situation case contains over quarters of the encoded packets for robust degree distribution. If we could promote the encoding efficiency for degree 2 situation, the LT encoding algorithm will be undoubtedly improved.

Fixing the degree distribution, another factor also plays an essential role to enhance LT performance, i.e., packets covering ratio. This ratio means how quickly the encoded packets will cover all the original packets. This factor is significant with the reason that all original packets must be covered, otherwise the receiver cannot recover all original packets. Consider the situation that the well-designed degree distribution has provided enough available decoding packets in each round; however, one of the original packets has never been chosen to be transmitted. Under such situation, the decoding is still a failure. Accordingly, covering the whole original packets as soon as possible will be effective to reduce the transmitting packets cost.

Recalling the degree 2 situation, we have shown that this situation occupies over quarters of whole transmitting packets. Thus, improving the packets covering ratio under degree 2 will be of great value. Assuming K packets are transmitted, so primary encoding algorithm costs $\binom{K}{2}$ solutions to pick 2 packets from the K packets. To reduce such cost, we predivide the K packets into two groups and picking one from each. For this proposal, only $\binom{K}{1} * \binom{K}{1}$ are cost. Taking $K = 10,000$ as an example, primary encoding algorithm has 49,995,000 solutions, however, the improved algorithm only cost 25,000,000 which is less than the half of the primary algorithm.

The modified encoding algorithm has been shown as follows:

Algorithm: ***Modified Algorithm for LT Code Encoding***

Input: Original Data S, Degree Distribution ρ, Data Packets Number K
Output: Encoded Packets T

procedure ENCODING(S, ρ, K)
  Divide Original Data S into K Packets $\{S_1, S_2, \cdots, S_K\}$, padding 0 if bits lack.
  Divide Packets $\{S_1, S_2, \cdots, S_K\}$ into two gourps S_A, S_B
  $i \leftarrow 1$
  repeat
    Picking Degree d based on Degree Distribution ρ
    if $d = 2$ **then**
      Seperately choosing u_1 from S_A and u_2 from S_B
    else
      Rondomly nonrepeated chooing $u_1, u_2, \cdots, u_d$ from packages.
    end if
    $T_i \leftarrow u_1 \oplus u_2 \oplus \cdots \oplus u_d$
    $i \leftarrow i + 1$
  until Recieving Correct Decoding ACK
end procedure

4 The Application of Fountain Code in Satellite Navigation System

The fountain code was first analyzed in the erasure channel with an impressive performance. Further, some researchers extend its application into other channel models as former mentioned. Meanwhile, some features belonging to fountain code,

like rateless, message recover inevitability are exactly fit the satellite channel model. Then it is a natural thought that applying the fountain code into satellite navigation system.

4.1 The Advantage Analysis of Applying Fountain Code into Satellite Navigation System

Before we analyze the advantage, we first discuss about the channel properties of the satellite navigation signal.

Two main problems are needed to be deal with the navigation signals. The first problem is the signal distortion caused by the interference from ionosphere, troposphere, and local surface. The second problem is the frequent consecutive burst errors, such errors often request large number of redundancies to preventing transmission failure.

To deal with such problems, the fountain code is an optimal candidate comparing with current applying channel code like LDPC in GPS L1C. The reasons are as follows. First, the message recovers inevitability of fountain code can guarantee the transmission success. Causer transmitter will unstop to generate transmitting packets until all the packets are recovered. Second, the rateless feature can reduce the former mentioned redundancy. Facing the situation that frequent burst errors often happen, the fixed rate must reserve enough redundancies. However, such redundancies will be unnecessary when the channel condition is good. Thus, the rateless code, i.e., fountain code, will improve such waste.

4.2 Preliminaries for Low-Earth Orbit Satellite

With former analysis, we can directly see that fountain code is perfectly suitable for satellite navigation system. Besides naive transplanting, a recently conducted experiment in November by NASA provides a brand-new prospect. In that experiment, LEo satellite is utilized to assistant GPS signal transmitting. This experiment also forecast that using LEo satellite could be an effective approach to improve the quality of navigation signals.

The Low-Earth orbit satellite is the satellite that occupies the orbit around earth with the altitude between 180 and 1240 km. With a closer distance from the Earth's surface, the LEo satellite enjoys a better communication than the Medium-Earth orbit satellite where almost all navigation satellites are belonging to GPS, Galileo, and Beidou.

4.3 The Application of Fountain Code in Satellite Navigation System

We combine two key techniques to realize an equivalent ensure channel, namely concatenated code and LEo satellites which has been introduced in last subsection. Further, such equivalent ensures channel that will be perfect for the application of fountain code in satellite navigation system.

The concatenated code was first presented by Forney in 1966 by naive concatenating block code and cyclic code. Forney also prove that the performance improvement would only be with polynomial-time decoding complexity that is increasing. Following this idea, we concatenate the fountain code with error-correcting code. Rather than directly concatenating, we separate the two encoders in different satellite to form an equivalent ensure channel.

In the transmitter, i.e., the navigation satellite, the original message will be first divided into packets. Then the transmitter encodes these packets with fountain code encoding. The navigation satellite will transmit these coded packets to the LEo satellite. The LEo satellite will not decode these packets, instead it will do the second-time encoding. LDPC or turbo code is suggested. After the inner encoding, LEo will forward the packets to the receiver. Here is a note that interleaving is needed for LDPC against the emerging of burst errors.

The decoders, both the inner and outer, are lying at the receiver. Rather than the routine sequential decoding, we have different designs. The decoder will first detect the error for the inner code, and make a judgment. If these errors are in the threshold, the inner decoder will correct them. Otherwise, this packet will be ensured. Thus, an equivalent ensures that the channel is generated for the outer code, which will be fountain code in our scheme. The inner decoder will send the corrected packets into the outer decoder to accomplish the fountain code decoding. Waiting for the all original packets recovered, the receiver will send a ACK to the transmitter to finish this round of message transmitting.

The transmission diagram is shown in Fig. 4.

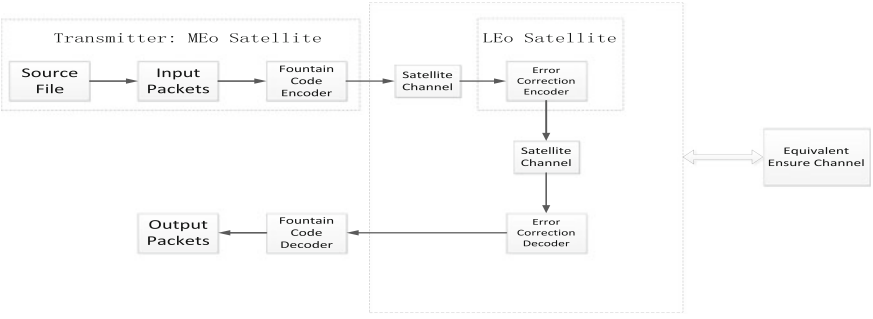

Fig. 4 Transmission diagram of proposed concatenated code

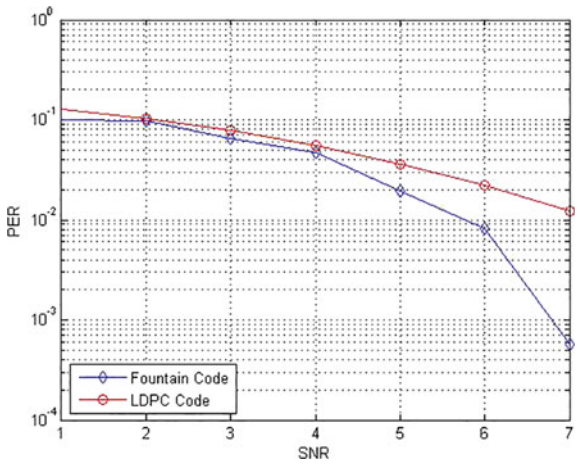

Fig. 5 Packets error ratio comparison for fountain code with LDPC code

4.4 Simulation Result of LT-LDPC Concatenated Code

To perform the proposed concatenated fountain code scheme, we simulate the situation by comparing the packet error ratio (PER) between the proposed code with LDPC which is used in GPS L1C. We choose LT code as the outer code and LDPC code as the inner code. We consider that 1000 packets has been transmitted, and set the rate of LDPC code as 0.5. Correspondingly, we assume 2000 packets have been received.

The simulation result is shown in Fig. 5. With the result we can see that with fixed SNR, the proposed code can correct more errors than LDPC code especially in high SNR region. Further, the ratelss and message recover inevitability feature belonging to fountain code makes it perfect suitable for the satellite navigation system.

5 Conclusions

The navigation signal is a significant factor to influence the quality of navigation service. However, the signal will suffer a bad distortion due to the satellite communication features. To deal with this problem, we apply the fountain code into navigation system. First, we briefly overview the fountain code with two practical scheme, namely LT code and Raptor code. Second, we modified the encoding algorithm of LT code to reduce the transmitting packets cost. At last, we apply the fountain code into navigation system with the help of LEo.

Some future work can be considered as follows. First, a novel degree distribution is desired for the particular satellite communication. Second, determining the factor c with theoretical analysis in Robust Soliton distribution is also a promising

way to improve the fountain code. And last, to improve the application in navigation system, different concatenated code approaches should be analyzed to seek out the optimal one.

Acknowledgments This work is supported by National Natural Science Foundation of China (No. 61101147), The National Basic Research Program of China (973 Program, No. 2012CB316100), Specialized Research Fund for Doctoral Program of Higher Education (No. 20110203120004), Natural Science Basic Research Plan in Shaanxi Province of China (Program No.2014JZ018), Science Research Plan in Shaanxi Province of China (No. 2013K06-15), The Fundamental of Research Funds for the Central Universities (No. K5051301006), The 111 Project (No. B08038), National Natural Science Foundation (No. 61472308)

References

1. Cassuto Y, Shokrollahi A (2015) Online fountain codes with low overhead. IEEE Trans Inf Theory 61(6):3137–3149
2. Hanzo L, Maunder RG, Chen H, Tafazolli R, Ma Y (2015) Hybrid-ARQ-aided short fountain codes designed for block-fading channels. IEEE Trans Veh Technol 99:1–12
3. Hussain I, Land I, Chan TH, Xiao M, Rasmussen LK (2014) A new design framework for LT codes over noisy channels. In: 2014 IEEE international symposium on information theory (ISIT). IEEE, pp 2162–2166
4. Luby M (2002) LT codes. In: Proceedings of the 43rd symposium on foundations of computer science. IEEE Computer Society
5. Shokrollahi A (2006) Raptor codes. IEEE Trans Inf Theory 52(6):2551–2567
6. Yen KK, Liao YC, Chen CL, Chang HC (2013) Modified robust soliton distribution (MRSD) with improved ripple size for LT codes. IEEE Commun Lett 17(5):976–979
7. Yue J, Lin Z, Vucetic B (2014) Distributed fountain codes with adaptive unequal error protection in wireless relay networks. IEEE Trans Wireless Commun 13(8):4220–4231
8. Zhang Q, Zhang S, Zhou W (2014) Enhanced LT decoding scheme in satellite communication. In: 2014 sixth international conference on wireless communications and signal processing (WCSP). IEEE, pp 1–6

A Comprehensive Evaluation Approach of Navigation Signal Performance Based on Multi-attribute Group Decision Making

Qing Liu, Yanhong Kou and Zhigang Huang

Abstract In the process of comprehensive performance evaluation of new-structure satellite navigation signals, some problems may be encountered including the wide varieties of performance indicators/attributes, the lack of a clear attribute system, the complex relationships and strong correlations among different attributes, the differences in user preferences of the significances of various attributes, and so on. Based on the comparative analysis of different models and methods for the fuzzy multi-criteria Group Decision Making (GDM) problems, this paper proposes a comprehensive signal performance evaluation approach that integrates multiple methods seamlessly. Firstly, a three-level signal attribute system is established based on Analytic Hierarchy Process (AHP). Next, the attributes at the bottom level are decorrelated and reconstructed by Fuzzy Clustering and Principal Component Analysis (PCA). Then the Technique for Order Preference by Similarity to Ideal Solution (TOPSIS) is employed to obtain the Relative Membership Degree (RMD) of each alternative signal option to each attribute unit. Finally, the overall performance of each alternative is calculated using the multi-attribute GDM model. The evaluation of six alternative modulations for GPS L1C signals based on theoretical analysis demonstrates the feasibility and effectiveness of the proposed approach. The approach provides an efficient means for the comprehensive performance evaluation of satellite navigation signals.

Keywords Satellite navigation signal · Multi-attribute group decision making · AHP · PCA · TOPSIS · Fuzzy clustering

Q. Liu · Y. Kou (✉) · Z. Huang
School of Electronic and Information Engineering, Beihang University, Beijing 100191, China
e-mail: kouy@buaa.edu.cn; xc1989love@buaa.edu.cn

J. Sun et al. (eds.), *China Satellite Navigation Conference (CSNC) 2016 Proceedings: Volume II*, Lecture Notes in Electrical Engineering 389,
DOI 10.1007/978-981-10-0937-2_2

1 Introduction

With the development of Global Navigation Satellite System (GNSS), various novel navigation signal structures have been proposed. Signal structure design is one of key tasks of GNSS design, and the scientific and comprehensive performance evaluation of different signal structures becomes of great importance for the achievement of function and performance goals of GNSS services.

Multi-criteria/multi-attribute decision making (MCDM/MADM) approaches have been widely applied in the fields of military affairs, transportation, healthcare, mining, hydraulic engineering, and so forth [1–7]. Nevertheless, few literatures can be found about applying these approaches in the evaluation of GNSS signal performances. Several related methods for GNSS signal performance evaluation have been mentioned/studied in [8], including the radar chart method, the expert scoring method, the linear weighting method, and the weighted Technique for Order Preference by Similarity to Ideal Solution (TOPSIS). These methods, however, need to be improved due to their inefficiency of dealing with subjectivity, lack of consideration of correlations among the attributes, or lack of quantitative analysis.

In order to solve these problems, this paper first establishes a hierarchical attribute system for satellite navigation signals. The signal attribute system can be divided into the following three levels: (1) The bottom level is composed of all the computable/measurable performance indicators, i.e., the attributes; (2) The middle level classifies these attributes into several groups, with one group named as an Attribute Unit (AU); (3) The top level forms the Group Decision Making (GDM) target and represents the overall performance of the signal. Then a fuzzy comprehensive evaluation approach is explored to act as the technical means for the optimal selection of signal alternatives, which takes advantage of Analytic Hierarchy Process (AHP), Principal Component Analysis (PCA), Fuzzy Clustering and weighted TOPSIS appropriately. Finally, taking six GPS L1C signal modulation alternatives as a case study [9], the evaluation results select the TMBOC (6,1,4/33) modulation meeting with the interface specification document IS-GPS-800.

2 Methodology

The proposed evaluation approach includes the following three steps: (1) to establish the three-level architecture of the signal attribute system for AHP; (2) to calculate the Relative Membership Degree (RMD) of each alternative signal option with respect to each AU; (3) to calculate the overall RMD of each alternative signal option.

2.1 Signal Attribute System

There is a wide range of attributes indicating different performances of satellite navigation signals. On the other hand, the relative importance of these attributes can vary significantly for different users and applications. As one of the most popular analytical techniques for complex decision making problems, AHP is firstly considered in our methodology to well characterize the signal option decision situation and efficiently incorporate objective as well as subjective attributes into the decision. Taking account of the definition, application requirements, and relevance of these attributes, as well as the summary of available theoretical data and test data for different signal options, a three-level signal attribute system is established for the decision making among different signal alternatives, as shown in Fig. 1. The specific attributes corresponding to the raw measurement/analysis data fall into the bottom level. The second level attributes can be obtained by classifying the first-level attributes with similar characteristics into an AU, such as the anti-interference capability, the measurement accuracy, the receiving threshold, and so forth. The third (top) level is the overall performance indicator corresponding to the evaluation result. This hierarchical architecture helps to reduce the workload, difficulty, subjectivity, and arbitrariness for the Experts, User representatives, and Decision makers (EUD) to assign weights to different attributes because only a few second-level attributes need to be weighted or, more simply, pairwisely compared according to the application preferences.

2.2 Fuzzy Optimization Model of One AU

The fuzzy optimization model of one AU includes the following two steps: decorrelation of the attributes and calculation of the RMD of each alternative to each AU.

2.2.1 Decorrelation of Attributes

Correlations among the attributes can be captured and reduced by employing fuzzy clustering and PCA.

AU Fuzzy Clustering

The attribute value (measured/calculated/estimated data) matrix for the decision problem with m attributes of the kth AU and n alternatives can be expressed as Eq. (1):

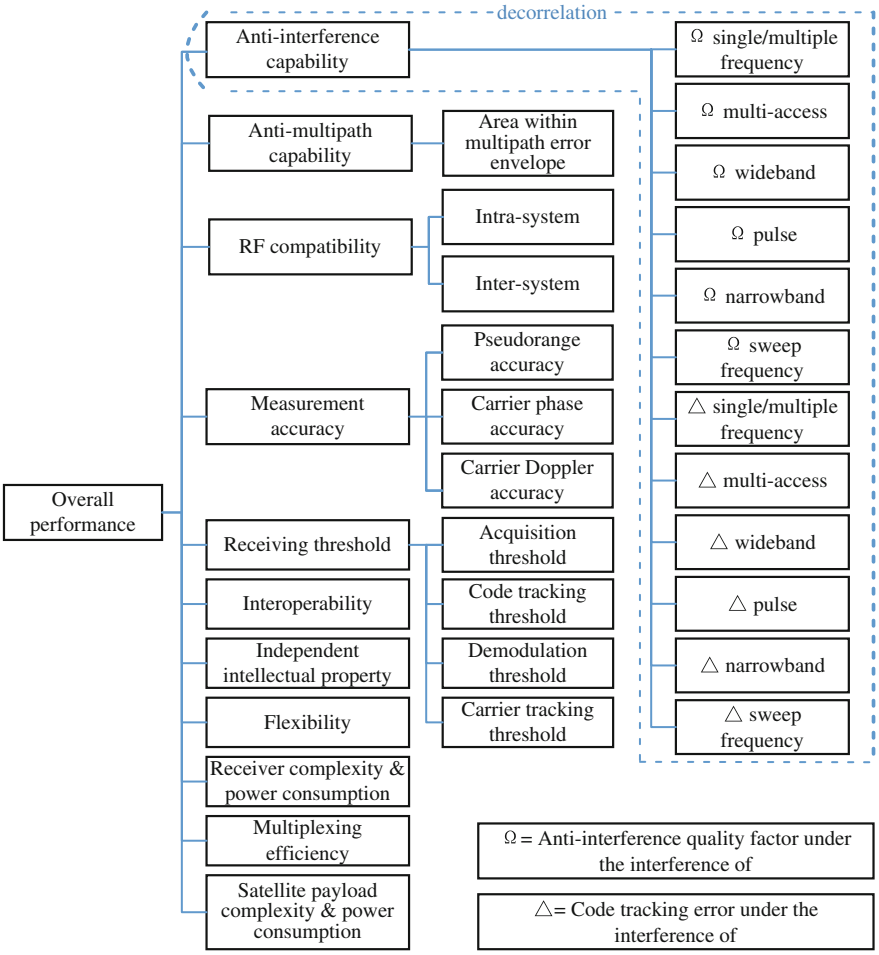

Fig. 1 Attribute system of satellite navigation signal

$$ {}_{1k}X = \begin{bmatrix} {}_{1k}x_{11} & {}_{1k}x_{12} & \cdots & {}_{1k}x_{1m} \\ {}_{1k}x_{21} & {}_{1k}x_{22} & \cdots & {}_{1k}x_{2m} \\ \vdots & \vdots & \vdots & \vdots \\ {}_{1k}x_{n1} & {}_{1k}x_{n2} & \cdots & {}_{1k}x_{nm} \end{bmatrix} = \left({}_{1k}x_{ij}\right)_{n\times m} \tag{1} $$

where $i = 1, 2, \ldots, n$; $k = 1, 2, \ldots, t$; $j = 1, 2, \ldots, m$; ${}_{1k}x_{ij}$ denotes the attribute value at the first level.

To make the attributes dimensionless and larger-the-better, the raw attribute value matrix can be normalized as follows:

$$ {}_{1k}X' = \begin{bmatrix} {}_{1k}x'_{11} & {}_{1k}x'_{12} & \cdots & {}_{1k}x'_{1m} \\ {}_{1k}x'_{21} & {}_{1k}x'_{21} & \cdots & {}_{1k}x'_{2m} \\ \vdots & \vdots & \vdots & \vdots \\ {}_{1k}x'_{n1} & {}_{1k}x'_{n1} & \cdots & {}_{1k}x'_{nm} \end{bmatrix} = \left({}_{1k}x'_{ij} \right)_{n\times m} \tag{2} $$

where

$$ {}_{1k}x'_{ij} = \frac{{}_{1k}x_{ij} - \overline{{}_{1k}x_j}}{{}_{1k}S_j} \quad \text{if attribute } j \text{ is a utility-type attribute} \tag{3} $$

$$ {}_{1k}x'_{ij} = 1 - \frac{{}_{1k}x_{ij} - \overline{{}_{1k}x_j}}{{}_{1k}S_j} \quad \text{if attribute } j \text{ is a cost-type attribute} \tag{4} $$

$$ \begin{aligned} \overline{{}_{1k}x_j} &= \frac{1}{n}\sum\nolimits_{i=1}^{n} {}_{1k}x_{ij} \\ {}_{1k}S_j &= \sqrt{\frac{1}{n}\sum\nolimits_{i=1}^{n} \left({}_{1k}x_{ij} - \overline{{}_{1k}x_j} \right)^2} \end{aligned} \tag{5} $$

The correlation matrix of Eq. (2) is calculated as

$$ {}_{1k}R = \left({}_{1k}r_{ij} \right)_{m\times m},\ {}_{1k}r_{ij} = \frac{\mathrm{cov}\left({}_{1k}x_i, {}_{1k}x_j \right)}{\sqrt{D\left({}_{1k}x_i \right) D\left({}_{1k}x_j \right)}} \tag{6} $$

Generally, since ${}_{1k}R$ is not a fuzzy equivalent matrix, its transitive closure ${}_{1k}R'$ should be further computed. By comparing the elements of ${}_{1k}R'$ with a threshold ${}_{1k}\lambda$, a matrix ${}_{1k}R'_{\lambda}$ with binary elements (0 or 1) is obtained. The attributes with value of 1 in one row/column can be classified into the same cluster.

The clustering results depend on the value of ${}_{1k}\lambda$. Assuming that ${}_{1k}R'_{\lambda}$ divides one AU into m_k clusters, $c_1, \ldots, c_l, \ldots, c_{m_k}$, where c_l $(l = 1, \ldots, m_k)$ represents the lth cluster, the evaluation objective function of ${}_{1k}\lambda$ can be estimated by Wang et al. [6]:

$$ {}_{1k}S = {}_{1k}\delta / {}_{1k}L \tag{7} $$

where ${}_{1k}\delta$ is the average Hamming distances [10] between the cluster centers and all the sample attributes, ${}_{1k}L$ is the minimum distance between different cluster centers. By choosing the best ${}_{1k}\lambda$ corresponding to the smallest ${}_{1k}S$, efficient and reasonable clustering can be achieved.

Construction of Composite Attribute of Each Cluster based on PCA

After the process of fuzzy clustering, it is essential to construct a new attribute for each cluster, which represents the composite performance of all the attributes in the cluster. The attribute values of the lth cluster of the kth AU are regrouped as

$$ {}_{1k}X'' = \begin{Bmatrix} {}_{1k}x''_{11} & \cdots & {}_{1k}x''_{1m_c} \\ \vdots & \ddots & \vdots \\ {}_{1k}x''_{n1} & \cdots & {}_{1k}x''_{nm_c} \end{Bmatrix} \tag{8} $$

where n is the number of the alternatives, m_c is the number of the attributes in this cluster, ${}_{1k}x''_{ij}$ keeps the attribute value of ${}_{1k}x'_{ij}$ in Eq. (2) and is reordered in the cluster. Normalizing Eq. (8) leads to ${}_{1k}Z = ({}_{1k}z_{ij})_{n\times m_c}$, where

$$ {}_{1k}z_{ij} = \frac{{}_{1k}x''_{ij} - \overline{{}_{1k}x''_j}}{{}_{1k}S''_j} \tag{9} $$

And

$$ \overline{{}_{1k}x''_j} = \frac{1}{n}\sum\nolimits_{i=1}^{n} {}_{1k}x''_{ij} $$

$$ {}_{1k}S''_j = \sqrt{\frac{1}{n}\sum\nolimits_{i=1}^{n}\left({}_{1k}x''_{ij} - \overline{{}_{1k}x''_j}\right)^2} $$

Thus the jth column vector of the normalized matrix has a zero mean and a unit variance $E({}_{1k}Z_j) = 0,\ D({}_{1k}Z_j) = 1$.

The correlation matrix of ${}_{1k}Z$ is

$$ {}_{1k}R_z = ({}_{1k}r_{ij})_{m_c\times m_c} = \frac{1}{n-1}\,{}_{1k}Z^T\,{}_{1k}Z \tag{10} $$

$$ {}_{1k}r_{ij} = \mathrm{cov}({}_{1k}Z_i, {}_{1k}Z_j) \tag{11} $$

Assuming that ${}_{1k}R_z$ has q eigenvalues greater than zero $(\lambda_1, \lambda_2, \cdots, \lambda_q)$, $\lambda_i > 0$, and the corresponding orthonormal eigenvectors are $A = (a_1, a_2, \cdots, a_q)$, q principal components can be computed by

$$ Y_{n\times q} = (y_1, y_2, \ldots, y_q) = {}_{1k}Z_{n\times m_c}A_{m_c\times q} $$

$$ \begin{bmatrix} y_{11} & \cdots & y_{1q} \\ \vdots & \ddots & \vdots \\ y_{n1} & \cdots & y_{nq} \end{bmatrix} = \begin{bmatrix} {}_{1k}z_{11} & \cdots & {}_{1k}z_{1m_c} \\ \vdots & \ddots & \vdots \\ {}_{1k}z_{n1} & \cdots & {}_{1k}z_{nm_c} \end{bmatrix} \begin{bmatrix} a_{11} & \cdots & a_{1q} \\ \vdots & \ddots & \vdots \\ a_{m_c1} & \cdots & a_{m_cq} \end{bmatrix} \tag{12} $$

As indicated by Yu [11], the principal components in Eq. (9) are independent

$$ \mathrm{cov}(y_i, y_j) = \begin{cases} 0 & i \neq j \\ \lambda_i & i = j \end{cases} \tag{13} $$

The contribution of the principal component y_i to the total variance is estimated as

$$\omega_i = \lambda_i \Big/ \sum_{j=1}^{q} \lambda_j \tag{14}$$

Ranking $y_1, y_2, \ldots, y_q$ in the descending order of $\omega_1 > \omega_2 > \cdots \omega_q$, the cumulative variance contribution of the first m_ρ principal components is:

$$\rho = \sum_{i=1}^{m_\rho} \lambda_i \Big/ \sum_{j=1}^{m_c} \lambda_j \tag{15}$$

Different value of ρ yield different reconstructed attribute $x_l^{new} = \sum_{i=1}^{m_\rho} \omega_i y_i$ as the composite performance evaluation of the lth cluster. In addition, large ρ allows more information kept in the newly constructed attribute.

If several clusters have been generated in the fuzzy clustering process for an AU, the above process should be repeated to reconstruct a separate attribute for each cluster.

2.2.2 Calculation of RMD to Each AU Based on Weighted TOPSIS

After the decorrelation of the attributes, a new attribute value matrix $\left({}_{1k}x^{\text{new}}\right)_{n\times m_k}$ for the kth AU is obtained. The weights of these reconstructed attributes can be determined by Wang [2]

$${}_{1k}\omega_j = \sum_{i=1}^{n} {}_{1k}rr_{ij}^{\text{new}} \Big/ \sum_{i=1}^{n} \sum_{j=1}^{m_k} {}_{1k}rr_{ij}^{\text{new}} \tag{16}$$

where ${}_{1k}\omega_j$ denotes the weight of the jth attribute of the kth AU, and ${}_{1k}rr_{ij}^{\text{new}} = \frac{{}_{1k}x_{ij}^{\text{new}} - \min_i\left\{{}_{1k}x_{ij}^{\text{new}}\right\}}{\max_i\left\{{}_{1k}x_{ij}^{\text{new}}\right\} - \min_i\left\{{}_{1k}x_{ij}^{\text{new}}\right\}}$ is the RMD of ${}_{1k}x_{ij}^{\text{new}}$.Using this objective weighting method, the trouble and arbitrariness of subjective weighting of a large number of attributes can be avoided.

According to the optimization rule of minimizing the sum of squares of the weighted distances to both the ideal and negative ideal solutions, the RMD of the ith alternative to the kth AU can be calculated by Wang [12]

$$u_{ik} = 1 \Big/ \left(1 + \left\{\sum_{j=1}^{m_k} \left[\omega_j\left(1 - {}_{1k}rr_{ij}^{\text{new}}\right)\right] \Big/ \sum_{j=1}^{m_k} \left[\omega_j \cdot {}_{1k}rr_{ij}^{\text{new}}\right]\right\}^2\right) \tag{17}$$

Equation (17) is the fuzzy optimization result representing the composite performance of each alternative to one AU. For an AU without decorrelation process, the same process of weighting and calculation of the RMD as shown Eqs. (16)–(17) can be conducted.

2.3 Multi-level Multi-attribute GDM Model

This model will output the final evaluation results by performing the following two steps: (1) assembly of the weights of attributes at the second level of AHP according to the judgements of all the EUDs; (2) calculation of the overall performance RMD of each alternative signal option.

2.3.1 Group Decision of Weights of AUs

In the previous section, one attribute for one AU has been obtained. The t attributes at the second level of signal attribute system are denoted as $O = \{o_1, o_2, \ldots, o_t\}$. Scaling the relative importance of the attributes using the Fuzzy degree value defined in Table 1, the Pairwise Comparison Matrix (PCM) [13] can be obtained

$$\beta = \begin{bmatrix} \beta_{11} & \beta_{12} & \cdots & \beta_{1t} \\ \beta_{21} & \beta_{22} & \cdots & \beta_{2t} \\ \vdots & \vdots & \vdots & \vdots \\ \beta_{t1} & \beta_{t2} & \cdots & \beta_{tt} \end{bmatrix} \tag{18}$$

where $\beta_{kl} = 1 - \beta_{lk}$ denotes the importance fuzzy degree of o_k relative to o_l. When o_k is more important than o_l, $0.5 < \beta_{kl} < 1$; when o_k and o_l are of the same importance, $\beta_{kl} = 0.5$; Otherwise $0 < \beta_{kl} < 0.5$.

The mood operators in Table 1 comes from the judgments of the EUDs. Since the navigation signals of different frequencies lay particular stress on different applications, different EUDs may be endowed with different weights for a specified signal. Assuming that α_k $(k = 1, \ldots, p)$ is the weight of the kth EUD and β_k represents the PCM given by the kth EUD, the p PCMs can be assembled by linear weighting

$$\bar{\beta} = \sum_{k=1}^{p} \alpha_k \beta_k \tag{19}$$

Table 1 Pairwise comparison scale of attributes according to mood operator

MO of the relative importance	Equally	Slightly more	Moderately more	Strongly more	Extremely more	Absolutely
FD	0.50	0.60	0.70	0.80	0.90	0.10

Annotation "MO" represents "mood operator", "FD" represents "fuzzy degree"

The normalized sum of a row in the matrix $\bar{\beta}$ represents the relative importance of the corresponding attribute

$$W_i' = \sum_{j=1}^{t} \bar{\beta}_{ij}, \quad i = 1, 2, \ldots t;\ i \neq j \tag{20}$$

$$W_i = W_i' \Big/ \sum\nolimits_{i=1}^{t} W_i' \tag{21}$$

Thus the weight vector of the t AUs is $W = (W_1, W_2, \cdots, W_t)^T$.

2.3.2 Calculation of Overall Performance RMD

Now that the RMD of each alternative corresponding to each AU has been given by Eq. (17) and the weight of each attribute given by Eq. (23), the final decision making vector can be obtained by simple linear weighting

$$U_{n\times 1} = \begin{bmatrix} U_1 \\ U_2 \\ \vdots \\ U_n \end{bmatrix} = \begin{bmatrix} u_{11} & u_{12} & \cdots & u_{1t} \\ u_{21} & u_{22} & \cdots & u_{2t} \\ \vdots & \vdots & \vdots & \vdots \\ u_{n1} & \cdots & \cdots & u_{nt} \end{bmatrix} \begin{bmatrix} W_1 \\ W_2 \\ \vdots \\ W_t \end{bmatrix} \tag{22}$$

where u_{ij} is the RMD of the ith alternative corresponding to the jth AU; U_i is the overall performance RMD of the ith alternative. So, the alternative with the maximum value of U_i represents the optimal signal option with the best overall performance.

3 Case Study

Taking the selection of GPS L1C signal modulation scheme as a case study, this section shows the evaluation process of the following six signal modulation options: BPSK(1), BPSK(2), BOC(1,1), TMBOC(4,1,4/33), TMBOC(5,1,4/33), and TMBOC(6,1,4/33). The raw value of each attribute is only based on theoretical calculation, with the preconditions and the attribute values shown in Tables 2 and 3 respectively. Note that only parts of the attributes in Fig. 1 have been taken into account. As shown in the first column of Table 3, the attributes have been grouped into six AUs. Additionally, the interoperability performance is calculated using the method proposed by Liu [14], and other attribute values are obtained according to the methods introduced in [15].

Table 2 Preconditions of theoretical calculation of signal performance

Parameter	Considerations	Value
Front-end bandwidth	Main lobe bandwidth of the signal	Main lobe bandwidth
Correlator spacing	$d < v/(2u)$	0.08 chip
DLL bandwidth	Typical receiver design	1 Hz
PLL bandwidth	Typical receiver design	15 Hz
Integration time	One code period	10 ms
Carrier to noise ratio (C/N0)	Nominal signal power level and thermal noise background	44 dB-Hz
Multipath to direct path ratio (MDR)	Typical value for test and analysis	−6 dB
L1 C/A signal power	Typical value for test and analysis of intra-system RF compatibility	−128.5 dBm
Interference to signal power ratio (C_I/C_s)	Typical value for test and analysis	40 dB
Interference	Typical parameters for test and analysis	Wideband: bandwidth covering signal main lobe
		Narrowband: 5 % of the main lobe bandwidth
		Pulse: 2 ms period, 200 us duration
		Single frequency: center frequency of the signal
		Sweep frequency: 1 kHz step, 1 ms period

Annotation "v" and "u" are originated from $BOC(u, v)$ signal parameters

The PCMs given by four user representatives has been assembled into

$$\beta = \begin{pmatrix} 0.5 & 0.45 & 0.6 & 0.25 & 0.35 & 0.65 \\ 0.55 & 0.5 & 0.65 & 0.3 & 0.4 & 0.7 \\ 0.4 & 0.35 & 0.5 & 0.15 & 0.25 & 0.55 \\ 0.75 & 0.7 & 0.85 & 0.5 & 0.6 & 0.9 \\ 0.65 & 0.6 & 0.75 & 0.4 & 0.5 & 0.8 \\ 0.35 & 0.3 & 0.45 & 0.1 & 0.2 & 0.5 \end{pmatrix} \tag{23}$$

Thus the weight vector of the 6 AUs is:

$$\omega = (\,0.1556 \quad 0.1722 \quad 0.1222 \quad 0.2389 \quad 0.2056 \quad 0.1056\,) \tag{24}$$

The 12 anti-interference attributes of the first AUs in Table 3 need to be decorrelated and reconstructed. According to Eqs. (2)–(6), the correlation matrix of the 12 raw attributes is

Table 3 Theoretical value of each attribute

Modulation / Attribute	BPSK (1)	BPSK (2)	BOC (1,1)	TMBOC (4,1,4/33)	TMBOC (5,1,4/33)	TMBOC (6,1,4/33)
Δ wideband (m)	12.78	4.00	3.17	0.86	0.66	0.54
Δ narrowband (m)	0.38	0.97	0.22	0.21	0.18	0.18
Δ single frequency (m)	1.37	0.59	5.99	1.56	1.24	1.05
Δ multi-access (m)	12.78	4.008	4.22	1.16	0.96	0.78
Δ pulse (m)	1.73	0.62	0.49	0.23	0.20	0.18
Δ multi-frequency (m)	2.53	4.11	1.03	1.00	0.78	0.39
Ω wideband	1.50	1.50	4.02	6.80	7.86	8.93
Ω narrowband	10.04	10.04	24.75	11.15	9.40	8.17
Ω single frequency	1	1	2.47	2.71	2.71	2.71
Ω multi-access	1.50	1.50	3.03	3.59	3.58	4.50
Ω pulse	1	1	2.24	2.47	2.47	2.47
Ω sweep frequency	43.31	43.32	45.70	42.18	41.74	41.49
Area within multipath error envelope (chip • m)	5.72	5.72	3.66	2.38	2.39	1.82
RF compatibility (dB)	0.14	0.10	0.09	0.07	0.07	0.06
Code tracking jitter (m)	0.92	0.46	0.38	0.16	0.14	0.14
Carrier tracking jitter (°)	1.98	1.98	1.98	1.62	1.62	1.62
Code tracking threshold (dB-Hz)	31.6	31.9	25.1	19.6	19.2	19.2
Carrier tracking threshold (dB-Hz)	26.47	26.47	26.47	24.73	24.73	24.73
Interoperability	0.32	0.33	0.57	0.57	0.57	0.57

Annotation "Δ" represents "code tracking jitter under the interference of"; "Ω" represents "anti-interference quality factor under the interference of"

$$
{}_{11}R = \begin{pmatrix}
1 & 0.280 & 0.036 & 0.997 & 1.000 & 0.528 & 0.804 & -0.053 & 0.788 & 0.798 & 0.789 & -0.361 \\
0.280 & 1 & -0.347 & 0.246 & 0.280 & 0.956 & 0.796 & 0.108 & 0.802 & 0.796 & 0.802 & -0.204 \\
-0.036 & -0.347 & 1 & 0.043 & -0.054 & -0.308 & -0.214 & -0.931 & -0.342 & -0.248 & -0.335 & -0.815 \\
0.997 & 0.246 & 0.043 & 1 & 0.995 & 0.498 & 0.783 & -0.124 & 0.757 & 0.774 & 0.759 & -0.422 \\
1.000 & 0.280 & -0.054 & 0.995 & 1 & 0.530 & 0.803 & -0.038 & 0.790 & 0.799 & 0.791 & -0.344 \\
0.528 & 0.956 & -0.308 & 0.498 & 0.530 & 1 & 0.926 & 0.042 & 0.924 & 0.932 & 0.924 & -0.293 \\
0.804 & 0.796 & -0.214 & 0.783 & 0.803 & 0.926 & 1 & 0.006 & 0.991 & 0.997 & 0.992 & -0.378 \\
-0.053 & 0.108 & -0.931 & -0.124 & -0.038 & 0.042 & 0.006 & 1 & 0.143 & 0.026 & 0.136 & 0.898 \\
0.788 & 0.802 & -0.342 & 0.757 & 0.790 & 0.924 & 0.991 & 0.143 & 1 & 0.991 & 1.000 & -0.249 \\
0.798 & 0.796 & -0.248 & 0.774 & 0.799 & 0.932 & 0.997 & 0.026 & 0.991 & 1 & 0.991 & -0.346 \\
0.789 & 0.802 & -0.335 & 0.759 & 0.791 & 0.924 & 0.992 & 0.136 & 1.000 & 0.991 & 1 & -0.256 \\
-0.361 & -0.204 & -0.815 & -0.422 & -0.344 & -0.293 & -0.378 & 0.898 & -0.249 & -0.346 & -0.256 & 1
\end{pmatrix} \tag{25}
$$

It can be seen that about 50 % of the elements in Eq. (25) are larger than 0.7. In the process of fuzzy clustering the minimal ${}_{11}S = 0.178$ (with ${}_{11}\delta$=1.49 and ${}_{11}L = 8.361$) can be achieved when using ${}_{11}\lambda$=0.7. Consequently, two clusters for the anti-interference AU are generated from the raw 12 attributes. With one attribute

reconstructed for one cluster by employing PCA, the correlation matrix of the new attribute value matrix $({}_{11}x^{\text{new}})_{6\times 2}$ becomes

$$ {}_{11}R^{\text{new}} = \begin{pmatrix} 1.0 & -0.25 \\ -0.25 & 1.0 \end{pmatrix} \tag{26} $$

It can be seen that the fuzzy clustering and PCA can effectively mitigate the correlation among the attributes and reduce the number of attributes as well.

The RMDs of the six AUs are calculated using weighted TOPSIS as introduced in Sect. 2.2, and then incorporated into the multi-level multi-attribute GDM model in Sect. 3. The overall performance RMD vector of the six alternatives is

$$ U = (\,0.21 \quad 0.3094 \quad 0.3064 \quad 0.8281 \quad 0.8258 \quad 0.8521\,) \tag{27} $$

Equation (27) ranks the six signal modulation options as follows: {TMBOC (6,1,4/33), TMBOC(4,1,4/33), TMBOC(5,1,4/33), BPSK(2), BOC(1,1), BPSK(1)}. The selected TMBOC(6,1,4/33) modulation coincides with the GPS LICP signal specification in the IS-GPS-800 document.

It is important to note that the short-list of signal attributes and the values of the attributes affect the evaluation results directly. Not all the signal attributes have been considered, and only the attribute values theoretically calculated with the ideal channel assumptions are inputted to the evaluation process of the case study. In practical applications, the signal performances will be degraded by channel imperfections to different extents for different signal structures. Nevertheless, the proposed evaluation approach is still applicable to the comprehensive performance evaluation of signal structures if complete attributes and practical values of attributes are incorporated. In addition to theoretical data, the testing or measured data of signal performances can also serve as the raw attribute values.

4 Conclusion

This paper has proposed a multi-attribute GDM approach for the comprehensive evaluation of the overall performances of satellite navigation signal options. The approach is an organic combination of AHP, fuzzy clustering, PCA, weighted TOPSIS, and GDM. On account of the complexity of raw signal attributes, a hierarchical attribute system has been established for using AHP to characterize the situation and efficiently incorporate objective and subjective factors into the decision. Correlations among the attributes are captured and reduced by fuzzy clustering and PCA. The subjective weighting necessary for the group decision-making is conducted by pairwise comparison of the relative importance of a few attribute units. The evaluation process of six GPS L1C signal modulation options has been shown as a case study. The proposed approach can mitigate the workload, difficulty,

subjectivity, and arbitrariness, and provide an effective means for comprehensive performance evaluation of satellite navigation signal options.

Some limitations in this paper and future work should be pointed out here: (1) Including more signal attributes will improve the reliability of the evaluation results, such as the receiver/payload complexity and power consumption, whereas the calculation and estimation of the attribute values are still under investigation. (2) The change of attribute values with different preconditions should also be included in the evaluation process, especially the degradations of signal performances under various imperfections of satellite payload, propagation, and receiver channels. (3) Reasonable integration of theoretical analysis, real measurements, and special test data is also worth exploring.

References

1. Xu B, Bao T (2011) Quantitative and comprehensive evaluation of qualitative index in dam safety monitoring. Adv Sci Technol Water Resour 31(5):59–63
2. Wang B (2008) Study on multi-layers and multi-objects system model for channel plan Fuzzy optimization. Dalian Maritime University
3. He J, Li Z, Wan F (2000) Method of analyzing qualitative index of comprehensive assessment for dam structure monitoring behaviour. Hydroelectric Energy
4. Liu D, Wu Z, Jia C (2005) Multi-layers and multi-objects fuzzy optimization model of main target ship. J Traffic Transp Eng
5. Meng Q, Zhao X, Zhou M (2007) Multi-attribute Fuzzy decision making for shipborne gunfire target optimum seeking. Fire Control Command Control
6. Wang HW, Shu-Lin LI, Chen N (2010) A method of solving the correlation of evaluation indices of aircraft survivability. J Air Force Eng Univ
7. Tan Y, Song W, Li T (2014) Application and research on consistency combination weights for mining method optimization by multi-objective decision. Chin J Eng 08:1115–1122
8. Ma X (2013) The research of comprehensive evaluation method for navigation signal waveforms performance. Huazhong University of Science and Technology
9. Hu X, Tang Z, Zhou H, Huang X (2009) Analysis on design principles of GPS and Galileo signal structure. Syst Eng Electron 10:2285–2293
10. Szmidt E, Kacprzyk J (2000) Distances between intuitionistic fuzzy sets. Fuzzy Sets Syst 114 (3):505–518
11. Yu J (2005) Multivariate statistical analysis and application. Sun yat-sen university press
12. Wang X (2003) A study on theories and methodologies for Fuzzy multi-objective decision making with their applications. Dalian University of Technology
13. Rao RV (2013) Decision making in the manufacturing environment using graph theory and Fuzzy multiple attribute decision making methods. Springer Series in Advanced Manufacturing. Springer, London. doi:10.1007/978-1-4471-4375-8_2
14. Liu W (2011) Study on the compatibility and interoperability of global navigation satellite system. Shanghai Jiaotong University
15. Kaplan ED, Hegarty C (2006) Understanding GPS: principles and applications. Artech House

Peak Position Detection-Based Acquisition Algorithm of Multiple Access Interference Resistance

Weina Hao and Jingyao Chen

Abstract This essay targets multiple access interference environment which is unclear to the PN sequence and investigates the reinforcing acquisition method of direct spread spectrum signal. This essay also puts forward peak position detection-based acquisition method of multi-access interference removal resistance, achieves the position information of cross-correlation interference with multi-peak characteristics through multiple detection decision, so as to remove the multi-access interference. Meanwhile, the frequency feature of the pseudo code correlation results is applied to reduce the false alarm probability through multifrequency joint detection. Both theoretical analysis and simulation results have verified the effectiveness of this method.

Keywords Direct spread signal acquisition · Multiple access interference · Peak position detection · Multiple frequency joint detection

In the space tracking and control system, the distance between responders and the ground station results in power differences of different signals, and strong signal influences the normal reception of weak signal through multi-access interference. Thus, improving multi-access interference resistance capability of signal acquisition has become an important research direction of space tracking and control technologies.

Conventional multi-access resistance algorithm removes interference through signal estimation, which needs the PN sequence information of multi-access interference. However, under some circumstances, the PN sequence of multi-access interference is unclear, so the improved acquisition strategy is needed. First of all, most research on acquisition algorithm of multi-access resistance makes

W. Hao (✉)
Academy of Opto-Electronics, Chinese Academy of Sciences,
No. 9 Deng Zhuang South Road, HaiDian District, Beijing 100094, China
e-mail: weinahao@163.Com; kramnana@sina.com

J. Chen
School of Information and Electronics, Beijing Institute of Technology,
Beijing, China

J. Sun et al. (eds.), *China Satellite Navigation Conference (CSNC) 2016 Proceedings: Volume II*, Lecture Notes in Electrical Engineering 389,
DOI 10.1007/978-981-10-0937-2_3

improvement in terms of techniques of detection decision of the correlation value. Main methods of correlation value detection include maximum detection [1], serial detection [2] and hybrid detection [3], and hybrid detection is more applicable to the FFT-based pseudo code parallel acquisition algorithm [4]. The main–sub ratio detection regards the ratio of maximum to submaximum value of the following group of frequency point results as detection decision, then compares the detection decision with detection threshold. The main–sub ratio detection has easy algorithm and CFAR characteristics, and has been widely applied in practical engineering [5]. The multi-peak detection method in reference [6] can be applied when the PN sequence of multi-access inteference is unclear. The autocorrelation peak of spread spectrum signal has only one autocorrelation main peak in a period of spreading code, while it has many cross-correlation peaks. Based on the cross-correlation feature of pseudo code, whether the current peak is a cross-correlation peak can be judged. If receivers make judgement that the current acquisition peak is a cross-correlation peak, this acquisition will be rejected. Reference [7] mentions to use the main–sub ratio as the acquisition algorithm of decision, which decreases the false alarm probability in the situation of interference resistance, yet it does not analyze the detection probability when strong multi-access signal exists.

When the PN sequence of multi-access interference is unknown, simple rejection of the cross-correlation peak mentioned in the above method reduces the false alarm probability of multi-access interference, but it does not significantly improve the detection probability. Therefore, it is necessary to investigate the acquisition algorithm when the pseudo code of multi-access interference is unclear.

1 Analysis of Algorithm Principles

The conventional multi-peak detection method makes use of different distribution features of autocorrelation peaks and cross-correlation peaks of the spreading code, detects whether cross-correlation interference exists in the process of signal acquisition, but it does not remove the cross-correlation interference. Thus, the acquisition performance is not desirable. Targeting this issue, the peak position information of cross-correlation interference can be applied to conduct interference zero setting, so as to remove multi-access interference. In addition, the peak position information can be acquired through multiple decisions by applying the multi-peak feature of cross-correlation function.

1.1 Detection Method of the Peak Position

The peak position detection-based acquisition method of multi-access interference removal needs to estimate the peak position information of cross-correlation interference when the PN sequence of multi-access interference is unclear, so as to conduct zero setting of the corresponding position of cross-correlation peaks in correlation

acquisition results. After the interference removal is completed, detection decision of peak-to-average ratio of correlation acquisition results can be performed.

This essay analyzes the algorithm performance by using the pseudo code with 0.1 ms period and 10.23 Mcps bit rate. The initial phase and generating polynomial of target pseudo code can refer to the PRN1 sequence of GPS satellites, and the initial phase and generating polynomial of interfering pseudo code can refer to the PRN2 sequence of GPS satellites.

The cross-correlation function of the PN sequence has the multi-peak feature and cross-correlation function of target pseudo code and interfering pseudo code has three possibilities, i.e., 63/1023, 1/1023, and −65/1023. The influence of cross-correlation function 1/1023 on correlation acquisition results can be omitted, so the cross-correlation function that needs to be removed is the cross-correlation peak value 63/1023 and −65/1023. Thus, the position estimation of cross-correlation peak value can be achieved by applying the correlation value as detection decision. In the FFT-based pseudo code parallel acquisition method, the Doppler frequency search applies the serial search method. Under a certain search frequency point, if the phase deviation of the corresponding pseudo code of interfering signal and target signal maintains unchanged, the peak position of cross-correlation interference in the acquisition results will be relatively fixed. Thus, in order to increase the reliability of position detection of cross-correlation peak value, it is necessary to conduct multiple detection decision. Main methods of detection decision include M/N decision, 1 + M/N decision, Tong detection, etc. This essay does not focus on multiple methods of detection decision, so the relatively simple M/N decision method is selected to conduct analysis here.

However, the correlation peak position achieved through peak position detection includes both cross-correlation peak and autocorrelation peak. If all correlation peak positions in the acquisition results are set zero, the autocorrelation peak will be lost and signal acquisition cannot be completed. Thus, when carrying out zero setting on the corresponding positions of correlation peaks in the acquisition result, the maximum of correlation peak should be kept as the acquired autocorrelation peak. Notably, maximum of the default cross-correlation peak before the multi-access interference removal represents the autocorrelation peak of target signal. Therefore, this algorithm can only achieve correct acquisition when the autocorrelation peak value is higher than cross-correlation peak value.

Based on the analysis above, the fundamentals of the acquisition method of peak position detection-based multi-access interference removal are as follows: the acquisition results of all phases in each search frequency point goes through peak position detection by using the multiple detection decision method in order, and recording all correlation peak positions. Then, among acquired correlation results under all frequency points, keeping the maximum value of the correlation peak and conducting zero setting of other correlation peaks, so as to remove the influence of cross-correlation peaks on acquisition performance. Next, performing peak–average ratio detection decision on correlation acquisition results after the zero setting of cross-correlation peaks and completing the detection period of the peak position detection-based acquisition method of multi-access interference removal.

1.2 Multiple Frequency Joint Detection Method

Based on the analysis above, the peak position detection-based multi-access interference removal algorithm can improve detection probability under fixed decision threshold. However, if only completing the detection period of the above acquisition method, the maximum of maintained correlation peaks cannot be ensured as auto-correlation peaks of target signal instead of cross-correlation peaks introduced by multi-access interference. Next, the influence of this algorithm on false alarm probability and its potential false acquisition as well as solutions will be discussed.

To inspect the influence of multi-access interference on corresponding false alarm probability and detection probability of each detection decision, the following four hypotheses should be considered:

1. H00 hypothesis: Target signal does not exist and receipt signal only contains Gaussian While Noise;
2. H01 hypothesis: Target signal does not exist and receipt signal only contains interfering signal and Gaussian While Noise;
3. H10 hypothesis: Target signal exists and receipt signal only contains target signal and Gaussian While Noise;
4. H11 hypothesis: Target signal exists and receipt signal contains target signal, interfering signal, and Gaussian While Noise;

Under the H00 hypothesis, receipt signal only contains Gaussian While Noise and peak position detection through multiple detection decision does not influence the peak value, so interference removal is not necessarily conducted and detection algorithm of correlation acquisition results will not be affected. Thus, the false alarm probability acquired by signal under the H00 hypothesis is not affected by peak position detection-based multi-access interference removal algorithm. While under the H01 hypothesis, in addition to Gaussian White Noise, receipt signal also contains interfering signal, so cross-correlation peak positions can be detected and removed through interference. As a consequence, the false alarm probability acquired under the H01 hypothesis will increase because of the application of peak position detection-based multi-access interference removal algorithm. Likewise, under the H11 hypothesis, applying the peak position detection-based multi-access interference removal might lead to false acquisition.

Under the circumstances of multi-access interference, the intermediate frequency combined signal model after receivers complete D/A switch can be represented as follows:

$$\begin{aligned} s(t) &= s_i(t) + s_j(t) + \eta(t) \\ &= A_i \cdot \mathrm{PN}_i(t-\tau_i) \cdot \cos\left[2\pi\left(f_I + f_{d,i}\right)t + \varphi_i\right] \\ &\quad + \sum_{\substack{j=1 \\ j\neq i}}^{M-1} A_j \cdot \mathrm{PN}_j\left(t-\tau_j\right) \cdot \cos\left[2\pi\left(f_I + f_{d,j}\right)t + \varphi_j\right] + \eta(t) \end{aligned} \tag{1}$$

In this formula, $s_i(t)$ is target signal; A_i represents the amplitude of target signal; $\mathrm{PN}_i(t)$ is the PN sequence of target signal; τ_j denotes the pseudo code of target signal; f_I is intermediate carrier frequency; $f_{\mathrm{d},i}$ represents Doppler frequency of target signal; φ_i is the carrier phase of target signal; $s_j(t)$ is target signal and A_j is the amplitude of interfering signal; $\mathrm{PN}_i(t)$ represents the PN sequence of interfering signal; τ_i is the pseudo code phase of interfering signal; $f_{\mathrm{d},j}$ is the Doppler frequency of interfering signal; φ_j represents the carrier phase of the interfering signal; M denotes the total number of channels of combined signals; $\eta(t)$ is Gaussian White Noise. It can be seen that the second item in formula 1 represents the multi-access interfering signal among receipt signals.

According to different frequency characteristics of autocorrelation function and cross-correlation function of pseudo code, the detection period of the above multi-access acquisition method of interference removal can be detected by means of multiple frequency joint detection method. The acquisition results under multi-access interference include autocorrelation result of target signal, the cross-correlation result of interfering signal as well as the noise item. The acquisition result $Z(\hat{\tau},\hat{f}_\mathrm{d})$ can be shown below:

$$\begin{aligned} Z\left(\hat{\tau},\hat{f}_\mathrm{d}\right) &= \frac{1}{2}A_i R_i(\Delta\tau_i)\mathrm{sinc}\left(\pi T_\mathrm{coh}\Delta f_{\mathrm{d,i}}\right)\mathrm{e}^{-j\varphi_i} \\ &\quad + \frac{1}{2T_c}A_j\mathrm{e}^{-j\varphi_j}\sum_{k=-\infty}^{+\infty}\mathrm{sinc}\left[\left(\Delta f_{\mathrm{d,j}}-\frac{k}{T_c}\right)T_\mathrm{coh}\right]\sum_{j\neq i}C_{i,j}\left(\frac{k}{T_c}\right)+n_z \end{aligned} \tag{2}$$

Next, the results of influence of Doppler frequency deviation on autocorrelation and cross-correlation are respectively analyzed from the perspective of single period coherent integration and multi-period coherent integration.

The autocorrelation part in the correlation acquisition result can be represented as follows:

$$Z_\mathrm{auto}\left(\hat{\tau},\hat{f}_\mathrm{d}\right) = \frac{1}{2}A_i R_i(\Delta\tau_i)\mathrm{sinc}\left(\pi T_\mathrm{coh}\Delta f_{\mathrm{d,i}}\right)\mathrm{e}^{-j\varphi_i} \tag{3}$$

When $\Delta\tau_i \approx 0$, $R_i(\Delta\tau_i) = 1$. The coherent integration is one pseudo code period; i.e., under the circumstance of 0.1 ms, the autocorrelation peak power when the Doppler frequency deviation is zero is regarded as the benchmark. The attenuation of autocorrelation peak power of target signals with different Doppler frequency deviations is shown in Fig. 1. It can be seen that attenuation of autocorrelation peak power conforms with characteristics of sinc function. When the Doppler frequency deviation is zero, the autocorrelation peak value is the biggest. When the Doppler frequency deviation is integral times of 10 kHz, i.e., at the zero point of sinc function, the autocorrelation peak power attenuation reaches the maximum value. As the Doppler frequency increases, the peak value of the side lobe of autocorrelation peak power function attenuates more.

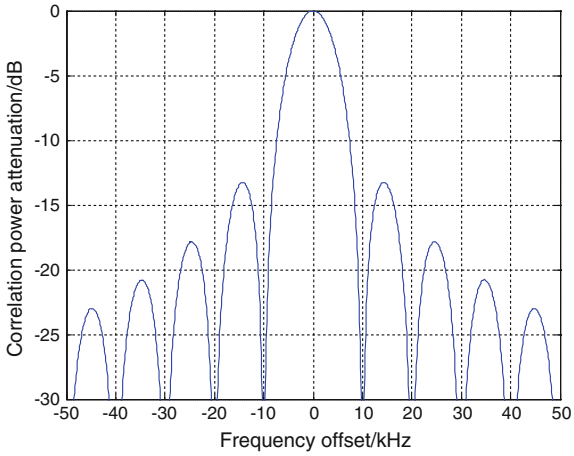

Fig. 1 Single period autocorrelation peak power attenuation of pseudo code with different Doppler frequency deviations

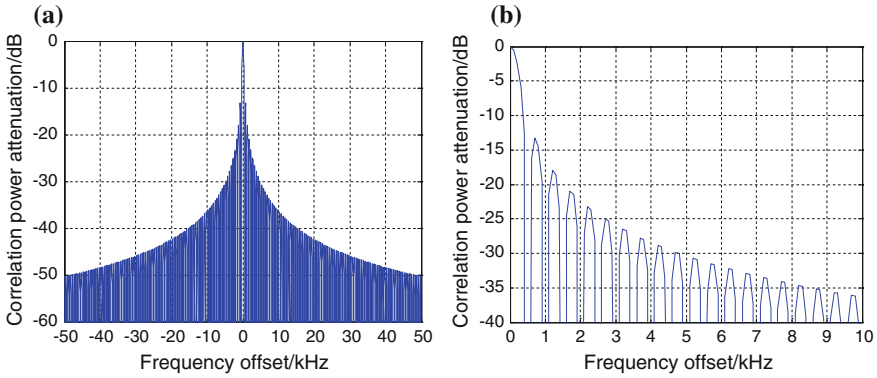

Fig. 2 Attenuation of multi-period autocorrelation peak power of pseudo codes under different Doppler frequency deviations

When the coherent integration is 20 pseudo code period (2 ms), the autocorrelation peak power when Doppler deviation is zero is regarded as the benchmark. Figure 2 shows the attenuation of autocorrelation peak power of target signal under different Doppler frequency deviations. Figure 2b is an enlarged scale of details in Fig. 2a when the Doppler frequency deviates from 0 to 10 kHz. It can be seen that under multi-period coherent integration, the attenuation of autocorrelation peak power complies with characteristics of sinc function. However, T_{coh} increases, so the position of the zero point of sinc function changes from the integral times of 10–500 Hz, but attenuation of the side lobe peak value of autocorrelation peak value still increases with the enlargement of Doppler frequency deviation.

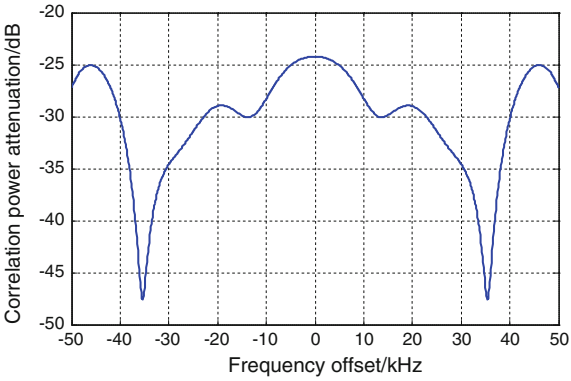

Fig. 3 Attenuation of single period cross-correlation peak value under different Doppler frequency deviations

The cross-correlation part in the acquisition result can be represented as follows [8]:

$$Z_{\text{cross}}\left(\hat{\tau},\hat{f}_{\text{d}}\right) = \frac{1}{2T_c}A_j e^{-j\varphi_j}\sum_{k=-\infty}^{+\infty}\text{sinc}\left[\left(\Delta f_{\text{d},j} - \frac{k}{T_c}\right)T_{\text{coh}}\right]\sum_{j\neq i}C_{i,j}\left(\frac{k}{T_c}\right) \quad (4)$$

When coherent integration is 1 pseudo code period (0.1 ms), for a certain fixed pseudo code phase difference, the autocorrelation peak power when Doppler frequency deviation is zero is regarded as the benchmark. Attenuation of cross-correlation peak value of target signal and interfering signal under different Doppler frequency deviations are shown in Fig. 3. It can be seen that the cross-correlation suppression capability of target signal on interfering signal is at worst around 24 dB. Theoretically, when Doppler frequency deviation is zero or integral times of the reciprocal of pseudo code period, cross-correlation interference has the strongest influence on correlation acquisition results. However, under single period coherent integration, attenuation of cross-correlation peak value of pseudo code under different Doppler frequency deviations does not significantly show the above characteristics.

When coherent integration is 20 pseudo code periods (2 ms), the autocorrelation peak power when Doppler deviation is zero is regarded as the benchmark. Figure 4 shows attenuation of cross-correlation peak power of target signal and interfering signal under different Doppler frequency deviations. Figure 4b is an enlarged scale of details in Fig. 4a when the Doppler frequency deviates from 0 to 10 kHz. It can be seen that under multi-period coherent integration, the zero point of sinc function is situated at the integral times of 500 Hz. Distinct from attenuation of autocorrelation peak power, attenuation of pseudo code cross-correlation peak value varies periodically with multiple frequency deviations. When Doppler frequency deviation is 0 or the integral times of 10 kHz, the peak power of pseudo code cross-correlation reaches the maximum value.

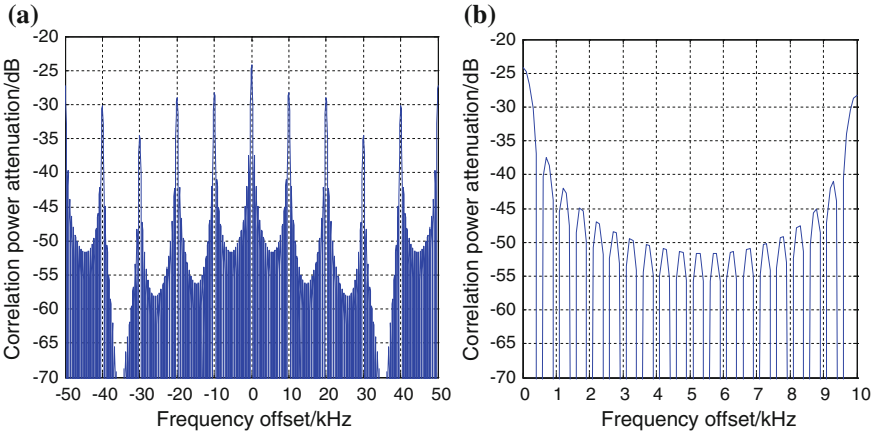

Fig. 4 Attenuation of multi-period cross-correlation peak power of pseudo code under different Doppler frequency deviations

Thus, when coherent integration has multiple pseudo code periods, if Doppler frequency deviation is the integral times of 10 kHz, attenuation of autocorrelation peak value is the most distinct, while attenuation of the peak value of cross-correlation is almost the same. Therefore, this feature can be used to distinguish autocorrelation peak and cross-correlation peak. In order to avoid the acquisition method of peak value position detection-based multi-access interference removal incorrectly treating the cross-correlation peaks of multi-access interfering signal as autocorrelation peaks of target signal, correlation results of all frequency points under corresponding pseudo code of correlation peaks can go through multifrequency joint detection. If the result complies with frequency characteristics of pseudo code autocorrelation function, this correlation peak is the autocorrelation peak and the corresponding Doppler frequency in the unit cell and the pseudo code phase represents the result of this acquisition. Otherwise, the correlation peak is the cross-correlation peak of interfering signal and the current acquisition result should be rejected.

Based on the analysis above, the design thought of multifrequency joint detection-based acquisition algorithm is as follows: first of all, under each frequency point, using the multi-peak feature of pseudo code cross-correlation function to detect the position information of cross-correlation interference and remove cross-correlation peak interference except the maximum value. Then, detecting the acquisition result and applying different frequency features of autocorrelation peaks and cross-correlation peaks to conduct multifrequency joint detection on the current acquisition result. If it is an autocorrelation peak, the acquisition result can be output; otherwise the acquisition of target signal is unsuccessful.

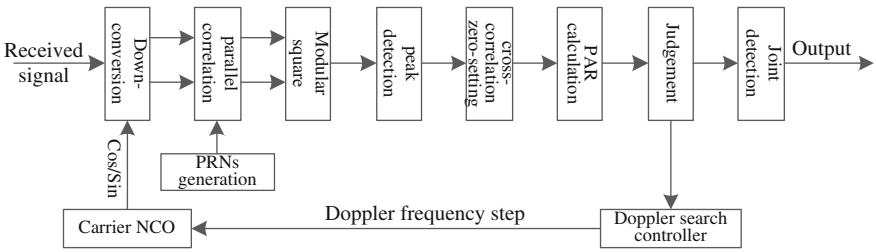

Fig. 5 Process of peak position detection-based acquisition method of multi-access interference removal

1.3 Summary of the Algorithm Process

The process of the peak position detection-based acquisition method of multi-access interference removal is shown in Fig. 5.

Detailed procedures of the process are shown below:

1. When acquisition starts up, the carrier NCO module receives the Doppler frequency word, the two-path orthogonal local carrier signal is generated and output to the down-conversion module.
2. The down-conversion module receives local carrier signal and input signal, and completes the Doppler frequency liftoff through orthogonal down-conversion algorithm, achieving path *I* (in-phase) baseband signal and path *Q* (orthogonal) baseband signal;
3. Pseudo code generator produces a pseudo code period of target signal with the length of one pseudo code period and output to parallel correlation modules;
4. In parallel correlation modules, the result of down-conversion and the local PN sequence produced by the local pseudo code generator go through parallel correlation, then output the correlation result;
5. Modular square module receives the parallel correlation result and conduct square algorithm after modular multiplication algorithm, then output the modular square result to the peak position detection module.
6. The peak position detection module conduct multiple correlation detection decision on all correlation results and output the acquisition result as well as the correlation peak result information to the cross-correlation peak zero-setting module;
7. Based on received information of correlation peak position, cross-correlation zero-setting module performs zero setting on module square value where correlation peaks appear except the maximum value in the result. Then, output the zero-setting module square result to the peak–average ratio so as to calculate modules;
8. Finding out the peak position from the correlation result output by correlation peak zero-setting module calculated through the peak–average ratio. Using data except the peak value to calculate the average noise value and output the

peak–average ratio (PAR) calculated by peak-to-noise average value to the decision module;

9. Detecting the peak–average ratio received by the decision module to calculate the peak–average ratio, and conducting detection decision with the threshold; if the peak–average ratio is smaller than the threshold, it means no signal has been acquired, and the Doppler search and control module will be notified; if the peak–average ratio is bigger than threshold, the peak–average ratio and the acquisition phase will be output to the Doppler search and control module;
10. In the Doppler search and control module, if the detection decision module does not exceed the threshold, the output Doppler frequency word will be updated, then enters procedure 1; if the detection decision module exceeds threshold, this peak–average ratio will be compared against the maximum peak–average ratio (the initial value is 0) stored previously. If it is larger than stored maximum peak–average ratio, maximum peak–average ratio, the acquisition phase and the current Doppler frequency word will be updated, then enters procedure 1;
    Under the control of the Doppler search and control module, repeating procedures 1 to 10 till completing searching all Doppler frequency words;
11. After the Doppler search and control module output all Doppler frequency words, if stored maximum peak–average ratio maintains 0, it means the initial acquisition is unsuccessful, then back to procedure 1; if stored maximum peak–average ratio is not 0, it means the initial acquisition is successful, stored acquisition phase and the acquisition results under corresponding multiple Doppler frequency points will be output to multifrequency joint detection modules;
12. Multifrequency joint detection modules conduct detection decision according to received pseudo code phase and its corresponding correlation results. If the correlation peak module value is significantly higher than other frequency points in a certain frequency point, this acquisition is successful, and this frequency point represents acquired Doppler frequency. The received pseudo code phase is acquired pseudo code phase and the acquisition result can be output; otherwise, the acquisition is unsuccessful, then back to procedure 1.

2 Verification of Algorithm Simulation

This section conducts simulation verification on the peak position detection-based acquisition method of multi-access interference removal through Monte Carlo simulation. This section also compares the conventional acquisition method with the peak position detection-based acquisition of multi-access interference removal (the acquisition method used in this essay), and the parametric setting is shown in Table 1.

Table 1 Simulation parametric setting

Parameter	Value	Unit
PN sequence of target signal	PRN1	–
PN sequence of interfering signal	PRN2	–
Speed of pseudo code	10.23	MHz
Frequency of intermediate frequency	15	MHz
Coherent integration time	0.5	Ms
Doppler search step	1	kHz

2.1 Simulation of Pre-detection Peak–Average Ratio

In order to conveniently observe the effect of the peak position detection-based acquisition of multi-access interference removal, simulation of acquisition correlation result of noise-free signal of interfering signal only in path 1 and pre-detection peak–average ratio is conducted.

1. No Doppler frequency deviation exists between multi-access interfering signal and target signal.

Figures 6 and 7 respectively represent the correlation results when no Doppler frequency deviation exists between multi-access interfering signal and target signal, and the two-dimensional correlation results acquired by noise-free signal before and after interference is removed. Applying the peak position detection-based acquisition of multi-access interference removal can remove certain cross-correlation interference and improve the pre-detection peak–average ratio. Under search frequency points with integral times of 10 kHz of the Doppler frequency difference of multi-access interfering signal, the influence of multi-access interfering signal on the acquisition result is the biggest and the correlation peak is kept after removing interference, among which the autocorrelation peak value of target frequency point is the largest.

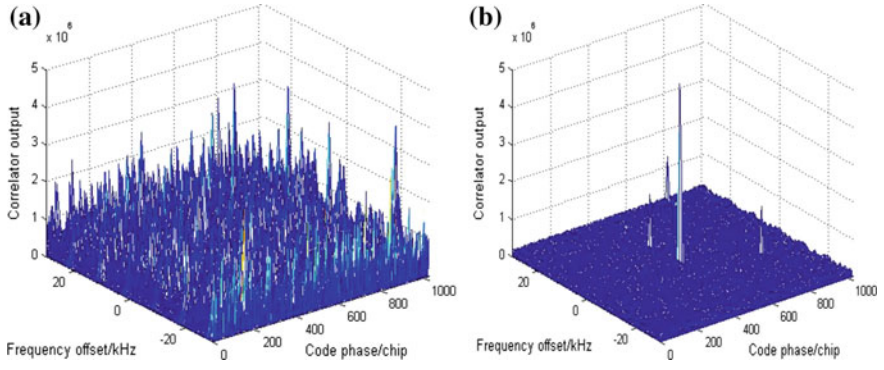

Fig. 6 Acquisition correlation results before and after noise-free signal interference removal (no frequency difference). **a** Before interference removal. **b** After interference removal

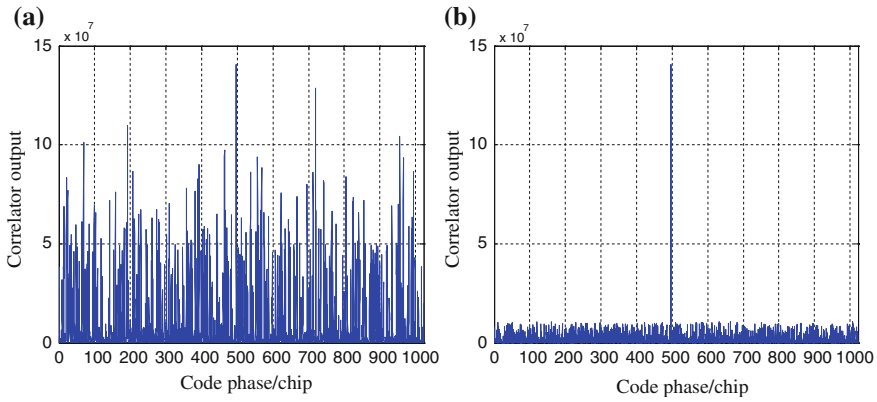

Fig. 7 Acquisition correlation result of signal frequency points before and after noise-free signal removal (no frequency difference). **a** Before interference removal. **b** After interference removal

2. Doppler frequency deviation exists between multi-access interfering signal and target signal.

Figures 8 and 9 respectively represent the acquisition two-dimensional search correlation results of noise-free signal before and after interference removal and correlation result of target frequency points when the Doppler frequency difference between multi-access interfering signal and target signal is 10 kHz. After applying the peak position detection-based acquisition of multi-access interference removal, certain cross-correlation interference can be removed under the circumstances of Doppler frequency difference. Pre-detection signal-to-noise ratio is improved, but certain cross-correlation peak is still maintained on nontarget frequency points.

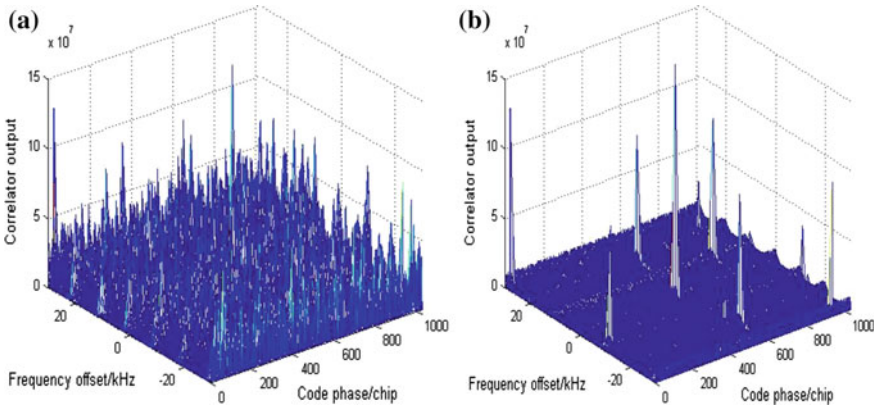

Fig. 8 Acquisition correlation results before and after removing the noise-free signal interference. **a** Before interference removal. **b** After interference removal

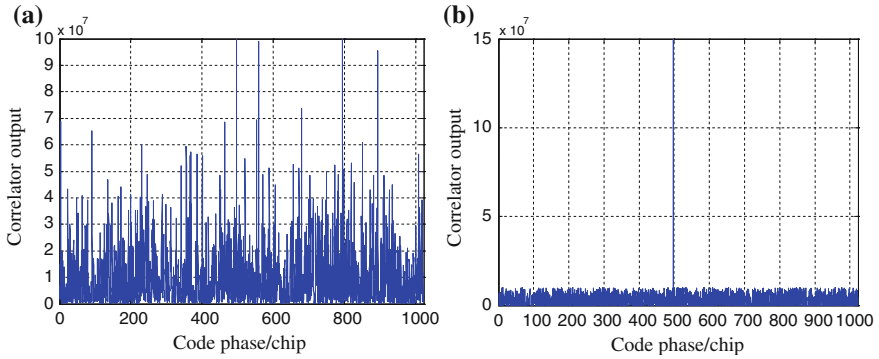

Fig. 9 Acquisition correlation results of target frequency points before and after removing the noise-free signal interference. **a** Before interference removal. **b** After interference removal

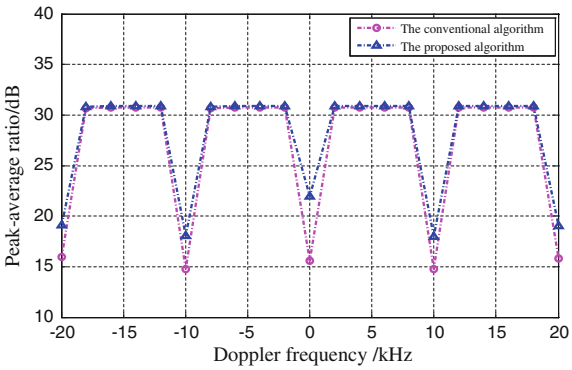

Fig. 10 Comparison of detection peak–average ratio before and after interference removal under different Doppler frequency deviations

When Doppler frequency deviation exists between multi-access interfering signal and target signal, the influence of cross-correlation interference on acquisition correlation results under different Doppler frequency deviations is distinct. Figure 10 shows the comparison between pre-detection peak–average ratio before and after interference removal under different Doppler frequency deviation. When the Doppler frequency deviation is 0 or the integral times of 10 kHz, cross-correlation interference has more significant influence on the acquisition result. The pre-detection peak–average ratio of conventional detection method is relatively low and the pre-detection peak–average ratio after interference removal is significantly increased, so the detection probability is improved. When applying the acquisition method investigated in this essay, the pre-detection peak–average ratio is the best when the Doppler frequency deviation is 0 and peak–average ratio increases about 7 dB. When the Doppler frequency deviation is the integral times of 10 kHz, the effect of interference removal is decreased. However, compared with the unprocessed situation, the peak–average ratio still increases above 3 dB. Under other Doppler frequency deviations, cross-correlation peaks are relatively small and the

pre-detection peak–average ratio is high, and interference removal is not necessary. Thus, the application of the algorithm of this essay does not influence the pre-detection peak–average ratio.

Based on the analysis above, applying the peak position detection-based acquisition method of multi-access interference removal can effectively remove interference and increase pre-detection peak–average ratio. However, when Doppler frequency difference exists between target signal and multi-access interfering signal and the difference is the integral times of 10 kHz, the effect of interference removal has certain decline.

2.2 *Simulation of False Alarm Probability*

In order to ensure the acquisition method in this essay conforms to the requirements of false alarm probability, the false alarm probability in receipt signal which only includes interfering signal is conducted simulation verification. Figure 11 shows the false alarm probability comparison of the peak position detection-based acquisition method of multi-access interference removal and the conventional acquisition method under different interfering signal SNR. With the application of the algorithm in this essay, when the multi-access interfering signal SNR is relatively low, the false alarm probability is a bit higher than that of conventional acquisition method. This is because the frequency feature of cross-correlation peaks is influenced by noise so that the effect of reducing false alarm is compromised. As the signal SNR of multi-access interference increases, the constant false alarm probability in the acquisition of this essay gradually declines and conforms to the requirements of constant false alarm detection. Thus, it is still necessary to compare the detection probability of conventional acquisition method and the method of this essay.

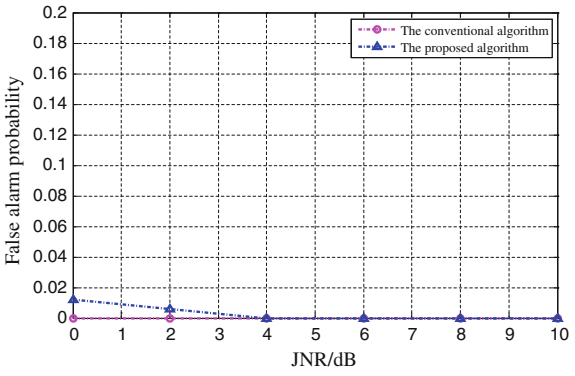

Fig. 11 False alarm probability under different interfering signal SNR

2.3 Simulation of Detection Probability

This section focuses on analyzing the acquisition performance of the peak position detection-based method of multi-access interference removal under the Gaussian channel. Two situations are considered: no Dopper frequency deviation exists between multi-access interfering signal and target signal; 10 kHz Doppler frequency deviation exists between multi-access interfering signal and target signal. The detection probability of the conventional acquisition method and the method in this essay is compared.

1. No Doppler frequency deviation exists between multi-access interfering signal and target signal.

Figure 12 compares the detection probability of the conventional acquisition method and the method of this essay under different target signal SNR when multi-access interfering signal SNR is 0 dB and no Doppler frequency deviation exists between multi-access interfering signal and target signal.

In the conventional method, when the target signal SNR is higher than −15 dB, the detection probability can achieve 90 % above; while the target signal SNR of this essay is higher than −17 dB, the detection probability can achieve 90 % above. Thus the acquisition sensitivity increases about 2 dB.

Figure 12 shows the detection probability comparison of the acquisition method of multi-access interference removal of the conventional method and the method of this essay under different SINR when the target signal SNR is −15 dB and no Doppler frequency deviation exists between the multi-access interfering signal and target signal (Fig. 13).

When the detection probability is above 90 %, the multi-access interference resistant capability of conventional acquisition method can achieve 15 dB, while that of this essay achieves around 17 dB. Thus the multi-access interference resistant capability improves about 2 dB.

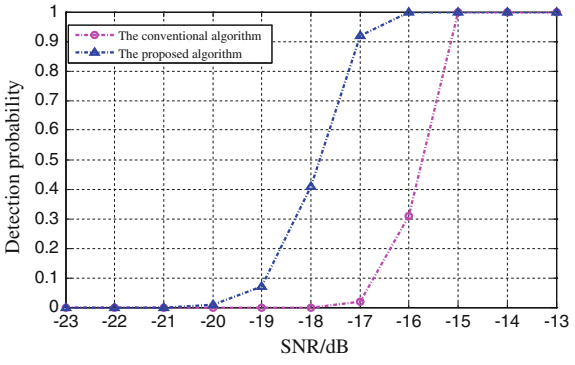

Fig. 12 Detection probability of algorithm under different target signal SNR (no frequency difference)

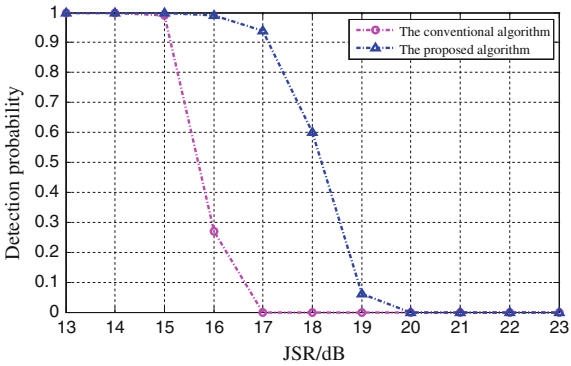

Fig. 13 Detection probability of algorithm under different SINR (no frequency difference)

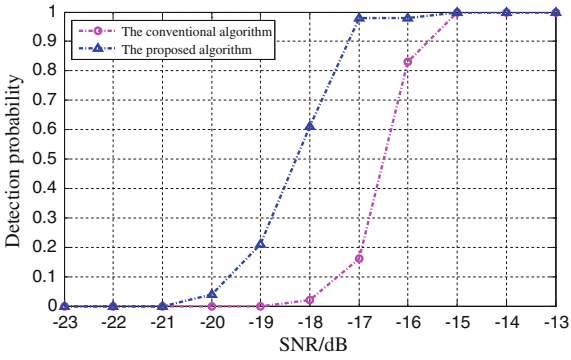

Fig. 14 Detection probability of algorithm under different target signal SNR (10 kHz frequency difference)

2. 10 kHz Doppler frequency deviation exists between multi-access interfering signal and target signal.

Figure 14 compares the detection probability of the conventional acquisition method and the method of this essay under different target signal SNR when multi-access interfering signal SNR is 0 dB and 10 kHz Doppler frequency deviation exists between multi-access interfering signal and target signal.

In the conventional method, when the target signal SNR is higher than −15.5 dB, the detection probability can achieve 90 % above; while the target signal SNR of this essay is higher than −17 dB, the detection probability can achieve 90 % above. Thus the acquisition sensitivity increases about 1.5 dB.

Figure 15 shows the detection probability comparison of the acquisition method of multi-access interference removal of the conventional method and the method of this essay under different SINR when the target signal SNR is −15 dB and 10 kHz Doppler frequency deviation exists between the multi-access interfering signal and target signal.

When the detection probability is above 90 %, the multi-access interference resistant capability of conventional acquisition method can achieve 16 dB, while

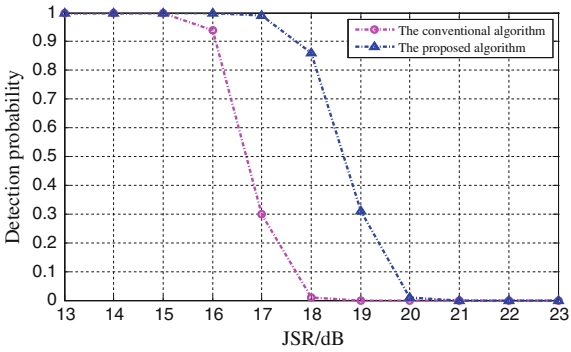

Fig. 15 Detection probability of algorithm under different SINR (10 kHz frequency difference)

that of this essay achieves around 17.5 dB. Thus the multi-access interference resistant capability improves about 1.5 dB.

Based on the analysis above, simultaneously applying the peak position detection-based acquisition method of multi-access interference removal can effectively achieve interference removal under the Gaussian channel, so as to improve the detection probability of signal acquisition. When the interfering signal SNR is fixed, applying this method can enhance the acquisition sensitivity; while when the target signal SNR is fixed, the application of this method can improve the multi-access interference resistance capability of acquisition. In addition, when 10 kHz Doppler frequency difference exists between multi-access interference signal and target signal, the multi-access interference resistance capability of this algorithm has certain decline compared with when no Doppler frequency difference exists.

3 Conclusion

This essay investigates the acquisition technique of multi-access interference removal when the PN sequence of interfering signal is unclear. Based on the design thought of applying cross-correlation interference position to remove interference and the multi-peak feature of pseudo code cross-correlation function, this essay put forward the acquisition method of multi-access interference removal based on peak position detection and illustrates the process of algorithm in detail. In terms of the increased acquisition false alarm probability and the potential false acquisition issue, this essay reduces the false alarm probability through multifrequency joint detection to complete the detection period of acquisition. This algorithm can improve multi-access interference resistance capability under different Doppler frequency deviations.

References

1. Corazza GE (1996) On the MAX/TC criterion for code acquisition and its application to DS-SSMA systems. IEEE Trans Commun 44(9):1173–1182
2. Polydoros A, Weber C (1984) A unified approach to serial search spread-spectrum code acquisition-part I: general theory. IEEE Trans Commun 32(5):542–549
3. Stirling-Gallacher RA, Hulbert AP, Povey GJ (1996) A fast acquisition technique for a direct sequence spread spectrum signal in the presence of a large Doppler shift. In: Proceedings of ISSSTA, vol 1, pp 156–160
4. Smidt J (2011) Statistical characterization of a constant false alarm detector for GNSS signals. In: International conference on localization and GNSS (ICL-GNSS), pp 98–103
5. Geiger BC, Soudan M, Vogel C (2010) On the detection probability of parallel code phase on the detection probability of parallel code phase. In: IEEE 21st international symposium on personal indoor and mobile radio communications, pp 865–870
6. Zheng B, Lachapelle G (2005) GPS software receiver enhancements for indoor use. In: Proceedings of ION GNSS, pp 1139–1140
7. Wang YQ, Wu SL (2011) New acquisition decision algorithm for multiple access interference suppression in DSSS system. J Syst Eng Electr 22(1):157–163
8. Qaisar SU, Dempster AG (2011) Cross-correlation performance assessment of global positioning system (GPS) L1 and L2 civil codes for signal acquisition. IET Radar Sonar Navig (2011)

Overall Performance Comparison of Three Dual-Frequency Constant Envelop Modulation Schemes for GNSS

Yang Gao, Chunxia Li, Li Fu and Henglin Chu

Abstract In Global Navigation Satellite Systems, dual-frequency constant envelop modulation scheme includes ACE-BOC, TD-AltBOC, and AltBOC. The three modulation schemes have pros and cons on single item evaluation index such as ranging precision, navigation message demodulation performance, et al., which cause difficulties for the comparison and final chosen. In this article, a method to evaluate the overall performance of navigation signals is proposed. This method takes the minimal signal power that satisfies some positioning precision as the evaluation index, which requires enough precise ranging as well as enough good navigation message demodulation at the same time, thus can reflect the overall performance of the signal in actual using. The overall performance of the three modulation schemes was compared by bed testing under conditions that the signal used the mainstream bit rate and channel encoding method. The bed testing results show that, for 3-D positioning precision better than 10 m, the ACE-BOC need the minimal signal power, 0.5–2.5 dB lower than that for TD-AltBOC and AltBOC, thus the ACE-BOC has the best overall performance of the three schemes.

Keywords Global navigation satellite systems · Dual-frequency constant envelop modulation scheme · Signal overall performance · Minimal signal power

1 Introduction

Dual-frequency constant envelop modulation is one important technique for GNSS signal design, which can modulate two navigation signals to the upper side band and the lower side band of a wide band signal to provide individual service as well as combined service, and usually used for Aeronautical Radio Navigation Service signal design. Currently, dual-frequency constant envelop modulation schemes include ACE-BOC [1–5], TD-AltBOC [6], and AltBOC [7] et al. Signal performance

Y. Gao (✉) · C. Li · L. Fu · H. Chu
Beijing Navigation Center, Beijing 100094, China
e-mail: bikong_001@aliyun.com; bikong_001@yahoo.com.cn

J. Sun et al. (eds.), *China Satellite Navigation Conference (CSNC) 2016 Proceedings: Volume II*, Lecture Notes in Electrical Engineering 389,
DOI 10.1007/978-981-10-0937-2_4

is one important reference for the final chosen of the three schemes, thus, signal designers and other researchers have made a lot of comparison [8]. However, this comparison mostly focused on single item evaluation index like ranging precision, demodulation performance, multipath performance, and compatibility. While under the premise of limited power and bandwidth, those items may compete with each other, for instance, the more signal power assigned to the pilot branch, the better ranging but the worse demodulation performance, and the more signal power assigned to the data branch, the better demodulation but the worse ranging performance, which may confuse the comparison and make the choice more difficult. Thus, a method to compare the overall performance instead of single item performance is needed. This paper suggests a method to compare the overall performance for the three modulation schemes. By considering the main differences among the three schemes, this method takes the minimal signal power that meets some positioning accuracy as the evaluation index, which requires signal ranging and demodulation performance good enough at the same time, thus can reflect the signal overall performance in actual using. By using this evaluating method, the three schemes performance was compared by bed testing. The bed testing took the mainstream bit rate and channel encoding method as the signal design conditions, and used navigation signal simulator and five kinds of receivers to got the minimal signal power (which is "acquiring threshold" and "tracking threshold" here) for each schemes. The result shows that, ACE-BOC scheme has the best overall performance, AltBOC, and TD-AltBOC have the similar overall performance.

2 Schemes and Differences

2.1 Modulation Schemes

To meet the dual-frequency Aeronautical Radio Navigation Service, GNSS needs to provide two signals in a wide band. Navigation satellites usually emit the two signals coherently, specifically, the satellite emits a wideband constant envelope signal, whose lower side band and upper side band provide the two signal service, and the two can also be received as one signal to get more precise service. Aeronautical Radio Navigation Service band is 1151–1215 MHz [8], which is named E5 in Galileo, L5 in GPS and B2 in BDS. Here, we take the name in BDS as reference, thus the lower side band signal is denoted as B2a, and the upper side band signal is denoted as B2b.

ACE-BOC, TD-AltBOC and AltBOC can all meet the previous mentioned Aeronautical Radio Navigation Service signal requirement. They all use 15.345 MHz carrier to modulate the B2a and B2b to the lower side band and the upper side band, the B2a and B2b signals both consists of data branch and pilot branch, and all branches use 10.23 Mbps pseudo noise (PN) code. The main

differences of the three schemes are in the multiplexing method and power assignment method of data and pilot branches.

TD-AltBOC uses time division multiplexing method, emits the pilot PN code chip and data PN code chip in even and odd time slots, respectively, thus the power ratio of pilot and data branches is 1:1 [6].

AltBOC uses phase division multiplexing method, modulates the data PN code and the pilot PN code on I and Q, respectively, and limited by the constant envelope constraint, the power ratio of pilot and data branches is 1:1 [7].

ACE-BOC also uses phase division multiplexing method, but different from AltBOC, it can assign the pilot and data power ratio arbitrary even under the constant envelop constraint. The concrete ACE-BOC scheme power ratio of pilot and data branches is 3:1 [1–5].

2.2 Performance Differences

There are many items for navigation signal evaluation, such as ranging precision, multipath performance, compatibility, demodulation performance etc. While for the three schemes focused in the paper, the compatibility and multipath performance may the same as they have the similar PN code rate, bandwidth and spectrum. The main difference is the power assignment way, comparing with AltBOC and TD-AltBOC, ACE-BOC assigns more power to pilot branches (the same with the newest GPS L1C signal [9, 10]), so ACE-BOC provides better potentials on tracking and ranging (1.76 dB better in theory), but worse ability on demodulation (3.0 dB worse in theory).

3 Overall Performance Evaluation Method

3.1 Evaluation Index Design

As introduced previously, the performance differences of ACE-BOC, TD-AltBOC and AltBOC are mainly caused by the power assignment ways. ACE-BOC provides way to assign the power ratio arbitrary, which brings more choices for signal design. While limited by the total signal power, different power assignment is essentially the competition of ranging performance and demodulation performance, so individually comparing the two performances is not important anymore, instead, in one assignment way, the signal overall performance in practical use is more significant.

For navigation signal, the overall performance consists of two parts: to provide enough accuracy ranging (or keeping receiver tracking), to provide right data demodulation and these two must be satisfied at the same time. For the whole navigation satellite system, to meet the overall performance, the lower power one

signal schemes needs, the easier the scheme is for the satellite implement; For the navigation users, to meet the overall performance, the lower power one signal scheme needs, the easier the scheme is for the receiver use. Apparently, for both the system and the users, the minimal signal power to meet the signal use is a key factor, so it can be taken as the evaluation index to compare the three schemes.

3.2 Evaluation Index Definition

Based on the previous analysis and the way that navigation receiver uses signals, two kinds of evaluation indexes are defined here, i.e., **acquisitioning threshold** and **tracking threshold**. The acquisitioning threshold is defined as the minimal signal power one signal scheme needed to make the receiver output specified accuracy positioning results in specified time in cold start condition. The tracking threshold is defined as the minimal signal power one signal scheme needed to keep the receiver output specified accuracy positioning results in specified time.

Here, the acquisitioning threshold reflects the difficulties receivers have to turn to synchronized state from unsynchronized state when using one signal scheme. The tracking threshold reflects the difficulties receivers have to keep the synchronized state when using one signal scheme.

3.3 Evaluation Index Analyzing Method

Signal performance can be analyzed in many ways such as theory, simulation and actual testing. Theory analysis and simulation method are applicable to the analysis of the single performance like ranging accuracy and demodulation performance, and are often under the assumption of single signal processing steady stage. While, for comparing the overall performance, the proposed evaluation index involves several signal processing stages, and including many transient stages, thus, the theory and simulation is not suitable anymore. The proposed evaluation index will be analyzed by testing ways.

4 Overall Performance Test and Comparison

4.1 Test Conditions

Some conditions must be determined before the acquisition threshold and tracking threshold test, because the thresholds relates to several factors besides the power assignment, those factors includes data bit rate, channel encoding method, receiver RF device and receiver algorithms.

(1) Data bit rate.
Data bit rate influences the demodulation performance. Currently, data bit rate used by satellite navigation system can be from 25 to 500 bps, and two mainstream bit rates are used here, which is 100 bps for B2a and 50 bps for B2b.
(2) Channel encoding method
Channel encoding promotes demodulation performance. Currently, channel encoding methods like Turbo and LDPC have already been used in navigation system. Here, take the GPS L1C as reference, the LDPC with encoding efficiency 2 is used for both B2a and B2b.
(3) Receivers
It is difficult to predict the future receiver level as the hardware and software of navigation receiver both develops fast. Here, we take five different receivers to compare the relative performance of the 3 modulation schemes, which can reflect the relative overall performance in current receiver level. Specifically, the receivers include two kinds of high precision receivers, two kinds of monitoring receivers, and one multifrequency compatible receiver.

4.2 Test Method

The bed test uses a navigation signal simulator to generate RF signals that can provide positioning results, by decreasing the signal power step by step, to get the acquisitioning thresholds and tracking thresholds of each modulation scheme in every receiver. The specific criteria are:

(1) Acquisitioning threshold criteria: the minimal signal power that make the receiver output 10 position results whose 3-D error all less than 10 m in 5 min under cold start conditions.
(2) Tracking threshold criteria: decreasing the signal power when the receiver has already steady output the right positioning results, the minimal signal power that make the ratio of the receiver 3-D position result better than 10 m higher than 95 % in 5 min.

The power decreasing step is 0.5 dB, and the PDOP in the simulation scenario is better than 2.

4.3 Test Results and Analysis

As the receiving sensitivity is one key performance index of the receiver, to avoid revealing sensitive information, the results shown later are corrected as follows:

The acquisitioning threshold and tracking threshold of TD-AltBOC in every receiver are all corrected to −133 dBm by adding some offsets, and the thresholds

of ACE-BOC and AltBOC in some receiver are corrected by adding the corresponding offset. After the corrections, the shown thresholds are not the absolute thresholds of the corresponding receivers, but the relative thresholds for different signal schemes are not changed, which do not affect the signal schemes comparison.

4.3.1 Acquisitioning Threshold Result

The acquisitioning thresholds of B2a and B2b signals are shown in Figs. 1 and 2, respectively.

For B2a signal, as Fig. 1 shows, the two high precision receivers and the two monitoring receivers show that ACE-BOC has the lowest acquisition threshold, 0.5–2.5 dB better than AltBOC and 0.5–2.0 dB better than TD-AltBOC. AltBOC and TD-AltBOC have pros and cons in different receivers; the difference is between 0.5 and 1.0 dB. The multifrequency receiver results are quite different, where the ACE-BOC has the highest acquisition threshold. This is due to that multifrequency receiver use the data branch as acquisition branch, which is designed for AltBOC but used directly for ACE-BOC.

For B2b sigal, as Fig. 2 shows, the results show the similar characteristic with that of B2a. The two high precision receivers and the two monitoring receivers show that ACE-BOC has the lowest acquisition threshold, 0.5–2.0 dB better than AltBOC and 0.5–2.5 dB better than TD-AltBOC. AltBOC and TD-AltBOC have pros and cons in different receivers; the difference is less than 0.5 dB. The multifrequency receiver B2b acquisition strategy also uses the data branch, thus the results is opposite to that of others.

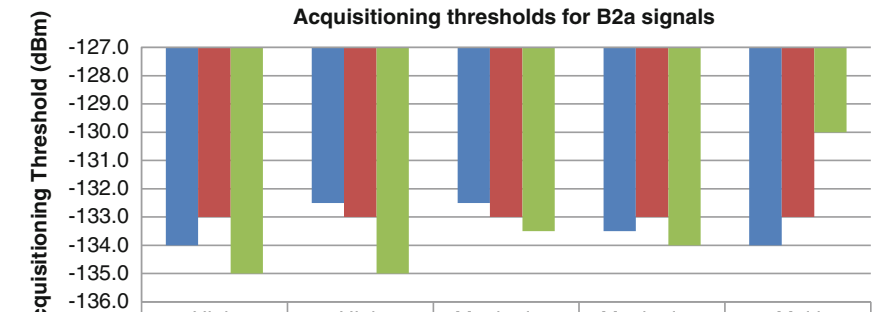

	High Precision A	High Precision B	Monitoring A	Monitoring B	Multi frequency
AltBOC	-134.0	-132.5	-132.5	-133.5	-134.0
TD-AltBOC	-133.0	-133.0	-133.0	-133.0	-133.0
ACE-BOC	-135.0	-135.0	-133.5	-134.0	-130.0

Fig. 1 Acquisition threshold comparison of the 3-scheme B2a

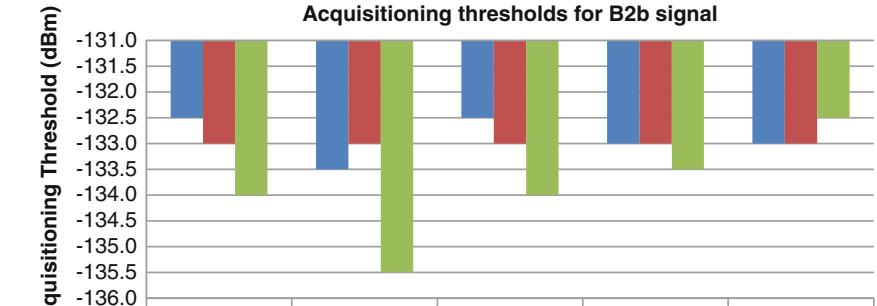

	High Precision A	High Precision B	Monitoring A	Monitoring B	Multi frequency
AltBOC	-132.5	-133.5	-132.5	-133.0	-133.0
TD-AltBOC	-133.0	-133.0	-133.0	-133.0	-133.0
ACE-BOC	-134.0	-135.5	-134.0	-133.5	-132.5

Fig. 2 Acquisition threshold comparison of the 3-scheme B2b

4.3.2 Tracking Threshold Result

The tracking thresholds of B2a and B2b signals are shown in Figs. 3 and 4, respectively.

For B2a signal, as Fig. 3 shows, except for monitoring receiver B, other receivers show that the ACE-BOC has the lowest tracking threshold, 1.0–2.5 dB better than AltBOC and 0.5–2.5 dB better than TD-AltBOC. AltBOC and

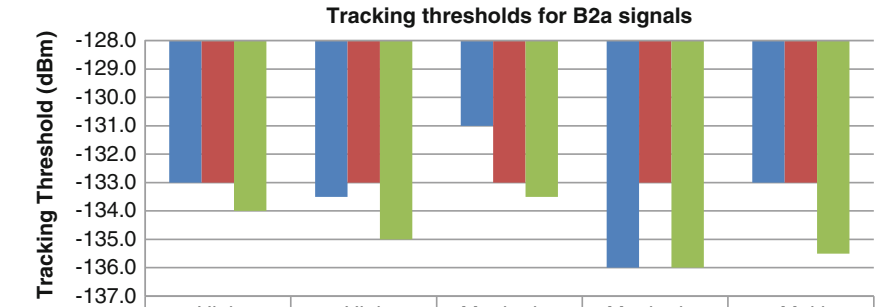

	High Precision A	High Precision B	Monitoring A	Monitoring B	Multi frequency
AltBOC	-133.0	-133.5	-131.0	-136.0	-133.0
TD-AltBOC	-133.0	-133.0	-133.0	-133.0	-133.0
ACE-BOC	-134.0	-135.0	-133.5	-136.0	-135.5

Fig. 3 Tracking threshold comparison of the 3-scheme B2a

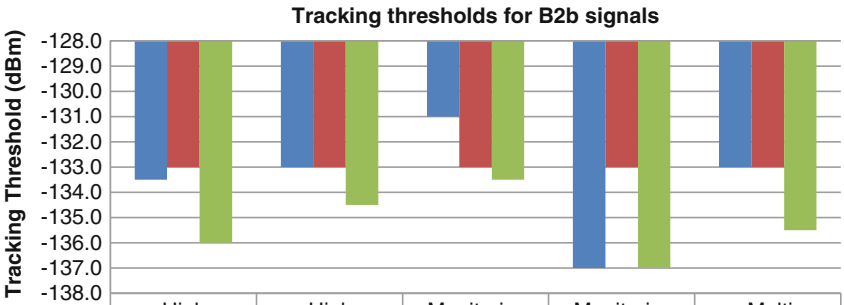

	High Precision A	High Precision B	Monitoring A	Monitoring B	Multi frequency
AltBOC	-133.5	-133.0	-131.0	-137.0	-133.0
TD-AltBOC	-133.0	-133.0	-133.0	-133.0	-133.0
ACE-BOC	-136.0	-134.5	-133.5	-137.0	-135.5

Fig. 4 Tracking threshold comparison of the 3-scheme B2b

TD-AltBOC. Tracking thresholds are the same in multifrequency receiver and high precision receiver A, and have pros and cons in high precision receiver B and monitoring receiver A, the difference is 0.5–2.0 dB. In monitoring receiver B, the threshold of AltBOC is 3.5 dB lower than that of TD-AltBOC, which is quite different from the theory result, it is reasonable to suspect that there might be some significant differences in signal processing strategies among different schemes, thus these results have low reference value.

For B2b signal, as Fig. 4 shows, the results show the similar characteristic with that of B2a. Except for monitoring receiver B, other receivers show that ACE-BOC have the lowest tracking threshold, 1.5–2.5 dB better than AltBOC and 0.5–3.0 dB than TD-AltBOC. Tracking thresholds of AltBOC and TD-AltBOC are the same in multifrequency receiver and high precision receiver B, and have pros and cons in high precision receiver A and monitoring receiver A, the difference is 0.5–2.0 dB. The result of monitoring receiver B has low reference value because of the same reason with that in B2a.

4.3.3 Results Analysis

As the multifrequency receiver's acquisitioning strategy is not well suited for all signal schemes, the monitoring receiver B might have significant differences in signal processing method, the corresponding results are not considered.

Based on above testing results, it can be seen that, nearly in all of the receivers, ACE-BOC has the lowest acquisitioning threshold and the lowest tracking threshold. It indicates that under the 50–100 bps data bit rate and popular encoding method, for the current receiver level (for all the receivers in the test, the absolute

acquisitioning threshold is −137 dBm, and the absolute tracking threshold is −150.5 dBm), demodulation is not the bottleneck factor of navigation signal receiving, thus assigning more power to pilot branch can improve the overall performance of signal, which means lower signal power to provide the same accuracy, or higher accuracy by using the same signal power.

5 Summary

For the main differences among the three BDS B2 frequency signal modulation schemes, this paper suggested an overall performance comparison method by testing the acquisitioning threshold and tracking threshold. Under the mainstream data bit rate and channel encoding method, the thresholds are tested by using navigation signal simulator and five kinds of receivers. The results shows that, ACE-BOC has the best overall performance, who's acquisitioning threshold and tracking threshold is 0.5–2.5dB lower than that of TD-AltBOC and AltBOC. It also indicates that, adaptation to the current message bit rate, encoding method, and receiver level, assigning more signal power to pilot branch and less power to data branch can be helpful to improve the signal overall performance.

References

1. Yao Z, Lu M (2012) Dual-frequency constant envelope multiplex with non-equal power allocation for GNSS. Electron Lett 48(25):1624–1625
2. Yao Z, Lu M (2013) Design, implementation, and performance analysis of ACE-BOC modulation. In: 26th International technical meeting of the ION satellite division (ION GNSS 2013), Nashville, Tennessee, 16–20 Sept 2013, pp 361–368
3. Yao Z, Lu M (2013) Constant envelope combination for components on different carrier frequencies with unequal power allocation. In: International technical meeting (ITM) of the Institute of Navigation, San Diego,CA, 28–30 Jan 2013, pp 629–637
4. Zhang J et al (2014) Applications and low-complex implementations of ACE-BOC multiplexing. In: International technical meeting of the Institute of Navigation, (ITM 2014), San Diego, California, 27–29 Jan 2014, pp 781–791
5. Yao Z et al (2016) ACE-BOC: dual-frequency constant envelope multiplexing for satellite navigation. IEEE Trans Aerosp Electron Syst 52(2):1–18
6. Tang Z et al (2010) TD-AltBOC: a new compass B2 modulation. In: Conference on China Satellite Navigation, Shanghai, China
7. Lestarquit L et al (2008) AltBOC for dummies or everything you always wanted to know about AltBOC. In: ION GNSS 2008, Savannah, GA, USA, pp 961–970
8. Zhu Y et al (2014) Comparative analysis of dual-frequency constant envelop multiplexing techniques for ARNS band. In: International technical meeting of the Institute of Navigation, (ITM 2014), San Diego, California, 27–29 Jan 2014, pp 792–801
9. Betz, J, et al (2006) L1C signal design options. In: National technical meeting of the Institute of Navigation, Monterey, CA, 2006, pp 685–697

10. Betz JW et al (2006) Description of the L1C signal. In: 19th International technical meeting of the satellite division (ION GNSS 2006), Fort Worth, TX, US, pp 2080–2091
11. Chen J, Wang M, Qian S (2011) Analysis of modernization GNSS navigation message's designing. J of Electron & Inform Technol 33(1):211–217

Research and Performance Analysis of Constant-Envelope Multiplex for BD B2 Signals

Ming-gui Cai, Nan Qi and Jun Xie

Abstract AltBOC (15, 10) is proposed to be the modulation mode of BD B2 global signals, which combines lower and upper lobes with four signals. The modulation makes users able to receive and process one lobe separately, or process two lobes coherently to achieve higher accuracy of position and navigation. AltBOC could also fulfill compatibility among BD, Galileo E5, and GPS L5. There have been lots of researches of B2 signals' solutions currently, but most of these only considered four signals with the same modulation mode and chip rate, which makes the choice of signals inflexible. Thus, we present two kinds of conditions that B2 signals have different modulation methods and chip rate, and three kinds of constant-envelope multiplex plans based on it to realize AltBOC modulation: non-symmetrical AltBOC, TD-AltBOC, and binary TD-AltBOC. The multiplex plans are simulated and multiplex efficiency of each one is given. Also the ranging accuracy, anti-multipath resistant, and anti-interference performance is shown to compare the three signals with the multiplex signals of B2 signals which are modulated as AltBOC (15, 10). Analysis results show the signals of the three multiplex plans have similar ranging accuracy, anti-multipath resistant, and anti-interference performance with the AltBOC (15, 10) signals. TD-AltBOC has the highest multiplex efficiency that is 100 % among the three plans. The multiplex schemes we present are able to combine signals with different modulation methods and chip rate as AltBOC modulation, which can achieve the same navigation performance to AltBOC (15, 10) signals and high multiplex efficiency, and these schemes could be new solutions for BD B2 signals.

Keywords BD · Constant-envelope multiplex · AltBOC · Performance evaluation

M. Cai (✉) · N. Qi
China Academy of Space Technology, Xi'an Branch, Xi'an, China
e-mail: 850139631@qq.com

J. Xie
China Academy of Space Technology, Beijing, China

J. Sun et al. (eds.), *China Satellite Navigation Conference (CSNC) 2016 Proceedings: Volume II*, Lecture Notes in Electrical Engineering 389,
DOI 10.1007/978-981-10-0937-2_5

1 Introduction

In 2001, CNES presented the AltBOC constant envelope modulation mode of four signals, realized four signals multiplex in two different frequency points, which was selected as Galileo E5 band signal modulation mode [1]. Because of the flexible use of AltBOC and considering the compatibility of GPS L5 and Galileo E5, BD global navigation satellite system is proposed AltBOC (15, 10) as B2 signal modulation mode.

The center frequency of AltBOC (15, 10) signal is located in the center of 1191.795 MHz, lower sideband at 1176.45 MHz, the same with GPS L5C and Galileo E5a, and upper sideband is located at 1207.14 MHz, the same with Galileo E5b. Upper and lower sideband contains data channel and pilot channel, each channel has the same energy [2]. There have been lots of researches on B2 frequency signal realization, such as TD-AltBOC proposed by Tang [3], and binary AltBOC proposed by Zhang [4], etc. But all these have only considered the four signals with the same modulation mode and chip rate, which makes the choice of signals inflexible. This article presents two kinds of B2 frequency signals with different modulation methods and code rate: one is using the center frequency point at 1207.14 MHz of BPSK (2) instead of the upper sideband data signal of AltBOC (15, 10), another one is adding the BPSK (2) signal with center frequency point is located at 1207.14 MHz to AltBOC (15, 10) four signals modulation. Based on these, three kinds of B2 constant envelope signal multiplexing methods are designed: asymmetric AltBOC, TD-AltBOC, and binary TD-AltBOC. Through the simulation analysis, three kinds of methods in which all can achieve B2 signal constant envelope multiplex. The binary TD-AltBOC plan has the highest multiplex efficiency which is 0 dB. Three kinds of solutions are compared with AltBOC (15, 10) and TD-AltBOC (15, 10) signals in power spectrum, code tracking precision, anti-jamming and anti-multipath, etc. The simulation results show that the three kinds of schemes of signals can achieve the same ranging accuracy, anti-interference, anti-multipath performance with AltBOC (15, 10) and TD-AltBOC (15, 10) signal, which can make signal modulation and code rate selection more flexible at the same time. Thus, the three solutions can be used as reference implementation scheme of B2 signals.

2 Four Signals Modulation with BPSK (2)

Baseband signal of standard four signals AltBOC (15, 10) can be represented as follows:

$$\begin{aligned} s(t) =& [d_A(t)\, c_{\mathrm{AD}}(t) + j\, c_{\mathrm{AP}}(t)][\mathrm{SC}_{\cos}(t) - j\, \mathrm{SC}_{\sin}(t)] \\ &+ [d_B(t)\, c_{\mathrm{BD}}(t) + j\, c_{\mathrm{BP}}(t)][\mathrm{SC}_{\cos}(t) + j\, \mathrm{SC}_{\sin}(t)] \end{aligned} \tag{1}$$

Where $d_A(t)$ is LSB data waveform, and $c_{\mathrm{AD}}(t)$ and $c_{\mathrm{AP}}(t)$ is LSB data and pilot pseudo-code waveform, respectively. $d_B(t)$ is USB data waveform, $c_{\mathrm{BD}}(t)$ and

$c_{BP}(t)$ is USB data and pilot pseudo-code waveform, respectively. For AltBOC (15, 10) signal, the data rate of upper and lower sideband can be different, but pn code rate of four signals is the same, which is 10.23 MHz. $SC_{cos}(t)$ and $SC_{sin}(t)$ is cosine subcarrier and sine subcarrier, respectively, which can be written as

$$\begin{aligned} SC_{cos}(t) &= \text{sign}(\cos(2\pi f_{SC} t)) \\ SC_{sin}(t) &= \text{sign}(\sin(2\pi f_{SC} t)) \end{aligned} \tag{2}$$

Where, f_{SC}=15.345 MHz.

If using the center frequency point in 1207.14 MHz of BPSK signal (2) replaced the USB data component signals, which can modulate BPSK (2) signal to the 1191.795 MHz first, then move up the spectrum through multiplication by complex subcarrier. Then the baseband signal of BPSK (2) can be shown as

$$s_{BPSK}(t) = d_{BPSK}(t)\, c_{BPSK}(t)[SC_{cos}(t) + j\, SC_{sin}(t)] \tag{3}$$

Where $d_{BPSK}(t)$ is data waveform of BPSK (2), $c_{BPSK}(t)$ is pseudo-code waveform which code rate is 2.046 MHz. Then the B2 signal can be written as follows:

$$\begin{aligned} s(t) =& [d_A(t)\, c_{AD}(t) + j\, c_{AP}(t)][SC_{cos}(t) - j\, SC_{sin}(t)] \\ &+ [d_{BPSK}(t)\, c_{BPSK}(t) + j\, c_{BP}(t)][SC_{cos}(t) + j\, SC_{sin}(t)] \end{aligned} \tag{4}$$

It is easy to verify that the signal according to (4) is not constant-envelope.

2.1 Asymmetric AltBOC

Paper [5] proposed an asymmetric AltBOC B1 signal constant envelope modulation mode, which can also be reference for B2 signal. The improved complex subcarrier can be represented as follows:

$$\begin{aligned} SC_d(t) =& \frac{\sqrt{2}}{4}\text{sign}\left[\cos\left(2\pi f_{SC} t - \frac{\pi}{4}\right)\right] \\ &+ \frac{1}{2}\text{sign}[\cos(2\pi f_{SC} t)] \\ &+ \frac{\sqrt{2}}{4}\text{sign}\left[\cos\left(2\pi f_{SC} t + \frac{\pi}{4}\right)\right] \end{aligned} \tag{5}$$

$$\begin{aligned} SC_p(t) =& -\frac{\sqrt{2}}{4}\text{sign}\left[\cos\left(2\pi f_{SC} t - \frac{\pi}{4}\right)\right] \\ &+ \frac{1}{2}\text{sign}[\cos(2\pi f_{SC} t)] \\ &- \frac{\sqrt{2}}{4}\text{sign}\left[\cos\left(2\pi f_{SC} t + \frac{\pi}{4}\right)\right] \end{aligned} \tag{6}$$

Further, the improved complex signal [5] can be represented as follows:

$$\begin{aligned} s(t) =& [s_{\mathrm{AD}}(t) + j\, s_{\mathrm{AP}}(t)] \left[\mathrm{SC}_d(t) - j\, \mathrm{SC}_d\left(t - \frac{T_{\mathrm{SC}}}{4}\right)\right] \\ &+ [s_{\mathrm{BPSK}}(t) + j\, s_{\mathrm{BP}}(t)] \left[\mathrm{SC}_d(t) + j\, \mathrm{SC}_d\left(t - \frac{T_{\mathrm{SC}}}{4}\right)\right] \\ &+ [s_{\mathrm{AP}}(t)\, s_{\mathrm{BPSK}}(t)\, s_{\mathrm{BP}}(t) + j\, s_{\mathrm{AD}}(t)\, s_{\mathrm{BPSK}}(t)\, s_{\mathrm{BP}}(t)] \cdot \\ &\left[\mathrm{SC}_p(t) - j\, \mathrm{SC}_p\left(t - \frac{T_{\mathrm{SC}}}{4}\right)\right] \\ &+ [s_{\mathrm{AD}}(t)\, s_{\mathrm{AP}}(t)\, s_{\mathrm{BP}}(t) + j\, s_{\mathrm{AD}}(t)\, s_{\mathrm{AP}}(t)\, s_{\mathrm{BPSK}}(t)] \cdot \\ &\left[\mathrm{SC}_p(t) + j\, \mathrm{SC}_p\left(t - \frac{T_{\mathrm{SC}}}{4}\right)\right] \end{aligned} \tag{7}$$

Where $T_{\mathrm{SC}} = 1/f_{\mathrm{SC}}$. The sub signals can be written as follows:

$$\begin{aligned} s_{\mathrm{AD}}(t) &= d_{\mathrm{AD}}(t)\, c_{\mathrm{AD}}(t) \\ s_{\mathrm{AP}}(t) &= c_{\mathrm{AP}}(t) \\ s_{\mathrm{BPSK}}(t) &= d_{\mathrm{BPSK}}(t)\, c_{\mathrm{BPSK}}(t) \\ s_{\mathrm{BP}}(t) &= c_{\mathrm{BP}}(t) \end{aligned} \tag{8}$$

2.2 TD-AltBOC

The realization of the TD-AltBOC signals expressions is shown as (4), four pseudo-code waveform signals can be represented as follows:

$$\begin{aligned} c_{\mathrm{AD}}(t) &= \sum_{l=-\infty}^{\infty} \sum_{k=0}^{N_{\mathrm{AD}}-1} C_{\mathrm{AD}}(k)\, p(t - (2N_{\mathrm{AD}}\, l + 2k)T_c) \\ c_{\mathrm{AP}}(t) &= \sum_{l=-\infty}^{\infty} \sum_{k=0}^{N_{\mathrm{AP}}-1} C_{\mathrm{AP}}(k)\, p(t - (2N_{\mathrm{AP}}\, l + 2k + 1)T_c) \\ c_{\mathrm{BPSK}}(t) &= \sum_{l=-\infty}^{\infty} p(t - 2\, l\, T_c) \sum_{k=0}^{N_{\mathrm{BPSK}}-1} C_{\mathrm{BPSK}}(k) p\left(\frac{t}{5} - (2N_{\mathrm{BPSK}}\, l + 2k)T_c\right) \\ c_{\mathrm{BP}}(t) &= \sum_{l=-\infty}^{\infty} \sum_{k=0}^{N_{\mathrm{BP}}-1} C_{\mathrm{BP}}(k)\, p(t - (2N_{\mathrm{BP}} + 2k + 1)T_c) \end{aligned} \tag{9}$$

Where N_{AD}, N_{AP}, $N_{BPSK,}$ and N_{BP} are pseudo-code yard length of four sub signals. T_c is code width of N_{AD}. $p(t)$ is the gate function can be represented as follows:

$$p(t) = \begin{cases} 1, & 0 \le t < T_c \\ 0, & others \end{cases} \tag{10}$$

3 Five Signals Modulation with AltBOC (15, 10) + BPSK (2)

This section increases the BPSK (2) to the original four AltBOC (15, 10) signals, to achieve a total of five constant envelope multiplex. To improve the multiplex efficiency, we choose the TD-AltBOC (15, 10) as four signals modulation mode.

Four-signal TD-AltBOC (15, 10) is equal to the dual channel AltBOC (15, 10) signal, can be represented as follows:

$$\begin{aligned} s(t) =& s_A(t)[\mathrm{SC}_{\cos}(t) - j\,\mathrm{SC}_{\sin}(t)] \\ &+ s_B(t)[\mathrm{SC}_{\cos}(t) + j\,\mathrm{SC}_{\sin}(t)] \end{aligned} \tag{11}$$

$S_A(t)$ and $S_B(t)$ use to broadcast signal, even time slot broadcast $S_{AD}(t)$ and $S_{BD}(t)$, and odd number slot broadcast $S_{AP}(t)$ and $S_{BP}(t)$. The complex signal baseband expression is as follows:

$$\begin{aligned} s(t) =& s_A(t)[\mathrm{SC}_{\cos}(t) - j\,\mathrm{SC}_{\sin}(t)] + s_B(t)[\mathrm{SC}_{\cos}(t) + j\,\mathrm{SC}_{\sin}(t)] \\ &+ s_{\mathrm{BPSK}}(t)[\mathrm{SC}_{\cos}(t) + j\,\mathrm{SC}_{\sin}(t)] \end{aligned} \tag{12}$$

Obviously, the complex signal is a constant envelope signals. It can be seen that the complex signal including all binary signals: S_A-$\mathrm{BOC}_{\cos}$, S_A-$\mathrm{BOC}_{\sin}$, S_B-$\mathrm{BOC}_{\cos}$, S_B-$\mathrm{BOC}_{\sin}$, S_{BPSK}-$\mathrm{BOC}_{\cos}$, S_{BPSK}-$\mathrm{BOC}_{\sin}$. POCET method can be used for the realization of the constant envelope multiplex, all signal amplitude phase relationships shown in the table below. We assume that all signals with the same power (Table 1).

On the basis of the above mentioned power and phase relationship, the optimal solution phases are provided using POCET algorithm search. The phases searched

Table 1 Modulation power/phase relationship of binary TD-AltBOC

Signal	S_A-$\mathrm{BOC}_{\cos}$	S_A-$\mathrm{BOC}_{\sin}$	S_B-$\mathrm{BOC}_{\cos}$
Power ratio	1	1	1
Phase	0°	±90°	0°/180°
Signal	S_B-$\mathrm{BOC}_{\sin}$	S_{BPSK}-$\mathrm{BOC}_{\cos}$	S_{BPSK}-$\mathrm{BOC}_{\sin}$
Power ratio	1	1	1
Phase	±90°	φ	φ ± 90°

Table 2 Phases of constant-envelope B2 signal

No.	1	2	3	4	5	6	7	8
θ(°)	0	26.6	90	63.4	−90.0	0	180	90
No.	9	10	11	12	13	14	15	16
θ(°)	90	63.4	116.6	90	180	90	153.4	116.6
No.	17	18	19	20	21	22	23	24
θ(°)	270	0	180	90	243.4	−90	206.6	180
No.	25	26	27	28	29	30	31	32
θ(°)	180	90	153.4	116.6	206.6	180	180	153.4
No.	33	34	35	36	37	38	39	40
θ(°)	333.4	0	0	26.6	296.6	333.4	270	0
No.	41	42	43	44	45	46	47	48
θ(°)	0	26.6	90	63.4	270	0	180	90
No.	49	50	51	52	53	54	55	56
θ(°)	296.6	333.4	270	0	270	296.6	243.4	270
No.	57	58	59	60	61	62	63	64
θ(°)	270	0	180	90	243.4	270	206.6	180

is shown in Table 2, the θ is arranged by S_A-$\mathrm{BOC}_{\cos}$, S_A-$\mathrm{BOC}_{\sin}$, S_B-$\mathrm{BOC}_{\cos}$, S_B-$\mathrm{BOC}_{\sin}$, S_{BPSK}-$\mathrm{BOC}_{\cos}$, S_{BPSK}-$\mathrm{BOC}_{\sin}$ code combination from the all 0 to all 1.

4 Multiplex Efficiency

The multiplex of navigation signal multiplexing efficiency defined as [6] follows:

$$\eta = \frac{P_{T-\mathrm{code}}}{P} = \frac{\sum_{n=1}^{N} |\mathrm{corr}_n|^2}{A^2} \tag{13}$$

Where $P_{T\text{-code}}$ is the transmitted signal power and $|\mathrm{corr}_n|^2$ is the nth signal power given by the receiver. N is the signal component number, and $P = A^2$ is the total power of the complex signal.

5 Code Tracking Accuracy

The lower bounds of code tracking error of the coherent loop can be expressed as [7] follows:

$$\sigma_T^2 = \frac{B_L}{C/N_0} \frac{1}{(\Delta\omega)^2} \tag{14}$$

$$\Delta f = \sqrt{\int_{-\beta_r/2}^{\beta_r/2} f^2 G_s(f)\mathrm{d}f} \tag{15}$$

Where $G_s(f)$ is the normalization of equivalent baseband signal power spectral density (Hz^{-1}) and β_r is receiving bandwidth (Hz). For comparison, this paper takes the form of Gabor bandwidth Hz as the unit.

6 Anti-interference Performance

In this paper, two types of interference are considered: narrowband interference and matching spectrum interference. Paper [8] gives the four main evaluation indicators of anti-jamming performance: demodulation and quality factor of narrow-band interference demodulation spectrum interference resistance matching quality factor, the code tracking quality factor of narrow-band interference and code tracking matching spectrum interference quality factor, which are discussed in this paper.

7 Anti-multipath Performance

The anti-multipath ability of navigation signal can be measured by noncoherent lead/lag delay lock loop code tracking multipath error envelope and average multipath error [9, 10]. Multipath error envelope is different multipath delay caused by multipath effect under the condition of maximum deviation, which can reflect a particular multipath delay multipath error under the condition of worst case as follows:

$$\varepsilon_\tau \approx \frac{\pm 2\tilde{a}_1 \int_{-\beta_r/2}^{\beta_r/2} S(f)\sin(-2\pi f\,\tilde{\tau}_1)\sin(\pi f\,d)\,\mathrm{d}f}{2\pi \int_{-\beta_r/2}^{\beta_r/2} f\,S(f)\,\sin(\pi f\,d)[1 \pm \tilde{a}_1\,\cos(2\pi f\,\tilde{\tau}_1)]\,\mathrm{d}f} \tag{16}$$

Where $\tilde{a}_1$ is the ratio of multiple drive signal with the direct signal amplitude, and $S(f)$ is the power spectrum of signal. d is the interval of lead correlator and lag correlator, and $\tilde{\tau}_1$ is multiple diameter signals relative to the extra time delay. The average time delay scope is as follows:

$$\varepsilon_a(\tilde{\tau}_1') = \frac{1}{\tilde{\tau}'}\int_0^{\tilde{\tau}_1'} \left[\frac{\left|\left(\varepsilon_\tau(\tilde{\tau}_1)|_{\tilde{\varphi}_1=0^o}\right)\right| + \left|\left(\varepsilon_\tau(\tilde{\tau}_1)|_{\tilde{\varphi}_1=180^o}\right)\right|}{2}\right] \mathrm{d}\tilde{\tau}_1 \tag{17}$$

8 Multiplex Efficiency

According to (13), constant envelope multiplex efficiency of asymmetric AltBOC, TD-AltBOC, and binary TD-AltBOC are 0, 1.08, and 0.75 dB, respectively. TD-AltBOC multiplex efficiency is highest, means the multiplex efficiency is 100 %. This is because the TD-AltBOC converts four-channel AltBOC to a double channel AltBOC, which in each time slot two signal transmissions are equivalent to linear superposition without bringing the intermodulation components.

9 Code Tracking Accuracy

Five kinds of Gabor complex signal bandwidth and the relationship between the receiver front-end bandwidth is shown in Fig. 1. Due to they have the same bandwidth, in the simulation they are set as 71.6 MHz, so these Gabor bandwidth have similar changing trend.

10 Anti-disturbance Performance

The anti-interference ability of five kinds B2 frequency complex signal are shown in Fig. 2. Simulation transmitting bandwidth is set to 71.6 MHz and receiving bandwidth is set to 60 MHz bandwidth, information rate is set to 50 bps. It is shown that AltBOC (15, 10) is best in demodulation narrow-band interference, demodulation

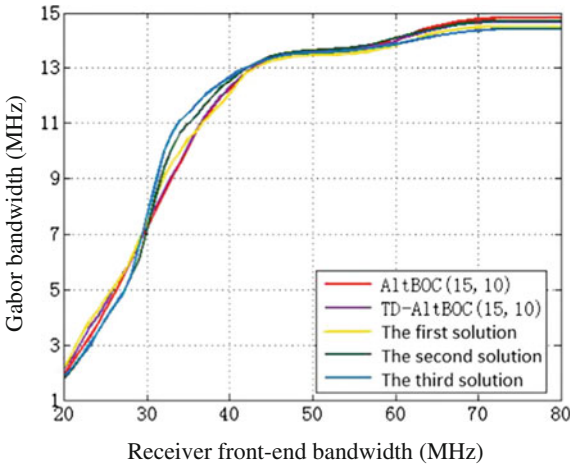

Fig. 1 Comparison of code tracking accuracy of B2 signals

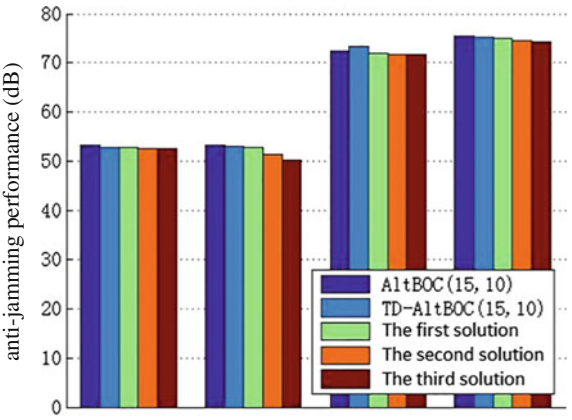

Fig. 2 Comparison of anti-disturbance performance of B2 signals

matching spectrum, code tracking performance of the optimal matching spectrum interference. TD-AltBOC (15, 10) signal has best code tracking narrow-band interference optimal performance.

11 Anti-multipath Performance

Multipath error envelope and multipath average error of five complex signal is as shown in Figs. 3 and 4, respectively. The transmitting bandwidth is set to 71.6 MHz, receiving bandwidth is set to 60 MHz. It can be seen that AltBOC (15, 10) and TD-AltBOC (15, 10) signal performance is basically the same and the best.

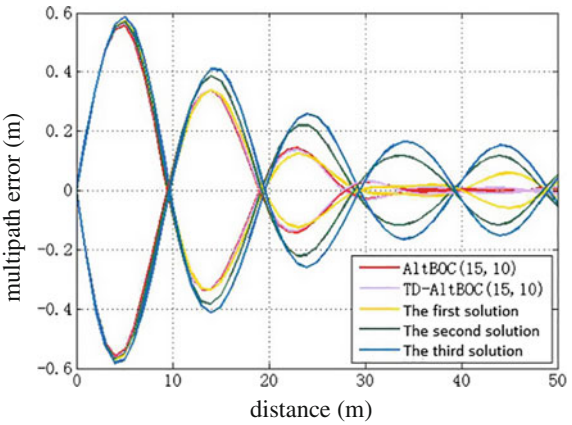

Fig. 3 Comparison of multipath error envelope of B2 signals

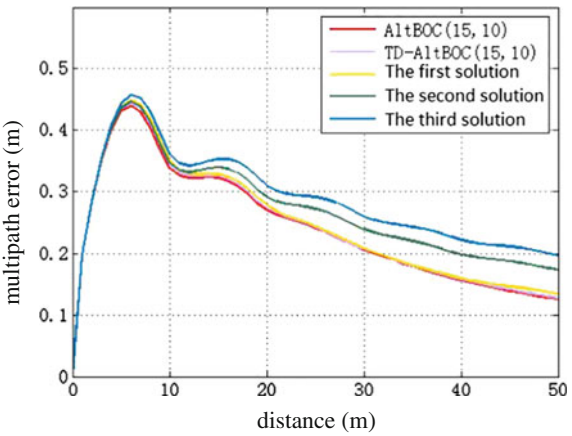

Fig. 4 Comparison of multipath average error of B2 signals

12 Conclusions

This paper presents two kinds of condition that B2 signals have different modulation methods and chip rate, three kinds of constant-envelope multiplex plans based on it to realize AltBOC modulation: non-symmetrical AltBOC, TD-AltBOC, and binary TD-AltBOC. Asymmetric AltBOC has the lowest multiplex efficiency but the performance is optimal; the TD-AltBOC multiplex efficiency is highest, performance is slightly less than asymmetric AltBOC; Binary TD-AltBOC, performance is relatively poor but multiplex efficiency is higher and using a lookup table to modulation, implementation is simple.

References

1. Lestarquit L, Artaud G, Issler J (2008) AltBOC for dummies or everything you always wanted to know about AltBOC. In: ION GNSS 21st international technical meeting of the satellite division, Institute of Navigation, Savannah, GA, Virginia, pp 961–970
2. Current and planned global and regional navigation satellite systems and satellite-based augmentations systems [OL] [2011-01-15]. http://ww.oosa.unvienna.org/pdf/publications/icg_ebook.pdf
3. Tang Z, Zhou H, Wei J et al (2011) TD-AltBOC: a new compass B2 modulation. Sci China Phys Mech Astron 50(6):1014–1021
4. Zhang K, Wang F (2011) Application of phase-optimized constant-envelope transmission method in compass signal design in the presence of finite da word-length effects. In: The 2nd China satellite navigation conference 2011
5. Zhu L, Yao Z, Feng Z (2012) Non-symmetrical ALTBOC multiplexing for compass B1 signal design. Tsinghua Univ (Sci&Tech) 06:869–873
6. Dafesh PA, Cooper L, Partirdge M (2000) Compatibility of the interplex modulation method with C/A and P(Y) code signals. Salt Lake City, UT: ION GPS 2000, pp 779–789, 19–22 September 2000

7. Spilker JJ Jr (1996) Signal structure and theoretical performance. In: Global positioning system: theory and applications, vol I. Progress in astronautics and aeronautics, vol. 163. American Institute of Aeronautics and Astronautics, Washington
8. Tang Z, Zhou H, Hu X et al (2010) Research in evaluation of compass navigation signal. In: The 1st China satellite navigation conference
9. Wallner S, Hein GW, Avila-Rodriguez JA (2006) Interference computations between several GNSS systems. In: Proceedings of ESA Navitec 2006, Noordwijk, The Netherlads
10. Tang Z, Hu X, Huang X (2009) Analysis of satellite navigation signal design performance against multipath. J Huazhong Univ Sci Technol 37(5):1–4

An Improved Approach of SFAP Algorithm for Suppressing Concurrent Narrowband and Wideband Interference

Yaohui Chen, Dun Wang, Peng Liu, Zhenxing Xu, Chanjuan Wei and Qijia Dong

Abstract Anti-jamming algorithm of Space-Frequency Adaptive Processing (SFAP) will fail when plural narrowband jammers in diverse directions fall into the same subfrequency band and the number of jammers exceeds the limitation that an antenna array can cope with. A well-known method called frequency excision was proposed to add into SFAP to remove these narrowband jammers. However, it is possible that narrowband interference cannot be detected correctly due to the existence of wideband interference. In such situation, this method becomes inapplicable. In this paper, a new approach of SFAP is proposed to cope with concurrent narrow and wideband jammers. It determines the weights of each sub-band based on the data from itself and adjacent sub-bands. Computer simulation with an antenna model of four elements in Y-form shows that the proposed approach improves the performance of SFAP significantly under concurrent narrow and wideband jammers and the increased implementation cost of the new approach is very small and can be negligible.

Keywords Space-frequency adaptive processing (SFAP) · Anti-jamming · Weight · Sub-band

1 Introduction

Satellite navigation system has been an indispensable tool for humans in political, scientific, economic, and military activities. Because it can provide 24-hour continuous, high-precision, three-dimensional position, velocity, and precise time information for all kinds of military and civilian carriers of global land, sea, air, space [1]. As a result of the satellite signals reached to the ground are quite weak (such as the minimum power of the L1 C/A code of GPS satellite signals are approximately −158.5 dBW, even weaker 20–30 dB than the receiver thermal

Y. Chen (✉) · D. Wang · P. Liu · Z. Xu · C. Wei · Q. Dong
Space Star Technology Co. Ltd, Beijing 102209, China
e-mail: Chen_yaohui10@163.com

J. Sun et al. (eds.), *China Satellite Navigation Conference (CSNC) 2016 Proceedings: Volume II*, Lecture Notes in Electrical Engineering 389,
DOI 10.1007/978-981-10-0937-2_6

noise) [2], it is susceptible to various types of radio frequency interference. Therefore, it is necessary to research anti-jamming technology for satellite navigation receiver.

The most commonly used navigation receiver anti-jamming techniques are mainly based on array antenna, such as spatial adaptive processing technology, Space-Time Adaptive Processing (STAP) technology, and Space-Frequency Adaptive Processing (SFAP) technology [3–5]. For pure spatial filtering algorithm with M elements, it can restrain M−1 jammers at most [6], but not apply to wideband interference. SFAP algorithm is a rejection technology of wideband interference. The wideband signals will be divided into multiple narrowband signals through FFT, and the spatial filtering processing will be carried out separately in each sub-band. Therefore, the anti-jamming algorithm of SFAP will get failed if the number of jammers in any sub-band exceeds the limitation that an antenna array can cope with. If plural narrowband jammers in diverse directions fall into the same sub-band and the number of jammers exceeds the limitation that an antenna array can cope with, the anti-jamming algorithm of SFAP will also failed, although other sub-bands are not exceeding. This will seriously affect the number of wideband jammers suppression. In order to make the SFAP algorithm suppress wideband interference as much as possible, the narrowband interference must be dealt with in advance. It is understood that there is a narrowband pretreatment method that filters narrowband interference through threshold detection in advance so that the SFAP algorithm has more freedom to suppress wideband interference. But this method of filtering the narrowband interference in advance requires that the narrowband interference can be detected correctly after FFT. Typically, narrowband and wideband jammers always exist at the same time. When the wideband interference is strong, it is possible that the narrowband interference will not be detected correctly after FFT due to the existence of the wideband interference. In such situation, this method becomes inapplicable. Now, the SFAP algorithm will failed if the number of jammers falling into a sub-band exceeds the limitation that an antenna array can cope with. Literature [7] proposes an approach of multi-order space-frequency algorithm, namely using adjacent sub-bands information to calculate the weights of the current bin, but the more adjacent sub-bands are used, the greater dimension of the matrix is needed and the greater the amount of calculation will be. In this paper, a new approach of SFAP is proposed to cope with concurrent narrow and wideband jammers. It determines the weights of each sub-band based on the data from itself and adjacent sub-bands, and the increased implementation cost of the new approach is very small and can be negligible.

This paper is organized as follows: Sect. 1 is the introduction. Section 2 introduces the SFAP algorithm model, and analyzes characteristics of the weights. Section 3 introduces the method of using adjacent sub-bands information to calculate the current sub-band filter weights. Section 4 shows the simulation carried out with four elements in Y-form. Finally, Sect. 5 summarizes the full text. Compared with the method of filtering narrowband interference by threshold detection before space-frequency anti-jamming and the method proposed in this

paper, the latter can solve the above problems very well and ensure the effectiveness of the SFAP algorithm.

2 SFAP Algorithm

2.1 SFAP Algorithm Model

The basic idea of the SFAP algorithm is that the outputs of the delay nodes after each element are Fourier transformed into frequency domain, then carry out adaptive filtering in frequency domain, finally recover the time domain outputs by inverse Fourier transform. Figure 1 shows the principle of space-frequency adaptive filter.

In Fig. 1, $\{w_{mk}\}$ are the unknown space-frequency weights, where $m = 1, 2, \cdots, M$ and $k = 1, 2, \cdots, N$. $\{x_{mn}(l)\}$ are the buffer data, where $m = 1, 2, \cdots, M$ and $n = 1, 2, \cdots, N$. $\{\tilde{x}_{mk}(l)\}$ are the outputs of buffer data after Fourier transform, where $m = 1, 2, \cdots, M$ and $k = 1, 2, \cdots, N$, note that index l denotes the block number.

The outputs of the kth bin for the lth block after Fourier transform use vector notation can be written as

$$\tilde{\boldsymbol{X}}_k(l) = [\tilde{x}_{1k}(l), \tilde{x}_{2k}(l), \cdots, \tilde{x}_{Mk}(l)]^T \tag{1}$$

where the superscript "T" denotes transpose.

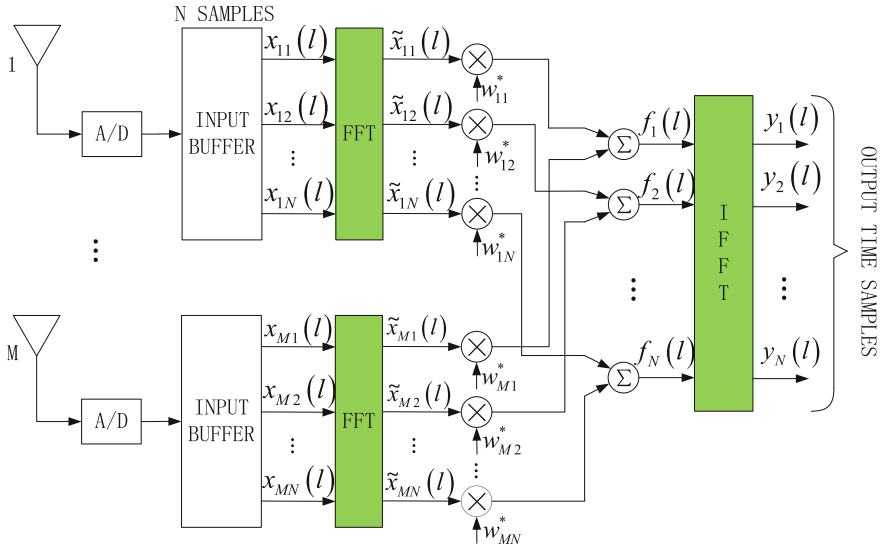

Fig. 1 Principle of space-frequency adaptive filter

Let L frequency domain samples be used to estimate the covariance matrix $\boldsymbol{R}_k$ for the kth bin. Then the kth bin covariance matrix $\boldsymbol{R}_k$ is given by

$$\boldsymbol{R}_k = \frac{1}{L}\sum_{l=1}^{L} \tilde{\boldsymbol{X}}_k(l)\tilde{\boldsymbol{X}}_k^H(l) \tag{2}$$

where the covariance matrix $\boldsymbol{R}_k$ is Hermitian matrix.

Using the Minimum Noise Variance (MNV) criterion can get the kth bin weights

$$\boldsymbol{W}_k = \alpha_k \boldsymbol{R}_k^{-1}\boldsymbol{s} \tag{3}$$

where $\alpha_k = 1/\boldsymbol{s}^H\boldsymbol{R}_k^{-1}\boldsymbol{s}$, $\boldsymbol{s}$ is the constraint vector, and is usually selected to be $[1, 0, \cdots, 0]^T$.

The kth bin output for the lth block after the anti-jamming filter is given by

$$f_k(l) = \boldsymbol{W}_k^H \tilde{\boldsymbol{X}}_k(l), 1 \le k \le N \tag{4}$$

Finally the outputs of the N bins after the anti-jamming filter are inverse Fourier transformed to obtain the time domain outputs. The nth time domain output for the lth block is given by

$$y_n(l) = \frac{1}{N}\sum_{k=1}^{N} f_k(l) e^{j\frac{2\pi}{N}(k-1)(n-1)}, 1 \le n \le N \tag{5}$$

2.2 Weights Characteristic Analysis

From the calculation formula of weights given by Eq. (3), one can see the following two points:

(1) The weights of each bin are calculated separately
From Eq. (3) one can see that the weights for each bin only use the information of this bin, and have nothing to do with other bins. Thus SFAP algorithm actually just divides the wideband signals into different sub-bands, but it actually uses spatial filtering algorithm in each sub-band. Therefore, the limitation on the number of jammers in the spatial filtering also exists in single sub-band of the SFAP algorithm, namely the SFAP algorithm will get failed if the number of jammers falling into a sub-band exceeds the limitation that an antenna array can cope with.

(2) α_k is real
Since the covariance matrix $\boldsymbol{R}_k$ is Hermitian matrix, so α_k is real. For weights calculation formula (3), the role of α_k is to make all weights in the same order of magnitude, and ensure that signal distortion does not occur. But when the

number of jammers falling into a sub-band exceeds the limitation that an antenna array can cope with, it will naturally cause interference that cannot be suppressed. The interference will be suppressed if one can modify the weights calculation formula to make the weights of corresponding sub-bands relatively small when the above condition happens. Based on this idea, this paper proposes an improved weights calculation method.

3 Improved SFAP Weight Calculation Method

This paper proposes a method to modify the weights calculation formula by using adjacent sub-bands information and reach the purpose of solving the above problems. In this paper, weights of each sub-band calculation using only their own band information are called first-order weights, weights of each sub-band calculation using two adjacent bins (one on each side) information are called second-order weights, weights of each sub-band calculation using four adjacent bins (two on each side) information are called third-order weights, and so on. Define:

First-order weights calculation formula is given by

$$\boldsymbol{W}_k = \frac{\boldsymbol{R}_k^{-1}\boldsymbol{s}}{\boldsymbol{s}^H\boldsymbol{R}_k^{-1}\boldsymbol{s}} \tag{6}$$

Second-order weights calculation formula is given by

$$\boldsymbol{W}_k = \frac{\boldsymbol{R}_k^{-1}\boldsymbol{s}}{\boldsymbol{s}^H\boldsymbol{R}_{k-1}^{-1}\boldsymbol{s} + \boldsymbol{s}^H\boldsymbol{R}_k^{-1}\boldsymbol{s} + \boldsymbol{s}^H\boldsymbol{R}_{k+1}^{-1}\boldsymbol{s}} \tag{7}$$

Third-order weights calculation formula is given by

$$\boldsymbol{W}_k = \frac{\boldsymbol{R}_k^{-1}\boldsymbol{s}}{\boldsymbol{s}^H\boldsymbol{R}_{k-2}^{-1}\boldsymbol{s} + \boldsymbol{s}^H\boldsymbol{R}_{k-1}^{-1}\boldsymbol{s} + \boldsymbol{s}^H\boldsymbol{R}_k^{-1}\boldsymbol{s} + \boldsymbol{s}^H\boldsymbol{R}_{k+1}^{-1}\boldsymbol{s} + \boldsymbol{s}^H\boldsymbol{R}_{k+2}^{-1}\boldsymbol{s}} \tag{8}$$

The largest amount of computation in the process of weight calculation is matrix inversion, and the amount of multiplication computation is M^3 order for an M order matrix. From the weights calculation formula, one can see that compared with first-order weights, the amount of computation of second-order and third-order weights does not increase observably, just increase a small amount of additive operation.

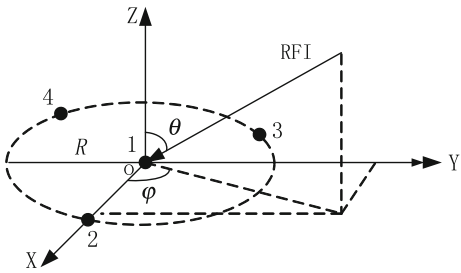

Fig. 2 Four elements in Y-form

4 Simulation and Verification

In order to verify the method proposed in this paper has advantages compared with the method of filtering narrowband interference by threshold detection after FFT, then the simulation is carried out with a Y-form of four elements, as shown in Fig. 2, one array element is in the center, the other three are uniformly distributed on the circumference with a radius of 0.4λ (0.0946 m). All elements are assumed to be isotropic antennas with no coupling. The bandwidth of the satellite signal is 20.46 MHz. The signals are downconverted to baseband and sampled at a rate of 62×10^6 samples/s.

The incident directions of the jammers are shown in Table 1.

4.1 Scene 1

First, reappear the issue that the anti-jamming algorithm of SFAP will get failed when the number of jammers falling into a sub-band exceeds the limitation that an antenna array can cope with.

This scenario contains one wideband jammer (interference NO.4) and three narrowband jammers (interference NO.1, 2, 3). The ISR (Interference-to-Signal Ratio) of each interfering signal at each antenna element is assumed to be 75 dB, and the SNR (Signal-to-Noise Ratio) of the desired signal at each antenna element is assumed to be −26 dB. For four elements in Y-form, each sub-band can cope

Table 1 The incident directions of jamming signals

Jammer #	Interference type	Bandwidth (MHz)	Frequency (MHz)	DOA (degrees) (azimuth φ, pitch θ)
1	Narrow band	0.0	1268.52	(0, 85)
2	Narrow band	0.0	1268.53	(60, 65)
3	Narrow band	0.0	1268.54	(150, 45)
4	Wide band	20.46	1268.52	(280, 85)

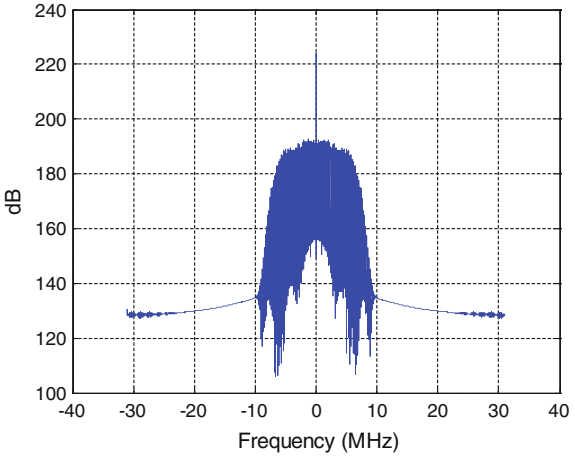

Fig. 3 Signal power spectrum (Gain) after LPF

with three jammers in maximum, while the first sub-band contains four jammers in this scenario which exceeds the limitation that the antenna array can cope with. The signals received by the antenna are downconverted to baseband through RF channel, AD sampling, digital down conversion, and low-pass filter. Figure 3 shows the power spectrum of the baseband signals which are carried out anti-jamming process.

Figure 4 shows the output signals power spectrum after anti-jamming processing with the existing SFAP algorithm. From Fig. 4 one can see clearly that the jammers are not suppressed. It shows that the SFAP algorithm will get failed when the number of jammers falling into a sub-band exceeds the limitation that an antenna array can cope with.

Next to verify that the method of filtering narrowband interference by spectrum analysis after FFT and the method proposed in this paper are both effective, when

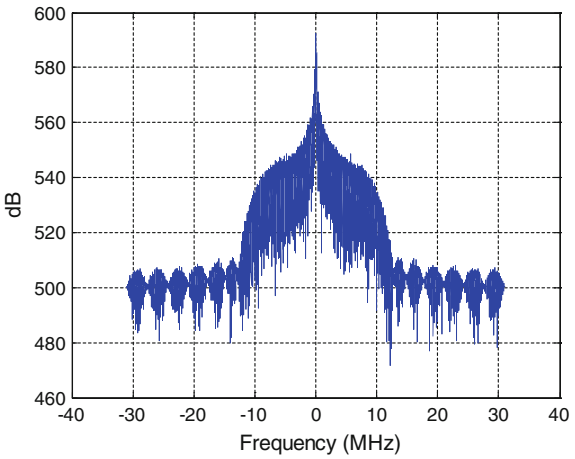

Fig. 4 Power spectrum (Gain) after space-frequency anti-jamming

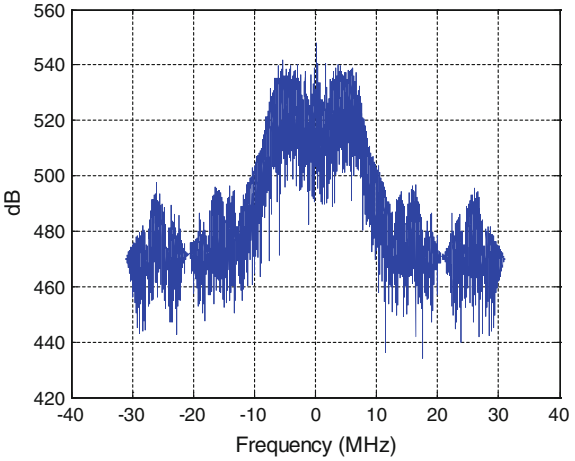

Fig. 5 Power spectrum (Gain) of space-frequency anti-jamming after narrowband filtering

the number of jammers falling into a sub-band exceeds the limitation that an antenna array can cope with and the narrowband interference can be detected correctly by spectrum analysis after FFT.

Jamming scenario remains the same, and from the power spectrum shown in Fig. 3 one can clearly identify the narrowband interference.

Figure 5 shows the power spectrum of the outputs of SFAP algorithm which filters narrowband interference by threshold detection in advance after FFT.

From Fig. 5 one can see that the narrowband interference is suppressed effectively in the way of filtering it in advance by threshold detection after FFT. Figure 5 shows its adjacent spectrum signals are also influenced when the narrowband interference is suppressed.

Figure 6 shows the power spectrum of the output signals after filtering with first-order, second-order, third-order and fourth-order weights proposed in this paper. From Fig. 6 one can see that the interference can be suppressed by the third-order and fourth-order weights, and other adjacent sub-bands spectrum signals do not have much impact.

Thus it can be seen that both methods are effective for the scenario that the narrowband interference can be detected correctly by the spectrum after FFT.

4.2 Scene 2

This section shows a scenario that the narrowband interference cannot be detected correctly by simple spectrum analysis after FFT. In this scenario, the traditional method of filtering narrowband interference is ineffective, while the new method proposed in this paper is effective.

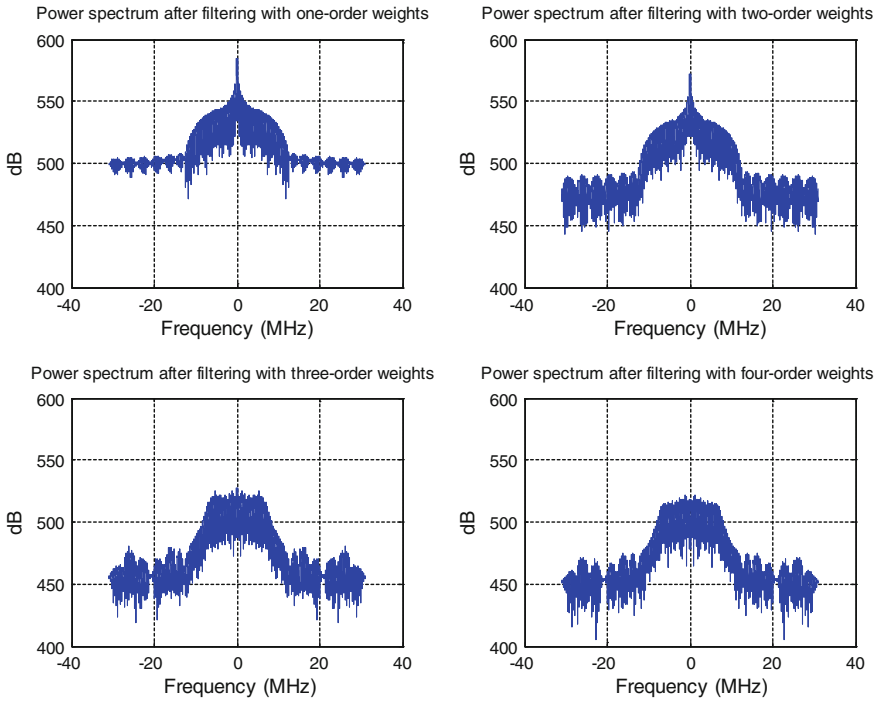

Fig. 6 Power spectrum (Gain) after filtering with improved weights

This scenario contains one wideband jammer (interference NO.4) and three narrowband jammers (interference NO.1, 2, 3). The ISR of wideband interference at each antenna element is assumed to be 75 dB, the ISR of narrowband interference is assumed to be 40 dB, and the SNR of the desired signal is assumed to be −26 dB. The signals received by the antenna are downconverted to baseband through RF channel, AD sampling, digital down conversion, and low-pass filter. Figure 7 shows the power spectrum of the baseband signals.

From Fig. 7 one can see that the narrowband interference spectrum is submerged under the wideband spectrum due to the wideband interference intensity is much stronger than the narrowband interference. The narrowband interference cannot be detected correctly by conventional spectrum analysis, so the method of filtering narrowband interference by threshold detection is inapplicable. The intensity of the narrowband interference is weaker than the wideband, which makes it difficult to be detected, though the ISR of the narrowband interference is also 40 dB that is strong enough to block the receiver to receive navigation signals.

Figure 8 shows the power spectrum of the output signals after filtering with first-order, second-order, third-order and fourth-order weights proposed in this paper. From Fig. 8 one can see there still is obvious residual narrowband interference in the signal spectrum when using the first-order and second-order weights

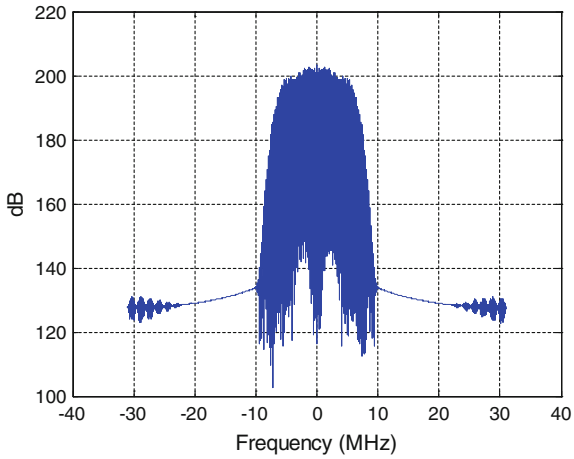

Fig. 7 Signal power spectrum (Gain) after LPF

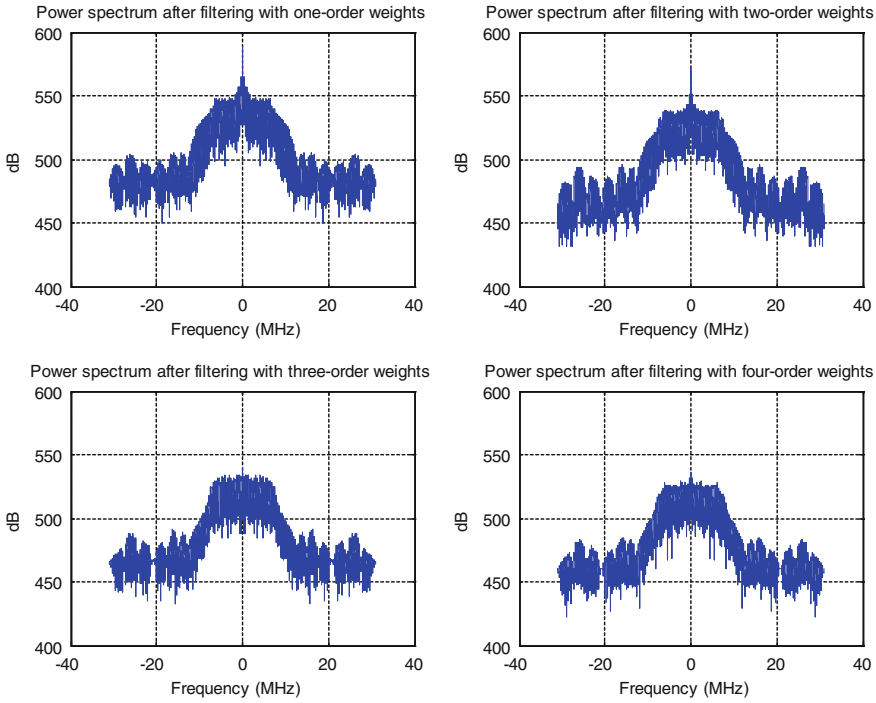

Fig. 8 Power spectrum (Gain) after filtering with improved weights

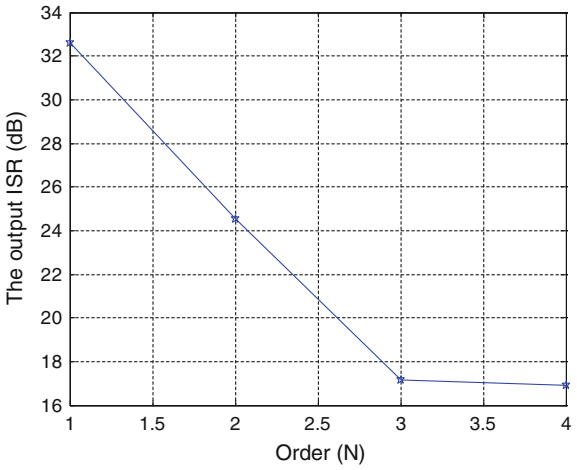

Fig. 9 The output ISR of different order weights

to filter interference. One can also see that the narrowband interference has been suppressed when use third-order and fourth-order weights to filter interference. The hybrid interference is suppressed effectively.

Figure 9 shows the output ISR after filtering with first-order, second-order, third-order and fourth-order weights proposed in this paper. From Fig. 9 one can see that the output ISR obviously improved after filtering with the third-order and fourth-order weights. As the satellite signals reached to the ground are quite weak, about 26 dB (at 20 MHz bandwidth estimation) lower than the receiver thermal noise, the results of Fig. 9 also confirmed that the hybrid interference has been effectively filtered out.

5 Summary

Focused on the issue that anti-jamming algorithm of SFAP will get failed when wideband and narrowband jammers exist at the same time and plural narrowband jammers in diverse directions fall into the same sub-band and the number of jammers exceeds the limitation that an antenna array can cope with, a new approach of SFAP is proposed to cope with concurrent narrow and wideband jammers. It determines the weights of each sub-band based on the data from itself and adjacent sub-bands. Computer simulation with an antenna model of four elements in Y-form shows that the method of filtering narrowband interference by multi-order weights proposed in this paper is obviously better than the method of filtering narrowband interference by threshold detection after FFT. The proposed approach improves the performance of SFAP significantly under concurrent narrow and wideband jammers and the increased implementation cost of the new approach is very small and can be negligible.

The future research is to analyze algorithm mechanism and the influence of the performance of weights order, and then the point is to analyze signal acquisition and tracking features on the receivers.

References

1. Guoqiang YU, Zhihe QIU (2000) Navigation and positioning: big dipper of the modern war [M]. National Defence Industry Press, Beijing
2. Kaplan ED, Hegarty CJ (2012) Understanding GPS principles and applications [M]. Publishing House of Electronics Industry, Beijing, p 96
3. Gupta IJ, Moore TD (2004) Space-frequency adaptive processing (sfap) for radio frequency interference mitigation in spread-spectrum receivers [J]. IEEE Trans Antennas Propag 52 (6):1611–1616
4. Godara LC (1995) Application of the fast fourier transform to broadband beamforming [J]. J Acoust Soc Am 98:230–240
5. Compton RT Jr (1988) The relationship between tapped delay-line and FFT processing in adaptive arrays [J]. IEEE Trans Antennas Propag 36(1):15–26
6. Yongliang W, Qianjun D, Rongfeng Li (2009) Adaptive array processing [M]. Tsinghua university Press, Beijing
7. Fante R, Vaccaro J (2000) Wideband cancellation of interference in a gps receive array [J]. IEEE Trans. Aerosp Electron Syst 36:549–564

Analysis and Simulation of Multi-beam Antenna Coverage for GEO Satellite Based on STK

Liangliang Guo, Yong Wei, Jianwen Li and Jun Zhao

Abstract Simulation analysis and modeling study of ground pointing and coverage characteristics of multi-beam antenna were presented for GEO communication satellite with small inclined angle which has the characteristics of short cycle, great visual range, and better flexibility. First, satellite positions were calculated based on the experiment of simulation of dynamics and orbital evolution. Secondly, the computational model of dynamic pointing of antenna based on offset control of attitude was obtained by analyzing these problems about the low-inclination orbit, the controlling of inclined orbit, and dynamic pointing of beam. Then the coverage rates were computed for different calibration stations and pointing deviation angle, respectively. The results show that the coverage rate of master control station was 100 % based on designed beam pointing when the orbit inclination equals 5.5°. However, under the same conditions, the coverage rate of auxiliary control station cannot achieve 100 % when azimuth angle and elevation angle are 0.4°. Finally, the process of verification about partial simulation was achieved by developing corresponding scenarios using STK, and it is proved that the research carried out in this paper is reliable.

Keywords Low-inclination orbit · Multi-beam antenna · Coverage · Modeling · Simulation · STK · Geostationary orbit satellite

L. Guo (✉) · Y. Wei · J. Li
Institute of Navigation and Aerospace Engineering, Information Engineering University, Zhengzhou 450001, China
e-mail: gllcumt@163.com

J. Zhao
Institute of Geospatial Information, Information Engineering University, Zhengzhou 450001, China

J. Sun et al. (eds.), *China Satellite Navigation Conference (CSNC) 2016 Proceedings: Volume II*, Lecture Notes in Electrical Engineering 389,
DOI 10.1007/978-981-10-0937-2_7

1 Introduction

Satellite communication is an important means of modern communication, which is attached to the advantages of large communication capacity, wide coverage, real time, high speed, and convenience. Currently, the realization of mobile satellite communication technology mainly adopts geostationary orbit satellite. In order to improve the effective utilization of the satellite, extend the use of time of the satellite or save fuel of the satellite, the scheme of using low-inclination orbit was usually implemented [1–3]. Along with a variety of development of wireless communication technology, spectrum space is getting increasingly crowded and there is a strong lack of available spectrum resources. Multiple-frequency reuse, spatial segregation, and polarization isolation of beam can be achieved by using multi-beam antenna on the GEO satellite. Meanwhile, the application of multi-beam antenna expands the available bandwidth and highly increases the transmission capacity so that the limited spectrum resources have been fully and effectively utilized.

Most of the existing antennas of satellite mobile communication system provide service via the multi-beam mode. Although the satellite can correct beam pointing deviation based on its own control system, it still cannot meet the requirements of beam pointing deviation of application system. Therefore, we need specific beam calibration system to improve beam pointing accuracy further. Many researches on coverage problems of the satellite multi-beam antenna have been conducted at home and abroad. Liu (2012) mainly made a detailed analysis about design and performance of multi-beam antenna for regional coverage of GEO [4]. Zhu et al. (2010) developed the mathematical model of covering service area using multi-beam antenna based on alternative approach of coordinate and realized the real-time dynamic effect of coverage of satellite multi-beam antenna under introducing orbit parameters and attitude parameters [5]. Considering offset control of attitude, Chen et al. (2014) established the optimization model of coverage and ameliorated the properties of coverage in service [6–8]. Han et al. (2015) intensively studied the influence of the attitude of GEO communication satellite on the pointing of spot beam antenna and combined the posture change of satellite with the communication of spot beam to enhance the reliability of the communication of spot beam [9].

The researches on the real-time pointing of multi-beam antenna and the properties of coverage in this paper are conducted based on coordinate transformation methods, which are fully considering the factors of orbit parameters of satellite, attitude-biased parameters, and the limitation of view. Then the computation method and simulation model are proposed. Meanwhile, an engineering example with antenna's coverage of one satellite is brought to show real timely the dynamic results of directional points on ground, which is very important to control beam pointing of mobile communication system.

2 Multi-beam Antenna Pointing Model with Controlling Attitude Offset

2.1 Definition of Coordinate System and Mutual Transformation

The five coordinate systems are involved in the process of establishing the beam pointing model. They are the terrestrial coordinate system $O_e = X_e Y_e Z_e(S_e)$, the equatorial geocentric inertial coordinate system $O_i = X_i Y_i Z_i(S_i)$, the satellite centroid orbit system $O_o = X_o Y_o Z_o(S_o)$, the southeast coordinate system $O_d = X_d Y_d Z_d(S_d)$, and the satellite body-fixed coordinate system $O_b = X_b Y_b Z_b(S_b)$, respectively. The definitions of these coordinate systems S_e,S_i,S_o and S_b can be found in the [10]. The coordinate system S_d is defined as follows: (Fig. 1)

Based on the definition of each coordinate system, the transformation matrices between different coordinate systems are shown as:

$$C_{ie} = R_z(-t_G) \tag{1}$$

$$C_{oi} = R_y(-u - \pi/2)R_x(i - \pi/2)R_z(\Omega) \tag{2}$$

$$C_{do} = R_z(\psi) \tag{3}$$

$$C_{bd} = R_y(\theta)R_x(\varphi) \tag{4}$$

where C_{ie} represents the transformation matrix from S_e to S_i; C_{oi} represents the transformation matrix from S_i to S_o; C_{do} represents the transformation matrix from S_o to S_d; C_{bd} represents the transformation matrix from S_d to S_b; t_G is the Greenwich right ascension; μ is the argument of latitude; Ω is the right ascension of satellite

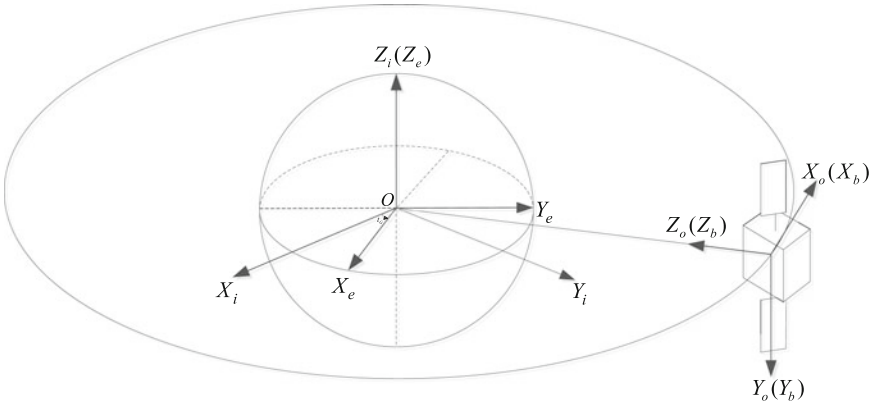

Fig. 1 The relationship between the different coordinate systems

ascending node; i is the orbital inclination; Ψ is the yaw angle; θ is the pitch angle; φ is the roll angle; R_x, R_y and R_z are the primitive rotation matrix for X-axis, Y-axis and Z-axis, respectively.

2.2 Computation of Intersection Point of Beam Pointing and Earth

In order to reduce the complexity of structural design of the satellite and accomplish continuous coverage for the service area in the alignment calibration system of beam for satellite mobile communication, let one beam of satellite unvaryingly point master control calibration station. Then, we maintain the pointing of another beam to auxiliary control calibration station through offset control of attitude. In this way the coverage of master control station and auxiliary control station are achieved. The covering theoretical model of multi-beam antenna pointing based on attitude regulating of satellite is proposed and expressed as follows:

By selecting the coordinate system S_d as the reference of attitude control and making full use of spherical triangle, the regular pattern of offset control

$$\psi = \text{arc tan}(\tan(i)\cos(u)) = \text{arc tan}(i\cos(\omega + f)) \tag{5}$$

is established with considering low-inclination orbit.

If the coordinates of the ground point that GEO satellite antenna points to the master control station are defined as (x_{e0}, y_{e0}, z_{e0}) and (x_{e1}, y_{e1}, z_{e1}) while the coordinates of satellite in the terrestrial coordinate system are given as $\left(x_{e0}^S, y_{e0}^S, z_{e0}^S\right)$ and $\left(x_{e1}^S, y_{e1}^S, z_{e1}^S\right)$ at the time t_0 and t_1, respectively, the pointing vectors $\overrightarrow{r_{e0}}$ and $\overrightarrow{r_{e1}}$ can be derived easily.

If we project the pointing vectors $\overrightarrow{r_{e0}}$ and $\overrightarrow{r_{e1}}$ to the southeast coordinate system, the pointing vector of $\overrightarrow{r_{d0}}$ and $\overrightarrow{r_{d1}}$ in coordinate system S_d can be formed and computed by

$$\begin{cases} \overrightarrow{r_{d0}} = C_{do}C_{oi}C_{ie}\overrightarrow{r_{e0}} \\ \overrightarrow{r_{d1}} = C_{do}C_{oi}C_{ie}\overrightarrow{r_{e1}} \end{cases} \tag{6}$$

It is required that one beam of satellite always points to the master control station, thus the attitude adjustment to satellite is essential. The X_b-axis of the satellite body-fixed coordinate system points to due east after the controlling of the yaw angle. The further fulfillment with perpetually pointing to the master control station need the conversion of pitching and rolling. That is the transformation process from the satellite body-fixed coordinate system to the southeast coordinate system. The transformation relationship from the southeast coordinate system to the satellite body-fixed coordinate system is as follows:

$$\begin{bmatrix} x_b \\ y_b \\ z_b \end{bmatrix} = \begin{bmatrix} \cos\theta & 0 & -\sin\theta \\ 0 & 1 & 0 \\ \sin\theta & 0 & \cos\theta \end{bmatrix} \begin{bmatrix} 1 & 0 & 0 \\ 0 & \cos\varphi & \sin\varphi \\ 0 & \sin\varphi & \cos\varphi \end{bmatrix} \begin{bmatrix} x_d \\ y_d \\ z_d \end{bmatrix} \tag{7}$$

where φ and θ are the offset angle of roll and pitch, respectively. When satellite is located in initial locations, three attitude parameters can be obtained as zero, namely $\overrightarrow{r_{b0}}$ is equal to $\overrightarrow{r_{b1}}$. Hence, we can find the required offset angle of attitude about rolling and pitching which insure the pointing to the master control station from one beam of satellite.

$$\begin{bmatrix} \varphi \\ \theta \end{bmatrix} = \begin{bmatrix} \arcsin(y_a/\sqrt{y_b^2+z_b^2}) - \arctan(y_b/z_b) \\ \arcsin(x_b/\sqrt{x_a^2+z_a^2}) - \arctan(x_a/z_a) \end{bmatrix} \tag{8}$$

Another beam points to the auxiliary control station at time t_0 that is a known value. Then the transformational relationship based on the offset control of attitude of the master control station is applied to the auxiliary control station so that the longitude and latitude of the ground at which another beam is pointing at time t_1 are to be determined. The pointing vector through iteration in its inertial system can be prepared for next calculations of latitude and longitude.

The vector triangle is composed of geocentric, satellite, and the intersection point with another beam center directing the earth. The vector equation is formed as follows:

$$\overrightarrow{r_{OF}} = \overrightarrow{r_{OS}} + \overrightarrow{r_{SF}} \tag{9}$$

where $\overrightarrow{r_{OF}}$ denotes the directing vector from geocentric to the intersection; $\overrightarrow{r_{OS}}$ denotes the directing vector from geocentric to satellite; $\overrightarrow{r_{SF}}$ denotes the directing vector from satellite to the intersection (Fig. 2).

The pointing vector of another beam in the inertial system S_i is described as $[x_{i1}^f, y_{i1}^f, z_{i1}^f]^{\mathrm{T}}$ at time t_1, its unit vector has been given. Moreover, the geodetic latitudes and longitudes of the intersection of beam pointing and the earth are marked as (λ, ϕ). (x_i^S, y_i^S, z_i^S) denotes the satellite position in the equatorial geocentric inertial coordinate system. Then, those values are substituted in vector equation.

$$R_E \begin{bmatrix} \cos\phi\cos(\lambda + t_G) \\ \cos\phi\sin(\lambda + t_G) \\ \sin\phi \end{bmatrix} = \begin{bmatrix} x_i^S \\ y_i^S \\ z_i^S \end{bmatrix} + \left|\overrightarrow{r_{SF}}\right| \begin{bmatrix} x_{i1}^f \\ y_{i1}^f \\ z_{i1}^f \end{bmatrix} \tag{10}$$

In the above equation, R_E is the radius of the earth; $\left|\overrightarrow{r_{SF}}\right|$ represents the distance from satellite to the ground directing point; λ, ϕ, and $\left|\overrightarrow{r_{SF}}\right|$ are unknown variables.

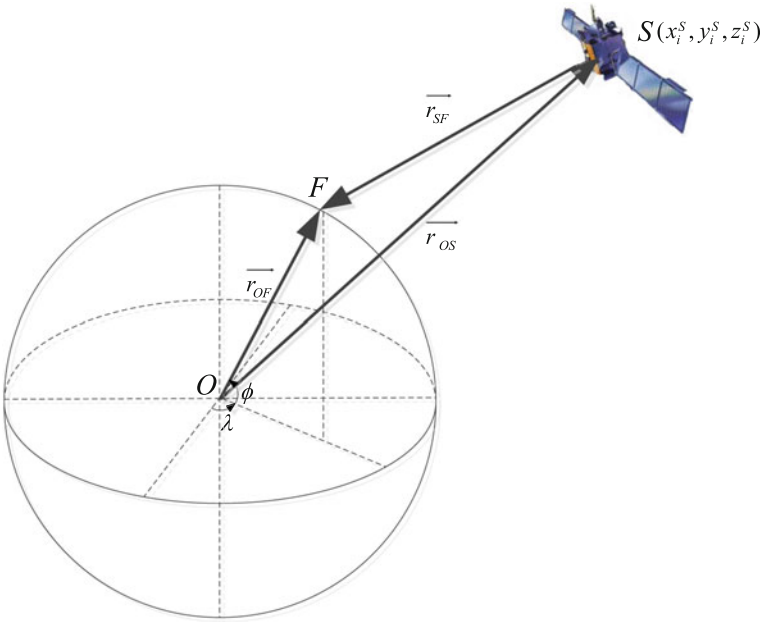

Fig. 2 The relationship between the vectors

The distance from satellite to the ground directing point based on above three equations is as below:

$$\left|\overrightarrow{r_{SF}}\right| = -\left[x_{i1}^f, y_{i1}^f, z_{i1}^f\right]^{\mathrm{T}} \cdot \left[x_i^S, y_i^S, z_i^S\right]^{\mathrm{T}} + \sqrt{x_i^S \cdot x_i^S + y_i^S \cdot y_i^S + z_i^S \cdot z_i^S - R_E^2} \tag{11}$$

Furthermore, we can compute (λ, ϕ) by

$$\begin{cases} \lambda = \arctan\left(\left(y_i^S + \left|\overrightarrow{r_{SF}}\right| y_{i1}^f\right) / \left(x_i^S + \left|\overrightarrow{r_{SF}}\right| x_{i1}^f\right)\right) - t_G \\ \phi = \arcsin\left(\left(z_i^S + \left|\overrightarrow{r_{SF}}\right| z_{i1}^f\right) / R_E\right) \end{cases} \tag{12}$$

The results attained from the above formula are really the geodetic latitude and longitude of the intersection of each sub-beam pointing and the earth when the satellite is in any orbital location. So, the above process can be used to analyze the dynamic coverage of multi-beam antenna of GEO satellite on low-inclination orbit. In addition, the trajectory of ground points of another antenna beam with pointing initially to the auxiliary control station can be obtained based on the computational model in this section under the condition that one beam points fixedly to the master control station.

3 Antenna Coverage Analysis

The coverage problems of satellite multi-beam antenna focus mainly on studying the relationship between beam coverage angle and beam coverage area. If we want to fulfill coverage for calibration station on the ground, it is necessary to adjust beam pointing angle and beam coverage angle in satellite transponder. During the process of analyzing coverage performances, the directing range of beam is affected by beam pointing angle, while the beam coverage area is depended on beam coverage angle.

Assuming the point A and B stand for the master calibration station and the auxiliary calibration station, respectively, we can solve the ground point location of another beam at each moment according to the computational flow of ground directing point described in Fig. 3 when one beam of satellite always point the A. The pointing vector of beam central visual axis is derived by combining satellite position with the coordinate of ground directing point every moment. Then, we can separately compute the angle of two pointing vector at every instant based on the vector that the satellite points to the master calibration station, as shown in Fig. 4. The circular beam is taken as an example, and obviously when the angle of two pointing vector is lesser than the angle of circular beam half angle, it can be indicated that the auxiliary calibration station is in the beam, namely the covered state.

In the calculated process, this paper does not directly calculate the spatial angle between the two directional vectors, but transfers firstly the two directional vectors respectively to the satellite body-fixed coordinate system. Then the azimuth angle and the elevation angle of the corresponding directions in body-fixed coordinate system are computed according to formula 13. In the end, we can determine

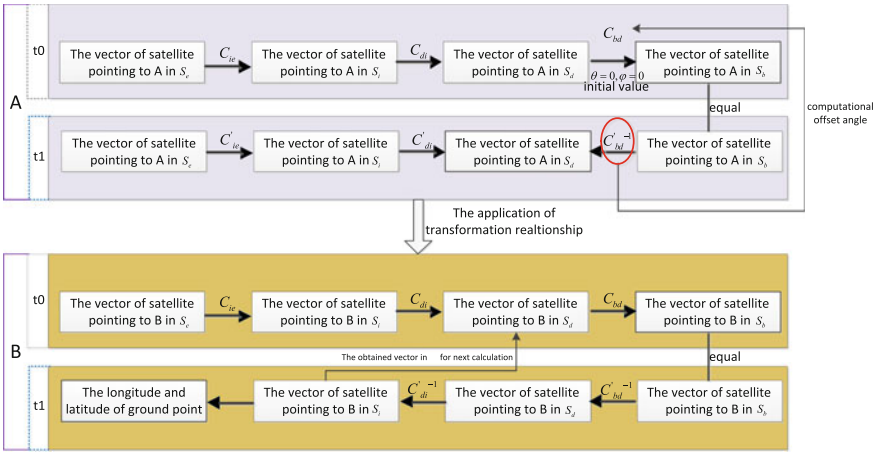

Fig. 3 Ground point calculation process of beam center los

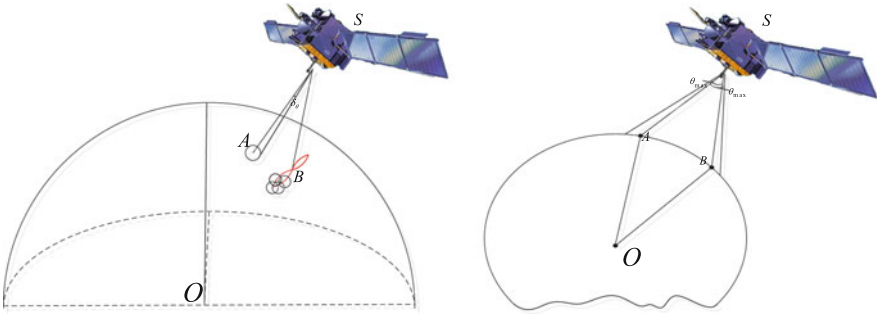

Fig. 4 Coverage analysis of main auxiliary calibration station

whether the master and auxiliary calibration station at this time stays in the covered state or not through threshold value.

$$\begin{cases} \alpha = \arcsin(y) \\ \beta = -\arctan(x/z) \end{cases} \tag{13}$$

In the above formula, α and β denote azimuth angle and elevation angle of the pointing vector, respectively; (x,y,z) is the pointing vector.

4 Example of Calculation and STK Simulation

This section will set up the simulation scene by STK 10.0 and complete the verification of partial simulation about the above process based on the trajectory calculation of ground point directed by beam main axis of sight and the theoretical analysis on the coverage of antenna [11, 12].

4.1 Trajectory of GEO Satellite Multi-beam Antenna Pointing in the Terrestrial Coordinate System

Computational parameters of the example are set as follows: the simulation time is from 20 May 2015 04:00:00 to 21 May 2015 04:00:00; the longitude of the stationary position of GEO satellite is 101.4°; the dynamic model is HPOP; the orbit inclination angle is 5.5°; the angle of circular beam half angle is 0.3°. The example chooses one master calibration station and seven auxiliary calibration stations to calculate. Their coordinates in the terrestrial coordinate system are *P*0(-1333909.546, 5326251.416, 3234479.112), *P*1(−2630791.785, 5233022.358, 2516419.324), *P*2(202128, 4629480, 4367960), *P*3(-2900330, 3505900, 4454620),

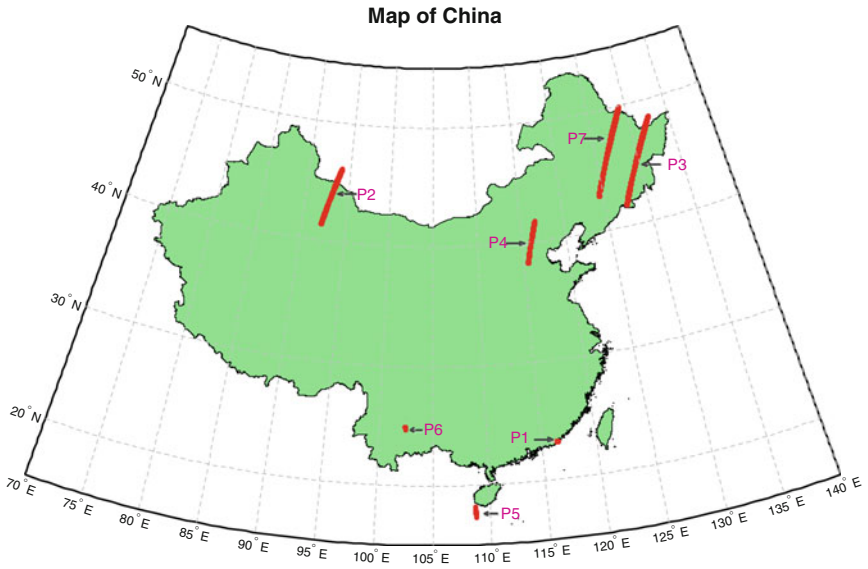

Fig. 5 Ground track of auxiliary calibration station

*P*4(−2170980, 4392640, 4069470), *P*5(−1975520, 5737320, 1958380), *P*6 (−1271280, 5641130, 2682090), and *P*7(−2649570, 3580560, 4549780). The location of satellite is obtained with sample interval 10 s. Moreover, the former and later epochs are t0 and t1, respectively.

The ground trajectory diagram of the auxiliary calibration station P1–P7 as shown in Fig. 5 can be got through programming calculation based on the preceding, given the computational procedures of the intersection of beam pointing and the earth, while the ground trajectory diagram by the simulation of STK can be found in Fig. 6.

The Figs. 5 and 6 show that the derivable directional regular pattern of the sub-beam central visual axis based on the analysis with selecting day as the orbital period, namely the ground trajectory of each auxiliary calibration station, is basically consistent with the simulation results of commercial software STK. Therefore, the pointing model of multi-beam antenna for controlling the offset of attitude built by the paper is reliable.

4.2 Coverage Analysis of GEO Satellite Multi-beam Antenna

The coverage scope of satellites is usually divided into many regions in multi-beam satellite communication system. We can equivalently design the following scheme

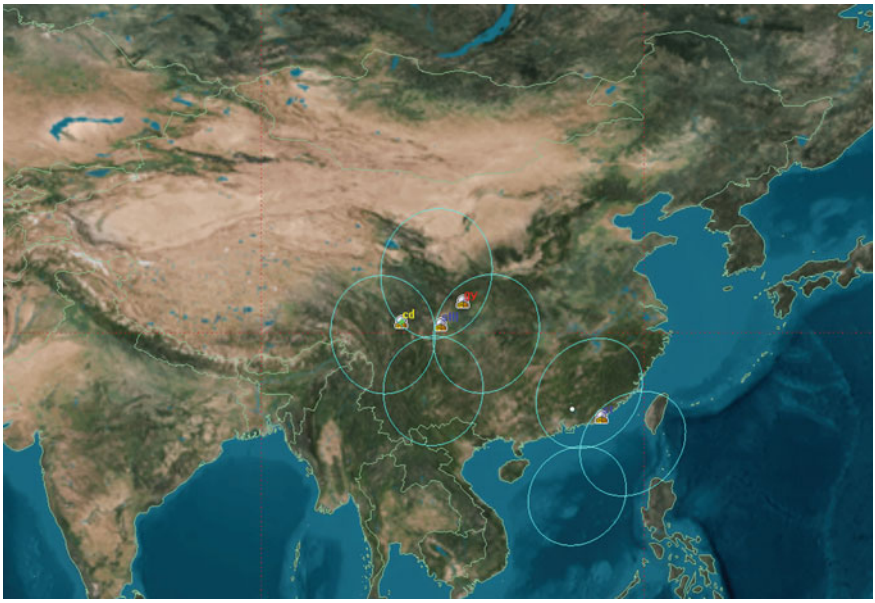

Fig. 6 Ground track of auxiliary calibration station based on STK

on the public earth surface covered by multiple beams based on the simulation experiment in part 1.4.1. We need, firstly, to compute the azimuth angles and the elevation angles of directional vector that the satellite points to the master calibration station and the auxiliary calibration station in the satellite body-fixed coordinate system, respectively. Then, we separately make difference to the azimuth angle and elevation angle. If the difference is greater than −0.4 and is lesser than 0.4, the coverage can be realized, otherwise it cannot be fulfilled.

We separately conduct the coverage analysis based on the 65 kinds of deviations as shown in Fig. 7, which take threshold ± 0.4° as criterion and define 3 days as the period. In the process of analysis, we introduce the coordinates of the master calibration station and the auxiliary calibration station in the terrestrial coordinate

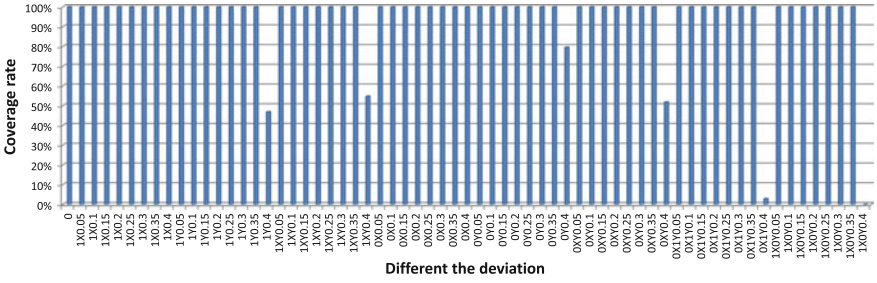

Fig. 7 Beam coverage of different deviations based on auxiliary calibration station

system and compute the coverage rate by programming when the values of deviation angle are different. The results show that the coverage rate of master control station was 100 % based on designed beam pointing when the orbit inclination equals 5.5°. However, under the same conditions, the coverage rate of auxiliary control station cannot achieve 100 % when azimuth angle and elevation angle are 0.4°.

Notes: 0 and 1 in front of *X*, *Y*, or *XY* denote the positive bias and the negative bias, respectively; *X* is the azimuth angle; *Y* is the elevation angle.

5 Conclusions

The paper mainly focuses on studying the pointing trajectory of multi-beam antenna of GEO satellite and provides the approach for determining the coverage of beam under the condition of considering the offset control of attitude and the method of coordinate transformation based on the satellite data offered by STK. The computational results by the method proposed in this paper are consistent with STK simulation, which proves the correctness of the theoretical model and the feasibility of coverage analysis. Therefore, the certain theoretical basis and reference can be provided for the pointing calibration of satellite beam and the design of multi-beam antenna of GEO satellite in low-inclination orbit.

References

1. Rao S, Hsu CC, Wang J (2010) Common aperture satellite antenna system for multiple contoured beams and multiple spot beams. IEEE Antennas Propag Soc Int Symp (APSURSI) 1–4
2. Rao S, Hsu CC (2008) Advanced multiple beam antenna system supporting multiple satellite communications services. Asia Pac Microwave Conf 2008:1–4
3. Letizia M, Zurcher JF, Fuchs B, Mosig JR, Skrivervik A (2011) Circularly polarized multi-beam lens antenna system for high altitude platforms. In: Proceedings of the 5th European conference on antennas and propagation, 1051–1055
4. Liu YA (2012) Geo satellite regional coverage multi-beam antenna design and performance analysis. Harbin Institute of Technology 72
5. Zhu JF, Li WH, He XS (2010) Modeling and simulation research on coverage characteristic of satellite multi-beam antenna. Commun Counter measures 110(2):32–35
6. Chen YJ, Zhou ZC, Qu GJ (2014) Coverage optimization of inclined geo satellite with multi-beam antenna. Chinese Space Sci Technol 1:10–17
7. Loh YP On antenna pointing control for communications satellite. AIAA-92–1940-CP:976–986
8. Liu Y, Liu G, Wu S (2006) Spot beam judgement algorithm of low earth orbit satellite mobile system. Chinese Space Sci Technol 26(3):59–66

9. Han X, Guo XZ, Qu HP (2015) Impact of attitude movement on spot beam pointing for geo communication satellites. J Spacecraft TT&C Technol 34(1):77–82
10. Qu GJ (2000) Spacecraft dynamics engineering. China Science Technology Press, Beijing
11. Bao K, Xu K, Xiang SX (2013) Analysis and simulation of spot beam coverage based on STK. Commun Technol 46(1):17–19
12. Yang Y, Wang Q (2005) Application of STK in computer simulation. National Defense Industry Press, Beijing, pp 124–132

Method of Navigation Message Broadcast Performance Analysis for GNSS

Jinxian Zhao, Jinping Chen, Caibo Hu, Dongxia Wang, Zhixue Zhang, Chunxia Liu and Wei Zhao

Abstract Navigation message is one of the basic data for the user to realize positioning. It is send to all users by the navigation signal and realizes the position and time function. The navigation message includes ephemeris prediction parameter, clock error prediction parameter, ionosphere delay model parameter, difference information, etc. The rationality of navigation message design relates directly the position efficiency, agility, and utilization ratio of channel link resource. The main factors of influencing performance of navigation message include navigation information parameter model, the message layout structure, message broadcast mode, channel error correction coding, etc. The message layout structure, the navigation message channel error correction coding, and message broadcast pattern associated with the message broadcast situation can be summarized to the navigation message broadcast performance. Navigation information parameter model is directly related to the user equivalent range error, and can be concluded to the user's using performance. Based on analyzing the performance element of navigation message, this paper deeply studied and analyzed the method of navigation message broadcast performance evaluation, and the calculated result is about GNSS at home and abroad. It supplies the basis for navigation message design of global satellite navigation system for our country.

Keywords Satellite navigation system · Navigation message · Message structure · Analysis of performance

1 Introduction

Navigation message is the important part of the satellite navigation signal, and it is made of ephemeris, clock error, correct parameter of ionosphere delay, almanac, differential correction, integrity, etc. These data are broadcast to user through

J. Zhao (✉) · J. Chen · C. Hu · D. Wang · Z. Zhang · C. Liu · W. Zhao
Beijing Satellite Navigation Center, Beijing 100094, China
e-mail: jinxian_zhao@sohu.com; 119481390@qq.com

J. Sun et al. (eds.), *China Satellite Navigation Conference (CSNC) 2016 Proceedings: Volume II*, Lecture Notes in Electrical Engineering 389,
DOI 10.1007/978-981-10-0937-2_8

satellite signal by means of binary data flow. The design of navigation message needs to insure the precision of parameter, timeliness of message, data transport rate and reliability, utilization ratio of link resource, expandability, and so on.

Design of navigation message takes the key role for the user performance; it is the basement of navigation and position. The content and structure of the navigation message also have a great influence on the design of receiver, the format of model and navigation parameter is different, and the algorithm of navigation and positioning is different. So, the contents of the navigation message and structure design are very important, and directly affect the whole satellite navigation system work way, the performance, and the design of the user, involving many aspects.

Navigation message structure in GPS NAV and GLONASS adopted the frame structure, and in modernization GPS and GALILEO, it has conducted a series of improvements from the message content and the parameters model to the message structure [1–4]. Result shows that the navigation message performance of different systems and the structure are different. Based on analyzing the performance element of navigation message, this paper deeply studied and analyzed the method of navigation message broadcast performance evaluation, and the calculated result is about GNSS at home and abroad.

2 Navigation Message Performance Factors

Navigation message design mainly includes the message content and its parameter model, the message layout structure, message broadcast mode, channel error correction coding, etc. So, we will focus on the above four aspects to carry out the navigation message performance analysis.

2.1 Message Content and Parameter Model

In order to realize the user function of PVT, message content broadcast by satellite system includes basis navigation message that desires high timeliness consisting of satellite ephemeris, clock error, satellite health, and so on. For aiding user capturing satellite signal, message includes non-timeliness extend navigation content such as almanac, and for improving the precision of navigation, some satellite system navigation message add the differential correction and integrity data. Therefore, the navigation message can be summarized as three types of information type:

1. Basic navigation information: ephemeris, clock error, correct parameter of ionosphere delay, satellite basic integrity information (including satellite health information and signal accuracy), UTC time deviation, as well as satellite channel time delay, etc. Such information is mainly used to meet the needs of the most basic navigation services, namely single-frequency and dual-frequency

single-point positioning services or multiple-frequency single-point positioning services.
2. Extended navigation information: almanac, earth orientation parameters of EOP, GNSS time deviation. It is mainly used to meet other than basic navigation service and enhanced service needs. The almanac information is mainly used for users to search satellite, EOP parameters for the user to calculate the satellite position transformation of different coordinate systems.
3. Enhanced navigation information: ephemeris difference correction, clock difference correction and the ionosphere correction of the grid, difference integrity information, etc. Such information is mainly used to meet the single-frequency or multifrequency wide-area enhanced service.

Various types of navigation information are broadcast to users in data model parameters, therefore the data expressed model for parameters is critical for system performance. In all kinds of navigation information, satellite position and clock error information is the core of the navigation message, its representation directly determines the accuracy of satellite orbit and clock, communication efficiency, etc.

2.2 Navigation Message Layout Structure

Navigation message layout structure refers to the reasonable arrangement for different types of data in the position of the message and the overall structure of the navigation message after determining the navigation message content composition, the navigation message parameter model expression, and makes the system to achieve optimal performance. It is a complicated system engineering, involving positioning principle and implementation technology, communication technology, and many other aspects. There are many factors to consider, the main factors are the following:

1. The determination of basic unit used in the message structure
   Message structure basic unit is the minimum length required in the message structure, such as the word in GPS NAV, the string in GLONASS, and the subframe in GALILEO system navigation message, and so on. It mainly depends on the navigation message parameters, real-time requirements, information rate, data update cycle, repetitive cycles, and other factors.
2. The overall structure design of navigation message
   The overall structure design of the navigation message is the overall arrangements for the message, it is the key step to solve the contradiction between the flexibility and data processing workload of user. Overall structure can be determined according to the total amount, the data updating period, data transmit rate, and the time user receiving all data. The existing message structure of the satellite navigation system such as GPS NAV [1] and GLONASS civil signal [5] used the fixed structure, its characteristic is that the data arrangement is with

subframe, frame, and superframe. There are strict corresponding relation between data and time. Also there is a block of data structure based on information type, such as new civilian GPS navigation message CNAV [2]. Others use the frame structure combined with a data block, such as GALILEO F/NAV [4].

3. Timing relationship between the navigation message and the system time
   Timing relationships between navigation message and the system time should consider two aspects. One is how to establish the relationship between the data frame and system time that makes the user to know the system time after receiving the navigation message. The other hand is that whether there is a fixed relationship between the navigation message and the system time. If there is a fixed relationship between message and the system time (such as GPS NAV), the navigation message need not set the data identification code, that is benefit to reduce the total amount of data, but the message structure is relatively fixed, the possibility of the modification is small. If the message and the system time have no fixed relationship, you must increase the data identification code (e.g., GPS CNAV).

For the navigation message structure, first the overall structure of the message is determined considering the various factors, and then the repetition cycle of the data should be confirmed combining the timeliness of data, at last the location of the various data of the message should be arranged reasonably.

2.3 Navigation Message Broadcast Pattern

During the navigation message broadcast pattern design, at first, the navigation message parameters constraints must be taken into account comprehensively, including the number of frequencies of the message broadcast used and real-time requirements of parameters, which determine the navigation message broadcast period and update period. From the parameters of the navigation message itself, the navigation message broadcast mode is restrained by real time of the information, functional requirements, physical properties, coupling, and self-consistent of the parameters, and it will also be affected by the signal system, the service performance requirements, and so on. So, considering the system information link resource, the design constraints of the navigation message broadcast pattern mainly include the following aspects: (1) the information rate, (2) the frequency points of the message broadcast, (3) the number of signal branches that broadcast message, (4) the navigation message layout structure; (5) system service performance requirements, (6) message parameters real-time requirements, etc. After determining various constraint conditions, the navigation message broadcast mainly involves two aspects: one is the order of each satellite navigation message broadcast and the other is the relative broadcast order design between the satellite and frequency [6, 7].

1. The navigation message broadcast order

The navigation message broadcast order refers to the broadcast moment of the different information contents, and it is influenced by the repetition period and update cycle of the parameters, the message layout structure, etc. Usually navigation message broadcast sequence in repeated period is the same, and in each update cycle, the corresponding information content can be broadcast at least once. For the fixed frame structure of the navigation message, the broadcast sequence is fixed, such as GPS NAV and GLONASS message structure. It is very conducive to users, but the flexibility and the message broadcast information link resources utilization rate are relatively low. Data block structure of navigation message broadcast order is relatively flexible, and it is only satisfied that the corresponding information in the update cycle can be broadcast one time. In an update cycle, the broadcast sequence of the different information can be different, such as GPS CNAV that can improve the flexibility of the message broadcast and the link utilization rate. For the combining format of the fixed frame structure and data block structure, such as GALILEO F/NAV, with the advantages of two kinds of layout structure, not only guarantees the update cycle of relatively high real-time basic navigation information, but also meets the needs of broadcast randomness of the non-real-time message.

2. Relative broadcast order between the satellite and frequency

Relative navigation message broadcast order between the satellite and frequency mainly refers to the broadcast order between different satellites and different frequencies, that is to say, the navigation message can be broadcast to the user through different frequencies and different satellites, and even different branches. Early GPS and GLONASS only have one frequency signals for civilian user, so there is no relatively broadcast order between frequencies. The message different satellite broadcast is about the same at one moment. When the information content is the same, such as correct parameter of ionosphere delay and almanac, there will be a waste and information redundancy phenomenon. After the modification of the GPS, in L1C, L2, and L5 frequency broadcast new civil signal, COMPASS and GALILEO system also broadcast public signal in multiple frequencies. Therefore, from optimizing the navigation message properties, the satellites and frequency cross broadcast way can be adopted to realize relative broadcast of the navigation message [4], such as almanac information can be broadcast between satellite, and the time of receiving all almanac can be shortened, EOP parameters and satellite time delay, can be broadcast between different frequencies that will shorten the user first positioning time and improve the users performance.

2.4 Navigation Message Channel Coding

Information in the process of transmission, affected by interference and power attenuation, gives error code. In order to ensure the navigation message

transmission reliability and improve antijamming, error control coding is usually used in the process of navigation message transferring to reduce the error rate. By adding redundancy in the message to determine whether there is an error in the process of transmission, on one hand can find errors and also can correct mistakes. Navigation message channel error correction coding from early hamming code to BCH code, and then development to the convolutional code and LDPC code, compiled code performance improves as the computing power and communication technology development. GPS NAV-adopted BCH code [1], GLONASS hamming code [5], GPS CNAV CRC + convolution code [2], GPS CNAV-2 BCH + LDPC + CRC + interweave [3], GALILEO system convolution + CRC + interweave [4]. The following table gives the performance characteristics of several common navigation message channel error correction codings (Table 1).

Table 1 Comparation of channel error correction coding for GNSS [8]

Coding	Definition	Performance
Hamming	Linear block code	• Higher coding efficiency, compiled code implementation simple • Error correction ability is limited, poor ability to resist burst error
BCH	Cyclic code, a subclass of the linear block code	• High coding efficiency, compiled code implementation simple • Error correction ability better than that of hamming code
Convolution	Supervise element is related with the information element of the current and former group	• Error correction ability better than that of block code, compiled code implement more complex than block code • Low coding efficiency
LDPC	Based on the parity check matrix of linear block codes	• Error correction ability close to theoretical limits, high coding gain, high error detection ability • Compiled code implementation complicated, low coding efficiency
CRC	Cyclic redundancy check code	• Error detection ability is very strong, and used to check burst error • Compiled code implementation simple
Interweave	By disrupting the original information sequence, bursted error will be transformed random errors	• Strong ability to resist burst error, no need to increase redundant information, coding efficiency unchanged • Decoder buffer and decoding delay increase

2.5 Summary

Through the above analysis, the main factors of influencing performance of navigation message include navigation information parameter model, the message layout structure, message broadcast mode channel error correction coding, etc. Therefore, the navigation message performance should be analyzed from the above four factors. The message layout structure, the navigation message channel error correction coding, and message broadcast pattern associated with the message broadcast situation, can be summarized to the navigation message broadcast performance, its specific performance is mainly manifested in the overall amount of the data within an information unit, Time to First Fix (abbreviated as TTFF), the time needed for user to receive a set of almanac data, the scalability of the message structure, channel link resource utilization, etc. Navigation information parameter model is directly related to the user equivalent range error(abbreviated as UERE), and can be concluded to the user's using performance, its specific performance can be achieved from all the message interaction effects, and also be analyzed from each respective information precision included in the message.

3 Navigation Message Broadcast Performance Evaluation Method and Case Analysis

Navigation message broadcast performance element is impacted on the performance differently, also each factor evaluation method is different. Some can make quantitative analysis, such as the required amount to send, information link resources utilization rate, some to quantitative analysis, such as extensibility of the message structure. Therefore, this article will assess the navigation message broadcast performance from the perspective of both qualitative and quantitative.

At present, the global satellite navigation system being built or building mainly includes the GPS, GLONASS, GALILEO, and COMPASS. The navigation messages of different systems are different. The following will analyze the navigation message broadcast performance of each system according to the methods putting forward before.

3.1 The Total Amount of Data Within the Information Unit

In the navigation message, all the information shall be broadcast at least once in a repeated cycle. So, the amount of data in an information unit is the amount of all the information content (except individual information such as text) broadcast once during the repeated cycle. Due to the different real-time and function requirements of the information, some information is broadcast only once in a unit, others are to

be repeated several times. If there are 'a' types of data, and have m_b (bits) in the 'b' number (b = 1, 2,…, a) type of data, within a information unit repeated time is j_n, and the total amount d_t (bits) can be calculated as expressions below:[9].

$$d\_t = \sum_{b=1}^{a} m_b \bullet n_b \tag{1}$$

According to the above expressions, we can see that the total amount of data is related with broadcast information type number and repeat time. The more the type number and the repeat time is, the greater the amount of data. The greater the amount of data required to broadcast in a fixed period of time, the higher the required information rate.

GPS consists of three types of navigation message: C/A code navigation message (also known as NAV) and C code navigation message (CNAV-2) in L1 frequency, and navigation message (CNAV) [1, 2, 3] in L5 frequency and L2 frequency. NAV is a fixed structure [1] made of superframe, frame, subframe, and every information unit consists of a superframe. Each superframe is made of 25 frames, each frame of 5 subframes, each subframe of ten words, each word of 30 bits. NAV information rate is 50 bps, repetition period of basic navigation information is 30s, almanac is 12.5 min. Therefore, the duration of an information unit is 12.5 min, and the total amount of data is 37,500 bits. CNAV adopts data block structure [2], the block length is 300 bits. Information type of data blocks is divided according to the different functions and real-time demands. CNAV currently consists of 15 kinds of information type, and information type extensible, and broadcast frequency of information types can be controlled through the ground. CNAV information rate is 50 bps, basic navigation information repeated cycles is 48s, almanac update period is 10 min. Therefore, the duration of an information unit is 10 min, and the total amount of data is 30,000 bits. CNAV-2 uses the message layout structure of fixed frame combined with a data block [3], and the frame is the basic format, each frame is composed of three subframe of different lengths. Each frame data length is 883 bit, and is broadcast in 18 s. Repetition period of the basic navigation information is 18s, Almanac repetition period is 15 min. Therefore, the duration of an information unit is 15 min, and the total amount of data is 44,150 bits.

GLONASS navigation message is a fixed layout structure made of superframe, frame, and string [5], each information unit consists of a superframe. Each superframe is made of 5 frames, each frame is 15 strings, and each string is made up of 100 bits. Repetition period of the basic navigation information is 30s, almanac repeated period is 2.5 min. Therefore, the duration of an information unit is 2.5 min, and the total amount of data is 7500 bits.

GALILEO navigation message includes F/NAV in E5a frequency, I/NAV in E5b and E1-B, and C/NAV in E6-B [4]. C/NAV mainly provides business services, and at present not announced specific message content. F/NAV uses message layout structure made of a fixed frame that consisted of frame, subframe, page, combined with a data block. Each frame is made of 12 subframes, each subframe is 5 pages,

and each page is made up of 256 bits. F/NAV contains 6 types of pages. In order to make the user to get all the satellite almanac in a shorter time, almanac is broadcast alternating between the satellites at the same time. Repetition period of the basic navigation data is 50s, each satellite almanac repeat period is 20 min. Therefore, the duration of an information unit is 20 min, and the total amount of data is 30,720 bits.

COMPASS uses message layout structure made of a fixed frame that consisted of superframe, frame, and subframe, combined with a data block [10]. Each information unit is composed of a superframe for MEO/IGSO satellites, and each superframe is made of 24 frames, each frame is 5 subframes, each subframe is ten words, and every word is made up of 30 bits. Repetition period of the basic navigation data is 30 s, almanac repeated period is 12 min. Therefore, the duration of an information unit is 12 min, and the total amount of data is 36,000 bits for MEO/IGSO. Each information unit is composed of a superframe for GEO satellites, and each superframe is made of 120 frames, each frame is 5 subframes, each subframe is ten words, and every word is made up of 30 bits. Repetition period of the basic navigation data is 30s, almanac repeated period is 6 min. Therefore, the duration of an information unit is 6 min, and the total amount of data is 180,000 bits for GEO.

3.2 The TTFF of User

User positioning time for the first time refers to the total time needed for the user from starting the work to finishing PNT calculating. The result is related with the navigation signal structure, capture performance of the user terminal, and other factors. Main purpose of this paper is to evaluate the performance of the navigation message structure, so TTFF here refers to the time from the start to receive navigation message to receive all the data required to PNT calculating. The complete information for PNT calculating includes basic navigation information such as satellite ephemeris prediction parameters, clock error prediction parameters, the ionosphere delay model parameter, satellite time delay, etc. TTFF is determined by the total data amount of basic navigation information, repetitive cycles, the information rate, and other factors.

Assuming that the data amount of basic navigation information is data_num (bits), the information rate is rate (bps), repetition period for basic navigation information is period (s), TTFF can be calculated through formula as below: [9] :

$$\begin{aligned} \mathrm{TTFF}_{\min} &= \mathrm{data\_num}/\mathrm{rate} \\ \mathrm{TTFF}_{\max} &= \mathrm{period} + \mathrm{data\_num}/\mathrm{rate} \\ \mathrm{TTFF}_{\mathrm{ave}} &= \frac{1}{2}(\mathrm{TTFF}_{\min} + \mathrm{TTFF}_{\max}) \end{aligned} \tag{2}$$

Table 2 The TTFF for user (s)

Navigation message	TTFF min	TTFF max	TTFF ave
GPS NAV	18	48	33
GPS CNAV	36	84	60
GPS CNAV-2	18	36	27
GALILEO F/NAV	40	90	65
GLONASS	10	40	25
COMPASS	18	48	33

When the TTFF is counted, without affecting the results, analysis is carried on according to the constraint conditions in the paper as follows: (1) the user is multichannel and can track all visible satellites and collect data at the same time; (2) the user positioning model adopts the basic navigation positioning. For calculation results, see Table 2.

3.3 The Time Needed for User to Receive a Set of Almanac

Almanac is simplified satellite ephemeris prediction parameters, and its real-time demand is not high. Almanac can help the user to select geometric factor (PDOP) optimal satellite and help to shorten the time of capturing satellite. The time taken for users receiving a set of complete almanac is related with amount of a unit of information, repetition period of almanac, information rate, and relative broadcast order between the satellite and frequency. Usually, each satellite will broadcast all Almanac of on-orbit satellites, the time user receiving all Almanac is equal to the duration of an information units. The statistics of the time needed for user to receive a set of almanac is given in Table 3.

3.4 The Scalability of the Message Structure

The scalability of the navigation message structure refers to when you need to add new message content or modify existing message content, it can be achieved without modifying the existing message layout structure, that is to say, the existing message structure should have reserved bits. The extensibility for fixed frame structure of the navigation message is mainly done by some reserved fields in the

Table 3 The time of entire almanac for user (min)

	GPS NAV	GPS CNAV	GPS CNAV-2	GALILEO F/NAV	GLONASS	COMPASS
Time	12.5	10	15	20	2.5	12

message and the data block structure of the navigation message by adding new data or information types. The reserved field will cause waste of information resources, reduce link resource utilization, and new data block of information types mode does not create the problem.

GPS NAV, GLONASS message structure is fixed, in order to improve the system scalability, reserved more undefined field, caused the waste of the link resource. GPS CNAV, GPS CNAV-2, and GALILEO F/NAV have the function of adding the data block or information types, when the system function needs extension to broadcast new information, it can simply be realized by adding new data block or information types, and their extensibility is better.

3.5 The Timeliness of Message Broadcast

The timeliness of the navigation message refers to whether navigation information can be updated timely that guarantees the normal work of the system and achieves enough accuracy, or the system failure can be timely reflected in the navigation message. For satellite orbit position, clock correction information, their timeliness is mainly implemented through the parameters prediction, so the efficiency of the message mainly refers to the real time of the integrity information, including the alarm time of the integrity and equivalent distance error precision. Equivalent distance error is associated with the relative position between user and satellite, and it depends on the specific integrity index requirements of navigation service. Integrity index is mainly aimed at the difference enhanced service, this article only discusses basic navigation service, and therefore, this function is not analyzed.

3.6 Utilization of Channel Link Resource

Channel link resource utilization refers to the ratio between the used information bits and all the amount of data in an information unit, it is the difference between "1" and the ratio of reserved information bits with all the amount of data.

For the fixed structure of the navigation message, assumed reserved information bits for r (bits), total data amount for s (bits), the channel link resource utilization η can be calculated as below:

$$\eta = 1 - \frac{r}{s} \tag{3}$$

For the flexible structure, channel link resource utilization adopted the following methods for evaluation:

Assumed,

Data: means all the data for the navigation message to broadcast,
data $= \{d_1, d_2, \ldots d_n\}$, d_i indicates the ith data type,
Length: indicates the data length in the navigation message,
length $= \{l_1, l_2, \ldots l_n\}$, l_i means the length of d_i,
Rate: means the information rate,
Data$B$: indicates the length of the data block,
Time: means the duration of the data block broadcast,
BloNum: means the total number of the data block,

Then the reserved bits for the data block di is as below:

$$R(i) = \begin{cases} \text{data}B - l_i (\text{data}B \geq l_i) \\ \left| \frac{l_i}{\text{data}B} \right| \text{data}B - l_i (\text{data}B < l_i) \end{cases} \tag{4}$$

The average reserved length per second produced.

$$\text{RPS} = \frac{\sum_{i=0}^{n} R(i)}{\text{BloNum} * \text{time}} \tag{5}$$

The channel link resource utilization η for the flexible structure can be calculated as below:

$$\eta = 1 - \frac{\text{RPS}}{\text{rate}} \tag{6}$$

Through the statistics method given above, channel link resource utilization, for GPS NAV, GLONASS, and COMPASS, uses the fixed structure methods to calculate, for CNAV, CNAV-2, and F/NAV, uses multiple data block calculation method. The system navigation message channel link resource utilization results statistics Table 4.

3.7 Use Performance of Navigation Message for User

Navigation message performance also includes user use performance, its overall performance evaluation usually adopts the user equivalent distance error method that calculates the equivalent distance error using pseudorange and the navigation

Table 4 Utilization ratio of link resource for GNSS

	GPS NAV	GPS CNAV	GPS CNAV-2	GALILEO F/NAV	GLONASS	COMPASS
Ratio	86.3 %	98.8 %	92.5 %	96.8 %	98 %	90.8 %

Table 5 Use performance of navigation message for GNSS (m)

	GPS NAV	GPS CNAV	GPS CNAV-2	GALILEO F/NAV	GLONASS	COMPASS
URE	1.5	0.8	0.6	0.5	1.5	1

message information, deducting the receiver's own measurement error, multipath error, etc. It contains the error term of the receiver's error itself, ionosphere delay correction error, tropospheric delay correction error, satellite position error, and clock error. Receiver's error is related on the development level of the user, the troposphere error associated with the model the receiver used, the ionospheric delay correction error, satellite position error, and clock error is associated with the algorithm adopted by the ground control segment. Since ionosphere delay correction error is in correlation with the location and time, user performance is mainly evaluated by comprehensive error about satellite position error and clock error, usually expressed in URE.

The use performance [11] for GPS, GALILEO, GLONASS, and COMPASS is analyzed in Table 5.

4 Conclusion

By analyzing the navigation message performance, the analysis results for GPS, GALILEO, GLONASS, and COMPASS are given in Table 6.

From above chart, we can see, the total amount of GLONASS is the least, GPS CNAV-2 is the most, and other four kinds of message comparative. The less total amount is benefit for shortening long data repetition period, especially the almanac data, it can be seen that repetition period of almanac for GLONASS is the shortest, this contributes to the user terminal capturing performance. CNAV-2 basic navigation information repeated period is the shortest, the parameters directly affect the performance of TTFF, $TTFF_{ave}$ for GLONASS is the shortest, and the user first positioning performance is the best. Channel link resources utilization rate of CNAV is very high, this also has very good flexibility at the aspects of extending and enhancing. GALILEO F/NAV information rate is relatively low, working together with its channel error correction coding that improves the reliability of message transfer, but the TTFF is longer, this is the compromise between two kinds of contradictions. In terms of user performance, CNAV-2 and F/NAV are the best. Repeated period of basic navigation information for CNAV-2 is the shortest with high information rate. Above all, considering TTFF, real-time demand in different parameters, channel link resource utilization, system function scalability, use performance of user, and CNAV-2 performance indicators have reached the high level, which is a kind of good navigation message.

Table 6 Performance evaluation for GNSS navigation message

	GPS NAV	GPS CNAV	GPS CNAV-2	GALILEO F/NAV	GLONASS	COMPASS
Total amount (bits)	37,500	30,000	44,150	30,720	7,500	36,000
Repeat period of almanac (min)	12. 5	10	15	20	2.5	12
Repeat period of basic navigation(s)	30	48	18	50	30	30
TTFFave (s)	33	60	27	65	25	33
Scalability And Flexibility	middle	better	good	good	Not good	middle
Utilization ratio (%)	86.3	98.8	92.5	96.8	98	90.8
Information rate (bps)	50	50	50	25	50	50
channel coding	BCH	CRC + convolutional	BCH + LDPC + CRC + interlaced	convolutional + CRC + interlaced	hamming	BCH + interlaced
URE (m)	1.5	0.8	0.6	0.5	1.5	1

References

1. INTERFACE SPECIFICATION (2012) I S—GPS—200—g
2. INTERFACE SPECIFICATION (2012) I S GPS—705—c
3. INTERFACE SPECIFICATION (2010) I S GPS—800—a
4. European Space Agency (2014) GALILEO open service signal in space interface control document (GAL OS SIS ICD) (Ver 1.2)
5. GLONASS INTERFACE CONTROL DOCUMENT (2008) (Ver 5.1)
6. Chen J (2011) Modern GNSS navigation message design analysis. J of electron and inf 33(1):211–217
7. Chen J (2010) Satellite navigation message design analysis. In: The first chinese satellite navigation academic conference (CSNC 2010)
8. Cao Z, Qian Y (2008) Modern communication principle, Tsinghua University Press
9. Chen N (2008). GNSS navigation message structure performance evaluation. J of Wuhan University, Info Sci, pp 512–515
10. China satellite navigation management office. (2013). BeiDou Navigation satellite system signal in space interface control document open signal (Version 2.0) http://www.beidou.gov.cn
11. Liu Z (2011) GNSS navigation message structure and the broadcast ephemeris analysis and design. In: 2nd China satellite navigation academic conference

A Novel Unambiguous W2 CCRW Multipath Mitigation Algorithm Applied to BOC (n, n) Signals

Shaojie Ni, Jing Pang, Kai Zhang, Chengtao Xu, Zhe Liu and Feixue Wang

Abstract In this paper, a novel unambiguous W2 CCRW multipath mitigation algorithm is applied to BOC (n, n) signals. We investigate a novel BOC (n, n) ambiguous tracking method with W2 code correlation reference waveform (CCRW) multipath mitigation algorithm. It is easily applied only by adding a rectangular gate function with no loss for the multipath mitigation performance.

Keywords GNSS receiver · W2 CCRW · BOC (n, n) · Multipath mitigation

1 Introduction

The BOC (n, n) signals would be broadcasted as same as L1C signals of GPS modernization program and Galileo E1 open service signals, This method of modulation is also planned to be used in compass system. The BOC (n, n) signals not only improve the spectral separation from the BPSK signal that is already existed, but the ability of anti-interference is greatly enhanced. The BOC (n, n) modulation can be regarded as the product of BPSK signal and a symbol of the square wave subcarrier, the spread spectrum waveform can be expressed as

$$g_{\mathrm{BOC}} = g_{\mathrm{BPSK}}(t)\mathrm{sgn}[\sin(2\pi f_s t)] \tag{1}$$

The frequency of $g_{\mathrm{BPSK}}(t)$ is $f_c = n \times 1.023$ MHz, the frequency of subcarrier is $f_s = f_c$ because of the existence of the subcarrier, the autocorrelation function of the BOC (n, n) signals is no longer a triangle but multi-peaked. Traditional narrow

S. Ni (✉) · J. Pang · K. Zhang · C. Xu · Z. Liu · F. Wang
National University of Defense Technology, Deya Road 109,
Changsha 410073, China
e-mail: nishaojie123@126.com

J. Sun et al. (eds.), *China Satellite Navigation Conference (CSNC) 2016 Proceedings: Volume II*, Lecture Notes in Electrical Engineering 389,
DOI 10.1007/978-981-10-0937-2_9

correlator and high resolution correlator (HRC) methods work well for BPSK modulation signals, but when they are applied to BOC signal, extra zero crossing points in discriminator outputs appear. This problem is exploited by most unambiguous tracking algorithms such as BOC-PRN method [1], shaping correlator [2], autocorrelation side-peak cancelation technique (ASPeCT) [3, 4], etc.

2 Signal Model

Multipath mitigation is another frontier for BOC (n, n) signal tracking. The solutions of popular class make use of particular reference code waveforms for the correlation operation. They have generically dubbed code correlation reference waveforms (CCRW) [5]. W2 CCRW is widely used in many GPS receiver manufactures [6–9] whose performance is much better than the traditional narrow correlator or high resolution correlator.

Moreover, how to achieve multipath mitigation with W2 CCRW and ambiguous tracking for BOC (n, n) signal at the same time is not fully exploited, Lee [10] discussed the W2 CCRW multipath mitigation performance for BOC (n, n), but without solving the problem of ambiguous tracking. Nunes et al. [11] solved the ambiguous tracking problem with W2 CCRW by the assistance of bump-jump technology, but it took a long time to judge the main peak to correlate each time and cost many times to adjust the local signal; there is certain complexity in the scheduling process and hardware implementation.

This paper proposed an ambiguous W2 CCRW tracking algorithm. On compared to traditional W2 CCRW, we added a series of local rectangular gates in the rising or falling edge of PRN code before modulated by subcarrier, as shown in Fig. 1.

W2 gate function and the rectangular gate function can be described mathematically as

$$w^{-}(t) = \sum_{k=0}^{\infty} g_{W2}(t - kT_c)c_k^{-} \tag{2}$$

$$a^{-}(t) = \sum_{k=0}^{\infty} g_{\mathrm{rec}}(t - kT_c)c_k^{-} \tag{3}$$

where c_k^{-} is the kth spreading code of BOC (n, n) before modulated by subcarrier and $g_{W2}(t)$ is the elementary window of W2, $g_{\mathrm{rec}}(t)$ is the elementary window of rectangular wave.

The receiver block diagram is shown in Fig. 2.

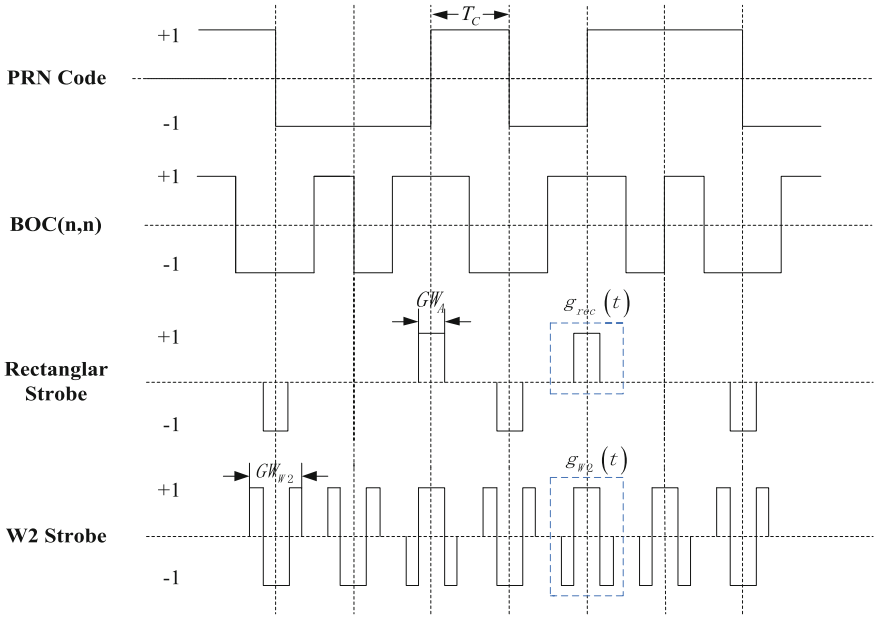

Fig. 1 Example of locally generated PRN code, corresponding BOC (*n*, *n*) signal with rectangular waveform

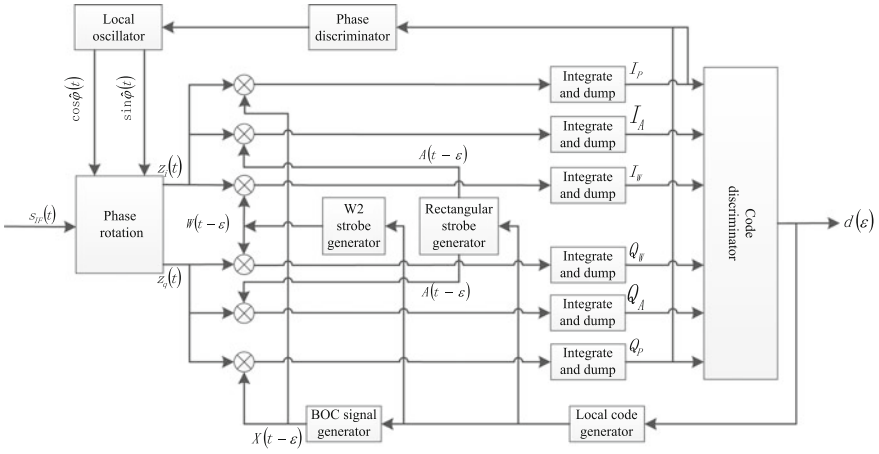

Fig. 2 Block diagram of receiver code and phase loops using unambiguous W2 CCRW

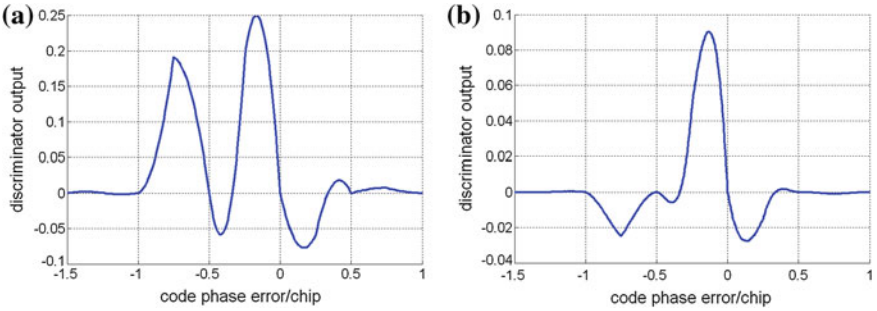

Fig. 3 Discriminator output of W2 CCRW and unambiguous W2 CCRW. **a** Discrimination curve of BOC (1, 1) signal with gate pulse width of 1/4 code chip. **b** Discrimination curve of BOC (1, 1) signal with square gate wave

The local pseudocode and the two gate functions are correlated by the received signal, respectively. The noncoherent joint discriminator can be shown as

$$\mathrm{d}(\varepsilon) = I_X(\varepsilon)I_W(\varepsilon)I_A(\varepsilon) + Q_X(\varepsilon)Q_W(\varepsilon)Q_A(\varepsilon) \tag{4}$$

where $I_X(\varepsilon)$ and $Q_X(\varepsilon)$ are the correlation of Z_i and Z_q with local code, $I_W(\varepsilon)$ and $Q_W(\varepsilon)$ are the correlation of Z_i and Z_q with the W2 CCRW gate function, $I_A(\varepsilon)$ and $Q_A(\varepsilon)$ are the correlation of Z_i and Z_q with the rectangular gate signal.

The discriminator output of W2 CCRW and ambiguous W2 CCRW under unlimited bandwidth condition are shown in Fig. 3a, b, wherein W2 gate width is 0.25 chips, additional waveform gate width is one chip. The ambiguous W2 CCRW code phase detector indicates: there is no zero crossing at the point of 0.5 chips, only at the delay of one chip with extra zero crossing, and the zero crossing cannot generate false lock. So the proposed method can effectively eliminate the W2 CCRW technology ambiguity in tracking BOC (n, n) signal.

3 Simulation Result

The numerical simulation method is used to verify the above conclusion. Specific simulation parameters are shown in Table 1.

As seen from Figs. 4 and 5 there is a stable fuzzy zero crossing point at −0.5 chips for the traditional CCRW algorithm, but the fuzzy zero crossing point disappears when using unambiguous CCRW algorithm, this demonstrates the effectiveness of the proposed algorithm in the paper.

Simulation result to compare multipath mitigation performance: The same gate width is used in the simulation which compares multipath error envelope of NC, HRC, W2 CCRW, and ambiguous W2 CCRW under the infinite bandwidth

Table 1 Simulation parameters

Simulation parameter	Setting value
Width of gate wave	1/4 chips
SNR	50 dBHz
Signal code frequency	1.023 Mcps
Signal bandwidth	Four times of code frequency
Coherent integration period	1 ms
Initial code phase error	−0.7 chips
Loop bandwidth	1 Hz

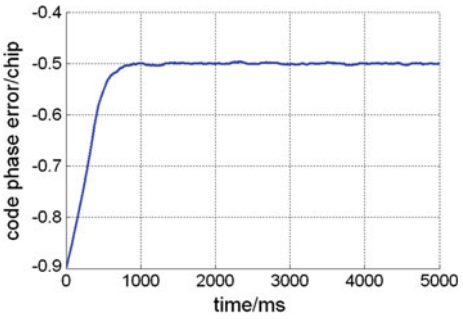

Fig. 4 Tracking error of traditional CCRW technique

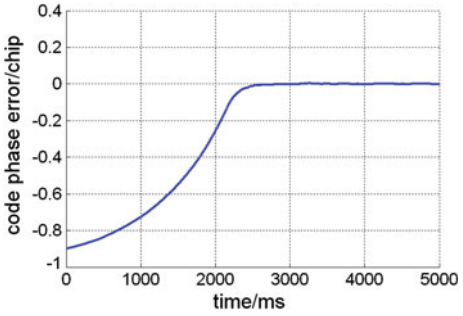

Fig. 5 Tracking error of unambiguous CCRW technique

condition, the result is shown in Fig. 6. The early-minus-late (E-L) space for NC is 0.25 chips. The E-L spaces for HRC are 0.25 chips and 0.5 chips. The gate function width is 0.25 chips for W2 and ambiguous W2. The rectangular gate width is one chip. The amplitude of multipath signal is half of direct signal. The figure indicates ambiguous W2 CCRW technology and W2 CCRW algorithm has the same multipath mitigation performance, both better than NC and HRC.

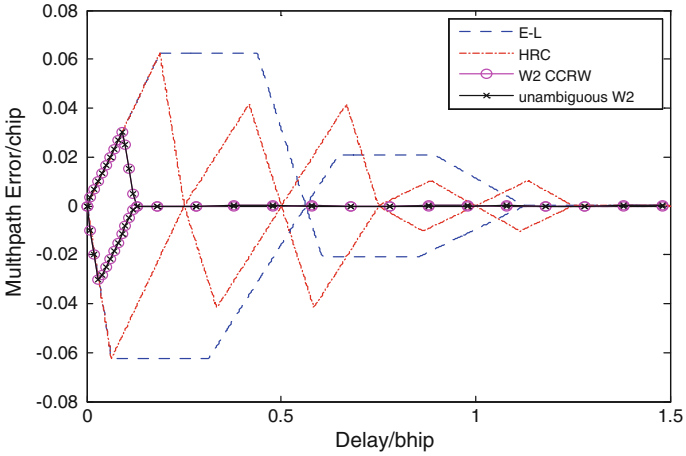

Fig. 6 Multipath error envelop comparison

4 Conclusion

We proposed an improved W2 CCRW technology by adding a rectangular gate wave in the chip-flipping place, false-locking in traditional W2 CCRW BOC (n, n) tracking can be eliminated conveniently and efficiently, with no loss in multipath mitigation performance.

References

1. Wu J, Dempster AG (2008) Symmetry analysis of the "BOC-PRN" delay locked loop discriminator. GPS Solution
2. Garin L (2005) The "shaping correlator", novel multipath mitigation technique applicable to GALILEO BOC (1, 1) modulation waveforms in hight volume markets. In: Proceedings of the ENC-GNSS
3. Nunes F, Sousa F, Leitão J (2008) Code correlation reference waveforms for multipath mitigation in MBOC GNSS receivers
4. Garin L, Rousseau J (1997) Enhanced strobe correlator multipath rejection for code and carrier. In: Proceedings of the 10th international technical meeting of the satellite division of the institute of navigation. Kansas City, Missouri, pp 16–19
5. Woo R (1998) Global positioning system receiver with improved multipath signal rejection. U.S. Patent Number 5,808,582 (Inventor: Woo R, Assignee: NavCom Technology, Date of Patent: 15 Sept 1998)
6. Garin L, Rousseau J (1997) Enhanced strobe correlator multipath rejection for code and carrier. In: Proceedings of the 10th international technical meeting of the satellite division of the Institute of Navigation, Kansas City, Missouri, pp 16–19
7. Hatch R, Keegan R, Stansell T (1997) Leicas code and phase multipath mitigation techniques. In: Proceedings of the national technical meeting of the Institute of Navigation, Santa Monica, California, pp 14−16

8. Stansell T (2000) Mitigation of multipath effects in global positioning system receivers. U.S. Patent Number 6,160,841 (Inventor: Stansell T, Assignee: Leica Geosystems, Date of Patent: 8 February 2000)
9. Hatch R (2000) Method and apparatus for code synchronization in a global positioning system receiver. U.S. Patent Number 6,023,489 (Inventor: Hatch R, Assignee: Leica Geosystems, Date of Patent: 8 Feb 2000)
10. Lee YC (2002) Compatibility of the new military GPS signals with non-aviation receivers. In: Proceedings of the ION 58th annual meeting/CIGTF 21st guidance test symposium, pp 581–597
11. Nunes F, Sousa F, Leitão J (2006) Gating functions for multipath mitigation in GNSS BOC signals. Submitted to the IEEE Transactions on Aerospace and Electronics Systems

Analysis and Correction of the Inter-frequency Clock Bias for BeiDou Satellites

Lin Pan, Xiaohong Zhang, Jingnan Liu, Xingxing Li and Xin Li

Abstract BeiDou provides triple-frequency signals for all operational satellites. However, an apparent inconsistency between triple-frequency carrier phases has been discovered. The satellite clock products derived from B1/B2 carrier phase observations cannot be used for B1/B3 based precise point positioning (PPP) without careful consideration of the inconsistency. The apparent inconsistency is known as inter-frequency clock bias (IFCB). Datasets collected at 37 globally distributed stations on fourteen consecutive days are employed to analyze the IFCB of BeiDou GEO (Geostationary Orbit), IGSO (Inclined Geosynchronous Orbit) and MEO (Medium Earth Orbit) satellites. A weighted epoch-differenced approach is proposed to estimate the IFCB. The results indicate that the IFCB is time- and satellite-dependent, and is irrelevant to the antenna types, station locations, satellite elevation and azimuth angles. The IFCB of GEO and IGSO satellites has a significant daily period. The IFCB varies within a range of –4 to +4 cm, and the RMS (root mean square) values of IFCB are smaller than 2 cm. There is a high correlation between IFCB of two adjacent days for part of GEO and IGSO satellites, and the RMS values of IFCB differences between two adjacent days for these satellites are usually smaller than 0.5 cm. When the extracted IFCB of the first day is used to correct the B1/B3 ionosphere-free carrier phase observations of the second day, the BeiDou PPP based on B1/B3 achieves higher positioning accuracy and smaller observation residuals.

Keywords Inter-frequency clock bias · Beidou · Triple-frequency · Precise point positioning

L. Pan (✉) · X. Zhang · J. Liu · X. Li
School of Geodesy and Geomatics, Wuhan University,
129 Luoyu Road, Wuhan 430079, China
e-mail: panlin@whu.edu.cn

L. Pan · X. Zhang
Collaborative Innovation Center for Geospatial Technology,
129 Luoyu Road, Wuhan 430079, China

X. Li
German Research Centre for Geosciences (GFZ), Telegrafenberg,
14473 Potsdam, Germany

J. Sun et al. (eds.), *China Satellite Navigation Conference (CSNC) 2016 Proceedings: Volume II*, Lecture Notes in Electrical Engineering 389,
DOI 10.1007/978-981-10-0937-2_10

1 Introduction

Currently, the American modernized GPS system, the European Galileo system, the Japanese Quasi-Zenith Satellite System (QZSS) and the Chinese BeiDou system all provide multi-frequency signals. The BeiDou system is a project made by China to develop an independent global navigation satellite system (GNSS), and all operational BeiDou satellites provide triple-frequency signals. The joint use of multi-frequency signals has become the trend of GNSS development. There are many advantages when using multi-frequency signals, such as improving the positioning accuracy and speeding up the ambiguity resolution process [1, 2]. However, there is an apparent inconsistency between triple-frequency carrier phases, which is known as inter-frequency clock bias (IFCB). Due to the influence of the IFCB variations, the satellite clock products derived from L1/L2 (B1/B2) carrier phase observations cannot be used for L1/L5 (B1/B3) based precise point positioning (PPP).

Montenbruck et al. [3] first noticed that periodical changes exist in L1/L5-minus-L1/L2 clock offset estimates, namely IFCB estimates, for the latest generation of GPS satellites, termed Block IIF. The results suggested satellite internal temperature variations due to varying sun illumination as the root cause of the IFCB variations, and the illumination itself depended on the sun–spacecraft–earth angles. With the development of BeiDou system, the IFCB variations between B1/B2 and B1/B3 carrier phases have been observed for GEO (Geostationary Orbit) and IGSO (Inclined Geosynchronous Orbit) satellites [4]. The IFCB is usullay estimated with a strategy in which the handling of ambiguities is needed, and thus the strategy is time consuming and complicated [3]. To reduce the computational burden, Li et al. [5] proposed an epoch-differenced (ED) approach to estimate the IFCB. The proposed approach removes the ambiguity parameters, and only ED IFCB remains. The IFCB of GPS Block IIF satellites and BeiDou GEO satellites was investigated with the ED approach [5–7]. The IFCB of QZSS satellites was also investigated and the results showed that it has no variation characteristics [8]. Most of the research works focused on the investigation of the time varying characteristics and the modeling of IFCB. The IFCB corrections still have not been applied to position determination. Hence many details have not been considered, such as the difference between a solar day and a sidereal day.

In this paper, datasets collected at 37 globally distributed stations on fourteen consecutive days are employed to analyze the characteristics of IFCB for BeiDou GEO, IGSO and MEO (Medium Earth Orbit) satellites. A weighted epoch-differenced approach is proposed for the IFCB estimation. The extracted IFCB of the first day is used to correct the B1/B3 ionosphere-free carrier phase observations of the second day, and then the performance improvement of BeiDou PPP based on B1/B3 is evaluated in terms of positioning accuracy and observation residuals.

2 IFCB Estimation Approach

The carrier phase observations on B1, B2 and B3 frequencies can form different ionosphere-free combinations. The geometric range and tropospheric delay can be removed by an operation of subtraction between two different ionosphere-free combinations, such as B1/B2 and B1/B3, and the remained terms are phase ambiguity and inter-frequency clock biases. The differenced ionosphere-free (DIF) observations can be expressed as [3]:

$$\mathrm{DIF}(\mathrm{B1},\mathrm{B2},\mathrm{B3}) = \mathrm{IF}(\mathrm{B1},\mathrm{B2}) - \mathrm{IF}(\mathrm{B1},\mathrm{B3}) = \mathrm{IFCB} + \mathrm{const}_{1,2} - \mathrm{const}_{1,3} \quad (1)$$

$$\mathrm{IFCB} = \mathrm{dT}_{1,2} - \mathrm{dT}_{1,3} \quad (2)$$

where $\mathrm{const}_{1,2}$ is the ambiguity of ionosphere-free combination formed with B1 and B2, and $\mathrm{const}_{1,3}$ is the ambiguity of ionosphere-free combination formed with B1 and B3. $\mathrm{d}T_{1,2}$ and $\mathrm{d}T_{1,3}$ are the satellite clock offsets derived from B1/B2 and B1/B3 carrier phase observations, respectively, and the difference between them is the IFCB.

Based on Eqs. (1) and (2), the IFCB can be estimated in a general clock estimation procedure [3, 9]. To reduce the computational burden, the ED approach is employed in this study. The ED approach proposed by Li et al. [5] is modified by taking into account the effects of measurement noises with different satellite elevation angles. A weighted epoch-differenced approach (WEDA) is proposed for the IFCB estimation in this contribution.

From Eq. (1), the following equation can be derived:

$$\mathrm{IFCB} = \mathrm{DIF}(\mathrm{B1},\mathrm{B2},\mathrm{B3}) - \mathrm{const}_{1,2} + \mathrm{const}_{1,3} \quad (3)$$

Assuming that there is no cycle slip between two adjacent epochs, the phase ambiguity items in Eq. (3) can be eliminated by an operation of epoch-difference between the DIF phase measurements of the two epochs. The ED IFCB at epoch m can be expressed as:

$$\Delta\mathrm{IFCB}(m) = \mathrm{DIF}(\mathrm{B1},\mathrm{B2},\mathrm{B3})(m) - \mathrm{DIF}(\mathrm{B1},\mathrm{B2},\mathrm{B3})(m-1) \quad (4)$$

where "Δ" represents the ED operator, and ΔIFCB is the ED IFCB. If the IFCB is time- and satellite-dependent, $\Delta\mathrm{IFCB}(m)$ should be the same for different stations. The dependence of IFCB on time and satellite will be testified in the next section. Assuming that there are n stations in the network, which improves the redundancy of the solutions, the ED IFCB at epoch m can be calculated through a weighted average over the entire network:

$$\Delta\mathrm{IFCB}(m)_{WA} = \left(\sum_{k=1}^{n} \Delta\mathrm{IFCB}(m)_k \cdot w_k\right) \Big/ \left(\sum_{k=1}^{n} w_k\right) \quad (5)$$

$$w = \begin{cases} \sin E & E < 40^\circ \\ 1 & E \geq 40^\circ \end{cases} \tag{6}$$

where E is the satellite elevation angle, and w is the weight of ΔIFCB for each station. Since the measurement noises start to increase significantly when the satellite elevation angles decrease to 40°, the ΔIFCB values with elevation angles below 40° are down-weighted.

It is assumed that the IFCB at the first epoch is zero, and the IFCB at epoch m can be calculated as follows:

$$\mathrm{IFCB}(m) = \sum_{t=2}^{m} \Delta\mathrm{IFCB}(t)_{WA} \tag{7}$$

According to Eq. (7), the IFCB at all epochs can be obtained. Assuming that there are p epochs in one day and the sum of IFCB at these epochs equals to zero, the final IFCB at epoch m can be described as:

$$\overline{\mathrm{IFCB}}(m) = \mathrm{IFCB}(m) - \left(\sum_{t=1}^{p} \mathrm{IFCB}(t) \right) \Big/ p \tag{8}$$

There may be a common constant bias in IFCB with respect to all epochs. The constant bias, however, is not a problem for PPP float solutions as it will be grouped with ambiguity term in parameter estimation process. But the bias will affect the fractional-cycle biases (FCB), which are essential for ambiguity fixing in PPP.

3 Results and Analysis

3.1 Data Description

Datasets collected at 37 globally distributed MGEX (Multi-GNSS Experiment) stations on November 1–14, 2015, are employed to analyze the IFCB. The geographical distribution of the stations is shown in Fig. 1. All stations were equipped with "Trimble NetR9" GNSS receivers which can produce BeiDou triple-frequency observations. All observations were recorded at a sampling interval of 30s, and the satellite elevation mask angle was set to 10°.

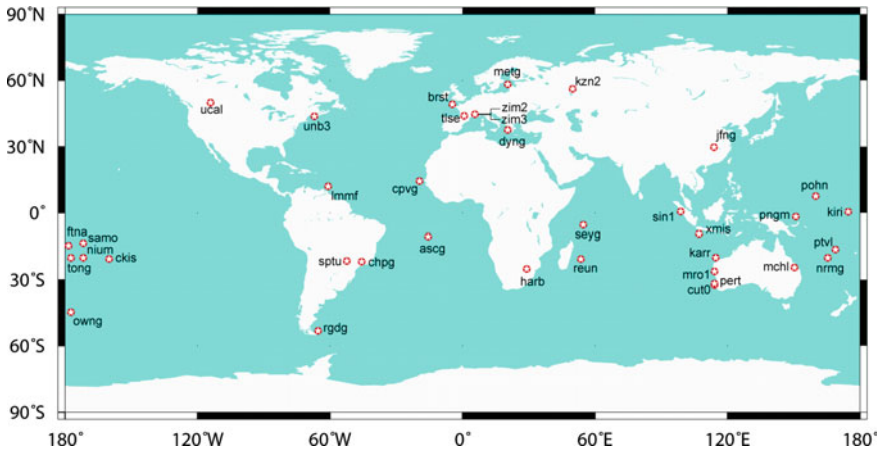

Fig. 1 Geographical distribution of 37 MGEX stations

3.2 IFCB Dependence Analysis

In order to analyze the dependence of IFCB, datasets from five stations on November 1, 2015 are adopted for the data processing. The five stations are located in different areas and set up with different types of antennas. Each station can track 10–13 BeiDou satellites. The detailed information of the five stations is listed in Table 1.

Alternatively, the IFCB can be acquired by subtracting an average DIF over each continuous ambiguity block from raw DIF values [4]. The detection and repair of cycle slips are carried out using triple-frequency measurements [10]. The absolute IFCB cannot be achieved through the above approach, and the tracking time of one satellite is different for different stations. Therefore, the IFCB values of the satellite at common epochs are different for different stations.

The IFCB of each BeiDou satellite at the five stations is obtained using the above approach, and the results are shown in Fig. 2. For the convenience of contrastive analysis, constant biases have been determined and added to the

Table 1 Station locations and antenna types of five stations

Station	Location		Antenna
	Latitude	Longitude	
CUT0	−32.00°	115.89°	TRM59800.00
JFNG	30.52°	114.49°	TRM59800.00
NRMG	−22.23°	166.48°	TRM57971.00
REUN	−21.21°	55.57°	TRM55971.00
SIN1	1.34°	103.68°	LEIAR25. R3

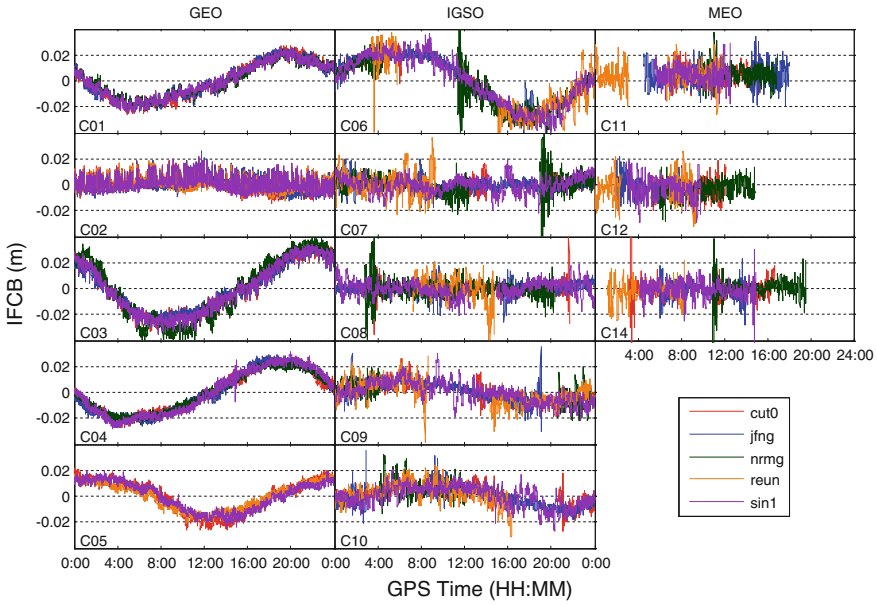

Fig. 2 IFCB of each BeiDou satellite at five stations on November 1, 2015

triple-carrier combination shown in Eq. (1) for each continuous tracking arc such as to minimize differences between stations at common epochs. It is obvious that the variations of IFCB of GEO satellites are consistent for different stations, and similar situations are also found in IGSO satellites C06, C09 and C10. For further analysis, Table 2 provides the correlation coefficients of IFCB between different stations at common epochs for each BeiDou satellite. The correlation coefficients between any

Table 2 Correlation coefficients of IFCB between different stations for each BeiDou satellite

		Sin1-cut0	Sin1-jfng	Sin1-nrmg	Sin1-reun
GEO	C01	1.00	0.99	0.99	–
	C02	0.73	0.76	–	0.76
	C03	1.00	1.00	0.98	–
	C04	0.99	0.98	0.99	–
	C05	0.97	–	–	0.94
IGSO	C06	0.96	0.97	0.94	0.90
	C07	0.40	0.47	0.23	0.14
	C08	0.26	0.12	−0.10	0.02
	C09	0.83	0.64	0.55	0.54
	C10	0.79	0.76	0.01	0.40
MEO	C11	0.39	0.31	0.22	0.39
	C12	0.64	0.42	0.54	0.33
	C14	0.37	0.25	0.08	−0.35

two stations are larger than 0.9 for C01, C03, C04, C05 and C06, and the corresponding values for C02 and C09 are larger than 0.7 and 0.5, respectively, indicating that the IFCB of these satellites is highly relevant for different stations. The lower correlation coefficients of other satellites may be partly due to the smaller trend terms in comparison to the dominant random errors of IFCB. Based on the above analysis, the IFCB is time- and satellite-dependent, and is irrelevant to the antenna types and station locations.

Figure 3 shows the IFCB values against the satellite elevation and azimuth angles. The IFCB shown in Fig. 2 is used. Different colors represent different BeiDou satellites. It is seen that there is no obvious dependence between IFCB values and elevation angles, or between IFCB values and azimuth angles. The IFCB of IGSO satellites C07 and C08 and all MEO satellites mainly shows the characteristics of measurement noises that the value increases as the satellite elevation angle decreases.

3.3 IFCB Estimates

The ED approach is feasible because the IFCB is time- and satellite-dependent. The WEDA proposed in this study is employed to process the datasets collected at 37 MGEX stations on November 1–14, 2015, and the IFCB of each BeiDou satellite on the fourteen days is shown in Fig. 4. The red curves are the low-frequency components of the raw IFCB time series, which are obtained with wavelet decomposition and reconstruction. The Symlet wavelet 'sym4' is employed. The operation is to test whether the high-frequency noises will affect the IFCB corrections in PPP. It is

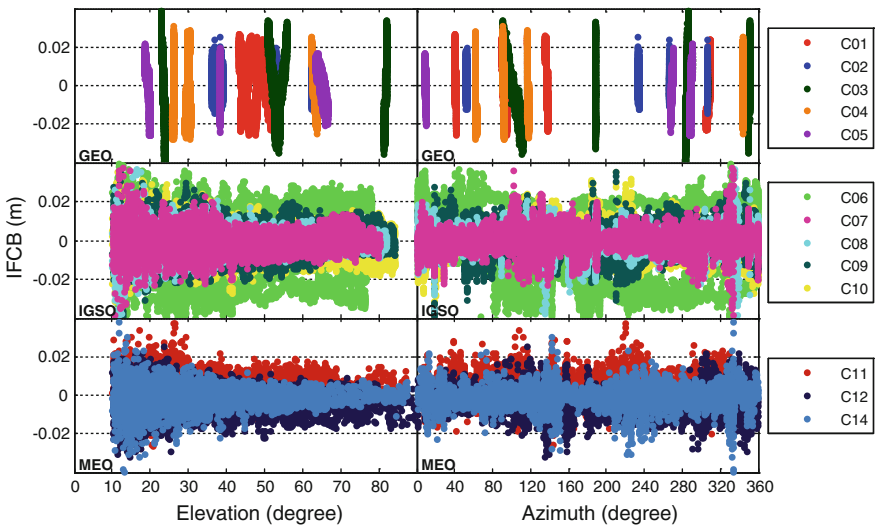

Fig. 3 Dependence of IFCB on the satellite elevation and azimuth angles

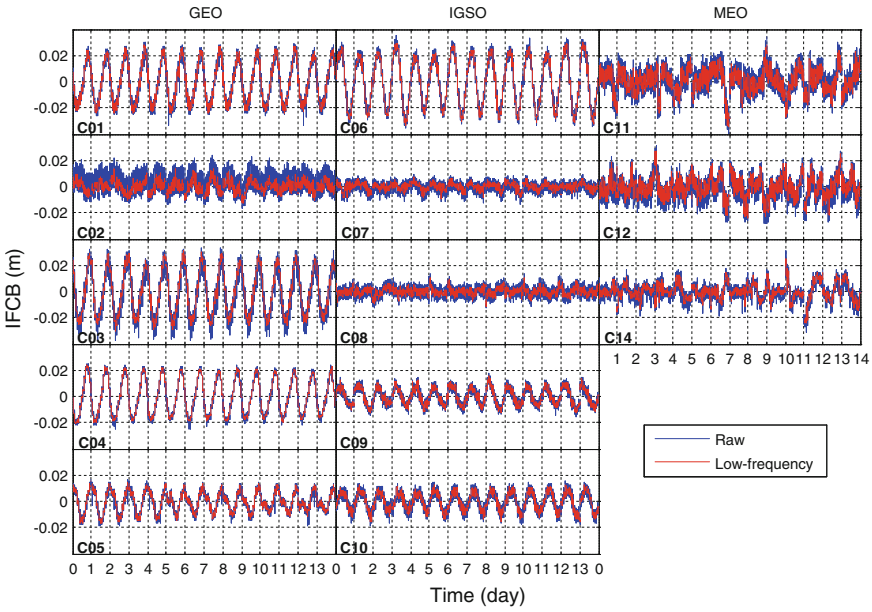

Fig. 4 IFCB of each BeiDou satellite on November 1–14, 2015

indicated that the IFCB varies within a range of −4 to +4 cm. The IFCB of part of GEO and IGSO satellites has obvious periodical behaviors, while it is not the case for the other satellites, which needs to be further analyzed.

The Fourier transform (FT) is able to depict the IFCB time series through amplitude versus frequency, revealing the frequency and the amplitude of each component. Thus, the spectral characteristics of IFCB time series can be investigated in the frequency domain. The discrete form of the FT is employed, since the IFCB time series here can be taken as a discrete signal with a sampling interval of 30s. In the frequency domain, the frequency range is from the fundamental frequency to the Nyquist frequency. The fundamental frequency, also the frequency resolution, can be calculated as $1/T$, where T is the time span of the signal, whereas the Nyquist frequency is half the sampling rate, i.e. 0.5/30 in this study. Figure 5 illustrates the fast Fourier transform (FFT) results of raw IFCB time series. The corresponding periods with peak amplitudes are marked in red. The peak amplitudes of all GEO and IGSO IFCB time series correspond to periods of 86,400s, whereas the periodicity of MEO ones is not obvious.

Figure 4 indicates that the IFCB varies within a range of −4 to +4 cm. For quantitative analysis, Fig. 6 shows the RMS (root mean square) statistics of raw IFCB time series over the fourteen days for each BeiDou satellite. The statistical results clearly demonstrate that the RMS IFCB is smaller than 2 cm for all satellites. C07 and C08 have the smallest IFCB with about 0.3 cm, while the RMS IFCB of C01, C03, C04 and C06 is larger than 1.3 cm.

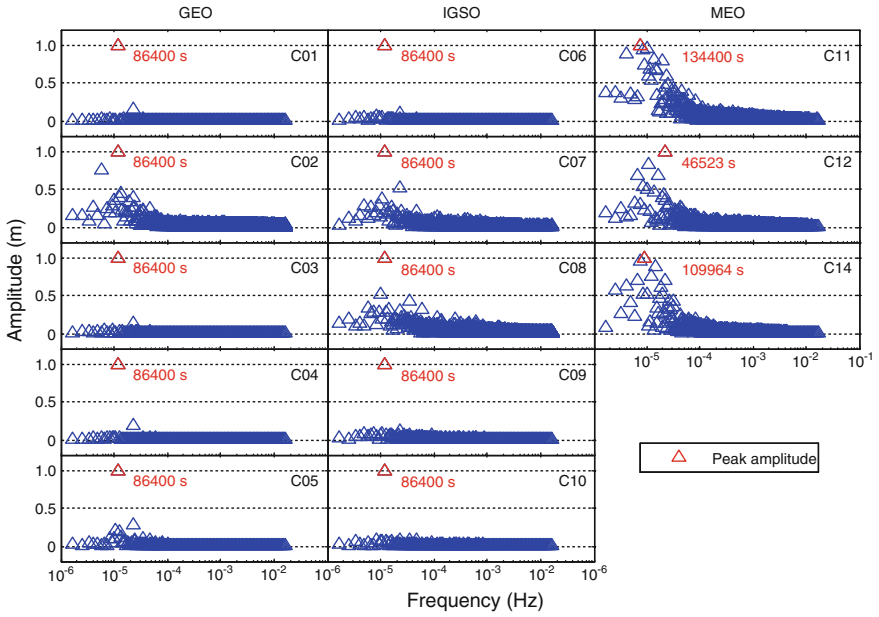

Fig. 5 FFT results of IFCB for each BeiDou satellite

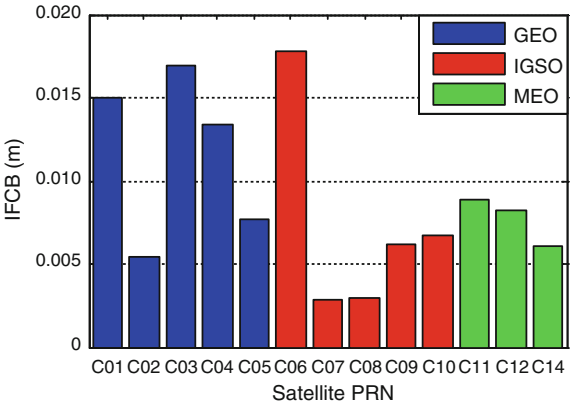

Fig. 6 RMS statistics of IFCB over fourteen days for each BeiDou satellite

In Eq. (5), the reliability and accuracy of $\Delta IFCB_{WA}$ between two adjacent epochs of one satellite are determined by the number of stations that are capable of tracking the satellite successfully at the two epochs. The sum of weights can reflect the number of the stations. Figure 7 shows the average values of the sum of weights at an epoch over all the available epochs of the fourteen days for each BeiDou satellite. The sum of weights for C02 and all MEO satellites is smaller than 7.0, while the C01 and C04 ones are larger than 15.0. The corresponding values of other satellites vary between 8.5 and 11.0.

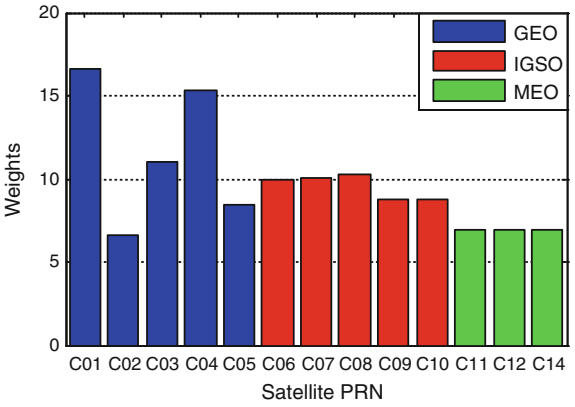

Fig. 7 Average values of the sum of weights at an epoch over all the epochs for each BeiDou satellite

3.4 IFCB Correction

Since the IFCB of GEO and IGSO satellites has a significant daily period, the extracted IFCB of the previous day can be used to correct the observations of the second day to improve the positioning accuracy. Before this, an additional work, the assessment of the differences of IFCB between two adjacent days, needs to be done. The correlation coefficients and RMS statistics of differences of IFCB between two adjacent days for GEO and IGSO satellites are plotted in Fig. 8. The raw IFCB time series given in Fig. 4 are used. The results demonstrate that the correlation coefficients for all GEO and IGSO satellites except the C02, C07 and C08 exceed 0.8, and almost all RMS values of IFCB differences for these satellites are smaller than 0.5 cm.

If the extracted IFCB of the previous day is employed, another factor should be considered, namely the difference between a solar day and a sidereal day. The difference value is about 236s. The orbit period of GEO and IGSO satellites is a sidereal day, while the observations refer to the GPS time which belongs to solar time. A time lag of 240s may be taken into account for the alignment of IFCB between two adjacent days with a sampling interval of 30s. To assess the influence of this factor, the results in Fig. 8 are re-computed with 240s lag, and then the differences between results with and without time lags are obtained. The average values of the differences over all days are displayed in Fig. 9. The results demonstrate that the time lags have no significant effects on GEO satellites. The correlation coefficients of IFCB between two adjacent days are increased by less than 0.08 for IGSO satellites, and the IFCB differences are reduced by less than 0.02 cm. Therefore, the effects of time lags on IGSO satellites are also little.

As to MEO satellites, the orbit repetition period is seven sidereal days. Therefore, the IFCB of the first seven days is compared with that of the second seven days for IGSO satellites. The time lag of one day is 240s, and thus the time lag of seven days is 1650s. The results indicate that no significant difference between results with and without time lags is found. The correlation coefficients of

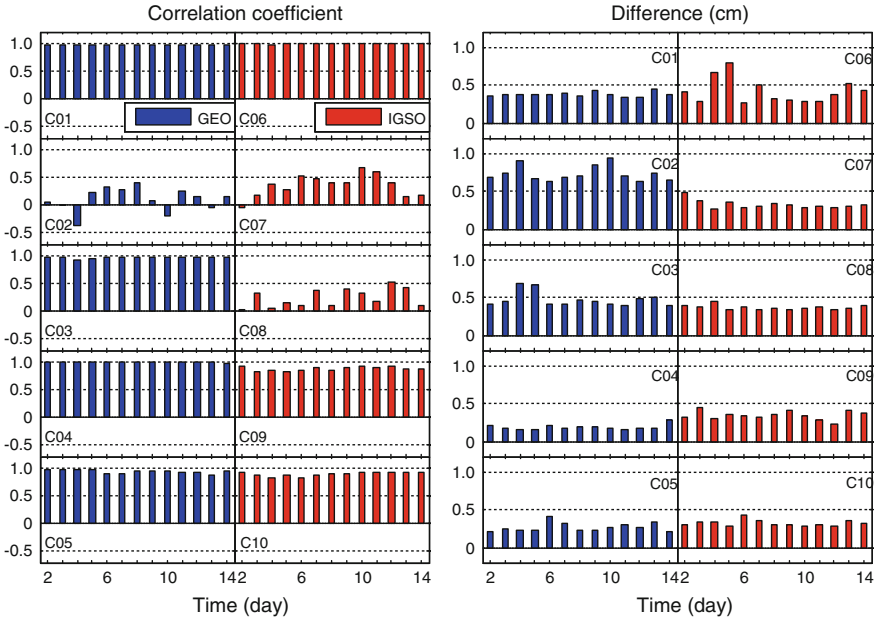

Fig. 8 Correlation coefficients and RMS statistics of differences of IFCB between two adjacent days for GEO and IGSO satellites

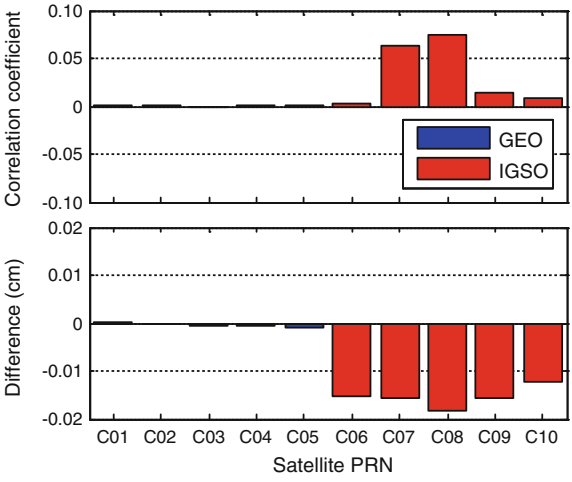

Fig. 9 Differences between results with and without 240s lag

IFCB between the first and the second seven days are smaller than 0.3 for all MEO satellites, and the RMSs of IFCB differences are approximately 1 cm.

Based on the above analysis, the IFCB of C02, C07 and C08 has an obvious daily period, but the differences of IFCB between two adjacent days for these

satellites are too large. The periodicity of IFCB is not significant for MEO satellites. Therefore, the derived IFCB of these satellites cannot be applied to correct the observations.

In order to assess the improvement of positioning performance due to IFCB corrections, the following three different strategies are employed for BeiDou PPP processing using datasets collected at stations cut0, jfng and sin1, which are covered by the BeiDou service of the Asia-Pacific area, on November 2–14, 2015. The three strategies can be described as:

Strategy 1: B1/B3 ionosphere-free carrier phase observations are adopted.
Strategy 2: B1/B3 ionosphere-free carrier phase observations are employed. The low-frequency components of IFCB extracted from the datasets of the previous day are used to correct the observations of the second day for C01, C03, C04, C05, C06, C09 and C10, while the weights of observations for other BeiDou satellites are down-weighted. The 240s lag is considered.
Strategy 3: B1/B2 ionosphere-free carrier phase observations are used.

In order to eliminate the effects of code biases, only carrier phase observations are used in BeiDou PPP. The a priori receiver clock offsets calculated through single point positioning (SPP) are employed to remove the rank deficiency between receiver clock and phase ambiguity parameters. The RMS statistics are calculated using the positioning errors over the last 15 min of each session, and then the average values of RMSs over 39 sessions at three stations on thirteen days are obtained. The RMSs of observation residuals over all the sessions for each BeiDou satellite are calculated. The results are given in Table 3. It is demonstrated that the positioning accuracy of Strategy 2 is improved by 28, 30 and 45 % over Strategy 1 in east, north and up directions, respectively, and the observation residuals are reduced by 0.1–0.8 cm. However, both the positioning accuracy and observation residuals of Strategy 2 are worse than those of Strategy 3, indicating that only partial IFCB between B1/B3 and B1/B2 observations is corrected. In addition, PPP

Table 3 Positioning errors and observation residuals for BeiDou PPP with three different strategies

		Strategy 1	Strategy 2	Strategy 3
Accuracy (cm)	East	1.79	1.28	0.86
	North	1.00	0.70	0.58
	Up	5.94	3.25	2.01
Residual (cm)	C01	3.45	2.66	1.86
	C03	2.02	1.43	1.28
	C04	3.79	3.16	2.86
	C05	4.32	4.19	3.62
	C06	3.26	2.58	2.25
	C09	2.77	2.40	2.24
	C10	2.76	2.31	2.16

results with raw IFCB and with low-frequency IFCB are compared, and no significant difference is found. Thus, the high-frequency noises do not affect the IFCB corrections for B1/B3 observations.

4 Conclusions

BeiDou provides triple-frequency signals for all operational satellites. The joint use of multi-frequency signals has become the trend of GNSS development. Multi-frequency signals can improve the positioning accuracy and accelerate the ambiguity resolution process. However, there is an apparent inconsistency between triple-frequency carrier phases, which is known as IFCB. The IFCB variations should be carefully considered. Otherwise, the satellite clock products derived from B1/B2 carrier phase observations cannot be used for B1/B3 based PPP.

Datasets collected at 37 globally distributed stations on fourteen consecutive days are employed to analyze the characteristics of IFCB for BeiDou GEO, IGSO and MEO satellites. A weighted epoch-differenced approach is proposed to estimate the IFCB. The results indicate that the IFCB is time- and satellite-dependent, and is irrelevant to the antenna types, station locations, satellite elevation and azimuth angles. The IFCB varies within a range of −4 to +4 cm, and the RMS values of IFCB are smaller than 2 cm. There is a high correlation between IFCB of two adjacent days for part of GEO and IGSO satellites, and the RMS values of IFCB differences between two adjacent days for these satellites are usually smaller than 0.5 cm. When the extracted IFCB of the first day is used to correct the B1/B3 ionosphere-free carrier phase observations of the second day, the positioning accuracy of the BeiDou PPP based on B1/B3 is improved by 28, 30 and 45 % in east, north and up directions, respectively, and the observation residuals are reduced by 0.1–0.8 cm.

Acknowledgment This study was supported by National Natural Science Foundation of China (Grant No. 41474025).

References

1. Elsobeiey M (2014) Precise point positioning using triple-frequency GPS measurements. J Navig 68(3):480–492
2. Geng J, Bock Y (2013) Triple-frequency GPS precise point positioning with rapid ambiguity resolution. J Geodesy 87(5):449–460
3. Montenbruck O, Hugentobler U, Dach R, Steigenberger P, Hauschild A (2012) Apparent clock variations of the Block IIF-1 (SVN62) GPS satellite. GPS Solutions 16(3):303–313
4. Montenbruck O, Hauschild A, Steigenberger P, Hugentobler U, Teunissen P, Nakamura S (2013) Initial assessment of the COMPASS/BeiDou-2 regional navigation satellite system. GPS Solutions 17(2):211–222

5. Li H, Zhou X, Wu B (2013) Fast estimation and analysis of the inter-frequency clock bias for block IIF satellites. GPS Solutions 17(3):347–355
6. Li H, Zhou X, Wu B, Wang J (2012) Estimation of the inter-frequency clock bias for the satellites of PRN25 and PRN01. Sci China Phy Mech and Astron 55(11):2186–2193
7. Li H, Chen Y, Wu B, Hu X, He F, Tang G, Gong X, Chen J (2013) Modeling and initial assessment of the inter-frequency clock bias for compass GEO satellites. Adv Space Res 51 (12):2277–2284
8. Hauschild A, Steigenberger P, Rodriguez-Solano C (2012) Signal, orbit and attitude analysis of Japan's first QZSS satellite Michibiki. GPS Solutions 16(1):127–133
9. Montenbruck O et al (2011) Flight characterization of new generation GNSS satellite clocks. In: International technical meeting of the satellite division (ION-GNSS-2011), Portland OR, USA, 21–23 Sept 2011
10. Zhao Q, Sun B, Dai Z, Hu Z, Shi C, Liu J (2015) Real-time detection and repair of cycle slips in triple-frequency GNSS measurements. GPS Solutions 19(3):381–391

Alternate Broadcasting Method of Navigation Message Among Satellites and Frequencies

Mengli Wang, Jinping Chen, Xiao Mao and Zhiqi Ma

Abstract Generally, navigation messages of all satellites and frequencies are broadcasted at the same beginning time. That is, receivers will receive the same message parameters from different satellites and frequencies at the same time. To compress the time of receiving navigation message, alternate broadcasting methods among satellites and frequencies are designed in this paper. Taking Beidou constellation as an example, messages relative to broadcasting turn among satellites and frequencies are optimized and designed. It is indicated that alternate broadcasting design among satellites and frequencies will improve the navigation message's timeliness effectively. And at the same time, system building cost need not be increased. The study is significant in quick prediction of satellites visibility and decreasing the first positioning time when the receiver is starting.

Keywords Broadcasting frequentness · Satellite visibility · Message separating · Alternate broadcasting

1 Introduction

Navigation message is an important part of satellite signal, and it is the navigation and position datum transferred from satellites to users in the form of binary code stream. Message performances are important that will affect system's services such as timeliness, flexibility, reliability, extensible, and users' cost directly. In recent years, design of navigation message is more important; for example, the navigation

M. Wang (✉) · J. Chen · X. Mao
Beijing Satllite Navigation Center, 100094 Beijing, China
e-mail: compass2020@126.com

Z. Ma (✉)
Beijing Information Technique Graduate School, Beijing 100094, China
e-mail: mazhiqi@126.com

J. Sun et al. (eds.), *China Satellite Navigation Conference (CSNC) 2016 Proceedings: Volume II*, Lecture Notes in Electrical Engineering 389,
DOI 10.1007/978-981-10-0937-2_11

message design for indoor messaging system [1], which is about message rate tradeoff design concerning message resolving time, bit error rate, and loss-of-lock; GLONASS being developed CDMA signal's message structure [2], which can be easily upgraded based on flexible row structure; message design, and estimation of wide argumentation system [3].

Message design factors include parameter content, frame structure, information rate, arranging format, broadcasting time series, etc. Broadcasting of navigation message concentrates on two aspects. The first is messages' broadcasting turn at each satellite; the second is messages' broadcasting turn among different satellites and frequencies. Generally, navigation messages of all satellites and frequencies are broadcasted at the same time beginning. That is, receivers will receive the same message parameters from different satellites and frequencies at the same time. Then the same messages will be redundancy, such as almanacs of all satellites. Therefore, Galileo system adopts alternate broadcasting method in F/NAV and I/NAV navigation messages. In this design, messages' relative broadcasting turn among satellites and frequencies is optimized [4], so messages that are received delay are decreased effectively.

This thesis takes Galileo navigation messages' design as reference, and further improves the alternate broadcasting method. The universal design method of navigation message is an alternate broadcasting method among satellites and frequencies and is raised in this thesis. Based on the universal method, message design of Beidou system is taken as an example, and its detailed design is afforded.

2 Alternate Broadcasting Method of Navigation Message among Satellites and Frequencies

Information contents of navigation messages include satellite clock bias parameters, group delay parameters, ephemeris parameters, ionospheric model parameters, almanac parameters, system time synchronization parameters, earth-orientation parameters, etc. Further, satellite clock bias parameters, group delay parameters, and ephemeris parameters are different broadcasted parameters by different satellites; ionospheric model parameters, almanac parameters, system time synchronization parameters, earth-orientation parameters are accordant broadcasted by different satellites. In the new design of this thesis, different message parameters will be parallelly broadcasted by different satellites and frequencies, while the same message parameters will be serially broadcasted by different satellites and frequencies. That is the main idea of navigation message that is alternate broadcasting among satellites and frequencies. By this method, navigation messages received from different satellites and frequencies at the same time could be compensated each other. The communication source could be utilized sufficiently and the navigation messages receiving time will be compressed effectively.

1. Messages alternate broadcasting design among satellites

Navigation message contents alternate broadcasted among satellites including parameters that corporately broadcasted in all satellites. For example, ionospheric model parameters, almanac parameters, system time synchronization parameters, and earth-orientation parameters. Design aim of alternate broadcasting is that the parameters are time-shared by different satellites, and users will receive the parameters side by side from all visual satellites. So that the receiving time will be decreased greatly.

Suppose the system constellation consists of M satellites; total length of navigation message alternate broadcasted in all satellites is K bit, and they have the same broadcast frequencies. According to their visibility, the constellation satellites are divided n groups, $n = 1, 2, 3\ldots M$. Each group has m satellites, and $m = M/n$., messages broadcasting turns of corresponding satellites among groups are conformably. Toward satellite messages broadcasting turns design of each group, the alternate broadcasting contents are divided into m parts with equal length. Each parts signed as $k_1, k_2, k_3 \ldots k_m$, respectively, where k is length and k = K/m (bit). The same information is broadcasted in different satellites by time-sharing. Users can receive parameters' different part from different satellites at the same time. The following is the design of definite broadcasting sequences. In the first satellite of SV-1, the messages broadcasting sequence is $k_1, k_2, k_3, \ldots k_m$; In the second satellite of SV-2, the messages broadcasting sequence is $k_2, k_3, \ldots k_m, k_1$; In the third satellite of SV-3, the messages broadcasting sequence is $k_3, k_4, \ldots k_m, k_1, k_2$; In the mth satellite of SV-m, the messages broadcasting sequence is $k_m, k_1, k_2 \ldots k_{m-1}$. The detailed design is shown in Fig. 1. In Fig. 1, t_0 is the initiative epoch broadcasting the first segment of navigation message, Δtm is broadcasting interval of each segment navigation message broadcasted in each satellite.

Alternate broadcasting turn of navigation messages among satellites shown in Fig. 1 is a universal design. Satellite grouping method of constellation is determined by satellite visibility. The fundamental principle is settling the visible satellites as a group at the same and the same region. Besides, the length k of each message section can be flexibly decided by message total length of K, constellation satellite number of M, and message frame length of N. If K is smaller corresponding to M and N; then k can be magnified properly by increasing satellite groups, for example, taking $n = 3$, $k = 3$ K/M. If K is bigger corresponding to M and N, then k can be magnified properly by decreasing satellite groups, for example, taking $n = 2$, $k = 2$ K/M.

2. Messages alternate broadcasting design among frequencies

Messages alternate broadcasted among frequencies could be all navigation parameters, such as satellite clock bias parameters, group delay parameters, ephemeris parameters, ionospheric model parameters, almanac parameters, system time synchronization parameters, earth-orientation parameters, etc. Messages are alternatively broadcasted among frequencies, and different section message could be broadcasted synchronously by different frequencies of the same satellite. Users can receive different messages from different frequencies at the same time, and messages' receiving delay will be decreased.

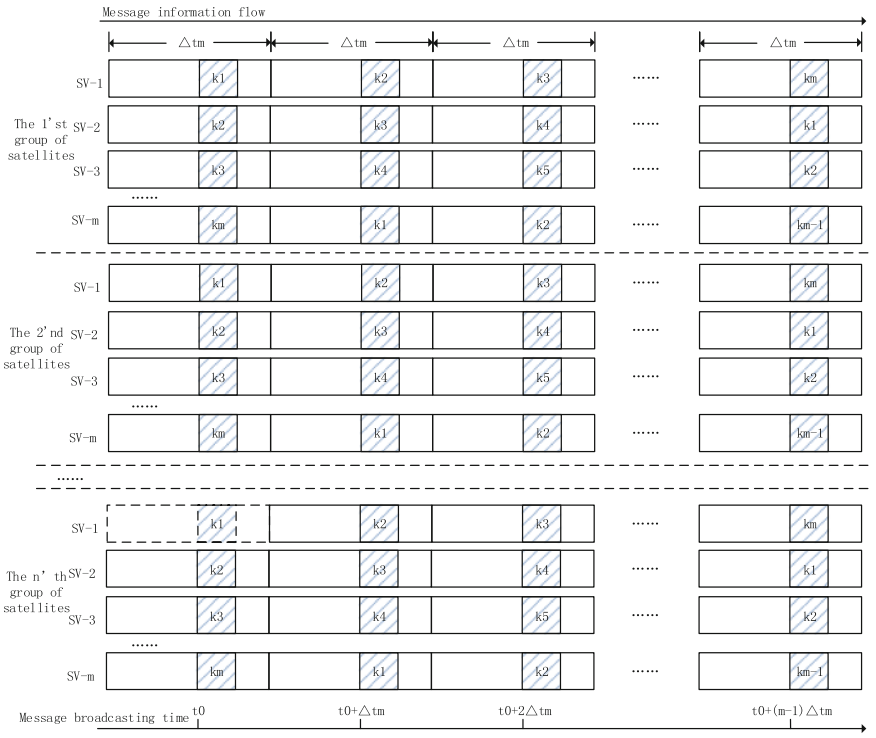

Fig. 1 Alternate broadcasting sequence of navigation messages among satellites

Suppose frequency number of each satellite is F. There have two kinds of messages need to be alternate broadcasted by the F frequencies. The first kind is broadcasted by its own satellite including clock bias parameters, group delay parameters, and ephemeris parameters, and their total length is P. This kind of messages needs higher broadcasting timeliness. The second kind is broadcasted by all satellites including ionospheric model parameters, almanac parameters, system time synchronization parameters, and earth-orientation parameters, and their total length is K. This kind of messages needs lower broadcasting timeliness. The following is the design of message broadcasting turn in multifrequency. Alternate broadcasting messages are divided into l sections with equal length. Each section length of the first kind of messages is p = P/F, and the sections are, respectively, signed as $p_1, p_2,\ldots p_F$. F or the first kind of messages, the specific design of alternate broadcasting turn in different frequencies is provided as follows. In the first frequency of f1, the alternate broadcasting sequence is $p_1, p_2,\ldots p_F$. In the second frequency of f2, the alternate broadcasting sequence is $p_2, p_3,\ldots p_F, p_1$. In the fth frequency of fF, the alternate broadcasting sequence is $p_F, p_1,\ldots p_{F-1}$. The second kind of messages will be alternate broadcasted among satellites and frequencies synchronously. According to forenamed in this thesis, the alternate broadcasting contents among satellites are divided into m sections with equal length, and the

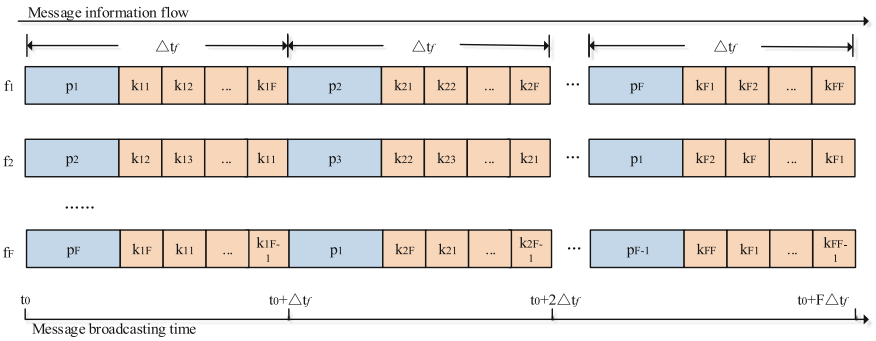

Fig. 2 Alternate broadcasting sequence of navigation messages among frequencies

length is k = K/m. Each section is signed as k_1, k_2, k_3, …k_m, respectively. For easy to be described, the sections are signed as k_x generally. Based on the number of frequencies, each section of k_x is divided into F parts again with equal length, and each part is signed as k_{x1}, k_{x2}, …k_{xF}, respectively. For the second kind of messages, the specific design of alternate broadcasting turn in different frequencies is provided as follows. In the first frequency of f1, the alternate broadcasting sequence is k_{x1}, k_{x2}, …k_{xF}. In the second frequency of f2, the alternate broadcasting sequence is k_{x2}, k_{x3}, …k_{xF}, k_{x1}. In the Fth frequency of fF, the alternate broadcasting sequence is k_{xF}, k_{x1}, …k_{xF-1}. The detail design is shown in Fig. 2. In Fig. 2, t_0 is the initiative epoch broadcasting the first segment of navigation message, Δtf is broadcasting interval of each segment navigation message broadcasted in each satellite.

3 Alternate Broadcasting Design of Beidou Navigation Messages

Constellation of Beidou system has 30 satellites. Each satellite has 3 frequencies named as B1, B2, and B3, and Beidou navigation messages are broadcasted by these three frequencies. Length of message frame is 300 bits, and the frame format is shown in Fig. 3.

Message parameters of Beidou system include satellite clock bias parameters, group delay parameters, ephemeris parameters, signal healthy status, precision of signal in space, ionospheric model parameters, system time synchronization parameters, earth-orientation parameters, and almanac parameters. Broadcasting frequency and data quantity are shown in Table 1. Further, ionospheric model parameters, system time synchronization parameters, earth-orientation parameters, and almanac parameters are broadcasted in all satellites with total length of K = 4997 bit, and these parameters can be alternate broadcasted among satellites and frequencies. Satellite clock bias parameters, ephemeris parameters and precision of signal in space are broadcasted in their own satellite with total length of

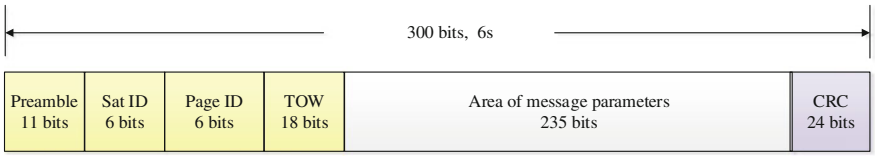

Fig. 3 Frame format of Beidou navigation message

Table 1 Broadcasting frequency and data quantity of Beidou navigation messages

Serial no.	Information contents	Least broadcasting frequency	Data quantity (bits)	Remark
1	Satellite clock bias parameters	30 s	79	Broadcasted in their own satellite
2	Group delay parameters (tgd)	30 s	24	Broadcasted in their own satellite and frequency
3	Ephemeris parameters	30 s	431	Broadcasted in their own satellite
4	Signal healthy status (HS)	30 s	10	Broadcasted in their own satellite and frequency
5	Precision of signal in space	30 s	33	Broadcasted in their own satellite
6	Ionospheric model parameters	5 min	74	Broadcasted in all satellites
7	System time synchronization parameters	5 min	165	Broadcasted in all satellites
8	Earth-orientation parameters	5 min	138	Broadcasted in all satellites
9	Almanac parameters (30 satellites)	5 min	4620	Broadcasted in all satellites

P = 543 bit, and these parameters can be alternate broadcasted among frequencies. Because group delay parameters and signal healthy status are different broadcasted in different satellites and different frequencies, they cannot be alternate broadcasted among satellites or frequencies.

Taking no account of constellation space signals' asymmetric covering, number of visible satellites is generally 10. So the 30 satellites are divided into three groups and satellite number of each group is m = 10. Messages broadcasting sequence of corresponding satellites among groups is conformed. First, messages alternate broadcasted among satellites are divided into 10 sections according to the broadcasting satellites, and the length of each section is 500 bits except that the last section is 497 bits. Second, each section is divided into three subsections according

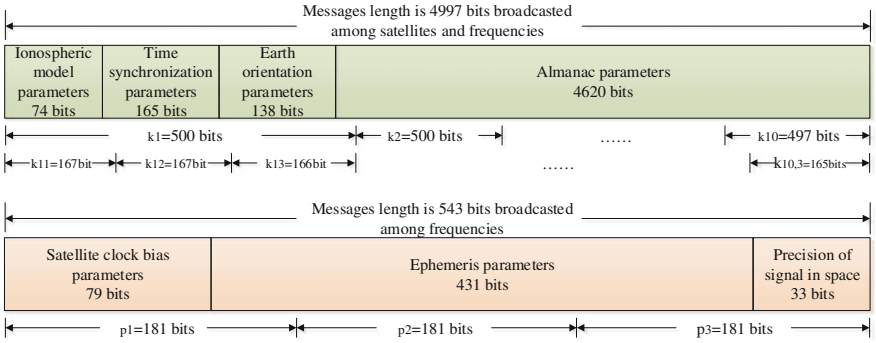

Fig. 4 Beidou message subsection for alternate broadcasting among satellites and frequencies

to the broadcasting frequencies, and the length of each subsection is 167 bits except that the last subsection that is 166 bits. In addition, the subsection length of the last section is 166 bits except that the last subsection is 165 bits. Messages alternate broadcasted among frequencies are divided into three sections according to broadcasting frequencies, and the length of each section is 181 bits. The detailed division is shown in Fig. 4.

According to the design method of alternate broadcasting among satellites and frequencies and the frame format of Beidou navigation messages provided preamble, alternate broadcasting design of Beidou messages is provided as follows. Limiting by the length of the article, three frequencies' message design of the first satellite is offered alone as shown in Fig. 5. To simplify the description, fillings of message parameter area are shown in the figure, while preamble, satellite ID, page ID, and Time of week have not been represented. In addition, Ab is vacant bits and unit of time is second in the figure. Time to broadcast 1 group and 1 section of messages is 30s. There, 1 group messages refer messages broadcasted by its own satellite and frequency, which include satellite clock bias parameters, group delay parameters, ephemeris parameters, signal healthy status, and precision of signal in space; 1 section messages refer messages broadcasted by all satellites. Comparing to the first satellite, sequences of messages broadcasted in all satellites are different are different in the second to the tenth satellites. That is, the arranging sequences of k_{x1}, k_{x2}, k_{x3} (x = 1,2,…10) will be different from Fig. 5, and the detailede design can pay respect to Fig. 1.

It is obvious that for single-frequency receivers, time to receive basic navigation messages is 18–30s and to receive one group of integrity almanac parameters is 300s. There, the basic navigation messages include satellite clock bias parameters, group delay parameters, ephemeris parameters, signal healthy status, and precision of signal in space. For multifrequency receivers, time to receive basic navigation messages is 6–24s, and time to receive almanac parameters is 12–30s. The messages' receiving delay is decreased greatly. For example, when the almanac

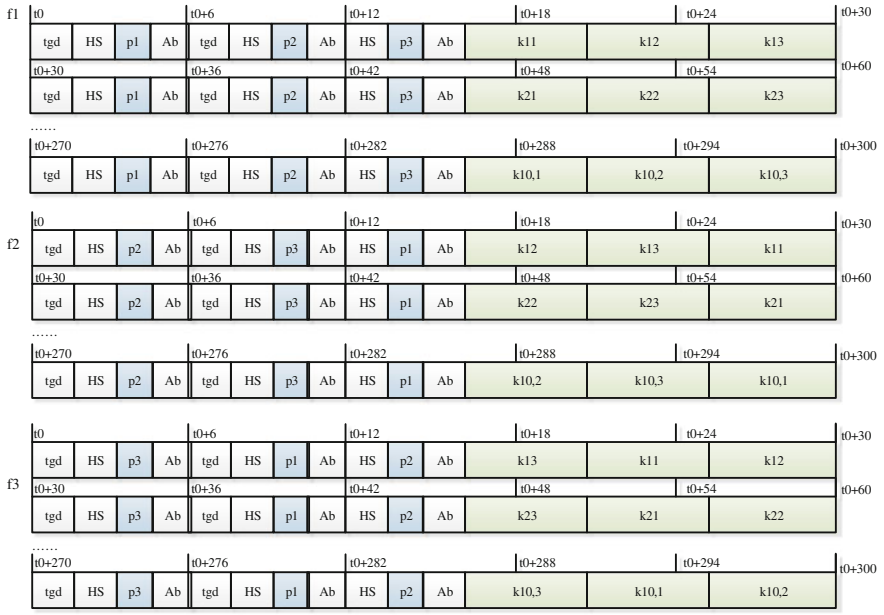

Fig. 5 Alternate broadcasting sequence of Beidou navigation messages among satellites and frequencies

parameters are received synchronously from 10 visible satellites, receiving time of almanac parameters will be decreased to less than 30s. There, it is supposed to be ideal condition and messages of the 10 satellites are alternate broadcasted.

4 Conclusion and Application

Alternate broadcasting method of navigation messages is perfected. A general design method for integrative alternate broadcasting among satellites and frequencies is provided. Taking Beidou constellation and navigation frame as an example, messages' alternate broadcasting sequences are designed in detail. By the way of alternate broadcasting among satellites and frequencies, messages' time efficiency will be improved effectively, while system building cost will not be increased. It is significant in application of satellite prediction, signal acquisition and decreasing of first position time when the receiver is started.

This thesis tries to perform a method for general design, which can provide references for designer of satellite navigation signals and messages. In the design example about Beidou system, there still have more spaces to optimize. For example, in the alternate broadcasting design among satellites and frequencies, messages division of alternate broadcasted messages can be replaced by definition

of different navigation pages to achieve messages' alternate broadcasting. Furthermore, thorough studies can be carried out in the following fields, such as messages' alternate broadcasting among different signals, alternate broadcasting about messages with different broadcasting frequencies, and satellites grouping strategic for alternate broadcasting among satellites.

Acknowledgment Foundation item: National Natural Science Foundation of China (41374038)

References

1. Sam P (2013) Analysis and testing of optimal navigation message rate for IMES. In: 26th International technical meeting of the ION satellite division, Sep 2013, pp 408–415
2. Povalyaev AA (2013) GLONASS navigation message format for flexible row structure. In: 26th International technical meeting of the ION satellite division, Sept 2013, pp 972–974
3. Wang M et al (2014) Design and evaluation of wide area augmentation navigation message In: Conference of statellite navigation (CSNC 2014), May 2014, pp 193–201
4. GAL OS SIS ICD. European GNSS (Galileo) (2014) Open service signal in space interface control document Vol 1(2): 2014

Part II
BDS/GNSS Augmentation Systems and Technology

Irregularities Detection and Bounding Variance Estimation in Ionospheric Grid Model

Dun Liu, Xiao Yu, Liang Chen and Jian Feng

Abstract The ways to detect ionospheric irregularities effects and construct a more effective bounding variance under ionospheric disturbance are presented in the paper. Ionospheric grid model is constructed to estimate the ionospheric delay and its bounding variance at grids. Then a chi-square detector is introduced to check the possible errors in measured ionospheric delays and the effectiveness of grid model. To improve the effectiveness of ionospheric error over bounding, additional term for ionosphere spatial decorrelation is used with an enlarging factor under disturbance condition. The validity of the method is assessed with GPS data from China area.

Keywords Ionosphere · Disturbance · Irregularity · Grid model · SBAS

1 Introduction

Ionospheric grid model is adopted in GNSS space-based augmentation system (SBAS). Both the grid ionospheric vertical delay (GIVD) and its confidence, the grid ionospheric vertical error (GIVE), at ionospheric grid points (IGPs) are estimated in ionospheric grid model. The confidence must bound the errors not only at the grids, but for all interpolated regions between the grids both for the nominal and the disturbed ionosphere condition.

The grid model is in essence a local planar fitting of the ionospheric delays on the thin shell model. Ionospheric disturbance destroys the assumption of ionospheric thin shell model causing uncertainty in ionospheric delay estimation. The estimated confidence is also affected to bound the delay strictly under disturbed ionospheric condition.

D. Liu (✉) · X. Yu · L. Chen · J. Feng
China Research Institute of Radio-Wave Propagation, Qingdao, Shandong, China
e-mail: dun.l@163.com

J. Sun et al. (eds.), *China Satellite Navigation Conference (CSNC) 2016 Proceedings: Volume II*, Lecture Notes in Electrical Engineering 389,
DOI 10.1007/978-981-10-0937-2_12

Unlike the idea in ionospheric physics, ionospheric disturbance (also refer to as irregularity) in grid model is defined as any abnormal ionospheric condition which destroys the assumption of the ionospheric thin shell model, including ionospheric storm, ionospheric anomaly in low latitude region, etc. These phenomena generally cause spatial variation of ionospheric delays in large range, while the temporal variation is relatively slow compared with updating frequency of broadcasting information. Special works have been conducted to take into account the ionospheric delay spatial variation and its correlation structure in grid model for quiet or stormy ionospheric condition [1–5].

In our previous works, spatial correlation structure of ionospheric delay over China area has been studied [6–8]. Here we will focus our efforts on detection of ionospheric irregularities in grid model to find more strict ways to bound the ionospheric error even under the disturbance condition.

In this paper the general way of estimating GIVD and GIVE in grid model is introduced first. In Sect. 2, a chi-square detector is introduced for ionospheric irregularities detection. In Sect. 3, an additional item for ionosphere space decorrelation is adopted with an enlarging factor under disturbance condition to improve the effectiveness of ionospheric error over-bounding. Validity of the method is evaluated with GPS data from China area in Sect. 4, with conclusion in the end.

2 Estimation of Ionospheric Delay and Its Confidence

In grid model, the ionospheric delay and its confidence at IGPs can be estimated by delay measurements at ionospheric pierce points (IPPs) around. Ionospheric delay measurements $I_{v,\,\mathrm{IPP}}$ and its error $\sigma^2_{I_v,\,\mathrm{IPP}}$ at IPPs can be expressed as:

$$I_{v,\,\mathrm{IPP}} = \begin{bmatrix} I_{v,\,\mathrm{IPP}_1} \\ I_{v,\,\mathrm{IPP}_2} \\ \vdots \\ I_{v,\,\mathrm{IPP}_N} \end{bmatrix} \tag{1}$$

$$\sigma^2_{I_v,\,\mathrm{IPP}} = \begin{bmatrix} \sigma^2_{I_v,\,\mathrm{IPP}_1} \\ \sigma^2_{I_v,\,\mathrm{IPP}_2} \\ \vdots \\ \sigma^2_{I_v,\,\mathrm{IPP}_N} \end{bmatrix} \tag{2}$$

Where $\sigma^2_{I_v,\,\mathrm{IPP}}$ is bounding variance for the IPPs which includes errors from measurement noise, multipath, and uncertainty caused by hardware bias. N is the number of available IPPs. Weighting matrix for these IPPs is

$$W^{-1} = \begin{bmatrix} \sigma^2_{I_v,\,\mathrm{IPP}_1} + \sigma^2_{\mathrm{decorr}} & \sigma_{\mathrm{bias},\,1,2} & \cdots & \sigma_{\mathrm{bias},\,1,N} \\ \sigma_{\mathrm{bias},\,1,2} & \sigma^2_{I_v,\,\mathrm{IPP}_2} + \sigma^2_{\mathrm{decorr}} & \cdots & \sigma_{\mathrm{bias},\,2,N} \\ \vdots & \vdots & \ddots & \vdots \\ \sigma_{\mathrm{bias},\,1,N} & \sigma_{\mathrm{bias},\,2,N} & \cdots & \sigma^2_{I_v,\,\mathrm{IPP}_N} + \sigma^2_{\mathrm{decorr}} \end{bmatrix} \tag{3}$$

Where, $\sigma^2_{\mathrm{decorr}}$ is residual error between delays at IPPs caused by spatial decorrelation of ionosphere [2, 7]. $\sigma_{\mathrm{bias},\,1,2}$ is uncertainty caused by hardware bias when the two IPPs share a common satellite or a common receiver [9].

A local coordinate system can be set up with its origin at IGP and with axis x and y pointing to East and North, respectively. Variable $[\hat{a}_0 \quad \hat{a}_1 \quad \hat{a}_2]$ is for delay estimate at IGP, and gradient of delays in East and North direction. $\hat{I}_{v,\,\mathrm{IGP}}$, the delay at IGP can then be derived by the planar fitting with measurements at IPPs around the IGP.

$$\hat{I}_{v,\,\mathrm{IGP}} = \hat{a}_0 + \hat{a}_1 \cdot \left(d_{\mathrm{IPP},\,\mathrm{IGP}} \cdot \hat{E}\right) + \hat{a}_2 \cdot \left(d_{\mathrm{IPP},\,\mathrm{IGP}} \cdot \hat{N}\right) \tag{4}$$

Where, $d_{\mathrm{IPP},\,\mathrm{IGP}}$ is range vector from IPP to IGP, $\hat{E}$, $\hat{N}$ are unit vector to eastward and northward, respectively. For an IGP, observation matrix is given by

$$G = \begin{bmatrix} 1 & d_{\mathrm{IPP}_1,\,\mathrm{IGP}} \cdot \hat{E} & d_{\mathrm{IPP}_1,\,\mathrm{IGP}} \cdot \hat{N} \\ 1 & d_{\mathrm{IPP}_2,\,\mathrm{IGP}} \cdot \hat{E} & d_{\mathrm{IPP}_1,\,\mathrm{IGP}} \cdot \hat{N} \\ \vdots & \vdots & \vdots \\ 1 & d_{\mathrm{IPP}_N,\,\mathrm{IGP}} \cdot \hat{E} & d_{\mathrm{IPP}_N,\,\mathrm{IGP}} \cdot \hat{N} \end{bmatrix} \tag{5}$$

Coefficients at each IGP can be solved by least square method

$$[\hat{a}_0 \quad \hat{a}_1 \quad \hat{a}_2] = \left[\left(\mathrm{GWG}^{\mathrm{T}}\right)^{-1}\mathrm{GW}I_{v,\,\mathrm{IPP}}\right]^{\mathrm{T}} \tag{6}$$

Then ionospheric delay at IGP is given by

$$\hat{I}_{v,\,\mathrm{IGP}} = \hat{a}_0 = [1 \quad 0 \quad 0]\left[\left(\mathrm{GWG}^{\mathrm{T}}\right)^{-1}\mathrm{GW}I_{v,\,\mathrm{IPP}}\right] \tag{7}$$

Error of ionospheric delay estimate is

$$\hat{\sigma}^2_{\hat{I}_{v,\,\mathrm{IGP}}} = \left[\left(\mathrm{GWG}^{\mathrm{T}}\right)^{-1}\right]_{1,1} = \begin{bmatrix} 1 \\ 0 \\ 0 \end{bmatrix}^{\mathrm{T}} \left(\mathrm{GWG}^{\mathrm{T}}\right)^{-1} \begin{bmatrix} 1 \\ 0 \\ 0 \end{bmatrix} \tag{8}$$

3 Construction of Statistic for Ionospheric Disturbance Detection

In essence the grid model is a planer fitting with delays at IPPs to predict delays at IGPs. Ionospheric disturbance detection can then be taken as "goodness-of-fit" test of the planar fitting method in ionospheric grid model.

The chi-square consistency check can be used to determine if measurements are consistent with model. For ionospheric grid model, measurements and its variance are known, together with model for delay estimation. So, a Chi-square detector could be used to check if the measured ionospheric delays are consistent with grid model (or the planar fitting method). When the chi-square statistic exceeds the threshold value, it means that there is error caused by ionospheric disturbance in delay measurements, or the assumption of thin shell model has been broken down by ionospheric disturbance. In this way, the ionospheric disturbance can then be detected.

The grid model can be evaluated around the IGP to provide estimates for each IPP

$$\hat{I}_{v,\,\mathrm{IPP}} \cong \begin{bmatrix} 1 \\ d_{\mathrm{IPP,\,IGP}} \cdot \hat{E} \\ d_{\mathrm{IPP,\,IGP}} \cdot \hat{N} \end{bmatrix} \left[\left(\mathrm{GWG^T} \right)^{-1} \mathrm{GW} I_{v,\,\mathrm{IPP}} \right] \tag{9}$$

The chi-square statistic is defined as

$$\begin{aligned} \chi^2 &\cong I_{v,\,\mathrm{IPP}}^T W \left\{ I - G^{\mathrm{T}} \left(\mathrm{GWG^T} \right)^{-1} \mathrm{GW} \right\} I_{v,\,\mathrm{IPP}} \\ &\cong I_{v,\,\mathrm{IPP}}^T W (I - P) I_{v,\,\mathrm{IPP}} \end{aligned} \tag{10}$$

The degree of freedom in chi-square distribution is the number of IPPs used for IGP delay estimation minus the number of parameters of the model (3 for planar fitting). For the given false alarm rate P_{fd}, the threshold can be calculated by chi-square distribution. If the chi-square statistic is above the threshold, then a problem may occur in the model or the measurements.

4 Consideration for Spatial Decorrelation and Disturbed Ionosphere Condition

For the chi-square statistic formed in last section, if errors are only slightly larger than the expected, it may also pass the chi-square test without triggering the detector. There is a probability of missing detection of big errors whose actual variance is larger than the expected. It may be caused by the imperfect ionospheric spatial decorrelation models or others. In these conditions, we should improve the

estimation of bounding variance (namely the GIVE of IGPs) so that the ionospheric delay error still can be bounded.

The statistic in Sect. 3 is formed under ideal ionospheric thin shell model. In the model ionospheric delays is taken as a smooth plane in local area, so that the ionospheric delay at IGP can be accurately estimated by planar fitting. Yet actually the ionospheric spatial decorrelation causes uncertainty in ionospheric delay distribution, which can be described by the ionospheric decorrelation model [1, 2, 7]. Error caused by this uncertainty in ionospheric delays could be resolved by adding an item σ^2_{decorr} in the estimation of confidence bound. σ^2_{decorr} could be estimated from ionospheric spatial decorrelation models [2, 7, 9].

For the slightly erroneous ionospheric delays that can pass the chi-sqaure detector, the failure mode follows the noncentral chi-square distribution. A method is proposed in Ref. 3 to enlarge the variances of all measured delays by the same factor R^2_{irreg} and then use the new distribution of failure model to determine the missed detection probability. The threshold would then be the value to meet both the false alarm rate P_{fd} and the miss detection probability P_{md} requirement. Given the P_{fd} and P_{md}, the factor R^2_{irreg} is given in (11) with χ^2_p the chi-square value that has p of the distribution below it.

$$R^2_{\text{irreg}}(P_{\text{fd}}, P_{\text{md}}) = \frac{\chi^2_{1-P_{\text{fa}}}}{\chi^2_{P_{\text{md}}}} \tag{11}$$

Considering the ionospheric spatial decorrelation and possible large error in the measured ionospheric delays, the bounding variance for a IGP can then be expressed as

$$\sigma^2_{\text{bound, IGP}} = R^2_{\text{irreg}}\left[\left(\text{GWG}^{\text{T}}\right)^{-1}\right]_{1,1} + R^2_{\text{irreg}}\sigma^2_{\text{decorr}} \tag{12}$$

5 Validation of Bounding Variance Estimation Method

The presented method of bounding variance estimation is validated with GPS data of 1st May 2009 (Day of year DOY 121) and 7th May 2009 (DOY 127) from China and its surrounding areas. The ionosphere is in quiet condition in DOY 121, while there is slight disturbance in DOY 127 (indicated by *Kp* index in Fig. 1).

In the analysis each IPP is taken as a virtual IGP. Ionospheric delay and its bounding variance at the virtual IGP can then be obtained with grid model. With the measured delay at the virtual IGP as real value, the delay error can then be derived and normalized with the estimated bounding variance. Effectiveness of the bounding variance can then be checked by analyzing the distribution of the normalized delay errors.

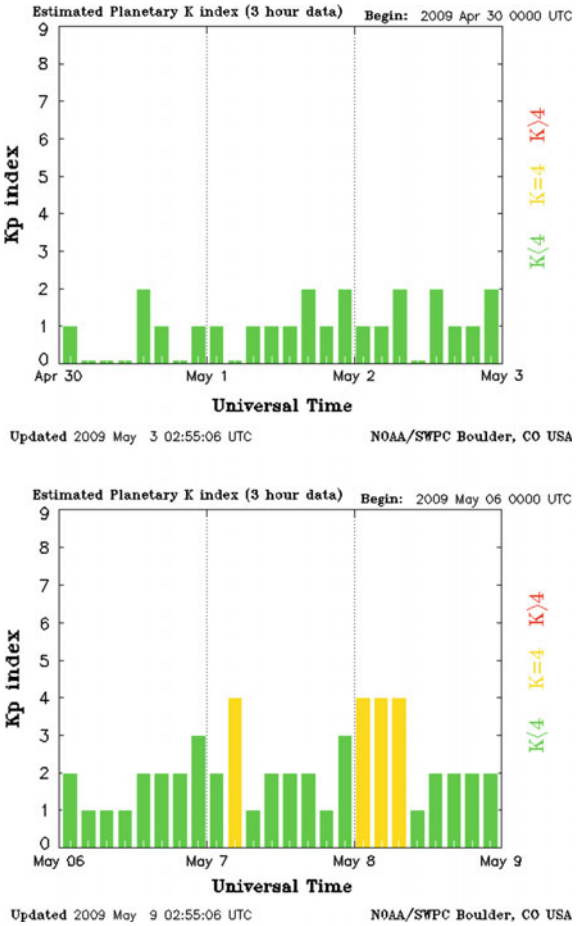

Fig. 1 Kp index for geomagnetic variation. The above is for April 30th–May 2nd 2009, the below for May 6th–May 8th 2009. *Green*, *yellow,* and *red* for quiet, moderate, and severe condition, respectively. (Courtesy of NOAA/SWPC boulder)

Figure 2 shows the distributions of the normalized delay errors with data from DOY121. Here the bounding variance is given by (13) and no σ^2_{decorr} and R^2_{irreg} terms are considered. It means only the errors from measured ionospheric delay and the imperfectness of grid model are taken into account.

$$\frac{I_{v,\,\text{IPP}} - \hat{I}_{v,\,\text{IPP}}}{\sqrt{\left[\left(\text{GWG}^{\text{T}}\right)^{-1}\right]_{1,1}}} \tag{13}$$

It can be seen that the distribution can be bounded effectively by the standard normal distribution, which means the predicted delays are effectively bounded by the bounding variance. Distribution from data of DOY127 is also given in Fig. 3. It can be seen the distribution exceeds the standard normal distribution.

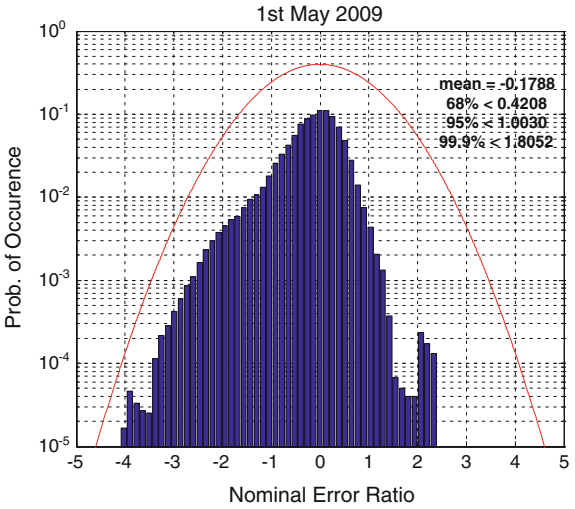

Fig. 2 The histogram of prediction error divided by nominal predicted error with (13) for May 1st 2009. *Red line* is for standard normal distribution

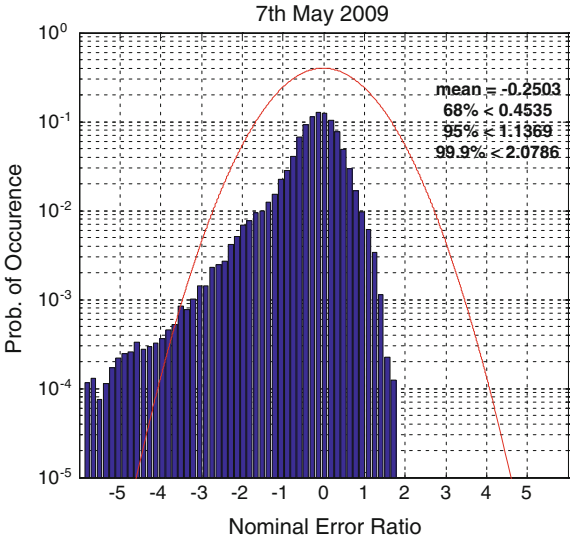

Fig. 3 The histogram of prediction error divided by nominal predicted error with (13) for May 7th 2009. *Red line* is for standard normal distribution

The ionosphere is quiet in DOY 121 while is slightly disturbed in DOY 127 as indicated by the *Kp* index. For calm ionosphere, the estimated delay can be effectively bounded by the bounding variance even without considering the ionospheric spatial decorrelation. Yet, this bounding variance is very much 'vulnerable' as shown by the exceeding of threshold even for a slightly disturbed ionospheric condition in low solar activity such as that of DOY 127 in 2009. The vulnerability will degrade the availability of system. Hence, the bounding variance of ionospheric delay errors should be appropriately increased to improve the availability of the system.

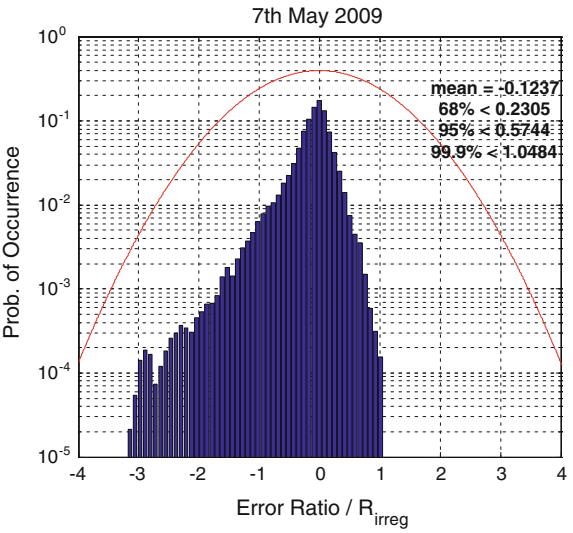

Fig. 4 The histogram of prediction error divided by nominal predicted error with (14) for May 7th 2009. *Red line* is for standard normal distribution

Then the ionospheric spatial decorrelation was considered in estimation of bounding variance and the factor R_{irreg}^2 was also taken into account for possible irregularity effects. The new error distribution was formed with the bounding variance which is given by (14) for DOY 127 (Fig. 4). Obviously, the distribution of ionospheric delay error can then be well bounded by standard normal distribution. It shows effectiveness of the new way of bounding variance estimation.

$$\frac{I_{v,\,\text{IPP}} - \hat{I}_{v,\,\text{IPP}}}{R_{\text{ireeg}}\sqrt{\left[\left(\text{GWG}^{\text{T}}\right)^{-1}\right]_{1,1} + \sigma_{\text{decorr}}^2}} \tag{14}$$

6 Conclusion

Ionospheric delay GIVD and its error GIVE can be estimated by ionospheric grid model. System integrity is realized by bounding the delays errors with GIVEs. Ionospheric disturbance destroys the premise of planar fitting in grid model, causing failure of grid model. A chi-square detector can be used to detect ionospheric disturbance. Detector parameters are derived from ionospheric delay measurements at IPPs.

There is a probability of missing detection of large errors whose actual variance is larger than the expected while the chi-square detector is not triggered. It may be caused by the imperfect ionospheric spatial decorrelation models under disturbance or other factors. Terms of σ_{decorr}^2 for ionospheric spatial decorrelation and R_{irreg}^2 for

possible ionospheric disturbance should be considered in estimation of ionospheric delay and bounding variance for IGP. Test with GPS data in China shows the effectiveness of the method.

References

1. Hansen A, Peterson E, Walter T, Enge P (2000) Correlation structure of ionospheric estimation and correction for WAAS. ION NTM 2000, pp 454–463
2. Hansen A, Walter T, Blanch J, Enge P (2000) Ionospheric spatial and temporal correlation analysis for WAAS: quiet and stormy. ION GPS 2000, pp 634–642
3. Blanch J, Walter T, Enge P (2002) Ionospheric threat model methodology for WAAS. Navigation 49(2):P103–P107
4. Blanch J, Walter T, Enge P (2001) Ionospheric threat model methodology for WAAS. ION AM 2001
5. Altshuler ES, Fries RM, Sparks L (2001) The WAAS ionospheric spatial threat model. ION GPS 2001, pp 2463–2467
6. Liu D, Zhen W (2012) The effects of china regional ionosphere on satellite augmentation system. Chinese J Radio Sci 27(1):195–203 (Ch)
7. Liu D, Zhen W, Chen L (2013) Ionospheric spatial correlation analysis for China area. CSNC 2013, Guangzhou
8. Liu D, Chen L, Chen L, Zhen W (2015) Ionospheric threat model methodology for China Area. CSNC 2015, Xian
9. Walter T, Hansen A, Blanch J, Enge P (2000) Robust detection of ionospheric irregularities. ION GPS 2000, pp 209–218

A New Method for Multiple Outliers Detection in Receiver Autonomous Integrity Monitoring

Jun Zhao, Taogao Dai and Chen Chen

Abstract Integrity of Global Navigation Satellite System (GNSS) includes the ability of a system to provide timely warnings to the user when the system should not be used for the intended operation. Receiver autonomous integrity monitoring (RAIM) is important for safety of life and liability critical applications. Outlier detection and fault exclusion are essential issues for RAIM so that GNSS positioning solutions are not susceptible to errors. Most of existing RAIM algorithms provide adequate integrity for only a single-satellite fault because there is an extremely small probability that significant simultaneous multiple outliers may occur. However, with the development and wide applications of multiple satellites navigation systems with multiple constellations, it is not realistic under assumption of a single outlier once again. RAIM will be required to detect the presence of multiple satellite failures. The study has proposed a new method to select the quasi-accurate observations by L_1 norm method and median and the principle of selecting quasi-accurate observations has been built. Then the quasi-accurate detection of outliers is employed to detect multiple outliers simultaneously. The detail analysis of GNSS single point position example has been conducted to assess the performance of the proposed approach. The results show that the new proposed method is capable of identifying and isolating multiple outliers accurately so that the reliable positioning solution is guaranteed.

Keywords RAIM · Outliers · Quasi-accurate detection · L_1 norm · Median · GNSS single point position

J. Zhao (✉)
Institute of Geospatial Information, Information Engineering University, Zhengzhou 450001, China
e-mail: zhaojun4368@163.com

T. Dai · C. Chen
Institute of Navigation and Aerospace Engineering, Information Engineering University, Zhengzhou 450001, China

J. Sun et al. (eds.), *China Satellite Navigation Conference (CSNC) 2016 Proceedings: Volume II*, Lecture Notes in Electrical Engineering 389,
DOI 10.1007/978-981-10-0937-2_13

1 Introduction

According to the International Civil Aviation Organization's definition of integrity, if the navigation system is not efficient for faults in satellites, the user should be alerted with a timely way [1–3]. Receiver autonomous integrity monitoring (RAIM) as a self-contained integrity monitoring method is researched extensively, which is based on the consistency check of satellite measurement used in a navigation solution [4–6]. In current, most of RAIM procedures are based on the assumption of a single fault, and the so-called parity method and *w*-test method are applied to detect a single outlier. The corresponding theories are studied intensively. But multiple outliers are absolutely possible in Global Navigation Satellite System (GNSS) positioning with the combined use of multiple navigation systems. Therefore, multiple outliers detection should be also paid more attention. In recent years, there are a few literatures for handling multiple outliers. For example, Angus (2006) proposed an extended method to compute the protection levels with multiple outliers, but there are no discussions about the outlier identification [7]. In the event of multiple outliers, generally the *w*-test for a single outlier as a common strategy is applied repeatedly until no further outliers. Hewitson and Wang (2006) have proved that it may lead to the wrong identifications [8]. The RAIM algorithms about two simultaneous faults have been also proposed [9, 10]. But a number of hypothesis tests should be made. Wang and wang (2007) suggested applying the robust M-estimation to mitigate the effect of multiple outliers on GNSS navigation [11]. Of course, other robust estimation methods like least median squares (LMS) method [12] can also achieve the goal. Knight and Wang (2009) compared the outlier detection procedures and robust estimation methods. The conclusion was that the mitigation and detection of outliers for a 100 % success rate was a very challenging task, let along if there are multiple outliers [13]. By bringing in the Gibbs sampler and classification variable, a new Bayesian RAIM method for multiple faults detection was proposed [14]. Through several numerical examples, this new method was demonstrated to be able to identify multiple outliers correctly. Unfortunately, it requires more complex computation of posterior probability. The more efficient methods may be highly desirable.

The quasi-accurate detection of outliers is a very convenient and practical method for detecting multiple outliers. The critical aspects for this method are the reasonable choice of quasi-accurate observations [15–17]. The least squares (LS) residuals or standardized residuals can be applied. As we known, the LS residuals are sensitive to outliers so that it leads to the masking and smearing for outlier identification. For correlated observations, the sensitive index based on sensitive analysis is constructed as a test statistic to select the quasi-accurate observations [18, 19]. In essence, it is to use the statistic with superior robustness for operations. In this paper, we will propose using the L_1 norm method and the median for combination as a new method and built the criterions to select the quasi-accurate observations.

The remaining of the paper is organized as follows. In Sect. 2, the GNSS pseudorange observations equation and the principle of quasi-accurate detection of outliers are briefly introduced. In Sect. 3, the L_1 norm method and median are proposed to select the quasi-accurate observations and the criterions for selection are built. In Sect. 4, to check the effectiveness of the new proposed method, the detail analysis about GPS real data is conducted. In the last section, some concluding remarks are given.

2 Multiple Outliers Detection in RAIM and the Principles of Quasi-Accurate Detection of Outliers

The GNSS pseudorange observations model can be expressed as follows [20]:

$$R_r^s(t_r, t_e) = \rho_r^s(t_r, t_e) - (\delta t_r - \delta t_s)c + \delta_{\text{ion}} + \delta_{\text{tro}} + \delta_{\text{tide}} + \delta_{\text{mul}} + \delta_{\text{rel}} + \varepsilon \quad (1)$$

where

$R_r^s(t_r, t_e)$	is measured pseudorange,
$\rho_r^s(t_r, t_e)$	is the geometric distance between the satellite at the emission time and the antenna at the reception time,
$(\delta t_r - \delta t_s)$	is the difference of time,
c	is the velocity of light,
δ_{ion}	denotes the ionospheric effects,
δ_{tro}	denotes the tropospheric effects,
δ_{tide}	denotes the Earth tide and ocean loading tide effects,
δ_{mul}	denotes the multipath effects,
δ_{rel}	denotes the relative effects and the remaining errors are denoted by ε

The linearized observation model in navigation can be defined by [21]

$$\boldsymbol{L} = \boldsymbol{A}\boldsymbol{X} + \boldsymbol{\Delta} \quad (2)$$

where $\boldsymbol{L}$ is the $n \times 1$ measurement vector, $\boldsymbol{A}$ is the $n \times t$ design matrix reflecting the geometric strength, $\boldsymbol{X}$ is the $t \times 1$ vector of unknown parameters. The expectation of Δ and its variance–covariance matrix are given by:

$$E(\boldsymbol{\Delta}) = \boldsymbol{A}\boldsymbol{X}, D(\boldsymbol{\Delta}) = \sigma_0^2 \boldsymbol{P}^{-1} \quad (3)$$

By employing the LS principle [21], the estimate of the unknown parameters is

$$\hat{\boldsymbol{X}} = \left(\boldsymbol{A}^{\mathrm{T}}\boldsymbol{P}\boldsymbol{A}\right)^{-1}\boldsymbol{A}^{\mathrm{T}}\boldsymbol{P}\boldsymbol{L} \quad (4)$$

the residual is

$$\boldsymbol{V} = \boldsymbol{A}\hat{\boldsymbol{X}} - \boldsymbol{L} = -\boldsymbol{R}\boldsymbol{L} \tag{5}$$

where $\boldsymbol{R} = \boldsymbol{I}_n - \boldsymbol{A}\left(\boldsymbol{A}^{\mathrm{T}}\boldsymbol{P}\boldsymbol{A}\right)^{-1}\boldsymbol{A}^{\mathrm{T}}\boldsymbol{P}$.

If one treats the model (2) to multiply by $\boldsymbol{R}$ with two sides, then one has

$$\boldsymbol{R}\boldsymbol{\Delta} = \boldsymbol{R}\boldsymbol{L} \tag{6}$$

because $\boldsymbol{R}\boldsymbol{A} = \boldsymbol{A} - \boldsymbol{A}\left(\boldsymbol{A}^{\mathrm{T}}\boldsymbol{P}\boldsymbol{A}\right)^{-1}\boldsymbol{A}^{\mathrm{T}}\boldsymbol{P}\boldsymbol{A} = \boldsymbol{O}$. In view of rank defect of the matrix $\boldsymbol{R}$, the estimate of real errors for (6) cannot be derived directly by LS method.Taking example by the idea of quasi-stable adjustment method [22], the real errors of model (6) can be estimated by adding the restricted conditions with the quasi-accurate observations. If one chooses the quasi-accurate observations with number $r(r > t)$, the corresponding observation equations consisting of those quasi-accurate observations can be denoted as

$$\boldsymbol{L}_r = \boldsymbol{A}_r\boldsymbol{X}_r + \boldsymbol{\Delta}_r \tag{7}$$

Similarly, we can derive following equations:

$$\boldsymbol{A}_r^{\mathrm{T}}\boldsymbol{Q}_r^{-1}\boldsymbol{V}_r = 0 \tag{8}$$

where $\boldsymbol{Q}_r$ and $\boldsymbol{V}_r$ are the cofactor matrix and residuals of the observations vector $\boldsymbol{L}_r$, respectively.

Of course, if the quasi-accurate observations are chosen reasonable, the observations in $\boldsymbol{L}_r$ should be clean and the corresponding residuals can be replaced by the real errors. After that, the new equation can be formed as

$$\boldsymbol{A}_r^{\mathrm{T}}\boldsymbol{Q}_r^{-1}\boldsymbol{\Delta}_r = 0 \tag{9}$$

Combing Eq. (6) with Eq. (9), the estimate of real errors can be derived by solving following model.

$$\begin{aligned} \boldsymbol{R}\boldsymbol{\Delta} &= \boldsymbol{R}\boldsymbol{L} \\ \boldsymbol{G}\boldsymbol{\Delta} &= 0 \end{aligned} \tag{10}$$

Here, $\boldsymbol{G} = \boldsymbol{A}_r^{\mathrm{T}}\boldsymbol{Q}_r^{-1}\boldsymbol{W}$ and $\boldsymbol{\Delta}_r = \boldsymbol{W}\boldsymbol{\Delta}$. Through constructing the Lagrange objective function

$$\Omega = (\boldsymbol{R}\boldsymbol{\Delta} - \boldsymbol{R}\boldsymbol{L})^{\mathrm{T}}\left(\boldsymbol{R}\boldsymbol{P}^{-1}\right)^{-}(\boldsymbol{R}\boldsymbol{\Delta} - \boldsymbol{R}\boldsymbol{L}) + 2\lambda^{\mathrm{T}}\boldsymbol{G}\boldsymbol{\Delta} \tag{11}$$

with differential to Δ and $\boldsymbol{\lambda}$, respectively, the estimate of real errors [18] is

$$\hat{\boldsymbol{\Delta}} = \left(\boldsymbol{PR} + \boldsymbol{G}^{\mathrm{T}}\boldsymbol{G}\right)^{-1}\boldsymbol{PRL} \tag{12}$$

If the observations are contaminated with outliers, the corresponding estimates of real errors will far away from other estimates of real errors, which are called "hive off" [15–19]. As a result, making using of the estimates $\hat{\boldsymbol{\Delta}}$, all the outliers can be identified and positioned correctly. After that, it can be estimated by LS method with mean-shift model.

3 The Selection of Quasi-Accurate Observations

The key procedure of the quasi-accurate detection of outliers is to obtain the quasi-accurate observations reasonable. In general, the residuals and standardized residuals can be applied [15–17]. For correlated observations, the sensitive index based on sensitive analysis is constructed to determine the quasi-accurate observations [18, 19]. Due to the sensitive of the residuals to outliers, the study has proposed the L_1 norm method and the median to build a rule for collecting the quasi-accurate observations.

Firstly, for the L_1 norm minimization problem, one can construct the objective function as follows:

$$\Omega = \boldsymbol{p}^{\mathrm{T}}|\boldsymbol{\Delta}| \tag{13}$$

where $\boldsymbol{p}$ is the $n \times 1$ vector consisting of the diagonal elements of the weight matrix. To eliminate the correlations of the observations, the Cholesky factorization

$$\boldsymbol{P}^{-1} = \boldsymbol{Q} = \boldsymbol{S}^{\mathrm{T}}\boldsymbol{S} \tag{14}$$

is conducted. After some transformations, the model (2) is reexpressed as follows:

$$\overline{\boldsymbol{L}} = \overline{\boldsymbol{A}}\boldsymbol{X} + \bar{\boldsymbol{\Delta}} \tag{15}$$

where $\overline{\boldsymbol{L}} = \left(\boldsymbol{S}^{\mathrm{T}}\right)^{-1}\boldsymbol{L}, \overline{\boldsymbol{A}} = \left(\boldsymbol{S}^{\mathrm{T}}\right)^{-1}\boldsymbol{A}, \bar{\boldsymbol{\Delta}} = \left(\boldsymbol{S}^{\mathrm{T}}\right)^{-1}\boldsymbol{\Delta}$. Then, the new objective function is built for model (15) as follows:

$$\Omega = \left|\bar{\boldsymbol{\Delta}}\right| \tag{16}$$

By introducing the slack variable with $\bar{\boldsymbol{\Delta}} = \beta - \gamma, \boldsymbol{X} = \xi - \psi$, the L_1 norm problem (16) is transformed into considering the following linear programming problem:

$$\min \Omega = [\,0 \quad 0 \quad \boldsymbol{h} \quad \boldsymbol{h}\,] \begin{bmatrix} \xi \\ \psi \\ \beta \\ \gamma \end{bmatrix} \tag{17}$$

subject to

$$[\,\overline{\boldsymbol{A}} \quad -\overline{\boldsymbol{A}} \quad \boldsymbol{I}_n \quad -\boldsymbol{I}_n\,] \begin{bmatrix} \xi \\ \psi \\ \beta \\ \gamma \end{bmatrix} = \overline{\boldsymbol{L}} \tag{18}$$

where $\boldsymbol{h} = [1, 1, \cdots, 1]$.

After solving the optimization problem with (17) and (18), the new residuals vector of the L_1 norm solution reads

$$\overline{\boldsymbol{V}} = \hat{\beta} - \hat{\gamma} \tag{19}$$

As a matter of fact, parts of components in $\overline{\boldsymbol{V}}$ got by L_1 norm method will be approximated as zero, which proves that those observations are clear. Consequently, those observations are treated as the first part of quasi-accurate observations. By deleting the corresponding residuals with the quasi-accurate observations, a new vector $\overline{\overline{\boldsymbol{V}}}$ can be constructed with the remaining residuals. Hence, the second part of quasi-accurate observations is those observations if the corresponding residuals of $|\overline{\overline{\boldsymbol{V}}}|$ are less than the given median of $\left|\overline{\overline{\boldsymbol{V}}}\right|$.

If the $k_1, k_2, \cdots, k_m$ observations are distinguished as the observations contaminated with outliers, the mean-shift model can be employed to estimate the outliers as follows:

$$\boldsymbol{L} = \boldsymbol{A}\boldsymbol{X} + \boldsymbol{H}_m \boldsymbol{Z}_m + \boldsymbol{\Delta} \tag{20}$$

where $\boldsymbol{Z}_m = [\boldsymbol{Z}_{k_1}, \boldsymbol{Z}_{k_2}, \cdots, \boldsymbol{Z}_{k_m}]^{\mathrm{T}}$ is the additional parameters with outliers, $\boldsymbol{H}_m = [\boldsymbol{H}_{k_1}, \boldsymbol{H}_{k_1}, \cdots, \boldsymbol{H}_{k_1}]$ is the corresponding coefficient matrix, $\boldsymbol{H}_{k_i} = [0, \cdots, 1, \cdots, 0]^{\mathrm{T}}$ is the unit vector with k_i component equal to zero.

The LS estimate of the outliers is

$$\hat{\boldsymbol{Z}}_m = \left(\boldsymbol{H}_m^{\mathrm{T}} \boldsymbol{P}\boldsymbol{R}\boldsymbol{H}_m\right)^{-1} \boldsymbol{H}_m^{\mathrm{T}} \boldsymbol{P}\boldsymbol{R}\boldsymbol{L} \tag{21}$$

and the estimate of the unknown parameters is

$$\hat{\boldsymbol{X}}_{Z_m} = \left(\boldsymbol{A}^{\mathrm{T}}\boldsymbol{P}\boldsymbol{A}\right)^{-1} \boldsymbol{A}^{\mathrm{T}} \boldsymbol{P}\left(\boldsymbol{L} - \boldsymbol{H}_m \hat{\boldsymbol{Z}}_m\right) \tag{22}$$

The estimate (22) can be considered as the improved estimate of the unknown parameters with the outliers.

4 Experiments and Results

To testify the effectiveness of the new proposed method, the GPS real data for BAKE station are collocated. The observable time is from 00:00:01 to 23:59:59 on 07-11-2015 and sample interval is 30 s. The elevation angle is 15°. The number of visible satellites for each epoch is displayed in Fig. 1.

To compare the w-test method and the new proposed method in this paper, three outliers of size 40 m are injected into pseudoranges with satellites G11, G17 and G19 for epoch 1262 and four outliers of size 30 m are injected into pseudoranges with satellites G5, G16, G18, and G20 for epoch 2442, respectively.

To prove that the LS residuals are not reliable to detect multiple outliers, the epoch 2442 is conducted as an example, and the results are plotted in Fig. 2. Figure 2 shows that the residuals for G22 and G29 are larger in addition to the G20, G5, G18, G16 with outliers. Therefore, one can make a conclusion that the LS residuals are not suitable for identifying the outliers.

For the L_1 norm method proposed in Sect. 3, the new residuals are obtained for each satellite with epoch 1262 and 2442, which is presented in Tables 1 and 2, respectively.

According to the rule of selecting the quasi-accurate observations proposed in Sect. 3, the observations with G28, G13, G18, and G15 for epoch 1262 should be determined as the first part of quasi-accurate observations. Then, by deleting the residuals with the quasi-accurate observations, one constructs a new residual vector with the remaining residuals. And the median of absolute values of the new vector is

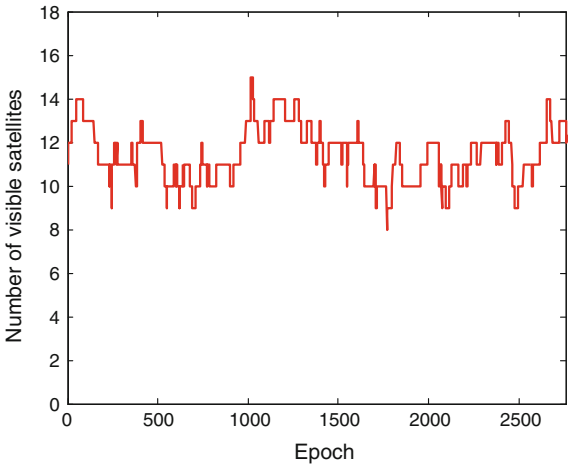

Fig. 1 The number of visible satellites for each epoch

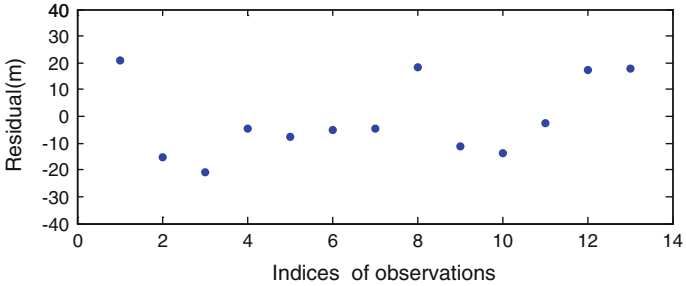

Fig. 2 LS residuals for epoch 2442 with outliers

Table 1 Residuals and choice of quasi-accurate observations for epoch 1262 with outliers

Satellite No.	Residuals	Selecting quasi-accurate observations
G24	−0.32108	+
G1	−0.51369	−
G7	0.34798	+
G30	−0.54608	−
G17	28.566	−
G28	−8.0911e–008	+
G19	37.286	−
G8	−0.42772	+
G22	0.079256	+
G13	−2.3604e–008	+
G11	33.979	−
G18	7.0756e–009	+
G15	−7.8949e–009	+

computed as 0.51369. The second part of quasi-accurate observations can be assigned easily. The specific results are presented in rank 2 of Table 1. The symbol "+" means that the observations are selected as the quasi-accurate observations, and the symbol "−" represents that the observations are non-quasi-accurate observations.

The same with the epoch 1262, for epoch 2442, the observations with G29, G27, G13 and G21 should be selected as the first part of quasi-accurate observations according to the residuals of the L_1 norm solution. Similarly, the corresponding residuals with the quasi-accurate observations are deleted so that the remaining residuals are formed as a new vector. And the median of absolute values of the new vector is computed as 0.89469. The second part of quasi-accurate observations is displayed in Table 2.

After getting the quasi-accurate observations, the real errors can be estimated by quasi-accurate detection of outliers in Sect. 2. The estimates of real errors for epoch 1262 and 2442 are shown in Figs. 3 and 4, respectively.

Table 2 Residuals and choice of quasi-accurate observations for epoch 2442 with outliers

Satellite No.	Residuals	Selecting quasi-accurate observations
G20	28.26	−
G22	−0.62012	+
G29	−7.7785e–016	+
G27	9.7451e–016	+
G13	−1.1339e–013	+
G8	−0.87078	+
G7	−0.87349	+
G5	11.794	−
G21	−3.116e–015	+
G15	−0.89469	−
G30	0.15237	−
G18	25.929	+
G16	11.725	−

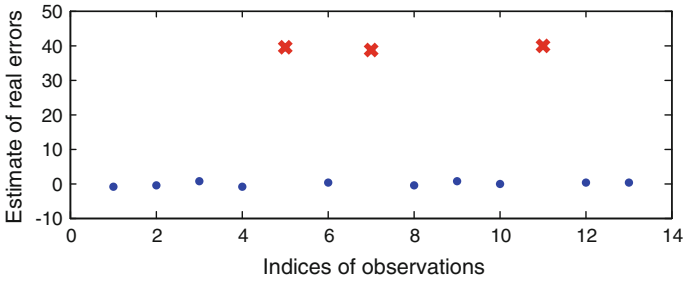

Fig. 3 Hive-off phenomena in estimates of real errors for epoch 1262 with outliers

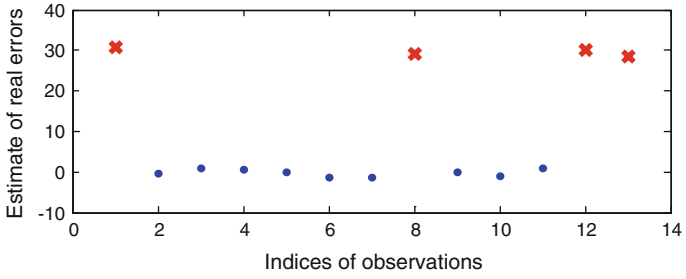

Fig. 4 Hive-off phenomena in estimates of real errors for epoch 2442 with outliers

In Fig. 3, the estimates of real errors for satellite G17, G19 and G11 are far away from others apparently, which is the "hive off" phenomenon. Therefore, those observations are considered as the outliers based on the principle of quasi-accurate

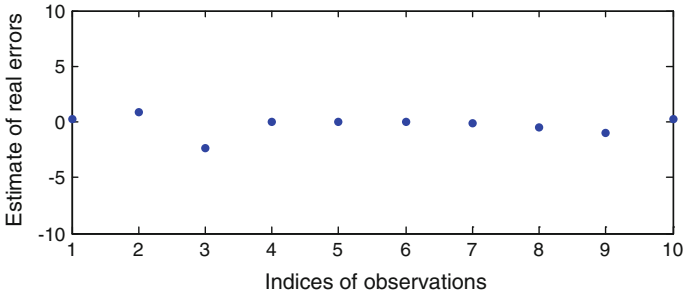

Fig. 5 Hive-off phenomena in estimates of real errors for epoch 2114 without outliers

detection of outliers. Similarly, in Fig. 4, the estimates of real errors for G20, G5, G18, and G16 are far away from other estimate of real errors so that those corresponding satellites are considered as being contaminated with outliers. On the basis of above analysis, all outliers are identified exactly with the simulated case.

However, in practical situations, one cannot judge that there are outliers or not in observations. Hence, the epoch 2114 without adding the outliers is analyzed by the proposed method. The estimates of real errors are given in Fig. 5, which indicates that all the observations are clear because there is no obvious "hive off" phenomenon. It can be used to prove that the proposed method do not identifying the clean observations as outliers. The effectiveness of the new proposed method for selecting quasi-accurate observations is verified strictly.

In order to comparing the w-test method for identifying multiples outliers, the epoch 2442 as an example is discussed. Because the variance of unit weight is unknown, the τ test is applied and the significance lever is chosen as 0.05. The detail results are given in Table 3. Apparently, the satellites G28 and G24 are mistaken as the satellites contaminated with outliers from Table 3, which demonstrates that the τ test is not proper for detecting multiple outliers.

After positioning the outliers, it can be estimated by LS method with mean-shift model. They are

$$[39.9118, 39.0033, 40.0491], [31.2204, 29.8135, 30.2389, 28.2318]$$

By adding the estimates of outliers into the contaminated observations, the revised observations will be derived, which can be used to get the positioning solutions.

The following three schemes will be employed to obtain the bias of positioning solutions.

Scheme 1: Computing the positioning solutions by the observations with outliers;
Scheme 2: Computing the positioning solutions by the revised observations with the estimates of outliers;
Scheme 3: Computing the positioning solutions by deleting the observations contaminated with outliers.

Table 3 The τ-test statistics with outliers and deleting outliers

Satellite No.	τ-test statistics				
	Without deleting outliers	Deleting the satellite G28	Deleting the satellite G17	Deleting the satellite G11	Deleting the satellite G19
24	0.14934	0.27745	0.49959	0.52351	**−1.8238**
1	−1.1607	−1.3536	−1.6182	−1.3884	0.39261
7	−0.27488	0.63509	1.744	2.0632	1.6872
30	−1.1182	−1.3835	−0.81863	−0.81102	–
17	1.7371	**2.0442**	–	–	–
28	**−1.9835**	–	–	–	−1.0169
19	1.4599	0.12229	0.37638	**2.4481**	–
8	−0.50355	−0.2459	−0.76505	−0.31337	−0.58178
22	0.00199	0.17812	−0.15692	0.13416	0.97004
13	−0.2785	−0.76912	0.057861	−0.23895	0.36031
11	1.498	1.3931	**1.7418**	–	–
18	0.16799	0.31065	0.36083	0.46316	−0.18776
15	0.061767	−0.77247	−0.52794	−0.78084	0.77081

The biases of positioning solutions for three schemes are plotted in Figs. 6, 7 and 8, respectively.

The Fig. 6 shows that the positioning solutions are strongly disturbed by the outliers. After identifying the outliers with the proposed approach and by adding the estimates of outliers into the appointed observations, the new positioning solutions are plotted in Fig. 7. Apparently, the bias of the positioning solutions is improved significantly. If one deletes the satellite observations contaminated with outliers,

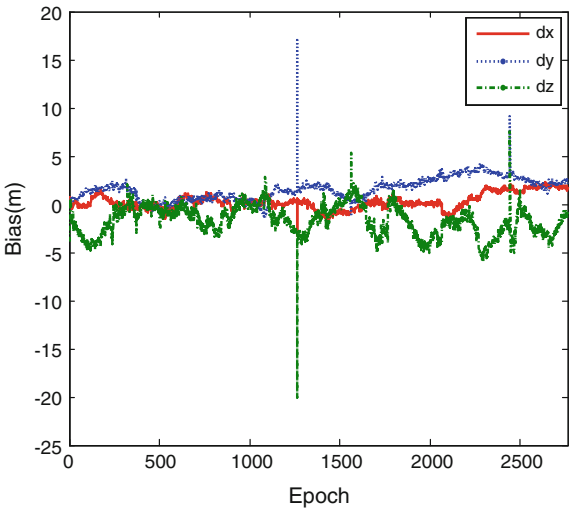

Fig. 6 The bias of positioning solutions with outliers

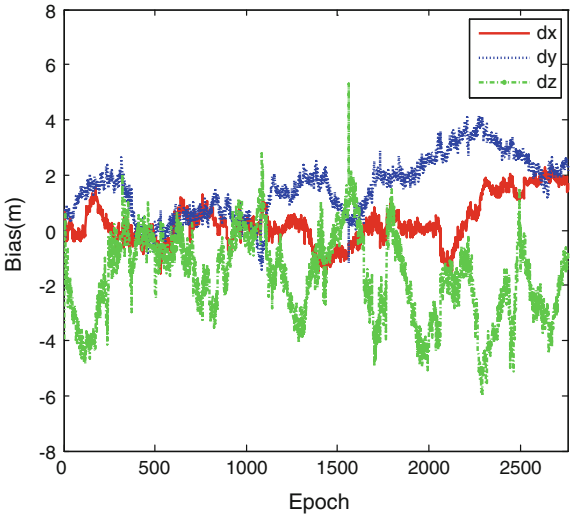

Fig. 7 The bias of positioning solutions with modified observations

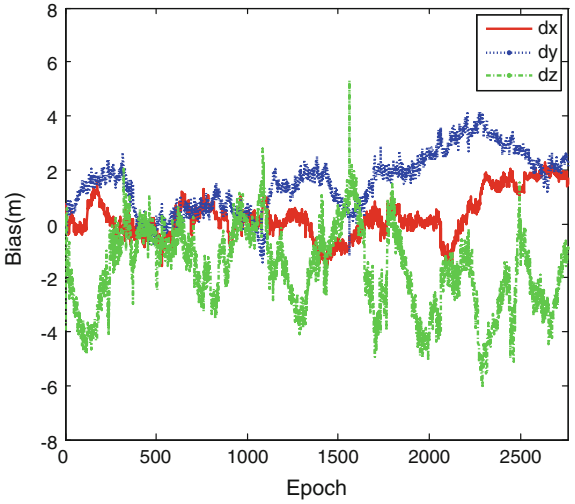

Fig. 8 The bias of positioning solutions with deleting the observations containing the outliers

one can also derive the improved positioning solutions, and the bias is smaller than those containing outliers. However, when the observations are limited, the redundant observations will be decreased by deleting the observations contaminated with outliers. Furthermore, some important information will be lost. Therefore, to modify the observations with the estimates of outliers may be a more reliable strategy.

5 Concluding Remarks

For the complexity of isolating multiple outliers in GNSS RAIM, the quasi-accurate detection of outliers is introduced to detect multiple outliers. The critical aspect for this method is to select the quasi-accurate observations reasonable. Therefore, the study has proposed a new method to choose the quasi-accurate observations, which can be divided into two parts. First, the L_1 norm method is suggested to obtain the robustifed residuals. If the residuals are approximated to zero, the corresponding observations will be treated directly as the first part of quasi-accurate observations. Then deleting those residuals, one can derive the new residuals vector and compute the median of absolute values of the new vector. As a result, the second part of quasi-accurate observations is the observations whose absolute values of the residuals of the new vector are smaller than the computed median. After that, the outliers can be identified by quasi-accurate detection of outliers through "hive off" of the estimates of real errors. After positioning the outliers, the LS method can be employed to estimate it with mean-shift model.

By analyzing the GPS real data, the results illustrate that the new method to select the quasi-accurate observations proposed in this paper is feasible and can identify multiple outliers in GNSS RAIM correctly so that the more reliable positioning solutions are guaranteed. The new proposed method in this paper can also be applied to RAIM algorithms for multiple constellation and integrated navigation with GNSS and inertial navigation.

Acknowledgments This research is sponsored by the National Natural Science Foundation of China (Grant No. 41174005, 41474009).

References

1. Obser P (2003) Integrity prediction and monitoring of navigation systems. Integricom publishers
2. Wang J, Obser P (2009) On the availability of fault detection and exclusion in GNSS reveiver autonomous integrity monitoring. J Navig 62(2):1–11
3. Hewitson S, Wang J (2007) GNSS receiver autonomous integrity monitoring with a dynamic model. J Navig 60(2):247–263
4. Brown R (1992) A baseline GPS RAIM scheme and a note on the equivalence of three RAIM methods. J Inst Navig 39(3):301–316
5. Parkinson B, Axelrad P (1988) Autonomous GPS integrity montoring using the pseudorange residual. Navig 35(2):49–68
6. Yang L, Knight N, Li Y, Rizos C (2013) Optimal fault detection and exclusion applied in GNSS positioning. J Navig 66:683–700
7. Angus J (2006) RAIM with multiple faults. Navigation 53(4):249–257
8. Hewitson S, Wang J (2006) GNSS receiver autonomous integrity monitoring (RAIM) for multiple outliers. J Navig 4(4):47–54
9. Liu J, Lu M, Cui X, Feng Z (2007) Theoretical analysis of RAIM in the occurrence of simultaneous two-satellite faults. IET Radar Sonar Navig 1(2):92–97

10. Knight N, Wang J, Rizos C, Han S (2009) GNSS integrity monitoring for two satellite faults. Int Glob Navig Satell Syst Soc IGNSSS Symp
11. Wang J, Wang J (2007) Mitigating the effect of multiple outliers on GNSS navigation with M-estimation schemes. Int Glob Navig Satell Syst Soc IGNSS Symp
12. Rousseeuw P (1984) Least median of squares regression. J Am Stat Assoc 79:871–880
13. Knight N, Wang J (2009) A comparison of outlier detection procedures and robust estimation methods in GPS positioning. J Navig 62(4):699–709
14. Zhang Q, Gui Q (2015) A new Bayesian RAIM for multiple faults detection and exclusion in GNSS. J Navig 68(3):465–479
15. Ou J (1999) Quasi-accurate detection of outliers (QUAD). Acta Geodaetical et Cartographica Sinica 28(1):15–20
16. Ou J (2000) Selection of quasi-accurate observations and "Hive off" phenomena about the estimators of real errors. Acta Geodaetica Cartogr Sin 29(1):5–10
17. Ou J (2002) Further on the principle, implementation and application of quasi-accurate detection method. Eng Surveying Mapp 11(4):3–6
18. Guo J, Ou J, Wang H (2007) Quasi-accurate detection of outliers for correlated observations. J Surveying Eng 133(2):129–133
19. Guo J (2007) Theory of model errors and its applications in GPS data processing. Institute of Geodesy and Geophysics, Chinese Academy of Sciences, Wuhan
20. Xu G (2007) GPS theory, algorithms and applications, 2nd edn. Springer, New York
21. Koch K (1999) Parameter estimation and hypothesis testing in linear models, 2nd edn. Springer-Verlag, New York
22. Zhou J (1980) Quasi-stable adjustment of monitoring networks. Special Publication, No.2, Institute of Geodesy and Geophysics, Chinese Academy of Sciences, Wuhan

Reliability and Separability Analysis of Integrated GPS/BDS System

Youlong Wu, Jinling Wang, Zhong Yang, Ling Yang and Gang Sun

Abstract With a hybrid constellation comprised of geostationary orbit (GEO) satellite, inclined geosynchronous orbit (IGSO) satellite and medium earth orbit (MEO) satellite, the BeiDou satellite navigation system (BDS) has the potential to provide navigation solutions with high accuracy and integrity, either as a standalone system or compensates with others. In this paper, the navigation performances of BDS are compared with GPS, in minimum detectable biases (MDBs), as well as fault separability capability are evaluated via simulation analysis. The MDB characteristics of different BDS satellites are summarized. For the GPS/BDS integrated system, the reliability and separability are all largely improved. In the integrated system the MDBs values for BDS MEO and IGSO and GPS satellites are both smaller than 6 m, while the values for the GEO satellite are between 8 and 9 m. The corresponding correlation coefficients between the fault detection statistics are all less than 0.5 and 80 % of them are smaller than 0.3. This ensures a higher probability of successfully identifying the fault, compared with the standalone systems.

Keywords Global positioning system (GPS) · Beidou navigation satellite system (BDS) · Reliability · Separability

Y. Wu (✉) · Z. Yang · G. Sun
College of Intelligent Science and Control Engineering,
Jinling Institute of Technology, Nanjing 211169, China
e-mail: youlong_wu@jit.edu.cn; youlong.wu@hotmail.com

J. Wang
School of Civil and Environmental Engineering,
University of New South Wales, Sydney, NSW 2052, Australia

L. Yang
College of Surveying and Geo-Informatics, Tongji University,
Shanghai 200092, China

J. Sun et al. (eds.), *China Satellite Navigation Conference (CSNC) 2016 Proceedings: Volume II*, Lecture Notes in Electrical Engineering 389,
DOI 10.1007/978-981-10-0937-2_14

1 Introduction

Positioning and navigation is highly needed in many applications such as aerospace, aviation, transportation, location-based services etc. Such high demand for positioning and navigation has been boosting the rapid development of GNSSs during the past half century. Current and prospective providers of GNSS systems are the American GPS, the Russian GLONASS, the European-controlled Galileo system, and the Chinese BeiDou Navigation Satellite System (BDS). Unlike other GNSS systems, BDS adopts a unique system design to approach its capability of providing high accuracy positioning services to China and Asia-Pacific region [1]. The system will be a constellation of 35 satellites, including 5 geostationary orbit (GEO) satellites and 30 non-geostationary satellites [27 in medium earth orbit (MEO) and 3 in inclined geosynchronous orbit (IGSO)], to offer the full operation capability [2]. With this unique constellation, the BDS system is aimed to significantly enhance the signal coverage and to improve the geometry strength for positioning, navigation, and timing purpose within the Asian Pacific area at the current stage of its development as well as globally by 2020.

To improve the overall performance of a navigation system, including accuracy, integrity, availability and continuity, fusing multiple constellations is surely the future tendency in the study of navigation field [3]. Navigation system integrity refers to the ability of the system to provide timely warnings to users when the system should not be used for navigation and therefore provide quality control to the system. Integrity monitoring of the navigation system can be achieved based on some kind of self-consistency check among the available measurement, independent of any external reference systems. Such kind of monitoring is referred to as receiver autonomous integrity monitoring (RAIM) [4]. Ideal RAIM method involves the detection, isolation, and exclusion of faulty measurement sources from the navigation solution. In the absence of integrity monitoring (which can be defined as a measure of the reliability of a computed result), users are not aware of the presence of faults or outliers and will trust positioning solution provided by their GPS receiver. Thus, assessing the RAIM performance is of great important for a satellite navigation system, especially for those life-critical applications.

In addition to real-time alert of a satellite failure, a GNSS RAIM system is also expected to provide a measure for the system reliability and separability. Reliability is an assessment of the capability of GNSS receivers to detect outliers. Separability refers to the system's ability to correctly identify the detected outliers from the measurements. The RAIM studies on multi-GNSSs have gained much attention for a long time. The RAIM availability in the GPS/GLONASS integrated system is investigated in [5]; the performance of Galileo standalone and GPS/Galileo integrated system in terms of system availability, reliability, and separability are compared in [6]; the availability and reliability analyses of GPS/Galileo integrated system are also studied in [7]; the RAIM performance of GPS, Galileo, BDS, and GPS/Galileo/BDS integrated system are analyzed in [8]; the benefits of BDS and

GPS/BDS integrated system compared to the GPS system standalone on the system availability and reliability aspects is discussed in [9].

The paper is organized as follows. The fundamentals of RAIM algorithms are given in Sect. 2. Section 3 introduces the mathematics of multi-constellation integration, including coordinate system, time system, and measurement weighting algorithms. In Sect. 4, simulations are given to assess the performance of BDS, GPS, and GPS/BDS integrated system, including the reliability and separability.

2 RAIM Algorithms

The linearized GNSS measurement model can be expressed as [10–12]

$$\boldsymbol{l} = \boldsymbol{A}\boldsymbol{x} + \boldsymbol{v} \tag{1}$$

where $\boldsymbol{v}$ is the n by 1 vector of residuals, $\boldsymbol{A}$ is the n by t design matrix, $\boldsymbol{x}$ is the vector of t unknown, and its estimated value is $\hat{\boldsymbol{x}}$, $\boldsymbol{l}$ is the n by 1 measurement vector containing the pseudo-range and the distances between satellites to receiver. The n by n positive definite variance covariance matrix $\boldsymbol{\Sigma}$ of the measurements is given by

$$D(\boldsymbol{l}) = \boldsymbol{\Sigma} = \sigma_0^2 \boldsymbol{Q} = \sigma_0^2 \boldsymbol{P}^{-1} \tag{2}$$

where σ_0^2 is the a priori variance factor, $\boldsymbol{Q}$ is the n by n cofactor matrix, and $\boldsymbol{P}$ is the n by n corresponding weight matrix.

The optimal estimates for the state parameters $\hat{\boldsymbol{x}}$ and the error covariance matrix $\boldsymbol{Q}_{\hat{\boldsymbol{x}}}$ are

$$\begin{cases} \hat{\boldsymbol{x}} = \left(\boldsymbol{A}^{\mathrm{T}}\boldsymbol{P}\boldsymbol{A}\right)^{-1}\boldsymbol{A}^{\mathrm{T}}\boldsymbol{P}\boldsymbol{l} \\ \boldsymbol{Q}_{\hat{\boldsymbol{x}}} = \left(\boldsymbol{A}^{\mathrm{T}}\boldsymbol{P}\boldsymbol{A}\right)^{-1} \end{cases} \tag{3}$$

From the least-squares principles the corresponding residual vector and the cofactor matrix are given by [12]

$$\begin{cases} \boldsymbol{v} = \left(\boldsymbol{I} - \boldsymbol{A}\left(\boldsymbol{A}^{\mathrm{T}}\boldsymbol{P}\boldsymbol{A}\right)^{-1}\boldsymbol{A}^{\mathrm{T}}\boldsymbol{P}\right)\boldsymbol{l} \\ \boldsymbol{Q}_{\boldsymbol{v}} = \boldsymbol{Q} - \boldsymbol{A}\left(\boldsymbol{A}^{\mathrm{T}}\boldsymbol{P}\boldsymbol{A}\right)^{-1}\boldsymbol{A}^{\mathrm{T}} \end{cases} \tag{4}$$

The most import components of the RAIM algorithm are outlier identification, reliability, and separability. They are briefly explained as below. More detailed information can be referred to [13, 14].

Once a fault has been detected with a global detection method, the w-test can then be used to locate the faulty measurement, the test statistic to assess the *i*th measurement can be formed as [10, 13]

$$w_i = \frac{\nabla_i}{\sigma_0 \sqrt{Q_{\nabla_i}}} = \frac{\boldsymbol{h}_i^{\mathrm{T}} \boldsymbol{P} \boldsymbol{Q}_v \boldsymbol{P} \boldsymbol{l}}{\sigma_0 \sqrt{\boldsymbol{h}_i^{\mathrm{T}} \boldsymbol{P} \boldsymbol{Q}_v \boldsymbol{P} \boldsymbol{h}_i}} \tag{5}$$

where $\boldsymbol{h_i}$ is a unit vector in which the *i*th component has a value equal to one and dictates the measurement to be tested.

The measure of internal reliability is quantified as the minimal detectable biases (MDBs), indicating the lower bound for detectable outliers. The MDB is the magnitude of the smallest error that can be detected for a specific level of confidence and is given by [12, 14]

$$MDB_i = \frac{\delta_0}{\sqrt{\boldsymbol{h}_i^{\mathrm{T}} \boldsymbol{P} \boldsymbol{Q}_v \boldsymbol{P} \boldsymbol{h}_i}} \tag{6}$$

where δ_0 is the theoretical non-centrality parameter that is computed via $\delta_0 = u_{1-\alpha/2} + u_{1-\beta}$ where α is the level of significance of the test and β is the power of the test. Equation (6) indicates that the MDBs are highly dependent on the number of the visible satellites and geometric distribution of the constellation.

The correlation coefficient between a pair of outlier statistics is given by [12]

$$\rho_{ij} = \rho_{ji} = \frac{\boldsymbol{h}_i^{\mathrm{T}} \boldsymbol{P} \boldsymbol{Q}_v \boldsymbol{P} \boldsymbol{h}_j}{\sqrt{\boldsymbol{h}_i^{\mathrm{T}} \boldsymbol{P} \boldsymbol{Q}_v \boldsymbol{P} \boldsymbol{h}_i} \cdot \sqrt{\boldsymbol{h}_j^{\mathrm{T}} \boldsymbol{P} \boldsymbol{Q}_v \boldsymbol{P} \boldsymbol{h}_j}} \tag{7}$$

The correlation coefficient has the property of $|\rho_{ij}| \leq 1$, where 1 and 0 correspond to full and zero correlation between the two test statistics, respectively. The larger the correlation between two test statistics, the more difficult it is to separate between these two statistics. We noted that locating a fault is based on the assumption that the redundant number is larger than 1. If the measurement redundancy is equal to 1, it may be able to detect the fault which however, cannot be identified, as all the identification test statistics are fully correlated in this case.

3 Multi-constellation System with Critical Parameters Design

When fusing multi-constellation and multi-frequency GNSS data, the number of available measurements is largely increased, so as to enhance the overall performance of the system. Nevertheless, the different characteristics of these individual

systems result in a number of issues to successful integration of these constellations, such as different coordinate systems, different time frames, as well as the variety of measurement accuracies. These issues will be discussed as follows.

Measurements from multiple satellite systems should be constructed in a unified space coordinate system. This step can be executed by transforming the coordinate system of BDS to the GPS coordinate frame using instance Bursa model with seven transformation parameters [8]

$$\begin{pmatrix} X \\ Y \\ Z \end{pmatrix}_2 = \begin{pmatrix} \Delta X \\ \Delta Y \\ \Delta Z \end{pmatrix} + (1+k) \begin{bmatrix} 1 & \Omega_Z & -\Omega_Y \\ -\Omega_Z & 1 & \Omega_X \\ \Omega_Y & -\Omega_X & 1 \end{bmatrix} \begin{pmatrix} X \\ Y \\ Z \end{pmatrix}_1 \tag{8}$$

where $(\Delta X \quad \Delta Y \quad \Delta Z)^{\mathrm{T}}$ is drifting parameter, $(\Omega_X \quad \Omega_Y \quad \Omega_Z)^{\mathrm{T}}$ is rotation parameter, k is scaling parameter.

In a multi-constellation system, the time difference between different systems should be considered. With a clock bias parameter for each system, the different time frames can be united to a unique frame. The observation model of N GPS satellites and K BDS satellites can then read [3, 9]

$$\begin{bmatrix} y_{N\times 1} \\ y_{K\times 1} \end{bmatrix} = \begin{bmatrix} G_{N\times 3} & 1_{N\times 1} & 0_{N\times 1} \\ G_{K\times 3} & 0_{K\times 1} & 1_{K\times 1} \end{bmatrix} \begin{bmatrix} \mathrm{d}x \\ \mathrm{d}y \\ \mathrm{d}z \\ \mathrm{d}t_{GPS} \\ \mathrm{d}t_{BDS} \end{bmatrix} + \begin{bmatrix} v_{N\times 1} \\ v_{K\times 1} \end{bmatrix} \tag{9}$$

where the subscripts N and K are the number of GPS and BDS satellites, referring to the size of the corresponding matrices or vectors, $\mathrm{d}t_{\mathrm{GPS}}$ and $\mathrm{d}t_{\mathrm{BDS}}$ denote the receiver clock errors for GPS and BDS systems, respectively.

In a multi-constellation system, the accuracies of the measurements from different GNSS systems are usually different. The measurement accuracy of MEO and IGSO satellites in BDS system are assumed to be the same as that of GPS [9]. While the measurement accuracy of GEO satellites equals to an amplification ratio on the foundation of MEO satellites. Generally, all measurement errors for the pseudo-ranges are assumed to be normally distributed with zero mean, as

$$\Delta\rho_{\mathrm{MEO}} \sim N\left(0, \sigma_M^2\right); \quad \Delta\rho_{\mathrm{IGSO}} \sim N\left(0, \sigma_I^2\right); \quad \Delta\rho_{\mathrm{GEO}} \sim N\left(0, \sigma_G^2\right) \tag{10}$$

where σ_M, σ_I and σ_G are the standard deviations of MEO, IGSO, and GEO satellites, respectively. In the simulation of this paper, it is assumed that $\sigma_M = \sigma_I = 1.5$m and $\sigma_G = 2.5$ m. It is also assumed that all the pseudo-range measurements are uncorrelated, and the cofactor matrix for measurements is expressed as follows

$$\boldsymbol{Q} = \mathrm{diag}\left(\sigma_M^2 \boldsymbol{I}_{m\times m}, \quad \sigma_I^2 \boldsymbol{I}_{n\times n}, \quad \sigma_G^2 \boldsymbol{I}_{k\times k}\right) \tag{11}$$

where the subscripts m, n, and k are the number of MEO, IGSO, and GEO satellites, respectively; and $\boldsymbol{I}$ means an identity matrix. Accordingly, the weight matrix for least-squares estimation is

$$\boldsymbol{P} = \boldsymbol{Q}^{-1} = \mathrm{diag}\left(\frac{1}{\sigma_M^2}\boldsymbol{I}_{m\times m},\quad \frac{1}{\sigma_I^2}\boldsymbol{I}_{n\times n},\quad \frac{1}{\sigma_G^2}\boldsymbol{I}_{k\times k}\right) \tag{12}$$

4 Numerical Experiments and Analysis

The accuracy of satellite positions is crucial in a positioning system. Generally, a satellite position can be determinated by using the Keplerian orbital elements such as semi-major axis, eccentricity, inclination, right ascension of ascending node, argument of perigee, and mean anomaly. For the simulation tests here, the Keplerian orbit parameters of BDS system [15] is listed in Table 1. The GPS satellite coordinates were determined by the precise ephemeris downloaded from the IGS website. During the whole simulation period, 32 GPS satellites and 35 BDS satellites were employed. The GPS and BDS sample intervals are both 1 s and masking elevation angle was set to be 15°. The ground tracks of BDS GEO and IGSO satellites are shown in Fig. 1. It shows that the trajectory of IGSO satellites forms an '8' and the trajectories of the three IGSO satellites are coincident. With this specific constellation, the signal coverage of BDS is further enhanced in the Asian pacific area. The parameters used for the reliability and separability analysis were set as $\alpha = 0.1\ \%$ and $\beta = 80\ \%$.

4.1 Reliability Performance

Figure 2 shows the change tendency of MDB values of GPS and BDS standalone system within 1000 s. It can be seen that during the simulated period the MDBs of GPS and BDS both vary from about 6 m to 20 m. For different satellites, the MDB

Table 1 Orbital parameters for BDS in simulation scenario

Orbit	MEO	GEO	IGSO
Semi-major axis/a (km)	27878.1	42164.17	42164.17
Inclination angle/i (°)	55	0	55
Orbit eccentricity/e	0	0	0
Argument of perigee/ω(°)	0	0	0
Ascending node/Ω(°)	0, 120, 240	58.75, 80, 110.5, 140, 160	118, 118, 118
Mean anomaly/M_0((°))	0, 15, 30, 75, 120, 165, 210, 255, 300	0	0, 120, 240

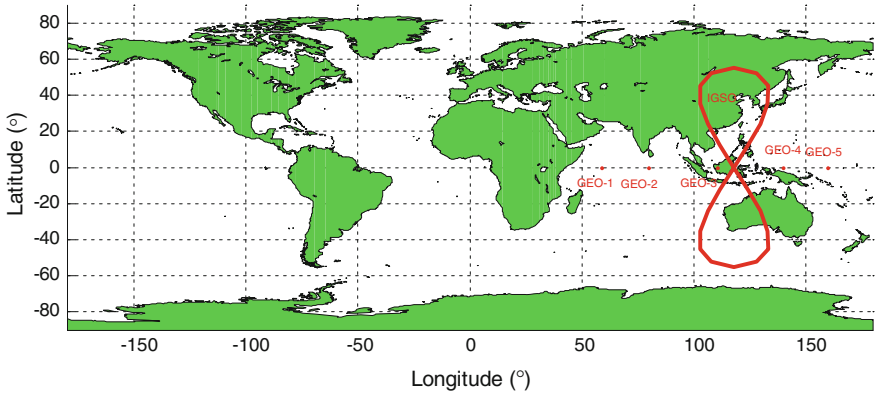

Fig. 1 Sub-satellite point track of BDS GEO and IGSO

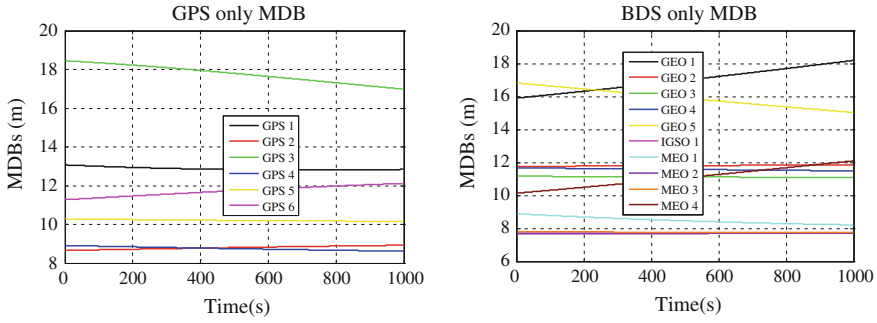

Fig. 2 MDBs for GPS and BDS measurements

values are different. This indicates that when a fault occurring on the measurement from different satellites, the system's capability of detecting the fault is different. Noted that although BDS GEO satellites are stationary respect to the ground, their MDBs values are still changed over time. This is due to the influence of other MEO satellites on the geometry strength of the constellation.

To compare with GPS and BDS standalone system, the MDBs of each satellite in the GPS/BDS integrated system are shown in Fig. 3. We can see that these MDB values are reduced significantly. Compared with Fig. 2, it can be seen that the maximum value of these MDBs decreases from 19 m to less than 13 m. It also shows that all the MDB values in the integrated system become much more stable over time. Similar as that in the BDS standalone system, the MDBs for GEO satellites are larger than those for MEO satellites, although all of them are reduced. It is noted that the measurements from GEO satellites are usually with a lower accuracy than MEO satellites due to a couple of reasons, such as lower elevation, longer observation distance, and so on.

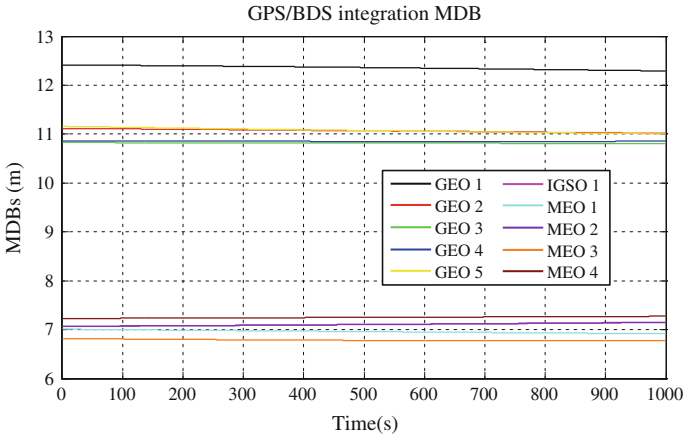

Fig. 3 MDBs for GPS/BDS measurements

4.2 Separability Performance

To evaluate the separability for faulty measurements in the GPS, BDS, and GPS/BDS integrated system, the correlation coefficient matrix for the w-test statistics of the three systems at the 100th second are shown in Figs. 4 and 5. In this simulation test, there were 6 GPS satellites and 10 BDS satellites in view. Figure 4 illustrates in the GPS and BDS system all the diagonal elements are one and all other elements are smaller than one, which means each test statistic is fully correlated with itself and partly correlated with others. The larger the value, the greater the correlation is. Comparing the two figures in Fig. 4, it can be seen that the correlation coefficients in BDS is generally smaller than those in GPS system. This

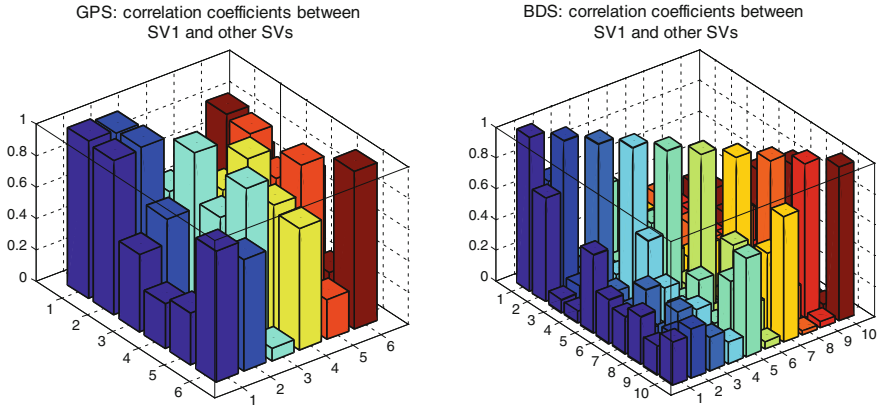

Fig. 4 Correlation coefficients for epoch 100 s of GPS and BDS only

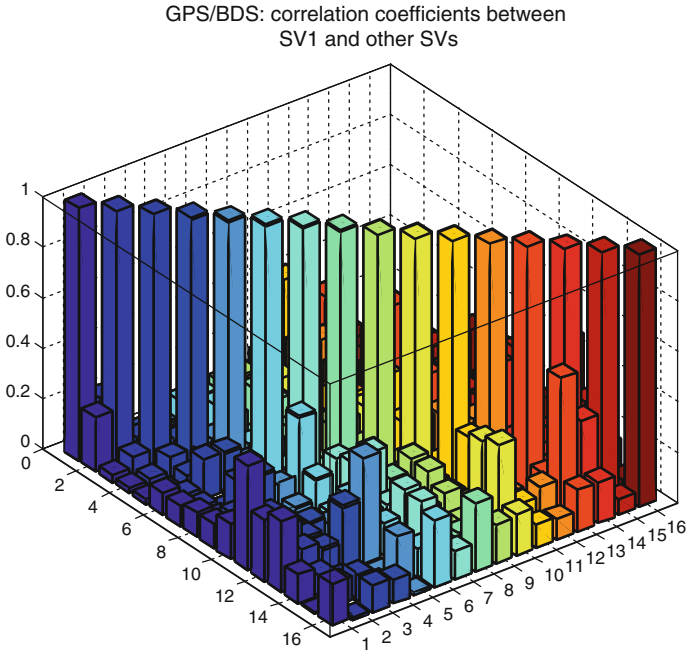

Fig. 5 Correlation coefficients for epoch 100 s of GPS/BDS integration

is because there are much more visible satellites in the BDS system, thus generating a better geometry. Figure 5 shows when fusing BDS and GPS systems, the correlation coefficients are all reduced dramatically, all of them are smaller than 0.5. While Fig. 4 illustrates nearly 30 % of the non-diagonal values are higher than 0.5. This means the capability of correctly identifying a fault in the integrated system is largely improved by increasing the redundancy number as well as enhances the geometry distribution.

To analyze the overall distribution condition of the correlation coefficients during the test, the correlation coefficients were divided into ten groups with steps of 0.1 and the numbers of the correlation coefficients with each interval are listed in Table 2. It is clear that nearly 30 % of the correlation coefficients in GPS standalone system exceeds 0.8, which indicates a disadvantaged condition for successfully identifying and excluding the fault between the two measurements. For BDS system the corresponding possibility is just 2 %. This means the fault detection and exclusion capability of the BDS is rather better than GPS system. When fusing GPS and BDS measurements, the number of visible satellites increased to 16. Increasing the number of visible satellites will accordingly enhance the geometry of the constellation, thus about 94 % of the correlation coefficients in the integrated system are smaller than 0.3, and no correlation coefficient is larger than 0.6. Consequently, by integrating GPS and BDS, the correlation coefficient

Table 2 Correlation coefficients over the whole time

	>0.8	0.8–0.7	0.7–0.6	0.6–0.5	
GPS (%)	29.08	15.38	4.99	7.73	
BDS (%)	2.01	0.31	2.11	7.97	
GPS/BDS (%)	0	0	0	0.83	
	0.5–0.4	0.4–0.3	0.3–0.2	0.2–0.1	<0.1
GPS (%)	6.31	8.80	15.99	3.48	7.95
BDS (%)	5.20	5.67	24.60	16.05	36.09
GPS/BDS (%)	1.63	3.77	9.07	35.58	49.11

between any two test statistics was in general reduced. This leads to a better performance of the fault detection and exclusion procedure in terms of increasing the identification success rate.

5 Conclusion and Remarks

BDS will provide navigation, positioning, and timing service to worldwide users by the end of 2020. In this paper the overall performance of BDS and GPS/BDS integrated system are analyzed and compared with GPS system, in terms of system reliability and separability. With the simulation tests, we can conclude that

1. The BDS ensures a good geometric coverage all over the world. Especially in Asia-Pacific area, the geometry strength is further enhanced compared with GPS system. The number of visible satellites, the dilution of precision, and the navigation accuracy are all increased. By introducing GEO satellites, not only the positioning accuracy and availability, but also the system reliability and integrity are largely improved.
2. The MDBs are highly dependent on the number of visible satellites and the geometric distribution of the constellation. Generally, the MDB values of GEO satellites are larger than MEO and IGSO satellites, due to the influence of elevation angle. When combining GPS with BDS, the MDB values for all satellites are obviously reduced and become much more stable over operation time.
3. When combining BDS with GPS system, the maximum correlation coefficients values are reduced to lower than 0.6 from higher than 0.8, as well as 97.5 % of the corresponding correlation coefficients values are lowered to 0.4. This shows a great improvement in the integrated system in terms of fault detection and exclusion capability.

References

1. Zhou S, Cao Y, Zhou J et al (2012) Positioning accuracy assessment for the 4GEO/5IGSO/2MEO constellation of COMPASS. Sci China Phys Mech Astron 55(12): 2290–2299
2. Yang Y, Li J, Xu J et al (2011) Contribution of the compass satellite navigation system to global PNT users. Chin Sci Bull 56(26):2813–2819
3. Hewitson S, Wang J (2006) GNSS receiver autonomous integrity monitoring (RAIM) performance analysis. GPS Solutions 10(3):155–170
4. Wang J, Ober PB (2009) On the availability of fault detection and exclusion in GNSS receiver autonomous integrity monitoring. J Navig 62(2):251–261
5. Hein GW, Pielmeier J, Zink T et al (1997) GPS and GLONASS RAIM availability analysis over Europe. ION GPS, pp 465–474
6. Ochieng WY, Sheridan KF, Sauer K et al (2002) An assessment of the RAIM performance of a combined Galileo/GPS navigation system using the marginally detectable errors (MDE) algorithm. GPS Solutions 5(3):42–51
7. Hewitson S, Kyu Lee H, Wang J (2004) Localizability analysis for GPS/Galileo receiver autonomous integrity monitoring. J Navig 57(2):245–259
8. Peng L, Jiang K, Duan X et al (2012) Receiver autonomous integrity monitoring parameter design and analysis for multi-constellation navigation. In: China satellite navigation conference, pp 15–27
9. El-Mowafy A (2013) ARAIM for vertical guidance using GPS and BeiDou. J Global Pos Syst 12(1):28–37
10. Knight NL, Wang J, Rizos C (2010) Generalised measures of reliability for multiple outliers. J Geodesy 84(10):625–635
11. Guo J, Ou J, Yuan Y (2010) Reliability analysis for a robust M-estimator. J Surv Eng 137(1):9–13
12. Yang L, Wang J, Knight NL et al (2013) Outlier separability analysis with a multiple alternative hypotheses test. J Geodesy 87(6):591–604
13. Hewitson S, Wang J (2010) Extended receiver autonomous integrity monitoring (eRAIM) for GNSS/INS integration. J Surv Eng 136(1):13–22
14. Wang J, Knight NL (2012) New outlier separability test and its application in GNSS positioning. J Global Pos Syst 11(1):46–57
15. Yang Y, Li J, Xu J et al (2011) Contribution of the compass satellite navigation system to global PNT users. Chin Sci Bull 56(26):2813–2819

Improving Extended Kriging with Chapman Model and Exponential Variation Function Model

Pan Liu and Rui Li

Abstract In the satellite-based augmentation system, the ionospheric error as one of the main error sources has a big influence on the navigation capability of single frequency user. At present, the IGD is estimated based on the distance-weighted algorithm and Kriging plane fitting algorithm with a single-layer shell model, in which ionosphere is equivalent to a thin shell at certain height. However, the error introduced by single-layer thin shell model leads to a poor precision of ionospheric delay estimation. In terms of this issue, some scholars proposed extended Kriging algorithm based on empirical model, but the accuracy is not high and are limited by experience. This paper proposes an extended tomography algorithm improving the estimation precision of extended Kriging algorithm using Chapman model instead of empirical model, and fitting the single Gaussian random delays. The analysis is made using ionospheric data collected from WAAS reference stations and CORS stations within the scope of the United States in this paper. First, we compare the fitting accuracy of Kriging algorithm and extended algorithm on each reference station, and analyze the improvement under the different ionospheric disturbance conditions and elevation angles. Then we compare the fixed delays based on the two methods. The results show that the fitting precision of the improved algorithm is increased by 10–50 %, especially in the case of low elevation angle, and the UIVE is also reduced by 5–40 %.

Keywords SBAS · Grid ionospheric correction · Tomography

P. Liu (✉) · R. Li
Beihang University, Beijing, China
e-mail: liupanlzu@yeah.net

R. Li
Collaborative Innovation Center of Geospatial Technology, Wuhan, China

J. Sun et al. (eds.), *China Satellite Navigation Conference (CSNC) 2016 Proceedings: Volume II*, Lecture Notes in Electrical Engineering 389,
DOI 10.1007/978-981-10-0937-2_15

1 Introduction

In the satellite-based augmentation system, the ionosphere error as the one of main error sources has a big influence on the navigation capability of single frequency user. At present, the widespread adoption of single-layer shell model calculate ionospheric grid to analysis the ionospheric characteristics between the reference stations and satellites. Wide area augmentation system (WAAS) and European Geostationary Navigation Overlay Service (EGNOS) using Kriging plane fitting and distance-weighted algorithm, respectively, to estimate the ionospheric delay at grid points, then broadcast ionospheric grid delay (IGD) and grid ionospheric vertical delay error (GIVE) to user. Finally, user selects near three or four grid points near IPP to calculate slant delay and confidence bound in user propagation path by bilinear interpolation to ensure the user's positioning accuracy and integrity.

But due to the large fluctuations of ionospheric in the solar geomagnetic storms, traditional single-layer shell method sets the ionosphere at the fixed height and hardly considers the ionospheric electron density in the vertical direction, so the accuracy is affected. In terms of this issue, some scholars proposed extended Kriging algorithm based on empirical model [1], but the accuracy is still limited because of the empirical coefficient listed in Table 1. This paper proposes an extended algorithm improving the estimation precision using Chapman model, which establishes a more accurate ionosphere model.

The algorithm analysis is made using ionospheric data collected from WAAS reference stations in this paper. First, we analyze both the estimation accuracy of different algorithms on each reference stations, and the improvement under different ionospheric disturbances and different elevations. Then we take the operational reference station continuously (CORS) stations as the users, and compare the slant delay values and confidence bound calculated by the three algorithms.

2 Ionospheric Delay Estimation

2.1 Extended Kriging Algorithm

Extended Kriging algorithm is mainly proposed by Juan blanch, which takes the ionospheric electron concentration in vertical direction and the distance correlation of the delay values into account, and introduces Gaussian random fields to establish multilayer thin shell structure based on the Kriging algorithm. This algorithm combines the advantages of Kriging algorithm and tTomography algorithm.

Table 1 The ionospheric coefficient of Empirical model

High (km)	350	400	450	500	550	600	650
φ_k	0.25	0.125	0.125	0.125	0.125	0.125	0.125

A p layers model is introduced instead of the single-layer thin shell, and a weighting factor ϕ_k is given to the k layer to describe the average weight of the electron concentration. The weighting factor are listed in Table 1, and:

$$\sum_k \varphi_k = 1 \tag{1}$$

As a regional model is established in each single layer, the ionospheric delay value can be equivalent to a mean value m plus a multidimensional Gaussian random field $r_k(x)$ dependent on the position of ionospheric pierce point x, assuming that Gaussian random fields of the layers are independent and identically distributed. Therefore, the vertical delay value of the k layer is equivalent to

$$I_{v,k} = \varphi_k \cdot (m + r_k(x)) \tag{2}$$

And the slant delay of the i measured on the k layer at the reference station is as follows:

$$I_{s,i} = \sum_{k=1}^{p} \varphi_k \cdot (m + r_k(x_{k,i})) \cdot ob_{k,i} \tag{3}$$

where $ob_{k,i}$ is the relative slant factor. Since r_k is independent of each other in different layers, the covariance of the projection values of the two propagation paths is given by

$$\begin{aligned} \operatorname{cov}(I_{s,i}, I_{s,j}) =& E\left(\left(\sum_{k=1}^{p} \varphi_k \cdot r_k(x_{k,i}) \cdot ob_{k,i}\right)\left(\sum_{k=1}^{p} \varphi_k \cdot r_k(x_{k,j}) \cdot ob_{k,j}\right)\right) \\ =& \sum_{k=1}^{p} \varphi_k^2 ob_{k,i} ob_{k,j} \operatorname{cov}\left(r_k\left(x_{k,i}\right), r_k\left(x_{k,j}\right)\right) \end{aligned} \tag{4}$$

Neglecting the measurement noise, the vertical delay value of grid point can be calculated using Kriging algorithm with Eq. (4), and then broadcasted to users. However, the vertical direction of the extended Kriging is limited by the fixed coefficient model, the improved accuracy is not high, and the specific coefficients are not given.

2.2 Improved Extended Algorithm

2.2.1 Chapman Model

Because of the ionospheric electron concentration is affected by solar activity, geomagnetic activity, season and time of day, a complete the theoretical analysis is

too complicated, so that we often established basic parameters to construct the empirical model of the ionosphere based on a large number of observations. The functions of the models include the Chapman function, the spherical harmonic function, and so on [2]. There are also many empirical models to choose from, which mainly include the international reference ionosphere model (IRI) and the parametric ionospheric model (PIM) [2].

The Chapman function is used to describe the distribution of electron density in the vertical direction, and the peak height of the electron density is obtained according to the changes of the atmospheric composition and the state of the sun, in which the electrons in the ionosphere are mainly concentrated between 100 and 1000 km. According to the IRI and the PIM models, we select the electron concentration peak model of the 450 km, as shown in the Chapman layer (Fig. 1):

Specific expressions are as follows:

$$\mathrm{Ch}(h, H_k) = \exp\left(1 + \frac{h_k - h}{H_k} - \exp\left(\frac{h_k - h}{H_k}\right)\right) \tag{5}$$

where, the peak point is h_k = 450 km, the model height is H_k = 90 km. The peak height of single-layer shell in WAAS is 350 km (Table 2).

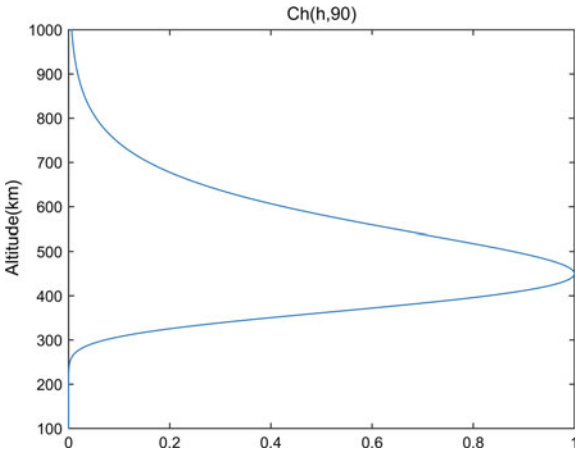

Fig. 1 Chapman layer

Table 2 The ionospheric coefficient of Chapman model

High (km)	360	450	540	630	720	810
φ_k	0.18	0.37	0.26	0.12	0.05	0.02

2.2.2 Exponential Variation Function Model

Ionospheric delay value varies slowly with time and the geographic location, so that the closer ionospheric pierce points have a higher correlation value in the thin shell model. So the ionospheric delay value is a special random variable, which is related to the location of the position. Because of the failure of the traditional probabilistic analysis method in describing the characteristics of delay value completely, the geostatistics variogram are introduced in single-layer shell Kriging, quantitatively describing spatial correlation of regionalized variables, and achieve better results [3].

This paper establishes a multilayer variation function model based on hierarchical technologies, which describe the characteristics of different propagation paths. Due to the delay value difference is 0 when the propagation paths are overlap (the delay value of the pierce point may have a larger deviation at the same position in single-layer shell), it overcomes the nugget effect (the discontinuity of starting point) in single-layer shell Kriging.

In each layer, the mean m of the delay value is deterministic as a plane trend term, so we only analyze the random items $r_k(x)$ in the delay value. Using the first-order plane fitting, we obtain the fitting coefficient by the least square method, and construct the difference of random entry to establish the corresponding experimental variation function.

The main steps are:

1. In the k layer, we obtain the position of the geometrical center at each pierce point pair for all the pierce points as the data source. The trend coefficient is obtained by all the points, except the selected pierce point pair, within the circle of radius 1200 km.
2. The mean value of the delay (m_i, m_j) is calculated using the fitting coefficient, and the difference of the slant delay value of the current layer $(I_{s,i} * \varphi_k, I_{s,j} * \varphi_k)$ is calculated.
3. The difference between the p layer and the random term of the space is obtained by $\Delta r_{ij} = \sum_{k=1}^{p} r_k(x_{k,i}) - \sum_{k=1}^{p} r_k(x_{k,j})$.
4. The random entry differences of all the points in the plane are obtained by traversing. We obtain the variation function values by the distance as the independent variable, then to carry on the drawing.

In this paper, we select 6 day's data with different ionospheric disturbances index Kp listed in Table 3 for analyzing. The results are shown in Fig. 2.

Table 3 Ionospheric disturbances index of Kp

Date	03.17	04.15	06.20	06.23	06.30	07.31
Kp	8	1	1	7	2	3

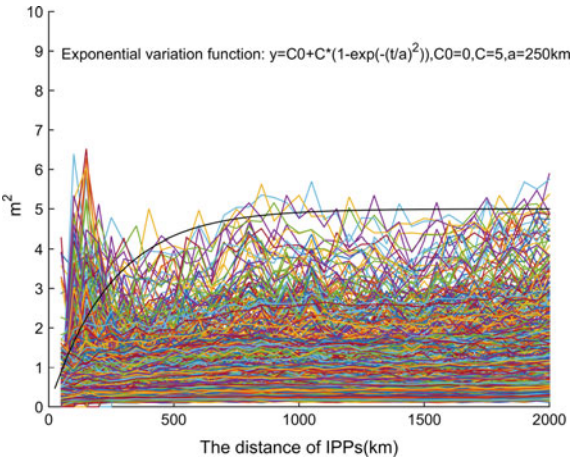

Fig. 2 Exponential variation function

According to the trend of the variation function, we select the experimental model variation function $\gamma(d) = C * (1 - \exp(-d/a))$ which is the black line, so the corresponding variance function is

$$\operatorname{cov}\left(r_k(x_i), r_k(x_j)\right) = f\left(\left\|x_i - x_j\right\|\right) = 5 \cdot \exp\left(-\frac{\left\|x_i - x_j\right\|}{250}\right) \tag{6}$$

2.2.3 The Calculation of Delay Value

According to the extended Kriging algorithm by Juan Blanch, we introduce the Chapman model and the exponential model of the regional variables above and calculate the vertical delay value of the grid points by Kriging algorithm [4]. Since the ionosphere estimation technique is linear, the slant delay value of the arbitrary propagation path is a linear combination of the measured values within a certain range. Assuming that there are n valid measurements, the ionosphere delay value is computed as follows:

$$\hat{I}_{\text{unknown}} = \sum_{i=1}^{n} \lambda_i \tilde{I}_{\text{mean},i} \tag{7}$$

As it meets the least mean square error criterion, the solution of the weighting coefficient is similar to that of Kriging method:

$$\lambda = (W - WG(G^{\mathrm{T}}WG)^{-1}G^{\mathrm{T}}W)c + WG(G^{\mathrm{T}}WG)^{-1}X_{\text{unknown}} \tag{8}$$

By solving Eq. 8, we obtained the weighted coefficients λ_i and the vertical delay value of the grid points can be calculated by Eq. 7.

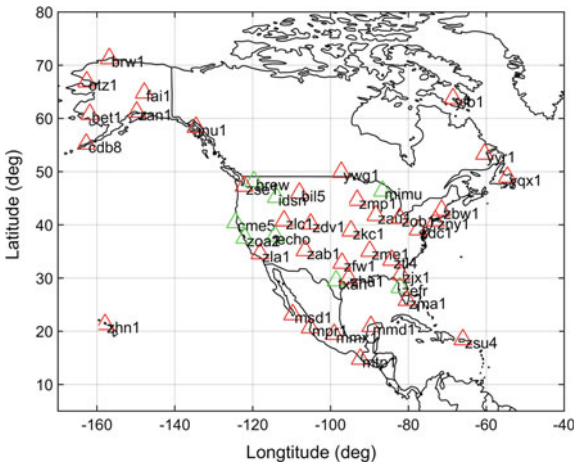

Fig. 3 The location of reference station

3 Algorithm Analysis and Results

The algorithm simulation is made using different disturbance ionospheric measurement data which collected from 38 WAAS reference stations and 8 CORS stations (red triangles and green triangles in Fig. 3, respectively) in 3 days of 2015. The cut-off angle of reference station observation takes 15° in improved algorithm, we select the delay values around 1200 km to estimate the point as the center of the circle, the minimum number of observation points is 10, and each layer of the pierce point data were selected in accordance with the 360 km.

3.1 Accuracy Analysis of Estimation Algorithm

We use the method of data deprivation to fit the remaining measurement pairs except the pair of satellite and station we selected, and then contrast the real value and the estimated value. In order to guarantee the accuracy of the algorithm, we excluded the data which have the same reference station with the estimated pair. At first, the root mean square and maximum of error to analyze the fitting accuracy of the planar Kriging algorithm, extended Kriging algorithm, and the improved algorithm, the results are as follows (Table 4).

Table 4 The error analysis between the three algorithms

	2015.06.20		2015.07.31		2015.03.17	
	RMS (m)	Max (m)	RMS (m)	Max (m)	RMS (m)	Max (m)
Kriging	0.427	14.069	0.431	6.172	0.817	19.783
Extended kriging	0.311	4.081	0.341	3.039	0.600	7.747
Improved algorithm	0.301	4.046	0.330	2.950	0.565	7.389

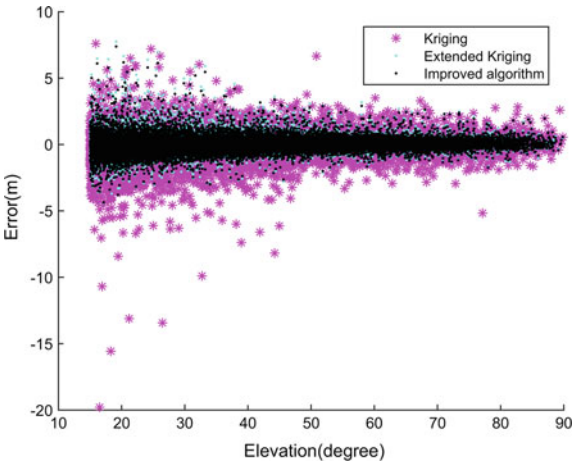

Fig. 4 The fitting errors of three algorithms

The ionospheric disturbance index Kp of the selected days are 1, 3 and 8, respectively. According to the results, we can see that the improved algorithm has a certain improvement in the fitting error.

Next we analyze the WAAS station fitting error condition in March 17th Fig. 4 is the comparison of the three algorithms, it can be seen that the improved method of fitting error value has a certain decrease especially in the case of low elevation, but there are also some larger errors. We list four reference stations in different locations to compare root mean square errors of the three algorithms in Fig. 5. The improved algorithm has an obvious improvement compared with the Extended Kriging algorithm and Kriging in the reference station at the center position

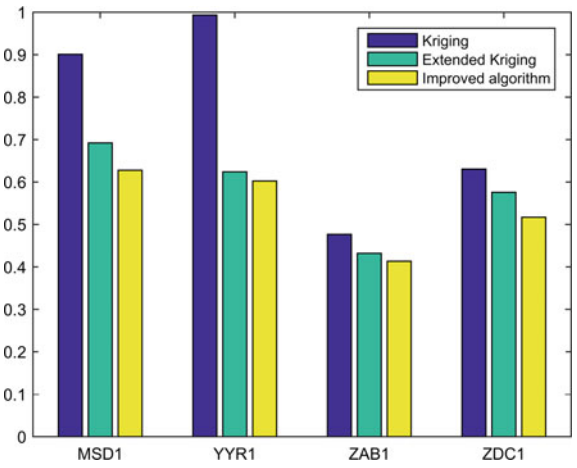

Fig. 5 Error variance histogram of reference stations

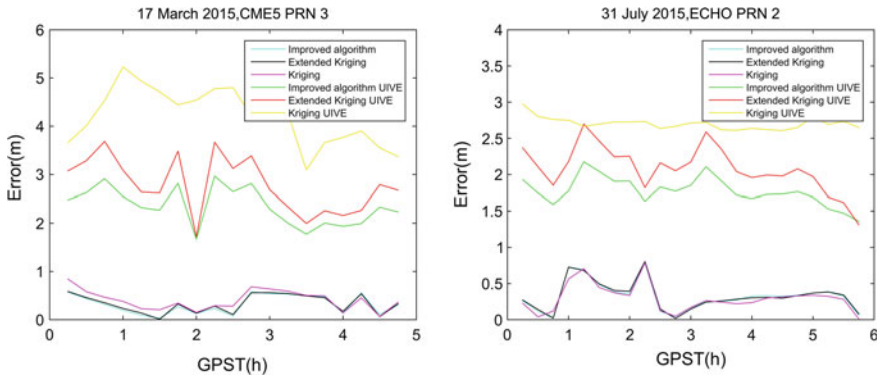

Fig. 6 IGD error and UIVE comparison of three algorithms

(ZAB1, ZDC1) and the edge position (MSD1, YYR1) of CONUS. But because the center location has lager quantity data, the model accuracy of three methods are similar, so the improvement is not obvious.

In summary, the improved algorithm has an improvement contrasted with Kriging and Extended Kriging especially in low elevation, and the fitting accuracy is improved by an average of 50 and 5 % compared with Kriging and Extended Kriging, respectively.

3.2 User Grid Correction Analysis

This paper selects 8 CORS stations as users plotted in Fig. 3, we interpolated the grid point delay values by WAAS measurement in the same time, and compared the accuracy of three algorithms by the difference between truevalue and its fitted value. We choose continuous observation of GPS satellite PRN 3 collected by station CME5 on March 17th when the Kp is 8 and GPS satellite PRN 2 collected by station ECHO on July 31st when the Kp is 3 to demonstrated in Fig. 6.

From Fig. 6 and Table 3, the improved algorithm is more fit for the user error bounding than Kriging, and the average reduction of UIVE is more than 40 %. Compared with Extended Kriging, improved algorithm also has some improvement, UIVE is reduced by 5 %. The UIVE bounding possibilities of the all three algorithms are all greater than 99.9 %, and the difference of the delay value is close and the root mean square differences reach a thousand points (Table 5).

Table 5 The correction performance of the three algorithms

Date	Kriging		Extended kriging		Improved algorithm		Reduction in kriging UIVE (%)	Reduction in extended UIVE (%)
	Error RMS (m)	UIVE bounding (%)	Error RMS (m)	UIVE bounding (%)	Error RMS (m)	UIVE bounding (%)		
03.17	0.453	99.98	0.463	99.94	0.466	99.94	44.7	8.2
06.30	0.303	100	0.304	100	0.304	99.98	43.2	2.8
07.31	0.347	100	0.349	99.95	0.350	99.95	41.6	3.3

4 Conclusion

This paper propose an ionospheric shell improved algorithm combining Chapman model and exponential variation function based on the Extended Kriging algorithm, to improve the fitting accuracy especially in low elevation and severe ionospheric disturbance condition. First, we use the observation data of the WAAS reference station in the continental United States to evaluate the accuracy of the three algorithms by the differences between the real value and the fitting estimate value. Then, we take CORS stations as users to validate error bounding.

The results indicate that the estimation accuracy of improved algorithm is improved by about 20–60 % than Kriging algorithm under the different Kp index, and improved by about 5 % than extended Kriging algorithm. However, the improvement is not obvious for the center station. At the end of the user, the three algorithms has nearly the same estimation accuracy, but the mean reduction percentage of UIVE is about 40–5 % for Improved algorithm over the Kriging algorithm and extended Kriging. In the vertical direction, the Chapman model we adopted is more flexible than extended Kriging. And we take the six layers Chapman model in which the peak value is 450 km, so the computational complexity has been reduced, while the accuracy has still been improved.

References

1. Blanch J, Walter T, Enge P (2004) A new ionospheric estimation algorithm for SBAS combining kriging and tomography. In: Proceedings of the institute of navigation national technical meeting
2. Hansen AJ (2002) Tomographic estimation of the ionosphere using terrestrial GPS sensors. ProQuest dissertations and theses; Thesis—Stanford University
3. Fengqiu J, Huan Zhigan SB (2010) Estimation method of ionospheric delay of IGP based on spatial variability. J Telemetry, Tracking Command, 31(4)
4. Blanch J (2004) Using kriging to bound satellite ranging errors due to the ionosphere. ProQuest dissertations and theses; Thesis—Stanford University

The Analysis of Availability and Integrity for Beidou-Based High Precise KINRTK

Guanlong Wang, Xiaowei Cui and Mingquan Lu

Abstract Generally kinematic navigation cannot be adapted for use in all environments, especially like the formation flying, UAV refuelling, SB-JPALS and spacecraft attitude control, because the base station is moving. Its requirement is that vertical position error be bounded to 1.1 m with an associated integrity risk for 10^{-7}. Carrier phase differential of Beidou can provide high accuracy, high availability, high integrity navigation. In this context, a robust processing methodology by optimally exploiting the complementary benefits of long duration geometric-free measurement filtering and satellite geometric redundancy for the cycle ambiguities fixing. Individual satellite wide lane ambiguity is used for cycle estimation by pre-filtering, prior to the moving station approach of base station. The four locations at china in which Beidou navigation availability and integrity performance that are sensitivite to the standard deviations of raw carrier and code phase measurement errors, measurement error correlation times and the filtering duration is quantified by simulation and evaluation.

Keywords Beidou · KINRTK · Measurement accuracy · Availability · Integrity

1 Introduction

Generally satellite-based navigation system with dynamic relative positioning, in which the base station is static, but it does not adapt to the new environment, especially like the ship-board joint precision approach and landing (SB-JPALS). The on-the-fly satellite navigation positioning relative to a moving reference (KINRTK) is being developed to provide high accuracy, high availability and high integrity for the base and rover both moving. The moving base calls for higher performance, the vertical accuracy limits with 0.4 m, vertical alert limit (VAL) for

G. Wang (✉) · X. Cui · M. Lu
Department of Electronic Engineering, Tsinghua University,
Zhong Guan Cun Bei Road, Beijing 100084, China
e-mail: wgl14@mails.tsinghua.edu.cn; dugubainian@sina.cn

J. Sun et al. (eds.), *China Satellite Navigation Conference (CSNC) 2016 Proceedings: Volume II*, Lecture Notes in Electrical Engineering 389,
DOI 10.1007/978-981-10-0937-2_16

Table 1 Pre-filtering time, the VDOP of CAT III and SB-JPALS availability requirements

	WLMQ	BJ	BZ	XM
CAT III				
15	3.791	2.960	2.441	2.388
12	3.801	2.948	2.459	2.419
30	3.804	2.945	2.459	2.457
40	3.808	2.943	2.459	2.457
SB-JPALS				
15	3.803	2.983	2.470	2.379
12	3.806	2.968	2.471	2.379
30	3.909	2.946	2.471	2.379
40	3.930	2.945	2.471	2.383

navigation system is 1.1 m, with an associated integrity risk of approximately 10^{-7}, and these integrity requirements be satisfied with a system availability of at least 99.7 % (Table 1 SB-JPALS of US navy) [1]. This research is focused on the availability and integrity performance of Beidou use for CAT III and SB-JPALS.

2 Measurement Models

Carrier phase can achieve centimetre-level navigation performance, but is dependent on the successful resolution of cycle ambiguities [1, 2]. The moving rover and moving base individually processes its own measurements. Before the un-differenced (UD) measurements that are received from moving rover and moving base to produce single-differenced (SD) and double-differenced (DD), pseudo ranges are combined to produce narrow lane pseudo ranges, combined carrier phase to produce wide lane phase ranges. Wide lane phases and narrow lane pseudo are combined to MW, that can be filtered to compute float wide lane ambiguities and its variances. The MW combination observation is defined as follows:

$$N_w = \frac{\Phi_w - R_n}{\lambda_w} - \frac{h_w - H_w}{\lambda_w} - \frac{m_w + e_w - M_n - E_n}{\lambda_w} \tag{1}$$

where R_n is narrow lane pseudo measurement. Φ_w is wide lane carrier phase measurement. M, m are multipath in pseudo and carrier phase. E, e receiver noise in pseudo and carrier phase. Multipath and noise, assume the mean value is 0, variance is σ^2. By low pass filter, consistent with the frequency content of multipath and noise, these effects can be filtered out to a very large extent, then the variance of the wide lane ambiguities estimate error can be written as follows:

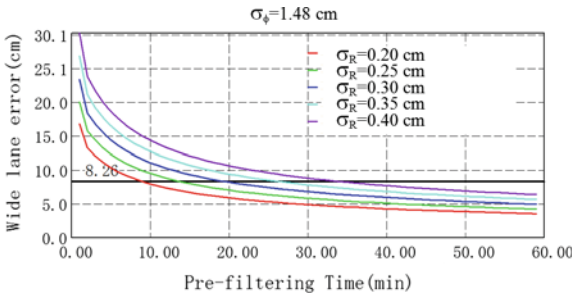

Fig. 1 Pre-filtering for wide lane ambiguity standard deviation

$$\sigma_{N_w}^2 = \left(\frac{1}{\lambda_1^2} + \frac{1}{\lambda_2^2}\right)\left(\sigma_\phi^2 + \left(\frac{\lambda_2 - \lambda_1}{\lambda_1 + \lambda_2}\right)^2 \sigma_R^2\right) \tag{2}$$

Generally, the range errors for both code and carrier are modelled as a first-order Gauss–Markov random process with a measurement error time constant of 1 min [2]:

$$\text{var} = \frac{2\sigma_w^2}{T/\beta} - \frac{2\sigma_w^2}{T^2/\beta^2}\left(1 - \exp\left(-\frac{T}{\beta}\right)\right) \tag{3}$$

where T is filter time, and β is the code measurement error time constant. Figure 1 quantifies the sensitivity of floating wide lane ambiguity estimate error, given $\sigma_\phi = 1.48$ cm, which is associated with the maximum error value of σ_w required to ensure a 10^{-8} total probability of incorrect wide lane integer ambiguity rounding for 8 satellites. As an example, given a geometric-free filtering duration of 30 min, the wide lane integers can be fixed with the specified integrity only if $\sigma_R < 37$ cm or small. This requirement for raw code error is stringent, but may be achievable using modern receivers [3].

3 Satellite Constellation Availability

Figure 2 shows four locations—WLMQ (Lon = 87.62767, Lat = 43.972815, 2015-6-30 ~ 2015-7-7), BJ (Lon = 116.334055, Lat = 39.999835, 2015-11-18 ~ 2015-11-21), BZ (Lon = 115.775683,Lat = 33.594111, 2015-4-10 ~ 2015-4-12), XM (Lon = 118.137048, Lat = 24.461383, 2015-6-30 ~ 2015-7-7), the vertical dilution of precision (VDOP) for SB-JPALS availability requirement of 99.7 % [4], with 1 min sampling interval, and 7.5° min-elevation angle masked.

The satellite constellations state probability model reference GPS, and assumes same state probability for each satellites. The use of VDOP in this preliminary analysis implicitly assumes that all satellite ranging errors (code or carrier phase) have equal variances. Table 1 gives the maximum VDOP of the CAT III after

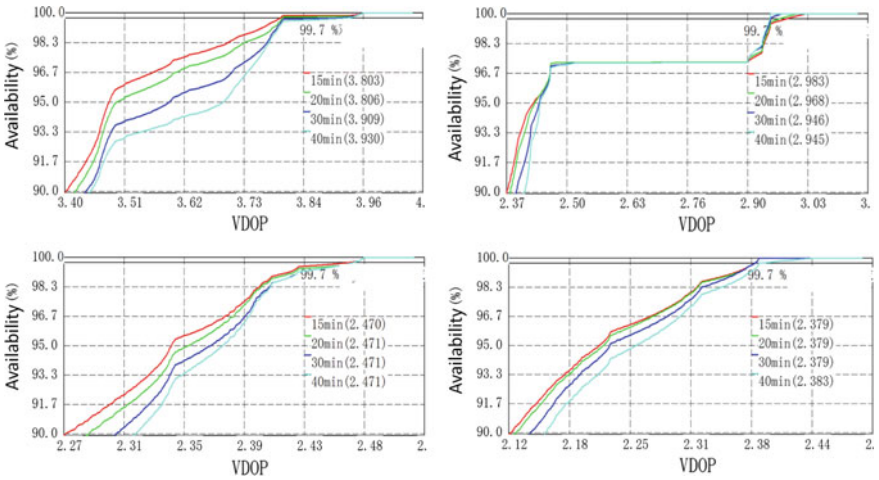

Fig. 2 (WLMQ, BJ, BZ, XM) VDOP of SB-JPALS availability pre-filtering time

5 min pre-filtering and SB-JPALS after 20, 30, 40 min pre-filtering availability at four locations. Given the maximum VDOP to meet the moving base relatively positioning availability specification, and assuming for a moment that the wide lane integer ambiguities are known and fixed, it is possible to compute the maximum permissible standard deviation for the wide SD carrier phase [1]:

$$\mathrm{VPL} = \sigma_{\Delta\phi,w} \cdot \mathrm{VDOP} \cdot K_{\mathrm{ffd}} < \mathrm{VAL} \tag{4}$$

where the VPL is the vertical protection level. $\sigma_{\Delta\phi,w}$ is the standard deviation for the wide lane SD carrier phase. K_{ffd} is the integrity multiplier corresponding to the integrity risk requirement of CAT III and SB-JPALS (K_{ffd} of CAT III is 6.11, and K_{ffd} of SB-JPALS is 5.33). VAL is vertical alert limit (for CAT III is 5.3 m, and for SB-JPALS is 1.1 m) [4]. Using 30 min pre-filtering time, the maximum carrier phase standard deviation to meet CAT III and SB-JPALS availability are given in Table 2. The relationship between the SD carrier phase and SD wide lane carrier standard deviation is given as follows: $\sigma_{\Delta\phi,w}5.58 \cdot \sigma_{\Delta\phi}$. From the above processing, the moving base relative positioning required availability of performance of Beidou is listed below:

Table 2 Carrier phase standard deviation for CAT III and SB-JPALS availability

	σ_{ϕ} (cm)	
	CAT III	SB-JPALS
WLMQ	2.04	0.47
BJ	2.64	0.63
BZ	3.16	0.75
XM	3.16	0.78

- For the availability of CAT III, the σ_ϕ must less than 1.48 cm, because to ensure a 10^{-8} total probability of incorrect wide lane integer ambiguity rounding for 8 satellites.
- For the availability of SB-JPALS, the most strictest requirements of σ_ϕ is 0.47 cm, at WLMQ. It is smaller σ_ϕ of performance of Beidou (0.2 cm) [3], and also which can ensure a reliable probability to cycle integers fixed.
- Increased usable satellite (decrease DOP value) will relax the σ_ϕ requirement.

4 Wide Lane Process

The wide lane measurement vector form is as follows:

$$\left[\Delta\nabla\phi_w^{ij}\right] = \left[G_{(n-1)\times 3} \quad I_{(n-1)\times(n-1)}\right]\begin{bmatrix}\lambda_w^{-1}b_{3\times 1}\\ \Delta\nabla N_{w,(n-1)\times 1}^{ij}\end{bmatrix} + v \tag{5}$$

where $G_{(n-1)\times 3}$ is the geometry matrix, $G_{(n-1)\times 3} = \left[-\left(l_r^1 - l_r^2\right)\ldots - \left(l_r^1 - l_r^n\right)\right]^T$, l_r^i is the line of sight vector to the satellite i. $I_{(n-1)\times(n-1)}$ is identity matrix. $\Delta\nabla N_w^{ij}$ is the DD wide lane cycle integer for satellite i, j. v is the DD wide lane carrier phase measurement error due to noise and multipath, and its covariance matrix is

$$P_{\phi_w} = 2\left(\left(\frac{\lambda_w}{\lambda_1}\right)^2 + \left(\frac{\lambda_w}{\lambda_2}\right)^2\right)\sigma_\phi^2\begin{bmatrix}2 & 1 & \cdots & 1\\ 1 & 2 & & \\ \vdots & & \ddots & \\ 1 & & & 2\end{bmatrix}_{(n-1)\times(n-1)} \tag{6}$$

It is simple to fuse the output of UD pre-filtering estimate of wide lane float ambiguities and its variance to produce the DD wide lane float ambiguities and its variances:

$$P_{\Delta\nabla\hat{N}_w} = 2\sigma_{N_w}^2\begin{bmatrix}2 & 1 & \cdots & 1\\ 1 & 2 & & \\ \vdots & & \ddots & \\ 1 & & & 2\end{bmatrix}_{(n-1)\times(n-1)} \tag{7}$$

At this point, DD widelane ambiguity error variance is dependent on the duration of pre-filtering for the individual satellites. The DD widelane ambiguities are difficult to treat as satellite individually [5]. To address this issue, we make use of Teunissen's LAMBDA or united cycle ambiguity decorrelation algorithm with integer bootstrapping [3–7]. This geometric redundancy implementation can compute ambiguity fix probability [8] to ensure the reliably ambiguity integer fix.

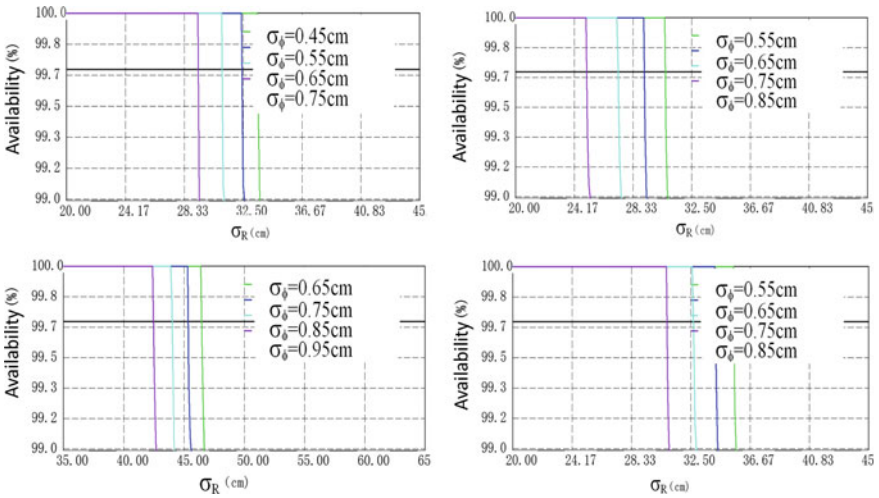

Fig. 3 (WLMQ, BJ, BZ, XM) σ_R and σ_ϕ for SB-JPALS after 30 min pre-filtering time

Assuming that the integer ambiguity has computed, substituting the result into (5). The residual DD carrier phase is $P_{\phi_{w,N}} = P_{\phi_w} + P_{\Delta\nabla\hat{N}_w}$. The well-known least square method is then used to resolve the moving rover position relatively moving base, and its relatively positioning error covariance matrix: $P_u = \left(G^T P_{\phi_{w,N}}^{-1} G\right)^{-1}$ where $G_{(n-1)\times 3}$ is the geometry matrix in (5). The vertical error standard deviation is $\sigma_v = \sqrt{P_{u,(3,3)}}$. Finally, the σ_v is scaled by the K_{ffd} to produce the VPL, which is compared with VAL (CAT III is 5.3 m, and SB-JPALS is 1.1 m) [4] determine whether sufficient performance is available for moving rover positioning relatively moving base.

Using the processing architecture [9] defined above, the availability and integrity of SB-JPALS requirement has been evaluated for various values of carrier phase and pseudo range error standard deviation at four locations are shown in Fig. 3 after 30 min pre-filtering with the pseudo range error time constant as 1 min, satellite min-elevation mask angle as 7.5°, positioning interval as 1 min. The pre-filtering times are 5 min (CAT III), 20, 30, and 40 min (SB-JPALS), carrier phase ranging error standard deviation meets the availability in Table 2, the required pseudo range error standard deviation list in Table 3.

The results of Beidou DD widelane carrier phase processing are follows:

- For the 99.7 % availability of SB-JPALS using DD widelane measurements to position, it is shown in Table 3 that when σ_ϕ meets the requirement, σ_R is of high requirement and is sensitive to pre-filtering time. As seen in the results, when pre-filtering time is 30 min, σ_R required in BJ is 29 cm, higher than the actual 33 cm code error performance of Beidou B_1 which is mentioned in [3], so to satisfy the pseudo range requirement, we need to extend pre-filtering time to

Table 3 σ_R and σ_ϕ for SB-JPALS, CAT level III

	Pre-filtering (min)	SB-JPALS (cm)			
		WLMQ	BJ	BZ	XM
σ_ϕ		0.45	0.65	0.75	0.75
σ_R	20	27	24	37	27
	30	33	29	43	32
	40	38	33	52	38
σ_R (CAT III)	5	66	65	93	73

at least 40 min. σ_R required in WLMQ and XM are 33 and 32 cm, respectively, which are equal or near to the actual code error of Beidou. Only σ_R required in BZ is larger than the actual code error of Beidou.

- For the 99.5 % availability of CAT III, the actual code error of Beidou can satisfy the requirement easily. Once σ_ϕ meets the requirement of ambiguity fixing probability, only 5 min is needed for pre-filtering, and the required σ_R can be relaxed to more than 65 cm.
- The relaxation effect of σ_ϕ on σ_R becomes weaker as σ_ϕ improves. As shown in Fig. 3, the relaxed range of σ_R narrow down for every 0.1 cm improvement in σ_ϕ.
- Once the availability of satellites reach to some extent, the relaxation effect of DOP on σ_R becomes weaker as DOP improves. For the same pre-filtering time of 30 min and σ_ϕ of 0.55 cm, the VDOP values in WLMQ and XM are 3.909 and 2.379, respectively, but σ_R are 32 and 35 cm, only 3 cm relaxation in σ_R.
- Figure 3 provides a result comparison of four different places with the σ_ϕ of availability of SB-JPALS required, and pre-filtering time. As we can see, for some cases, VDOP in BJ is better than the one in WLMQ while the requirement for σ_R is more stringent. VDOP in BZ and XM are basically the same while the requirement of σ_R in BZ is much relaxed. Since the data was collected in different seasons (WLMQ and XM in July, BZ in April, and BJ in November), we do not know whether the availability and integrity performance of Beidou system are related to the seasons, which will be studied in our future work.

5 B_1/B_2 Process

Once the DD widelane cycle integers have been determined, one can step down to B_1 DD ambiguities. The geometry-free combination of carrier phase also is a linear combination of N_1 and N_2. The geometry-free measurement is modelled as follows:

$$\Phi_1 - \Phi_2 = \left(\frac{\lambda_2^2}{\lambda_1^2} - 1\right) I_1 + (\lambda_1 N_1 - \lambda_2 N_2) + (h_1 - h_2) + (m_1 + e_1 - m_2 - e_2) \quad (8)$$

where the geometry-free phase measurement has three components. The iono error is less than B_1 measurement, only $0.59I_1$. However, it has increased multipath and noise. The geometry-free ambiguity can be determined very precisely by filtering out the effects of multipath and noise. Then, as moving rover approaches the moving base, the iono term becomes negligibly small allowing accurate determination of the $\lambda_1 N_1 - \lambda_2 N_2$. Based on this approach [9], the accuracy N_1 and its corresponding variance to each of the satellites are determined:

$$\hat{N}_1 = \left(1 - \frac{\lambda_1}{\lambda_2}\right)^{-1} \left(N_w - \frac{1}{\lambda_2}(\Phi_1 - \Phi_2)\right) \tag{9}$$

$$\sigma_{N_1}^2 = \sigma_{N_2}^2 = \frac{2}{(\lambda_2 - \lambda_1)^2}\sigma_\phi^2 = 630.76\sigma_\phi^2 \tag{10}$$

Generally, the above simultaneous equations of widelane and geometry-free ambiguity is started to process only when the moving rover is near the moving base. The B_1 DD measurements will be produced, then the B_1 DD ambiguity float values are estimated and its corresponding covariance matrix is produced.

As widelane has same architecture, the B_1 ambiguities can be resolved using LAMBDA algorithm or united ambiguity decorrelation [7, 8] with integer bootstrapping fixing cycle integer, substituting the result into B_1 DD measurement, it is possible to eliminate the DD integer ambiguity like widelane approach, compute σ_v, scaled by the K_{ffd} to produce the VPL, which is compared with VAL to determine whether sufficient performance is available for moving rover positioning relatively to the moving base.

After 30 min pre-filtering duration, assume that widelane integer ambiguity has been fixed. Almost in the same time, the B_1 DD ambiguities can be fixed. Simulated results for four locations (WLMQ, BJ, BZ, and XM) σ_ϕ using B_1 DD measurements is shows in Fig. 4.

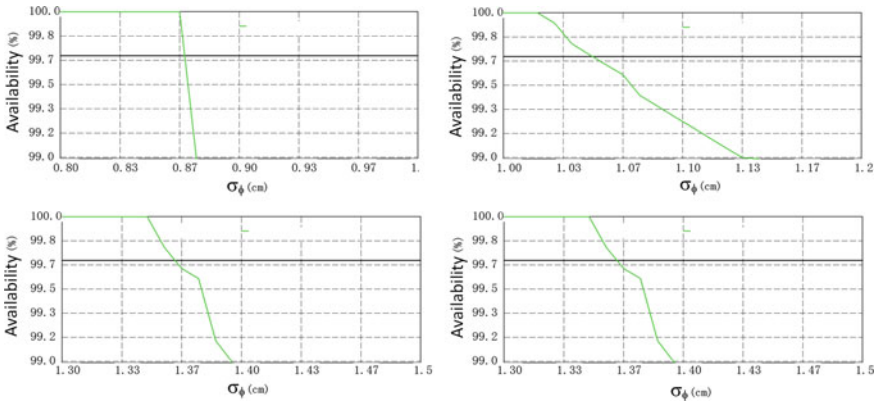

Fig. 4 (WLMQ, BJ, BZ, XM) σ_ϕ for SB-JPALS after 30 min pre-filtering time

From the simulated results, comparison with the results on the prior (wide lane), it provides further performance improvement:

- The requirement for σ_ϕ when we use B_1 DD measurements to position is much relaxed than the situation when we use DD widelane measurements. For example, for the availability of SB-JPALS, σ_ϕ required in BJ is relaxed from 0.65 to 1.02 cm.
- An availability comparison of four different areas is shown in Fig. 4. It is seen that the relaxed range of σ_ϕ in BJ is the most obvious, and the requirement for σ_ϕ in BJ when we use B_1 DD measurements is less strict than the one in XM, which is in contrast to the widelane situation. The requirements for σ_ϕ in WLMQ and XM are almost the same. By contrast, the requirement for σ_ϕ in BZ is the loosest, which is larger than 1.3 cm.
- For the availability of CAT III, the simulation results show that it takes only 5 min to fix both widelane ambiguities and single-frequency ambiguities, and the requirement for σ_ϕ is less strict than the SB-JPALS situation. Limited by the space, the simulated results are not plotted in this paper.

6 Conclusions

This paper was focused on the availability and integrity of performance of Beidou using for CAT III and SB-JPALS at four locations (WLMQ, BJ, BZ, XM). Based on a robust algorithm by optimally combining the complementary benefits of geometric-free code and carrier range filtering and geometric redundancy cycle ambiguity fixing. Two processing (DD wide lane and DD B_1) methodologies were simulated to compute the required ranging error standard deviation of pseudo and carrier phase to meet the availability and integrity of required by CAT III and SB-JPALS. These conclusions were listed follows:

- The pseudo and carrier phase range error performance provided by Beidou satellite navigation system can both satisfy the requirement for the availability and integrity of CAT III and SB-JPALS. Among the four experiment places, for SB-JPALS, the strictest requirement for carrier phase error standard deviation is 0.47 cm in WLMQ, the strictest requirement for pseudo range error standard deviation is 33 cm in BJ. For CAT III, the required pseudo range error standard deviation can be relaxed to 65 cm, when the carrier phase range error standard deviation equals to SB-JPALS.
- For the availability of CAT III using the DD widelane processing, it takes only 5 min to pre-filter while, in contrast, for the availability of SB-JPALS, the requirement for pseudo range error standard deviation is quite strict, which is 27 cm in BJ under 30 min pre-filtering time, so we have to extend pre-filtering time to at least 40 min to relax the required pseudo range error standard deviation to 33 cm, the actual pseudo range error performance of Beidou.

- After fixing the DD ambiguities of B_1, the requirement for carrier phase error standard deviation becomes looser. The required carrier phase error standard deviation in WLMQ which is the strictest among four places is relaxed from 0.47 to 0.87 cm.

Specially, the availability and integrity of performance of Beidou for moving base at WLMQ, BJ, BZ, XM, the performance at BZ is the best. Comparing to XM, they have about equal VDOP, it is just different in navigation season. Whether the performance of Beidou navigation system is related to such factors as the season is also needed long time to study. In the simulation, this paper assuming that the carrier phase without lock and cycle slip, but in the practical, how to detect and repair cycle slip, ionospheric scintillations, base station measurements extrapolation and interpolation in epoch, is the subject of continuing work.

References

1. Mohmaed AH, Sehwarz KP (1998) A simple and economic algorithm for GPS ambiguity resolution on the fly using a whitening filter. Navig J Inst Navig 45(3):P221–P231
2. Heo M-B, Pervan B (2006) Carrier phase navigation architecture for shipboard relative GPS. Aerosp Electron Syst 42(2):P670–P679
3. Yang YX, Li JL, Wang AB et al (2014) Preliminary assessment of the navigation and positioning performance of BeiDou regional navigation satellite system. Science China Earth Sci 57:144–152. doi:10.1007/s11430-013-4769-0
4. Xu JY, Yang YX, Li JL et al (2013) Integrity analysis of COMPASS and other GNSS combined navigation. Sci China Earth Sci 56:1616–1622. doi:10.1007/s11430-013-4647-9
5. Teunissen PJG (1994) A new method for fast carrier phase ambiguity estimation. In: Proceedings of IEEE PLANS'94, Las Vegas, NV, pp 562–573, 11 Apr 1994
6. Liu LT (1999) A new approach to GPS ambiguity decorrelation. J Geodesy 73(9):P478–P490
7. He HB, Yang YX (2001) Real-time estimation of a prior variance-covariance for GPS observations. Acta Geodaetica et Cartographica 30(1):P42–P47
8. Teunissen PJG, Odijk D, Joosten P (1998) A probabilistic evaluation of correct GPS ambiguity resolution. In: Proceedings of the 18th international technical meeting of the satellite division of the institute of navigation (ION GPS 1998), Nashville, TN, pp 1315–1323
9. Dogra S, Wright J, Hansen J (2005) Sea-based JPALS relative navigation algorithm development. In: Proceedings of the 18th international technical meeting of the satellite division of the institute of navigation (ION GNSS 2005), Long beach, CA, pp 2871–2881

Research on GPS RAIM Algorithm Using PF Based on PSO

Ershen Wang, Rui Li, Tao Pang, Pingping Qu and Zhixian Zhang

Abstract To solve the problem of basic particle filter (PF), a novel GPS receiver autonomous integrity monitoring (RAIM) method was proposed, which was based on an algorithm combining particle swarm optimization particle filter (PSO-PF) with likelihood ratio test. The test statistic of fault satellite detection was set up, and the probability distribution of the log-likelihood ratio test statistic was analyzed. The consistency test is undertaken by checking the cumulative log-likelihood ratio (LLR) of system states. The velocity and position of particles were updated by particle swarm optimization algorithm, which make the particles of PF approximate the true system state to improve the posterior probability density of system state. Collecting the raw GPS data, the proposed algorithm was verified. The simulation result demonstrates that the proposed algorithm can effectively detect and isolate fault satellite under conditions of non-Gaussian measurement noise.

Keywords Global positioning system (GPS) · Receiver autonomous integrity monitoring (RAIM) · Particle swarm optimization (PSO) · Particle filter

1 Introduction

Global navigation satellite system (GNSS) is a space-based radio navigation system, the construction of satellite constellation in the space to achieve all weather, global, continuity of precise three-dimensional positioning capability. Among the four systems, GPS is the most mature development one. Now China's Beidou satellite navigation system (BDS) has now entered the stage of global networking construction. There are over 20 orbiting satellites, which are expected to complete

E. Wang (✉) · R. Li
Beihang University, Beijing, China
e-mail: wes2016@sau.edu.cn; wes2016@126.com

E. Wang · T. Pang · P. Qu · Z. Zhang
School of Electronic and Information Engineering, Shenyang Aerospace University, Shenyang, China

J. Sun et al. (eds.), *China Satellite Navigation Conference (CSNC) 2016 Proceedings: Volume II*, Lecture Notes in Electrical Engineering 389,
DOI 10.1007/978-981-10-0937-2_17

construction in 2020. Satellite navigation systems, mostly in high orbits, contained the time parameter of the receiver and the satellite, the atmospheric propagation delay, multipath effects, etc. There could be some errors in the coordinate solution. In addition, the satellite signal transmission is easy to be affected by topography, and it is difficult for the system to meet positioning requirements in the canyon, jungle and urban built-up area. Thus, the integrity of the navigation system is an important measure of the navigation system, especially for high reliability requirements of aviation users; integrity monitoring system is onboard navigation systems which are indispensable.

At present, to realize the target that the navigation system integrity monitoring can achieve the following three points: the first is the satellite autonomous integrity monitoring (SAIM); the second is the receiver autonomous integrity monitoring (RAIM); the third is to enhance the system [1]. Where RAIM technology detected and isolated faults mainly in two ways: first, through the redundant information, and second, through other auxiliary equipment (altimeter, inertial navigation, etc.). Currently, the development of different navigation systems, making visible satellites doubled, RAIM algorithm based on redundant information receiver brought out a new vitality.

To solve performance variation problem of RAIM algorithm based on Kalman filter in the process of dealing with non-Gaussian noise, a lot of researchers combined the particle filter (PF) algorithm and RAIM algorithm, but in PF algorithm exists the problem that particle degradation and resampling caused loss of diversity of particles, this paper introduces the particle swarm optimization algorithm (PSO) to optimize the particles more accurately to represent the true sample distribution of the probability density function, and its combination with the likelihood ratio method to achieve integrity monitor.

2 Particle Filter Algorithm Based on Particle Swarm Optimization

PF is based on Monte Carlo method and recursive Bayesian statistical filtering method. The basic idea is based on the experience distribution of the system state vector producing a collection of random samples (particles) in the state space, based on adjusted information of the particles weight and position in the process measurement to correct initial experience conditional distribution, it is effective nonlinear filtering technology.

Describe the dynamic system state equation and observation equation is:

$$X_k = f(x_{k-1}, w_{k-1})$$
$$Y_k = h(y_{k-1}, v_{k-1})$$

Among them, X_k as the state vector, Y_k as the measurement vector, f as the state transfer function, h as the transfer function between the state vector and the observation vector, w_{k-1} is the system noise, v_{k-1} is the observation noise [2].

In the standard PF, because the particles produced degradation introduced resampling technique which can reduce particle invalid particles, but resampling will bring new problems, for example, in many occasions, the resampling will not only increase the computational burden, but also generates a sample depletion phenomenon, some weights larger particles will be selected multiple times, the result contains many duplicate particle. This leads to a loss of diversity among the particles [3, 4]. To solve this, shortcoming in the PF can combine intelligent optimization methods with PF. Particle swarm optimization (PSO) algorithm is a swarm intelligence optimization algorithm, which is incorporated PF, can effectively improve the sampling process.

PSO algorithm, each particle was updated with their speed, size, and location status on the basis of individual extremes and global extreme [5–7]. In the n-dimensional space, after several iterative calculation, got the individual extreme $P_i = (p_{i1}, p_{i2}, \ldots, p_{in})$, calculated from the initial time to the current time produced the optimal solution; Global extreme $G = (g_1, g_2, \ldots, g_n)$ is the group of optimal solution searched in the entire particle swarm for from the initial time to the present time. Updated formula is as follows:

$$V_i = w * V_i + c_1 * \text{Rand}() * (P_i - X_i) + c_2 * \text{Rand}() * (G - X_i)$$
$$X = X_i + V_i$$

In the formula, Rand is random numbers between (0, 1); w as the inertia coefficient; c_1 and c_2 Collectively referred to as learning factors, in general $c_1 = c_2 = 2$. Typically, w larger, then the algorithm has strong global search capability, w smaller tends to local search.

From above the formula, PF and PSO algorithm has many similarities [8–10]. First, PSO finds the optimal value by constantly updating the velocity and position of the particles in the search space, and PF approximates the system's true posterior probability distribution through constantly updating the particle's location and weight; second, PF algorithm, the maximum weight of the particles showed that the value is very close to the real system state, and particle swarm optimization represents the search space optimal value points through the particles which have a maximum fitness value; third, PSO algorithm and particle filtering algorithm have their own motion mechanism.

Based on the above three points, the PSO algorithm can integrate into the PF algorithm to optimize the performance of standard particle filtering algorithm.

Defined particle fitness function is as follows:

$$\text{fitness} = \exp\left[-\frac{1}{2R}(y_{\text{new}} - y_{\text{pre}})^2\right]$$

In the formula, y_{new} is the latest measured value, y_{pre} is the prediction of the measurement value of the particle, R is the noise variance. Use the fitness function values to push the particle swarm to move to the optimal solution particles. PSO optimized PF algorithm is as follows:

(1) Initial the particle collection. At time $k = 0$, sampling N particles as: $\{x_0^i, i = 1, 2, \ldots, N\}$.
(2) Calculated particle fitness values. $k = k + 1$, Calculated the fitness value of each particle by the formula 4.
(3) Calculated the particle weight. The modified weights calculated are as follows:

$$w_k^i = w_{k-1}^i * \text{fitness}(x_k^i).$$

Update particle velocity and position using formulas 1.2 and 1.3, the updated particle position is $\{x_k^j, j = 1, 2, \ldots, N\}$. Using the formula $q(x_{0:k}|Y_k) = q(x_0)\prod_{j=1}^{k} q(x_j|x_{0:j-1}, Y_j)$ normalized weights, $w_k^i = w_k^i / \sum_{i=1}^{N} w_k^i$.

(4) Particle resampling. Calculated N_{eff} by the formula $\hat{N}_{\text{eff}} = \frac{1}{\sum_{i=1}^{N} (w_k^i)^2}$ and compared with threshold value $N_{\text{threshold}}$ if $N_{\text{eff}} < N_{\text{threshold}}$, then proceed particle resampling. After resampling, particle collection $\{x_k^j, w_k^j\}_{i=1}^{N}$ which contains weight mapped to the particle samples $\left\{x_k^m, \frac{1}{N}\right\}_{m=1}^{N}$.
(5) PSO_PF result output:
The system state value estimate: $\hat{x}_k = \sum_{m=1}^{N} w_k^m x_k^m$. Variance estimation:

$$P_k = \sum_{m=1}^{N} w_k^m (x_k^m - \hat{x}_k)(x_k^m - \hat{x}_k)^T.$$

(6) Determine whether the algorithm is end or not. If not completed, then return to the Step (2); otherwise, exit algorithmic process.

Through the above process, the particles tend to high likelihood region so reduce the needed number of particles for PF and for improve the effects of each particle making poor particle phenomenon resolved.

3 RAIM Algorithm Based on PSO-PF

Combining RAIM algorithm of GNSS systems with PSO optimized PF algorithm detects and identifies the fault satellite. According to the measured value from the receiver, do high precision estimation of the system state with the PSO-PF algorithm, establish a log-likelihood ratio (LLR) test statistic for satellite fault detection and identification. Calculated the measured value LLR of different satellites at various times, and accumulated in a limited length of the window function,

respectively, obtained cumulative logarithmic likelihood ratio corresponding to time [11–14]. After conducting conformance testing, in which way satellite fault and the number of fault satellite can be determined.

3.1 The System State Equation and Measurement Equation

System state equation for GNSS:

$$X_k = F_{k-1}X_{k-1} + \mu_{k-1}$$

Measurement equation for GNSS:

$$\rho^i(k) = R^i(k) + c * \Delta\delta^i + T^i(k) + I^i(k) + E^i(k) + v^i(k)$$

In the formula, $X_k = [r_x, r_y, r_z, \Delta\delta]^T$, is the three-dimensional position coordinates and receiver clock error; F is transfer matrix, When the receiver static, F is unit matrix; μ is state process noise. ρ^i is pseudorange value of the ith satellite $\left(S_x^i, S_y^i, S_z^i\right)$ to receiver; $R^i = \sqrt{\left(S_x^i - r_x\right)^2 + \left(S_y^i - r_y\right)^2 + \left(S_z^i - r_z\right)^2}$ is geometrical distance of the ith satellite to receiver; c is the light-speed; $\Delta\delta^i$ is clock error of the ith satellite to receiver; T^i is the troposphere delay; I^i is the ionosphere delay; E^i is the ephemeris errors; v^i is the observation noise.

The navigation data that the receiver received comprises a satellite position information $\left(S_x^i, S_y^i, S_z^i\right)$, pseudorange ρ^i, clock error $\Delta\delta^i$, ephemeris errors E^i, tropospheric delay T^i, and ionosphere delay I^i.

Assuming there are nine satellites used for calculating at the present time, and where there is a failure satellites. Among them, y1, y2, y3, y4, y5, y6, y7, y8, and y9 is the measured value of the current moment. Sub-PSO-PF Q(Q = A, B, C, D, E, F, G, H, and J) is the input measurement subset of PSO-PF filter. $\{\hat{x}^Q, p^Q(y)\}$ (J = A, B, C, D, E, F, G, H, and J) is the state estimation and likelihood probability density of the PF given. The main PSO-PF is used to handle all nine measurements to make accurate estimate about state of the system $\hat{x}^M$ and its probability density function $p_M(y)$, while the other six NNWA-PF as an auxiliary PF is mainly used to process five measurements among the six, to calculate the state estimation $\hat{x}^q$ and their probability density function $p_q(y)$ (q = A, B, C,…, J), the results will be used to construct test statistics. Therefore, figure out the normalized weights each time of the main PSO-PF and each auxiliary PSO-PF, the cumulative LLR used for x consistency test can be acquired, thus detect the system whether failure.

3.2 Principle of LLR Test Used in the RAIM

By calculating the cumulative LLR function at each time $s_j^k(d) = \sum_{r=j}^{k} \ln \frac{\frac{1}{N}\sum_{i=1}^{N} \tilde{w}_r^d(i)}{\frac{1}{N}\sum_{i=1}^{N} \tilde{w}_r^A(i)}$, the decision function for consistency detecting is as follows: $\beta_k = \max_{k-U+1 \le j \le k} \max_{1 \le d \le U} S_j^k(d) > \tau$.

In the equation, U as the window function, It contains each time observation before the current time, τ is the decision threshold, When $\beta_k > \tau$, that is, the system detects a fault, it should set the alarm, and the current time is represented as t_a, then use the formula $g = \arg\max_{1 \le d \le D} s_{t_a}^k (k > t_a)$ determine the number of the fault satellite.

CLLR S_j^k for fault detection function has the following characteristics: With the increasing detection time k, and in the case of the system working properly, S_j^k function curve as a whole stable, occasional fluctuations; When the system data is changed in a moment, S_j^k function creates a negative direction curve drift before the data change, after the data change produced an obvious positive curve drift, which have a greater change rate curve, use this feature, whether the GNSS system failure can be determined.

The process of RAIM algorithm based on PSO-PF algorithm is as follows:

(1) Initializing particle, let the receiver for initial coordinates (r_x, r_y, r_z), according to initial receiver coordinate generating N main PSO-PF initial particle collection $\{x_0^{\text{main}}(i), i = 1, 2, \ldots, N\}$ and fraction of N sub-PSO-PF fraction initial particle collection $\{x_0^q(i), i = 1, 2, \ldots, N\}$, and $x_0^q(i) = x_0^{\text{main}}(i)$.

(2) Repeat the process for $I \sim IX$ in k moment:

I. Particle state prediction. Initialized particles collection $\{x_0^{\text{main}}(i), i = 1, 2, \cdots, N\}$ and $\{x_0^q(i), i = 1, 2, \ldots, N\}$ into the GNSS state equation. Get the predicted value of the particle state $x_{k|k-1}^{\text{main}}(i)$ and $x_{k|k-1}^q(i)$.

II. Calculate the particle fitness. According to the receiver received navigation information, let the coordinate value be (S_x^q, S_y^q, S_z^q), clock error $\Delta\delta$, ephemeris error E^q, ephemeris errors E^i, tropospheric delay T^q, and ionosphere delay I^q and $x_{k|k-1}^{\text{main}}(i), x_{k|k-1}^q(i)$ of the qth satellite into the measurement equation of GNSS, calculated for each particle to the q satellite pseudorange prediction value $\bar{\rho}_{k|k-1}^q(i)$. Let the receiver received actual pseudorange value be ρ^q and predict pseudorange values $\bar{\rho}_{k|k-1}^q(\mathrm{i})$ into the fitness formula, calculate the fitness value of each particle and calculate the weight of each particle.

III. Update particle velocity and position. According to individual optimal values and global optimum updated particle velocity and position, get the optimal new particle $\bar{x}_{k|k-1}^{\text{main}}(i)$ and $\bar{x}_{k|k-1}^q(i)$;

IV. Normalize particle weight. Make the corresponding particle weights normalized, The normalized value is $\tilde{w}_k^{\text{main}}(i)$ and $\tilde{w}_k^q(i)$.
V. Calculate the cumulative log-likelihood ratio.
VI. Calculate the fault decision function β_k.
VII. Determine fault detection.
If $\beta_k < \tau$, It said the failure of the current time is not detected, jump to IX.
If $\beta_k < \tau$, It indicates that there is a failure detected, record the alarm time which is $t_a = k$, jump to VIII.
VIII. Identify the fault satellite. Under $t_a = k$ condition, calculate the maximum value of CLLR of sub-PSO-PF module, to know the fault satellite number, and complete the fault satellite recognition.
IX. Resample and status update. Calculate the effective particles number $\bar{w}_{k|k-1}^{\text{main}}(i)$ and $\bar{w}_{k|k-1}^q(i)$, and compare with a threshold value N_{eff} to determine whether there is need resampling or not. If resampling, modify the resampling particle as $x_{k|k-1}^{\text{main}}(i)$ and $x_{k|k-1}^{\text{main}}(i)$, the weight is $\frac{1}{N}$. Finally, update the system status $X_k = \sum_{i=1}^{N} w_k^i X_{k|k-1}(i)$.

4 Experiment and Simulation Analysis

In this section, by using the raw data of GPS receiver in the May 29, 2014 as the algorithm analysis, the length of time for data collection is 86,400 s, there are 32 satellites and without fault, the receiver positioning accuracy is 2.0 m.

Get information from the raw data required by the algorithm, satellite coordinate information, pseudorange value, ionosphere error, tropospheric, and other information. To validate the algorithm, select the valid data length 1000 s time, there are nine satellites that meet the PVT calculating, satellite numbers are 1, 12, 14, 15, 17, 22, 24, 26, and 28.

To validate effectiveness of the algorithm for satellite fault detection and identification, at the time t = 500 s, in the original trouble-free observation pseudorange values of the No. 1 satellite, artificially adding different deviation, analyse the detection situation of algorithms for different deviation.

In this algorithm validation experiments, the number of particles N = 50, alarm thresholds $\tau = 20$, window function length selected as U = 30, particle swarm optimization iterations K = 10. In time t = 500 s, the original observations Pseudo of the Ith satellite were added in 10, 20, and 30 m step deviation. As can be seen from Figs. 1, 2, and 3, at time t < 500 s, under different bias the decision function is relatively small, and that is $\beta < \tau$. And there was no satellite failure. After t = 500 s, the decision function under different bias appears larger increase, indicating that at the moment there is satellite fault detected.

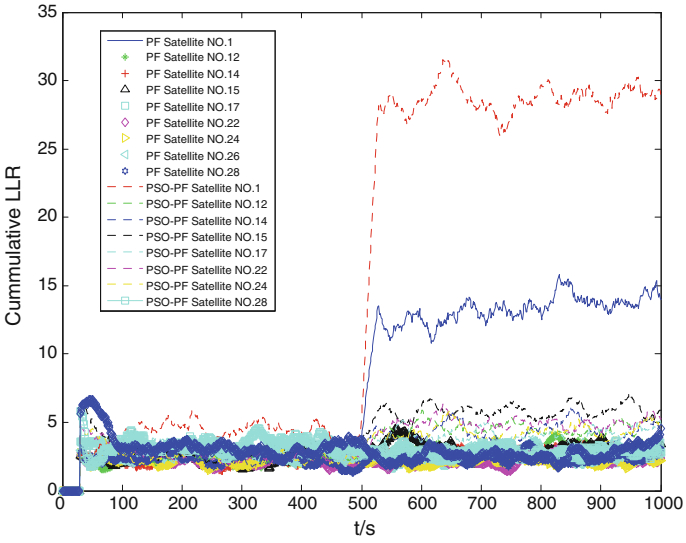

Fig. 1 Cumulative LLR under 10 m step failure condition

As can be seen from Figs. 4, 5, and 6, at different bias, each satellite in time t = 500 s, its CLLR values that have emerged grow dramatically. In the case of 10, 20, and 30 m, the greater the deviation, the greater CLLR value of the fault satellites, and the algorithm can more easily identify the fault satellites.

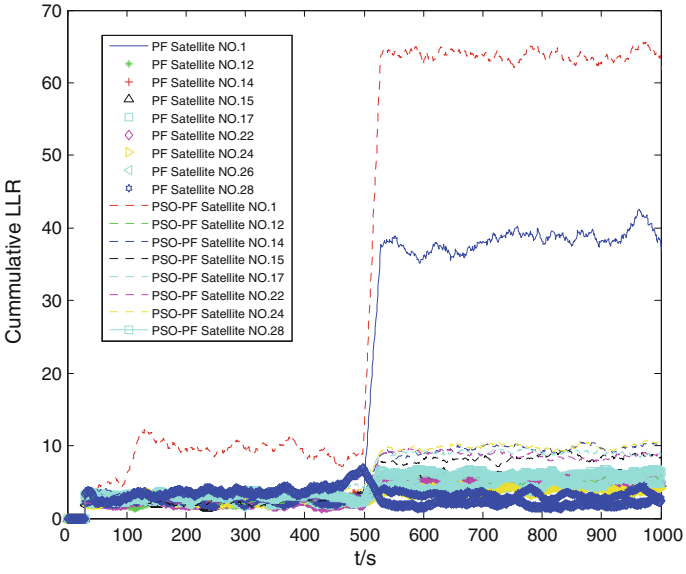

Fig. 2 Cumulative LLR under 20 m step failure condition

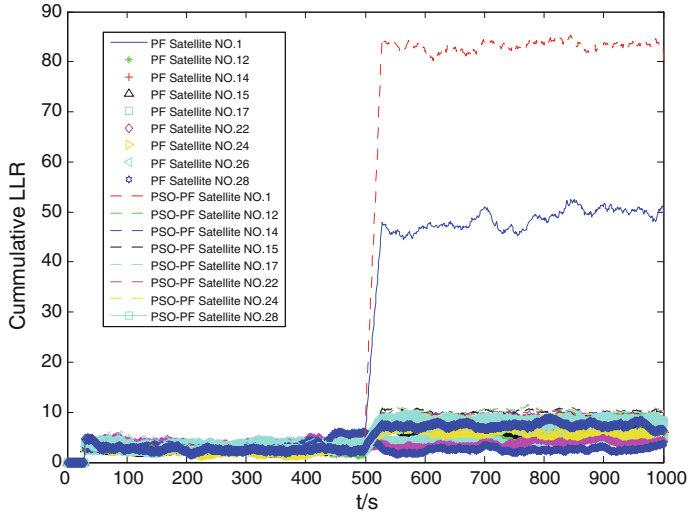

Fig. 3 Cumulative LLR under 30 m step failure condition

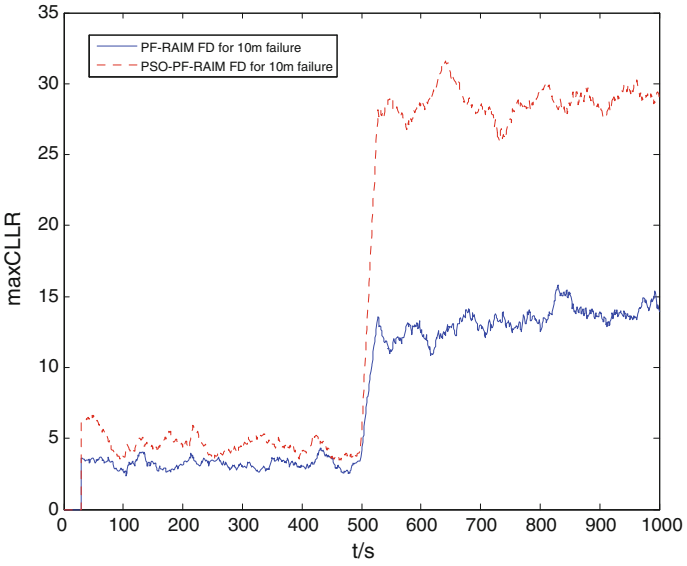

Fig. 4 Decision function for fault detection under 10 m step failure condition

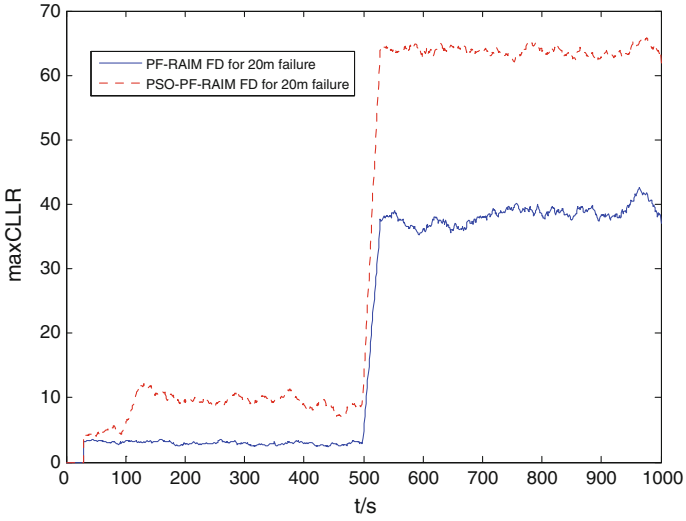

Fig. 5 Decision function for fault detection under 20 m step failure condition

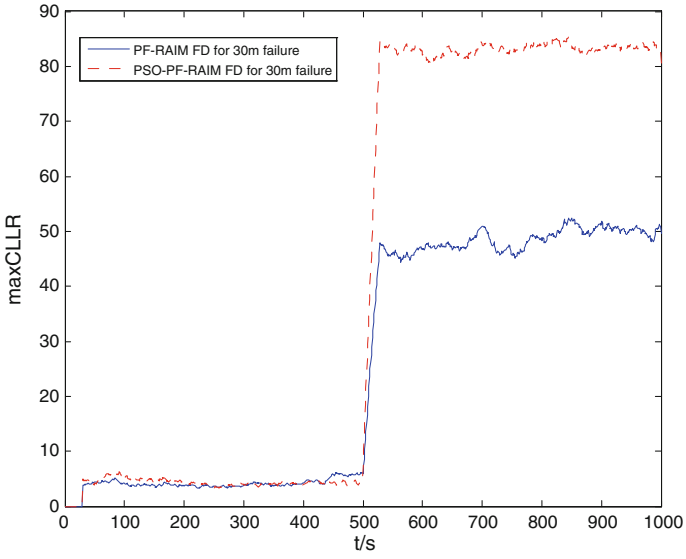

Fig. 6 Decision function for fault detection under 30 m step failure condition

As can be seen from Table 1, under different pseudorange deviations the average effective number of particles is more than 43 for PSO-PF algorithm. RAIM algorithm based on PSO-PF has enough effective number of particles in the process of detection and identification of the satellite failure.

Table 1 Average effective number of particles under different deviation ($N = 50$)

Deviation (m)	Average effective number of particles for PSO-PF
10	44.3819
20	44.3649
30	43.5810

5 Conclusion

In this paper, the particle swarm optimization PF algorithm for GPS RAIM was proposed, through the establishment of satellite fault detection and identification model, using the accumulated log-likelihood ratio test method to complete satellite integrity monitoring. Receiving the GPS receiver satellite's data, different values of the pseudorange step bias were artificially added in order to verify the fault detection and identification capability of RAIM algorithm based on PSO-PF. The results showed that: at adding different pseudorange bias case, PSO-PF-RAIM algorithm can effectively detect satellite failure, and identifies the number of failure satellite. Experimental studies have shown that RAIM algorithm combining PSO optimizes PF algorithm, implements satellite fault detection and fault satellite identification function is available and effective. The improved algorithm for the study of China's BDS navigations receiver autonomous integrity monitoring, and improves the accuracy of GPS positioning which has a certain significance.

Acknowledgment This study is funded by the National Basic Research Program of China (973 Program) (2010CB731805), the National Natural Science Foundation of China (61571309 & 61101161), and the Joint Funds of the Natural Science Foundation of Liaoning Province (2013024003).

References

1. Lu D, Chen X (2009) Algorithm for global navigation satellite system receiver autonomous integrity monitoring. Comput Eng 35(11):10–12
2. Wang E, Pang T, Li X, Zhang Z (2015) Improved particle filter algorithm based on genetic algorithm and neural network for GPS positioning data processing. Chin J Electron Dev 2015 (2)
3. Doucet A, Godsill S, Andrieu C (2000) On sequential monte carlo sampling method for Bayesian filtering. Stat Comput 10:197–208
4. Chen Z, Bo Y, Wu P, Yu S (2013) A Chaos particle swarm optimization particle filter algorithm. Electron Opt Control 20(1):36–40
5. Fang Z, Tong G, Xu X (2007) Particle swarm optimized particle filter. Control Decis 22(03):273–277
6. Krohiling RA (2004) Gaussian swarm: a novel particle swarm optimization algorithm. In: Proceedings of the IEEE conference on cybernetics and intelligent systems, pp 272–276
7. Gao Y, Xie S (2004) Particle swarm optimization algorithms based on simulated annealing. Comput Eng Appl 40(01):47–50

8. Kadirkanathan V, Li P, Jaward MH et al (2002) Particle filtering based fault detection in non-linear stochastic systems. Int J Syst Sci 33(4):259–265
9. Wei T, Huang Y, Chen CLP (2009) Adaptive sensor fault detection and identification using particle filter algorithms. IEEE Trans Syst Man Cybern Part C Appl Rev 39(2):201–213
10. Cheng Q, Varshney PK (2007) Joint state monitoring and fault detection using distributed particle filtering. In: Conference record of the forty-first Asilomar conference on signals, systems and computers, 2007. ACSSC 2007. IEEE, pp 715–719
11. Li P, Kadirkamanathan V (2001) Particle filtering based likelihood ratio approach to fault diagnosis in nonlinear stochastic systems. IEEE Trans Syst Man Cybern Part C Appl Rev 31(3):337–343
12. Zhang Q, Campillo F, Cerou F et al (2006) Nonlinear system fault detection and isolation based on bootstrap particle filters. In: 44th IEEE conference on decision and control, 2005 and 2005 European control conference. CDC-ECC '05. IEEE, pp 3821–3826
13. Legland F, Oudjane N (2000) Stability and approximation of nonlinear filters in the Hilbert metric, and application to particle filters. In: Proceedings of the IEEE conference on decision and control, pp 1585–1590
14. Rosihan, Indriyatmoko A, Chun S et al (2006) Particle filtering approach to fault detection and isolation for GPS integrity monitoring. Proceedings of 2006 ION GNSS, ION, Fort Worth, TX, pp 873–881

Fingerprint Positioning Method of Satellite Signal Based on Probability Distribution

Li Yang, Di He, Peilin Liu and Wenxian Yu

Abstract To enhance the GNSS localization quality degraded by signal blockage and multipath reflections in urban areas, a fingerprint positioning method of satellite signal based on probability distribution has been proposed to improve the satellite positioning accuracy. We utilize the difference of the probability distribution of different positions to perform an accurate positioning in this paper. The probability distribution of the signal parameter at a certain position can be obtained with the 3-D ray-tracing method, and then we can establish a fingerprint database by figuring out the probability distribution curves of the signal parameters at different locations. Finally, a matched filter method, which is used to match the actual received signal parameters with the fingerprint information in the database, can be used to realize the positioning task. The proposed fingerprint positioning method based on probability distribution greatly reduces the similarity of fingerprint information at different positions, so it can perform better than the traditional nearest neighbor method. The theoretical analysis and simulation results show that the proposed approach can improve the accuracy of positioning.

Keywords Satellite positioning · Location fingerprint · Probability distribution · Signal parameters · Positioning accuracy · 3-D ray-tracing algorithm

1 Introduction

The rapid development of the mobile processing technique has led to the strong demand of location-based services (LBS). The needs for accurate positioning have become increasingly urgent, including the indoor and outdoor environments.

L. Yang (✉) · D. He · P. Liu · W. Yu
Shanghai Key Laboratory of Navigation and Location-Based Services,
School of Electronic Information and Electrical Engineering,
Shanghai Jiao Tong University, 200240 Shanghai, China
e-mail: yangli0525@sjtu.edu.cn; 270668996@qq.con

J. Sun et al. (eds.), *China Satellite Navigation Conference (CSNC) 2016 Proceedings: Volume II*, Lecture Notes in Electrical Engineering 389,
DOI 10.1007/978-981-10-0937-2_18

As the main outdoor positioning and navigation technology, the dependence on satellite positioning technology has increased gradually in many areas. Meanwhile its deficiency in positioning accuracy has attracted more and more attention. In the common indoor/outdoor location system, the time of arrival (TOA), time difference of arrival (TDOA), or received signal strength (RSS) of the measured signal are usually used to measure the distance between the transmitter and receiver, and the angle of arrival (AOA) is utilized to determine the relationship between space angles. At present, the main positioning methods include triangulation, mobile network-based location technique and fingerprint positioning method.

Triangulation method [1, 2] uses the geometric properties of triangle to estimate the location of the target, and it consists of two types: lateration and angulation. Lateration, which is also called distance measurement technique, computes the distance by measuring TOA or TDOA, etc., to locate an object, while angulation technique computes angles relative to several references to determine the position of an object. Triangulation method has the advantage of less work and convenience. However, due to the measurements of TOA, TDOA, and AOA are susceptible to outside influence and the demand for the system hardware is higher, there exits great difficulties in the implementation process.

Mobile network-based positioning technology [1, 3] requires each cell which has its own identification number, and it determines the position by collecting the identification number of the cell where the mobile terminal is located. When the target comes into a certain cell, this cell should be registered, at the same time its corresponding identification number is recorded in the positioning system's database.

Fingerprint positioning method [4–6] contains two stages: offline stage and online stage. The main purpose of the offline stage is to collect the signal parameters at each sampling point of the received area, including RSS, AOA, etc., and to establish the fingerprint database. At the online stage, we figure out the estimated location by matching the collected signal parameters with the fingerprint information. This fingerprint positioning method not only has high precision but also is convenient to implement.

Deterministic method and probabilistic distribution method [7–11] are the two major positioning methods of fingerprint technique. The deterministic method measures and saves the mean of the signal characteristic parameters in the offline phase, and matches the fingerprint database to realize localization by calculating Euclidean distance in the online phase. While the probability distribution method calculates and saves probability distribution of the signal parameters at the first step, and then estimates the location of the object with the bayesian method. Compared with the deterministic fingerprint positioning approach based on the mean of the parameters, the probability distribution method can make full use of the previous measured data, depict the probability distribution of the signal parameters at each specific position more accurately, thereby it can reduce the similarity of fingerprint information at different positions significantly. So, the probabilistic distribution-based fingerprint

method is applied in this paper to reduce the positioning error and improve the positioning accuracy.

Presently, 3-D ray-tracing method [12] is widely used in predicting the geometric paths of the signal and evaluating the performance of the positioning system. Ray-tracing algorithm is based on the electromagnetic theory, the uniform theory of diffraction and the geometrical theory of optics. All the possible paths from transmitter to receiver can be predicted by simulating the propagation paths of transmitted signal. Therefore, in order to reduce the workload of the fingerprint positioning method in offline stage, we consider simulating the propagation path of satellite signal with the 3-D ray-tracing model, and implement satellite signal positioning task by using probability distribution-based fingerprint method under the simulation environment.

2 Multiparameter Fingerprint Positioning Method Based on Probability Distribution

Due to the influence of such factors as the movement of the satellite, signal interference and noise, the signal parameters at the same place are varying, whose change regularity obeys normal distribution. So, compared with the deterministic fingerprint positioning approach, the probability distribution method depicts the signal parameters at each specific position more accurately, reduces the similarity of fingerprint information at different positions significantly. The traditional probability distribution method uses only one parameter, such as RSS, to establish the fingerprint database. However, our researches show that using multiple signal parameters as fingerprint information can reduce the positioning error. On the basis of the previous research [3], therefore, we put forward a multiparameter fingerprint positioning method based on probability distribution.

Probability distribution-based fingerprint method calculates the posterior probability by matching the parameters of the object with that of the reference point in the database, and uses the location with maximum probability as the estimated position. As multiple sampling results show that the signal parameters at a fixed position obey Gaussian probability distribution, we utilize the statistical mathematical expectation and variance to describe the distribution features of signal parameters of each reference point.

2.1 Offline Sampling Stage

The main task of the offline stage is to calculate the mean and variance of the signal parameters of each reference point at the receiving area and to record them in the

fingerprint database. The fingerprint information contains RSS, AOA, phase difference of arrival (PDOA), and time delay (Td). AOA consists of an elevation angle (EA) and an azimuth angle (AA) in the 3-D space, PDOA is the phase difference between the minimum and the rest of the incident paths or the reflection paths that arrive in the receiving area.

For a certain set of actual signal parameters x (contains RSS, AOA, PDOA, and T_d), it is generally considered obeying a normal distribution $N(\mu, \sigma^2)$, statistical parameters are μ and σ^2. The likelihood function is described as:

$$L(\mu, \sigma^2) = \prod_{i=1}^{n} \frac{1}{\sqrt{2\pi}\sigma} e^{-\frac{(x_i-\mu)^2}{2\sigma^2}} \tag{1}$$

Apply logarithmic transformation to function (1):

$$\lg L(\mu, \sigma^2) = -\frac{n}{2}\lg(2\pi) - \frac{n}{2}\lg(\sigma^2) - \frac{n}{2\sigma^2}\sum_{i=1}^{n}(x_i - \mu)^2 \tag{2}$$

Likelihood equations are:

$$\begin{cases} \frac{\partial \lg L(\mu,\sigma^2)}{\partial \mu} = \frac{1}{\sigma^2}\sum_{i=1}^{n}(x_i - \mu)^2 = 0 \\ \frac{\partial \lg L(\mu,\sigma^2)}{\partial \sigma^2} = -\frac{n}{2\sigma^2} + \frac{1}{2\sigma^4}\sum_{i=1}^{n}(x_i - \mu)^2 = 0 \end{cases} \tag{3}$$

Solve Eq. (3) to obtain the maximum likelihood estimation of μ and σ^2:

$$\mu^* = \bar{x} = \frac{1}{n}\sum_{i=1}^{n} x_i \tag{4}$$

$$\sigma^{*2} = \frac{1}{n}\sum_{i=1}^{n}(x_i - \bar{x})^2 \tag{5}$$

When the sample space is large enough, the maximum likelihood estimation μ^* and σ^{*2} can be considered as the true value. On the offline stage, we collect the parameters of each signal path (including direct path and multipath) which arrives at the reference point, and calculate the maximum likelihood estimation of the mean and variance of the signal parameters which contain RSS, EA, AA, PDOA, and Td. Then, we combine the coordinate X_t ($t = 1, 2, \ldots N$, N stands for the number of all the reference points) of each reference point with the mean vector and variance

vector to establish a fingerprint database. The mean vector $\vec{\mu}$ and variance vector $\vec{\sigma^2}$ can be described as:

$$\begin{aligned}\vec{\mu} &= (\mu_1, \mu_2, \ldots \mu_n) \\ &= E(\overbrace{\text{RSSI, EA, AA, PDOA, Td}}^{LOS}, \overbrace{\text{RSSI, EA, AA, PDOA, Td, }\ldots}^{NLOS}) \\ \vec{\sigma^2} &= (\sigma_1^2, \sigma_2^2, \ldots \sigma_n^2) \\ &= D(\overbrace{\text{RSSI, EA, AA, PDOA, Td}}^{LOS}, \ldots \overbrace{\text{RSSI, EA, AA, PDOA, Td, }\ldots}^{NLOS})\end{aligned} \tag{6}$$

where n is the total number of the vector.

2.2 Online Positioning Stage

On the online stage, the position is estimated by matching the collected signal parameter vector with the fingerprint information in the database. The core idea of the match method is probability distribution. At each reference point, the conditional probability or posterior probability of the object can be computed according to its measured signal parameter vector, and then the position with the maximum probability can be regarded as the estimated position. According to the bayes formula, assumed that the real-time collected signal parameter vector of a target is S, the posterior probability can be computed as follows:

$$p(X_t/S) = \frac{p(S/X_t)p(X_t)}{p(S)} \tag{7}$$

where $p(X_t)$ is the prior probability of being at location X_t, and it is always assumed to be uniform distribution; $p(S/X_t)$ is called the likelihood function; $p(S)$ has weak correlation with the specific reference position, so it is seen as constant. Equation (7) can be simplified as:

$$p(X_t/S) \propto p(S/X_t) \tag{8}$$

Equation (8) shows that the maximum likelihood probability can be used to represent the maximum posterior probability. Suppose that the sampled signal parameter vector of an object is:

$$\begin{aligned}S &= (S_1, S_2, \ldots S_n) \\ &= (\overbrace{\text{RSSI, EA, AA, PDOA, Td}}^{\text{LOS}}, \overbrace{\text{RSSI, EA, AA, PDOA, Td, }\ldots}^{\text{NLOS}})\end{aligned} \tag{9}$$

Assuming that every parameter is independent on each other, the maximum likelihood probability can be computed as:

$$p(S/X_t) = \frac{1}{\sqrt{(2\pi)^n \prod_{i=1}^{n} \sigma_i}} \exp\left(-\frac{1}{2} \sum_{i=1}^{n} \frac{(S_i - \mu_i)^2}{\sigma_i^2} \right) \tag{10}$$

The likelihood probability at any reference point can be given according to formula (10), finally the position with the maximum probability is considered as the estimated location (x, y, z).

$$(x, y, z) = \max_{(x,y,z)} \frac{p(S/X_t)}{\sum_{t=1}^{N} p(S/X_t)}. \tag{11}$$

3 Simulation Results and Discussions

We take the balcony in the Microelectronics Building at Shanghai Jiao Tong University (shown in Fig. 1a) as a real site, and build a 3-D model of the balcony and the walls around it (shown in Fig. 1b). Then we set the simulation parameters such as the reflection coefficient of the walls and the satellite signal frequency, etc. The receiving area is divided into many small grids averagely and the center of each grid is regarded as the reference point. According to the ray-tracing method, we can predict the propagation path of the signal, and calculate the RSS, PDOA, etc., of each path. Due to the influence of such factors as noises, the mean and variance of the signal parameter which can describe its probability distribution are recorded into the fingerprint database. At last, we can implement the positioning task by matching the database to get the maximum posterior probability.

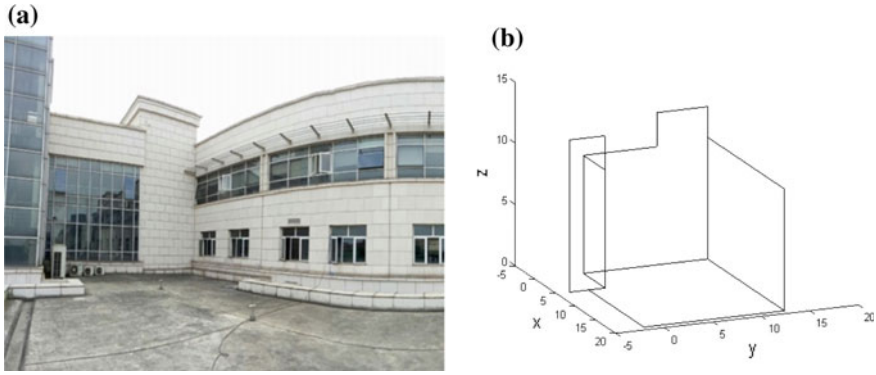

Fig. 1 The real scene and 3-D model of the balcony. **a** The real scene of the research. **b** The 3D simulated model

No more than two once-reflected paths (or twice-reflected paths) and one LOS path are simulated in our research in order to reduce the computational complexity. Consequently, at most five paths (one LOS path, two once-reflected paths, and two twice-reflected paths) would be simulated at a reference point, if exists. On the online stage, we calculate the posterior probabilities that the point to be located is positioned at each reference point in the database. The point with maximum probability is regarded as the estimated position. The whole process of the MPPD method is depicted in Fig. 2.

In order to verify the feasibility of the proposed MPPD method, 200 receiving samples are selected randomly to match the fingerprint. In this simulation experiment, the grid density is 100 grids per square meter, which determines the size of the fingerprint. Figure 3 shows the positioning results of the proposed MPPD approach, where the green '*' represents the selected experimental position and the

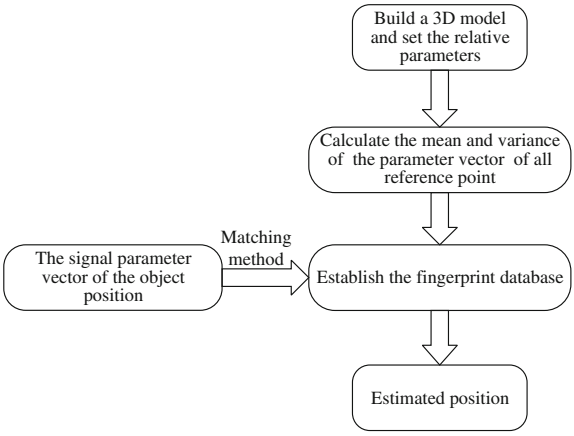

Fig. 2 Block diagram of the proposed MPPD method

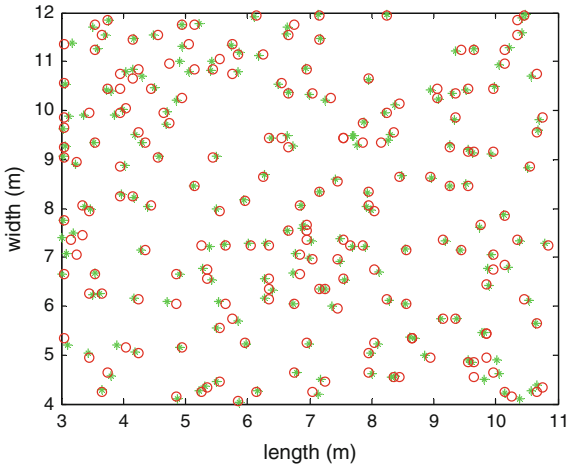

Fig. 3 Positioning result of the proposed MPPD method

red ‘o’ is the estimated position. The simulation result indicates that the proposed MPPD method achieves accurate location.

The fingerprint information used in the traditional single parameter fingerprint method is RSS or Td, but the positioning accuracy cannot meet our demands. In the previous study, we have proposed a multiparameter nearest neighbor fingerprint method, whose positioning accuracy has been improved. In the same simulation environment, we make some experiments using the proposed MPPD method, multiparameter nearest neighbor (MPNN) method, single parameter probability distribution (SPPD) method, and single parameter nearest neighbor (SPNN) method, respectively. The positioning error of the four methods under different grid densities is showed in Fig. 4.

It is obvious from Fig. 4 that, under the same grid density, the proposed MPPD method has a smaller positioning error compared with MPNN, SPPD, and SPNN. Additionally, the positioning error of the MPPD method reduces with the rise of the grid density. Table 1 shows that increasing grid density appropriately can improve the positioning accuracy, but it suffers from high computational complexity. According to the results in Fig. 4 and Table 1, when the grid density exceeds 100 grids per square meter, the increasing of accuracy rate is little while that of the computation time is awful. For this reason, the grid density of 100 grids per square meter is appropriate in the practical applications.

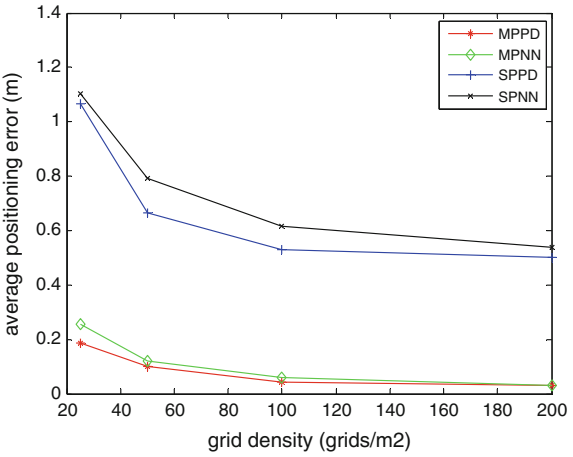

Fig. 4 The average positioning error of four different methods under different grid densities

Table 1 Comparison of position errors and computation time of MPPD under different grid densities

Grid density (grid/m^2)	Average positioning error (cm)	Total computation time (s)
25	18.63	5.76
50	9.94	20.68
100	4.41	93.59
200	3.01	320.10

4 Conclusion

A multiparameter fingerprint positioning method of satellite signal based on probability distribution is presented to improve the positioning accuracy in this paper. The 3-D ray-tracing method is applied in the simulation of satellite signal, and the positioning task can be realized with the difference of the probability distribution of signal parameter at different points. First, we build a 3-D model of the real scene and set the reflection coefficient of the walls, the frequency of the satellite signal, etc. Then the receiving area is divided into many small grids averagely and the center of each grid is regarded as the reference point. Due to the uncertainty of the signal parameters, the probability distribution of the signal parameter is recorded in the fingerprint database. According to the ray-tracing method, we can predict the propagation path of the signal, and calculate the RSS, PDOA, etc. of each path, and then the mean and variance of the signal parameter which can describe its probability distribution are put into the database. At last, we can implement the positioning task by matching the database to get the maximum posterior probability.

The experimental results verify the feasibility of the MPPD method. The comparisons with the conventional fingerprint method show that the MPPD method really has improvement in the positioning accuracy, and the location accuracy increases with the rise of the grid density. However, when the grid density exceeds 100 grids per square meter, the increasing of accuracy rate is little while that of the computation time is awful. Considering the contradiction between computation and positioning accuracy, the grid density of 100 grids per square meter is appropriate in the practical applications.

Acknowledgments This research work is supported by the Important National Science and Technology Specific Project of China under Grant No. 2016ZX03001022-006, the Major Project of Second Generation Satellite Navigation System of China under Grant No. GFZX03010422, the National Natural Science Foundation of China under Grant Nos. 91438113 and 61573242, the Shanghai Science and Technology Committee under Grant Nos. 14511100300 and 15511105100, the Shanghai Pujiang Program under Grant No. 14PJ1405000, the Shanghai Qingpu Industry-University-Research Project under Grant No. 2015-4, and the ZTE Corporation and University Joint Research Project under Grant No. CON1511060024.

References

1. Liu H, Darabi H, Banerjee P et al (2007) Survey of wireless indoor positioning techniques and systems. IEEE Trans Syst Man Cybern Part C Appl Rev 37(6):1067–1080
2. Wang Y, Yang X, Zhao Y et al (2013) Bluetooth positioning using RSSI and triangulation methods. In: IEEE 10th consumer communications and networking conference (CCNC), IEEE, pp 837–842 (2013)
3. Yang L, He D, Liu P (2015) Dynamic fingerprint positioning method of satellite navigation signal based on 3-dimensional modeling scene. In: Proceedings of the 28th international technical meeting of the satellite division of the institute of navigation (ION GNSS + 2015), Tampa, Florida, September 2015, pp 2134–2141

4. Zou D, Meng W, Han S (2014) An accuracy estimation algorithm for fingerprint positioning system. In: 2014 fourth international conference on instrumentation and measurement, computer, communication and control (IMCCC), IEEE, pp 573–577 (2014)
5. Lin TN, Lin PC (2005) Performance comparison of indoor positioning techniques based on location fingerprinting in wireless networks. In: 2005 international conference on wireless networks, communications and mobile computing, vol 2. IEEE, pp 1569–1574
6. Hossain S, Ariffin SHS, Fisal N et al (2012) Accuracy enhancement of fingerprint indoor positioning system. In: 2012 third international conference on intelligent systems, modelling and simulation (ISMS), IEEE, pp 600–605 (2012)
7. Le Dortz N, Gain F, Zetterberg P (2012) WiFi fingerprint indoor positioning system using probability distribution comparison. In: 2012 IEEE international conference on acoustics, speech and signal processing (ICASSP). IEEE, pp 2301–2304
8. Roos T, Myllymäki P, Tirri H et al (2002) A probabilistic approach to WLAN user location estimation. Int J Wireless Inf Networks 9(3):155–164
9. Lin M, Yubin X, Mu Z (2010) Accuracy enhancement for fingerprint-based WLAN indoor probability positioning algorithm. In: 2010 first international conference on pervasive computing signal processing and applications (PCSPA), IEEE, pp 167–170
10. Youssef MA, Agrawala A, Udaya Shankar A (2003) WLAN location determination via clustering and probability distributions. In: Proceedings of the first IEEE international conference on pervasive computing and communications, pp 143–150
11. Song Y, Yu H (2008) A RSS based indoor tracking algorithm via particle filter and probability distribution. In: 4th international conference on wireless communications, networking and mobile computing, WiCOM'08. IEEE, pp 1–4
12. Liang G, Bertoni HL (1998) A new approach to 3-D ray tracing for propagation prediction in cities. IEEE Trans Antennas Propag 46(6):853–863
13. Kumar R, Petovello, MG (2014) A novel GNSS positioning technique for improved accuracy in urban canyon scenarios using 3D city model. In: Proceedings of the 27th international technical meeting of the satellite division of the institute of navigation (ION GNSS + 2014), Tampa, Florida, pp 2139–2148

Study and Experimental Analysis of Advanced RAIM Algorithm Based on BDS/GPS Multi-constellation

Fei Niu, Pengfei Zhang, Junyi Xu and Meijun Fan

Abstract Receiver autonomous integrity monitoring (RAIM) is the key approach to monitor the integrity of global navigation satellite system (GNSS). The paper focuses on the RAIM algorithm based on multi-constellation. According analysis, the performance of ARAIM is validated. It is shown that Advanced RAIM method based on double constellations is effective for the users requiring high level of integrity, continuity, and availability. The performance of LPV-200 can be achieved.

Keywords GNSS · Integrity · ARAIM

1 Introduction

In the past few years, to ensure the integrity of navigation and positioning, receiver autonomous integrity monitoring (RAIM) algorithm is widely used in the navigation of civil aviation route to the nonprecision approach [1–8]. Through conclusion and summary on the past RAIM algorithms, it can be found that the existing RAIM algorithms have some shortcomings, mainly reflected in the following points: (1) Algorithms primarily meet the integrity requirements of the horizontal direction, and they have no integrity requirements for vertical direction, however, with the improvement of application requirements, the vertical direction to the integrity requirements is more important; (2) The hypothesis that at most one satellite failure

F. Niu (✉) · J. Xu · M. Fan
Beijing Satellite Navigation Center, Beijing, China
e-mail: niufei009@sina.com

J. Xu
e-mail: xujunyi-025@163.com

M. Fan
e-mail: magurate@msn.com

P. Zhang
School of Aerospace Engineering, Beijing Institute of Technology, Beijing, China
e-mail: successful.2008@163.com

J. Sun et al. (eds.), *China Satellite Navigation Conference (CSNC) 2016 Proceedings: Volume II*, Lecture Notes in Electrical Engineering 389,
DOI 10.1007/978-981-10-0937-2_19

occurs at a certain moment is true when the alert limit is 556 m for NPA navigation, however, the situation that multiple failures occur simultaneously should be taken into consideration for higher performance standards. (3) The understanding and modeling of the ranging errors are relatively rough, and for higher requirements of navigation stage, the small measurement error on the normal navigation signals can not be ignored. Sometimes, some small measurement errors are relatively constant in an approach period, therefore they can not be considered as a random error, but a deviation one.

With the rapid development of Beidou satellite navigation system and the European Galileo system and the recovery of Russia's GLONASS constellation, the future GNSS will coexist as four global satellite navigation system, it has a good application prospects for RAIM processing method based on multi-constellation. Based on this trend, the US GEAS Group (GPS Evolutionary Architecture Study Group) put forward the concept of Advanced RAIM (ARAIM) [9, 10], and the design goal is the performance of LPV-200, but so far, the research of ARAIM based on multiple systems still should be improved. As to this problem, this paper put forward Advanced RAIM algorithm based on BDS/GPS multi-constellation, and carries on the analysis of test data to verify the performance of the algorithm.

2 Basic Characteristics and Design Goals

The main characteristics of the new algorithm based on BDS/GPS multi-constellation is as follows: applications for multi-constellation, auxiliary support of ground monitoring system. Its basic structure consists of ground support system and receiver algorithm. The core function of ground support system is monitoring the space-signal performance of different satellites in different navigation systems and supporting the application of multi-constellation by generating some system integrity parameters which are transmitted to the receiver. The main function of the receiver algorithm is to detect and identify the failures through receiving observed signal of multi-constellation and ground integrity support information, and to provide navigation services which can satisfy the performance requirements. As shown in Fig. 1.

The basic process flow of the receiver is divided into three parts: the input, output, and processing flow, as shown in Fig. 2. Input parts include: observations and navigation messages of different constellations, ground support integrity information, application requirements. After input the three kinds of information, carrying on positioning and RAIM algorithm of multi-constellation. If the algorithm flow is true, the navigation service will be carried on to meet the performance requirements, otherwise, it will alarm.

Compared with the traditional RAIM, the external difference is the new multi-constellation fusion RAIM introduces multi-constellation and multi-frequency navigation signals information and it has the support of ground integrity information, the internal difference is the improvement of the model and algorithm, and. the most basic difference is the design performance objectives. The design goal of traditional

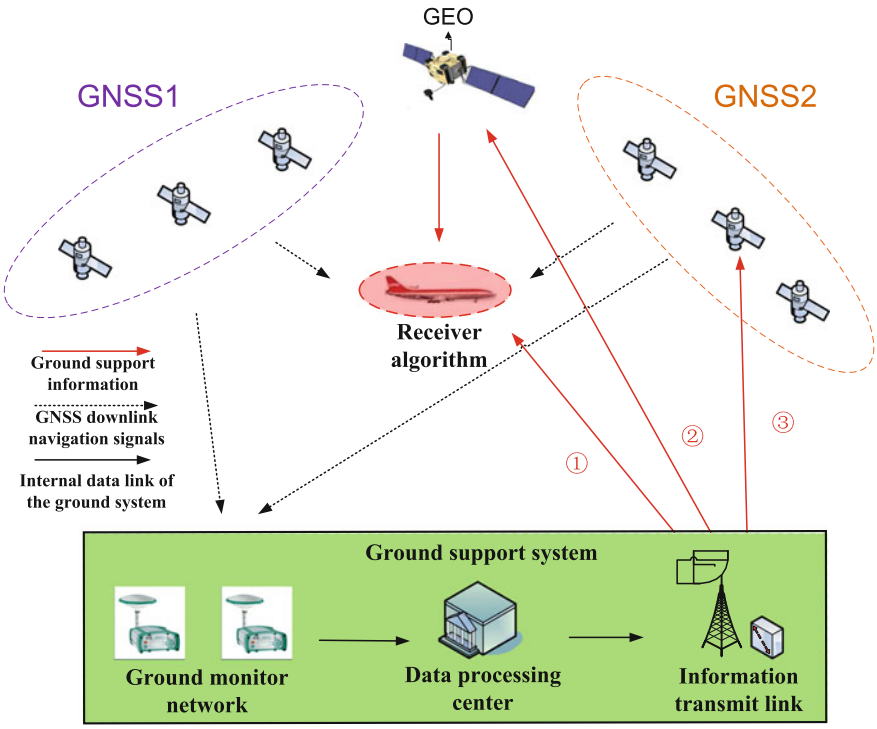

Fig. 1 The basic framework outline of new RAIM algorithm based on BDS/GPS multi-constellation

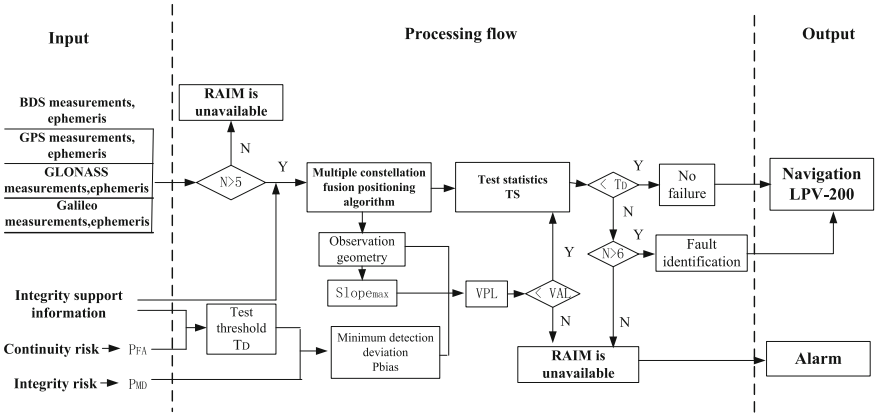

Fig. 2 The processing of the new RAIM algorithm

Table 1 Several navigation performance standard indicators

	LPV-250	LPV-200	CAT I
Horizontal accuracy (m)	16	16	16
Vertical accuracy (m)	20	4	4
Time to alert (m)	6 s	6 s	6 s
Horizontal alert limit (m)	40	40	40
Vertical alert limit (m)	**50**	**35**	**10**
Integrity risk	2×10^{-7}/approach	2×10^{-7}/approach	2×10^{-7}/approach
Continuity risk (s)	8×10^{-6}/15	8×10^{-6}/15	8×10^{-6}/15
Availability (%)	99	99	99

RAIM is NPA, so it does not provide vertical navigation. The new multi-constellation RAIM is designed to support both horizontal and vertical navigation at LPV-200 stage. Table 1 shows three performance standards, namely LPV250, LPV200, and CAT I precision approach.

3 The Basic Method of Data Processing Based on Multi-constellation

The first problem to solve the multi-constellation fusion application is to identify the differences between different navigation systems, and eliminate the impact on the difference. The main differences of different navigation systems are shown in Table 2.

The problem focuses on the two aspects of the unity of the space-time system and the performance of space signal. For the performance differences between the different systems of space signal, it can be reflected by the ground support integrity information. The following figure shows several parameters of ground support integrity information provided by the GEAS. Their core role is to make the user to calculate the σ_{UERE} priori values of different satellites, as shown in Table 3.

Table 2 Difference analysis of different systems

	Coordinate system	Time system	Signal	Ephemeris	Space signal performance/URE (m)
BDS	CGCS2000	BDT	CDMA	Kepler orbit elements	1–2
GPS	WGS84	GPST	CDMA	Kepler orbit elements	0.5–2
GLONASS	PZ-90	UTC (Soviet Union)	FDMA	Position and velocity	1–3
Galileo	GTCF	GST	CDMA	Kepler orbit elements	0.5 (Forecast)

Table 3 The parameters of ground support integrity information

Parameters	Meaning	Explanation
URE	Space signal error	The parameters based on the accuracy performance, is a conventional statistical based on assumption of Gaussian distribution
Nominal_Bias	Space signal deviation	The parameters based on the accuracy performance, the mean value of space signal system deviation
URA	Space signal accuracy	The parameters based on the integrity performance, it is mainly to meet the requirements of life safety. The corresponding parameters need to carry out probability envelope of the non-Gauss error distribution, the value is more conservative than URE
Max_Bias	Extreme space signal deviation	The parameters based on the integrity performance, the maximum value of space signal deviation
Psat	Satellite priori probability of failure	Associated with satellite reliability index
Flag	Integrity flag	It is used to indicate whether the satellite states comply with the above five parameters or not, reflect the timeliness of the five parameters

4 Receiver Algorithm

4.1 Positioning Algorithm and the Test Statistics

GNSS pseudorange observation model can be expressed as follows:

$$y = Gx + \varepsilon\ W \tag{1}$$

In the formula, y is an observed value of pseudorange free vector. n is the number of visible satellites; G is an $n \times 4$ dimensional observed value of design matrix; x is the four-dimensional parameter vector, including three user location correction parameters and a receiver clock offset correction parameter; ε is an observed value of n dimensional pseudorange noise vector, if there is a deviation, $\varepsilon + b$ is used to express; W is an observed value of $n \times n$ dimensional random model weight matrix. σ_0 is an error of unit weight.

Under the $H0$ assumption (no failure occur), the navigation solution of the observation is expressed as:

$$\widehat{x}_0 = S_0 \cdot y \tag{2}$$

In the formula, S_0 is a space transformation matrix:

$$S_0 = (G^T W_{\mathrm{URA}} G)^{-1} G^T W_{\mathrm{URA}} \tag{3}$$

In the formula, W_{URA} is a random model weight matrix based on URA. The nth element is a function of the error of the nth URA and the receiver:

$$W_{\mathrm{URA},n} = \frac{1}{\sigma^2_{\mathrm{URA},n} + \sigma^2_{\mathrm{user},n} + \sigma^2_{\mathrm{iono},n} + \sigma^2_{\mathrm{tropo},n}} \tag{4}$$

In the formula, $\sigma_{\mathrm{user},n}$ is the error of receiver, including the observation noise and multipath error. $\sigma_{\mathrm{iono},n}$ is ionospheric delay error. $\sigma_{\mathrm{tropo},n}$ is tropospheric delay error.

Under the $H1$ assumption (a failure occurs), the navigation solution of RAIM algorithm is expressed as:

$$\widehat{x}_n = S_n \cdot y \tag{5}$$

$$S_n = (G^T M_n W_{\mathrm{URA}} G)^{-1} G^T M_n W_{\mathrm{URA}} \tag{6}$$

In the formula, M_n is an n-dimensional diagonal matrix, the nth diagonal element is 0.

Structure test statistic d_n:

$$d_n = |\widehat{x}_n - \widehat{x}_0| \tag{7}$$

Detection threshold in the vertical direction is D_n:

$$D_n = K_{\mathrm{ffd},n} \cdot \sigma_{dv,n} + \sum_{i=1}^{N} |\triangle S_n(3,i)| \cdot \mathrm{Nominal\_Bias}\ (i) \tag{8}$$

$$\triangle S_n = S_n - S_0 \tag{9}$$

In the formula, $K_{\mathrm{ffd},n}$ is confidence quantile, which is determined by the probability of false alarm, n = 1, 2,…, N, $\sigma_{dv,n}$ is the standard deviation in the vertical direction. The second term of the right formula of D_n is the projection of the bias terms of distance domains in the vertical direction. Considering the worst case, assuming that the direction is consistent, the absolute value is taken.

$$\sigma_{dv,n} = \sqrt{dP_n(3,3)} \tag{10}$$

$$dP_n = \triangle S_n W^{-1}_{\mathrm{URE}} \triangle S^T_n \tag{11}$$

In the formula, W^{-1}_{URE} is a random model coordinated factor matrix based on URE.

4.2 Multi-constellation Processing

If the user can receive navigation signal of multi-constellation, formula (1)–(11) also applies equally. The difference is that observation matrix and unknown parameters are different. The observation matrix of a single constellation can be expressed:

$$G = \begin{bmatrix} e_1^T & -1 \\ e_2^T & -1 \\ \vdots & \\ e_N^T & -1 \end{bmatrix} \tag{12}$$

In the formula, e_k is observations cosine vector of the k-th satellite. When the second navigation constellation is added for positioning, the time offset of the two systems is estimated as an unknown parameter. The unknown parameter is $(\triangle x, \triangle y, \triangle z, \triangle t, \triangle t_{21})^{\mathrm{T}}$. Among them, $\triangle t_{21}$ is systematic deviation of second satellite navigation systems and the first satellite navigation system. At this point G can be expressed by the following:

$$G = \begin{bmatrix} \begin{bmatrix} & 0 \\ G_1 & 0 \\ & \vdots \\ & 0 \end{bmatrix} \\ \begin{bmatrix} & 1 \\ G_2 & 1 \\ & \vdots \\ & 1 \end{bmatrix} \end{bmatrix} \tag{13}$$

When the third constellation is added, it can be analogized in accordance with this method.

4.3 The Method with Multi-frequency Navigation Signal

The maximum advantage of the multi-frequency navigation signal is to eliminate the ionospheric delay error by the combination of the observations without the influence of ionosphere. In principle, it will improve the accuracy of navigation positioning. However, the combination of multi-frequency navigation signals also bring some problems. For example the combination of the observables without the influence of ionosphere will enlarge the receiver noises. Such as multipath effect

and observation noise. The measurement variance of the pseudorange will be transformed from the following:

$$\sigma_{\text{single}}{}^2 = \sigma^2{}_{\text{URA},n} + \sigma_{\text{iono},n}{}^2 + \sigma_{\text{tropo},n}{}^2 + \sigma_{\text{user},n}{}^2 \tag{14}$$

to

$$\sigma_{\text{double}}{}^2 = \sigma^2{}_{\text{URA},n} + \sigma_{\text{tropo},n}{}^2 + \sigma_{\text{user},n}{}'^2 \tag{15}$$

Therefore, the RAIM algorithm based on multi frequency navigation signal needs to consider the problem caused by the observation of multi frequency combination.

4.4 VPL Calculation

PL calculation of the new RAIM algorithm is used to analyze the availability of the algorithm. It is determined by the maximum value between the $H0$ assumption VPL_{H0} and the $H1$ assumption VPL_{H1}, if it is less than alert limit VAL, the algorithm meets the requirements of availability.

Under the assumption of $H0$, VPL based on all observations is calculated by the following formula:

$$\text{VPL}_0 = K_{\text{md},0} \cdot \sigma_{v,0} + \sum_{i=1}^{N} |S_0(3,i)| \cdot \text{Max\_Bias}\ (i) \tag{16}$$

In the formula

$$\sigma_{v,0} = \sqrt{P_0(3,3)} \tag{17}$$

$$P_0 = \left(G^T W_{\text{URA}} G\right)^{-1} \tag{18}$$

In the formula, $K_{\text{md},0}$ is confidence quantile under the assumption of $H0$.

Under the assumption of $H1$, VPL based on all observations is calculated by the following formula:

$$\text{VPL}_n = D_n + K_{\text{md},n} \cdot \sigma_{v,n} + \sum_{i=1}^{N} |S_n(3,i)| \cdot \text{Max\_Bias}\ (i) \tag{19}$$

In the formula, $K_{\mathrm{md},n}$ is confidence quantile under the assumption of the n-th satellite failure occurs.

$$\sigma_{v,n} = \sqrt{P_n(3,3)} \tag{20}$$

$$P_n = (G^T M_n W_{\mathrm{URA}} G)^{-1} \tag{21}$$

The final vertical error protection limit is expressed as:

$$\mathrm{VPL} = \mathrm{Max}\{\mathrm{VPL}_0, \mathrm{VPL}_n\}. \tag{22}$$

4.5 Calculation and Analysis

In this paper, the data collection is carried out on the roof of the building through UR240-CORS-II GPS/BDS dual-system four-frequency receiver. The approximate true position is obtained by using RTK with data of BJFS station. During the calculation in this paper, the priori user equivalent range error (UERE) of single frequency is set as 4 m, and that of dual-frequency is set as 2 m. The detailed distribution is shown in Table 4.

The continuous 800 s static data is calculated and analyzed, then analysis of sequence diagram of VPE (positioning error in vertical direction) and VPL (protection level in vertical direction) which is based on single system single frequency and dual-system single-frequency are shown in Fig. 3.

The VAL is the vertical protection limit in the figure, as it can be seen from Fig. 3 that the VPE value and VPL value based on GPS/BDS dual system are better than the VPE value and VPL value based on the GPS and BDS single system respectively at the same period. This is due to the increase in the number of visible satellites with the increase of the constellations, and then the observations for calculation increase, so that the results are optimized. Meanwhile, from Fig. 1c it can be seen that the VPL value based on GPS/BDS dual system is less than the vertical alert limit (35 m) of LPV-200. This means that integrity in the vertical direction based on GPS/BDS dual system can be achieved navigation application requirements in the aviation approach stage of LPV-200.

Table 4 The prior values of different errors

Error sources	UERE of single frequency (m)	UERE of dual frequency (m)
Relative errors of satellite	1.5	1.5
Ionospheric delay	3.5	0.0
Tropospheric delay	0.8	0.8
Receiver noise and resolution	0.8	0.9
Multipah	0.5	0.7
Total	4.0	2.0

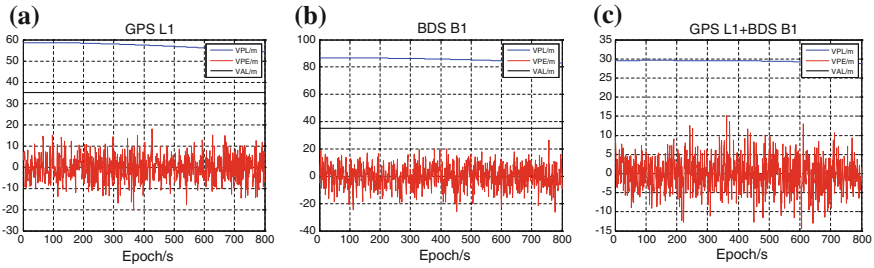

Fig. 3 Sequence diagram of positioning error in vertical direction and protection level in vertical direction

Statistical analysis of the positioning error in vertical direction and protection level in vertical direction of single system single frequency, single system dual frequency, dual system single frequency and dual system dual frequency are shown blow.

Quantitative statistical results of positioning error in vertical direction are shown in Table 5.

As can be seen from Fig. 4 and Table 5, the dual-frequency positioning error in vertical direction and vertical RAIM availability were better than the results of a single frequency under the same conditions, and integrity in the vertical direction of dual-system single-frequency and dual-system dual-frequency can be achieved navigation application requirements in the aviation approach stage of LPV-200. For the combination of dual-frequency navigation signals, it can eliminate the ionosphere effect, however, it will enlarge the noise of receiver, therefore, the standard deviation of positioning error in vertical direction will increase in this situation. This is because the paper does not use the relevant filtering algorithm to eliminate the noise of the receiver. If a combination of multi-frequency signal is used, filtering the noise of the receiver is required.

In order to analyze the sensitivity of fault deviation, this paper adds fault deviation in the pseudorange of a certain visible satellite, and the fault deviation is increased from 5 to 150 m, and the increasing step is 5 m. Figure 5 shows the fault

Table 5 Statistical results of positioning error in vertical direction

	Vertical positioning error (m)		
	Deviation	Standard deviation	RMS
GPS L1	−0.3832	3.0726	3.0765
GPS L1/L2	−0.1896	4.1578	4.1552
BDS B1	−0.2505	5.1436	5.1433
BDS B1/B2	−0.1562	6.2658	6.4582
GPS L1+BDS B1	0.0892	3.4465	3.4437
GPS L1/L2+BDS B1/B2	0.0345	3.6441	3.6430

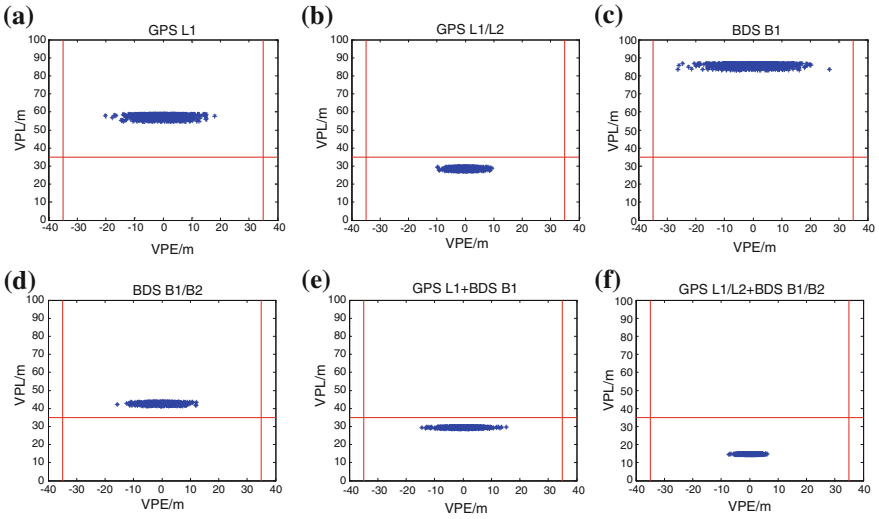

Fig. 4 Statistical analysis of positioning error in vertical direction and protection level in vertical direction

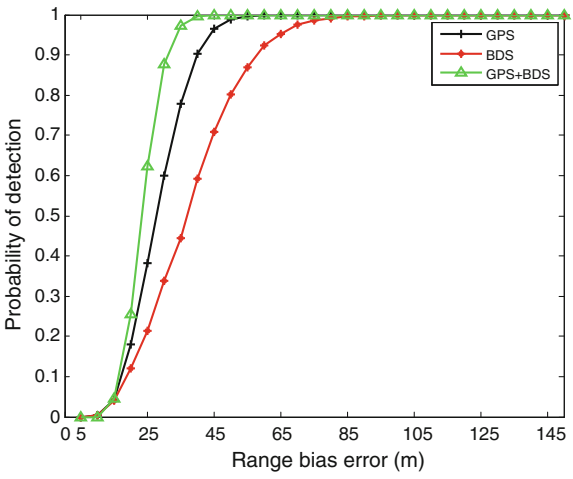

Fig. 5 Probability of fault detection

detection probability of RAIM algorithm of GPS single frequency, BDS single frequency, and GPS/BDS single frequency respectively.

As can be seen from the figure, when the fault deviation is less than 40 m, the fault detection probability of GPS/BDS dual constellation is significantly higher than that of the single constellation. With the increase of the fault deviation, the fault detection probability of the dual constellations reaches 100 %.

5 Conclusion

Advanced RAIM algorithm based on BDS/GPS multi-constellation is studied in this paper, and the experimental analysis is carried out. The analysis results show that compared with the single constellation, the vertical integrity under the condition of GPS/BDS dual constellation has improved significantly, which can be achieved navigation application requirements in the aviation approach stage of LPV-200. Meanwhile, the RAIM algorithm is more sensitive to the small deviation under the condition of dual constellation. The fault detection probability is improved under the same condition than that of the single constellation. However, for the combination of dual-frequency navigation signals, although it can eliminate the ionosphere effect, it will also enlarge the receiver noise. In the case of not taking filtering algorithm, the standard deviation of positioning error in vertical direction will increase in the situation of the combination of dual-frequency navigation signals. In the future work, observation noise and multipath effect caused by a combination of multi-frequency signal observations will be weakened by the introduction of filtering algorithm, thereby the integrity in vertical direction will be improved under the combination of multi-frequency signal.

Acknowledgments This work was supported by the National Natural Science Foundation, China (No. 41374038 and No. 41304031).

References

1. Lee YC (1986) Analysis of range and position and position comparison methods as a means to provide GPS integrity in the user receiver. In: Proceedings of the annual meeting of the ION, Seattle, WA, June 1986
2. Lee YC (2004) Investigation of extending receiver autonomous integrity monitoring (RAIM) to combined use of Galileo and modernized GPS. In: ION GNSS 17th international technical meeting of the satellite division of the Institute of Navigation. ION GNSS 2004. Institute of Navigation, Long Beach, CA, pp 1691–1698
3. Hewitson S, Lee HK, Wang J (2004) Localizability analysis for GPS/Galileo receiver autonomous integrity monitoring. J Navig 57(2):245–259
4. Yu M, Chen W, Li Z, Chen YQ (2004) Improvement on integrity and reliability of vehicle positioning by a new map matching method. In: ION GNSS 17th international technical meeting of the satellite division of the Institute of Navigation. ION GNSS 2004. Institute of Navigation, Long Beach, CA, pp 2086–2094
5. Syed S (2004) GPS based map matching in the pseudorange measurement domain. In: ION GNSS 17th international technical meeting of the satellite division of the Institute of Navigation. ION GNSS 2004. Institute of Navigation, Long Beach, CA, pp 241–252
6. Fei N (2008) Theory and technique on GNSS integrity augment. Dissertation Submitted to Information Engineering University. Zheng Zhou (in Chinese)
7. Chen JP (2001) Research if GPS integrity augmentation. Zheng Zhou: Institute of Surveying and Mapping, Information Engineering University, 2001 (in Chinese)

8. Zhong BJ, Lin LY (2004) New developments on integrity monitoring technology of satellite navigation system. Surveying Mapp Sci 29(1):64–67 (in Chinese)
9. GNSS Evolutionary Architecture Study Phase I—Panel Report, February 2008
10. Phase II of the GNSS Evolutionary Architecture Study, February 2010

Signal-in-Space Accuracy Research of GPS/BDS in China Region

Si Sun and Zhipeng Wang

Abstract As one of the most important performance indicator of satellite navigation, Signal-In-Space Accuracy (SISA), which is usually characterized by Signal-In-Space Range Error (SISRE), directly affects the positioning accuracy, integrity, and other performance indicators. This paper analyzes SISA of GPS and BDS using SISRE based on the Worst User Location (WUL). Considering that the signal coverage in China region is irregular, the traditional geometric method is not applicable, therefore this paper proposes Geometric Approximation Algorithm (GAA) that can obtain accurately the WUL in global region and China region. The calculation interval is set at 30 s, and the time span is from January 11, 2015 to November 21, 2015, then we separately calculate the difference of broadcast ephemeris and precise ephemeris of GPS and BDS to get orbit errors and clock errors. Finally, we form data sets of global region and China region, thus we can calculate the RMS URE using their data sets. The results shows that, in China region, the average RMS URE of 32 GPS satellites is 0.68 m, and, average RMS URE of 13 BDS satellites is 1.38 m. We also find that average RMS URE based on WUL is greater than that based on integration method by about 16 % for GPS and 28 % for BDS.

Keywords Signal-In-Space Accuracy · Signal-In-Space Range Error · Worst User Location · Geometric Approximation Algorithm

Zhipeng Wang research focuses on the combination algorithms of Ground Based Augmentation System (GBAS) and Satellite-Based Augmentation System (SBAS), also Advanced Receiver Autonomous Integrity Monitoring (ARAIM).

S. Sun (✉) · Z. Wang
School of Electronic and Information Engineering, Beihang University, Beijing, China
e-mail: 1455929251@qq.com

Z. Wang
e-mail: wangzhipeng@buaa.edu.cn

J. Sun et al. (eds.), *China Satellite Navigation Conference (CSNC) 2016 Proceedings: Volume II*, Lecture Notes in Electrical Engineering 389,
DOI 10.1007/978-981-10-0937-2_20

1 Introduction

Recently, GPS, as the most advanced navigation system, whose SISA has been very stable and is being upgraded in the trend. Beidou navigation satellite system (BDS) [1] has been running smoothly for 3 years since it is officially providing services for Asia-Pacific region at the end of 2012.

BDS's performance in China region has drawn much attention, and, researches about SISA increase in recent years [2–5]. While, at present, BDS is local system, so, its statistical characteristics of SISA mainly reflect the situation in China region. In order to compare objectively the SISA performance of GPS and BDS in China region, we should also consider the SISA performance of GPS within China region rather than its global SISA performance. The scope of China region in this paper is set at 55°S–55°N, 55°E–180°E (actually including the Asia-Pacific region).

SISRE is the measurement of orbit error and clock error [6, 7] in the direction of pseudorange, which is often used to depict the SISA. SISRE is often calculated by empirical formulas [8, 9], shown in formula 1–3, deduced by integral idea, which reflects the average level of SISA (referred to AURE). But for the users in aviation, maritime fields and so on, where life safety is highly valued, they concerns more about the worst level of SISA in their activities region, thus, this paper studies the SISRE based on the WUL [10, 11] within China region of GPS and BDS (referred to WURE). Then, this paper compares WURE with AURE to find their difference. The key to calculate the SISRE is to obtain WUL accurately, well, taking into account the irregularity of intersection domain between signal coverage and China region, it is difficult for traditional geometric method to address the WUL, therefore, Geometric Approximation Algorithm (GAA) is proposed in this paper, which is also applicable to solving global WUL.

Formulas used in the integration method are as follows:

$$\mathrm{SISURE}_{\mathrm{GPS}} = \sqrt{(0.98R - T)^2 + 0.141^2(A^2 + C^2)} \tag{1}$$

$$\mathrm{SISURE}_{\mathrm{BDS(GEO,IGSO)}} = \sqrt{(0.99R - T)^2 + \frac{1}{127}(A^2 + C^2)} \tag{2}$$

$$\mathrm{SISURE}_{\mathrm{BDS(MEO)}} = \sqrt{(0.98R - T)^2 + \frac{1}{54}(A^2 + C^2)} \tag{3}$$

2 Geometric Approximation Algorithm

The core of GAA is to find the potential WULs (we call them User unified) on the borderline including the only WUL, then, gets the projection values of orbit error vector in the direction of "User-Satellite" vector determined by there User (referred

to OEP). Finally, find maximum |OEP − CE| (abbreviated as WOEP) combined with clock error (referred to CE), whose corresponding User is WUL.

2.1 Two Cases of WUL Distribution

As shown in Fig. 1, global WUL at any point can be completely determined by three variances: satellite position, orbit error vector and clock error, which can be only one of the following two cases.

Assuming that the angle formed by υ vector and OS vector is ω (if ω is greater than 90°, ω should minus 90°).

(a) If $\omega > \beta$, WUL is on the borderline. υ_1 belongs to this case, so, WUL is either A or B and scope of OEP is $[l_{min}, l_{max}]$;
(b) If $\omega < \beta$, WUL is either within the coverage domain or on the borderline. υ_2 belongs to this case, so, WUL is one of A, B and C and scope of OEP is $[\min(OEP_A, OEP_B), \|\upsilon_2\|]$.

To judge which point above is WUL, we need to combine clock error. In case a, it is incorrect to deduce that A point is WUL thinking that l_{max} is greater than l_{min}.

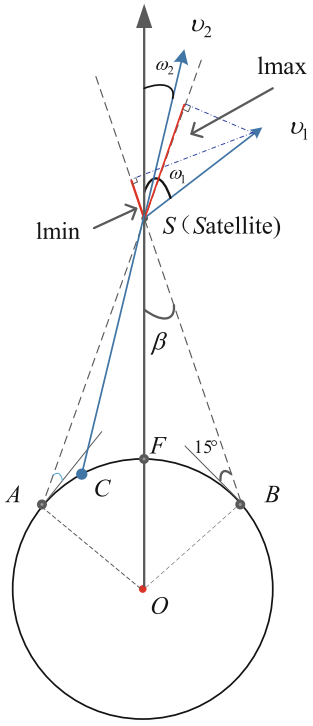

Fig. 1 Two cases of WUL distribution, *Note O* is the center of earth in ECEF, *S* is satellite, the plane is on the cross section between plane determined by *OS* vector and orbit error vector, the satellite elevation angle is 15°, *A*, *B* is intersection point of signal beam with surface of ellipsoid, *F* is subastral point of *S*, *C* is intersection point of orbit error vector and surface of ellipsoid

The reason is simple, although $|\mathrm{OEP}_A| > |\mathrm{OEP}_B|$, while, the case $|\mathrm{OEP}_A - \mathrm{CE}| < |\mathrm{OEP}_B - \mathrm{CE}|$ might exists, and even exists the case that $|\mathrm{OEP}_B - \mathrm{CE}| = 0$, obviously, A is not reasonable WUL we expect. Therefore, the corresponding point of maximum $|\mathrm{OEP} - \mathrm{CE}|$ is actual WUL. Results show that the RMS URE will be reduced by about 10 % if we use the WUL determined by maximum |OEP| instead of maximum $|\mathrm{OEP} - \mathrm{CE}|$. Similarly, in case b, the point to which $\max[|\mathrm{OEP}_A - \mathrm{CE}|, |\mathrm{OEP}_B - \mathrm{CE}|, |\|\upsilon_2\| - \mathrm{CE}|]$ corresponds is WUL.

2.2 *Principle of Geometric Approximation Algorithm*

Figure 2 shows the basic principle of GAA ideas. The core is to find the maximum point and minimum point to determine the OEP range. We only need to find all potential WULs by searching the borderline, then calculate the angle formed by "User-Satellite" vector and υ vector to see how far there User from the maximum point or the minimum point. Searching scope reduced sharply after several searches, and User on the borderline gradually approach to the maximum point or minimum point. Finally, we end searching until the search interval is less than a given value, and the two points with maximum angle and minimum angle are taken as potential WULs.

The borderline is divided into the following two categories:

1. In case a, the signal coverage domain boundary is borderline, which can be referred as category I;
2. In case b, the borderline is composed by points on the ellipsoid surface satisfy that the angle between *OS* vector and "User-Satellite" vector equals ω, which can be referred as category II (Actually, the borderline has two separate closed parts, and note that the part which has a minus elevation angle should be excluded).

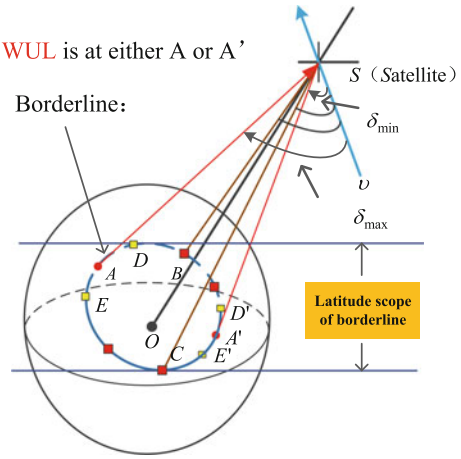

Fig. 2 Principle of GAA *Note S* is satellite, *A*–*E* points are Users, *AS* is one of "User-satellite" vectors, $\delta_{\min}$ and $\delta_{\max}$ is minimum angle and maximum angle among angles formed by there "User-satellite" vectors and υ

2.3 Steps of Geometric Approximation Algorithm

The steps for global WUL are as follows:

1. Judge which case WUL belong to

   When $\omega > \beta$, WUL belong to case a
   When $\omega < \beta$, WUL belong to case b;

2. According to longitude of subastral point F, we can get latitude scope of I borderline. Then divide equally the latitude scope into 10 parts by 10 points in Fig. 2, and calculate the corresponding longitude of there points on borderline. Finally, we get 10 points on the borderline with determined position;
3. Calculate the angle between the υ vector and the "User-Satellite" vector, then, find the corresponding points of the minimum angle and the maximum angle of them, namely A and A′ in Fig. 2;
4. Select nearest surrounding points of A and A', there are D, E and D', E', then, continue to divide the latitude scope limited by D, E or D', E' into 10 parts, and find two points which have the minimum angle and the maximum angle. Continuing to operate like this until the division interval meets certain precision;
5. Consuming that the two points found in last time are W and W', we can find the WUL according to their cases in step 1:

   Case **a**: the corresponding point of $\max[|\mathrm{OEP}_W - \mathrm{CE}|, |\mathrm{OEP}_{W'} - \mathrm{CE}|]$ is WUL
   Case **b**: the corresponding point of $\max[|\mathrm{OEP}_W - \mathrm{CE}|, |\mathrm{OEP}_{W'} - \mathrm{CE}|, |\|\upsilon\| - \mathrm{CE}|]$ is WUL.

If there is intersection region between signal coverage domain and China region, the WUL within China region exists. Now, we divide borderline of China region into 4 sections (up, down, left, right section), taking into account signal borderline, there are 5 sections. Most of the time, the intersection borderline consists of 3 or 4 (some of them may not be complete) of all 5 sections.

The steps for China region WUL are as follows:

1. In case **a**: Searching borderline II and find C point, then, determine whether C is in the intersection region

   if in, the WUL in China region belongs to the case a
   if not, the WUL in China region belongs to the case b
   In case **b**: it is easy to understand, the WUL in China region belongs to case b;
2. Divide each section of intersection borderline and searches each section, finally, we can find which section the maximum and minimum angle belong to;
3. Find the WUL within China region according to the steps for global WUL.

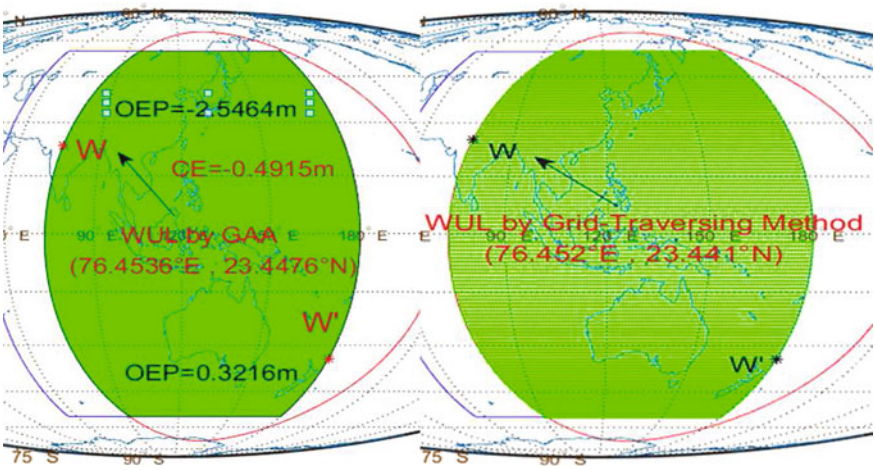

Fig. 3 WUL calculated by GAA and Grid-Traversing method

Table 1 Input data for calculating WUL

Input date		Result
Satellite position (m) X: −3.230832846e+07 Y: 2.704930956e+07 Z: −1.113637782e+06 CE: −0.4915 m	Orbit error (m) X: 6.5523 Y: 6.5838 Z: 4.6245	Geometric Approximation Algorithm (76.4536°E, 23.4476°N) Grid-Traversing method (0.001° * 0.001°) (76.452°E, 23.441°N)

2.4 Result of Geometric Approximation Algorithm

Figure 3 shows the WUL within China region of BDS satellite (PRN number is 1), at the 90,000 s of 1828 GPS week, by Geometric Approximation Algorithm and Grid-Traversing Method (0.001° * 0.001°). Table 1 gives the corresponding orbit error and satellite position in ECEF coordinate system and the outcomes. Note that the digit on the third decimal place of the outcomes for the limited interval of Grid Traversing Method other than the precision of GAA itself. After testing a large number of data, results show that GAA has a high enough precision.

3 Process of Calculating SISRE

3.1 Data Resources

The data resources used are from January 11, 2015 to November 21, 2015. For GPS, this paper uses broadcast ephemeris of brdcddd0.yyn format provided by

International Geodynamic Service (IGS) and precise ephemeris of apcwwwd format provided by National Geospatial-Intelligence Agency (NGA). For BDS, this paper uses broadcast ephemeris of brdmyyy0.yyp format and precise ephemeris of gbmwwwd.sp3 format both provided by IGS.

3.2 *Brief Data Processing Process*

First, obtaining data initial set of orbit and clock error using the difference of broadcast ephemeris and precise ephemeris with interval time of 30 s. Second, Fig. 4 shows the brief process for different data sets. Calculating WULs of global

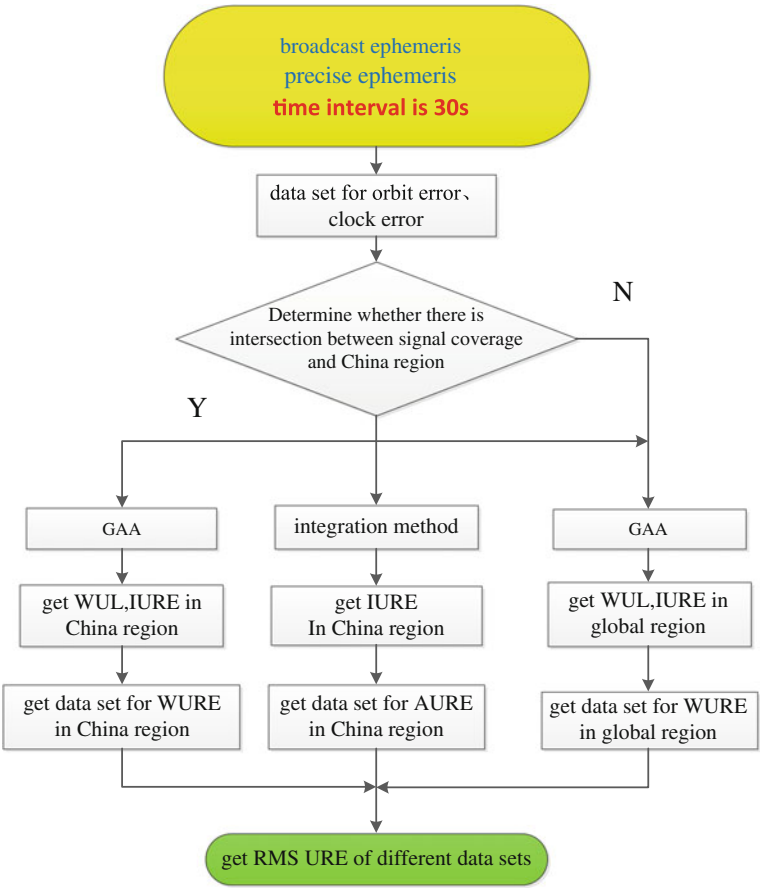

Fig. 4 Brief process for different data sets

region and China region (if exists). Finally, getting RMS URE in different regions using different data sets through the following formulas.

$$\mathrm{WOEP} = \left\| \overrightarrow{v} \right\| \cos(\delta) \tag{4}$$

$$\mathrm{IURE} = \mathrm{WOEP} - \mathrm{CE} \tag{5}$$

$$\mathrm{URE}_{\mathrm{rms}} = \sqrt{\left(\sum_{1}^{N} \left(\mathrm{IURE}^2 \right) \right) / N} \tag{6}$$

Note: IURE is instantaneous URE.

4 Result and Analysis

4.1 URE Comparison of GPS and BDS

Using WURE data set in China region and WURE data set in global region, we obtain results showed in Figs. 5 and 6. Figure 5 shows the RMS WOEP, RMS CE, and RMS URE of GPS in China region and global region. Note that the corresponding results in global region are placed in the middle position of each items of bar graph with black color. Figure 6 shows the results of BDS, given that MEO satellites are global satellites unlike GEO satellites and IGSO satellites, whose

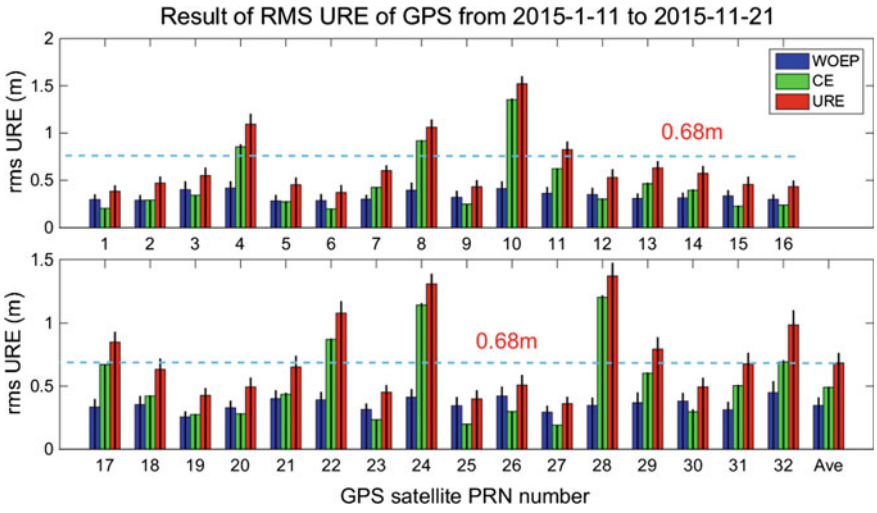

Fig. 5 Statistical results of GPS SISRE

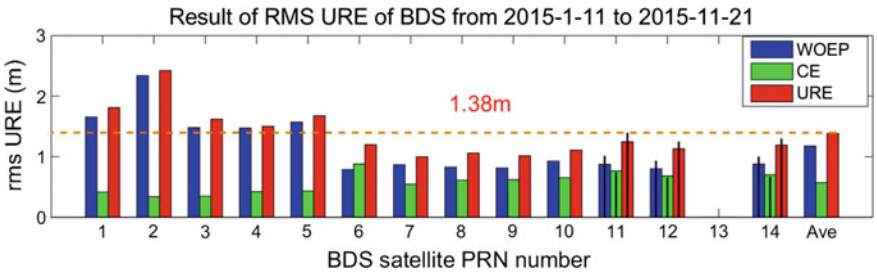

Fig. 6 Statistical results of BDS SISRE

Table 2 Average RMS URE of WOEP, CE and URE

System	Region	WOEP	CE	URE
GPS	China (m)	0.345	0.490	0.684
	Global (m)	0.408	0.492	0.761
	C/G (%)	84.6	–	**89.9**
BDS	China (m)	1.176	0.569	1.382
	Global (m)	1.265	0.561	1.463
	C/G (MEO) (%)	87.0	–	**90.8**

results in global region are also displayed. The average RMS value of all satellite in different systems is given in Table 2.

The results show that in the Chinese region, the average RMS URE of 32 GPS satellites is 0.68 m, for 13 BDS satellite, the value is 1.38 m, so, we can draw a conclusion that the SISA of GPS is better than BDS. For BDS itself, the SISA of GEO (PRN number is 1–5) satellite is worse than that of IGSO and MEO. The reason may be that GEO satellites are relatively static.

Form global view, for GPS and MEO satellites of the BDS satellite, the SISA performance in the China region is slightly better than its global performance, which can be explained from two aspects:

First, the statistical method is based on WUL, so, the larger the selected region, the worse the WUL become, in other words, the WUL in China region is actually embodied in the global region.

Second, because of the long distance between satellite and earth, the β showed in Fig. 1 is small (about 10°), thus resulting in a small distinguish of SISRE results based on the WUL in different areas of signal coverage domain.

4.2 Results of WURE and AURE

Using the WURE data set of AURE data sets both in China region, RMS URE are given in Fig. 7.

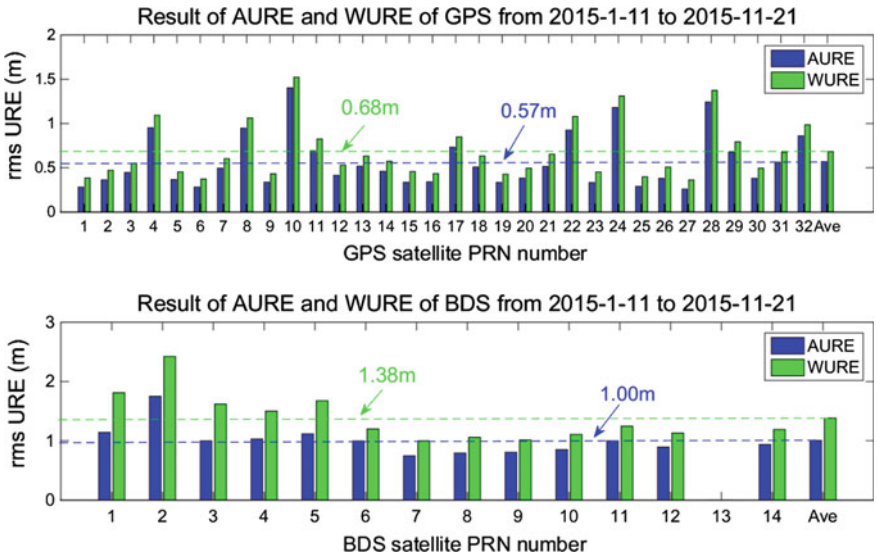

Fig. 7 Statistical results of WURE and AURE

The results show that the RMS URE by WUL method is greater than that by integration method for both GPS and BDS in China region. Average RMS URE based on WUL is greater than that based on integration method by about 16 % for GPS and 28 % for BDS.

5 Conclusion

This paper analyzes SISA of GPS and BDS in the China region based on WUL method, and compares with the results by integration method. The following conclusions are obtained:

1. In China region, the average RMS URE of GPS is 0.68 m, average RMS URE of BDS is 1.38 m, so, at present, the SISA for GPS is abut twice better than that of BDS. Both orbit error and clock error should be upgraded for BDS, if BDS wants to keep its competition with GPS in China region.
2. In China region, average RMS URE based on WUL is greater than that based on integration method by about 16 % for GPS and 28 % for BDS, in some sense, the results reflect the difference between upper level and average level of BDS's SISA is larger than that of GPS, in other words, GPS is more stable on SISA for its small fluctuations.

Acknowledgment The authors would like to give thanks to many other people in the CNS/ATM lab for their advice and interest. The work was carried out with financial supports under National Natural Science Foundation of China (Grant No. 61501010), Beijing Municipal Natural Science Foundation (Grant No. 4154078) and Aeronautics Science Foundation (Grant No. 2015ZC51035).

References

1. China Satellite Navigation Project Center (2009) Compass/Beidou navigation satellite system development. CSNPC, Beijing
2. Liu S (2015) The analysis of GNSS SIS accuracy. In: CSNC 2015
3. Chen G (2015) Assessment of BDS Signal -in-Space accuracy and standard positioning performance during 2013 and 2014. In: CSNC 2015
4. Gao WG (2013) Test and evaluation on Signal -in-Space accuracy of BDS. In: CSNC 2013
5. Wen YL (2013) Research on URE calculation method of GNSS. In: CSNC 2013
6. Cohenour C, Van Graas F (2011) GPS orbit and clock error distribution. Navigation 58(1): 17–28
7. Langley RB, Jannasch H, Peeters B, Bisnath S (2000) The GPS broadcast orbits: an accuracy analysis. In: 33rd COSPAR Scientific Assembly, Warsaw
8. Ananda MP, Berstein H, Bruce R (1984) Autonomous navigation of the global positioning system satellite, Seattle
9. U.S. Department of Defense (2008) Global positioning system standard positioning service performance standard
10. Shao JF, Washington Y (2005) An efficient worst user location algorithm for the generation of the Galileo integrity flag. In: Proceedings of Institute of navigation global navigation satellite system (ION GPS), Sep, 2005:11–22. Long Beach, pp. 0–0
11. Li ZH (2011) Study of GNSS SIS error worst user location algorithm. J Navigation 64: S91–S101

The Performance Testing Method of Optical Fiber Time Synchronization in BeiDou Ground-Based Navigation Signal Net

Tingsong Tang, Na Zhao, Yun Zhao, Xing Chen, Fengjuan Wu, Zhen Qiu and Changjie Liu

Abstract In BeiDou ground-based navigation signal net, the technology of optical fiber time and frequency transfer, whose design precision excels 0.5 ns, is used to realize the time synchronization between ground stations. Limited by condition and precision, some techniques such as TWSTFT and satellite common-view are not suitable for optical fiber time synchronization testing. In this paper, the clock travel method based on cesium clock with high precision is used to test the performance of optical fiber time synchronization, and its handling process is discussed in detail. At the same time, the main error sources are analyzed in this paper. The closed-loop result of outfield testing excels 0.4 ns, which validates the feasibility of the method. Meanwhile, unilateral delay of optical fiber device is calibrated, and time delay of 100 ns level is detected, which is important for system data processing.

Keywords Moving clock way · Ground-based navigation · Optical fiber · Time synchronization

1 Introduction

Satellite navigation system is the important foundation in the field of spatial information. According to the "three steps" development strategy of BeiDou satellite navigation system (BDS), the construction task of regional satellite navigation system has been completed at the present stage, and formally opened to the service at the end of 2012 [1, 2].

Currently, the capability of BeiDou regional satellite navigation system is not as good as GPS. At the same time, because the system uses a mixture of GEO, IGSO,

T. Tang (✉) · N. Zhao · Y. Zhao · F. Wu · Z. Qiu · C. Liu
Beijing Satellite Navigation Center, Beijing 100094, China
e-mail: tang_tingsong@163.com

X. Chen
Peking University, Beijing 100871, China

J. Sun et al. (eds.), *China Satellite Navigation Conference (CSNC) 2016 Proceedings: Volume II*, Lecture Notes in Electrical Engineering 389,
DOI 10.1007/978-981-10-0937-2_21

and MEO satellite constellation [1–3], the satellite signal in complex area is shaded seriously, and available satellite amount to the user is decreased significantly. That results in the decrease of system service continuously. Therefore, in order to enhance the competitive ability in the BDS, the BeiDou ground-based navigation signal network research is developed. At present, the research tasks have been completed, the demonstration area is establishing at Chengdu Longquanyi district, and the demonstration application of beidou navigation foundation network will be finished by the end of 2015.

Establishment and maintain of time datum in ground-based navigation signal network is implemented using the time–frequency transmission technology via optical fiber [4–9]. The distance between two sites in demonstration is 1–5 km, the distance of fiber path between site and time–frequency reference source is greater than 100 km (beeline distance 40 km), and time synchronization accuracy within 0.5 ns is designed. The target is rigorous, and the time–frequency benchmark and terminal are separated at different locality. That brings a difficult point how to accurate determination of the optical fiber time synchronization accuracy. Usual time synchronization methods with nanosecond level includes satellite common-view and two-way satellite time and frequency transfer (TWSTFT). Time synchronization precision of TWSTFT can be reached 1–2 ns, but it needs a whole set of communication equipment to send and receive the measurement data transmission with cost dearly. Satellite common-view generally in 5–10 ns is not satisfying for the measured target accuracy of 0.5 ns.

Moving clock way has the characteristics of high precision and lower cost. In this paper, a moving clock way based on high-precision cesium clock is presented [10, 11], the time synchronization accuracy between 1 pps passing through 126 km fiber path and the reference signal was tested, and the closed-loop error is less than 0.4 ns. The measurement results can be used as optical fiber delay correction reference for time and frequency transfer equipment.

2 Basic Principle of Time and Frequency Transfer via Optical Fiber

In the examination, 1 pps and 10 MHz signals outputting by beidou synchronous station (main station) atomic clocks were used as the time–frequency benchmark. A physical connection was established through optical fiber link between main station and slave station, and through two sets of time–frequency transmission system, bidirectional transmission of time–frequency signal and data information between the stations was implemented using WDM technology. The basic principle is shown in Fig. 1.

During bidirectional transferring of time pulse, frequency signal, and the data information, six channels of optical fiber can be used, channel 1 and channel 2 for time

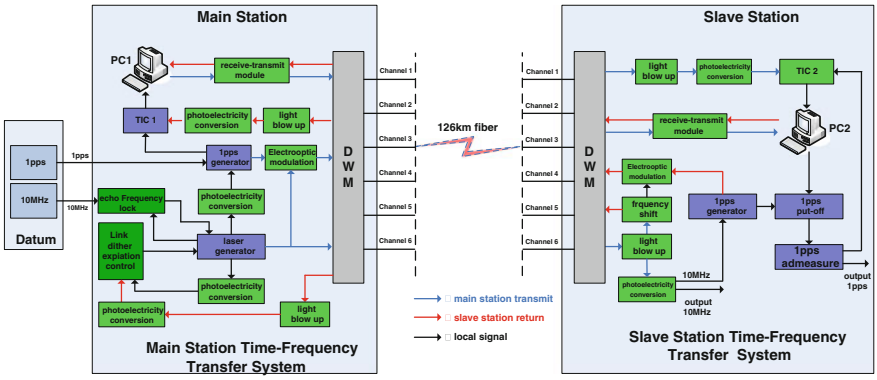

Fig. 1 Basic principle of time and frequency transfer via optical fiber

pulse signal, channel 3 and channel 4 for frequency signal, channel 5 and channel 6 for data information. Through online monitoring and real-time compensation method, the pulse signal and frequency signal can be corrected. Then the precision frequency transfer and time synchronization between master station and from the station are finished.

In fiber frequency transfer, nonlinear optical frequency shift technique was adopted to realize the judgment and compensation of phase noise at the whole link. In fiber time synchronization, by comparing the two-way time, adjust the 1 pps delay and then realize the time synchronization between master station and slave station.

3 Test Method

A high-precision cesium clock is equipped at main station. A benchmark 1 pps and a cesium clock 1 pps are connected up the time interval counter. The benchmark 1 pps as close signal, the cesium clock 1 pps as open signal, by measuring the time difference value, calculate relative frequency deviation Δf between the cesium clock and the reference signal. At the moment t_1, benchmark 1 pps T_{ref1} as close signal, cesium clock 1 pps T_{Cs1} as open signal, accessed time interval counter and measured. Put the result X_1 into the computer for storage.

Then the cesium clock is conveyed to substation (cesium clock charged by UPS). At the moment t_2, substation 1 pps signal as close signal, cesium clock 1 pps signal as open t signal, accessed time interval counter and measured, deposited the measurement data X_2 in data collection computer. Equipment connection diagram is shown in Fig. 2.

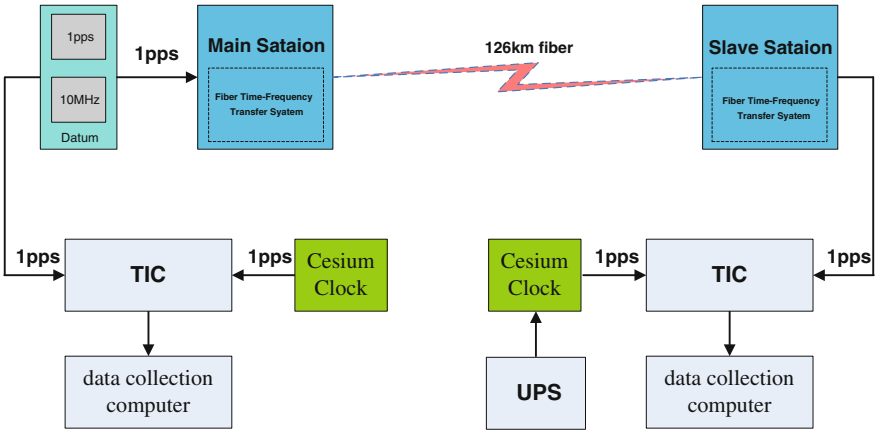

Fig. 2 Equipment connection diagram

Data processing is as follows:

At the moment of t_1, compute the difference X_1 between cesium clock 1 pps signal T_{Cs1} and the reference 1 pps signal: $T_{\text{ref}1}$ as formula (1):

$$X_1 = T_{Cs1} - T_{\text{ref}1} \tag{1}$$

When cesium clock conveyed to substation, at the moment of t_2, compute the differenceX_2 between cesium clock 1 pps signal T_{Cs2} and the reference 1 pps signal: $T_{\text{ref}2}$ as formula (2):

$$X_2 = T_{Cs2} - T_{\text{ref}2} \tag{2}$$

From moment t_1 to moment t_2, cesium clock error due to the change of state named τ, if reference signal is considered as least in the process, the following formula can be established.

$$T_{Cs2} - \tau = T_{Cs1} + (t_2 - t_1)f_{Cs} \tag{3}$$

$$T_{\text{ref}2} = T_{\text{ref}1} + (t_2 - t_1)f_{\text{ref}} \tag{4}$$

In formula (3) and (4), f_{Cs} is cesium clock frequency accuracy, and f_{ref} is reference signal frequency accuracy.

From formula (3)–(4), we can get formula (5):

$$\begin{aligned} T_{Cs2} - T_{\text{ref}2} - \tau = {} & T_{Cs1} - T_{\text{ref}1} \\ & + (t_2 - t_1)f_{Cs} - (t_2 - t_1)f_{\text{ref}} \end{aligned} \tag{5}$$

Put formula (1), (2) into formula (5), and we can get formula (6):

$$X_2 - \tau = X_1 + (t_2 - t_1)(f_{Cs} - f_{\text{ref}}) \tag{6}$$

Then we can get formula (7) as follows:

$$\tau = (X_2 - X_1) - (t_2 - t_1)\Delta f \tag{7}$$

As a result, we can get τ, which is the time synchronization error between the reference signal and substation.

4 The Test Results

In June of 2015, the time synchronization precision scene test was implemented in Chengdu ground-based navigation signal network demonstration area using the moving clock way, with OSCILLOQUARTZ b—5585 PRS cesium clock made in Swiss. Before moving, 2 h data was collected. The relative frequency deviation between the reference signal and cesium clock was calculated whose value was 2.5E-13. The time difference curve is shown in Fig. 3. Two substations' 1 pps signals were tested, and the results are shown in Tables 1 and 2.

Table 1 shows that nearly 5 hours of the test, closed-loop error of moving clock way is 0.31 ns, while time synchronization accuracy requirements via optical fiber is 0.5 ns. Therefore, it is feasible to time synchronization accuracy test in the ground-based navigation signal optical fiber network. Table 2 shows that there are time deviations from −60 to 92 ns between two substations and main station, which caused by cable and fiber time–frequency transmission equipment delay. The delay should be calculated before the formal operation of ground-based navigation signal network, and deducted in the process of data processing.

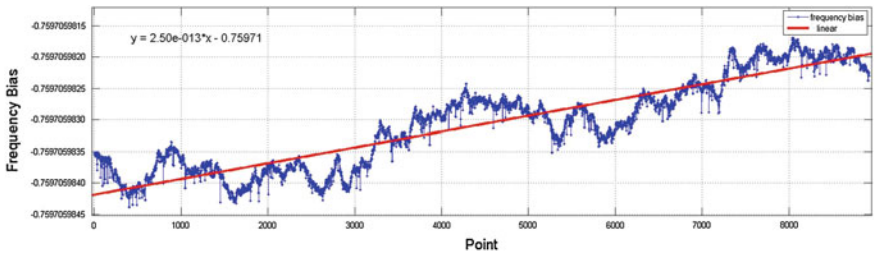

Fig. 3 Time difference curve between reference signal and cesium clock

Table 1 Closed loop result with moving clock way

Location	Time	1 pps(local) – 1 pps(Cs) (s)	Phase change (ns)	Time deviation (ns)
Main station	2015-06-18 08:31:22	0.964778843226	4.40	0.31
Main station	2015-06-18 13:24:23	0.964778839138		

Table 2 Substation test result with moving clock way

Location	Time	1pps(local) − 1pps(Cs) (s)	Phase change (ns)	Time deviation (ns)
Main station	2015-06-18 08:31:22	0.964778843226	1.29	−60.71
Substation 1	2015-06-18 09:57:19	0.964778781230		
Main station	2015-06-18 08:31:22	0.964778843226	2.01	91.62
Substation 2	2015-06-18 10:45:11	0.964778932838		

5 Conclusions

When moving, affected by the temperature, speed, vibration, and so on, the state of cesium clock is constantly changing. Therefore, the relative frequency deviation compared with the prior value can be different, and it is not fixed. That is the main error source of moving clock way. In order to ensure the accuracy of method, it is necessary to weaken the above factors with corresponding measures.

The test results show that the moving clock way can evaluate 100 km time synchronization accuracy via optical fiber effectively and has beneficial reference value for similar projects. Moving clock way is suitable for short fiber in time synchronization accuracy test. In the future, optical fiber time synchronization technology is applied to the long distance (thousand kilometers) or network development. It is a new challenge for the researchers to implement the sub-nanosecond test.

References

1. Liu J (2013) Status and development of the Beidou navigation satellite system. J Telemetry Tracking Command 34(3):1–8
2. Jia R, Dong X, Li X, Chen L (2015) Analysis on Signal-In-Space error of Beidou navigation satellite system. J Equip Acad 26(1):84–87
3. Li H, Qian S, Gao W, Zhou J, Li J, Jiao W (2014) The constellation stability promotion approaches for compass (BeiDou) regional navigation and positioning system. J Sci Sinica Phys Mech Astron 44:621–629. doi:10.1360/132012-1027

4. Zhang F, Hou D, Guo H, Zhao J, Zhang Z (2010) Timing delay jitter compensation of a fiber link with active delay compensation. J Acta Optica Sinica 30(3):671–675
5. Chen X, Zhang J, Lu J, Lu X, Tian X, Liu B, Wu H, Tang T, Shi K, Zhang Z (2015) Feed-forward digital phase compensation for long distance precision frequency dissemination via fiber network. Opt Lett 40:371–374
6. Chen X, Zhang J, Lu J, Cui Y, Lu X, Lv Z, Tian X, Ci C, Liu B, Wu H, Tang T, Shi K, Zhang Z (2015) Ultrastable frequency dissemination based on feed-forward digital phase compensation technology. In: Conference on lasers and electro-optics (CLEO 2015)
7. Chen X, Lu J, Zhang J, Cui Y, Lu X, Lv Z, Tian X, Ci C, Liu B, Wu H, Tang T, Shi K, Zhang Z (2015) Simultaneous microwave frequency transfer and time synchronization based mode-locked pulse train over 120 km fiber. In: 11th conference on lasers and electro-optics Pacific Rim (CLEO-PR 2015)
8. Lu J, Chen X, Cui Y, Lu X, Ci C, Zhang X, Liu B, Wu H, Tang T, Shi K, Zhang Z (2015) Stable frequency dissemination in commercial optical fiber with nonlinear wavelength shift for feedback comparison. In: 10th International conference on ultrafast optics 2015
9. Zhang Z (2011) Advances in high repetition rate femtosecond fiber lasers. J Acta Optica Sinica 31(9):0900130-1–0900130-8
10. Qu L, Li B (2010) Study on the high accuracy time transfer methods in the short distance. J Astronaut Metrol Measur 30(2):64–67
11. Wei Z (1993) Time comparison and delay determination by moving clock way 51–53

The Improvement of the Positioning Accuracy in Search and Rescue with Two Satellites

YanRong Xue, ShaoJun Feng, Washington Yotto Ochieng, Xin Zhang and ZhenJun Zhang

Abstract The efficiency of search and rescue (SAR) heavily relies on the positioning accuracy, so high positioning accuracy is very important in the procedure of SAR, especially when searched and rescued object (SARO) dropped into the place where the number of the visible satellites is very small. It is necessary to know the position of the SARO using as less satellites as possible because of the signal sheltered. Combining with the principle of time and frequency difference of arrival (TDOA and FDOA, respectively) and differential technology of positioning error correction in global positioning system (GPS), pseudorange differential positioning method basing on TDOA and FDOA is put forward in the procedure of SAR with two satellites. By choosing the proper reference object (RO), the pseudorange correction of RO is used to correct pseudorange of the SARO so that more accurate position of SARO is solved. Finally, simulation results show that the positioning accuracy can be improved and can precede 5 km after differential by selecting RO and SARO which are within 1000 km apart for pseudorange differential technology.

Keywords Pseudorange differential · Positioning error · Positioning accuracy · TDOA · FDOA

Y. Xue (✉)
National Time Service Center, Chinese Academy of Sciences,
Xi'an 710600, China
e-mail: yrxue1203@ntsc.ac.cn

Y. Xue · S. Feng · W.Y. Ochieng · X. Zhang · Z. Zhang
Department of Civil and Environmental Engineering,
Imperial College London, London SW7 2AZ, UK

X. Zhang · Z. Zhang
School of Aeronautics and Astronautics, Shanghai Jiao Tong University,
Shanghai 200240, China

J. Sun et al. (eds.), *China Satellite Navigation Conference (CSNC) 2016 Proceedings: Volume II*, Lecture Notes in Electrical Engineering 389,
DOI 10.1007/978-981-10-0937-2_22

1 Introduction

Nowadays, the work of search and rescue (SAR) depends on the satellite's navigation system. To a great extent, the efficiency of SAR heavily relies on the positioning accuracy of the system, so high positioning accuracy is very important in the procedure of SAR. Especially when searched and rescued object (SARO) dropped into the place where the number of the visible satellites is very small. It is necessary to know the position of the SARO using as less satellites as possible because of the signal sheltered. So in this paper, the position of SARO is obtained using dual-satellite location system. Dual-satellite location system is based on joint positioning technology of time difference of arrival (TDOA) and frequency difference of arrival (FDOA), simultaneously the time difference and frequency difference information of the same radiation source on the ground getting to the two satellites is measured to determine the location of the signal source. The positioning way decreases the number of platforms and the number of receiving channels, reduces the difficulty actualizing and cost of the system, and real-time and positioning performance of which is higher than that of the single-platform approach, compared with other commonly positioning technology, which has much merit like few desired channel number, short positioning time, high positioning precision, and broad application prospects in the aviation and aerospace positioning. Therefore, domestic and foreign experts in the field of dual-satellite location system make a lot of research and discussion. Initially, TDOA and direction measurement were used to achieve the positioning and performance of the two were analyzed [1, 2], then the time difference and the frequency difference of positioning technology was researched [3], including error analysis and accuracy estimation [4, 5]. Domestic scholars have also carried out algorithm research of the time difference and the frequency difference dual-satellite location [6, 7]. Positioning accuracy can achieve 10 km or so by using current algorithm, which is relatively poor. Therefore, differential method is applied to three satellites location by some scholars [8], but almost no scholars study differential techniques applying to dual-satellite location. Yanrong Xue and Xiaohui Li researched the position differential technology of GPS positioning error correction method applied to positioning error correction technology of the dual-satellite location for the first time [9], which has taken as a critical step for the study of the location and also improves the positioning accuracy, but the accuracy is not high enough, and there are some limitations in the application of this method, so which need to be studied continuously. Combining with pseudorange differential in the application of GPS, in this paper, pseudorange differential method based on TDOA and FDOA in the dual-satellite location is put forward innovatively, and the positioning accuracy of the system is analyzed.

2 The Principle of Pseudorange Differential Based on TDOA and FDOA in the Dual-Satellite Location

View of observations existing errors in the positioning of the TDOA and FDOA of dual-satellite location, which can refer to the principle of error corrections in the process of GPS pseudorange differential, the pseudorange differential method is applied to observations of time difference and frequency difference in the dual-satellite for differential correction. Furthermore, all radiation sources on the ground use the same system configuration, the correlation between the two parts is strong and space of application in pseudorange differential is more extensive. Therefore, we can use the pseudorange differential method for error corrections to improve the positioning precision of dual-satellite location system.

The principle of pseudorange differential in dual-satellite location system means that SARO uses pseudorange difference corrections from RO to satellite 1 and satellite 2 to correct pseudorange difference from SARO to satellite 1 and satellite 2, then distance difference from SARO to the two satellites close to the true value is obtained. SARO uses FDOA corrections from RO to satellite 1 and satellite 2 to correct FDOA from SARO to satellite 1 and satellite 2, FDOA from SARO to the two satellites close to the true value is obtained. Finally, TDOA, FDOA, and the Earth ellipsoid equation are used to achieve the more accurate positioning of SARO in data processing center on the ground.

Let the coordinate of the RO be (x_0, y_0, z_0), the coordinate of SARO be (x, y, z), first pseudorange difference between RO and the two satellites is measured at receiving station

$$\rho_0^{s2} - \rho_0^{s1} = r_0^{s2} - r_0^{s1} + \Delta\rho_0^s + \Delta\rho_0 \tag{1}$$

where r_0^{s1}, r_0^{s2} is the geometric distance from RO to satellite 1 and satellite 2, respectively, which can be calculated according to the position of RO and satellite broadcast ephemeris, namely

$$r_0^{s2} = \sqrt{(x_{s2} - x_0)^2 + (y_{s2} - y_0)^2 + (z_{s2} - z_0)^2} \tag{2}$$

$$r_0^{s1} = \sqrt{(x_{s1} - x_0)^2 + (y_{s1} - y_0)^2 + (z_{s1} - z_0)^2} \tag{3}$$

where $\Delta\rho_0^s$ indicates ranging error related with the position of RO on the ground and satellite locations, $\Delta\rho_0$ indicates ranging error related with the receiver.

Pseudorange corrections of the satellites are calculated by the following formula in the data processing center on the ground:

$$\Delta\rho = (r_0^{s1} - r_0^{s2}) - (\rho_0^{s1} - \rho_0^{s2}) \tag{4}$$

where pseudorange from SARO to satellite 1 and satellite 2 is ρ^{s1}, ρ^{s2}, respectively, TDOA close to the true value obtained using pseudorange correction to correct pseudorange difference of SARO:

$$\begin{aligned} c\Delta t' &= \rho^{s2} - \rho^{s1} + \Delta\rho \\ &= \sqrt{(x_{s1}-x)^2 + (y_{s1}-y)^2 + (z_{s1}-z)^2} \\ &\quad - \sqrt{(x_{s2}-x)^2 + (y_{s2}-y)^2 + (z_{s2}-z)^2} \end{aligned} \tag{5}$$

Similarly, FDOA of SARO is corrected.

First FDOA with errors between RO and the two satellites is measured, that is, Δf_r, FDOA close to the true value from RO to satellite 1 and satellite 2 can be obtained using the position of RO, the satellite broadcast ephemeris and satellite real speed source, that is Δf_0

$$\begin{aligned} \frac{c\Delta f_0}{f_0} &= \frac{x_{s2}-x_0}{r_2}v_{x2} + \frac{y_{s2}-y_0}{r_2}v_{y2} + \frac{z_{s2}-z_0}{r_2}v_{z2} \\ &\quad - \frac{x_{s1}-x_0}{r_1}v_{x1} + \frac{y_{s1}-y_0}{r_1}v_{y1} + \frac{z_{s1}-z_0}{r_1}v_{z1} \end{aligned} \tag{6}$$

Frequency corrections of the satellites are calculated by the following formula:

$$\Delta F = \Delta f_0 - \Delta f_r \tag{7}$$

where FDOA from SARO to satellite 1 and satellite 2 is Δf, FDOA close to the true value is obtained using frequency correction to correct FDOA with errors of SARO, that is $\Delta f'$:

$$\begin{aligned} \frac{c\Delta f'}{f_0} &= \frac{c(\Delta f + \Delta F)}{f_0} = \frac{x_{s2}-x}{r_2}v_{x2} + \frac{y_{s2}-y}{r_2}v_{y2} \\ &\quad + \frac{z_{s2}-z}{r_2}v_{z2} - \frac{x_{s1}-x}{r_1}v_{x1} + \frac{y_{s1}-y}{r_1}v_{y1} + \frac{z_{s1}-z}{r_1}v_{z1} \end{aligned} \tag{8}$$

Let the Earth's semi-major axis be a, the Earth's semi-minor axis be b, the Earth ellipsoid equation be

$$\frac{x^2}{a^2} + \frac{y^2}{a^2} + \frac{z^2}{b^2} = 1 \tag{9}$$

The position of the SARO is solved using the differential Eqs. (5), (8), and (9) to achieve high-precision positioning. The whole process mentioned above is shown in Fig. 1.

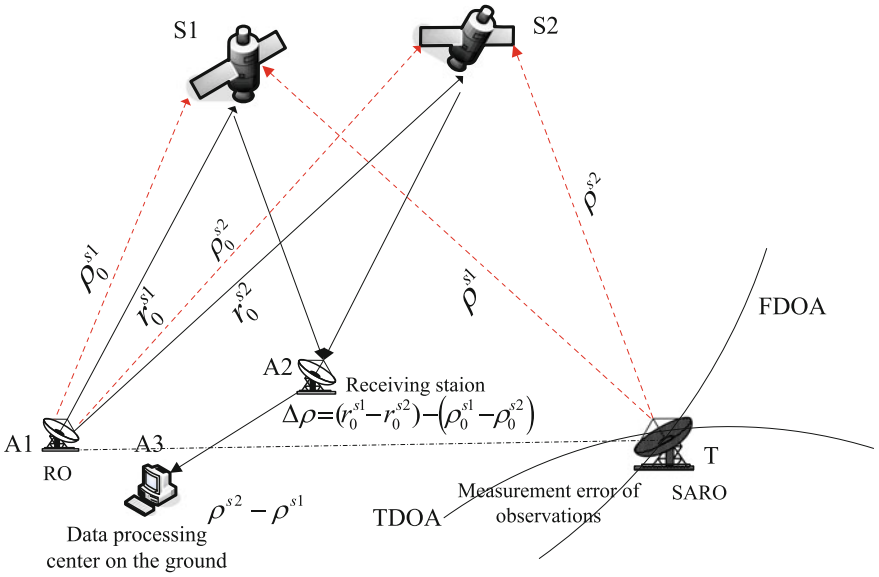

Fig. 1 The principle of pseudorange differential about TDOA and FDOA in dual-satellite location system

3 Results and Discussions of the Experiment

In order to verify the application of the pseudorange differential in dual-satellite location system, pseudorange differential positioning error of time difference and frequency difference in dual-satellite location is simulated, the process of the simulation is shown in Fig. 2. Take Earth's ellipsoid semi-major axis a = 6378137 m, semi-minor axis b = 6356752.314 m, the speed of light c = 299792458 m/s, the carrier frequency of radiation source is 10 GHz while transmitting.

Assuming that the longitude and latitude of the two satellites is 125°, 29.4°, 125°, 30.5°, respectively, when the signal of radiation source is received by them,

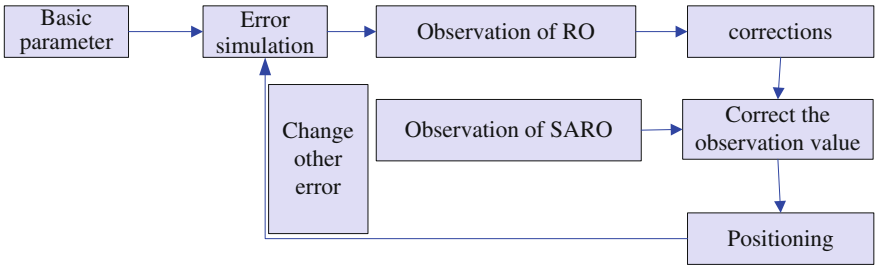

Fig. 2 Simulation diagram of pseudorange differential in dual-satellite location system

their orbital altitude is 800 km, adding in ephemeris error. According to the current level of error control, take the time difference measurement accuracy $\sigma_t = 100$ ns, the Doppler frequency difference measurement accuracy $\sigma_f = 10$ Hz, and let satellite 1 and satellite 2 have same speed, $v_{1x} = v_{2x} = 743.8$ m/s, $v_{1y} = v_{2y} = 3228.6$ m/s, $v_{1z} = v_{2z} = 6503.2$ m/s, respectively.

In order to analyze the results more comprehensively and accurately while simulating, we select the SARO and RO being within 1000 km apart for pseudorange differential. Figure 3 gives curve graph of accuracy comparison before and after differential, when the SARO and RO are within 1000 km apart.

Figure 2 shows the SARO and RO are selected and remain within 1000 km for differential, in the whole, differential effect is particularly evident and the positioning accuracy after differential is increased to less than 5 km from 8 km before differential.

From the above case comprehensively, the pseudorange differential for the SARO is taken, which can improve the positioning accuracy, so you can use pseudorange differential method to improve the positioning accuracy of the SARO, which is one of the most effective ways to increase the positioning accuracy of the dual-satellite location system. However, from the above analysis, selecting the RO being in close proximity to the SARO for differential, the effect of pseudorange differential will be better, and they should better remain in the distance within 1000 km, of course, just as using position differential of positioning error correction, in reality, if you cannot timely find a suitable RO, which being more than

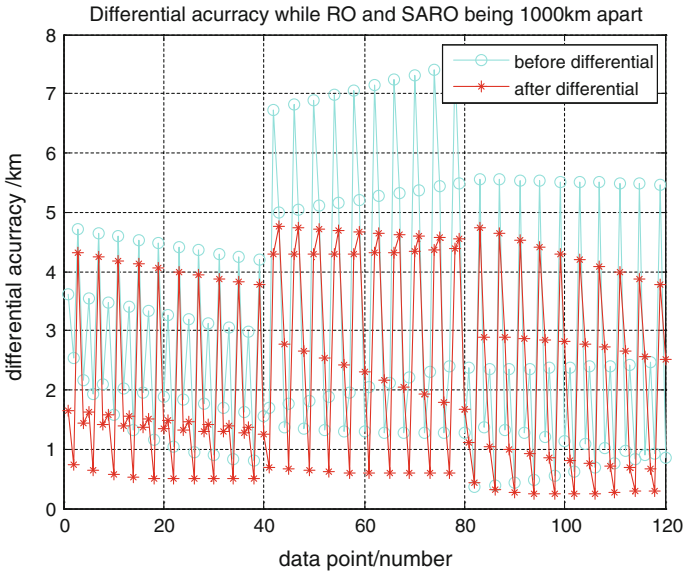

Fig. 3 Curve graph of accuracy comparison before and after differential of SARO and RO being within 1000 km apart

thousands of kilometers away from SARO are also selected for differential, although the effect of differential is not more obvious than that of within 1000 km, but the results of this differential also have a certain reference value, and the accuracy of the location will also be improved.

4 Conclusions

In this paper, a new method about error correction is proposed on the basis of time difference and frequency difference of the dual-satellite location system, and the principle of pseudorange differential based on the system is also put forward. By means of simulation test, the effect of differential and positioning accuracy of pseudorange differential are analyzed, positioning accuracy using pseudorange differential to correct pseudorange of the SARO is increased to better than 5 km from the current 10–20 km, so that more accurate position of SARO is solved, which has taken an important step for improving positioning accuracy of dual-satellite location. This is also a new method that corrects positioning error of location, which has important theoretical and application value, as well as practical value for the future development of the dual-satellite location system.

References

1. Wegnero LH (1971) On the accuracy analysis of airborne techniques for ly locating electromagnetic emitters. Report R-722-PR, Rand Corp.: available from National Technical Information Service as ASTIA D.C. AD 729 767
2. Torrieri DJ (1984) Statistical theory of location systems. IEEE Trans Aerosp Electron Syst 20(2):183–198
3. Ho KC, Chan YT (1997) Geolocation of a known altitude object from TDOA and FDOA measurements. IEEE Trans Aerosp Electron Syst 33(3):770–783
4. John JM (2008) TOA/FOA geolocation error analysis, SANDIA REPORT, Sandia National Laboratories
5. Engel U (2009) A geolocation method using TOA and FOA measurement. In: Proceedings of the 6th workshop on positioning, navigation and communication, WPNC 2009. IEEE Computer Society Publisher, Piscataway, pp 77–82
6. Zhang Y, Sheng WD, Guo FC et al (2007) Low orbit dual-satellites location algorithm and its precision analysis. J Chin Inertial Technol 15(2):188–192 (in Chinese)
7. Guo FC, Fan Y (2008) A method of dual-satellites geolocation using TDOA and FDOA and its precision analysis. J Astronaut 29(4):1381–1386 (in Chinese)
8. Liu JY, Kang GH, Yue YZ et al (2007) Integrated navigation system of three-star Beidou/SINS based on pseudo-range difference. J Chin Inertial Technol 15(4):445–448 (in Chinese)
9. Xue YR, Li XH, Xu LX et al (2012) Research on position differential method of dual-satellites TDOA and FDOA in location system. In: IEEE international frequency control symposium proceedings. IEEE Computer Society Publisher, Washington DC, pp 481–485

An Enhanced Global Positioning Technology and Precision Verification of BDS

Jin Wang, Qin Zhang, Guanwen Huang, Rui Tu, Wenju Fu and Pingli Li

Abstract Precise point positioning (PPP) technology is a positioning enhancement technique that can cover a large area and reduce the cost of positioning. With the support of real-time precise orbit and clock offset products, the global real-time PPP can be realized, which greatly improves the effectiveness and availability of the results. First, in this paper, the global real-time precise orbit and clock offset can be calculated by the BeiDou global continuous tracking station. Then the BeiDou global-enhanced message is designed, the frequency and the type of broadcasting-enhanced message are analyzed. Finally, the real-time PPP accuracy of BDS is studied. The actually measured numerical example shows that the real-time PPP based on BDS can achieve decimeter-level position accuracy in the Asian-Pacific region.

Keywords The enhanced global positioning · Beidou navigation satellite system · Precise orbit determination · Real-time PPP

J. Wang (✉) · Q. Zhang (✉) · G. Huang · W. Fu · P. Li
College of Geology Engineering and Geomantic, Chang'an University,
Xi'an 710054, Shaanxi, China
e-mail: jwang1989@163.com

Q. Zhang
e-mail: zhangqinle@263.net.cn

G. Huang
National Key Laboratory of Geographic Information Engineering,
Xi'an 710054, China

R. Tu
National Time Service Center, Chinese Academy of Sciences,
Xi'an 710600, Shaanxi, China

J. Sun et al. (eds.), *China Satellite Navigation Conference (CSNC) 2016 Proceedings: Volume II*, Lecture Notes in Electrical Engineering 389,
DOI 10.1007/978-981-10-0937-2_23

1 Introduction

The BeiDou navigation satellite system (BDS) officially began to provide regional services at the end of 2012. So far, China has launched 20 BeiDou navigation satellites. The global service capability will be formed and the world-class global satellite navigation system will be built by 2020. Therefore, the positioning performance of BDS is being of great concern. Based on the global tracking station network, the real-time precise positioning service system further enhances these advantages of PPP technology on wide coverage and time-sensitive, which has become a hot GNSS application research.

PPP dependents on the precise products of satellite orbit and clock offset. Therefore, the real-time precise satellite orbit and clock offset products are the key to realize real-time PPP and directly affects the accuracy of real-time precise positioning results. At present, there is quite a lot of research on the GPS real-time PPP, many organizations and researchers have done a lot on the performance of it. In 2007, IGS set up a real-time experimental program to provide real-time orbit and clock offset products. The RTG software developed by JPL has been used in WASS, GDGPS, MSAS, and other real-time systems for practical application. For the GPS, it can achieve 0.1 and 0.2 m accuracy for the horizontal and vertical components. ESOC developed RETINA software, which can realize 0.2–0.45 ns accuracy for the real-time clock offset; NRC achieved updating satellite rapid orbit once an hour and clock offset once 2 s; RTNET software of BKG has provided 1 Hz real-time clock offset which the accuracy more than 0.5 ns. Based on PANDA software, Wuhan University built a wide area real-time precision positioning prototype system which can achieve GPS real-time PPP service. Its accuracy is better than 0.1 and 0.2 m for the horizontal and vertical components, respectively. With the construction and perfect of MGEX tracking net built by IGS and iGMAS tracking network led by China, the global real-time monitoring network for BDS has been implemented. The performance of BDS real-time PPP gets more and more attention. Some institutions and scholars in China have been done some research. Zhu Yongxing used postscript orbit and clock offset to simulate real-time kinematic PPP, achieved decimeter level of accuracy in the Chinese [1]. With the increase of real-time observation station and the ability to enhance real-time communication, the accuracy of BDS real-time will be improved. Based on this, a global real-tim- enhanced positioning system and its precision verification of BDS are introduced.

2 The Composition and Realization of the Global-Enhanced Real-Time Positioning System of BDS

The global-enhanced real-time positioning system of BDS mainly contains the real-time reference station network, data processing center, broadcast link, and the client [2]. The main workflow of the system is: the data processing center real-time receive and process data transmitted by reference station network, generate real-time orbit and clock offset products. The differential data can be obtained by comparing the real-time orbit and clock offset with broadcast ephemeris. The differential data will be written into enhanced cable and be spread to client by the internet. The client receives the real-time observed data and differential data to precise positioning. The specific processes are showed in Fig. 1.

Based on the global-enhanced real-time positioning system of BDS, this paper achieved the precision verification of BDS global real-time PPP. In this paper, the satellite orbit update sonce 1 h and the clock offset is estimated by 1 Hz's real-time observed data. The differential data is used to realize real-time PPP of BDS. There are several stations to get result of PPP for verifying the performance of global real-time PPP. The coding and spread of real-time differential data are achieved by the software compiled by Chang'an University Beidou Analysis and Service Center. Communication protocol of data broadcasting adopts Ntrip protocol and TCP/IP protocol, the data format adopts RTCM3.0, data broadcast link uses 3G wireless communication mode.

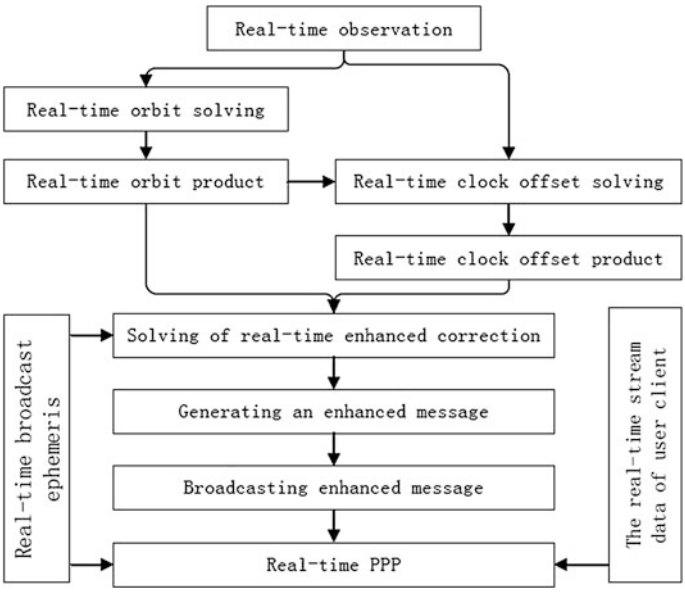

Fig. 1 The calculation process of real-time PPP

3 Real-Time Orbit Solving Strategy

38 global monitoring stations of BDS in iGMAS and MGEX are selected to consist of the global Beidou satellite orbit monitoring network. The predicted orbit was calculated by the 24-hours real-time observation data.

The brief processing of the orbit determination is as follows: first, the initial orbit can be obtained with the broadcast ephemeris, and the integral of variational equation can be implemented. Then errors are corrected using undifferenced observation and the observation will be linearized. Finally, we obtain the values of unknown parameters and then obtained the satellite orbit products [3, 4].

In order to get the relatively smooth real-time satellite orbit products, the sliding window method is used [5]. First, the real orbit is solved with n hours the ground monitoring station observation data before and related table files once an hour, and then according to the extrapolation model, obtained n hours predicted orbit as a real-time orbit. After the data was calculated using the sliding window method, namely the calculation after a period of real-time orbit, remove the first arc section of the measured data, added a recent arc segment of the measured data, processing the next real-time orbit determination. Specific process diagram is shown in Fig. 2.

4 Real-Time Clock Offset Solving Strategy

At present, the product accuracy of the ultra-fast predicted clock offset is only 3 ns, the equivalent distance error is 0.9 m, which is much lower than the nominal precision of 75 ps final clock offset products. Its accuracy and stability limit the accuracy of real-time PPP [6–8]. Foreign scholars achieve the GPS satellite real-time clock offset solution accuracy which is superior to 0.2 ns [9, 10]. However, the research on real-time satellite clock error estimation algorithm for BDS is less.

The real-time clock offset is estimated usually using non-difference model and epochs difference model. In this paper, 21 monitoring stations are selected from the MGEX and iGMAS tracking network, and the non-difference model is adopted to estimate the 1 Hz BDS satellite clock offset.

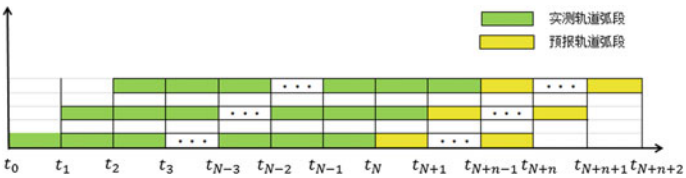

Fig. 2 The calculating method of sliding window

Known station coordinates satellite orbit, the pseudorange and phase of the ionosphere-free combination of observation values as the clock error estimation observation, you can get the non-difference observation model [11].

$$\left.\begin{aligned} \upsilon_{Lc}(k) &= \delta t_{\mathrm{r}}(k) - \delta t_s(k) + m(k)\delta T(k) + B + l_{Lc}(k) \\ \upsilon_{\mathrm{Pc}}(k) &= \delta t_{\mathrm{r}}(k) - \delta t_s(k) + m(k)\delta T(k) + l_{Pc}(k) \end{aligned}\right\} \quad (1)$$

k are epochs, δt_r and δt_s denote the clock offset parameters of receiver and satellite, respectively, δT and m denote the zenith wet delay and the mapping function of zenith wet delay, respectively, B is the ambiguity of Ionosphere-free combination observed values, l_{Lc} and l_{Pc} denote the difference between the phase observation or code observation and the calculated value. υ_{Lc} and υ_{Pc} denote the residuals of phase and code observations, respectively.

System deviation of satellite clock offset in the position can be the absorbed into receiver clock offset and ambiguity parameters and it does not affect the results of positioning. The NNOR's receiver clock offset is selected as reference clock to solve satellite clock offset and other receivers' clock offset compared to the reference clock. For the parameter estimation, phase-winding error, satellite phase center variation, solid tide correction, correction of ocean loading tide, Earth rotation correction, relativistic effects, and so on are corrected using correction model. The satellite clock offset, receiver clock offset, and ambiguity parameters are set as unknown parameters to estimate the influence of troposphere delay of the dry component and adopt Sasstamoinen empirical model to correct, zenith wet delay is set as unknown parameters to piecewise estimate and to estimate a set of parameters once 1 h.

5 The Real-Time PPP Algorithm of the Client of BDS

Real-time positioning of the client is using the real-time PPP of BDS model. The real-time PPP selects undifference carrier phase and pseudorange as the observation value. The ionospheric error is eliminated using the ionosphere-free combination observation. The troposphere delay error and the receiver error are estimated by introducing unknown parameters [12]. The observation equation:

$$\left.\begin{aligned} P &= \rho + c(dT_{\mathrm{j}} - dT^i) + m \cdot ZPD + \varepsilon_p \\ \varphi &= \rho + c(dT_j - dT^i) + m \cdot ZPD + N^i + \varepsilon_\varphi \end{aligned}\right\} \quad (2)$$

P denotes the ionosphere-free code observation; φ denotes the ionosphere-free phase observation; ρ represents the geometric distance between satellite (X^i, Y^i, Z^i) and receiver (X_j, Y_j, Z_j); c denotes the speed of light; dT_j and dT^i denote the clock offset parameters of receiver and satellite, respectively; ZPD and m denote the zenith wet delay and the mapping function of zenith wet delay, respectively; N^i is

the ambiguity of Ionosphere-free combination observed values; ε_p and ε_φ denote the random error of code and phase observation, respectively.

6 The Preliminary Design of Global-Enhanced Message

In this paper, the enhanced message is designed by referencing the RTCM 3.0 standard message format. According to the updated rate and the accuracy of a variety of products, the enhanced message is designed to improve the performance of real-time PPP. The specific content is showed in Table 1.

7 Result and Discussions

In this paper, the experiment of estimating real-time orbit, real-time clock offset, broadcasting-enhanced message, and real-time PPP last for 6 days using the data of day of the year from 318 to 323 in 2015. 10 stations are selected to verify the accuracy of the global-enhanced real-time positioning technology.

Table 1 Specific content of real-time enhanced message of BDS

	Parameter	Unit	Period
Orbit	PRN (satellite No)	无	5 min
	IODE (age of ephemeris data)	s	
	Dx/Dy/Dz (correction of X/Y/Z coordinate)	m	
	Ddx/Ddy/Ddz (correction rate of X/Y/Z coordinate)	m/s	
	Time-of-day applicability t0 (reference moment of orbit correct)	s	
Clk offset	PRN (satellite No)	无	
	IODCS (age of slowly varying clock offset)	无	180 s
	Da0 (constant term of clock offset correction)	s	
	Da1 (one degree term of clock offset correction)	s/s	
	Time-of-day applicability t0 (reference moment of slowly varying clock offset)	s	
	IODCF (age of slowly varying clock offset)	无	1 s
	Dclk (correction of fast varying clock offset)	s	
	t01 (reference moment of fast varying clock offset)	s	
Ionosphere	Grid points(ionosphere grid point ID)	无	5 min
	IGP VDE (ionosphere perpendicular delay of grid point)	m	
	Effective range: latitude −85 to 85, longitude −175 to 175, Grid resolution: 5。*5。		

7.1 The Accuracy Analysis of Real-Time Orbit and Clock Offset

In this paper, we processed 6 days' real-time orbit and compared it with final ephemeris of GFZ to get the residual series of RMS. In Figs. 3 and 4, the average accuracy is 194.0 cm, 24.9 cm for GEO satellite, MEO/IGSO satellite. GEO satellites orbit accuracy was significantly lower than the other two kinds of satellites. The C02 statistical precision of C02 GEO satellite reached 8.72 m, far lower than similar GEO satellites, therefore the accuracy of the statistics is the exclusion of C02.

We selected the results of the 318th day of the year in 2015 to show the accuracy of real-time clock offset. The real-time clock offset results are compared with the final precise clock of GFZ used quadric difference. The clock of C01 satellite is the reference clock, and then the STD value of different satellite is showed in Fig. 5. In

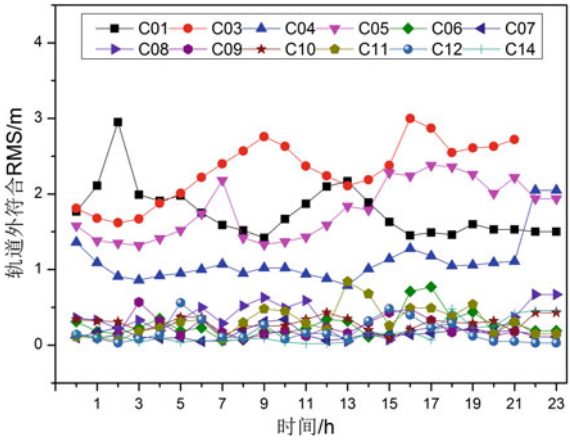

Fig. 3 The external accuracy of orbit precision in 2015-318

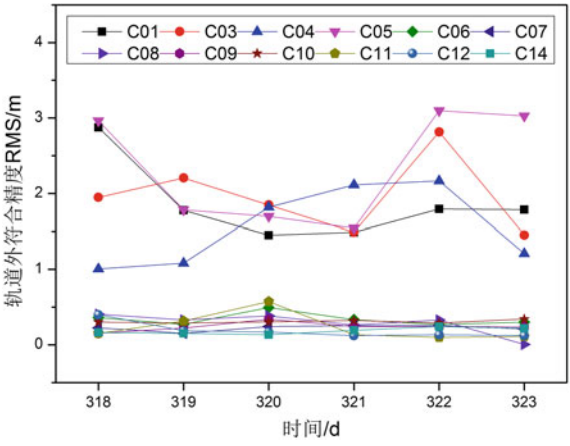

Fig. 4 The external accuracy of orbit precision about 6 days

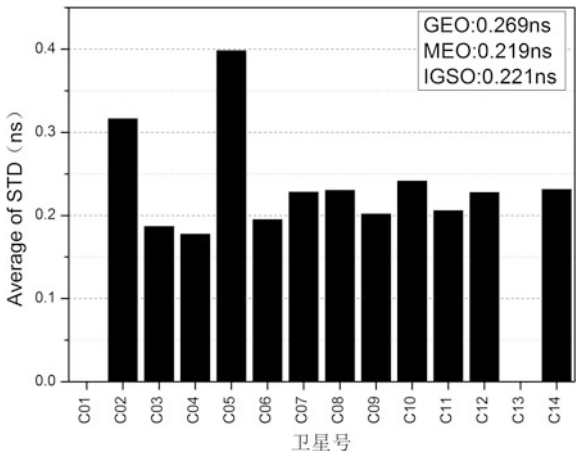

Fig. 5 The external accuracy of clock offsets precision

Fig. 5, the accuracy of real-time clock offset is better than 0.4 ns, 0.3 ns for the MEO satellites and MEO/IGSO satellites.

7.2 Precision Verification of BDS Global-Enhanced Real-Time PPP

10 stations are selected to verify the accuracy, which includes 4 stations in the territory of China, overseas 6 stations (3 stations in Africa, 2 stations in Australia, 1 station in South Asia). Its specific distribution is showed in Fig. 6.

1. **Precision verification of stations in China**

The BJF1, KUN1, JFNG, SHA1 are selected to analyze the accuracy of the enhanced real-time PPP in China. The time of processing is 1 to 24 h. The snx

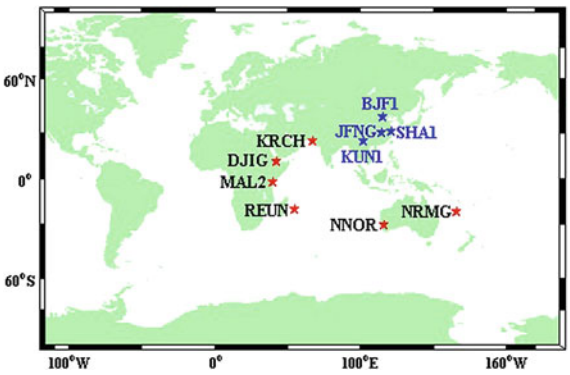

Fig. 6 The distribution stations of monitoring network

product provided by Chang'an University Beidou Analysis and Service Center was adopted to be as reference coordinate of stations to get the residual of positioning. The results of 318th day in 2015 are showed in Fig. 7, 8, 9 and 10.

In Table 2, it shows that the decimeter real-time positioning accuracy in three directions can be achieved in China. The average residuals are 0.223, 0.272, and 0.469 m for the directions of north, east, up-coordinate component, respectively.

2. **Precision verification of overseas stations**

The NRMG, NNOR, MAL2, KRCH, DJIG, REUN are selected to analyze the accuracy of the overseas-enhanced real-time PPP. For overseas stations, the number of satellite be observed is less than in China, therefore, the time of positioning is not fixed and long enough. The time of each station for positioning is more than 7 h. The results of 318th day in 2015 are showed in Figs. 11, 12, 13, 14, 15, and 16.

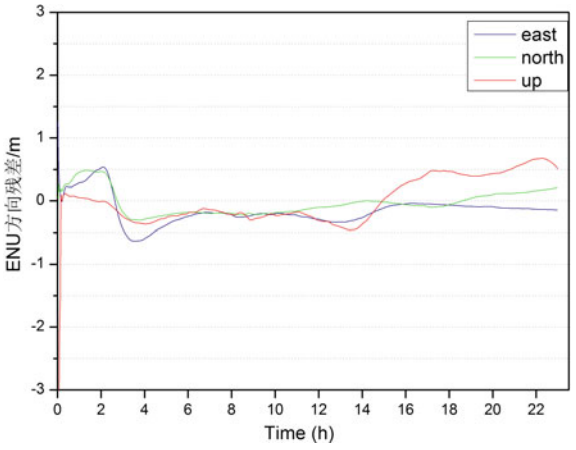

Fig. 7 The error of real-time PPP for KUN1

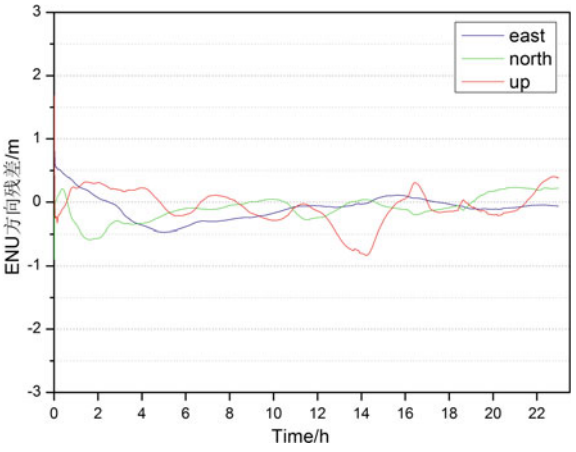

Fig. 8 The error of real-time PPP for JFNG

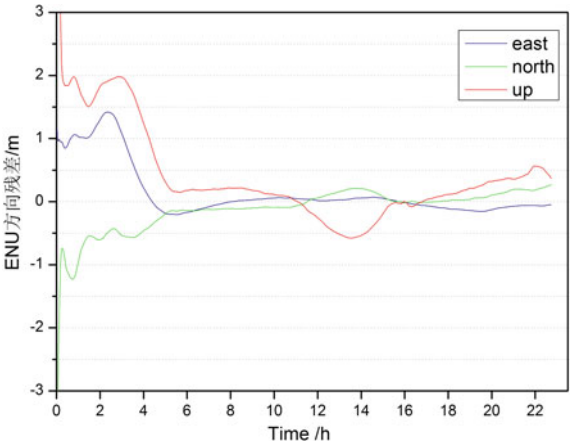

Fig. 9 The error of real-time PPP for BJF1

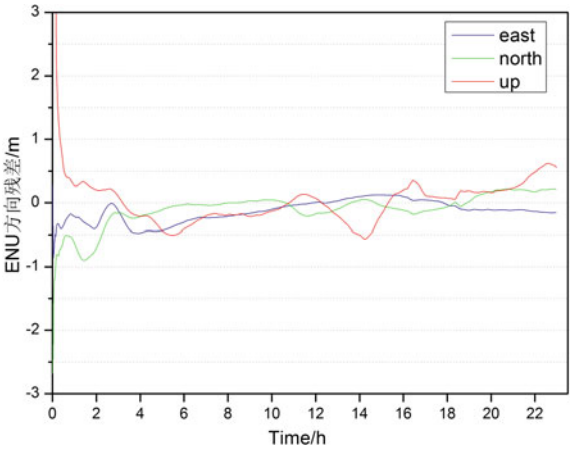

Fig. 10 The error of real-time PPP for SHA1

Table 2 The average residual of real-time PPP in China (318–323, in 2015)

Station	North (m)	East (m)	Up (m)
KUN1	0.1976	0.2708	0.6067
BJF1	0.2413	0.4007	0.7162
JFNG	0.2137	0.2132	0.2761
SHA1	0.2396	0.2015	0.2771

In Table 3, it shows that the decimeter real-time positioning accuracy in three directions also can be achieved for the overseas stations. The average residual are 0.267, 0.365, 0.501 m for the directions of north, east, up-coordinate component, respectively. Obviously, the accuracy is lower compared with the stations in China.

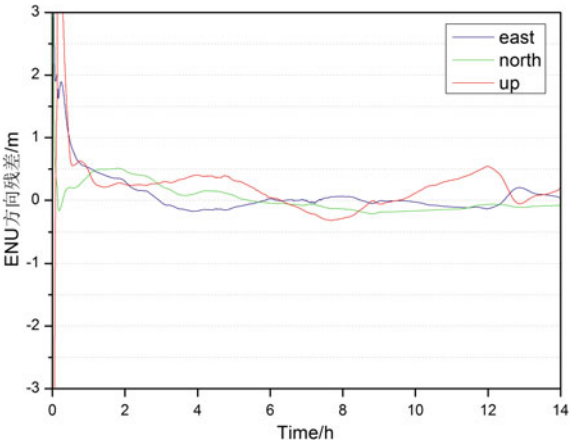

Fig. 11 The error of RT PPP for NRMG

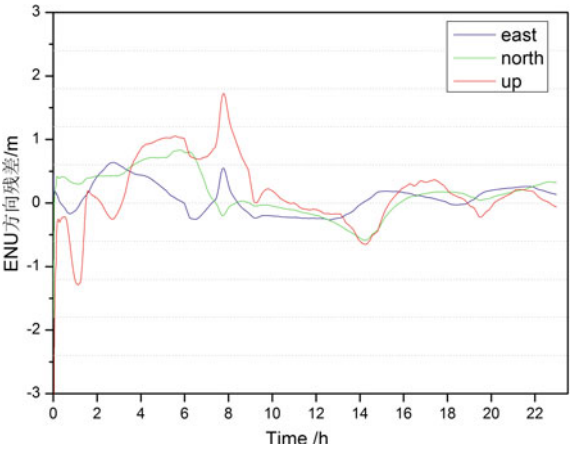

Fig. 12 The error of RT PPP for NNOR

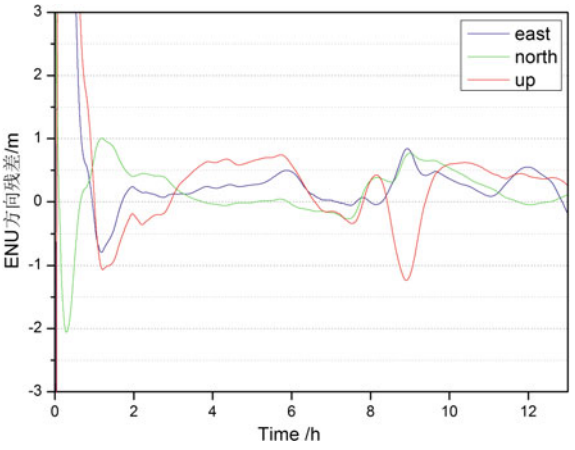

Fig. 13 The error of RT PPP for MAL2

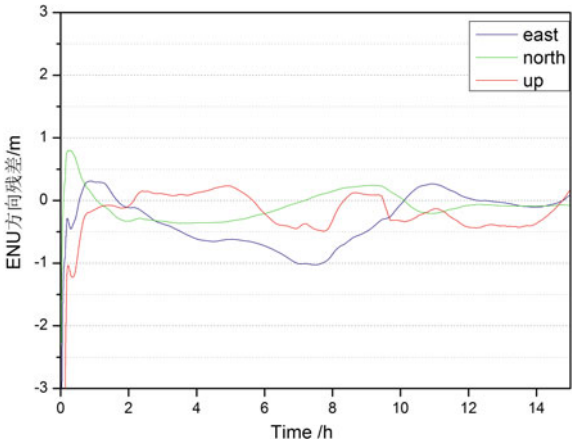

Fig. 14 The error of RT PPP for KRCH

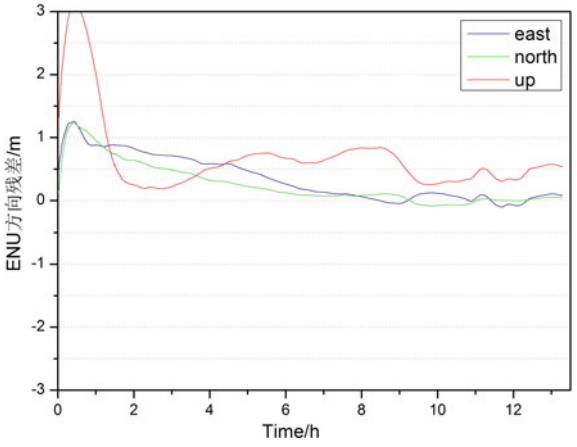

Fig. 15 The error of RT PPP for DJIG

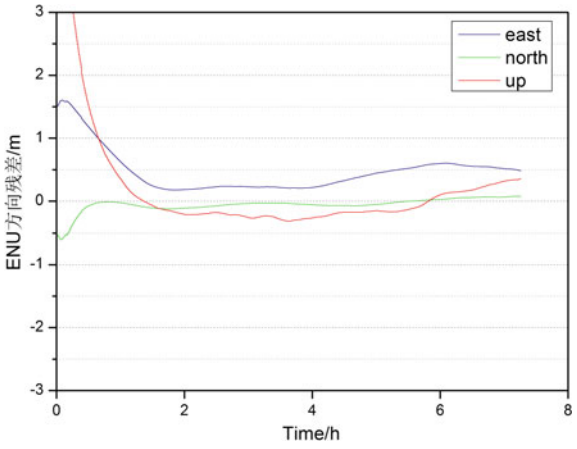

Fig. 16 The error of RT PPP for REUN

Table 3 The average residual of real-time PPP for the overseas stations (318–323, in 2015)

Station	North (m)	East (m)	Up (m)
NRMG	0.2108	0.1994	0.2869
NNOR	0.3697	0.2483	0.5461
MAL2	0.3462	0.3115	0.4998
KRCH	0.2646	0.5436	0.7555
DJIG	0.2888	0.4153	0.5507
REUN	0.1205	0.4719	0.3646

8 Conclusions

In this paper, real-time clock offset and orbit estimation and global-enhanced real-time PPP of BDS are realized. Through the various stations, the results of real-time positioning show that: within the scope of the Beidou satellite navigation system to provide services, the real-time PPP based on BDS can achieve decimeter-level position accuracy.

In China, an accuracy of 0.3 and 0.5 m can be achieved for the horizontal and vertical coordinate components based on only BDS observations. For overseas stations, accuracies are 0.4 and 0.6 m for the horizontal and vertical components, respectively. The positioning accuracy of overseas stations is lower than the stations in China, the reason is that the number of overseas stations is short and the number of satellites be observed is not enough compared with the stations in China. At present, the Beidou satellite constellation has not been fully established and there is still relatively small number of global monitoring stations. With the Beidou satellite constellation improvement and global tracking station network developing, this will further improve the calculation accuracy of real-time orbit and clock offset, thereby further improving the accuracy of the global-enhanced real-time PPP of BDS.

Acknowledgments This research was supported by the project of National Natural Science Fund (41104019, 41104022, 41304033, and 41504006), Project of Chinese Hydropower Engineering Consulting Group of science and technology (GW-KJ-2012-21), the Special Fund for Basic Scientific Research of Central Colleges (Grant No. 310826165014, Chang'an University). The authors would like to thank The open foundation of National Key Laboratory of Geographic Information Engineering (2013ADL-DW0103), The open fund of Sate Key Laboratory of Geographic Information Engineering (SKLGIE2013-Z-2-1) and Central University Research Funds (2014G1261051), The National Natural Science Foundation of China, Light of West China, for their support, and to the editor and anonymous referees for their valuable suggestions.

References

1. Zhu Y, Feng L, Jia X et al (2015) The PPP precision analysis based on BDS regional navigation system. Acta Geodaetica Cartogr Sin 44(4):377–383
2. Shi C, Lou Y, Song W, Cai H The prototype system and preliminary results of wide area real time precision positioning

3. Li J (1995) Satellite precision orbit determination. Chinese People's Liberation Army Publishing House, Beijing
4. He S, Wu B, Chen J (2011) Orbit predictions for GPS satellites using IGS ephemeris. Annals of Shanghai Observatory Academia Sinica 32:25–34
5. Lou Y, Shi C, Ge M et al (2008) GPS real time orbit determination and initial results analysis. Geomatics Inf Sci Wuhan Univ 33(8):815–817
6. Heo YJ, Cho J, Heo MB (2010) Improving prediction accuracy of GPS satellite clocks with periodic variation behavior. Meas Sci Technol 21:073001. doi:10.1088/0957-0233/21/7/073001
7. Huang GW, Zhang Q, Li HT et al (2012) Research on quality variation of GPS satellite clocks on-orbit using IGS clock products. Adv Space Res 51:978–987. doi:10.1016/j.asr.2012.09.041
8. Huang GW, Zhang Q et al (2013) Real-time clock offset prediction with an improved GPS satellite clocks model. GPS Solution. doi:10.1007/s10291-013-0313-0
9. Bock H, Dach R, Jaggi A, Beutler G (2009) High-rate GPS clock corrections from CODE: support of 1 Hz applications. J Geod 83(11):1083–1094. doi:10.1007/s00190-009-0326-1
10. Zhang XH, Li XX, Guo F (2010) Satellite clock estimation at 1 HZ for realtime kinematic PPP applications. GPS Solut (in press). doi:10.1007/s10291-010-191-7
11. Ge M, Chen J, Douša J, Gendt G, Wickert J (2012) A computationally efficient approach for estimating high-rate satellite clock corrections in realtime. GPS Solut 16:9–17. doi:10.1007/s10291-011-0206-z
12. Zhang X (2006) Accuracy analysis of dynamic precise point positioning. Glob Positioning Syst 01:7–11+22

Research and Application on Enhanced Reception Techniques Based on Distributed Antennas in Ground Station

Ke Zhang, Zengjun Liu, Hang Gong, Zhicheng Lv, Xiangwei Zhu and Guangfu Sun

Abstract In order to enhance navigation warfare capabilities of ground station, miniaturization and motorization is a trend. However, the demand of antenna aperture for downlink signal processing is diversity. Then contenting the diversity of antennas is a major factor that restricts the development of ground control systems. For the demand of multi-target tracking and single target enhancing, based on the characteristics of precise-time synchronization between ground stations of satellite navigation systems, an enhanced reception techniques based on distributed antenna system (DAS) is proposed with a plurality of distributed small aperture as the basic element. With the knowledge of wave direction, phase difference between the received signals is computed and compensated. Then downlink signal synthesis is realized which means larger aperture synthesizing antenna is achieved and the ability of receiving signal is enhanced. Numerical analysis shows that when the phase compensation accuracy is up to 0.2, synthesizing efficiency can reach to 75 % within the scanning range [π/18, π/2]; while a digital multi-beam antenna can only reach about 70 % at elevation angle of 30°. Distributed enhanced reception techniques, by arraying small aperture to achieve flexible combinations and configurations of beam and gain, can be applied to ground station for miniaturization and self-propelled construction and improve the multi-target tracking and controlling capability of satellite navigation and aerospace based on flexibility and low cost of small-diameter antenna.

Keywords Ground station · DAS · Signal enhancing · Phase compensation · Synthesizing efficiency

K. Zhang (✉) · Z. Liu · H. Gong · Z. Lv · X. Zhu · G. Sun
National University of Defense Technology, Deya Road 109,
Changsha 410073, China
e-mail: zhane0915@163.com

J. Sun et al. (eds.), *China Satellite Navigation Conference (CSNC) 2016 Proceedings: Volume II*, Lecture Notes in Electrical Engineering 389,
DOI 10.1007/978-981-10-0937-2_24

1 Introduction

Satellite navigation system [1] is mainly divided into the satellite constellation, ground controlling, and monitoring network and user receiving equipment. Ground controlling and monitoring network, also known as ground control system, is responsible for monitoring, command and control satellite constellation, including monitoring downlink navigation signals, updating navigation data, solving satellite anomalies, and other functions. For example, the downlink navigation signal processing requires a variety of antenna aperture with the measurement fields, modulation and time domain analysis respectively. In addition, with the BDS system towards the globalization process, constellation has also been improved. In order to accomplish tasks in both peacetime and wartime, the future ground station is able to not only track the usual multi-target in the visual region, but also enhance the single target in war region.

Existing ground control systems typically employ large aperture reflector antenna or a digital multi-beam antenna for receiving satellite signal, which means at any time a satellite can only built chain with one ground station antenna, such signal processing architecture has many disadvantages:

- Low system reliability. Since the signal processing chain is so concentrated that system reliability is low, and the capability for anti-strike and anti-jamming is weak in navigation warfare situation;
- Limited system performance. Large-diameter reflector antenna is advantageous for single target enhancement, but is limited of multi-target tracking capability. Digital multi-beam antenna is better for multi-target tracking, but its capability of low elevation tracking and single target enhancing and some other aspects is slightly weaker;
- High construction costs. The receiving G/T of a single antenna is mainly limited by the diameter. So to improve receiving sensitivity, antenna aperture increases exponentially. But large-diameter antenna requires seriously the installation site, construction technology, and construction costs increase substantially.

DAS can be used to effectively compensate for these deficiencies in three areas of existing ground control systems.

DAS [2] is generalized to multiple antennas system in accordance with certain rules. Since it has obvious advantages in the use of space resources, on the one hand it is more flexible to be installed, and on the other hand it can work as an alternative array. DAS has become the key technology to enhance the frequency efficiency of wireless communication, and it is a trend of the future for wireless communication system architecture development. Therefore it is also the research hotspot in recent years. In mobile communications [3, 4], DAS can fight large-scale fading [5], reduce transmission power, and increase system capacity.

DAS is widely used in the field of astronomical observation applications, such as Square Kilometer Array (SKA) [6]. The mid-SKA shown in Fig. 1 includes

Fig. 1 Geometry of SKA

190 reflector antennas with surface diameter 15 m and with antenna bandwidth 350 MHz–20 GHz while physical aperture of the entire array is 42737 m^2. Beamforming is achieved by phase control and time synchronization through the optical fiber. NASA Space Communication and Navigation Architecture Recommendations [7], raised by SCAWG for 2005–2030, had proposed next six key technologies, including the downlink arraying technology. It gave some advice to make use of distributed and flexible small aperture antenna to achieve the objective of a large aperture array.

In this paper, the enhanced reception techniques based on distributed antenna system was studied on condition that satellite navigation system was with high-precision time features [8]. On the one hand a single antenna with independent signal processing functions meets the needs of multi-target tracking; on the other hand, single target enhancements can be achieved through the signal synthesizing. With the knowledge of signal direction and wave way error between distributed antennas, the phase difference was calculated integrating channel delay data between the antennas. Finally the signal was synthesized through the phase compensation and synthetic efficiency [9] was proposed as the evaluation index.

2 Antenna Requirement

Currently the receiver using omnidirectional antenna can meet the needs for frequency domain analysis, including signal spectrum and power analysis. This section focuses on demand of antenna diameter for time domains analysis, such as spreading code correctness analysis and time domain waveform analysis.

2.1 The Requirement for Spreading Code Correctness Analysis

For continuous spreading code correctness analysis, bit error rate (BER) 10^{-3} is enough to discern whether the chip generates errors under normal circumstances. The relationship between BER P_b and carrier-to-noise ratio (CNR) is

$$P_b = \frac{1}{2}\mathrm{erfc}\left(\sqrt{\frac{C/N_0}{R_b}}\right) \tag{1}$$

where, erfc(·) is complementary error function, R_b represents data rate. C/N_0 denotes CNR.

If we need to monitor the navigation signals of simple BPSK signal whose code rate is 10.23 MHz, the CNR 77.5 dBHz is required. After the GPS Modernization, signals are BOC modulated, so BER calculation not only can simply master key code rate but also take subcarriers into account. Altboc(15,10) modulated signal, for example, the total code rate including the main code and subcarrier is 30.69 MHz, then CNR 82.3 dBHz is required for chip correctness analysis.

2.2 The Requirement for Time Domain Waveform Analysis

Analysis of chip distortion first needs to recover code chip waveform with 100 % correctness. In the case of 10.23 and 30.69 MHz code rate, the corresponding minimum requirement for CNR is 80.1 and 84.9 dBHz, respectively.

The time domain waveform of QPSK modulated signal with the code rate of 10.23 MHz and CNR 75 dBHz, 85 dBHz was simulated, respectively. Noise loop bandwidth is 10.23 MHz and time domain waveform is shown in Fig. 2.

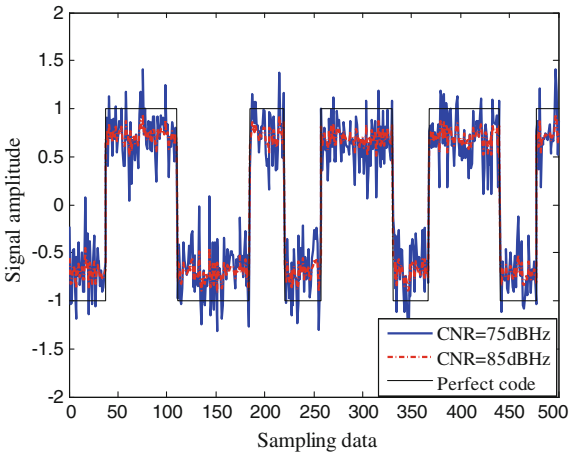

Fig. 2 The time domain waveform with different CNR

Table 1 Antenna aperture needs for signal quality analysis

Analysis project		CNR	Aperture
Time domain	Time domain waveforms	84.9 dBHz	22.5 m
	Spreading code symbol correctness	82.3 dBHz	16.5 m
Modulation	Vector diagram	65 dBHz	2.5 m
Correlation	Correlation peak distortion	52 dBHz	0.6 m
Measurement	Pseudo range and carrier phase	Omnidirectional antenna	
Frequency	Spectrum		

Obviously, compared to 75 dBHz, time domain waveform of 85 dBHz was easier to judge and the correct rate was higher.

2.3 Statistical Antenna Aperture

Assuming that the LNA gain is 60 dB, the noise temperature is 50 K, and antenna efficiency is 0.6. The antenna aperture for diversity domain signal analysis is calculated, as shown in Table 1.

From Table 1, the time domain waveform analysis of the new BOC signal requires the highest CNR, at least 84.9 dBHz, and the antenna diameter is 22.5 m. If the user does not need to analyze the time domain waveform, then the most demanding of the antenna is the spreading code symbol correctness, and the requirements for its antenna diameter is 16.5 m. When ground station is constructed on the motive platform, the recommended aperture of antennas is 2–3 m. A single antenna at this time can only be used to analyze signal in the amount of frequency domain, modulation domain, correlation domain, and measuring domain. In this situation, enhancing technology needs to improve the analysis ability of the system.

3 Distributed Signal Enhancing Techniques

Distributed signal enhancing techniques use distributed antenna as node to receive signals, and the received signal enhancement is completed by signal synthesis. During signal synthesis, the key point is to achieve the precise spatial location of distributed antennas, high-precision time synchronization, channel delay calibration, and so on.

3.1 Principle of Distributed Signal Receiving Architecture

Schematic distributed signal receiving architecture is shown in Fig. 3a, b. By scanning beam to a satellite, the same signal is received by distributed antennas

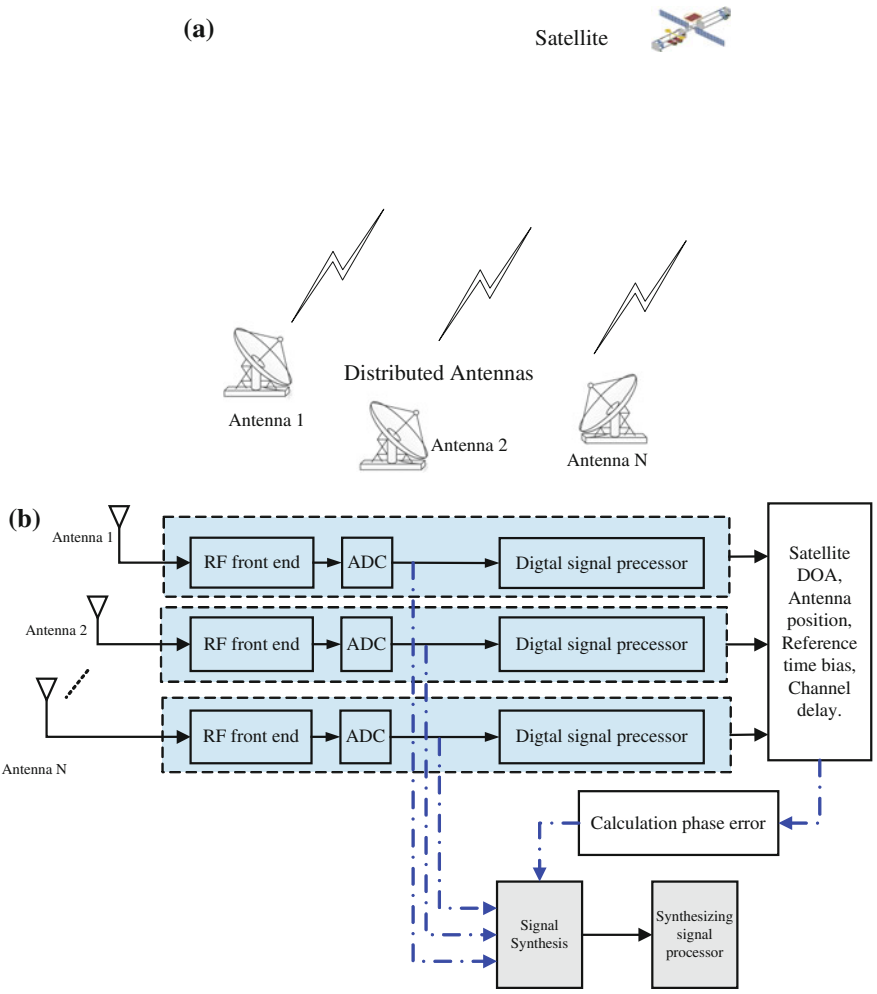

Fig. 3 Architecture of signal receiving based on DAS. **a** DAS. **b** Architecture of signal receiving

which are distributed to one or more ground stations. On the one hand received downlink navigation signal in a single antenna is analyzed independently in the frequency domain and measured domain under the conditions of low CNR. On the other hand, the signal after sampling of each antenna is transmitted through fiber to centralized processing nodes to synthesize.

At the same time, the existing satellite ground station has to measure the direction of arriver (DOA) of satellite signal, antenna location, clock error between station and channel delay, and some other data. Then all information will be transferred to a centralized processing node where they are integrated and phase error is calculated between antennas. In the centralized processing node, signals are

synthesized by adjustment phase relationship in accordance with the calculated phase error. Synthesizing signal is sent to the signal processor for processing at last.

Distributed signal receiving architecture fully makes use of the flexibility and low-cost advantages of small-diameter antenna, no need to change the architecture of the receiving links of original ground station. So ground stations are able to keep the original functions separately. Since the antenna diameter of a single node is reduced, it is beneficial for single station to be miniaturized and motorized. At the same time, beam and gain can be flexibly arrayed according to the tasks by lots of small-diameter antenna which means the distributed architecture is compatible for multi-target tracking and single target enhancing.

3.2 Key Technology Analysis

According to the principle above, the core of distributed architecture is used to calibrate the benchmark of spatial-time. So the key technology is to achieve the precise spatial location of distributed antennas, high-precision time synchronization, channel delay calibration, and signal long-distance transmission.

Precise physical location of the distributed antenna reference point can be measured by precise point positioning (PPP) [10]. Currently, a single GPS receiver with dual band and dual code can achieve a global-scale accuracy of 2–4 cm level in condition of the fast static position.

High-precision time synchronization can be achieved by fiber two-way time synchronization [11]. Research has shown that the frequency stability is better than 1×10^{-13} s when the frequency signal is transmitted over 100 km and time synchronization accuracy is less than 1 ns.

Channel delay calibration can be completed by offline calibrating the channel delay from LNA to the ADC and online monitoring the delay variation value through digital loop and analog loop as shown in Fig. 4 where the calibrating signal is generated by the measuring signal generator. And delay caused by antenna can be pre-calibrated in an anechoic chamber initially [12].

Fiber optic cable can be used to transmit signal over long distance. Currently, the digital signal optical transmission technology has become more mature.

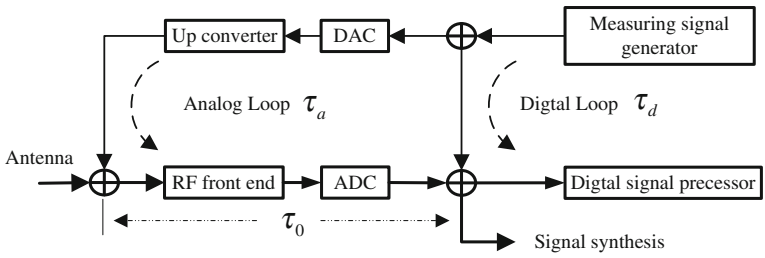

Fig. 4 Principle of channel delay measurement

4 Distributed Signal Synthesis Principle

Distributed signal synthesis is the key of distributed processing architecture. In this section the synthesizing efficiency is defined according to the electromagnetic wave propagation mechanism; and then the impact of residual phase error on synthesizing efficiency is analyzed after phase compensation. In this paper, antennas distributed in local area are considered which means far-field condition between satellites and DAS is satisfied. The constraint can not only reduce error source but also make the system control easily.

4.1 Definition of Synthesizing Efficiency

First a reference coordinate is set up in Fig. 5 where reference phase point is set as the coordinate origin and z-axis is perpendicular to the tangent plane of the earth at the reference phase point, i.e., the direction of the earth geocenter pointing to the reference phase point. The x-axis points to south direction, and the y-axis is vertical to the plane. The position of ith receiving antenna is identified as (R_i, θ_i, ϕ_i) while the transmitting antenna position is (r_0, θ_0, ϕ_0).

According to wave propagation theory, in a free-space radio wave propagation conditions, the field strength of transmitting antenna signal is

$$\boldsymbol{E_i} = \frac{f_t(\theta_{ti}, \phi_{ti}) \cdot I_0 \cdot \boldsymbol{r_i}}{|\boldsymbol{r_i}|^2} \cdot C_i \cdot \exp(-j \cdot \boldsymbol{k_i} \cdot \boldsymbol{r}_i) \tag{2}$$

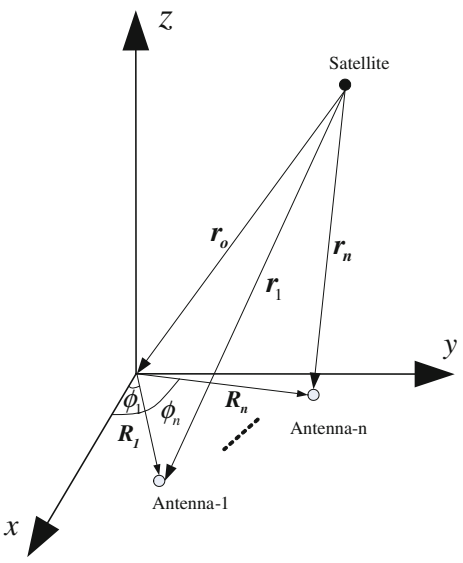

Fig. 5 Principle of signal synthesis based on distributed antennas

where $f_t(\theta_{ti}, \phi_{ti})$ denotes transmitting pattern, (θ_{ti}, ϕ_{ti}) denotes the direction of wave propagation when compared to the phase center of transmitting antenna, I_0 is the excitation current, C_i represents the electromagnetic field affected by the ionosphere, troposphere, and other parameters, $\boldsymbol{k}_i$ is the wave vector constant.

For distributed array consisting of N elements, the synthesized field strength E from the satellite at centralized processing nodes is

$$\boldsymbol{E} = \sum_{i=1}^{N} f_i(\theta_{ri}, \phi_{ri}) \cdot \boldsymbol{E_i} \cdot \exp(2\pi f_c \tau_i) \tag{3}$$

where $f_i(\theta_{ri}, \phi_{ri})$ denotes receiving pattern and τ_i represents phase delay due to received link cable channel while f_c denotes the frequency of carrier wave. (θ_{ti}, ϕ_{ti}) denotes the direction of incoming wave when compared to the phase center of transmitting antenna. The power density is proportional to the square of the electric field amplitude, so the synthesizing efficiency η can be defined as

$$\eta = \left| \sum_{i=1}^{N} |C_i| \exp(-j\varphi_{i1}) \right|^2 \tag{4}$$

where φ_{i1} denotes the phase error refer to reference phase point. In (4), in order to simplify the analysis, some assumptions are made.

- Receiving antennas are distributed on the same plane, so $\theta_i = 0$. The array aperture D_a should meet $D_a \leq \sqrt{R \cdot \lambda/2}$, where R represents the distance between the satellite and the center of the array.
- Since the elements are in close proximity, and work in the low-frequency band, it is reasonable that for each array element C_i is constant.
- The receiving pattern is equal for each distributed element.
- Ground stations are divided into a master and several slaves, and the master station is set as phase reference point at the origin of coordinates.

4.2 Phase Compensation Principle

According to (4), the phase error between the slave and the master is:

$$\begin{aligned} \varphi_{i1} &= (\boldsymbol{k}_i \cdot \boldsymbol{r}_i - \boldsymbol{k}_1 \cdot \boldsymbol{r}_1) + 2\pi f_c(\tau_i - \tau_1) \\ &= \frac{2\pi}{\lambda} R_i \cos(\phi_i - \phi) \cos\theta_0 + 2\pi f_c(\tau_i - \tau_1) \end{aligned} \tag{5}$$

where $i = 1$ indicates the master signal, other signals from the slaves, and R_i represents the distance from the slaves and the master. In the right of (5), the first term is the wave path-difference, while the second term is channel delay.

The ground station has to measure the DOA of satellite, antenna location, clock error and channel delay between stations. Then all data are transferred to a centralized processing node where they are integrated and phase error is calculated between each antenna. In the centralized processing node, signals are synthesized by adjustment phase relationship in accordance with the calculated phase error.

However, the precision of relative positioning accuracy and the channel delay calibration is limited, (5) can be simplified to the following (6) after phase-compensated where β_i is the residual phase error. In order to avoid introducing additional synthesizing ambiguity [13], we constraints $\beta_i \in [-\pi, \pi]$.

$$\eta = \left| \sum_{i=1}^{N} \exp(-j \cdot \beta_i) \right|^2 \tag{6}$$

After the phase compensation, the received downlink signals achieve the coarse synchronization. Obviously, this method does not require array geometry, and antenna can be installed or selected flexible based on demand of ground stations.

5 Numerical Analysis of the Synthesizing Efficiency

The residual phase error is mainly composed of wave path-difference error due to the relative positioning errors and the channel delay calibration error between array elements, as defined in (7) as follows:

$$\beta_i/2\pi = (\Delta R_i/\lambda) \cdot \cos(\phi_i - \phi) \cdot \cos\theta + f_c \Delta\tau_i \tag{7}$$

where ΔR_i denotes the relative positioning error of distance R_i, and $\Delta R_i/\lambda$ obeys normal distribution $N\left(0, \sigma_1^2\right)$, where σ_1 represents the relative positioning precision factor of receiving antenna with respect to reference phase point. $\Delta\tau_i$ represents the phase error of τ_i, and $f_c\Delta\tau_i$ obeys normal distribution $N\left(0, \sigma_2^2\right)$, where σ_2 represents the channel delay calibration precision factor. And then $\beta_i/2\pi$ obeys normal distribution $N(0, \sigma_2)$, where σ represents the phase compensation precision factor.

We defined that $\cos(\phi_i - \phi) = 1$, which means synthesizing efficiency under the most adverse conditions was studied. In the simulation four distributed antennas were chosen, and 1000 satisfies the above constraints scenes were randomly generated, then the average value was set as the synthesizing efficiency in this phase error conditions.

Figure 6 shows the influence of two types of phase errors on signal synthesizing efficiency at different elevation. It is easy to find from the figures that the signal synthesizing efficiency significantly reduced with the increase of the phase error. By

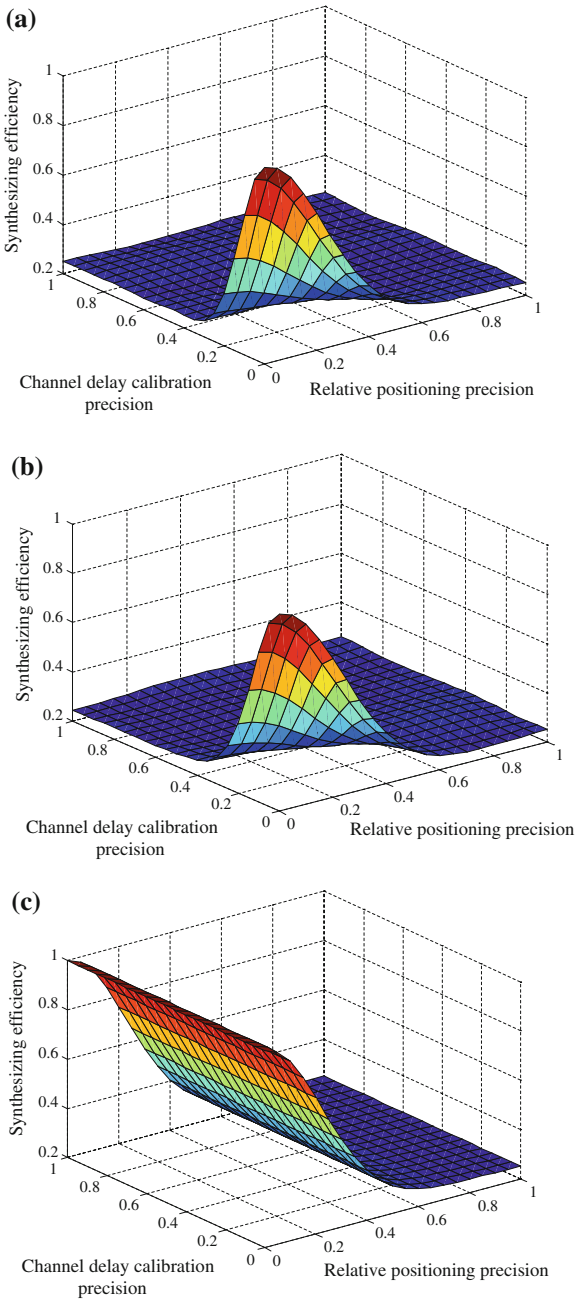

Fig. 6 Influence of phase error on synthesizing efficiency in a 4 elements array. **a** Elevation 10°. **b** Elevation 30°. **c** Elevation 90°

Table 2 Constraint between synthesizing efficiency and phase compensation precision

Number	Synthesizing efficiency (%)	Phase compensation precision
1	95	0.08
2	90	0.12
3	85	0.15
4	80	0.17
5	75	0.2

comparison of Fig. 6a, b, the higher the antenna beam scanning elevation the higher synthesizing efficiency in the condition of the same relative positioning precision and channel delay calibration precision. At the same value of precision, the channel delay calibration precision has a greater impact on synthesizing efficiency compared than the relative positioning precision.

In addition, under the condition $\sigma_1 = 0$, the trends of synthesizing efficiency with σ_2 is equivalent to the trends with σ, as shown in Fig. 6c. Statistical synthesizing efficiency under typical phase compensation precision is shown in Table 2.

When antenna elevation beam scanning range is $[\pi/18, \pi/2]$, phase precision is required to not exceed 0.2 to achieve a synthesizing efficiency of 75 %. And synthesizing efficiency can be improved by reducing the power combining elevation beam scanning range while the antenna relative positioning precision determined.

6 Conclusion

In this paper, with the background of the navigation signal quality analysis, combining with flexibility of small-diameter antenna and utilization of existing resources, distributed antenna array signal enhancing techniques in ground station was analyzed, and the main conclusions are as follows:

- Beam and gain can be flexibly arrayed by lots of small-diameter antenna which means the distributed signal enhancing techniques is compatible for multi-target tracking and single target enhancing.
- PPP, fiber two-way time synchronization and transmission technology can solve the demand for the distributed signal processing.
- When antenna elevation beam scanning range is $[\pi/18, \pi/2]$, phase compensation precision shall not exceed 0.2 to achieve synthesizing efficiency of 75 %.

The techniques can be applied to satellite navigation, space TT and C ground stations and other areas for miniaturization and low power construction. The architecture can improve monitoring capabilities for downlink signal. Also it is conducive to strengthen the flexibility of ground stations and warfare capability of the overall system navigation.

References

1. Elliott DK, Christopher JH (2006) Understanding GPS: principles and application, 2nd edn. Artech House Inc., Boston
2. Wang Y, Xiao L, Su X et al (2013) Joint transmit antenna selection in distributed antenna system. J Tsinghua Univ (Sci Technol) **53**(7):951–954
3. Baoling LIU et al (2005) MIMO detection algorithm based on generalized distributed antenna array systems. J Beijing Univ Posts Telecommun 5(28):38–41
4. Yin QY, Jia SQ, Zuo SL et al (2013) A distributed multi-antenna space hopping transceiver technique. J Xi'an Jiaotong Univ 1(47):1–6
5. da Silveira MW, Odendaal JW, Joubert J (2001) Same cell co-channel interference reduction using multiple spatially distributed adaptive array systems. Sig Process 81:2059–2068
6. Jw Lazio T (2013) The square kilometre array pulsar timing array. Class Quantum Gravity 30:1–14
7. SCAWG (2006) NASA space communication and navigation architecture recommendations for 2005–2030. NASA's Glenn Research Center, Cleveland, pp 1–165
8. Zhu XW (2007) Key technology study on time synchronization in satellite navigation system. National University of Defense Technology, Changsha
9. Xu G, Xu Y, Shi MY et al (2013) Impact of random phase error on microwave power Synthesizing efficiency. High Power Laser Part Beams 25(11):2914–2918
10. Zhang XH, Guo F, Li XX (2012) A novel Stop & Go GPS precise point positioning (PPP) method and its application in geophysical exploration and prospecting. Surv Rev 44(327):251–255
11. Zhang J, Zhou DM (2014) Research on time two-way transfer with single wavelength single fiber. J Optoelectron Laser 25(10):1968–1976
12. Balanis CA (1982) Antenna theory: analysis and design. Harper & Row Publishers, New York
13. Guochang Xu (2007) GPS theory, algorithms and application, 2nd edn. Springer, Berlin

Signal Design of High Accuracy Terrestrial Pseudolites System in BeiDou RDSS Frequency Band

Chenglong He and Baoguo Yu

Abstract Beidou high precision terrestrial navigation system is a passive and independent navigation system composed of terrestrial pseudolites and built for high precision positioning purpose. In the frequency band (2.4835–2.5 GHz) where RDSS works, a comprehensive analysis was made to such design factors as bandwidth, modulation, message, and time-hopping pattern in the signal design of BeiDou terrestrial pseudolites system from the perspective of compatibility and high-precision ranging, with the emphasis on the signal ranging performance, compatibility between ground signal and signal in space as well as the influence of near-far effect between terrestrial pseudolite signals to receiver ranging. Upon it, another analysis was made to the design requirements for subcarrier modulation mode and pseudolite time-hopping pattern. On the basis of 10,230-long Weil code, a time-hopping terrestrial pseudolite signal was developed. Besides, a semi-physical verification platform was built, which was used to verify the high precision positioning performance of the interested signal. The signal test results showed that it enabled the receiver to gain a near 4 cm static positioning accuracy.

Keywords Beidou terrestrial pseudolite · High precision positioning · Multiple access interference (MAI) · Subcarrier modulation · Time-hopping (TH) pattern

1 Introduction

Restricted by uncertainty due to signal propagation error and signal masking problem, it is difficult for a satellite navigation system to implement high precision positioning and continuous positioning in a complex environment without other supports such as differential units. With the capability of transmitting the signals similar to navigation GNSS signal, pseudolites can be used to transmit redundant

C. He (✉) · B. Yu
State Key Laboratory of Satellite Navigation System and Equipment Technology,
No. 589 West Zhongshan Road, Shijiazhuang, China
e-mail: hechenglong743@sina.com

J. Sun et al. (eds.), *China Satellite Navigation Conference (CSNC) 2016 Proceedings: Volume II*, Lecture Notes in Electrical Engineering 389,
DOI 10.1007/978-981-10-0937-2_25

navigation signals so as to improve the coverage of satellite navigation signal, the positioning continuity in a masking environment and the geometric distribution of satellite navigation signal in addition to better ranging accuracy, and easiness to achieve high precision positioning performance independently. In recent years, the technology of independent pseudolites system has received more attention and development. For example, Locata uses the signal in ISM frequency band and TimeLoc time synchronization technique to have achieved centimeter-level positioning accuracy, which has been applied to such applications as mining, bridge monitoring, and shooting range measurement.

BeiDou high precision terrestrial navigation system is a passive independent navigation system composed of terrestrial pseudolites and established for high precision positioning purpose. In the design of pseudolite signal to be working in *S* band for RDSS, it is required to consider information, frequency domain, and time domain for high-precision ranging purpose as well as the compatibility with RDSS GNSS signal. Based on an analysis of spectral separation coefficient and multiple access interference compatibility, particular importance should be attached to the design of subcarrier modulation and TH pattern, so as to improve the compatibility between the internal and the external of the pseudolite navigation system.

2 High-Precision Terrestrial Pseudolites System

The terrestrial pseudolites system is composed of several static pseudolites whose exact positions are known. Under the condition of high-precision time synchronization among these pseudolites, it is possible to achieve positioning by receiving the navigation signals broadcasted from four or more pseudolites. Since terrestrial pseudolites are characterized by supporting millimetre-precision coordinate measurement, short signal propagation path, free from the ionospheric effect and stratospheric effect and less influence by the medium sublayer of the tropospheric layer, it is easy to achieve high precision positioning performance with the support of good geometric layout.

In a terrestrial pseudolites system with a fixed central node, when the central node of the terrestrial pseudolites system is synchronized with a space system by means of satellites time service, the receiver can achieve positioning jointly with GNSS signal and pseudolite signal. Comparing with most radio navigation technologies, pseudolites make full use of the ranging advantage and technical achievements of spread-spectrum signal to achieve high-performance positioning without the help of a differential system. With such features of low cost and deployment convenience, a pseudolites navigation system can be deployed in a masking environment like indoors, mountainous area or jungle to provide continuous navigation service or provide backup navigation capability when the navigation satellite signals are interfered in.

Working in BeiDou RDSS frequency band, a high-precision terrestrial pseudolites system is designed, with the major design considerations as follows:

- The RDSS frequency band can provide about 16 MHz bandwidth resource. Since the more high-frequency components exist in the signal power spectrum and the wider is Gabor bandwidth, the better antinoise and anti-multipath performance will be achieved. For a navigation receiver, the design bandwidth is typically within 20 MHz; therefore, bandwidth resource is available in this frequency band.
- Since the RDSS frequency band is only used for navigation and short message communication of BeiDou Navigation System, it is not required to give complicated multisystem compatibility analyses, preferable in design space in comparison with *L* band.
- It is compatible with some hardware resources of RDSS receiver in addition to better hardware compatibility and functional expandability in comparison with ISM frequency band.

There are three fundamental problems to resolve for a terrestrial pseudolites system to achieve high precision positioning independently, i.e., how to achieve high-precision time synchronization, how to achieve high-precision ranging and how to restrain the environmental errors in ranging. To overcome the above three problems to the maximum, it is required to take full consideration of such factors as signal bandwidth, pseudocode, message rate, and contents in the signal design, thus to satisfy the requirements for receiving, ranging, multipath mitigation, noise suppression, and information updating rate. On the other hand, the near-far effect among pseudolites may cause inter symbol interference in a specific environment, which might even become the dominant source to ranging error. When the pseudolites are about to work in GNSS frequency band, it must be assured that the GNSS signal receiving will not be affected even if positioning compatibility is not achievable. Therefore, consideration must be given to the assessment and improvement of signal compatibility in signal design.

Here, for the design of pseudolite signal, an analysis and assessment is given to the most critical internal and external system compatibility in RDSS frequency band in addition to relevant signal parameter design.

3 Compatibility Analysis of Pseudolite/RDSS Signals

Signal compatibility of navigation systems refers to the mutual effects between signals resulting from a series of signal processing like acquisition, tracking, and positioning are acceptable. The terrestrial navigation signal, which is about to work in RDSS frequency band, must be compatible with the GNSS signal.

For a band spread system, the interference between different signals is essentially the multiple access interference between code streams after down conversion, which depends on channel filtering, signal spread-spectrum codes, and subcarrier

modulation codes. When the spread-spectrum codes are unknown, it is possible to assess the frequency spectrum generated from subcarrier modulation codes. Here, SSC and code tracking spectral sensitivity coefficient (CT_SSC) are used for assessment of the compatibility between terrestrial pseudolite signal and RDSS signal.

By estimating the composition of equipper interference signal in the power spectrum envelope of the desired signal, SSC is used to reflect the effect of the interference signal to the CNR of the desired signal.

$$\mathrm{SSC} = \frac{\int_{-\mathrm{Br}/2}^{\mathrm{Br}/2} G_{\mathrm{s}}(f) G_{\mathrm{i}}(f) H(f) \mathrm{d}f}{\int_{-\mathrm{Br}/2}^{\mathrm{Br}/2} G_{\mathrm{s}}(f) H(f) \mathrm{d}f} \tag{1}$$

Where, Br represents the processing bandwidth of the receiver, $G_{\mathrm{s}}(f)$ and $G_{\mathrm{i}}(f)$ represent the power spectra of the desired signal and the interference signal, respectively, and $H(f)$ represents the transfer function of filter. When the transfer function of filter is 1, SSC may be simplified as

$$\mathrm{SSC} = \int_{-\mathrm{Br}/2}^{\mathrm{Br}/2} G_{\mathrm{s}}(f) G_{\mathrm{i}}(f) \mathrm{d}f \tag{2}$$

By estimating the overlap level of the intersystem signal power spectrum components in different frequency bands, CT_SSC is used to reflect the effect of interference signal to the ranging performance of the desired signal. Assuming the interval between the lead-lag correlators is Δ, then CT_SSC can be expressed as

$$\mathrm{CT\_SSC} = \frac{\int_{-\mathrm{Br}/2}^{\mathrm{Br}/2} G_{\mathrm{s}}(f) G_{\mathrm{i}}(f) H(f) \sin(\Delta \pi f)^2 \mathrm{d}f}{\int_{-\mathrm{Br}/2}^{\mathrm{Br}/2} G_{\mathrm{s}}(f) H(f) \sin(\Delta \pi f)^2 \mathrm{d}f} \tag{3}$$

If the extreme interval of narrow band correlators is $\Delta \to 0$, then the above expression can be simplified as

$$\mathrm{CT\_SSC} = \frac{\int_{-\mathrm{Br}/2}^{\mathrm{Br}/2} G_{\mathrm{s}}(f) G_{\mathrm{i}}(f) f^2 \mathrm{d}f}{\int_{-\mathrm{Br}/2}^{\mathrm{Br}/2} G_{\mathrm{s}}(f) f^2 \mathrm{d}f} = \frac{\mathrm{C\_SSC}}{\int_{-\mathrm{Br}/2}^{\mathrm{Br}/2} G_{\mathrm{s}}(f) f^2 \mathrm{d}f} \tag{4}$$

Where C_SSC represents the code tracking spectrum splitting coefficient. Hence, to suppress the interference between the terrestrial pseudolite signal and the RDSS signal, it is required to reduce the overlap level of intersystem signal power spectra in the signal spectrum design, prevent the spectrum peak from occurring at the same frequency point, and reduce the overlap of high-frequency spectrum components.

In the design of terrestrial pseudolite signal spectrum in RDSS frequency band, there are two or three concerns, i.e., how to acquire the signal ranging advantage by

Table 1 Candidate modulation modes for a terrestrial pseudolite system

No	Modulation mode	Center frequency (MHz)
1	$BOC_s(4,1)$	2491.75
2	$BOC_c(4,2)$	2491.75
3	$BOC_s(4,2)$	2491.75
4	$BOC_c(4,2)$	2491.75
5	AltBOC(4,1)	2491.75
6	AltBOC(4,2)	2491.75
7	BPSK(1)	2491.75 ± 4.092
8	BPSK(2)	2491.75 ± 4.092
9	BOC(2,1)	2486.635
10	BOC(2,2)	2487.658

utilizing the bandwidth resource and provide a space for improving message rate, how to acquire noise suppression and multipath mitigation advantages by increasing the high-frequency signal components in the conditions of high bandwidth, and how to improve the system application value by maximizing the compatibility with the RDSS GNSS signal. Under the above guideline, the potential modulation modes of a terrestrial pseudolite system are provided in Table 1.

Assuming that the processing bandwidth Br of receiver is 16 MHz, the comparison of the major parameters between different modulation modes shown in Table 2.

Where, the serial number No = 0 represents QPSK(4) modulation used by RDSS GNSS signal with the center frequency at 2491.75 MHz. Based on the calculation results shown in the above table, it is known that BPSK(1)\BPSK(2)\BOC(1,1) can reduce the chance of peak overlap with RDSS GNSS signal by means of frequency offset; however, the ranging performance is still poor due to

Table 2 Comparison of candidate modulation modes for a terrestrial pseudolite system

No	SSC	C_SSC	Main bandwidth (MHz)	Gabor (dBHz/main bandwidth)	Gabor (dBHz/16 MHz)
0	−67.8822	−7.1719	8.184	70.47	71.97
1	−79.9343	−13.5313	10.23	74.49	74.85
2	−86.0652	−14.1860	10.23	74.83	75.11
3	−76.9239	−10.5207	12.276	74.68	74.70
4	−83.0562	−11.1790	12.276	74.96	75.24
5	−82.0963	−13.1484	10.23	75.31	75.45
6	−79.0864	−10.1407	12.276	75.40	75.45
7	−77.4322	−8.3604	6.136	71.67	–
8	−75.6634	−7.7858	6.136	71.95	–
9	−74.3484	−8.9664	8.184	71.35	–
10	−72.1192	−6.6324	8.184	72.46	–

relatively fewer high-frequency components and the signal compatibility is poor due to too much spectrum overlap of BOC(2, 2).

In terms of multipath mitigation performance, the interval between lead-lag correlators are different in different modulation modes. Besides, there are a great variety of optimization modes, e.g., multi-correlator processing; therefore, it is impossible to make a perfect assessment. Since different modulation modes have different advantages in multipath mitigation, noise suppression, and signal compatibility, it is required to compromise in compatibility, positioning performance, and bandwidth when selecting pseudolite modulated signal.

4 Intrasystem Compatibility Analysis of Pseudolites System

In comparison with a satellite navigation system, the signal link of a terrestrial pseudolite system is relatively stable; therefore, the intrasystem near-far effect in a terrestrial pseudolite system is not simply the CNR effect, but what is more, the effect of multiple addresses among signals to ranging.

Since the signal of a terrestrial pseudolite system is constant for a short time, the MAI effect to ranging is used to assess the intrasystem compatibility here. For a static receiver, the received signal can be expressed as

$$\begin{cases} \mathrm{r}(t) = \mathrm{s_r}\ (t) + \sum\limits_{i=1}^{\mathrm{m}} \mathrm{s}_i(t) + \mathrm{n}(t) \\ \mathrm{s}_i(t) = p_i\ d_i\ \mathrm{P}_i\ (t_i)\ \mathrm{e}^{j\theta_i} \end{cases} \tag{5}$$

Where $\mathrm{S_r}(t)$ represents the desired signal, $\mathrm{S}_i(t)$ represents the received other pseudolite signal and multipath signal, p_i represents the relative power of the interference signal, d_i and P_i represent the relative message and pseudocode data, respectively, τ_i represents the relative time delay of signal and θ_i represents the relative phase magnitude. Then the correlation output of the desired signal is expressed as

$$\mathrm{R} = \mathrm{R}_r + \sum_{i=1}^{m} p_i d_i \mathrm{R}_{r,i}(\tau_i)\cos(\theta_i) + \mathrm{n}(t) \tag{6}$$

If the interval between the lead-lag correlators of a receiver is 2d, then

$$\sum_{i=1}^{m} p_i d_i \mathrm{R}_{r,i}(d)\cos(\theta_i) \neq \sum_{i=1}^{m} p_i d_i \mathrm{R}_{r,i}(-d)\cos(\theta_i) \tag{7}$$

The interference signal will bring effect to the ranging error δt. In static or low dynamic positioning condition, the relative time delay τ of a terrestrial pseudolite

system between intrasystem signals is approximately constant. The constant ranging offset generated for a short time will make the expectation of ranging error $E(\delta t) \neq 0$.

Assuming a single channel of interference signal, the main peak slope of the desired signal is $\pm k_r$, an interference correlation peak of slope k_u exists in the main peak, the delay between the correlation right end and the correlation center of the desired signal is $\Delta\tau$ and the pseudocode width is T, then in the interval

$$\Delta\tau \in \left[\left(\frac{p_i d_i k_u \cos(\theta_i)}{k_r} + 1\right)d, \left(\frac{p_i d_i k_u \cos(\theta_i)}{k_r} - 1\right) + T\right] \tag{8}$$

the maximum ranging error that is possible to occur can be expressed as

$$\delta t_{\max}(k = k_u) = \frac{k_u}{k_r} p_i d_i d \cos(\theta_i) \leq \frac{k_{u,\max}}{k_r} p_i d_i d \tag{9}$$

When both ranging signal and interference signal are received, since their cross-correlation forms are the same and the slopes k_r of their normalized correlation peaks are approximately the same, the maximum ranging error incurred thereby can be expressed as

$$\delta t_{\max} = \frac{k_{u,\max}}{k_r p_i^2} d d_i \tag{10}$$

In case of multipath interference, cross-correlation would bring about more complicated effects. When it becomes worse, a number of cross-correlation peaks overlap with one another and create a ghost peak, which might cause error trapping or even error lock. With reference to Eqs. (9) and (10), it is concluded that MAI has constant ranging effect to the signal in static link, which is highly correlated with the power ratio and the correlation slope ratio. When signal A is less affected by Signal B in terms of ranging, the effect of Signal B to Signal A might be higher by p_i^2 times.

As per Eq. (9), the techniques to suppress the ranging effect between terrestrial pseudolite signals include using low-correlation pseudocodes family and reducing the signal power difference. When it is difficult to resolve the problem by means of pseudocodes, it is possible to suppress the interference between signals in frequency domain or in time domain by means of frequency division or time division, i.e., use TH-DS/CDMA or FH-DS/CDMA modes in signal transmitting control of terrestrial pseudolites.

In time-hopping mode, the terrestrial pseudolite signal can be expressed as

$$\begin{cases} s_{\mathrm{TH}}^{(i)}(t) = s_i(t) \times \mathrm{T}^{(i)}\left(\left\lfloor (t - \varepsilon^{(i)}(t))/\mathrm{T_{DS}} \right\rfloor\right) \\ \mathrm{T}^{(i)}(n) = 1 \backslash 0 \end{cases} \tag{11}$$

Where, $\mathrm{T}^{(i)}(n)$ represents the TH sequence composed of 1 and 0, $\varepsilon^{(i)}(t)$ represents the protective time slot synchronized regularly and TDS represents the pseudocode period. Different pseudolites must satisfy that

$$\mathrm{T}^{(i)}\left(\left\lfloor (t-\varepsilon^{(i)})/\mathrm{T_{DS}}\right\rfloor\right) \neq \mathrm{T}^{(j)}\left(\left\lfloor (t-\varepsilon^{(j)})/\mathrm{T_{DS}}\right\rfloor\right) \tag{12}$$

As a TH type, only a pseudolite is allowed to transmit signal at any time. The protective time slot $\varepsilon^{(i)}(t)$ might be accumulated due to different distances from a receiver, which would cause changed time slot when receiving two adjacent TH signals. Let us assume that $\Delta\varepsilon(t0)$ represents the time slot between the signals coming from pseudolite 1 and pseudolite 2 at the moment t0, $l^{(1)}$ and $l^{(2)}$, respectively, represent the distances between the receiver and pseudolite 1/pseudolite 2 when pseudolite 1 signal arrives and pseudolite 2 signal disappears. Regardless of the system synchronous error and the clock error drift of receiver, then, when $l^{(1)} - l^{(2)} < c\Delta\varepsilon(t0)$, the receiver will simultaneously receive the signals coming from pseudolites 1 and 2 within the interval of $[t_0\text{-}\Delta\varepsilon(t0),t_0]$. Here, we define the TH collision coefficient at the receiver is

$$k = \frac{l^{(1)} - l^{(2)} - c\Delta\varepsilon(t0)}{c\mathrm{T_{DS}}} \tag{13}$$

At the receiver end, the TH interference signal truncated by proportion k still causes cross-correlation interference. Taking U(t) as step signal, the interference in the correlation process of the truncated signal can be expressed as

$$\begin{cases} \mathrm{R}_{\boldsymbol{I}} = [s_{\boldsymbol{I}}(t)\mathrm{Y}(t) \otimes s_{\mathrm{Q}}(t)]\cos\phi_{\boldsymbol{I}}(t)\mathrm{H}(t) \\ \mathrm{Y}(t) = \mathrm{U}(t + k\mathrm{T_{DS}}) - \mathrm{U}(t + \mathrm{T_{DS}}) \\ t \in [0, \mathrm{T_{DS}}] \end{cases} \tag{14}$$

The ranging interference generated by cross-correlation is also subject to Eq. (9), but the effect level to ranging is also related to k. In the terrestrial pseudolite system, restricted by receiver sampling range and deployment conditions, the actual coverage area of a single pseudolite is not too large; plus, considering the limited front-end bandwidth of receiver and the design length of available pseudocodes, the TDS will not be less than 100us; therefore, within the collision, the following expression is typically satisfied.

$$l^{(1)} - l^{(2)} - c\Delta\varepsilon(t0) \leq cT_{DS} = 30\mathrm{Km} \tag{15}$$

In other words, in a service area where the range difference is not more than 30 km, no collision will happen between non-adjacent TH signals and a terrestrial pseudolite signal may be exposed to the interference of two adjacent TH signals at most.

For TH/DS-CDMA pseudolites system, three factors should be taken into account in the design of TH pattern.

First, a terrestrial pseudolite system is required to have good spacial distribution to reduce the DOP distribution within the coverage area in addition to satisfying the requirement for signal ranging performance; therefore, the more pseudolites are required if possible to meet the deployment needs. However, along with the increase of pseudolite number, the ranging updating rate will decrease under the effect of TH signals; therefore, a high-precision pseudolites system is virtually a capacity-restricted system. In the design of TH pattern, compromise is required between updating rate and system capacity.

Secondly, when the capacity is maximized, it is required to cancel or reduce the protective time slot between TH blocks. In such a case, for two adjacent to TH signals, there must be a zone that satisfies $k > 0$. In other words, there must be a zone where the ranging is affected due to partial collision between two signals; and there must be a zone where no collision occur at all because the range difference is reversible. In high precision positioning, it will be ideal that the desired signal is not partially collided by two adjacent TH blocks in a certain TH period. The receiver may also make use of the track data in this period for high-precision ranging even if the desired signal is interfered in all other periods. This design requirement can be expressed as

$$\begin{aligned} &\forall i \neq j \neq v,\ \exists \mathrm{n}_0,\ n_1 \in [1, N/M] \\ &\begin{cases} \mathrm{T}^{(i)}(n_0) = \mathrm{T}^{(j)}(n_0 - 1) = \mathrm{T}^{(v)}(n_0 + 1) = 1 \\ \mathrm{T}^{(i)}(n_1) = \mathrm{T}^{(j)}(n_1 + 1) = \mathrm{T}^{(v)}(n_1 - 1) = 1 \end{cases} \end{aligned} \tag{16}$$

Where, N represents the number of TH blocks corresponding to the system TH period and M represent the system capacity. In other words, the desired signal will not be affected by the lead or lag collision with the two adjacent signals. As per Eq. (16), it is possible to know the preliminarily constraint to capacity and period in the TH pattern.

$$M(M-1) \leq \frac{N}{M} \tag{17}$$

For example, in a system whose design capacity is 5, the TH period should never be less than 20TDS; in a system whose design capacity is 10, the TH period should never be less than 90TDS.

Finally, pseudorandom nature is required in the TH pattern to improve the synchronizing speed of the TH pattern and to satisfy the non-collision ranging requirement expressed in Eq. (16). It must be noted that in a pseudolites system oriented to regional passive positioning users, the dynamic TH pattern concerning users' locations is not practical. In dynamic positioning, to assure the uniformization of pseudolite ranging information updating rate, macroscopic uniform

distribution is required for $T^{(i)}(n)$ layout of pseudolites in the pseudorandom TH pattern, i.e.,

$$\begin{aligned} &\forall t,\ i \neq j \\ &P(T^{(i)}(\lfloor t/T_{\mathrm{DS}} \rfloor) = 1) = P(T^{(j)}(\lfloor t/T_{\mathrm{DS}} \rfloor) = 1) = \frac{1}{M} \end{aligned} \tag{18}$$

The frame-structured pseudolite signal will satisfy this requirement. Specifically, try to divide a TH-sequenced full period into several frames of the same length. All the pseudolites must transmit signals at equal probability within every frame. In this way, the TH sequences from M psuedolites will form the system TH pattern.

$$R_{\mathrm{TH}} = \begin{bmatrix} \mathrm{Frame1} \\ \mathrm{Frame2} \\ \cdots\cdots \\ \mathrm{Frame}\frac{N}{M} \end{bmatrix} = \begin{bmatrix} 1 & 2 & 3 & 4 & \ldots & M \\ 4 & 2 & 1 & M & \ldots & M-m \\ \ldots & \ldots & \ldots & \ldots & \ldots & \ldots \\ 2 & 5 & 3 & 1 & \ldots & M-n \end{bmatrix} \tag{19}$$

The layout of frame-formated TH can be known with several $M \times M$ sequential shift matrixes by means of pseudorandom permutation line.

5 Test and Verification

A group of terrestrial pseudolite signals are designed in response to the signals working in RDSS frequency band, which are summarized as follows:

- Center frequency: 2491.75 MHz
- Modulation mode: $\mathrm{BOC_C}(4,1)$
- System capacity: 5
- Pseudocode: 10230Weil/1.023Mcps
- Message: 500 bit/20 bps
- TH pattern: pseudorandom 5×50

A semi-physical simulation and verification platform was established with the aid of hardware to test the ranging and positioning performance of the signal in IF band. On the platform, the pseudolite baseband signal board was used to generate five pseudolite baseband signals at the preset range difference. In the test, the pseudolite time synchronization error and the clock error drift were not set.

The system compatibility was assessed by means of sampling the observation data of the pseudolite signal and simulating the RDSS GNSS signal. In the test, the thermal noise was approximately −171dBmW/Hz and the received power was set to −170 to−130 dBW. SSC was estimated with reference to the power spectrum envelope. With interference simultaneously coming from five psuedolites, the results show that maximum effect was approximately 3 % when an RDSS receiver tried to receive in 8 MHz bandwidth.

The signal positioning measurement data sampled from other than the central zone were recorded and analyzed, with the result shows the MAI effects at different pulses when random TH pattern was used. In the non-collision zone, the minimum positioning accuracy was 1.5 cm. In case of collision and powerful pseudolite interference signal, the positioning error was diverged to 20–30 cm. In the testing process, the mean positioning error in several positioning tests was approximately 4 cm.

6 Conclusion and Prospect

This paper describes the signal design of a terrestrial pseudolite system working in RDSS frequency band. The emphasis is set on intrasystem and intersystem compatibility and high precision positioning in the analyses and design. An analysis is made to the collision effect to ranging due to range difference in TH signal format and the critical design factors for TH pattern. With the aid of a semi-physical test platform, the compatibility and positioning performance of a pseudolite signal was verified. The test result shows that the system positioning accuracy was approximately 4 cm on average and 1.5 cm to the maximum, which verified the performance of this pseudolite signal.

In the future, more work will be done for further optimization of the signal design, function expansion, and integration with pseudolite time synchronization.

References

1. Cobb HS (1997) GPS pseudolites: theory, design and applications. California Stanford University, The GNSS Signal
2. Edward Alan LeMaster (2002) Self-Calibrating Pseudolite Arrays: theory and experiment. California Stanford University, The GNSS Signal
3. Matsuoka M, Rock SM, Bualat MG (2004) Autonomous deployment of a self-calibrating pseudolite Array for Mars rover navigation. Position Location and Navigation Symposium, pp 733–739
4. LeMaster EA, Matsuoka M, Rock SM (2002) Field demonstration of a Mars navigation system utilizing GPS pseudolite transceivers. Position Location and Navigation Symposium, pp 150–155
5. LeMaster EA, Matsuoka M, Rock SM (2003) Mars navigation system utilizes GPS. Aerospace and Electronic Systems Magazine, pp 3–8
6. CETC54: Interface control document for OTE, Vol 1 Revision 0'
7. Luan Rui Xu, Weiming JL, Lihua Z (2009) Time synchronization technologies for pseudolites positioning system. Meas & Control Technol 06:43–46
8. Rizos C, Roberts G, Barnes J, Gambale N (2010) Experimental results of locata: a high accuracy indoor positioning system, International Conference on Indoor Positioning and Indoor Navigation, Switzerland, pp 15–17 Sep 2010
9. Barnes J et al (2006) A positioning technology for classically difficult GNSS environments from Locata. In Symposium on Position Location and Navigation IEEE/ION, pp 715–721

Wireless Time Synchronization for Multiple UAV-Borne Pseudolites Navigation System

Chenglong He, Baoguo Yu and Zhixin Deng

Abstract Pseudolites system provide positioning service based on a ranging process similar to Global Navigation Satellite System (GNSS) that need all transmitters have consistent reference time and frequency. In airborne pseudolites navigation system applications, all UAVs are move continually and it is impossible to achieve real-time precision flight trajectories, which have more challenge for wireless time synchronization. This study provides a method based on direct two-way time and frequency transfer (TWTFT) link that calculate the clock difference by ranging differential delay and error compensating without UAVs' accurate position. In addition, analysis of the synchronization performance in high dynamic and jamming situation will be showed by showing the effect of pseudolites clock drift, Sagnac and unsymmetrical interference. A software simulation and hardware test results are provided.

Keywords Pseudolites · Synchronization · Sagnac · Frequency shift

1 Introduction

Promoting receivers' performance in denial and degraded environment is a key goal of GNSS modernization process. A set of technical methods were implemented to reach the goal include design new signals of high associate gain code, transmit through on-board multi-beam antenna, embed efficiency receiving and positioning methods and so on. Pseudolites is a transmitter effectively enhances the received signal power, quantity and geometric distribution by providing extra navigation signal and ranging process similar to satellite navigation [1]. Moreover,

C. He (✉) · B. Yu · Z. Deng
State Key Laboratory of Satellite Navigation System and Equipment Technology,
No. 589 West Zhongshan Road, Shijiazhuang, China
e-mail: hechenglong743@sina.com

J. Sun et al. (eds.), *China Satellite Navigation Conference (CSNC) 2016 Proceedings: Volume II*, Lecture Notes in Electrical Engineering 389,
DOI 10.1007/978-981-10-0937-2_26

positioning system composed of several pseudolites support independent operation mode where precise time synchronization among the transmitters is needed [3–5].

Time synchronization methods of early pseudolites systems are based on GPS timing which higher than 30 ns [1]. To achieve ns-level accuracy, [6] provide a method that ranging differential delay between a monitor station and all pseudolites which are fixed positioned within narrow bounds. While in moving situation such as the system composed of several UAVs, the time-varying trajectory and straight constant distance between arbitrary transmitters lead the methods inappropriate. To satisfy the need of certain application [7] provides a macro-analysis of two-way time and frequency transfer synchronization method for airborne pseudolites system. The paper will provide an exhaustive description of the effects of clock drift on TWTFT accuracy, and the synchronization performance under dynamics and jamming. To support the analysis a set of theoretical experiments were developed in state key laboratory and its microwave darkroom. The paper is organized as follows. Section 2 will provide a detailed description of the synchronization method and clock difference calculate process. Section 3 will provide the effects of clock characteristics on synchronization error. Then Sects. 4 and 5 will analysis the synchronization performance under dynamics and jamming. Finally Sects. 6 and 7 will show the steps of experiment and its results to support the above discussion.

2 TWTFT for UAV-Borne Pseudolites

Traditional pseudolites system adopted wireless method ranging and contrasting signal transmit distances from each pseudolite $1 \sim N$ to a fix or ascertained coordinate point to calculate the time differences. The synchronization process could be described as,

$$\rho_i = l_{i,0} + g_{i,T} + g_{0,R} + \tau_{i,0} + c(\delta t_0 - \delta t_i) + \varepsilon,\ i = 1 \sim N \tag{1}$$

The monitoring receiver calculate pseudo-ranges ρ_i of each transmitter composing of linear distance from pseudolite to receiver $l_{i,0}$, group delay of transmitter $g_{i,T}$ and receiver $g_{0,R}$, tropospheric delay $\tau_{i,0}$, clock error difference $\delta t_0 - \delta t_i$ of receiver and transmitter error ε caused by thermal noise, multi-access interference and multipath. The clock difference of pseudolites could be figured out by

$$\delta t_i - \delta t_j = \frac{1}{c}(\rho_j - l_{j,0} - g_{j,T} - \tau_{j,0} - \rho_i + l_{i,0} + g_{i,T} + \tau_{i,0}) + \varepsilon \tag{2}$$

It could achieve satisfactory synchronization accuracy of ns-level even ps-level after adopting superior error modification methods for tropospheric and group delay [8–10]. However, its performance severely relies on the signal propagation model's precision and the position accuracy of receiver and pseudolites, additionally, and the clocks' shift during the synchronization process which will be analyzed later.

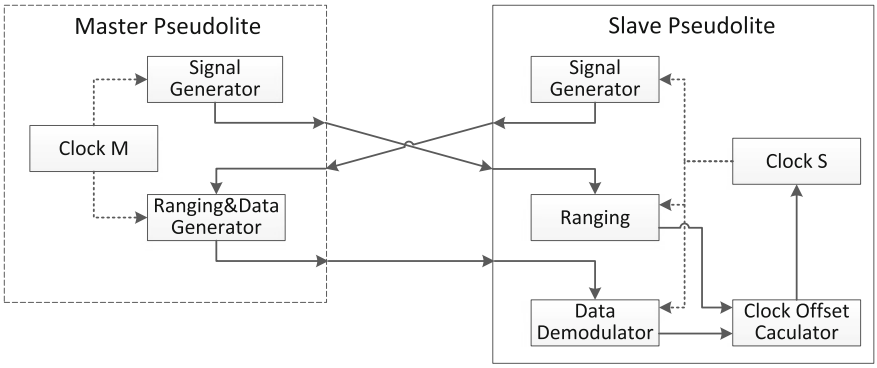

Fig. 1 Signal transmit and processing of TWTFT

To avoid the insufficient, a position irrelevant method TWTFT is adopted, as shown in Fig. 1. The slave pseudolite (SPL) is defined as the transmitter that adjust its clock to consistent with the master pseudolite (MPL), which wouldn't change its clock or just consistent with GNSS.

The pseudolites transmits ranging signal to each other at presupposed time points $t_i = \{t_0, t_1, t_2, t_3 \cdots\}$, and the ranging results of MPL and SPL could be described as

$$\begin{cases} \rho_M = l_{S,M} + g_{S,T} + g_{M,R} + \tau_{S,M} + c(\delta t_M - \delta t_S) + \varepsilon \\ \rho_S = l_{M,S} + g_{M,T} + g_{S,R} + \tau_{M,S} + c(\delta t_S - \delta t_M) + \varepsilon \end{cases} \tag{3}$$

The subscripts of l and τ stand of signal transmitted direction, for example, $l_{S,M}$ means the linear distance from SPL to MPL. The ranging result ρ_M will be transmitted in MPL signal with the time point index for calculation matching.

For the transmit antenna (TX) and receive antenna (RX) of pseudolite are close to each other or a same antenna by duplex measurements, the pair of space links are almost the same, which means

$$\begin{cases} l_{S,M} \approx l_{M,S} \\ \tau_{S,M} \approx \tau_{M,S} \end{cases} \tag{4}$$

Additionally, transmitter and receiver group delays would be regarded as the same in the case that all pseudolites are composed of same hardware. As a result, the time difference could be figured out in slave pseudolite by

$$\begin{aligned} \delta t_S - \delta t_M &\approx \frac{1}{2c}(\rho_S - \rho_M) + (g_{S,T} - g_{M,T} + g_{M,R} - g_{S,R}) \\ &\approx \frac{1}{2c}(\rho_S - \rho_M) \end{aligned} \tag{5}$$

A significant advantage is there is no need to calculate the precise position of pseudolites and the space transmit errors, which is more applicable for airborne pseudolites system. While TWTFT severely relies on the consistency and symmetry of bidirectional links, all conditions that caused asymmetrical ranging would affect the synchronization performance certainly, which include the clock drift, Sagnac effect and jamming.

3 Effects of Pseudolites Clock Drift

Accurately, the ranging signals' real transmit time points of MPL and SPL $\{t_{\mathrm{MT}}, t_{\mathrm{ST}}\}$ satisfied

$$\begin{cases} t_{\mathrm{MT}} + \delta t_M(t_{\mathrm{MT}}) = t_i \\ t_{\mathrm{ST}} + \delta t_S(t_{\mathrm{ST}}) = t_i \end{cases} \tag{6}$$

The real received time points are

$$\begin{cases} t_{\mathrm{MR}} = t_{\mathrm{ST}} + \frac{1}{c}(l_{S,M} + g_{S,T} + g_{M,R} + \tau_{S,M}) \\ t_{\mathrm{SR}} = t_{\mathrm{MT}} + \frac{1}{c}(l_{M,S} + g_{M,T} + g_{S,R} + \tau_{M,S}) \end{cases} \tag{7}$$

Hence the clock error of bidirectional ranging process based on different time, as a result Eq. (3) could be described as:

$$\frac{\rho_S - \rho_M}{c} \approx \delta t_S(t_{\mathrm{ST}}) + \delta t_S(t_{\mathrm{SR}}) - \delta t_M(t_{\mathrm{MT}}) - \delta t_M(t_{\mathrm{MR}}) \tag{8}$$

Another considerable factor is the ranging result transmitting delay, which include modulate delay d_{Mod} and group delay of MPL, free space transmit delay, demodulate delay d_{Dem} and group delay of SPL. The final time point of SPL processing is

$$t_{\mathrm{SP}} = t_{\mathrm{MR}} + d_{\mathrm{Mod}} + d_{\mathrm{Dem}} + \frac{1}{c}(l_{M,S} + g_{M,T} + g_{S,R} + \tau_{M,S}) \tag{9}$$

According to Eqs. (6)–(9), the synchronization error caused by clock would be

$$\sigma_{Clock}(t_{\mathrm{SP}}) = [\delta t_S(t_{\mathrm{SP}}) - \delta t_M(t_{\mathrm{SP}})] - \frac{\rho_S - \rho_M}{2c} = f(\delta t_S) - f(\delta t_M) \tag{10}$$

which includes the clock drift error of SPL and MPL:

$$\begin{cases} f(\delta t_S) = \delta t_S(t_{\mathrm{SP}}) - \frac{\delta t_S(t_{\mathrm{ST}}) + \delta t_S(t_{\mathrm{SR}})}{2} \\ f(\delta t_M) = \delta t_M(t_{\mathrm{SP}}) - \frac{\delta t_M(t_{\mathrm{MT}}) + \delta t_M(t_{\mathrm{MR}})}{2} \end{cases} \tag{11}$$

A simplified model of clock output frequency, frequency drift are

$$\begin{cases} f_{\text{out}} = (f_0 + \Delta f_0) \times [1 + h(T, F, \varphi)] + p(k, t) + \omega \\ \Delta f_{\text{out}} = f_{\text{out}} - f_0 \end{cases} \tag{12}$$

which includes the standard frequency f_0 and its difference Δf_0, temperature-frequency and force-frequency effect $h(T, F, \varphi)$ (φ is direction of force), aging drift $p(k, t)$ and random noise ω. For the clock drift is caused by frequency drift, during time period (t_1, t_2) it could be

$$\Delta\delta t = \delta t(t_2) - \delta t(t_1) = \frac{1}{f_0} \int_{t_1}^{t_2} \Delta f_{\text{out}}(t) \mathrm{d}t \tag{13}$$

the clock drift in Eq. (11) could be expressed as

$$\begin{cases} f(\delta t_S) = \dfrac{1}{f_0} \left[\displaystyle\int_{\text{ST}}^{\text{SP}} \Delta f_{S,\text{out}}(t) \mathrm{d}t - \frac{1}{2} \int_{\text{ST}}^{\text{SR}} \Delta f_{S,\text{out}}(t) \mathrm{d}t \right] \\ f(\delta t_M) = \dfrac{1}{f_0} \left[\displaystyle\int_{\text{MT}}^{\text{SP}} \Delta f_{M,\text{out}}(t) \mathrm{d}t - \frac{1}{2} \int_{\text{MT}}^{\text{MR}} \Delta f_{M,\text{out}}(t) \mathrm{d}t \right] \end{cases} \tag{14}$$

Equations (10) and (14) show the clock drift effect on synchronization performance, which mainly based on the difference of transmit time points and clock frequency accuracy rather than stability. To suppress the clock drift effect, accuracy clocks and frequency correction methods should be applied.

Additionally, for all UAVs are distributed within a region of 300 km and coarse synchronization methods are applied, $t_{\text{SR}} - t_{\text{ST}}$ and $t_{\text{MR}} - t_{\text{MT}}$ are no more than 1 ms, the drift effect mostly due to the modulate and demodulate delay at data speed of 50 or 100 bps, which means UAV high speed data links and special data design are needed.

4 Synchronization Performance Under Dynamics

The dynamics of UAVs would cause asymmetrical ranging in free space of the pair of pseudolites, which is defined as the Sagnac effect [11, 12]. According to Eq. (7), the bidirectional ranging signal transmit paths are

$$\begin{cases} l_{S,M} = \left| \vec{P}_S(t_{\mathrm{MT}} + \dfrac{1}{c} g_{S,T}) - \vec{P}_M(t_{\mathrm{MR}}) \right| \\ l_{M,S} = \left| \vec{P}_S(t_{\mathrm{SR}}) - \vec{P}_M(t_{\mathrm{MT}} + \dfrac{1}{c} g_{M,T}) \right| \end{cases} \tag{15}$$

The $\left\{ \vec{P}_S(t), \vec{P}_M(t) \right\}$ in the equation are the positions of SPL and MPL at an appointed time. As shown in Fig. 2, all UAVs are move toward unpredicted directions continually during the signal transmit period, which lead inconsistent paths.

The UAVs' movement vector are defined as

$$\begin{cases} \vec{M}_S = \vec{P}_S(t_{\mathrm{MT}} + \dfrac{1}{c} g_{S,T}) - \vec{P}_S(t_{\mathrm{SR}}) \\ \vec{M}_M = \vec{P}_M(t_{\mathrm{MT}} + \dfrac{1}{c} g_{M,T}) - \vec{P}_M(t_{\mathrm{MR}}) \end{cases} \tag{16}$$

the difference of the paths would be

$$\begin{aligned} & l_{M,S} - l_{S,M} \\ & = \left| \vec{P}_M(t_{\mathrm{MR}}) - \vec{P}_S(t_{\mathrm{MT}} + \frac{1}{c} g_{S,T}) + \vec{M}_S + \vec{M}_M \right| - l_{S,M} \\ & \in \left[-\left| \vec{M}_S + \vec{M}_M \right|, \left| \vec{M}_S + \vec{M}_M \right| \right] \end{aligned} \tag{17}$$

maximum of $\left| l_{M,S} - l_{S,M} \right|$ would be

$$\left| l_{M,S} - l_{S,M} \right|_{\max} = \left| \vec{M}_S \right| + \left| \vec{M}_M \right| \tag{18}$$

which occurred when the pair UAVs flying in a line with contrary directions.

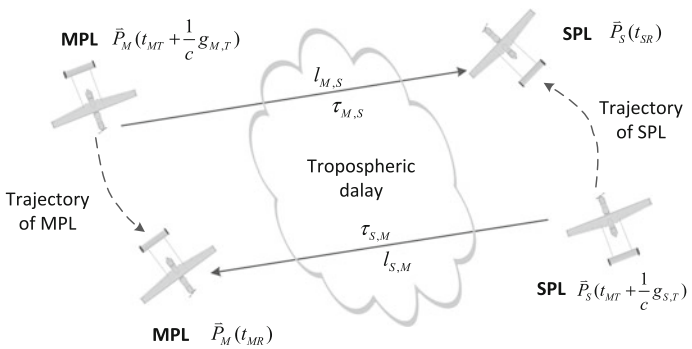

Fig. 2 Bidirectional ranging signal transmit paths of TWTFT

In UAVs steadily flying condition, the movement vectors closely approximates

$$\begin{cases} \vec{M}_S \approx \vec{V}_S(t_{\mathrm{SR}}) \times (t_{\mathrm{SR}} - t_{\mathrm{MT}} - \frac{1}{c} g_{S,T}) \\ \vec{M}_M = \vec{V}_S(t_{\mathrm{MR}}) \times (t_{\mathrm{MR}} - t_{\mathrm{MT}} - \frac{1}{c} g_{M,T}) \end{cases} \tag{19}$$

In view of Eqs. (17) and (19), correction methods based on velocity measurement, direction measurement and ascertainable route planning are suitable for the condition for it could predict and calculate the paths' difference. However the methods are inapplicable for dynamical UAVs with unascertained routes and the Sagnac effect might cause high synchronization error. For example, two UAVs move in 300 m/s, the bidirectional ranging transmit delays are similar to 1.5 ms, the error caused by movement would up to

$$\sigma_{\mathrm{Sag}} = \pm \frac{1}{c} \times 300 \text{ m/s} \times 1.5 \text{ ms} \times 2 \approx \pm 3 \text{ ns} \tag{20}$$

As shown in Fig. 3, an existent special situation that the varied topography might cause one path obstructed or diffraction while another keeps linear transmit, this would cause serious effect for the obstructed path has great ranging error. To avoid the unexpected effect on synchronization performance by topography, all UAVs should flying at suitable altitudes.

Another considerable factor of the Sagnac effect is the difference of tropospheric delays, which is severely relies on the temperature and humidity, while all the parameters would not evidently change within several milliseconds so that the error is generally ignored.

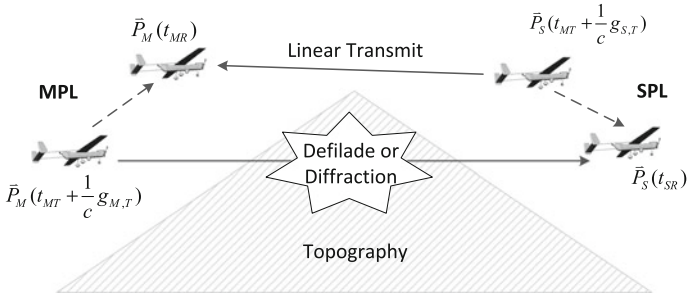

Fig. 3 Topography cause one path obstructed or diffraction

5 Synchronization Performance in Jamming

The bidirectional signals are ranging separately by MPL and SPL, a prominent problem is that if the UAVs are in different electromagnetic environment the ranging results would be asymmetrical too. Concretely, the UAVs would suffer not only the deceptive and barrage jamming but also the intra-system multi-access interference (MAI). In consideration of general situations, the paper would discuss the MAI effect on synchronization performance only.

All UAVs would receive two or more ranging signals in pseudolites system for they are all omnidirectional transmitted. In a M pseudolites system, the received signal by one pseudolites (PS0) would be

$$r(t) = \sum_{m=1}^{M} A_m d_m(t - T_{\mathrm{md}}) c_m(t - T_{\mathrm{md}}) \cos(2\pi f_m t + \varphi_m) + \varepsilon \tag{21}$$

The parameters $\{A_m, d_m, T_{md}, c_m, \varphi_m\}$ are the relative received power, data, delay, PRN code and carrier phase of ranging signals of PS1 $\sim$ PSm, and f_m is their carrier frequency. If not consider of the loop tracking error, the multi-access signals after receiver code correlation process of PS1's signal would become

$$\sum_{m=2}^{M} A_m E(\varphi) \int_{-\infty}^{\infty} \mathrm{d}_1 \mathrm{d}_m(\alpha - T_{\mathrm{md}}) R_{\mathrm{cmc1}}(T_{\mathrm{md}} - T_{1\mathrm{d}}) h(t - \alpha) \mathrm{d}\alpha \tag{22}$$

the $E(\varphi)$ is the mean fading of MAI due to frequency and code phase difference, which could be described as

$$E(\varphi) = \frac{1}{T_c} \int_{0}^{T_c} \cos[\varphi_1 - \varphi_m + (f_1 - f_m)t] \, \mathrm{d}t \tag{23}$$

T_c is the correlation time. It could be seen that cross correlation curve adding to autocorrelation curve might cause tracking error, which is relied on the code property, relative power and carrier phase.

A rough path design of all UAVs is applied to enhance the position performance which has the property that each UAV could only receive one strong signal except the synchronized ranging signal, as shown in Fig. 4.

As a result, number of pseudolites in Eqs. (21) and (22) would satisfied $M = 2$ which include synchronized source PS1 and interference source PS2, and maximum of the ranging error caused by MAI would be

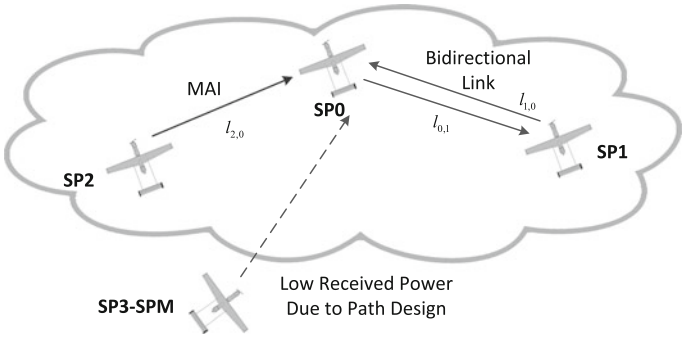

Fig. 4 Intra-system MAI of the pseudolites of rough path design

$$\sigma_{\mathrm{MAI}} = \frac{A_2 K_{\mathrm{cor}}}{A_1 K_{\mathrm{sel}}} d_2 d_1 L \cos(\varphi_2 - \varphi_1) \tag{24}$$

In Eq. (24), L is the half width of the phase discriminator, K_{cor} and K_{sel} are the slopes of auto correlation peak

$$\begin{cases} K_{\mathrm{cor}} = R_{12}\left(\left\lceil \frac{l_{1,0}-l_{2,0}}{cT_{\mathrm{code}}} \right\rceil T_{\mathrm{code}}\right) - R_{12}\left(\left\lfloor \frac{l_{1,0}-l_{2,0}}{cT_{\mathrm{code}}} \right\rfloor T_{\mathrm{code}}\right) \\ K_{\mathrm{sel}} = R_{11}(0) - R_{11}(-T_{\mathrm{code}}) \end{cases} \tag{25}$$

T_{code} is the PRN code's width.

For example, if the correlation gain of the codes is similar to 30 dB, L equal to half of the code width, the codes transmit speed is 5.115 MHz and the UAVs are at similar distance, the error caused by MAI would be

$$\sigma_{\mathrm{MAI}} = \pm 0.5 \times 10^{-\frac{30}{20}} \times \frac{c}{5.115\ \mathrm{MHz}} \approx \pm 0.9\ \mathrm{m} \tag{26}$$

which is equivalent to synchronization error of $\pm 3ns$.

6 Simulations of the System Synchronization Performance

The simulations are aim at verifying the synchronization performance in dynamic remedy the lack of standard clock and real-time performance evaluate method in authentic flying. All the simulations are developed by Matlab and STK. The flying parameters of simulated UAVs are showed in Table 1.

The simulated ranging signals of all pseudolites are of a same frequency and bandwidth. The PRN codes are chosen from BeiDou B1I. The clock drifts of pseudolites are simulated as slow variables within ±1 ns/s. A frequency correction

Table 1 Flying and pseudolites parameters

	UAV0 (MPL)	UAV1 (SPL)	UAV2	UAV3
Velocity	300 m/s			
Altitude (km)	20	20	15	15
Latitude (N)	36	36	34.5	34
Longitude (E)	100	102	100	103
Trajectory	Hover (left turn)			
Radius (km)	6	8	6	8
Offset (m)	10	10	15	15

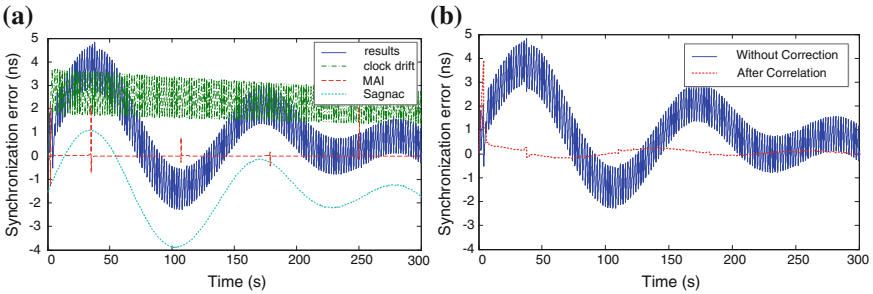

Fig. 5 Synchronization error and its composition, **a** without frequency correction methods, **b** adopting correction methods

method which estimates the frequency error by synchronization error data fitting is adopted to improve the real-time performance for comparative analysis.

The group delays of transmitting and ranging processes are simulated as a constant 2 ms, and the tropospheric delays are ignored. The modulation and demodulation delay of the ranging results data is simulated as 2 s, which determine the frequency of time synchronization up to 0.5 Hz. The synchronization results without frequency correction methods are showed in Fig. 5a A correlation method that estimates error within ranging period by ranging data filtering was adopted and the synchronization performance is showed in Fig. 5b The correlation method reduces the effect of both clock drift and Sagnac and reach the accuracy of ± 0.3 ns after convergence process.

7 Experiments of the System Synchronization Performance

To verify the synchronization performance by TWTFT in pseudolite system, a principle airborne pseudolites system (PAPS) was developed in state key laboratory.

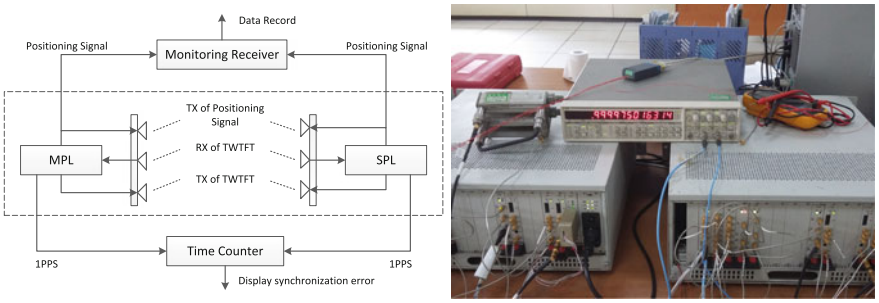

Fig. 6 The test structure and environment of PAPS

The TWTFT signal of PAPS is designed in a different frequency of the broadcast positioning signal to avoid self-interference in a UAV, and the ranging result is transmitted as a part of data in ranging signal. To improve the tracking precision, the code rate is designed as 10.23 MHz. In consideration of the calculation of integer ambiguity resolution, the ranging signal is transmitted in two frequencies. Another attempted experiment that using a time-hopping signal structure to restrain the intra-system MAI is developed too. All the pseudolites are used a commercial rubidium clock, which have an approximate linear drift within ± 0.5 ns/s. To restrain the effect of temperature and force on clock, environment control and adapt modules and clock drift correction methods are applied. Additionally, a self-calibrating method is applied for calculate the group delay real-timely. The synchronization error would be broadcasted in SPL positioning signal without adjusting clock until in excess of ± 10 ns.

A set of wired test experiments were developed to support the principle synchronization process, which composed of two pseudolites (SPL and MPL) and a time counter to display the synchronization error by comparing 1PPS signals of the pair pseudolites. The test structure and environment of PAPS is showed in Fig. 6.

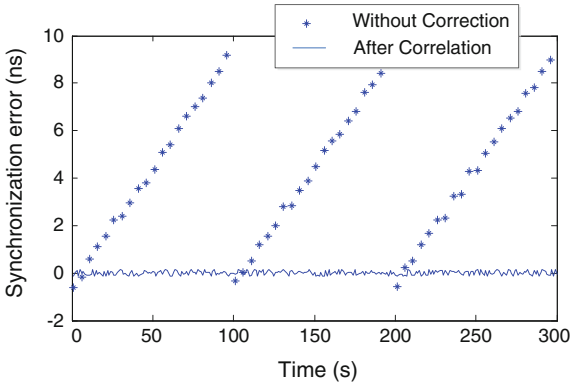

Fig. 7 Synchronization performance of PAPS

The synchronization results are showed in Fig. 7. The error has a linear variation within the bidirectional ranging results transmitting cycle without frequency correction method. While after correlation method is adopted the performance has an obvious improvement that astringing to ± 0.3 ns.

The experiments showed that TWTFT could reach high synchronization performance without using positions of all pseudolites. However, the tests are developed in static situation and the ranging between SPL and MPL approximates 30 m, for which it could hardly evaluate the performance in true flying situation. Flight tests and further experiments should be carried on in future.

8 Conclusions

In this paper a synchronization method for multiple UAV-borne pseudolites system and its performance in flight situation have been presented. The method is independent of signal propagation model and positions of pseudolites to adapt the flight situation. A rigorous analysis showed that the clock drifts, Sagnac and MAI have attentional effects on synchronization performance. To improve the performance a set of technique methods are mentioned. The simulations and experiments not only showed the performance of basic TWTFT, but also showed the improvement of correlation methods. A principle system is developed and reaches ± 0.3 ns synchronization performance. For future pseudolites systems the synchronization method would be further improved and more flight experiments would be developed.

Acknowledgments The authors would like to thank the Work Group of PAPS and Dr. Deng for proving experiments and data.

This work is supported by the Fundamental Research Funds of Laboratory (XX131450001).

References

1. Cobb HS (1997) GPS pseudolites: theory, design and applications (PhD thesis), California Stanford University
2. LeMaster EA (2002) Self-calibrating pseudolite arrays: theory and experiment (PhD thesis), California Stanford University
3. Matsuoka M, Rock SM, Bualat MG (2004) Autonomous deployment of a self-calibrating pseudolite array for mars rover navigation, In: Symposium on position location and navigation, pp 733–739
4. LeMaster EA, Matsuoka M, Rock SM (2002) Field demonstration of a Mars navigation system utilizing GPS pseudolite transceivers, In: Symposium on position location and navigation, pp150–155
5. LeMaster EA, Matsuoka M, Rock SM (2003) Mars navigation system utilizes GPS, Aerospace and Electronic Systems Magazine, pp 3–8
6. CETC54 Interface Control Document for OTE Vol 1 Revision 0

7. Luan R, Xu W, Jiang L, Zhang L (2009) time synchronization technologies for pseudolites positioning system. Meas Control Technol 06, pp 43–46
8. Rizos C (2010) Experimental results of locata: a high accuracy indoor positioning system. In: International Conference on indoor positioning and indoor navigation, Switzerland, pp 15–17 Sept 2010
9. Barnes J, (2006) A positioning technology for classically difficult GNSS environments from Locata, In: Symposium on position location and navigation (IEEE/ION), pp 715–721
10. Montillet JP (2007) Achieving centimeter-level positioning accuracy in urban canyons with Locata technology. J of Glob Positioning Syst. 6: 158–165
11. Yu L, Lu L, Wang R, Jing J, Wu C, Zhu Z, Zhang B (2013) Analysis of the sagnac effect on the accuracy of the long haul optical fiber time transfer system. Frequency and Time Forum European, pp 303–305
12. Tseng WH, Feng KM, Lin SY, Lin HT, Huang YJ, Liao CS (2011) Sagnac effect and diurnal correction on two-way satellite time transfer. IEEE Trans on Instrum and Meas pp 2298–2303

A Wide Area Differential Correction Algorithm Research Adapted Differential Satellite Statuses

Wei Zhong, Yuanhao Yu and Hua Huang

Abstract In order to solving the problems, for example: the BeiDou wide area differential system(WADS) now only has one correction which cannot adapt differential satellite statues as normal status, phase adjustment status, orbit maneuver status, Next generation BeiDou WADS is dependent more on system's data, other WADS algorithms such as WAAS are not suitable for BeiDou constellation structure which has GEO and IGSO satellite, so a BeiDou WADS algorithm is proposed to compute four-dimensional differential correction including satellite clock error and ephemeris RTN errors, only based on monitoring receiver. At last, based on real observations of BeiDou system and the verified results show that the influences of satellite phase adjustment and orbit maneuver are reduced and the positioning uncertainty is remarkably depressed.

Keywords Wide area difference · Enhance · Monitoring receiver · Position

1 Introduction

With more and more application of GPS, GLONASS, and BeiDou, the positioning precision, the continuance and integrity of service cannot satisfy senior user's demand, for example in precision geodetic mapping and aviation precision near. With space-based or ground-based enhancement system, the disadvantage of basic service can be remedied. Therefore, WAAS (USA), EGNOS (Europe), MSAS

W. Zhong (✉) · Y. Yu · H. Huang
No. 27, ShiBu Farm Road, Litchi Ditch, Sanya, Hainan, China
e-mail: zhongwei_820@163.com

Y. Yu
e-mail: yyhpla@126.com

H. Huang
e-mail: huanghuafly@163.com

J. Sun et al. (eds.), *China Satellite Navigation Conference (CSNC) 2016 Proceedings: Volume II*, Lecture Notes in Electrical Engineering 389,
DOI 10.1007/978-981-10-0937-2_27

(Japan), and QZSS (Japan) are developed. These organizations are independent of GPS, GLONASS system, and can supply ephemeris errors, satellite clock error and ionospheric grid correction to an authorized user.

2 Basic Principle

The basic principle of WADS is as follows: first, different kinds of error are distinguished and modeled; second, corrections of different errors are computed and broadcast to user; finally, with these corrections, the influence of errors is weakened, and user's positioning precision is improved. The errors of WADS include: satellite orbit error, satellite clock error, ionosphere delay error, and so on. With WADS corrections, URE is better than 1 m, and positioning precision can be down to 3 m.

Now, by ground monitoring the station with exact coordinate, BeiDou WADS calculates the URE (called equivalent clock error) to modified positioning errors (including satellite orbit errors and clock error). Through verification of experiment, equivalent clock error is effective to broadcast ephemeris error and clock error of health satellite, but it is not adaptive to the situations such as satellite orbit maneuver, satellite phase adjustment, and so on. If satellite orbit error and clock error are separated to compute relative correction, the usability and precision of BeiDou WADS can be improved (Fig. 1).

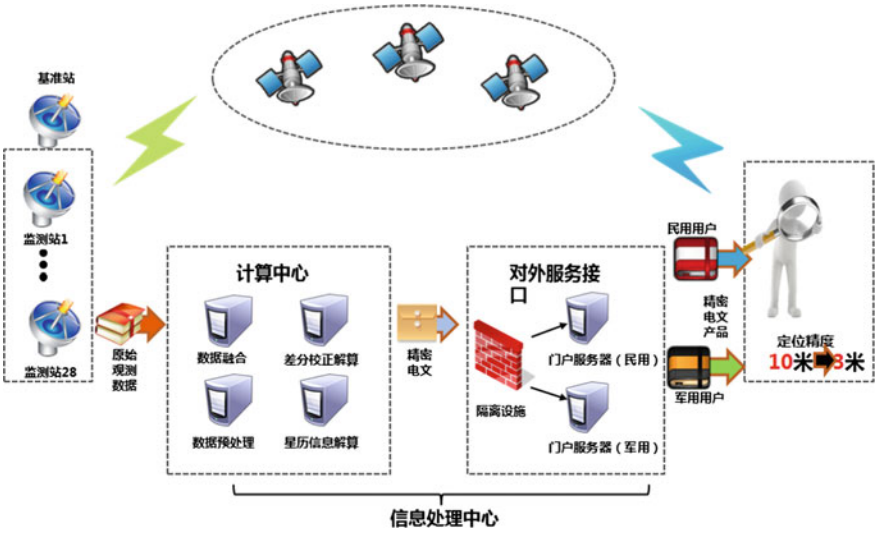

Fig. 1 WADS principle

3 Four-Dimensional WADS Correction Algorithm

Because of hybrid constellation of BeiDou with high orbit satellite and medium orbit satellite, the space environment and orbit control method are different from GPS, and DOP value of the high orbit satellite is several times than medium orbit. Therefore, the WADS algorithm can reduce the influence of high DOP value and improve positioning precision, which reduces four-dimensional calculation to three-dimensional calculation by the separation of satellite clock error from orbit errors.

The main problem is how to separate satellite clock error from orbit errors. The separation algorithm has been proposed by some scholars [1], and has completed simulation verification. But the algorithm must further consider the situations such as the constellation of BeiDou, the performance of atomic clock on the satellite, and the frequent phase adjustment and orbit maneuver. A BeiDou four-dimensional WADS correction algorithm is based only on monitoring receiver data is proposed, which adapts different situations of satellite with relative separation method, common view method, code noise and multipath correction method, and minimum variance method.

3.1 The Relative Separation Method of Satellite Orbit Error and Clock Error

Figure 2 shows the principle of relative separation. Step 1, the pseudo-range of ground monitoring receiver must be pretreatment. Step 2, the URE of monitoring receiver 1 is set as satellite clock correction. Step 3, satellite orbit corrections of monitoring receivers

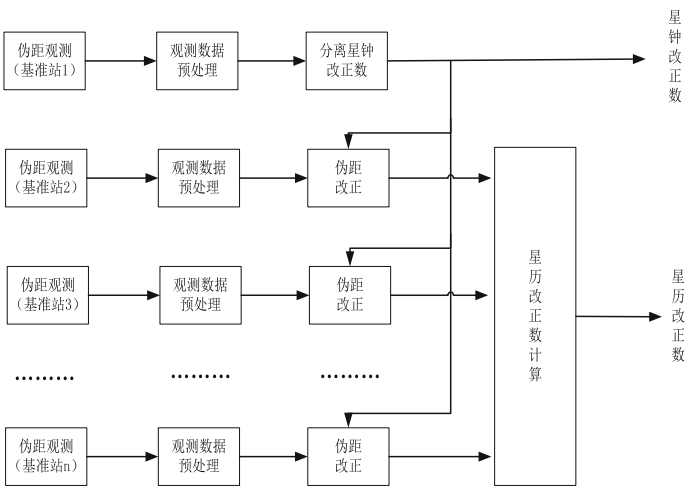

Fig. 2 Relative separation algorithm

2 − n are computed with clock correction calculated in step 2, and it realizes the relative separation of satellite orbit error and clock error. The residual of all monitoring receivers are just as follows: $\Delta\rho_1 - \Delta\rho_1, \Delta\rho_2 - \Delta\rho_1, \Delta\rho_3 - \Delta\rho_1, \Delta\rho_n - \Delta\rho_1$.

Through pretreatment, different kinds of delay such as ionosphere [2], troposphere are removed. The residual of monitoring receiver 1 $\Delta\rho_1$ is set as satellite clock error which in fact includes satellite orbit error and clock error. So all the users in overlay area make equivalent modification $\Delta\rho_1$.

The residuals of monitoring receivers 2− n subtracting $\Delta\rho_1$ means that the satellite position calculating by broadcast ephemeris is shifted $(\Delta x, \Delta y, \Delta z)$, and the residuals of all monitoring receivers are reduced to zero. Formula 1 shows how to calculate the satellite orbit correction:

$$\begin{bmatrix} \Delta x \\ \Delta y \\ \Delta z \end{bmatrix} = \begin{bmatrix} \frac{x-x_1}{r_1} & \frac{y-y_1}{y_1} & \frac{z-z_1}{z_1} \\ \frac{x-x_2}{r_2} & \frac{y-y_2}{y_2} & \frac{z-z_2}{z_2} \\ \cdots & \cdots & \cdots \\ \frac{x-x_n}{r_n} & \frac{y-y_n}{y_n} & \frac{z-z_n}{z_n} \end{bmatrix} \times \begin{bmatrix} \Delta\rho_1 - \Delta\rho_1 \\ \Delta\rho_2 - \Delta\rho_1 \\ \cdots \\ \Delta\rho_n - \Delta\rho_1 \end{bmatrix} \tag{1}$$

(x, y, z) is satellite position calculating by broadcast ephemeris; $(x_\mathrm{i}, y_\mathrm{i}, z_\mathrm{i})$ is monitoring receiver position; r_i is the distance between satellite and monitoring receiver.

3.2 *Time Synchronization of Monitoring Receivers with Common View*

In satellite orbit error and clock error relative separating, $\rho_i - \rho_1$ contains clock error between monitoring receiver i and 1. The original algorithm removes clock error by single difference, but it does not adapt BeiDou because reference satellite must be selected. The new algorithm does not take reference satellite, and adopt common view method to removes clock error between monitoring receiver i and 1.

The algorithm is as follows [3]: first, the atomic clock of monitoring receiver 1 is taken as reference clock considering its high stability:

$$t_{\mathrm{sta}.M} = \frac{1}{P_{\mathrm{sta}.M}} \sum_{j=1}^{N} \frac{\rho_M^j}{\sigma^2_{\rho_M^j} + (\mathrm{URA}^j)^2} \tag{2}$$

$t_{\mathrm{sta}.M}$ is reference clock; ρ_M^j is residual smoothed by carried phase; $\sigma^2_{\rho_M^j}$ is measuring precision; $P_{\mathrm{sta}.M}$ is power.

Second, monitoring receivers i and 1 have $N_{i,M}$ satellites in common view, single difference is

$$\Delta_{i,M}^{j} = \Delta\rho_{i}^{j} - \Delta\rho_{M}^{j} \tag{3}$$

In regional network, satellite ephemeris projection error can be ignored [3]. Clock mutual difference of monitoring receivers i and 1 is

$$\mathrm{dclk}_{\mathrm{sta},i} = \Delta t_{\mathrm{sta}.i} - \Delta t_{\mathrm{sta}.M} = \frac{1}{N_{i,M}} \sum_{j=1}^{N_{i,M}} \Delta_{i,M}^{j} \tag{4}$$

The clock of monitoring receiver 2 − n is $\mathrm{Staclk}_i = \mathrm{dclk}_{\mathrm{sta},i} + \Delta t_{\mathrm{sta}.M}$. Finally, the residuals $\Delta\rho_{i}^{j}$ of monitoring receiver 2 − n subtract Staclk_i, and monitoring receiver 2 − n synchronize to monitoring receiver 1, so clock errors between different monitoring receivers are removed.

3.3 Eliminating Multipath

After repairing the carrier phase and evaluating the combined integer ambiguity and channel delay, multipath can be effective by eliminating CNMC method.

3.3.1 Cycle Slip Detection and Repair

With dual frequency pseudo-range/carrier phase combination method [4], the cycle slip greater than 2 cycles can be detected and repaired, and by the dual frequency ionospheric residual method [5], the 0.5–2 cycle can be detected and repaired.

When the ionospheric delay variation is small in adjacent epoch, cycle slip can be detected by

$$\begin{aligned} \Delta N_{i,j} = N_{i,j}(t+1) - N_{i,j}(t) &= \varphi_{i,j}(t+1) - \varphi_{i,j}(t) \\ &- (p(t+1) - p(t))/\lambda_{i,j} - \frac{a_{i,j} + \beta}{\lambda_{i,j}} (I(t+1) - I(t)) \end{aligned} \tag{5}$$

$\varphi_{\mathrm{i,j}}(t) = i\varphi_1(t) + j\varphi_2(t)$ is dual frequency combined observation; $\lambda_{\mathrm{i,j}} = c\ /(\mathrm{if}_1(t) + \mathrm{jf}_2(t))$; $p(t) = (p_1(t) + p_2(t))\ /2$; $\alpha_{\mathrm{i,j}} = (4620\mathrm{i} + 5929\mathrm{j})\ /(4620\mathrm{i} + 3600\mathrm{j})$, β is 1.323.

The algorithm uses $\varphi_{1,-1}(t)$ and $\varphi_{-7,9}(t)$ to detect and repair cycle slip. The cycle slip of $\varphi_1(t)$ and $\varphi_2(t)$ are:

$$\begin{aligned} \Delta N_1 &= \frac{9\Delta N_{1,-1} + \Delta N_{-7,9}}{2} \\ \Delta N_2 &= \frac{7\Delta N_{1,-1} + \Delta N_{-7,9}}{2} \end{aligned} \tag{6}$$

Dual frequency pseudo-range/carrier phase combination can detect cycle slip greater than 2 cycles, and the rest part is detected by dual frequency ionospheric residual method.

Dual frequency ionospheric residual method detects cycle slip by calculating the ionospheric delay variation of different epochs. Ignoring the measurement noise and multipath, the phase difference of adjacent epoch is as follows:

$$\Delta\Phi(t) = \Delta_{\text{ion}}(t+1) - \Delta_{\text{ion}}(t) + \frac{f_1}{f_2}\Delta N_2 - \Delta N_1 \tag{7}$$

If $\Delta\Phi$(t) is less than 0.28, there is no cycle slip; if $\Delta\Phi$(t) is approached to an integer, $f1$ frequency have $\Delta\Phi(t)$ cycle slip; if $\Delta\Phi(t)f1/f2$ is approached to an integer, $f2$ frequency have $\Delta\Phi(t)$ cycle slip;

3.3.2 CNMC Algorithm

CNMC [3] algorithm calculates the multipath with recursive algorithm, and it is initialed as below:

$$\begin{aligned} \text{CMCB}_i(t_0) &= P(t_0) - \phi(t_0) - \Delta I(t_0) \\ \text{CMC}(t_0) &= 0 \end{aligned} \tag{8}$$

The follow-up is

$$\begin{aligned} \text{CMCB}_i(t) = \text{CMCB}_i(t-T) \\ + \frac{1}{n}\left(P_i(t) - \phi_i(t_0) - \Delta I_i(t_0) - \text{CMCB}_i(t-T)\right) \end{aligned} \tag{9}$$

$$\text{CMC}_i(t) = P_i(t) - \phi_i(t_0) - \Delta I_i(t_0) - \text{CMCB}_i(t) \tag{10}$$

$P_i(t)$ is pseudo-range; $\phi_i(t_0)$ is carrier phase; $\Delta I_i(t_0)$ is ionospheric delay; T is recursive interval.

4 Experiment Analysis

In order to verify the algorithm effect when the satellite is in normal status, phase adjustment status or orbit maneuver status, the data of June 18, 2012, June 19, 2012, and June 20, 2012 were used to calculate satellite orbit correction and clock correction, then these corrections were added to position calculation. The results were as follows.

First, the enhancement effect was verified when all satellites were normal. In June18, 2012, there was no abnormal BeiDou satellite. The monitoring receivers of low latitude station, medium latitude station and high latitude station were used to calculate satellite orbit correction and clock correction to verify position enhancement effect. The effect of low latitude station was shown in Figs. 3 and 4. Other stations' effect were shown in Table 1. Therefore, when satellites were normal, algorithm could reduce the uncertainty to 50 %. Meanwhile, with the normal data of June 19, 2012, June 20, 2012, and June 21, 2012, algorithm could reduce the uncertainty to 30–50 %.

Second, the enhancement effect was verified when the phase of a satellite was adjusting. On June 20, 2012 10:27:10–10:57:26, a satellite was in phase adjustment status. Monitoring receiver of high latitude station was used to verify the

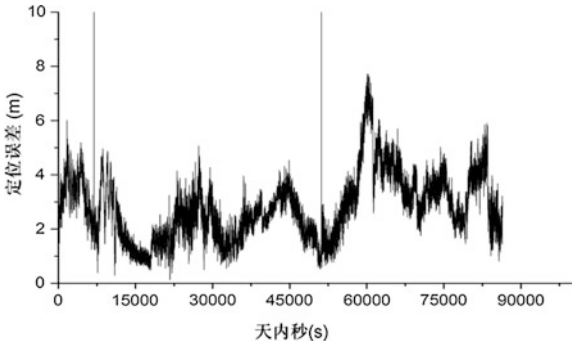

Fig. 3 Position error of low latitude area (no enhancement)

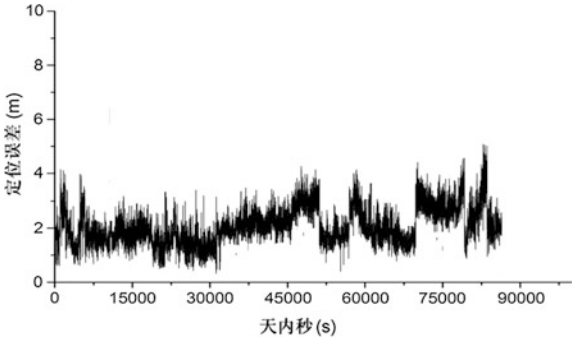

Fig. 4 Position error of low latitude area (enhancement)

Table 1 Analyses of the uncertainty

Latitude		Accuracy of position (m)	Uncertainty of a kind (m)
Low latitude	No enhancement	2.76	1.21
	Enhancement	2.07	0.67
Medium latitude	No enhancement	2.54	1.52
	Enhancement	2.65	0.61
High latitude	No enhancement	4.68	3.15
	Enhancement	4.75	1.56

enhancement effect, and it is shown in Figs. 5 and 6. Different stations had the same enhancement effect at the same time. So, algorithm could effectively remove the influence of phase adjustment.

Finally, the enhancement effect was verified when a satellite was in recovery period after orbit maneuver. In June 21, 2012 00:00:00–08:00:00, a satellite was in

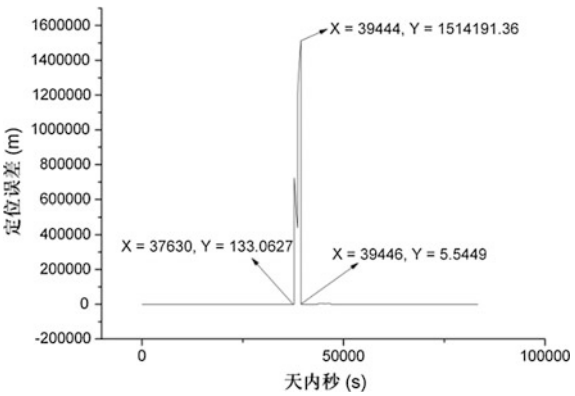

Fig. 5 Position error of high latitude area (no enhancement and the atomic clock phase of one satellite was adjusting)

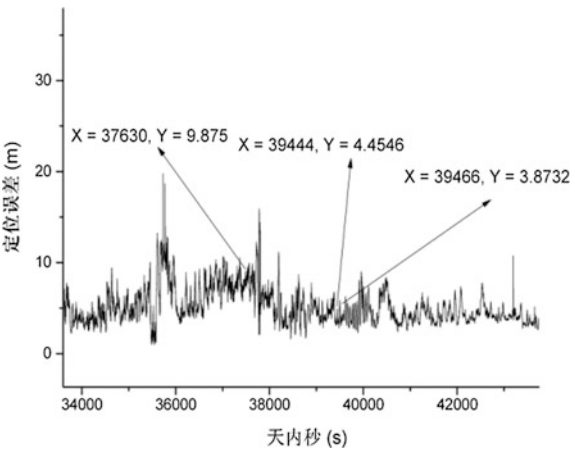

Fig. 6 Position error of high latitude area (enhancement and the atomic clock phase of one satellite was adjusting)

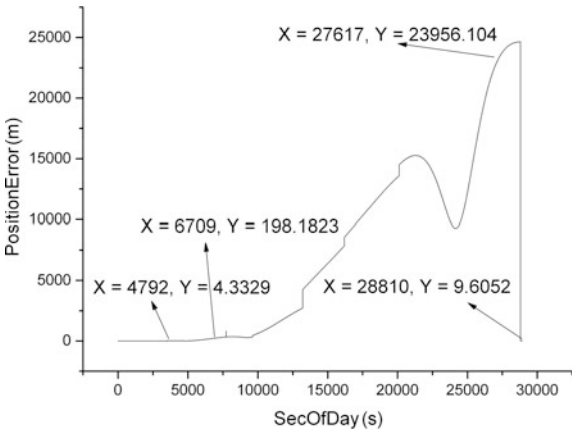

Fig. 7 Position error of low latitude area (enhancement and oribt maneuver)

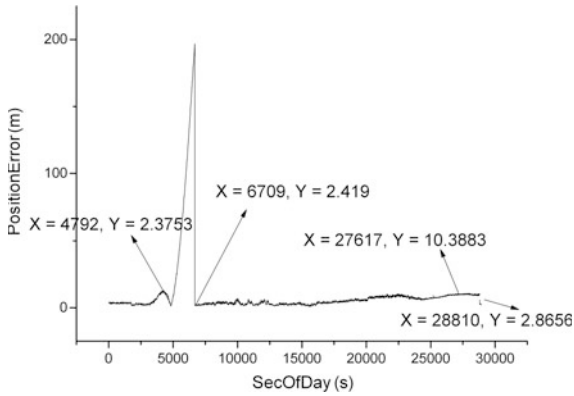

Fig. 8 Position error of low latitude area (enhanced and oribt maneuver)

recovery period after orbit maneuver. Monitoring receiver of low latitude station was used to verify the enhancement effect, and it is as shown in Figs. 7 and 8. So, the algorithm could effectively reduce the influence of orbit maneuver. In the 4792–6709 period, there were less than 4 monitoring receivers which were used to calculate satellite orbit correction and clock correction, so there was no enhancement effect.

5 Summary

Based on monitoring receiver data, solving the problem of satellite orbit and clock relative separation, overcoming the influence of selecting reference satellite, and eliminating the clock errors between different monitoring receivers and multipath, through the verification by the real data of BeiDou, it is proved that algorithm can

reduce the influence of phase adjustment and orbit maneuver, and effectively reduce the uncertainty to 30–50 %. Therefore, this algorithm not only satisfies the normal demand of position enhancement, but also is able to get the correct position of user with the data of abnormal satellite, when the integrity of the navigation system is abnormal or visible normal satellite is less than 3. But timing is not correct because the algorithm introduces reference clock error, and it is next step to solve this problem.

References

1. Cheng-lin C et al (2009) A novel wide-area differential method on separated calculation of satellite clock error and ephemeris errors. J of Astronautics, 30(6): 2166–2167
2. Wan C (2010) The study of dual frequency ionospheric correction methods based on GPS. J Sci & Technol Info 21:439
3. Yue-ling C (2014) Studies on the wide-area differential correction and integrity monitoring for the regional satellite navigation system of BeiDou. Astronomical Observatory, Shanghai p 4067
4. Han S (1995) Theory and applications of the combinations of GPS dual frequency carrier phase observations. J Acta Geodaetica At Cartographica Sinca. 21(2):9–13
5. Jianjun F (2007) Research on the theory and method of data processing of the precise GNSS system with three frequencies. Nat Univ of Defense Technol, p 60

Performance Analysis of INS-Aided GNSS Carrier Loop for Tracking Weak Signal

Xuwei Cheng, Xiaqing Tang, Meng Wu, Junqiang Gao and Shulei Chen

Abstract For the sake of steadily tracking carrier signal under high dynamic or low C/N_0 (carrier to noise power ratio) environments, during various tracking loop structure of GNSS (global navigation satellite system) receivers' design process, the INS-aided tracking loop architecture is adopted. The performance of the tracking loop with and without INS-aided are analysed, respectively, and experimentally validated. The all models of error sources affecting the tracking performance of the INS-aided PLL and FLL is built and quantified. Then, based on the principle of minimizing the tracking error, an optimal adaptive bandwidth designing method is proposed. Meanwhile, the dynamic stress noise is compensated by the INS completely and the relationship between the tracking performance and the INS devices' quality is deduced. The results show that the tracking error for tracking weak signals is still under the given threshold at small bandwidths by INS aiding.

Keywords Optimal bandwidth · INS-aided · Loop tracking error · Weak signal

1 Introduction

With the rapid development of navigation technology, reliability of GNSS navigation has gradually become a topic of concern by the military and civil user, and research on tracking weak GNSS signal has also become a hot topic. The most challenged problem of GNSS receiver design and application lie in how to improve system robustness, but accuracy [1]. For military purpose, the highest reliable navigation and guidance ability were needed. In such harsh environment, the signal power will be low 10–30 dB than the normal, which illustrates that the designer

X. Cheng (✉) · X. Tang · M. Wu · J. Gao · S. Chen
Department of Control Engineer, Academy of Armored Force Engineering, 100072 Beijing, China
e-mail: chengxuwei0872@126.com

X. Tang
e-mail: tangxiaqing_001@163.com

J. Sun et al. (eds.), *China Satellite Navigation Conference (CSNC) 2016 Proceedings: Volume II*, Lecture Notes in Electrical Engineering 389,
DOI 10.1007/978-981-10-0937-2_28

must consider advanced means to improve receiver's performance, in order to acquire signals effectively and steadily tracking them.

When it comes to improve receiver's performance for tracking weak signals, two terms are involved: adopting more advanced antenna design or digital signal processing, on the other hand, eliminating Doppler affection with multi-sensor information fusion, such as GNSS/INS (inertial navigation system) integration [2, 3], which complete carrier loop tracking with utilizing INS aiding GNSS receivers, and enhance receiver's acquiring and tracking ability [4], moreover, lessen the user's dynamic affection to tracking loop performance [5–7].

This paper analyzes error types and quantizing of PLL, and compares the affection of PLL noise error models [8] with external aiding. After comparing and analyzing the influence during parameters design processing of PLL, based on the principle of minimizing the tracking error, a kind of adaptive bandwidth adjusting method was adopted with INS aiding. Meanwhile, we analyzed the effect of tracking performance different accuracy grades of the core components of INS.

2 Design of Carrier Tracking Loop with INS-Aided

The conventional INS/GNSS integration only involves compensating the INS's error, once the receiver's accuracy declines, the system performance will be greatly influenced. While the deep integration completes the signal replica by control NCO with the corrected INS information, thus the code/carrier tracking loop is finished.

2.1 INS Aiding PLL Design

We can see from Fig. 1 that the code and frequency loop are simultaneously working during GNSS signal tracking, both the loop coupling with each other.

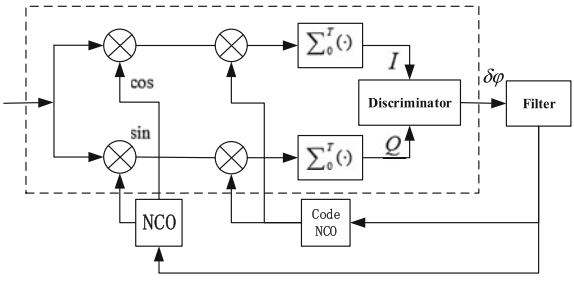

Fig. 1 The traditional tracking loop model

The FLL is more sensitive to dynamic stress than DLL, and more easily loss lock for its longer wavelength than code, so, the PLL has got more attention than DLL.

FLL-assisted PLL loop filter design can improve PLL performance in certain, after converting to pure FLL, the loop is remain easily loss lock. So under dynamic applying environment, the adaptively adjusting method of PLL bandwidth is needed [9]. For the INS information for integration system can be easily got, which can be utilized to tracking PLL to improve tracking performance. Meanwhile, with the C/N_0 (carrier to noise power ratio) of received broadcast signal and measured dynamic stress information, the dynamic tracking ability dramatically can be enhanced [10, 11]. Figure 2 shows the INS aiding PLL structure model.

Where $\phi_r(s)$ is input; $\omega_\phi(s)$ is phase noise; $\hat{f}_d$ and $\delta\hat{f}_d$ are Doppler estimator and clock frequency error, respectively, provided by navigation filter of INS.

$$\phi_{\mathrm{PLL}}(s) = H_1(s)\phi_r(s) + H_2(s)\omega_\phi(s), \tag{1}$$

where $H_1(s) = \frac{\frac{a_{\mathrm{INS}}}{s+a_{\mathrm{INS}}}s + F(s)}{s + F(s)}$, $H_2(s) = \frac{F(s)}{s+F(s)}$, and a_{INS} is the equivalent bandwidth of INS' Doppler aiding, The performance of PLL mainly depends on the loop filter. For a traditional second PLL, if the filter $F(s)$ of a proportion and integral part is $K(s+a)/s$. And the loop bandwidth can be obtained as

$$B_n = \frac{1}{2\pi|H(0)|}\int_0^\infty |H(j\omega)|^2 \mathrm{d}\omega = \frac{\omega_n}{2}\left(\zeta + \frac{1}{4\zeta}\right) \tag{2}$$

The loop bandwidth is the most important parameter affecting the GNSS receiver's tracking performance, while the dynamic and controlling noises ability contradicts with each other. Smaller bandwidth can control the loop noise under certain value, thus the loop works with smaller tracking error, if the bandwidth is too small, the dynamic ability cannot be meet. Taking loop type, order and the sensibility to the dynamic all into consideration, the tracking loop scheme with INS aiding is designed as third-order PLL with INS aiding and third-order DLL with second FLL.

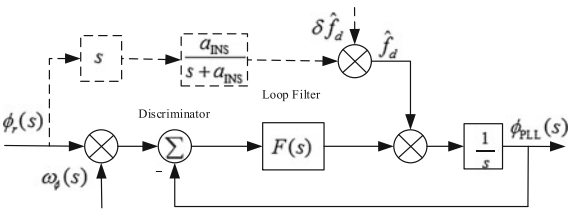

Fig. 2 The PLL model with INS aiding

2.2 Estimating C/N_0 of GNSS Signal

Adopt the narrow-wide-band power ratio method, during the measured period T, calculating the non-coherent accumulation wide-band power $P_{\mathrm{w}}(k)$ and coherent narrow-band power $P_{\mathrm{n}}(k)$ respectively, then, we can obtain

$$P_{\mathrm{w}}(k) = \left[\sum_{i=1}^{M}\left(I_i^2 + Q_i^2\right)\right]_k \quad P_{\mathrm{n}}(k) = \left[\sum_{i=1}^{M} I_i\right]_k^2 + \left[\sum_{i=1}^{M} Q_i\right]_k^2 \tag{3}$$

where, I_i and Q_i represent the in-phase and quadra-phase signals within the given pre-detection integration time (1 ms) respectively.

In order to weaken noises' influence, calculate Eq. (5) K times continuously. Thus, the C/N_0 can be expressed as follows:

$$C/N_0 = 10\lg\left[\frac{M\left(\bar{P}_{\mathrm{n/w}}(k) - 1\right)}{T\left(M - \bar{P}_{\mathrm{n/w}}(k)\right)}\right] \bar{P}_{\mathrm{n/w}}(k) = \frac{1}{K}\sum_{k=1}^{K} P_{\mathrm{w}}(k)/P_{\mathrm{n}}(k) \tag{4}$$

where $(C/N_0)_{\mathrm{Hz}} = 10^{\frac{C/N_0}{10}}$ (Hz). Generally, if the C/N_0 is lower, all kind of estimating methods will be affected, a longer time T (such as $M > 25$) is needed for calculating the necessary measure information [12], while the noise and respond time all need to be taken into consideration.

3 Analysis of PLL Tracking Error

3.1 PLL Tracking Error

During the PLL regular work, numerous sources of measurement errors are in each type of tracking loop. The dominate sources of phase errors are phase jitter and dynamic stress error, respectively. The 1-sigma rule threshold for the PLL tracking loop for the two-quadrant arctangent phase discriminator is therefore

$$\delta_{\mathrm{PLL}} = \theta_e/3 + \delta_j = \theta_e/3 + \sqrt{\delta_{\mathrm{PLL}t}}^2 + \delta_v^2 + \theta_A^2 \le 15^\circ \tag{5}$$

where θ_e represents dynamic stress error, δ_j is 1-sigma phase jitter from all sources except dynamic stress error, namely thermal noise $\delta_{\mathrm{PLL}t}$ and other colored noises, including vibration-induced oscillator jitter δ_v and Allan variance-induced oscillator jitter. While the discriminator is realized as a simple multiplication of the I and Q signals, the thermal noise is given by

$$\delta_{\mathrm{PLL}t} = \frac{360}{2\pi}\sqrt{\frac{B_n}{C/N_0}\left(1+\frac{1}{2TC/N_0}\right)} \tag{6}$$

where the one-side PLL loop bandwidth is presented as B_n, T is the pre-detection integration time. For a given T, $\delta_{\mathrm{PLL}t}$ is a function of B_n and C/N_0. The second term of Eq. (7) represents the effects of squaring loss. To improve the performance of a traditional receiver in tracking a weak signal, either increase the coherent averaging time or decrease the carrier tracking loop bandwidth.

The dynamic stress error can be obtained from the steady state error, which depends on the loop bandwidth and order. For a third-order loop with minimum mean square error, the dynamic stress error can be expressed as follows:

$$\theta_{e3} = \frac{\mathrm{d}^3R/\mathrm{d}t^3}{\omega_0^3} = 0.7845\frac{\mathrm{d}^3R/\mathrm{d}t^3}{B_n^3} \tag{7}$$

where $\mathrm{d}^nR/\mathrm{d}t^n$ defines maximum LOS (Light of Sight) acceleration dynamic.

The vibration-induced oscillator phase noise is a complex problem, generally, the equation for empirical vibration-induced oscillator jitter can be expressed as:

$$\delta_v = \frac{360f_L}{2\pi}\sqrt{\int_{f_{\min}}^{f_{\max}} S_v^2(f_m)\frac{P(f_m)}{f_m^2}\mathrm{d}f_m} \tag{8}$$

where f_L is carrier frequency, $S_v(f_m)$ is oscillator vibration sensitively, f_m is the random vibration modulation frequency, and $P(f_m)$ is the power curve of it.

Allan variance phase noise is completely determined by experience. $\Delta\theta_A$ defines RMS jitter into PD due to the oscillator, thus,

$$\theta_A = 160\frac{\delta_A f_L}{B_n} \tag{9}$$

For third-order loop, the short-term Allan variance is $\delta_A = 2.25\Delta\theta_A/\omega\tau$. Where $\omega = 2\pi f$ is input frequency, τ is short-term stability gate-time range.

3.2 Error Analysis of PLL with INS Aiding

In the deep integrated GNSS/INS system, the dynamic stress noise is greatly reduced by INS information aided, which estimates the Doppler frequency and compensates the dynamic to PLL. After compensating, the total error of PLL consists of thermal noise, measurement error caused by the INS core component' errors, not the antenna's

acceleration of the motions in LOS [13]. Ideally, the tracking error of the PLL of GNSS/INS system can be expressed as follows:

$$\delta_{\mathrm{PLL}} = \sqrt{\delta_{\mathrm{PLL}}^2 + \theta_{\mathrm{INS}}^2} \leq 15^{\circ} \tag{10}$$

For a third-order PLL in the deep integrated GNSS/INS system, the dynamic stress error is expressed as follows:

$$\theta_{\mathrm{INS}} = \frac{1}{3}\alpha^3 \cdot \frac{\delta_{\mathrm{INS}}}{(B_n)^3} \cdot 360 \cdot \frac{f_L}{c}, \delta_{\mathrm{INS}} = B + g\gamma(0) + gDt \tag{11}$$

In Eq. (13), δ_{INS} presents the error vector of the acceleration in LOS, c is speed of light, B is the accelerometer bias, g is the gravity acceleration, D is the gyro bias, and $\gamma(0)$ is the initial misalignment error, t is the drift time.

4 Design of Optimal Bandwidth

Without external aiding, the loop bandwidth is designed by pre-estimate dynamic of GNSS satellites to vehicle and C/N_0. While the dynamic stress error be completely compensated with INS. The oscillator vibration and Allan variance jitter are neglected, the tracking error is a function of four parameters, expressed as follows:

$$\delta_{\mathrm{PLL}} = \frac{1}{3}\frac{\mathrm{d}^n R/\mathrm{d}t^n}{(B_n/\alpha)^n} + \frac{\lambda}{2\pi}\sqrt{\frac{B_n}{C/N_0}\left(1 + \frac{1}{2TC/N_0}\right)} \tag{12}$$

For a given loop, the order and T are all known, assume the INS information and LOS dynamic are known, then the loop bandwidth can be designed according to the estimation of minimum C/N_0 of received signal. Taking the derivation of bandwidth relative to time and setting $\partial\delta_{\mathrm{PLL}}/\partial B_n = 0$, the optimal PLL bandwidth which ensures the absolutely stable tracking capability can be obtained as follows:

$$B_{n,\mathrm{optiomal}} = \left\{ \left(\frac{2n}{3}\frac{\mathrm{d}^n R/\mathrm{d}t^n}{(1/\alpha)^n}\right)^2 / \left(\frac{\lambda}{2\pi}\right)^2 \frac{C/N_0(1 + 2TC/N_0)}{2TC/N_0} \right\}^{\frac{1}{2n+1}} \tag{13}$$

For known maximum dynamic compensated by INS aiding, with variational C/N_0, the bandwidth and its minimum threshold must be redesigned. For $\delta_{\mathrm{PLL}t}$ calculation, we must seek optimizing algorithm, such as GA (genetic algorithm), iteration and interpolation algorithm, taking all factors into consideration, choose the iteration algorithm.

(a) Suppose the tracking error is only caused by maximum dynamic stress error, then, B_n is obtained with rewritten Eq. (7);
(b) Estimating C/N_0, using B_n to calculate thermal noise and other terms;
(c) Calculating total tracking error $\sqrt{\delta_{\mathrm{PLL}t}^2 + \delta_v^2 + \delta_s^2 + \theta_A^2}$ with the results of (*a*) and (*b*), substituting to Eq. (5), the dynamic stress error is obtained as $\theta_e \leq \varsigma - 3\sqrt{\delta_{\mathrm{PLL}t}^2 + \delta_v^2 + \delta_s^2 + \theta_A^2}$;
(d) Substituting the result of (*c*) to Eq. (13), updated B_n is obtained;
(e) Repeating (*b*)–(*e*) until the updated B_n difference between two iteration lower than the given threshold (0.5 Hz).

5 Experiments and Analysis

5.1 Analysis of Optimal Bandwidth of PLL Without INS Aiding

As to verify the tracking error difference between with and without INS aiding, Fig. 3 shows the relationship between C/N_0, dynamic stress error and total tracking error of traditional third-order PLL of different noise bandwidth.

When the received signal's C/N_0 is lower, the tracking error will be above the tracking error threshold which leads to poor tracking performance. Assume the bandwidth is given 8 Hz, only the dynamic acceleration within 5 g/s can ensure tracking error less than threshold. While B_n = 15 Hz, and C/N_0 = dB-Hz, the dynamic ability of receiver only can reach 2 g/s. So, if for high acceleration dynamic, a higher order loop or the external aiding information must be involved.

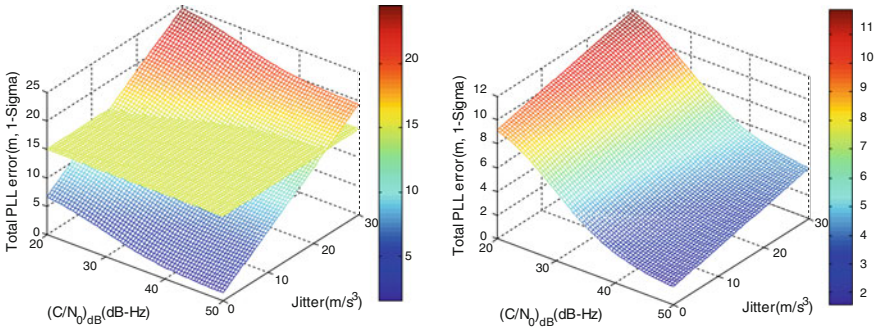

Fig. 3 Third-order PLL total tracking error versus different noise bandwidth T = 1 ms

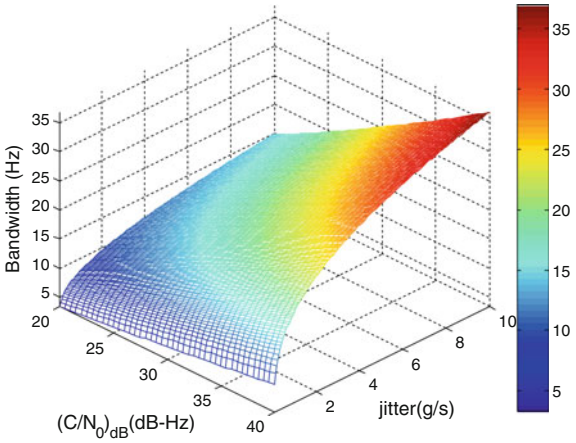

Fig. 4 Third-order PLL optimal bandwidth versus C/N_0 and jitter dynamic $T = 1$ ms

Figure 4 shows the third PLL optimal bandwidth of receiver antenna under 10 g/s, for 40 dB-Hz signal, the dynamic stress is 2.5 g/s, the bandwidth at least reach 24 Hz, the loop can hold the best tracking performance. While for the weaker 30 dB-Hz signal, the 3rd PLL loop bandwidth need to design as 16 Hz.

Figure 5 compares the tracking error of different strength signals with and without INS aiding for the given d^nR/dt^n is 10 g/s. It is noted that the optimal bandwidth is determined by minimum error criterion, and the minimal bandwidth is defined by the point of intersection with tracking threshold (15°).

Under the same dynamic, to track 35 dB-Hz signal, the optimal bandwidth and the minimal bandwidth of third need to design as 14 and 31 Hz. But for 25 dB-Hz signal, the tracking error will exceed the tracking threshold in any case bandwidth setting. Hence, for high dynamic application environment, once the useful signal is

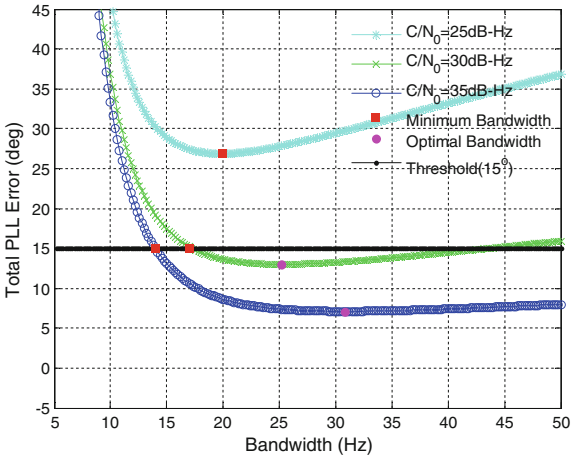

Fig. 5 Third loop phase error versus B_n with different C/N_0 ($T = 1$ ms)

covered by noise, the PLL without INS aiding is unable to make tracking error below tracking threshold only by adjust bandwidth parameter.

5.2 Analysis of Optimal Bandwidth of PLL with INS-Aided

Similarly, calculating the optimal bandwidth and the minimal bandwidth of PLL with INS aiding. Figure 6 shows that the tracking error of different strength signals with INS aiding for the given $d^n R/dt^n$ is 10 g/s.

Figure 6 indicates that with the signal C/N_0 increase, the tracking ability decreases obviously. For example, $T = 2$ ms, only if the C/N_0 greater than 25 dB-fHz, the loop can successfully track signal; Same condition, third-order loop error is less than second order. For the $d^n R/dt^n$ is 10 g/s and 25 dB-Hz signal, the optimal bandwidth and the minimal bandwidth of third loop need to design as 1 and 2 Hz respectively; setting $T = 10$ ms, the result shows that the signal below 20 dB-Hz can, the tracking error is acceptable, at the same time, the bandwidth is still a small value. Compared with $T = 1$ ms, tracking weak signal ability is improved sharply.

Above all, at the high dynamic environment and weak signal application occasion, INS aiding PLL tracking performance is superior to pure PLL. Table 1

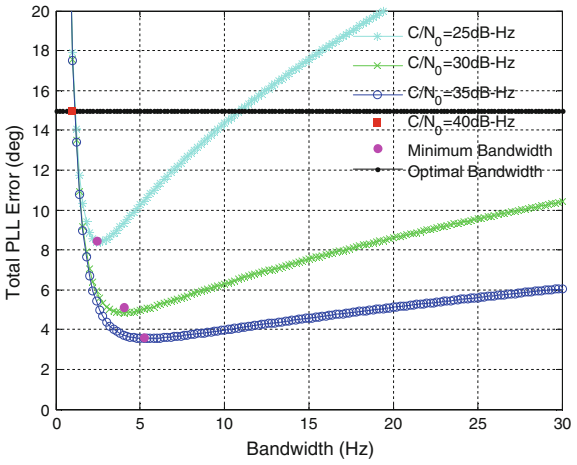

Fig. 6 The bandwidth and tracking error of third-order PLL with INS aiding ($T = 2$ ms)

Table 1 Third-order PLL tracking error comparison versus INS aiding

C/N_0/dB-Hz	No aiding			INS aiding		
	Threshold /Hz	Optimal bandwidth/Hz	Tracking error/(°)	Threshold/Hz	Optimal Bandwidth/Hz	Tracking error/(°)
25	–	–	>27	1	2	8
30	17	27	13	1	4	5
35	14	31	7	1	5	4

summarizes the tracking error results of third-order PLL with and without INS aiding at 10 g/s maximum LOS acceleration. It is thus clear that with INS aiding, the tracking ability of weak signal is dramatically improved.

5.3 *The Effect of the INS Accuracy on the PLL Performance*

The compensated result of dynamic stress error is determined by INS components' accuracy, therefore, choosing different grade IMU is a crucial problem of GNSS/INS deep integration system. So, Fig. 7 compares the effect of dynamic stress noises with different accuracy grade of INS components. Table 2 lists the performance index of three kinds of different accuracy grades of INS components.

Figure 7 indicates that the dynamic stress noise decreases as the IMU quality increase. For a poor accuracy IMU (such as MEMS), INS errors still have a considerable effect on the loop tracking performances. For the higher accuracy INS components, the dynamic stress noise is far less than the threshold, and which can be neglected. Therefore, the conclusion can be drawn that to pursue better tracking performance, a higher quality IMU should be used, e.g. the tactical is enough.

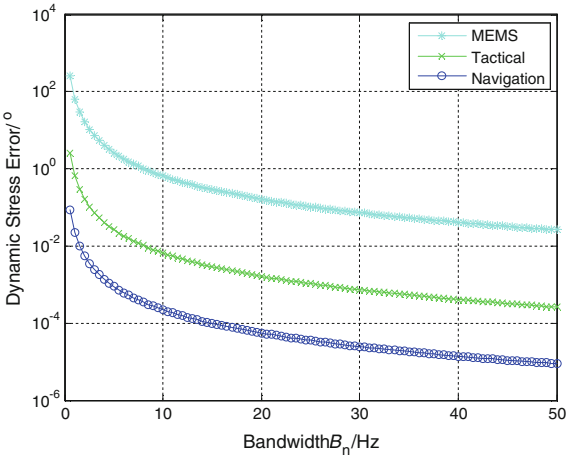

Fig. 7 The effect of dynamic stress noises with different accuracy grade INS components

Table 2 Performance index of three kinds of different accuracy grade INS components

	MEMS	Tactical	Navigation
Gyro bias	100°/h	1°/h	0.01°/h
Accelerometer bias	10 mg	0.1 mg	0.01 mg

6 Conclusion

In order to make GNSS receiver work normally for weak signal, this paper analyzes the tracking loop noises in detail, and derives the optimal bandwidth of carrier loop with INS-aid. The results show that the tracking error can be kept minimum with adjusting bandwidth adaptively based on C/N_0 of the received signals. Meanwhile, the effect of dynamic stress noise induced by receiver antenna's dynamics be decreased with INS aiding, namely, the optimized bandwidth setting can restrain loop noises, and the tracking error can effectively decreased.

It is complex for receiver to track weak signals, while with INS information, with more precise Doppler frequency estimator, the tracking loop lose lock uneasy. For the compensation effect of dynamic stress error is determined by the accuracy grade of the INS devices, so tactical IMU will enough for improve signal tracking performance of GNSS/INS deep coupling system, which is helpful for integration navigation design to pursue higher accuracy and reliability.

References

1. Alireza R, Demoz GE, Dennis M (2008) A Carrier loop architectures for tracking weak GPS signals. IEEE Trans AES 44(2):697–710
2. Lashley M, Bevly DM (2013) Performance comparison of deep integration and tight coupling. Navigation 60(3):159–178
3. Lashley M, Bevly DM (2008) A Comparison of the performance of a non-coherent deeply integrated navigation algorithm and a tightly coupled navigation algorithm. In: Proceedings of the 21st international technical meeting of the satellite division of the institute of navigation, Savannah, GA, USA
4. Sul GP, Ho Cheol J, Jeong WK et al (2011) Magnetic compass fault detection method for GPS/INS/magnetic compass integrated navigation systems. Int J Control Autom Syst 2:276-28
5. Kaplan ED, Hegarty CJ (2006) Understanding GPS: principle and applications, 2nd edn. Artech House, Boston
6. Borre K, Akos D (2005) A Software-defined GPS and Galileo receiver: single-frequency approach. In: ION 18th international technical meeting of the satellite division. Long Beach, CA, USA
7. Soloviev A (2010) Tight coupling of GPS and INS for urban navigation. IEEE Trans AES 46 (4):1731–1746
8. Ye P, Zhan XQ, Fan CM (2011) Novel optimal bandwidth design in INS-assisted GNSS phase lock loop. IEICE Electron Express 8(9):650–656
9. Li CJ, Yang SX (2012) Optimization of carrier tracking loop for GPS high dynamic receivers. J Beijing Inst Technol 21(2):164–171
10. Miao JF, Chen W, Sun YR et al (2011) Adaptively robust phase lock loop for low C/N carrier tracking in a GPS software receivers. Acta Autom Sin 37(1):52–60
11. Wang XL, Li YF (2012) An innovative scheme for SINS/GPS ultra-tight integration system with low-grade IMU. Aerospace Sci Technol 23(1):452–460
12. Groves PD (2005) GPS signal-to-noise measurement in weak signal and high-interference environments. Navigation 52(2):83–92
13. Qin F, Zhan XQ, Du G (2013) Performance improvement of receivers based on ultra-tight integration in GNSS-challenged environments. Sensors 13(12):16406–16423

Part III
Multi-sensor Fusion Navigation

The Multipath Fading Channel Simulation for Indoor Positioning

Shengchang Yu, Zhongliang Deng, Jichao Jiao, Shu Jiang, Jun Mo and Fuhai Xu

Abstract In recent years, with the increasing living standards, LBS (location-based service) has been gradually integrated into all aspects of daily life. However, compared to the outdoor environment, indoor environment is very complex. In this paper, we discuss the problem of TC-OFDM (time divided CDMA-OFDM superimposed signal system) multipath interference in the design of indoor positioning receiver based on the terrestrial broadcasting network. In the TC-OFDM system, because of the complexity of the indoor environment, the problem of multipath, especially the short-delay multipath, is particularly severe, which causes a serious impact on the receiver signal acquisition and tracking performance. Through theoretical analysis and mathematical simulation, we specify the characteristics of the fading channel in the indoor location and influence of the multipath signal. We also build the models of signals through the MATLAB software. Through the analysis in this paper, we can understand the propagation characteristics and the main error sources of the indoor signal better, furthermore, we provide theoretical basis for the system optimization in the future.

Keywords Indoor location · Multipath interference · Fading channel

Foundation project: The National High Technology Research and Development Program ("863" Program) of China (No. 2015AA124101). The National Science Foundation of China (No. 61401040).

S. Yu (✉) · Z. Deng · J. Jiao · S. Jiang · J. Mo · F. Xu
School of Electronic Engineering, Beijing University of Posts and Telecommunications, Beijing, China
e-mail: yushengchang@bupt.edu.cn

J. Sun et al. (eds.), *China Satellite Navigation Conference (CSNC) 2016 Proceedings: Volume II*, Lecture Notes in Electrical Engineering 389,
DOI 10.1007/978-981-10-0937-2_29

1 Introduction

The current mainstream positioning system includes American positioning system GPS, Compass China, European Galileo, Russia's GLONASS, and other satellite positioning systems. Satellite positioning system can obtain precise positioning accuracy in the outdoor environment, but due to occlusion of the building, it has more limitation in application of the indoor environment. With the increasing development of social progress and people's living standard, location-based services under the indoor environment have gained more and more attention. Research in related fields is becoming positioning technology research focus [1].

TC-OFDM (time divided CDMA-OFDM superimposed signal system) positioning system discussed herein is designed for the indoor complex environment, which can provide wide-area high-precision indoor location services. The current mainstream high-precision positioning systems use CDMA (Code Division Multiple Access) technology. So, TC-OFDM system is based on CDMA and the CDMA signal is superimposed on the mobile broadcast signals or mobile communication signal. Without affecting original system performance, TC-OFDM system provides users with high-accuracy location-based services. CDMA system has strong antijamming performance, high spectrum efficiency, confidentiality for advantages, but still could not overcome multipath problems. Multipath is one of the major sources of error in the receiver. The paper analyzes the indoor environment multipath fading channel characteristics. The impact of multipath signals is quantitatively analyzed and finally we carry out modeling and simulation in MATLAB [2]. The paper provides a theoretical basis for future anti-multipath indoor environment optimization design.

2 Brief Introduction of Mobile Fading Channel

In recent years, with the increasing people's living standards, the demand for mobile communications is also increased and research of mobile fading channel has become a hot topic. In the process of radio transmission, the simplest of form is the free space propagation. The so-called free space propagation refers to homogeneous media space with the permittivity and permeability of 1 [3]. The space has characteristics of conductivity of 0 and isotropic. Calculated as:

$$L_S(\mathrm{dB}) = 32.45 + 20\lg f + 20\lg d \tag{1}$$

Among the equation, L_S is the free space path loss; f is the operating frequency in units of MHz; d is the propagation path in units of Km. The actual mobile channel not only has the free space path loss, but also has additional propagation path loss. Signal is primarily affected by multipath signal interference, communication object movement, and so on, which makes the modeling for mobile fading channel more difficult.

3 Research for Indoor Multipath Fading Channels

3.1 Indoor Fading Channel Model

This article focuses on indoor positioning multipath fading channel. Indoor positioning system structure diagram is shown in Fig. 1. In the figure, pseudo-satellite station transmits a positioning signal and the signal through a complex channel eventually reaches positioning receiver to calculate location information [4].

Multipath propagation effects mainly show up on the expanding delay and frequency selectivity decline. Figure 2 shows the positioning signal model through a multipath fading channel model.

Wherein $s(t)$ stands for the TC-OFDM baseband signal; ω_c is the RF carrier frequency; $h(t, \zeta)$ is the channel impulse response; $r(t)$ is the actual signal received by the receiver.

3.2 Indoor Multipath Channel Model

In the TC-OFDM signals, CDMA signal, which is composed of PN sequence and superimposed on the carrier signal, is actually used for ranging. So, this article

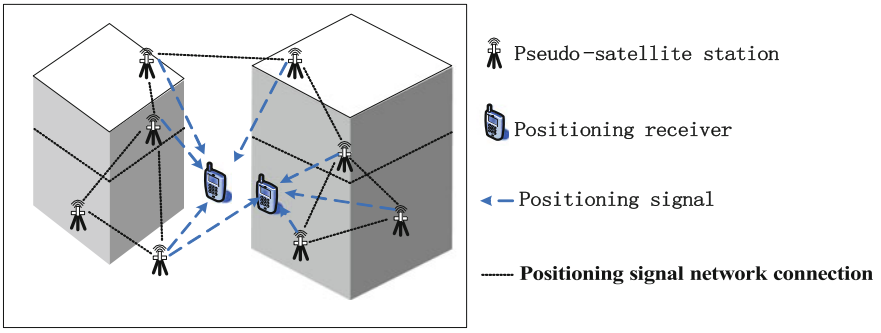

Fig. 1 Indoor positioning system structure diagram

Fig. 2 Fading channel model

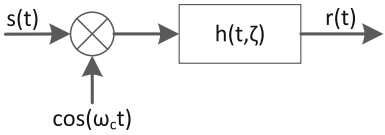

focuses on the CDMA signal analysis and ignores OFDM signal. The baseband signal is described as:

$$s(t) = AD(t)C(t) \tag{2}$$

Among the equation, A is the amplitude of the baseband signal; $D(t)$ is a data message; $C(t)$ is the spreading code. When the receiver demodulates the signal, it needs to carry on the coherent integration for the spread spectrum signal. The autocorrelation function of the variation of the phase difference of the spread spectrum code can be expressed as:

$$R_c(\zeta) = \frac{1}{T_c}\int_0^{T_c} C(t)C(t+\zeta T_c)\mathrm{d}t \tag{3}$$

Among the equation, T_c is the pseudocode period; ζ is normalized code phase. Under the unlimited bandwidth, the auto correlation value is a linear function within the range of one chip. We let $H(T,$ zeta) for mobile fading channel complex low-pass impulse response, then auto correlation function of $H(T,$ zeta) is

$$\begin{aligned} R_h(\Delta t;\zeta_1,\zeta_2) &= \frac{1}{2}E[h^*(t;\zeta_1)h(t+\Delta t;\zeta_2)] \\ &= \varphi_h(\Delta t;\zeta_1)\delta(\zeta_1-\zeta_2) \end{aligned} \tag{4}$$

In the equation, when the $\Delta t = 0$, $\varphi_h(\Delta t;\zeta_1)\delta(\zeta_1-\zeta_2)$ is called multipath density function (MIP, multipath intensity profile) [5]. For Rayleigh fading channels, $h(t,\ z)$ is a zero-mean complex Gaussian random process. If you do not consider the effect of noise, the signal received by the receiver is as follows:

$$r(t) = Re\{A\tilde{r}(t)\mathrm{e}^{\mathrm{j}\omega_c t}\} \tag{5}$$

Among them

$$\begin{aligned} \tilde{r}(\mathrm{t}) &= \int_{\tau t}^{\infty} D(t-\zeta)C(t-\zeta)h(t,\zeta)\mathrm{d}\zeta \\ &= \sum_{k=0}^{\infty}\int_{kT_c}^{(k+1)T_c} D[t-\tau(t)-\zeta]\cdot C[t-\tau(t)-\zeta]\cdot h[t,\tau(t)+\zeta]\mathrm{d}\zeta \end{aligned} \tag{6}$$

Type of $\tau(t)$ represents the channel change delay. Since the actual channel is a causal system, so we set when $\zeta < \tau(t)$, the value of $h(t,\ \zeta)$ is zero in the process of derivation. Because of the nature of the spreading code, the chip level is invariant in a chip-level time. Therefore, in Eq. (6), the internal factor of integral number can be put forward, so we can see

$$\widetilde{r}(t) = \sum_{k=0}^{\infty} D[t - \tau(t) - \zeta] \cdot C[t - \tau(t) - \zeta] \cdot h_k(t) \tag{7}$$

Among them

$$h_k(t) = \int_{kT_c}^{(k+1)T_c} h[t, \tau(t) + \zeta] \mathrm{d}\zeta \tag{8}$$

As can be seen from the above equation, $h_k(t)$ is uncorrelated zero-mean complex Gaussian random process, and its variance is as follows:

$$\sigma_k^2(t) = \frac{1}{2} E[h^*(t)h(t)] = \frac{1}{2} \int_{kT_c}^{(k+1)T_c} \varphi_h(0, \tau(t) + \zeta) \mathrm{d}\zeta \tag{9}$$

It assumed that when $\zeta > \tau(t) + (L + 1)T_c$, then $\varphi(0, \zeta) = 0$, therefore Eq. (7) can be derived as:

$$\tilde{r}(t) = \sum_{k=0}^{L} D[t - \tau(t) - kT_c] \cdot C[t - \tau(t) - kT] \cdot h_k(t) \tag{10}$$

In the $h_k(t) = a_k(t)\mathrm{e}^{\mathrm{j}\theta_k(t)}$, we can know $a_k(t)$ obeys the Rayleigh distribution and $\theta_k(t)$ obeys the uniform distribution from characteristics of Rayleigh Road. As mentioned above, you can see the indoor multipath fading channel will affect the amplitude and phase of TC-OFDM signals. The signal receiving and positioning precision of the positioning receiver will be impacted.

4 Simulation and Analysis of the Indoor Multipath Fading Channel

4.1 Single-Path Rayleigh Fading Channel Simulation

The probability of Rayleigh fading distribution is shown in Fig. 3.

From the analysis shown in the last chapter, we can know that fading channel should be Rayleigh distribution under the condition of non-line of sight and the maximum Doppler frequency shift is 200 Hz single-path Rayleigh fading channel. The simulation is shown in Fig. 4.

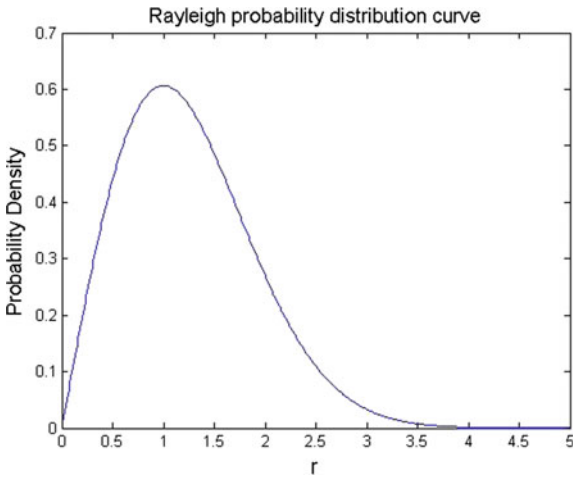

Fig. 3 Rayleigh probability distribution curve

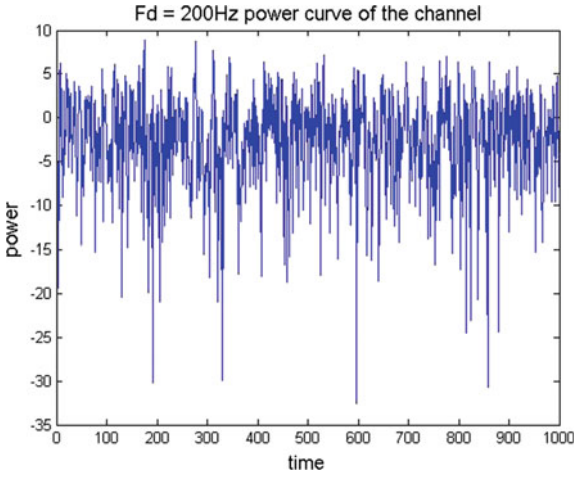

Fig. 4 Single-path Rayleigh fading channel

4.2 Multipath Rayleigh Fading Channel Simulation

Rayleigh fading channel simulation of the multipath fading channel is shown in Fig. 5. The simulation signal is a common indoor positioning short multipath signal with the smaller code retardation of direct signal and multipath signal and the smaller Doppler frequency.

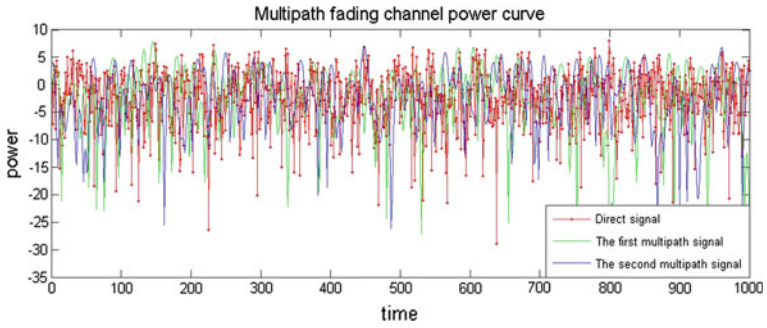

Fig. 5 Multipath Rayleigh fading channel

From the above chart, we can see that when the positioning signal reaches the receiver through reflection, refraction, scattering, and other multiple paths, the total signal strength obeys Rayleigh distribution. If the receiver moves or for other reasons, the signal strength and phase characteristics can be led to change.

5 Conclusion

This paper outlines the current development status of indoor positioning and mobile fading channel and then focuses on the multipath fading channels in the indoor complex environment. We carry out modeling. The main work is to quantify a channel model and multipath interference, and we provide a theoretical basis for the latter positioning receiver multipath technology research.

References

1. Yingchun Li (2008) Modeling and simulation of mobile fading channels. Shanghai University, Shanghai
2. Xie G (2009) Principles of GPS and receiver design. Publishing House of Electronics Industry, Beijing, pp 376–384
3. Chen L, Wan G, Feng Z (2004) The simulation of multi-path fading channel in mobile communication based on matlab. J Jiangxi Sci Technol Normal Univ 05:78–81
4. Deng Z, Li X, Ma W, Fang Y, Zeng H (2015) Design and implementation of indoor & outdoor positioning service platform based on Beidou and base station system. In: The 5th China satellite navigation conference
5. Deng Z, Yu Y, Yuan X, Wan N (2013) Situation and development tendency of indoor positioning. China Commun

Research on Ranging/GNSS Localization Based on Pollution Collaborative Positioning via Adaptive Kalman Filter

Lin Zhang, Baowang Lian and Hao Yan

Abstract Collaborative positioning in many applications has broad prospects especially in the complex and weak environment. However, complicated and changeable environment has brought challenges to robust and precision fusion filter methods. To this end, this paper put forward the collaborative positioning algorithm based on adaptive Kalman filtering (CPAKF) according to the maximum likelihood criterion which can adaptively adjust process noise covariance and observation noise covariance, make the fusion filtering adapt to the changeable and complex noise environment, and have a certain anti-interference performance. Then, the pollution collaborative positioning algorithm (PCP) is presented which can achieve isolation of pollution nodes, make the other nodes clear by collaborative positioning and improve the accuracy of all peer nodes in the network ultimately. Simulation analysis of multi-use standalone as well as collaborative positioning based on the traditional kalman and adaptive kalman filtering. Compared to the traditional standalone kalman-based positioning algorithm (SKF), the collaborative positioning algorithm based on adaptive kalman filtering (CPAKF) is much better. Besides, the PCP with much smother curve can avoid pollution nodes affecting others which performs best among three positioning algorithms.

Keywords Adaptive kalman filter · GNSS · Terrestrial ranging · Pollution collaborative positioning

1 Introduction

In recent years, navigation and positioning technology has penetrated almost every aspect of our lives including national economic construction, national defense construction, and scientific research. The main application areas of the civil aspects

L. Zhang (✉) · B. Lian · H. Yan
Northwestern Polytechnical University, Xi'an 710129, China
e-mail: linlin_1106@126.com

J. Sun et al. (eds.), *China Satellite Navigation Conference (CSNC) 2016 Proceedings: Volume II*, Lecture Notes in Electrical Engineering 389,
DOI 10.1007/978-981-10-0937-2_30

are geodetic survey, resources exploration, monitoring deformation, transportation, city comprehensive serves, and telecommunications network, etc. However, with the improvement of variety of service, higher requirements for accuracy, environment and positioning technologies of navigation and positioning are put forward. Accordingly, kinds of enhanced techniques have emerged related to global satellite navigation system (GNSS) to improve the positioning accuracy and availability. Differential GNSS, ground and satellite-based augmentation system, pseudolite positioning, multi-sensor integrated navigation and other technical approaches have been adopted to assist GNSS positioning. And the high accuracy of navigation and positioning is considered especially in the case of GNSS signal cannot be covered, for instance, indoor, canyon, and underground environment. With the continuous development of communication technology, the information service network in the future must be integrated with a variety of technologies, sharing information, adapting to a variety of environment which promotes the production of collaborative positioning and navigation technology. All shared information in the network is utilized for users to provide location services. Particularly, the distributed collaborative positioning technology based on the ranging technology (ranging) and GNSS is attracting more and more attention due to potential application in the future.

Collaborative positioning [1–4] network is equipped with distributed N users and S satellites. The main idea of ranging/GNSS collaborative positioning is to utilize the pseudorange measurements and terrestrial range measurements of all users in the network to complete PVT. In addition to pseudorange measurements, ephemeris, locations, and observations, all can be shared between users which can assist to capture weak signal, achieve data fusion and then improve the positioning accuracy. At present, terrestrial ranging technology can be achieved based on the received signal strength (RSS) and time of arrival (TOA). The collaborative positioning is analyzed based on Bluetooth, WIFI, and ultra wideband (UWB) by Politecnico Di Torino team [5, 6]. In addition, they also have studied the dedicated short range communication (DSRC) system. In terms of data fusion [7, 8], the least square (LS), kalman filtering (KF), unscented kalman (UKF), particle filter (PF), and sum product algorithm are also made progressed.

In this paper, the collaborative positioning algorithm based on adaptive kalman (CPAKF) and the pollution collaborative positioning (PCP) algorithm are presented. Compared to traditional standalone kalman-based (SKF) positioning algorithm, CPAKF-based with a smother curve is much better than SKF-based positioning algorithm and error probability distribution (EPD) is more concentrated especially in harsh environment. In order to improve the accuracy of all users in the network, the PCP algorithm which isolates the polluted nodes and assists the polluted nodes is analyzed.

2 Ranging/GNSS Collaborative Positioning Model

2.1 System Model

Given a collaborative positioning network with decentralized U peer nodes and S satellites. For any user i, the state model with three dimensional position and velocity, clock error and clock drift, expressed in meters

$$\begin{aligned} \hat{x}(t) &= \{x_i^t, y_i^t, z_i^t, c_i^t, v_{x_i}, v_{y_i}, v_{z_i}, \dot{c}_i^t\}; \\ c_i^t &= c \cdot \delta t_i, i = 1, 2, \ldots U; \end{aligned} \tag{1}$$

where x, y, z, $v_{x_i}, v_{y_i}, v_{z_i}$ denote the three dimensional position and velocity respectively, c is the speed of light, δt_i is the clock error of receiver.

The state time evolution is modeled by

$$\begin{aligned} \hat{x}_i(t) &= f(\hat{x}_i(t-1), \omega_i^t) \\ \omega_i^t &\sim N(0, Q_i^t) \end{aligned} \tag{2}$$

where $f(\cdot)$ is the state transition function which evolves the state of node i in time given its previous state $\hat{x}_i(t-1)$, and ω_i^t is the process noise vector distributed with zero mean and covariance matrix Q_i^t.

Then, the state variable system model of node i can be indicated by

$$\hat{x}_i(t) = F_i \cdot \hat{x}_i(t-1) + G_i \cdot \omega_i^t \tag{3}$$

F and G is given as

$$F_i = \begin{bmatrix} I_{4\times4} & TI_{4\times4} \\ 0_{4\times4} & 0_{4\times4} \end{bmatrix}, G_i = \begin{bmatrix} 0.5T^2 I_{4\times4} \\ TI_{4\times4} \end{bmatrix} \tag{4}$$

where I is the identity matrix, and T is the time interval.

2.2 Observation Model

The collaborative positioning is observed through pseudorange ρ from nodes to their visible satellites and terrestrial range measurements d from peer to peer. For each node i, measurements of collaborative positioning $z_i(t)$ with observation function $h(\cdot)$ is expressed as

$$\begin{aligned} z_i(t) &= h(\hat{x}_i(t), v_i(t)) \\ &= \begin{bmatrix} z_{\rho_i} \\ z_{d_i} \end{bmatrix} = \begin{bmatrix} h_{\rho_i}(\hat{x}_i(t), v_{is}(t)) \\ h_{d_i}(\hat{x}_i(t), v_{ij}(t)) \end{bmatrix} \quad \text{where } i, j = 1, 2, \ldots, N \\ v_i(t) &\sim N(0, R_i(t)) \end{aligned} \tag{5}$$

where $v_i(t) = [v_{is}(t), v_{ij}(t)]^{\mathrm{T}}$ is the observation noise vector distributed with zero mean and covariance matrix

$$R_i(t) = \mathrm{diag}(R_{is}(t), R_{ij}(t)) \tag{6}$$

Pseudorange observation function of node i is computed with

$$h_{\rho_i}(t) = \sqrt{(x_i - x_s)^2 + (y_i - y_s)^2 + (z_i - z_s)^2} + c_i, \tag{7}$$

The Jacobian matrix of pseudorange observation is give by

$$H_{\rho_i} = \begin{bmatrix} \frac{\partial h_{\rho_i}}{\partial x_i} & \frac{\partial h_{\rho_i}}{\partial y_i} & \frac{\partial h_{\rho_i}}{\partial z_i} & \frac{\partial h_{\rho_i}}{\partial v_{x_i}} & \frac{\partial h_{\rho_i}}{\partial v_{y_i}} & \frac{\partial h_{\rho_i}}{\partial v_{z_i}} & \frac{\partial h_{\rho_i}}{\partial c_i} & \frac{\partial h_{\rho_i}}{\partial \dot{c}_i} \\ \vdots & \vdots & \vdots & \vdots & \vdots & \vdots & \vdots & \vdots \end{bmatrix} \tag{8}$$

In order to simply analyze, the terrestrial ranging observation function between peer i and j is only given

$$h_{d_{i,j}}(t) = \sqrt{(x_i - x_j)^2 + (y_i - y_j)^2 + (z_i - z_j)^2} \tag{9}$$

Partial derivatives of the function

$$\begin{aligned} \Delta h_{d_{i,j}} &= \begin{bmatrix} \frac{\partial h_{d_{i,j}}}{\partial x_i} & \frac{\partial h_{d_{i,j}}}{\partial y_i} & \frac{\partial h_{d_{i,j}}}{\partial z_i} & \frac{\partial h_{d_{i,j}}}{\partial c_i} \end{bmatrix} \\ \Delta h_{v_{i,j}} &= \begin{bmatrix} \frac{\partial h_{d_{i,j}}}{\partial v_{x_i}} & \frac{\partial h_{d_{i,j}}}{\partial v_{y_i}} & \frac{\partial h_{d_{i,j}}}{\partial v_{z_i}} & \frac{\partial h_{d_{i,j}}}{\partial \dot{c}_{x_i}} \end{bmatrix} = [0, 0, 0, 0] \\ \Delta h_{d_{j,i}} &= \begin{bmatrix} \frac{\partial h_{d_{i,j}}}{\partial x_j} & \frac{\partial h_{d_{i,j}}}{\partial y_j} & \frac{\partial h_{d_{i,j}}}{\partial z_j} & \frac{\partial h_{d_{i,j}}}{\partial c_j} \end{bmatrix} = -\Delta h_{d_{i,j}} \\ \Delta h_{v_{j,i}} &= [0, 0, 0, 0] \end{aligned} \tag{10}$$

The Jacobian matrix of ranging observation is expanded as follows:

$$H_{di} = \underbrace{\begin{bmatrix} 0 & \cdots & \overbrace{[\Delta h_{d_{i,j}}, \Delta h_{v_{i,j}}]}^{i} & \cdots 0 \cdots & \overbrace{[\Delta h_{d_{j,i}}, \Delta h_{v_{j,i}}]}^{j} & \cdots & 0 \\ \vdots & \cdots & \vdots & \cdots & \vdots & \cdots & \vdots \\ 0 & \cdots & \overbrace{[\Delta h_{d_{i,k}}, \Delta h_{v_{i,k}}]}^{i} & \cdots 0 \cdots & \overbrace{[\Delta h_{d_{k,i}}, \Delta h_{v_{k,i}}]}^{k} & \cdots & 0 \end{bmatrix}}_{U} \tag{11}$$

2.3 Mutil-use Collaborative Positioning Model

According to the system model and observation model above, the collaborative positioning system and observation model with U peer nodes and S satellites is given by

$$X = [\hat{x}_1, \ldots, \hat{x}_U]^{\mathrm{T}} \tag{12}$$

$$F = \mathrm{diag}(F_1, \ldots F_U), G = [G_1, \ldots, G_U]^{\mathrm{T}} \tag{13}$$

$$Q = \mathrm{diag}(Q_1, \ldots, Q_U) \tag{14}$$

$$Z = [z_{\rho_1}, \ldots z_{\rho_U}, z_{d_1}, \ldots, z_{\rho_{d_U}}]^{\mathrm{T}} \tag{15}$$

$$H_\rho = \mathrm{diag}(H_{\rho_1}, \ldots, H_{\rho_U}) \tag{16}$$

$$H_d = [H_{d_1}, \ldots H_{d_U}]^{\mathrm{T}} \tag{17}$$

$$H = \begin{bmatrix} H_\rho \\ H_d \end{bmatrix}, R = \mathrm{diag}(R_i, \ldots, R_U) \tag{18}$$

3 Estimation Algorithm

The main work of multi-use collaborative positioning estimation algorithm is to estimate the position via fusion filter based on all measurements, including GNSS and terrestrial range measurements. According to Eqs. (12)–(18), kalman filter and adaptive KF of collaborative positioning are respectively analyzed below.

3.1 Kalman Filter

(1) Predict step

The transition matrix F is used to predict a prior state and covariance at the current time given the previous posteriori estimates

$$X(t/t-1) = FX(t-1) \tag{19}$$

$$P(t/t-1) = FP(t-1)F + GQG^T \tag{20}$$

(2) Update step
Innovation, filter gain and state covariance are computed as

$$b_t = \tilde{Z}(t) = Z(t) - h(x(t/t-1)) \tag{21}$$

$$K(t) = P(t/t-1)H^T(HP(t/t-1)H^T + R)^{-1} \tag{22}$$

$$P(t) = (I - K(t)H)P(t/t-1) \tag{23}$$

(3) State estimate
With the filter gain correct the state estimate

$$X(t) = X(t/t-1) + K(t)\tilde{Z}(t) \tag{24}$$

3.2 Adaptive Kalman Filter

The criterion of maximum likelihood estimation is to estimate the state from the perspective of maximum probability of observation, not only to consider the change of innovation but also the innovation covariance matrix.

Assuming the measurements follow Gaussian distribution

$$P(z\backslash\alpha)_t = \frac{1}{\sqrt{(2\pi)^m |C_{b_t}|}} \mathrm{e}^{-\frac{1}{2}b_t^T C_{b_t}^{-1} b_t} \tag{25}$$

where α is the adaptive parameter, C_{b_t} is innovation covariance matrix, and m is the number of measurements.

Making $\partial \ln P/\partial\alpha$, and after simplification

$$\sum_{t=t_0}^{n} [tr\{C_{b_t}^{-1}\frac{\partial C_{b_t}}{\partial\alpha}\} - b_t^T C_{b_t}^{-1}\frac{\partial C_{b_t}}{\partial\alpha}C_{b_t}^{-1}b_t] = 0 \tag{26}$$

For a fixed-length memory filter, the innovation sequence will be considered inside the estimation window of size N and t represents the moving epoch inside the window. Where t_0, n in the above formula can be indicated as $N = n - t_0 + 1$.

The innovation covariance matrix and predict state covariance is expanded as

$$\begin{aligned} C_{b_t} &= R(t) + HP(t/t-1)H^T \\ P(t/t-1) &= HP(t)H^T + Q. \end{aligned} \tag{27}$$

Taking the results of above to Eq. (26)

$$\sum_{t=t_0}^{n} tr\left\{\left[\frac{\partial R(t)}{\partial \alpha}+H_t\frac{\partial Q(t-1)}{\partial \alpha}H_t^T\right]\left[\frac{\partial R(t)}{\partial \alpha}+H_t\frac{\partial Q(t-1)}{\partial \alpha}H_t^T\right]\right\}=0 \tag{28}$$

The simplification of Eq. (28), respectively

$$\begin{cases}\sum\limits_{t=t_0}^{n} tr\{C_{b_t}^{-1}[C_{b_t}-b_t b_t^T]C_{b_t}^{-1}\}=0\,, & \alpha=R\\ \sum\limits_{t=t_0}^{n} tr\{K(t)HP(t/t-1)-K(t)b_t b_t^T K^T(t)\}=0, & \alpha=Q\end{cases} \tag{29}$$

The observation noise and process noise of the adaptive kalman filtering collaborative positioning is indicated by

$$\begin{cases}\hat{C}_{b_t}=\frac{1}{N}\sum\limits_{t=t_0}^{n} b_t b_t^T\\ \hat{R}(t)=\hat{C}_{b_t}-H(t)P(t/t-1)H^T(t)\end{cases}$$
$$\begin{cases}\Delta x_t=K(t)b_t\\ \hat{Q}(t)=\frac{1}{N}\sum\limits_{t=t0}^{n}\Delta x_t\Delta x_t^T+P(t)-FP(t-1)F^T\end{cases} \tag{30}$$

4 Experimental Results

4.1 Static Test

In this section, the performance of KF and AKF-based collaborative and traditional standalone positioning with real satellites position are analyzed. In the test, the observation started at 19:00 Beijing time on June 5, 2015. The ephemeris on June 5, 2015 of Beijing time is used to compute the position of satellites whose PRN including 5, 15, 21, 20. The position of peer node A is taken as the origin of the reference system with the geodetic coordinate system $(34.0314^{\circ}, 108.76350^{\circ}, 422.2764613^{\circ})$. The position of static peer node A, B, and C in ENU are respectively $A=(0,0,0)$, $B=(40,0,0), C=(40,40,0)$.

Pseudorange and terrestrial range measurements are corrupted by additive white Gaussian noise with standard deviation $\sigma_\rho=5$ and $\sigma_d=0.2$ m respectively. And peer node A is simulated in harsh environment with standard deviation $\sigma_{\text{add}}=50$ m duration of 100 epochs from epoch 500 to epoch 599 which is defined as pollution phase. Then, the standalone positioning based on Kalman (SKF), the collaborative positioning based on Kalman (CPKF) and adaptive Kalman (CPAKF) are carried out in 2000 epochs. Figures 1, 2 and 3 are the positioning error results and EPD of peer node A, B, and C respectively. The RMSE of SKF, CPKF, CPAKF are seen in Table 1.

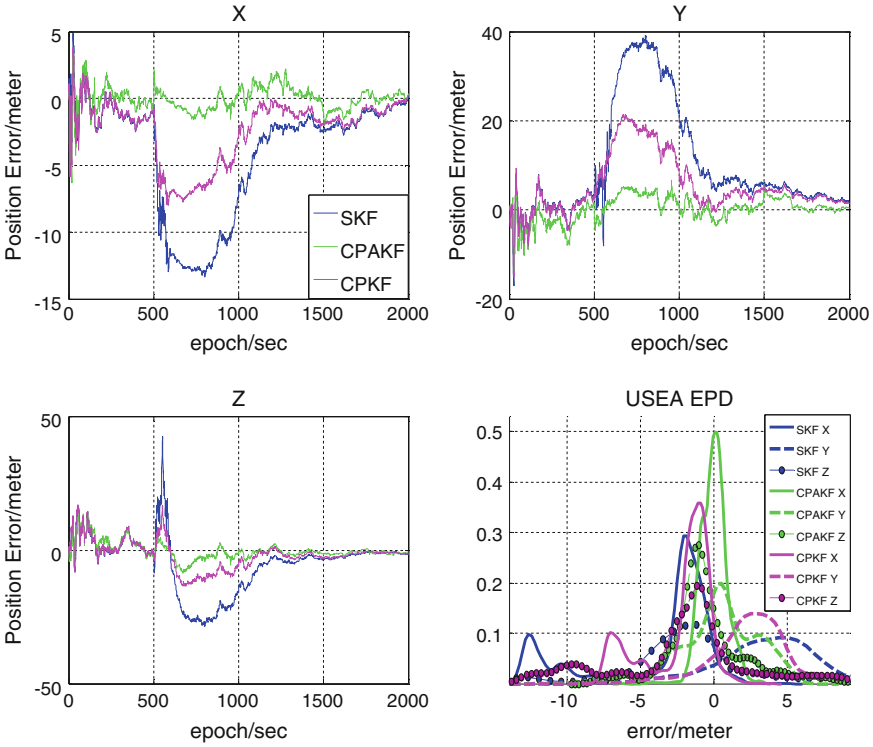

Fig. 1 Position error of static node *A*

Figure 1 shows the positioning results of peer node *A* in ECEF in harsh environment. In the pollution phase, the curve of SKF-based position error fluctuates enormously in all directions which means it is much easily affected by harsh environment. And the maximum positioning error reaches 40 m from epoch 500 to the highest point of epoch 600 which is consistent with the pollution phase. Besides, it can be noticed from the EPD of node *A* that, compared to the SKF-based and CPKF-based positioning algorithm, the EPD of CPAKF-based positioning algorithm is most moving closer to the middle. And it is obvious that CPKF-based positioning can reduce the error of results and the fluctuation of error, and the CPAKF-based positioning which can smooth the error curve and have the optimal performance among the three algorithms.

It is can be seen that the collaborative localization algorithm of CPKF-based and CPAKF-based greatly reduces the error of the user A, but the error jitter of user A indeed affects the positioning results of user B and C. Figures 2 and 3 and Table 1 together show that instead of getting smother, the CPKF-based and CPAKF-based positioning error of node *B* and *C* turned into larger than SKF-based positioning in the pollution phase. The RMS of former is 2–3 m larger than SKF-based positioning, and the latter is larger than SKF-based positioning in *Z* direction of node

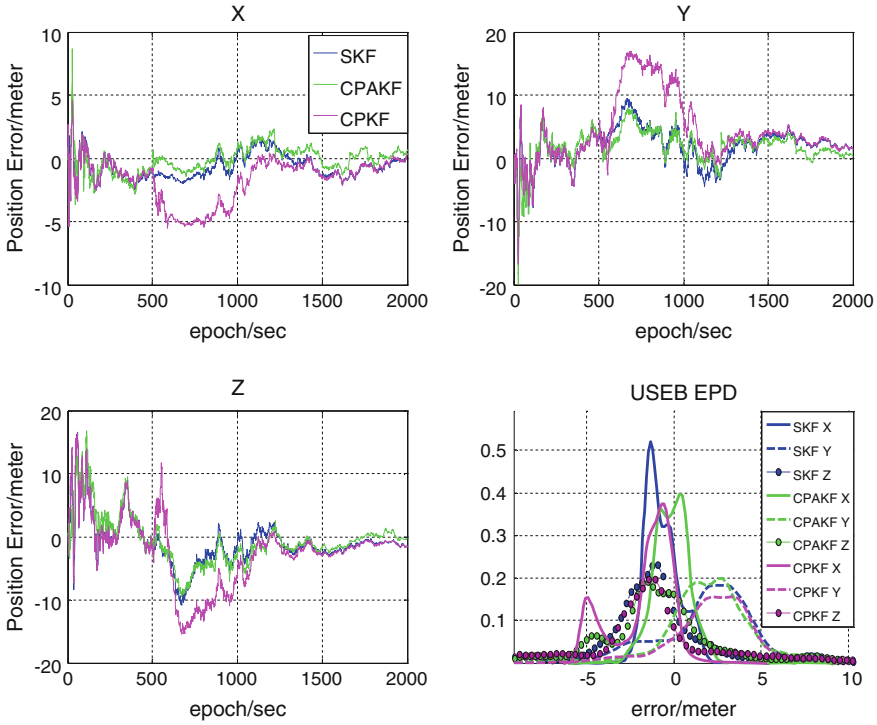

Fig. 2 Position error of static node *B*

B and in *X*, *Y* direction of node *C*. The EPD result of SKF-based positioning is much closer to the middle area which is quite different from that of node *A*. In other words, the collaborative localization algorithm (CPKF, CPAKF) makes the node *A* in the harsh environment affect the positioning accuracy of other nodes, which accordingly reduces collaborative positioning performances.

4.2 Pollution Collaborative Positioning Algorithm

The conclusions from the analysis above are that the method of collaborative positioning can increase the error of other non-polluted nodes due to interdependence relationship between nodes. Consider this circumstance, the PCP algorithm based on AKF is proposed which can achieve isolation of pollution nodes, make the other nodes clear by cooperative positioning and improve the accuracy of all peer nodes in the network ultimately.

The PCP algorithm requires clock synchronization among all peer nodes. In the practical application, the threshold *G* which is used to determine the pollution nodes

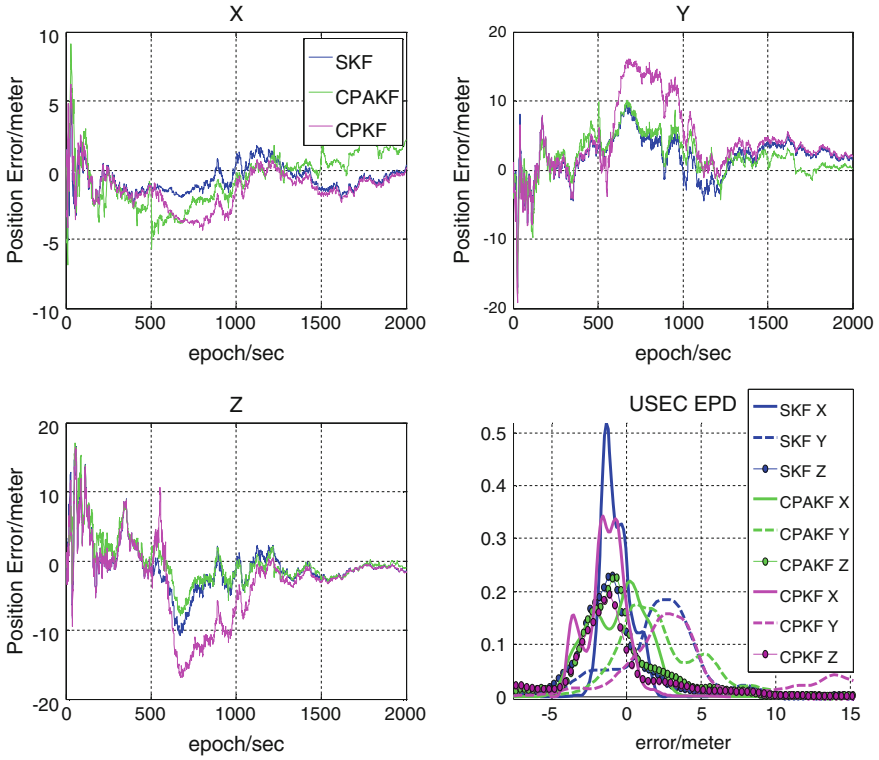

Fig. 3 Position error of static node *C*

Table 1 RMSE of SKF, CPKF, and CPAKF-based positioning

RMS (m)		SKF	CPKF	CPAKF
A	X	5.9741	3.3036	0.9084
	Y	15.9807	8.3928	2.8885
	Z	11.7431	5.5303	3.2650
B	X	1.1929	2.4391	1.0751
	Y	3.5815	6.8182	3.2825
	Z	3.7321	5.8806	3.8667
C	X	1.1929	1.9216	2.0067
	Y	3.5815	6.5723	3.7342
	Z	3.7321	6.1932	3.4737

can be tested under different environment conditions based on innovation sequences in advance. The above approach will be considered in next work. The flow chart is shown in Fig. 4.

Fig. 4 Flowchart of PCP

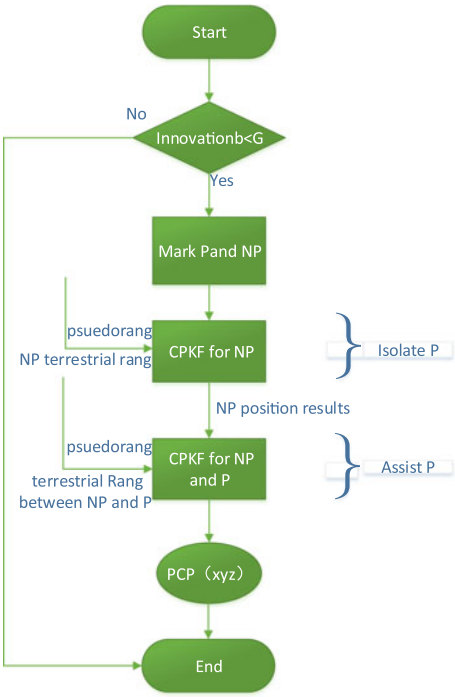

The PCP algorithm is described as follows:

1. To determine whether the innovation sequences exceed the threshold G and mark the polluted nodes as 'P' based on innovation sequences. The rest of the nodes are marked as 'NP'. Otherwise, end of the algorithm.
2. Compute the position coordinates of NP with pseudoranges from NP to satellites and terrestrial range measurements of NP after the state equation and observation equations were established which means completing insulating the nodes P.
3. According to position coordinates of NP in step 2, pseudoranges from P to satellites and terrestrial range measurements from P to NP, the state equation and observation equations of P were established which means NP assisting P positioning.
4. Output the position results of NP and P.

Figures 5, 6 and 7 show the positioning results of node A, B, and C based on CPAKF and PCP. The simulation data is the same as before and the pollution phase is always starts from epoch 500 to 599. The node P including peer node A and the node NP including peer node B and C are still not changed in this test. As it is seen from Figs. 5, 6, and 7 that, the curve of PCP is more smother than CPAKF in pollution phase. The RMSE is shown in Table 2 also illustrates the point that the error of PCP algorithm is significantly less than that of CPAKF which contribution

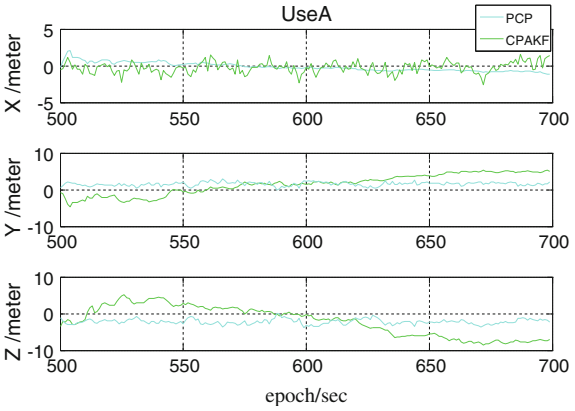

Fig. 5 Positioning results of node *A* based on CPAKF and PCP

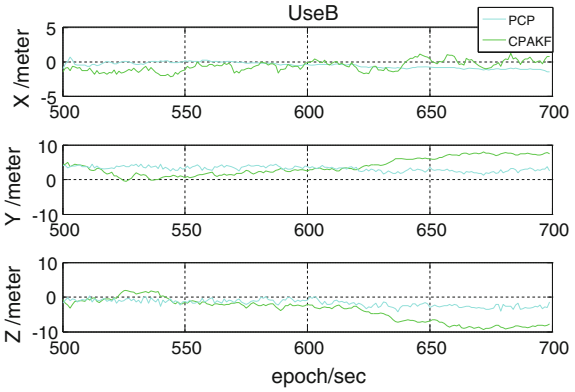

Fig. 6 Positioning results of node *B* based on CPAKF and PCP

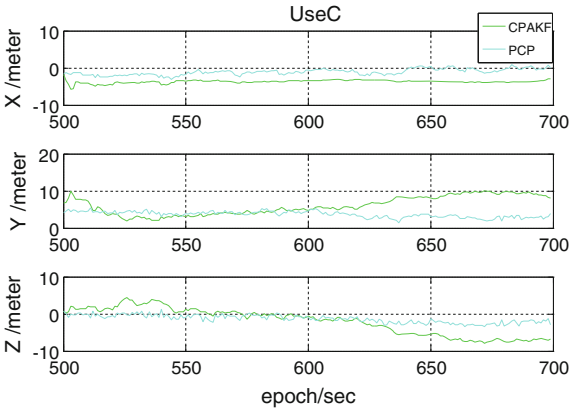

Fig. 7 Positioning results of node *C* based on CPAKF and PCP

Table 2 The RMSE of the static model based on CPAKF and PCP in pollution phase

RMS (m)		CPAKF	PCP
A	X	0.8060	0.6012
	Y	3.1006	1.6693
	Z	4.5385	2.3204
B	X	0.9844	0.6682
	Y	4.5164	3.2253
	Z	5.0469	1.9826
C	X	3.7121	1.3389
	Y	6.5618	3.7754
	Z	4.0942	1.6957

to isolating the node *P* and the node NP also helping *P* to position, so that all the users in the network can reduce the error.

4.3 Dynamic Model Trajectory Test

Peer node *A* and *C* are static users with the both same coordinates in static experiments before. Peer node *B* makes uniform circular motion in *E* direction taking the node *A* as circle center with 40 m radius and 1 m/s velocity. In this test section, *B* as the pollution node *P*, *A* and *C* as non-pollution node NP with their ENU coordinates are *A*(0, 0), *B*(0, 40, 0), *C*(40, 40, 0). The motion trajectory of dynamic model is described in Fig. 8. The RMS of the model based on SKF, CPAKF and PCP is in Table 3.

Figure 9 shows positioning results of dynamic model. It is clear that the position error of dynamic node *B* is a little greater than that of static nodes. For dynamic node *B*, the CPAKF-based positioning algorithm is more closer to the true trajectory than SKF-based. However, it is conclusion that the PCP-based algorithm has the

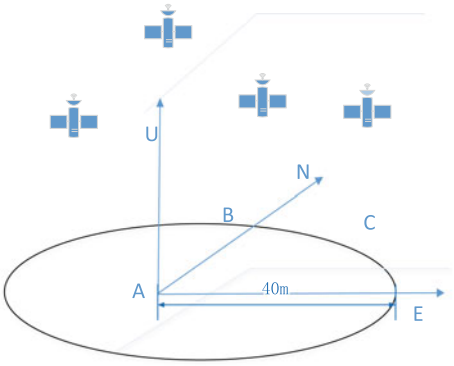

Fig. 8 Trajectory of dynamic model

Table 3 The RMS of the dynamic model based on SKF, CPAKF, and PCP

RMS (m)		SKF	CPAKF	PCP
A	X	1.5002	1.4864	1.4464
	Y	4.5502	4.6414	4.5667
	Z	5.4871	4.7432	4.2264
B	Z	4.5811	5.8567	5.3612
	Y	7.2981	4.1677	3.3661
	Z	9.9308	4.4452	4.2368
C	X	1.5002	1.5032	1.5680
	Y	4.5502	4.6190	3.5943
	Z	5.4871	5.2960	5.2403

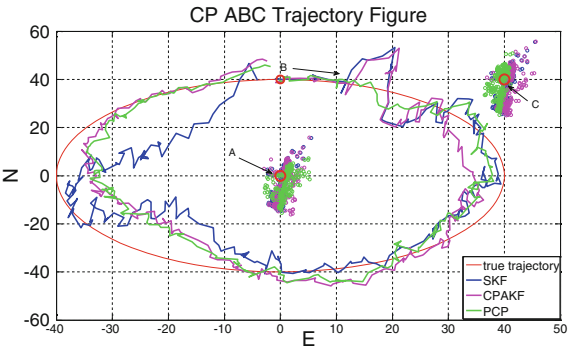

Fig. 9 Positioning of dynamic model

best performance among three algorithms. For the static node *A* and *C*, the CPAKF-based is better than SKF-based in some directions and PCP-based is most closest to the real coordinates due to isolating the dynamic node *B*.

5 Conclusions

The system model and observation model of multi-user collaborative positioning are proposed, respectively. Multi-user KF-based collaborative positioning, AKF-based collaborative positioning and PCP algorithms are analyzed. Based on simulation data, the condition of harsh environment is simulated, and three nodes static and dynamic models of standalone positioning and collaborative positioning are analyzed. Simulations reveal that the collaborative positioning solution showed greater accuracy over traditional standalone positioning method, especially the RMSE of pollution node is much smaller than that of the standalone positioning and obviously the adaptive KF is better than KF. However, the algorithm of the collaborative positioning can increase the error of other non-polluted nodes due to interdependence

relationship. Consequently, the PCP algorithm is presented which can achieve isolation of pollution nodes, make the other nodes clear by collaborative positioning and improve the accuracy of all peer nodes in the network ultimately.

Acknowledgments We are grateful to the reviewers for their comments and suggestions. This work was supported by the key laboratory project of science and technology innovation of Shaanxi Province (Grant no. 2013SZS15-K01).

References

1. Mauricio AC, Francesco S, Roberto G et al (2010) Spirito, hybrid GNSS-ToA localization and tracking via cooperative unscented kalman filter. In: IEEE 21st international symposium on personal, indoor and mobile radio communications workshops, pp 272–276
2. Huang B, Yao Z, Cui X et al (2015) Dilution of precision analysis for GNSS collaborative positioning. IEEE Trans Veh Technol 64(5):427–437
3. Mourikis AI, Roumeliotis SI (2006) Performance analysis of multi-robot cooperative localization. IEEE Trans Robot 22(4):666–681
4. Cardinali R, De Nardis L, Di Benedetto MG et al (2006) UWB ranging accuracy in high- and low-data-rate applications. IEEE Trans Microwave Theory Tech 54:1865–1875
5. Garello R, Lo Presti L, Corazza GE et al (2012) Peer-to-peer cooperative positioning part I: GNSS-aided acquisition. InsideGNSS 7(2):55–63
6. Garello R, Samson J, Spirito MA et al (2012) Peer-to-peer cooperative positioning part II: hybrid devices with GNSS and terrestrial ranging capability. InsideGNSS 7(4)
7. Caceres MA, Penna F, Wymeersch H et al (2011) Hybrid cooperative positioning based on distributed belief propagation. IEEE J Sel Areas Commun 29(10):1948–1958
8. Wymeersch H, Lien J, Win MZ (2009) Cooperative localization in wireless networks. Proc IEEE 97(2):427–450

Dynamic Weighted Data Fusion Algorithm Based on TDOA/RSSI for Indoor Location

Chenyang Zhai, Zhongliang Deng, Jichao Jiao, Ning Li, Yan Zhou and Cheng Li

Abstract With the rapid development of wireless communication, wireless location technology has attracted more and more attention. However, the wireless communication environment is becoming complex. Just relying on only one positioning technology cannot meet the need of the precise positioning. Therefore, a proper fusion algorithm should be used for obtaining higher accuracy. In this paper, we propose a new algorithm based on the TDOA/RSSI data fusion. In this algorithm, the linear regression is used to reduce the interference of small probabilities to get the precise RSSI positioning result. Then, a dynamic weighted data fusion is performed at the decision level by combining the TDOA positioning result. By comparing to the normal TDOA algorithm, the results show that the proposed algorithm solves the problem of location ambiguity and weak robustness, and further improves the positioning accuracy.

Keywords TDOA/RSSI · Linear regression · Dynamic weight · Data fusion

1 Introduction

With the development of wireless communication, wireless location technology has attracted more and more people's attention. In recent years, the rapid development of the mobile communication and the Internet makes wireless location technology

Foundation project: The National High Technology Research and Development Program ("863" Program) of China (No. 2015AA124103). The National Natural Science Foundation of China (No. 61401040). The National Science and Technology Support Program of China (No. 2014BAK12B00).

C. Zhai (✉) · Z. Deng · J. Jiao · N. Li · Y. Zhou · C. Li
School of Electronic Engineering, Beijing University of Posts and Telecommunications, Beijing, China
e-mail: chia91@163.com

J. Sun et al. (eds.), *China Satellite Navigation Conference (CSNC) 2016 Proceedings: Volume II*, Lecture Notes in Electrical Engineering 389,
DOI 10.1007/978-981-10-0937-2_31

more widely in military, production and all areas of the human life. In support of four global navigation satellite systems, the outdoor location services have broad access to people's lives. However, there is no mature system to support indoor location technology. With the increasing number of large buildings, the demand for indoor location services is increasing. The indoor location technology gradually becomes a new hot spot of competition. In commercial applications, public safety and other aspects, the indoor location services will also have a more promising future [1].

In recent years, a large number of indoor positioning systems appear. According to the principle of positioning, they can be divided into the following categories: positioning based on identification code, positioning based on fingerprint and positioning based on geometric relationship. Through geometric positioning technology, we can get the positioning result by the geometric relationship of the ranging. Due to increasingly complex wireless communication environment, a single location algorithm cannot meet the needs of precise positioning. Multi-sensors fusion algorithm is becoming the main trend targeting [2]. On the basis of TDOA-based positioning technology, RSSI-based positioning technology is assisted to get more precise and more stable positioning result.

2 RSSI Ranging Processing

The value of RSSI is an indicator of the energy of received signal. Its value is related to the distance. The gradient model that is commonly used for wireless signal transmission is the theoretical model [3]. Equation is as follows:

$$[p_r(d)]_{\mathrm{dBm}} = [p_r(d_0)]_{\mathrm{dBm}} - 10n\lg\left(\frac{d}{d_0}\right) + X_{\mathrm{dBm}} \tag{1}$$

where d is the distance between the receiver and the transmitter. d_0 is the reference distance. $p_r(d_0)$ is the distance from the reference point of the received signal power. $p_r(d)$ is the received signal power at the receiver. X_{dBm} is a zero mean Gaussian variables that indicates how the received signal power changes in case that the distance is fixed. n is the path loss exponent and it is usually obtained from the actual measurement. The more obstacles there are, the greater n will be.

In practical application, a simplified gradient model is commonly used, as follows:

$$[p_r(d)]_{\mathrm{dBm}} = [p_r(d_0)]_{\mathrm{dBm}} - 10n\lg\left(\frac{d}{d_0}\right) \tag{2}$$

For ease of expression and calculation, d_0 is usually taken as the reference distance of 1 m.

$$[p_r(d)]_{\mathrm{dBm}} = \mathrm{RSSI}_0 - 10n\lg(d) \tag{3}$$

Turn the value of received sign into the form of RSSI. The final form of the equation is as follows:

$$\mathrm{RSSI} = \mathrm{RSSI}_0 - 10n\lg(d) \tag{4}$$

where RSSI_0 is the reference of field strength. RSSI is the measured field strength. Equation (4) is the classical RSSI ranging model. It shows a relationship of RSSI and d. RSSI_0 and n are empirical values, and they are closely related to the specific wireless signal propagation environment. We should get their values in specific experiments [3].

In order to make the model meet the wireless signal propagation characteristics in the current environment and get higher precision by RSSI ranging. We must get the optimal RSSI_0 and n in current indoor environment. Linear regression analysis is usually used to estimate RSSI_0 and n. The equation is as follows:

$$\rho_i = -10\lg d_i, \quad i = 1, 2, \ldots N \tag{5}$$

$$n = \sum_{i=1}^{N}(\rho - \bar{\rho})\mathrm{RSSI}_i / \sum_{i=1}^{N}(\rho - \overline{\rho})^2 \tag{6}$$

$$\mathrm{RSSI}_0 = \overline{\mathrm{RSSI}} - n\bar{\rho} \tag{7}$$

$$\bar{\rho} = \frac{1}{N}\sum_{i=1}^{N}\rho_i \tag{8}$$

$$\overline{\mathrm{RSSI}} = \frac{1}{N}\sum_{i=1}^{N}\mathrm{RSSI}_i \tag{9}$$

where N is the number of measured values in the ranging experiment. By linear regression, we get the ranging model in the current indoor environment accurately. The ranging model can clearly show the corresponding relationship between field strength and distance.

3 TDOA Location Algorithm

Through TDOA positioning technology, we can estimate the position of the unknown node. Figure 1 shows the positioning principle of TDOA. A value of TDOA corresponds to a hyperbolic. Multiple values of TDOA correspond to multiple hyperbolic. The intersection point is the result of the position [4]

Where $AP_1(x_1, y_1), AP_2(x_2, y_2), AP_3(x_3, y_3)$ are the coordinates of beacon nodes and $POS(x, y)$ is the coordinate of unknown node. The hyperbolic equation is shown as follows:

$$\begin{cases} \sqrt{(x_1 - x)^2 - (y_1 - y)^2} - \sqrt{(x_2 - x)^2 - (y_2 - y)^2} = d_{1,2} \\ \sqrt{(x_2 - x)^2 - (y_2 - y)^2} - \sqrt{(x_3 - x)^2 - (y_3 - y)^2} = d_{2,3} \\ \sqrt{(x_3 - x)^2 - (y_3 - y)^2} - \sqrt{(x_1 - x)^2 - (y_1 - y)^2} = d_{3,1} \end{cases} \tag{10}$$

where $d_{1,2}$ is the range difference between POS to AP_1 and POS to AP_2. In the same way we can know $d_{2,3}$ and $d_{3,1}$. According to the measured time and the relationship of time between distance, distance can be calculated.

The method of Taylor series expansion is commonly used to solve the hyperbolic equations. It is a recursive algorithm that requires an initial estimated position. In the case of providing the initial position, the algorithm can get accurate results.

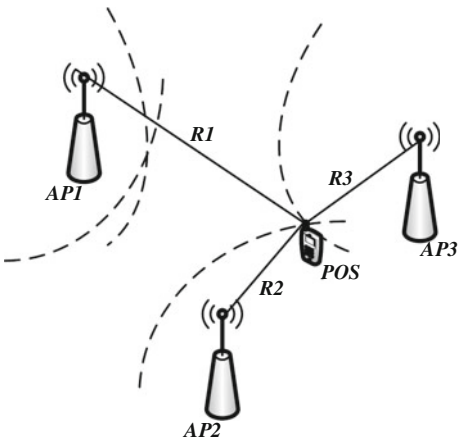

Fig. 1 Principle of TDOA positioning technology

4 Fusion Algorithm

4.1 The Proposed Algorithm

We can solve hyperbolic equations to get accurate results by the method of Taylor series expansion. However, the method requires an initial estimate of the actual location to ensure convergence [5]. Therefore, the initial position is calculated by RSSI positioning technology. Then we get the final result by data fusion of two positioning results. The process is as in Fig. 2.

4.2 The Initial Position Estimate

The algorithm obtains an initial position by the RSSI location algorithm. Though Eq. (4), we can know the ranging model is different in different physical environments. Therefore, before positioning calculation, we must get $RSSI_0$ and n in order to establish an accurate RSSI ranging model. The accuracy of the ranging model influences the positioning accuracy of subsequent calculations in a large extent. In order to obtain a more accurate mapping between RSSI and distance for improving positioning accuracy, RSSI ranging experiments is conducted in the field. Then, we collect large numbers of date and process them to obtain the optimal $RSSI_0$ and n [6]. Finally, the distance measurement model is set up, which is in line with the current environment.

Ranging model can clarify the relationship between RSSI and distance in the current environment. We can obtain the RSSI positioning results by measuring RSSI. The equation is as follows:

Fig. 2 Algorithm flowchart

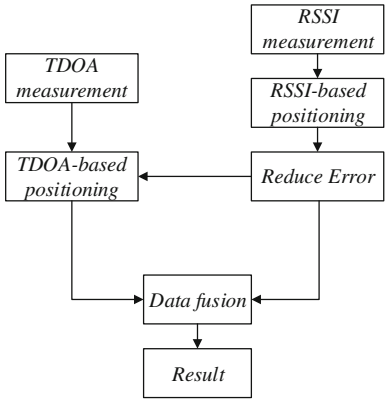

$$\begin{cases} \sqrt{(x_1 - x)^2 - (y_1 - y)^2} = d_1 \\ \sqrt{(x_2 - x)^2 - (y_2 - y)^2} = d_2 \end{cases} \tag{11}$$

4.3 The First Layer Data Fusion

Through RSSI positioning technology, we can get a stable positioning result. But the method of Taylor series expansion requires an initial estimate close to the actual location to ensure convergence. Therefore, the RSSI positioning results are checked to remove the abnormal data. Then we average the remaining positioning results. A stable position close to the actual position will be calculated. It acts as the initial position of TDOA Taylor series expansion method. Through recursion, it improves the position estimation. Finally, we will get the TDOA positioning result.

4.4 The Second Layer Data Fusion

The received signal beacon nodes of TDOA may appear insufficient. In order to improve the stability and accuracy of positioning results, a second data fusion should be conducted in precise positioning process. The positioning result of TDOA is fused with the positioning result of RSSI in the decision level. Since the positioning accuracy of TDOA and RSSI positioning technology varies greatly. We cannot fairly treat the results obtained in different ways in the data fusion. Given TDOA positioning accuracy is higher, we allocate TDOA location a higher weight. The model of the results is as follows:

$$\mathrm{POS} = a\mathrm{POS}_{\mathrm{tdoa}} + b\mathrm{POS}_{\mathrm{rssi}} \tag{12}$$

where $\mathrm{POS}_{\mathrm{tdoa}}$ is the result of TDOA positioning and $\mathrm{POS}_{\mathrm{rssi}}$ is the result of RSSI positioning. a and b stand for the weights of the two kinds of positioning results. In the positioning process, based on the received signal quantity of TDOA, the weight is dynamic changed. Then, the final positioning result will be obtained by the best linear weighted data (Table 1).

Table 1 The data of weighted dynamic allocation

Sign number	1	2	3	4	5	6
a	0	0	0.8	0.9	0.95	0.95
b	1	1	0.2	0.1	0.05	0.05

5 Results

5.1 Ranging Results

We select the laboratory corridor as experimental environment to conduct ranging model experiment. Experimental environment is as shown in Fig. 3. During the experiment, only one beacon node opens in the central corridor as the transmitter. The receiver is placed at different distances from the transmitter. We receive one hundred sets of data at every point of the twenty receivers. Then, the mean value of the one hundred sets of data is used as the field strength of the point of receiver. After the experiment, the other beacon nodes are turned on in turn to repeat the experiment for five times. Finally, we can get one hundred sets of data.

After collecting data, the data will be progressed by linear regression analysis and obtain the value of RSSI_0 and n. Finally, we can get the ranging model in the laboratory corridor:

$$\mathrm{RSSI} = -41.2 - 20\lg(d) \tag{13}$$

Figure 4 shows the data points obtained from the ranging experiment and the RSSI ranging model curve.

5.2 Locating Results

Based on the TDOA/RSSI fusion location algorithm, we carry out experiments in different numbers of beacon nodes positioning environment. The RMRS of positioning results is used as the positioning accuracy, such as the equation:

$$\mathrm{RMSE} = \sqrt{(x - X)^2 + (y - Y)^2} \tag{14}$$

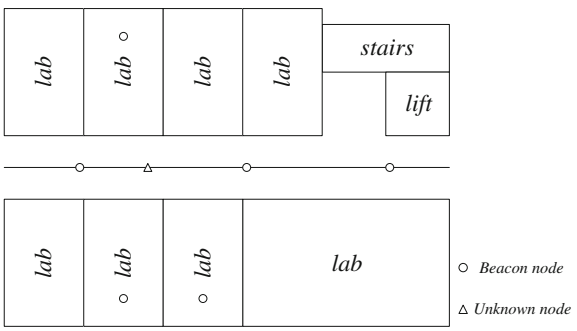

Fig. 3 Experimental environment

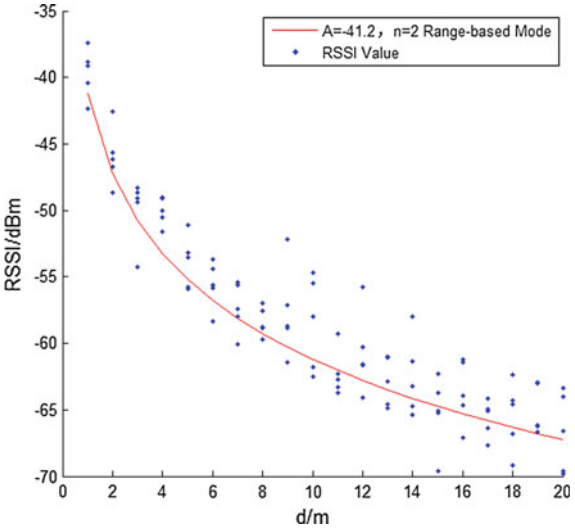

Fig. 4 Experimental data and RSSI ranging model curve

where (x, y) is the coordinate of the final result, and (X, Y) is the coordinate of the actual position. By analysing the mean square error of positioning results, we can compare TDOA/RSSI fusion location algorithm with TDOA location algorithm in positioning accuracy and stability. The result is shown as Figs. 5 and 6.

The results show that TDOA/RSSI fusion algorithm can get accurate positioning results in the more complex indoor environment. The algorithm solves the problem that TDOA algorithm cannot get accurate position where the number of beacon nodes is insufficient. Moreover, the mean and variance of the root mean square error

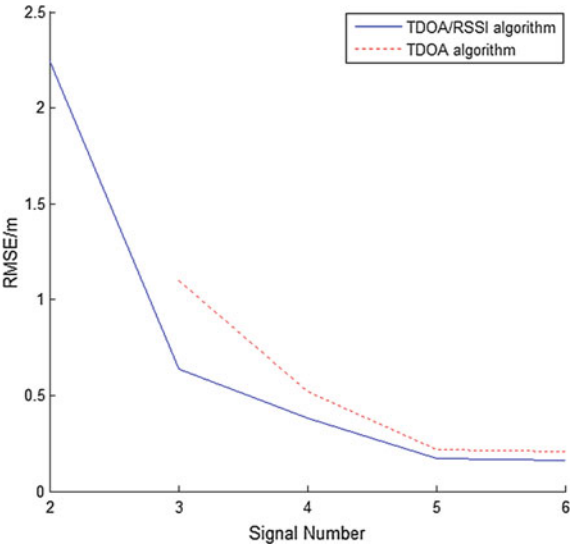

Fig. 5 Mean of the root mean square error

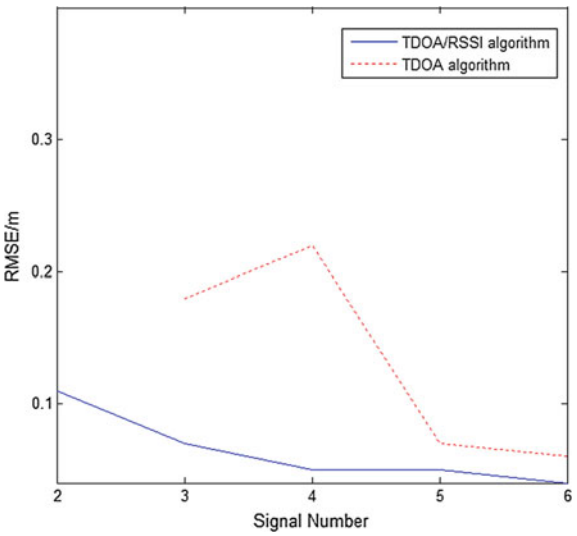

Fig. 6 Variance of the root mean square error

of TDOA/RSSI fusion location algorithm are less than TDOA location algorithm. So it has higher positioning accuracy and better stability than TDOA location algorithm.

6 Conclusion

This article describes a fusion location algorithm based on TDOA/RSSI for solving the shortage of vague positioning and robustness caused by TDOA location algorithm. We get the ranging model of the current environment by the ranging experiment and calculate initial positioning point by RSSI positioning technology. Then we use two layers of data integration to achieve the final precise positioning point. The results show that the fusion location algorithm can effectively increase the success rate of positioning and stability, and the positioning accuracy is also improved slightly.

References

1. Zhang L, Yu Y (2014) Indoor positioning applications and services of mobile phone. J Navig Positioning 2(4)
2. Zhao F, Zhao Q, Chen H (2011) TDOA localization algorithm based on RSSI weighted data fusion. J Guilin Univ Electron Technol 31(4)
3. Wang Q (2012) Research on an indoor positioning technology based on RSSI ranging. Electron Sci Tech 25(6)

4. An Q, Deng Z, Zhao X, Wang K (2014) Indoor positioning algorithms based on multidimensional information. In: China satellite navigation conference, CSNC 2014-proceedings, vol 305 LNEE, pp 617–625
5. Deng P (2002) Investigation of mobile station location in celluar network. Southwest Jiaotong University, ChengDu
6. Fang Z, Zhao Z, Guo P, Zhang Y (2007) Analysis of distance measurement based on RSSI. Chin J Sensor Actuators 20(11)

Fast Acquisition Algorithm in GNSS/INS Ultra Tightly Integrated Navigation System Based on Steady State Judgment

Wei He and Baowang Lian

Abstract GNSS receiver usually use the match filter and FFT to get the code phase and carrier frequency. However, it is hard to get the code phase and carrier frequency under high dynamic condition, and the match filter and FFT will occupy huge hardware resource. The INS (inertial navigation system) can assist the GNSS receiver to get the carrier frequency. It can also improve the calculate efficiency. But the carrier frequency acquisition error can also affect the carrier frequency lock. It may affect the GNSS signal track. To solve this problem, this paper proposed a fast acquisition algorithm in GNSS/INS ultra tightly integrated navigation system based on steady state judgment. This algorithm can effectively lock the carrier frequency under high dynamic condition. And this algorithm can also judge the acquisition condition to control the switch between acquisition and tracking to improve higher carrier frequency tracking accurate.

Keywords Ultra tightly integrated navigation system · Fast acquisition · Steady state judgment · Error tracking

1 Introduction

For GNSS receiver, the existing serial acquisition method would take a long time. Many researchers deeply studied the quickly acquisition methods for the GNSS receiver [1, 2]. However, these methods would take a lot of hardware resources, and the cost of the project implementation is high. At the same time when the code rate is very high, existing methods are difficult to acquire the carrier frequency under high dynamic conditions.

W. He (✉) · B. Lian
Northwestern Polytechnology University, Xi'An 710072, China
e-mail: heweizj@163.com

B. Lian
e-mail: Bwlian@126.com

J. Sun et al. (eds.), *China Satellite Navigation Conference (CSNC) 2016 Proceedings: Volume II*, Lecture Notes in Electrical Engineering 389,
DOI 10.1007/978-981-10-0937-2_32

In the ultra tightly integrated system, we can use the INS to assist the tracking loop of the GNSS receivers to improve the acquisition and tracking performance under high dynamic and low SNR conditions [3–5]. Use INS to estimate the carrier frequency GNSS receiver can assist the fast acquisition of satellite signals [6], but because of the RF channel frequency error, the satellite position and velocity calculation error and INS calculation error, the existing INS assisted GNSS receivers fast acquisition method would cause the Doppler shift estimation error. The Doppler shift estimation error may cause the ultra tightly integrated tracking loop error .

This paper first analyzed causes and impact of the Doppler shift estimation error. Through analysis and simulation the Doppler shift estimation error may cause the GNSS/INS ultra tightly integrated tracking loop error tracking. This paper proposed a fast acquisition algorithm based on steady judgment, this algorithm uses Kalman filter and steady judgment formula to decide whether the system has completed the acquisition of the carrier frequency and whether the system can enter GNSS/INS ultra tightly integrated tracking loop. The simulation results show that the fast acquisition algorithm based on steady state judgment can effectively accomplish the acquisition of the satellite signal under high dynamic conditions. Meanwhile the fast acquisition algorithm can effectively analyze the carrier frequency draw state, make up for the shortcomings of existing algorithms to improve ultra tightly integrated navigation system performance under high dynamic conditions.

2 Doppler Shift Estimation Error Modeling

Through the INS calculation and satellite almanac calculation the Doppler frequency shift information f_{dop} can be estimated. In practical applications the Doppler shift estimation value exist error $\delta f_{\text{forecast}}$.

$\delta f_{\text{forecast}}$ contains δf_A, δf_C, δf_{INS}, δf_{Sat} and δf_{IFc}, with the amount of error of five. δf_A is the carrier frequency error caused by almanac calculation error, δf_C is the carrier frequency error caused by RF channel frequency error, δf_{INS} is the carrier frequency error caused by INS calculation error, δf_{Sat} is the carrier frequency error caused by satellite signal frequency error, δf_{IFc} is the carrier frequency error caused by the local IF frequency error. δf_{Sat} and δf_{IFc} are very small, so the two errors can be ignored.

2.1 RF Channel Frequency Error

Satellite navigation signals through an antenna into the RF channel to complete the down conversion work, the RF signal down to IF signal. When there is no Doppler shift between the navigation satellite and the GNSS receiver, the IF signal is the standard intermediate frequency f_{IF}. In the ideal case, the intermediate frequency f_{IF} is confirmed to be a fixed value, but due to the influence of the oscillator frequency

error, there is an error δf_C between the actual standard intermediate frequency f_{IFm} and preset standard intermediate frequency f_{IF}.

The RF channel frequency error δf_C can be calculated and stored by the data fusion filters to assist the carrier frequency acquisition, but the error is in the almanac is valid for seven days will still change with the outside temperature changes [7] Therefore, the proposed RF channel frequency error δf_C is RF channel frequency error is the change from last calculation to this acquisition.

2.2 The Almanac Calculation Error

When there is no external auxiliary ephemeris data to assist the navigation signal acquisition, the receiver can only use the existing almanac information. The almanac is the summary form of broadcast ephemeris which can be used to assist the navigation signal acquisition. Compared with the ephemeris, almanac information satellite navigation systems lack orbit perturbation parameters, thus the almanac calculation results contains error. At the same time the almanac lack the necessary parameters to calculate the satellite velocity. It needs to be calculated using the position information. Therefore, there will be an error in the satellite velocity calculation.

2.3 INS Calculation Error

The positioning, velocity and attitude calculation error will accumulate as the INS calculation. Therefore, the position error caused by the INS calculation will have an impact on the satellite's orientation vectors D. As the same reason inertial navigation solution velocity caused by the velocity calculation error and orientation vectors D will also have an impact on satellite Doppler shift, thereby generating the carrier frequency acquisition errors.

3 The Influence of Doppler Shift Estimation Error on GNSS /INS Ultra Tightly Integrated Navigation System

Through the previous analysis, In practical applications the Doppler shift estimation value exist error $\delta f_{\mathrm{forecast}}$. At this time if the system transferred directly into the GNSS/INS ultra tightly integrated tracking loop, although the INS can eliminate the dynamic stress on phase lock rings, but because of the Doppler shift estimation error $\delta f_{\mathrm{forecast}}$, equivalent to the aid an initial frequency error into the phase tracking loop, if the value is too large, due to the limited performance of the carrier phase

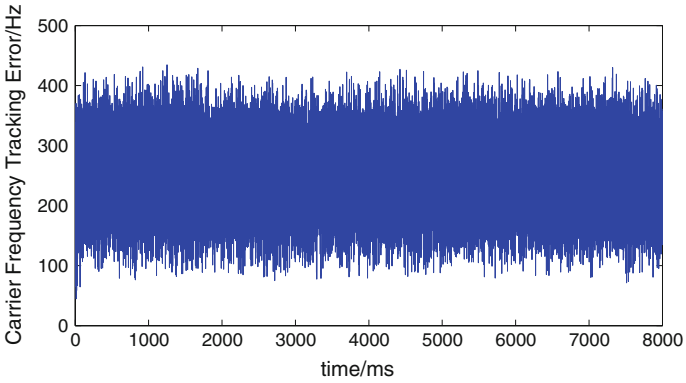

Fig. 1 Carrier frequency tracking error of [6]

tracking loop [8], the tracking error tracking loop will enter the error tracking state. In order to verify this conclusion, this paper designed the following simulation.

GPS IF signal generated by matlab, simulation satellites No. Is 03, the carrier is in a stationary state, the signal IF is 4.2 MHz, code frequency is 1.023 MHz, signal sampling frequency is 39 MHz, the relevant accumulated time is 1 ms, CNR is 44 dB-Hz, simulation time is 8 s, carrier frequency estimation error is 200 Hz, after acquisition the system directly enter the ultra tightly integrated tracking loop. The simulation results of the method proposed by [6] are shown in Fig. 1.

Figure 1 shows the tracking error of the carrier frequency in the vicinity of 250 Hz jitter. It means the tracking error tracking loop entered the error tracking state.

And in this state, the loops still maintain the carrier and code tracking, the accumulation of relevant results is big. Figure 2 is accumulation results comparision between error tracking and unlock. The accumulation results of error tracking

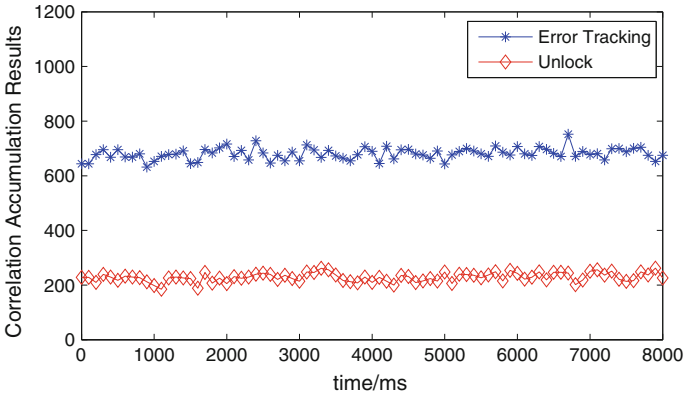

Fig. 2 Correlation accumulation results Comparison

is much bigger than the unlock state. Wrong track status may not be recognized as a baseband processing unit out of lock, tracking loops of the receiver is "spoofing."

From the above analysis it shows that for ultra tightly integrated system, [6] proposed a fast acquisition algorithm which ignores the impact to tracking loop caused by carrier frequency estimation error, it may lead ultra tightly integrated system into error tracking state. Therefore, the use of INS auxiliary carrier frequency acquisition after completion, can not be directly enter the ultra tightly integrated tracking loop, we should eliminate the frequency error.

4 Fast Acquisition Algorithm Based on Steady State Judgment

In practical applications the Doppler shift estimation value exist error $\delta f_{\text{forecast}}$, if directly enter the ultra tightly integrated tracking loop, it will cause the error tracking. We should start with the existing 2FLL + 3PLL tracking loop traction until the Doppler shift error is small enough before enter the ultra tightly integrated tracking loop. But for integrated navigation systems, you can not get the exact difference between the actual carrier frequency f_C and the carrier frequency f_L which is got from the existing 2FLL + 3PLL tracking loop. Therefore it is hard to judge the carrier frequency draw effect of the existing 2FLL + 3PLL tracking loop.

Within a short period of time, the difference between the carrier frequency assisted by INS and the real carrier frequency can be seen as a fixed value. Therefore the existing 2FLL + 3PLL tracking loop can firstly pull the carrier frequency to a small range, the difference between the carrier frequency assisted by INS and the carrier frequency which is got from the existing 2FLL + 3PLL tracking loop should be stable, it means the change rate of the difference should be zero.

Combination of the above analysis, in order to effectively and rapidly judge the tracking loop switch state, proposed the fast acquisition algorithm based on steady judgement.

Fast acquisition algorithm flow chart is shown in Fig. 3, firstly is the Kalman filter, the input of the Kalman filter is the difference between the carrier frequency assisted by INS and the carrier frequency which is got from the existing 2FLL + 3PLL tracking loop. Then the change rate of the difference will be sent to the steady state judgement unit, if the steady state judgement result is yes, the

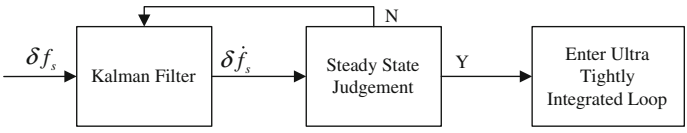

Fig. 3 Steady state judgment algorithm

acquisition is completed, the system will enter the ultra tightly integrated loop. If the result is no, then continue with the steady judgement, until judgment is yes.

The state vector of the Kalman filter $\mathbf{x_k}$ is as formula (1), where δf_s is the carrier frequency difference between the INS estimation value f_{forecast} and the value f_L from 2FLL + 3PLL tracking loop as formula (2). $\delta \dot{f}_s$ is the change rate of the frequency difference, the state equation of the system as formula (3), where $\mathbf{w}$ is the system noise, the state transition matrix, such as the formula (4), where t is the data refresh rate.

$$\mathbf{x_k} = \begin{bmatrix} \delta f_s & \delta \dot{f}_s \end{bmatrix} \tag{1}$$

$$\delta f_s = f_{\text{forecast}} - f_L \tag{2}$$

$$\mathbf{x_k} = \mathbf{\Phi_{k/k-1}} \mathbf{x_{k-1}} + \mathbf{w_{k-1}} \tag{3}$$

$$\mathbf{\Phi_{k/k-1}} = \begin{bmatrix} 1 & t \\ 0 & 1 \end{bmatrix} \tag{4}$$

The observation vectors $\mathbf{y_k}$ is the frequency difference observations. The measurement equation is as follow, $\mathbf{v_k}$ is the measurement noise.

$$\mathbf{y_k} = \mathbf{H_k} \mathbf{x_k} + \mathbf{v_k} \tag{5}$$

$\mathbf{H_k}$ is the measurement matrix which is shown as follow.

$$\mathbf{H_k} = \begin{bmatrix} 1 & 0 \end{bmatrix}_{1\times 2} \tag{6}$$

The steady state judgment is as follow. When the result of the Kalman filter N times meet the steady state judgment formula (7). The steady state judgement result is yes. The acquisition is completed. The system will enter the ultra tightly integrated loop. Th_s is the steady state judgment threshold.

$$\left| \delta \dot{f}_s \right| < \text{Th}_s \tag{7}$$

5 Simulation and Analysis

In order to verify the proposed algorithm, we designed the following simulation. The simulation parameters as 1.4, the carrier frequency error is captured 310 Hz, simulation time is 8 s. The dynamic model is JPL high dynamic model [9].

After serial code acquisition stage, the system enter the carrier frequency acquisition stage. Through the simulation, the steady state judgment results are shown as Fig. 4. In the first 0.5 s steady state judgment unit judge the state of the tracking loop is steady, the loop will be transferred to the ultra tightly integrated tracking loop.

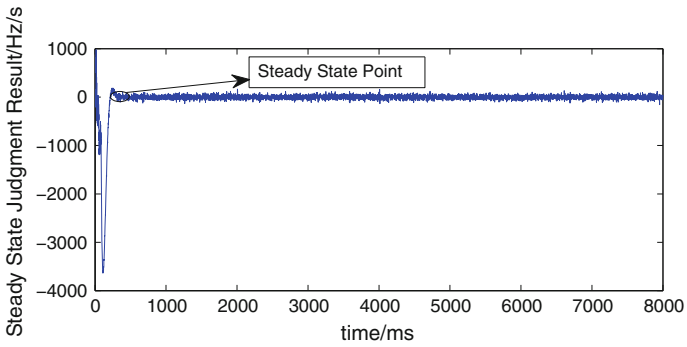

Fig. 4 Steady state judgment result

Through the simulation, the carrier frequency and phase tracking error comparison is shown as Fig. 5. You can see from Fig. 5, the accuracy of the fast acquisition algorithm based on steady state judgment is the highest, and there is no error tracking problem. Although directly into 2FLL + 3PLL tracking loops can also avoid error tracking problem, but under high dynamic conditions in order to ensure the tracking of the satellite navigation signals, the loop bandwidth is set too large, carrier frequency and carrier phase tracking accuracy is low.

Qin et al. [6] proposed fast acquisition algorithm did not pull the frequency acquisition error, after the acquisition is completed and system turn into the tracking loop. Since the carrier Doppler shift estimation error is large, the carrier frequency is error tracked at 250 Hz. It means the tracking error tracking loop entered the error tracking state. The fast acquisition algorithm based on steady state judgment can effectively accomplish the acquisition of the satellite signal under high dynamic conditions.

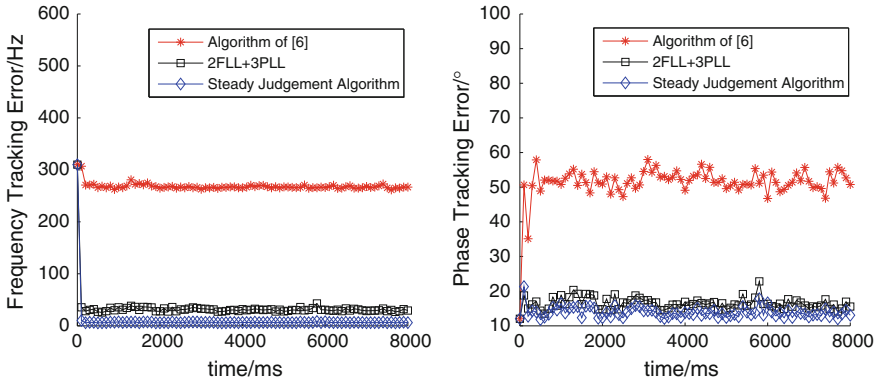

Fig. 5 Carrier frequency and phase tracking error comparison

6 Conclusion

This paper mainly studied the INS assisted GNSS receiver quickly acquisition technology. First, this paper analyzed the Doppler shift estimation error and the influence on GNSS/INS ultra tightly integrated navigation system. Second, this paper proposed a fast acquisition algorithm based on steady state judgment to eliminate the error tracking caused by the Doppler shift estimation error.

Simulation results show that the fast acquisition algorithm based on steady state judgment can effectively accomplish the acquisiton of the satellite signal under high dynamic conditions. Meanwhile, the fast acquisition algorithm can effectively analyze the carrier frequency draw state, make up for the shortcomings of existing algorithms to improve ultra tightly integrated navigation system performance under high dynamic conditions.

References

1. Sun CC et al (2008) signal acquisition and tracking using a parallel approach. IEEE/ION, pp 1332–1340
2. Kong SH (2013) A deterministic compressed gnss acquisition technique. IEEE Trans Veh Technol 62(2):511–521
3. Babu R et al (2008) Analysis of ultra-tight gps/ins integrated system for navigation performance. signal processing. In: International Conference on signal processing communications and networking, pp 234–237
4. Xie F et al (2014) Adaptive robust ultra-tightly coupled global navigation satellite system/inertial navigation system based on global positioning system/BeiDou vector tracking loops[J]. Radar Sonar & Navig IET 8(7):815–827
5. Qin F et al (2014) Improvement of global navigation satellite system signal acquisition using different grade inertial measurement units for high dynamic applications. Radar, Sonar & Navig 8(3):233–241
6. Qin F et al (2014) Improvement of global navigation satellite system signal acquisition using different grade inertial measurement units for high dynamic applications. IET Radar Sonar Navig 8(3):233–241
7. Huang X et al (2015) 100-MHz low-phase-noise microprocessor temperature-compensated crystal oscillator. IEEE Trans Circuits Syst II Express Briefs 62(7):636–640
8. Mengali U et al (1997) Synchronization techniques for digital receivers. Pisa University of Pisa, pp 92–95
9. Hinedi S, Statman JL (1988) High-dynamic GPS tracking final report. Jet Propulsion Laboratory, pp 10–15

Research on Horizontal Line Fitting Algorithm Based on Robust Estimation

Chonghui Li, Yabo Luo, Yong Zheng and Chao Zhang

Abstract Celestial bodies and horizontal line could be imaged simultaneously by fisheye camera, and then the inclination of vessel could be calculated by steps of horizontal line extraction and horizontal line fitting. However, some noise points may be mistakenly seen as horizontal line points in extraction step. Meanwhile, the position of some points extracted from the image may have large error. To solve these problems, this paper first introduces the Robust estimation, and based on it a horizontal line fitting algorithm has been established. The experiment shows that the model can effectively exclude the impact of noise points, limit utilize abnormal points, and take full advantage of high-precision horizontal line information, by which vessel inclination angle accuracy is improved from 46.4″ to 37.2″.

Keywords Robust estimation · Celestial navigation · Equal weight · Horizontal line fitting · Projection model

1 Introduction

Celestial navigation is a technique for determining one's geographic position (or space position) and orientation by the observation of identified stars, identified planets, the Sun, and the Moon. Its basic principles are a combination of rudimentary astronomical knowledge and spherical trigonometry [1, 2]. It is an important kind of autonomous navigation methods, which has the advantages of not easy to be disturbed, simple equipment, and the positioning error does not accumulate over time. Standard celestial navigation relies on quartermasters skilled in

C. Li (✉) · Y. Zheng · C. Zhang
Zhengzhou Institute of Surveying and Mapping, Zhengzhou 450052, Henan, China
e-mail: lichonghui6501@126.com

Y. Luo
College of Water Conservancy and Environmental Engineering of Zhengzhou University, Zhengzhou 450001, Henan, China

J. Sun et al. (eds.), *China Satellite Navigation Conference (CSNC) 2016 Proceedings: Volume II*, Lecture Notes in Electrical Engineering 389,
DOI 10.1007/978-981-10-0937-2_33

the use of sextant and paper-and-pencil sight-reduction techniques. It was seen as an important alternative to GPS that could be used to determine a ship's position when GPS may not be available at the most critical times. Additionally, the "STCW78/95 Convention" published by International Maritime Organization (IMO) also explicitly provides that mariners must have the ability to use celestial bodies to determine the ship's position [3, 4].

The determination of horizontal datum is the precondition of realized celestial navigation. In traditional marine celestial navigation, the determination of horizontal datum is realized by utilizing sextant to observe the horizontal; this method has such disadvantages as low efficiency and low accuracy. Nowadays, celestial navigation equipment has gradually developed into a star sensor with large field of vision, which can image multiply celestial body at the same time, and then realize navigation and positioning through solve integrated information of the image coordinates of celestial bodies, the imaging time and the theoretical position of celestial bodies. Furthermore, if utilizing a fisheye camera to image the celestial bodies and horizontal simultaneously, then we could determine the attitude of the vessel by fitting the horizontal line in the image, thereby the horizontal datum is determined [5].

After imaged the horizontal line by the fisheye camera, first we need to extract the contour point of horizontal line in the image, and then need to fit the contour points according to the projection model of the fisheye camera. However, such circumstance like mistakenly identify image noise as a contour point are widely exist in the contour points extracting process, which lead to some outliers in the contour points. Meanwhile, even though the points were correctly extracted, some large error points are also possibly included. In order to solve this problem, robust estimation was introduced to assign the weights of the contours points, therefore, the accuracy of celestial navigation could be improved.

2 Horizontal Line Projection Principle

2.1 Fisheye Camera Projection Model

Fisheye camera is composed of fisheye lens and imaging sensor, it always has a super wide field of view (FOV), typically wider than 180° × 360°. It uses the "non-similar" theory, hence large distortion would be lead-into the imaging shape of the horizontal line, which requires distortion correction of the horizontal line in the image treatment process.

The projection model of general camera is

$$r = f \tan\theta. \tag{1}$$

In which, θ denotes semiangular field, f denotes focal length of the fisheye camera, r denotes the distance between projection point of celestial object and principal point in the image plane. When θ infinite approaching 90°, r approaching infinite, therefore

Eq. (1) could not realize. However, fisheye camera utilizing the "non-similar" theory, commonly used fisheye projection models includes equidistance projection model, equisolid projection model, and orthogonal projection model, etc. [6].

In this paper, the equisolid projection model was taken as an example for analysis, and its projection formula is

$$r = 2f \sin\left(\frac{\theta}{2}\right). \tag{2}$$

The projection point deviation from the ideal location of the point of the camera imaging system due to reasons such as design, manufacture, and assembly error is called optical distortion. Distortions generally include radial distortion, decentering distortion, and in-plane distortion. But in the final image, the radial distortion is the main problem. The decentering distortion and in-plane distortion are very small and could be neglected. In the case of only considering the radial distortion, the error of distance between projection point of horizontal line and the principal point could be expressed as the error of semiangular field of corresponding horizontal line point [7].

According to Eq. (2), semiangular field under equisolid projection model could be calculated as

$$\theta = 2\arcsin\left(\frac{r}{2f}\right) \tag{3}$$

In which

$$r = \sqrt{(x - x_0)^2 + (y - y_0)^2}. \tag{4}$$

Since the existence of optical distortion, the actual projection formula which even nominally equisolid projection model is not as shown in Eq. (3).

Due to the radius distortion, we introduce a distortion model as [5, 7]

$$\theta = 2\arcsin\left(\frac{r}{2f}\right) + k_1\left(\arcsin\left(\frac{r}{2f}\right)\right)^2 + k_2\left(\arcsin\left(\frac{r}{2f}\right)\right)^3 + k_3\left(\arcsin\left(\frac{r}{2f}\right)\right)^4. \tag{5}$$

Equation (5) is the fisheye camera equisolid projection polynomial distortion model.

2.2 Horizontal Line Projection Principle

As shown in Fig. 1, assume over the sea, the height of observation point O from sea surface is h, and the earth radius is R, the line of sight which observed the horizon is

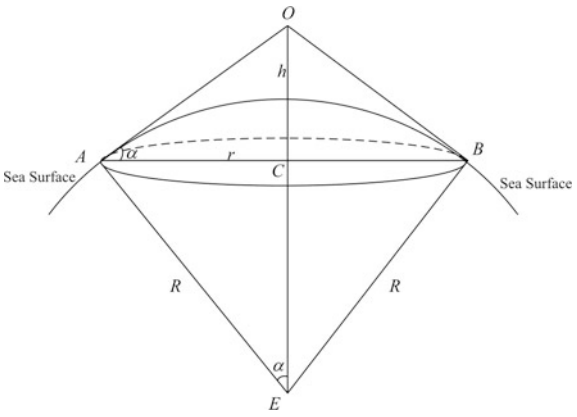

Fig. 1 The observe principle of horizontal line

a straight line which both through the observation point and tangent with the sea surface, connected all of the points of tangency we could observed the circular horizontal line.

In Fig. 1, E denotes the earth center, OA and OB are two optical line of sight which could observe horizontal line, respectively, the depression angle of them are both α, A and B are two points of tangency, connected all of the points of tangency we could observe the circular horizontal line. The center of which is C, and the radius of which is r. Then the projection principle of horizontal line is shown in Fig. 2.

In Fig. 2, $\vec{n}$ is the unit principle optical axis vector of the lens, $\vec{z}$ is the unit local vector points to the opposite direction of gravity, the angle between them is denoted as i. Assuming that $P(x, y)$ is a point on the horizontal line, the argument and semiangular field of which are φ and θ, respectively. And the corresponding projection point in the

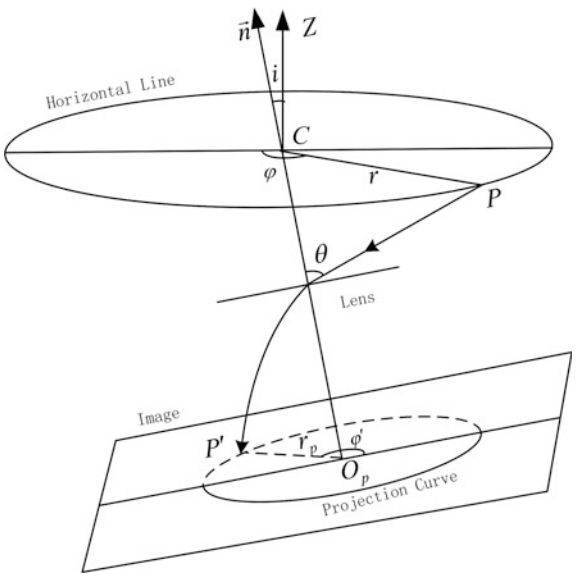

Fig. 2 Projection principle of horizontal line

image plane is P', the argument of which is φ', the distance between P' and O_P is r'. Then according to the projection principle, θ could be calculated as

$$\theta = \arccos \frac{R \sin i \cos \varphi - \sqrt{h^2 + 2Rh}\cos i}{R + h}. \tag{6}$$

In which, the argument φ in the horizontal plane could be calculated according to the corresponding argument φ' in the image plane

$$\varphi = \begin{cases} \arctan(\tan\ \varphi' \cos i) - \pi & -\pi < \varphi' < -\frac{\pi}{2} \\ \arctan(\tan\ \varphi' \cos i) & -\frac{\pi}{2} \le \varphi' \le \frac{\pi}{2} \\ \arctan(\tan\ \varphi' \cos i) + \pi & \frac{\pi}{2} < \varphi' \le \pi \end{cases}. \tag{7}$$

In order to realize unified representation, set φ_0 the angle between the shortest radius and the X-axis of image coordinate. If the anticlockwise rotation angle of the radius vector of a horizontal line contour point (x_j, y_j) from the X-axis of image coordinate is φ'_j, then the angle between the radius vector and shortest radius is $\varphi' = \varphi'_j - \varphi_0$, therefore, Eq. (7) changed as

$$\varphi = \begin{cases} \arctan(\tan(\varphi'_j - \varphi_0)\cos i) - \pi & -\pi < (\varphi'_j - \varphi_0) < -\frac{\pi}{2} \\ \arctan(\tan(\varphi'_j - \varphi_0)\cos i) & -\frac{\pi}{2} \le (\varphi'_j - \varphi_0)_j \le \frac{\pi}{2} \\ \arctan(\tan(\varphi'_j - \varphi_0)\cos i) + \pi & \frac{\pi}{2} < (\varphi'_j - \varphi_0)_j \le \pi \end{cases} \tag{8}$$

In which, φ'_j could be calculated by the image coordinate of the horizontal line contour point as

$$\varphi'_j = \begin{cases} \arcsin \frac{y_j - y_0}{\sqrt{(x_j - x_0)^2 + (y_j - y_0)^2}} & x_j - x_0 \ge 0 \\ \arcsin \frac{y_j - y_0}{\sqrt{(x_j - x_0)^2 + (y_j - y_0)^2}} + \pi & x_j - x_0 \le 0 \end{cases} \tag{9}$$

In which, x_0 and y_0 are, respectively, the abscissa and ordinate of the principle point. Therefore, we can obtain the theoretical semiangular field of the horizontal line contour point according to Eqs. (6), (8) and (9).

3 Horizontal Line Fitting Method

3.1 Error Equation

Assume the coordinate of principle point is (x_0, y_0), and the coordinate of one horizontal line contour point is (x_j, y_j), then the length of the radius vector r_j is

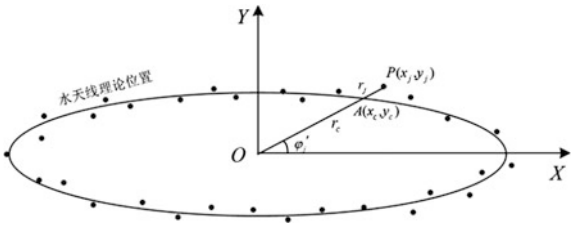

Fig. 3 Horizontal line fitting based on distance restriction

$$r_j = \sqrt{(x_j - x_0)^2 + (y_j - y_0)^2}. \tag{10}$$

The direction angle φ'_j in the image is

$$\varphi'_j = \begin{cases} \arcsin \frac{y_j - y_0}{\sqrt{(x_j - x_0)^2 + (y_j - y_0)^2}} & x_j - x_0 \geq 0 \\ \arcsin \frac{y_j - y_0}{\sqrt{(x_j - x_0)^2 + (y_j - y_0)^2}} + \pi & x_j - x_0 \leq 0 \end{cases}. \tag{11}$$

However, the theoretical location of the horizontal line corresponding to direction angle φ'_j is $A(x_c, y_c)$, which is shown as Fig. 3.

According the above analysis, if utilizing the equisolid projection polynomial distortion model, the theoretical length r_c of the radius vector corresponding to point A need to be solved iteratively. Then the error equation could be established by the length difference as

$$v_j = r_j - r_c. \tag{12}$$

There were just two unknown parameters i and φ_0 in Eq. (12), if we extract more than two horizontal line contour points, the two parameters could be calculated according to least square method. Due to Eq. (12) is a nonlinear equation, it need to be linearized in the least square process. However, there were higher term and anti-trigonometric function in the equation, and r_c need to be calculated iteratively, these problems lead to difficult to linearization, so the horizontal line fitting method based on distance restriction is unusefulness.

Actually, according to the distance r_j between each contour point and the principle point, the corresponding semiangular field of each contour point could be calculated. Besides, the theoretical semiangular field could be calculated according to Eq. (6). Therefore, the error equation could be established by the observed semiangular field and its theoretical value. In practice, due to there is anti-trigonometric function in Eq. (6), the calculated quantities are too much to linearize the equation, so the semiangular field is instead by its cosine function. The error equation is as follows:

$$v = \cos\hat{\theta} - \cos\theta_j. \tag{13}$$

In which, $\cos\theta_j$ denotes the cosine of semiangular field of horizontal line contour point, it could be calculated by

$$\theta_j = 2\arcsin\left(\frac{r_j}{2f}\right) + k_1\left(\arcsin\left(\frac{r_j}{2f}\right)\right)^2 + k_2\left(\arcsin\left(\frac{r_j}{2f}\right)\right)^3 + k_3\left(\arcsin\left(\frac{r_j}{2f}\right)\right)^4. \tag{14}$$

Among them, k_1, k_2, k_3 and f are known camera parameters, r_j denotes the length of radius vector of the ith contour point. $\cos\hat{\theta}$ denotes the theoretical cosine value of semiangular field of the contour point which corresponding to image direction angle φ'_j. First, the direction angle $\hat{\varphi}$ on the horizontal plane could be calculated as

$$\hat{\varphi} = \begin{cases} \arctan(\tan(\varphi'_j - \hat{\varphi}_0)\cos i) - \pi & -\pi < (\varphi'_j - \hat{\varphi}_0) < -\frac{\pi}{2} \\ \arctan(\tan(\varphi'_j - \hat{\varphi}_0)\cos i) & -\frac{\pi}{2} \le (\varphi'_j - \hat{\varphi}_0)_j \le \frac{\pi}{2} \\ \arctan(\tan(\varphi'_j - \hat{\varphi}_0)\cos i) + \pi & \frac{\pi}{2} < (\varphi'_j - \hat{\varphi}_0)_j \le \pi \end{cases}. \tag{15}$$

Then $\cos\hat{\theta}$ could be calculated as

$$cos\hat{\theta} = \frac{R\,\sin\hat{i}\cos\hat{\varphi} - \sqrt{h^2 + 2Rh}\cos\hat{i}}{R + h}. \tag{16}$$

In which, the two unknown parameters inclination $\hat{i}$ and drift angle $\hat{\varphi}_0$ could be calculated according to the least square method.

Equation (13) is a nonlinear equation, it needs to be linearized in the least square process. Assume the initial value of $\hat{i}$ and $\hat{\varphi}_0$ are i_0 and φ_{00}, respectively, the corresponding correction are $\delta\hat{i}$ and $\delta\hat{\varphi}_0$; then according to Taylor series expansion, the error equation become [8]

$$v_j = \left(\frac{\partial(\cos\hat{\theta})}{\partial\hat{i}}\right)_0 \delta\hat{i} + \left(\frac{\partial(\cos\hat{\theta})}{\partial\hat{\varphi}_0}\right)_0 \delta\hat{\varphi}_0 + \cos\hat{\theta}_0 - \cos\theta_j \tag{17}$$

In which

$$\frac{\partial(\cos\hat{\theta})}{\partial\hat{i}} = \frac{R\sin^2 i\sin\varphi\,\tan(\varphi'_j - \varphi_0) + (R\cos i\cos\varphi + \sqrt{h^2 + 2Rh}\,\sin i)(1 + (\tan(\varphi'_j - \varphi_0)\cos i)^2)}{(R + h)(1 + (\tan(\varphi'_j - \varphi_0)\cos i)^2)} \tag{18}$$

$$\frac{\partial(\cos\hat{\theta})}{\partial\hat{\varphi}_0} = \frac{R\sin i\cos i\sin\varphi}{(R+h)\cos^2(\varphi_j' - \varphi_0)(1+(\tan(\varphi_j' - \varphi_0)\cos i)^2)} \tag{19}$$

Order

$$A = \begin{bmatrix} \frac{\partial(\cos\hat{\theta})}{\partial\hat{i}} & \frac{\partial(\cos\hat{\theta})}{\partial\hat{\varphi}_0} \end{bmatrix} \tag{20}$$

$$\delta\hat{X} = \begin{bmatrix} \delta\hat{i} & \delta\hat{\varphi}_0 \end{bmatrix}^T \tag{21}$$

$$l = A\hat{X}_0. \tag{22}$$

Among them, A denotes the coefficient matrix, $\hat{X}$ denotes the correction vector of unknown parameters, l denotes the free term vector of error equation, order V denotes the residual vector, and they could be represented as

$$v = A\delta\hat{X} + l. \tag{23}$$

If the initial value $\hat{X}_0$ is given, Eq. (23) could be solved according to the least square method. However, there exist some unavoidable outliers and some unavoidable large error observations those would lead to obtain low accuracy attitude parameters. In order to solve this problem, the robust estimation is introduced to improve the accuracy of the parameters.

3.2 Robust Estimation

Robust estimation is proposed for least squares estimation which does not have the characteristic of the anti-interference. It is an estimation which can both relief the affect of outlier and has a high efficiency [9–12].

In order to eliminate or reduce the impact of outliers and large deviation observations on estimates, set $\bar{P}$ as equivalent weight matrix and its diagonal element is $\bar{p}_i$; then according to Eq. (13) we obtain

$$A^T\bar{P}A\hat{X} + A^T\bar{P}l = 0. \tag{24}$$

The robust M estimation of unknown parameters is

$$\hat{X} = -\left(A^T\bar{P}A\right)^{-1}A^T\bar{P}l. \tag{25}$$

The posterior covariance matrix of $\hat{X}$

$$\sum_{\hat{X}} = \sigma_0^2 \left(A^T \bar{P} A\right)^{-1} A^T \bar{P} P^{-1} \bar{P} A \left(A^T \bar{P} A\right)^{-1}. \tag{26}$$

To get the solution we generally use iterative method, the $k+1$ times iterative solution is

$$\hat{X}^{k+1} = -\left(A^T \bar{P}^k A\right)^{-1} A^T \bar{P}^k l. \tag{27}$$

The element of $\bar{P}^k$ is

$$p_i^k = p_i \omega_i^k, \omega_i^k = \frac{\psi\left(v_i^k\right)}{v_i^k} \tag{28}$$

v_i^k is the residual component of k time iterative solution.

We could conclude from the principle of robust estimation that a kind of ρ function is corresponding to a kind of M estimation. Various equivalent weight functions have been put forward [9–12]. A good equivalent weight function should assign outlier zero weight, decreases doubtful observation's weight. IGG3 scheme is a commonly used equivalent weight function [13, 14].

$$\psi(\tilde{v}_i) = \begin{cases} \tilde{v}_i & |\tilde{v}_i| \le k_0 \\ k_0 \left(\frac{k_1 - |\tilde{v}_i|}{k_1 - k_0}\right) & k_0 \le |\tilde{v}_i| \le k_1 \\ 0 & k_1 \le |\tilde{v}_i| \end{cases} \tag{29}$$

As for independent observation situation, equivalent weight function is

$$\bar{p}(\tilde{v}_i) = \begin{cases} 1 & |\tilde{v}_i| \le k_0 \\ \frac{k_0}{|\tilde{v}_i|} \left(\frac{k_1 - |\tilde{v}_i|}{k_1 - k_0}\right)^2 & k_0 \le |\tilde{v}_i| \le k_1 \\ 0 & k_1 \le |\tilde{v}_i| \end{cases} \tag{30}$$

In Eq. (30), the value of k_0 and k_1 is, respectively, 1.5 and 3.0, $\tilde{v}_i$ is for standardization residual, which is

$$\tilde{v}_i = \frac{v_i}{m_{v_i}} \tag{31}$$

In Eq. (31), v_i is observation residual, m_{v_i} is mean error to v_i, m_{v_i} is calculated by followed equation.

$$m_{v_i} = \sigma_0 \sqrt{\frac{1}{p_i} - A_i (A^T P A)^{-1} A_i^T} \tag{32}$$

In Eq. (32), σ_0 is unit weight of error; p_i is the weight of observations, A_i is the i line of the matrix A, and it is the i error equation coefficient vector [15].

First, the residual of each horizontal line contour point could be calculated according to the least square method, then the equal weights could be calculated by substituting the standardized residual into Eq. (30), and finally the ultimate robust estimation value of $\hat{X}$ could be obtained by iterated as Eq. (27).

4 Analysis and Examples

In order to clarify the steps of the horizontal line fitting algorithm based on robust estimation and verify the effectiveness and the accuracy of the algorithm, a group of horizontal line contour points were taken as example. There were 494 contour points extracted from the image, as shown in Fig. 4.

The horizontal line fitting steps based on robust estimation are as follows:

(1) First utilizing the least square method to calculated the estimate value of inclination $\hat{i}$ and direction angle $\hat{\varphi}_0$ in the image plane, and the residual vector V of the cosine value of semiangular field.
(2) Calculate the robust estimate value of the parameters and their residuals, and then recalculate the standard residuals and equal weights.
(3) Calculate the robust estimate value of inclination $\hat{i}$ and direction angle $\hat{\varphi}_0$ according to Eq. (27), and calculate their mean square error (MSE) according to Eq. (26).

Finished above-mentioned steps, the equal weight of the horizontal line contour points are shown as follows:

In Fig. 5, there are 4 points with 0 weight, 59 points with weight between 0 and 1, and other 431 points with 1 weight. It indicated that 4 points were eliminated as

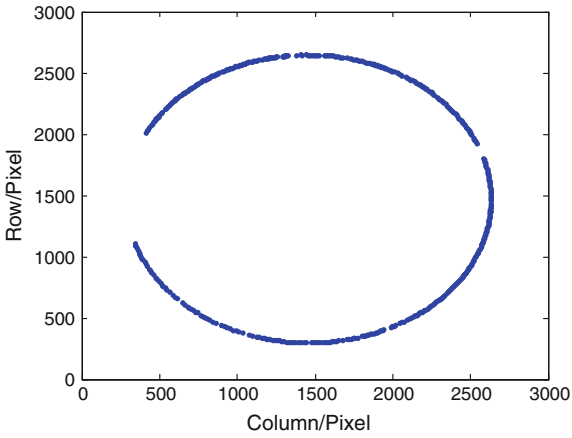

Fig. 4 Horizontal line points restricted from fisheye picture

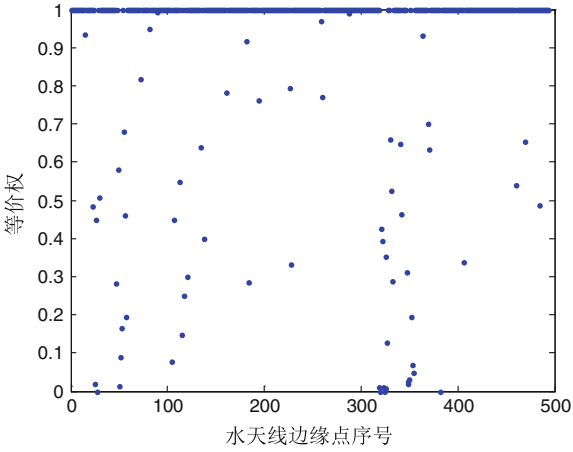

Fig. 5 Equal weight of horizontal line contour points

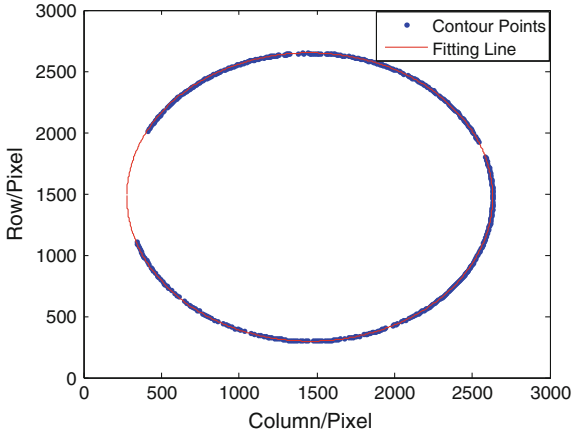

Fig. 6 Horizontal line fitting curve based on robust estimation

outliers, 59 points were reduced their weights, and other 431 points were seen as high-precision contour points to calculate the vessel attitude parameters according to the robust estimation. The fitting curve based on robust estimation is shown as follow Fig. 6.

In order to verify the accuracy of the fitting algorithm based on robust estimation, the robust estimation method and the least square method were used to fit the horizontal line contour points in 10 images, respectively. The MSE of the obtained inclination parameter is shown as follows.

The mean MSE of the 10 images according to least square method is 46.4″, while the mean MSE of the 10 images according to robust estimation method is 37.2″. It also could be seen in Fig. 7 that the MSE of robust estimation method is obviously less than the MSE of the least square method. These indicate that the

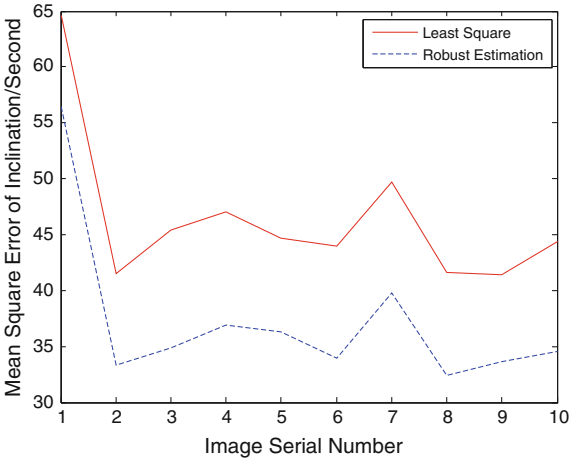

Fig. 7 Mean square error of estimate inclination angle

robust estimation method improved the accuracy of horizontal line fitting by weaken the influence of the noise contour points.

According to the above example and analysis, we could reach a conclusion that the horizontal line fitting algorithm based on robust estimation not only could successfully fit the horizontal line image by fisheye camera, but also could reduce the influence of the noise points and finally improve the accuracy of the vessel attitude parameters.

Acknowledgment This work is supported by Natural Science Foundation of China (NSFC) numbered 11373001 and 41374042.

References

1. Ji B, Feng H (1998) How to develop of astronomical navigation across to the 21st century. Navig technology Analecta of the turn of century. Xi'an: Chinese Institute of Electronics Navigation Branch, pp 30–38 (Ch)
2. Wang A (2007) Modern celestial navigation and its key technologies. J Electron 12: 2347–2348 (Ch)
3. Fang J, Ning X (2006) The theory and application of celestial navigation. Beijing University of Aeronautics and Astronautics Press, Beijing (Ch)
4. Hu W, Wu G, Huang L (2002) Research on marine electronics sextant angle sensor system. J Shanghai Marit Univ 23(3):17–20 (Ch)
5. Li C (2013) Research on marine celestial navigation technology based on fish-eye camera. Zhengzhou Institute of Surveying and Mapping (Ch)
6. Wang Y (2006) Fisheye lens optical. Science Press, Beijing (Ch)
7. Yuan Y (2012) Research on fish-eye camera stellar calibration technology. Zhengzhou Institute of Surveying and Mapping (Ch)
8. Sui L, Song L (2004) Theory of errors and measure adjustment foundation. PLA Press, Beijing, pp 188–190 (Ch)
9. Yang Y (1996) Adaptive robust least squares estimate. J Surv Map 25(3):206–211 (Ch)

10. Yang Y, He H, Xu G (2001) Adaptively robust filtering for kinematic geodetic positioning. J Geodesy 75:P109–P116
11. Yang Y (1999) Robust estimation of geodetic datum transformation. J Geodesy 73:268–274
12. Yang Y, Song L, Xu T (2002) Robust estimator for correlated observations based on bifactor equivalent weights. J Geodesy 76:353–358
13. Yang Y (1994) Equivalent weight principle–parameter adjustment model robust least squares solution. Bull Survey Map 6:33–35 (Ch)
14. Yang Y, FuMei W (2006) Critical value variable robust estimation equivalent weight function. J Surveying Mapp Sci Technol 23(5): 317–320 (Ch)
15. Song L (2009) Program design of surveying adjust. National Defense Industry Press, Beijing, pp 116–117 (Ch)

A Weak Signal Acquisition Method for Indoor Passive Location on Mobile Communications

Chuang Wang, Zhongliang Deng, Aihua Hu, Yao Zhang, Wei Zhao and Shuyue Dong

Abstract Under the indoor environment, since the attenuation of signal intensity of the mobile phone is caused by traversing multiple building walls, the signal strength that the receiver captured is pretty weak. Unfortunately, the existing indoor passive location receivers based on CDMA cannott capture that weak signal under such circumstances, hence it is urgent to propose a reasonable acquisition method to solve this problem. This paper starts from the existing signal capture methods based on CDMA communication system, by studying all the uplink channels in this system that are suitable for indoor passive location, preferentially chooses the RACH (Random Access Channel) signal after researching on the reverse channel of CDMA communication system. However, the existing signal acquisition method in CDMA system is not suitable for the weak RACH signal acquisition. This paper redesigns the local code generator and the acquisition process, and finally achieved the weak signal acquisition in CDMA system. Experimental results show that this method cannot only improve the signal to noise ratio of weak signal acquisition decision, but also has a great reference value for post disaster rescue and rescue detection station research based on CDMA mobile phone.

Keywords Indoor passive location · CDMA detection station · Weak signal acquisition · RACH

Foundation project: The National High Technology Research and Development Program ("863" Program) of China (No. 2015AA124101). The National Natural Science Foundation of China (No. 61401040). The National Science and Technology Support Program of China (No. 2014BAK12B00).

C. Wang (✉) · Z. Deng · A. Hu · Y. Zhang · W. Zhao · S. Dong
School of Electronic Engineering, Beijing University of Posts and Telecommunications, Beijing, China
e-mail: chuangwang2014@bupt.edu.cn; wcbeiyou12@126.com

J. Sun et al. (eds.), *China Satellite Navigation Conference (CSNC) 2016 Proceedings: Volume II*, Lecture Notes in Electrical Engineering 389,
DOI 10.1007/978-981-10-0937-2_34

1 Introductions

In recent years, criminal activities and natural disasters frequently happened all over the world, which have a strong impact on people's daily life. As a result, there is an urgent need for positioning technology in order to improve the criminal surveillance and reconnaissance capabilities as well as to rescue trapped personnel, and thus to well promote the peaceful development of society [1]. However, the traditional indoor and outdoor positioning systems, such as GNSS, ZigBee, Wi-Fi and so on [2], are all users active positioning which require users or client program on the mobile devices to initiate a positioning request. Therefore, the traditional indoor and outdoor positioning systems are not suitable for this special occasion.

With the popularity of mobile phones and the improvement of satellite navigation and positioning system, the indoor passive location based on mobile phone has gradually become the research hotpot. However, the CDMA communication system is very difficult because of its high degree of confidentiality. At present, domestic and foreign research in the field of indoor passive location is still at the blank stage. The acquisition of weak signal is a prerequisite for the realization of passive location of the receiver under complex indoor environment. In order to improve the acquisition sensitivity of the mobile phone signal, the signal to noise ratio (SNR) of indoor passive detection station must be improved. There are two existing ways to capture the weak signal, one is to improve the transmission power of the terminal, and the other is to increase the coherent or non-coherent integration time in the receiving end [3, 4]. This method of this paper belongs to the category of passive localization, that is to say, to achieve positioning without changing the existing mobile communication system. So it is unable to improve the acquisition sensitivity by increasing the transmission power of the mobile terminal. According to the CDMA communication system, the mobile phone's signal is discontinuous and non-periodic except for the reverse pilot channel. However, the reverse pilot channel is transmitted along with the traffic channel, which is not suitable for the indoor passive positioning environment. Therefore, this paper starts from two aspects of the search for the higher transmission power of the mobile phone signal and the increase of local coherent or non-coherent integration time, and finds that RACH signal not only has large transmission power and a sudden strong signal, and very suitable for indoor passive location of signal acquisition [5]. By improving the existing pilot acquisition method, the acquisition of RACH signal has been achieved. What is more, the signal to noise ratio is improved when the RACH signal is captured. The experimental simulation is carried out for the proposed algorithm afterwards. It turns out that when the signal to noise ratio of the signal is SNR = −30 dB, the maximum peak is still higher than the second peak for nearly 7 dB.

2 Research on the Acquisition Method of Passive Location About CDMA

2.1 The Existing CDMA Signal Acquisition Method

The existing CDMA signal acquisition methods are all based on the pilot channel which includes the F-Pilot and the R-Pilot channel in the CDMA communication system, to achieve synchronization between base station and users. The data transmitted by the pilot channel is all zero, and the Walsh function is the zero sequence of the 64 bits, which only added the phase and orthogonal short PN codes, then directly transmitted after the carrier modulation. Therefore, the received pilot signal:

$$\begin{aligned} r(t) &= \sqrt{\frac{2E_c}{T_c}}[C_I(t)\cos(\omega_0 t+\psi_\omega)+C_Q(t)\sin(\omega_0 t+\psi_\omega)]+n(t) \\ &= \sqrt{\frac{2E_c}{T_c}}[C'_I(t)\cos\omega_0 t+ C'_Q(t)\sin\omega_0 t]+n(t) \end{aligned} \tag{1}$$

where $C'_I(t) \triangleq C_I(t)\cos\psi_\omega + C_Q(t)\sin\psi_\omega$, $C'_Q(t) \triangleq C_Q(t)\cos\psi_\omega - C_I(t)\sin\psi_\omega$, is a short I road pseudo code, $C_Q(t)$ is a short Q road pseudo code; E_c is the code $C_I(t)$ slice energy, and T_c is the code slice period, and ψ_ω is the initial carrier phase; When the receiver receives the $r(t)$, the RF signal is reduced to 0 IF with analog down-conversion processed, and the Walsh code of this signal is then processed by coherent integration and noncoherent integration, and the result of the integral and local threshold value is the output of acquisition decision. If the result is greater, the program will enter the tracking loop, whereas, according to the search strategy, set a new code phase to continue detection. The capture block diagram of the signal [6] is shown in Fig. 1: where $X(t)$, $Y(t)$ are the signals of the short pseudo code stripped. The signal expression is as follows:

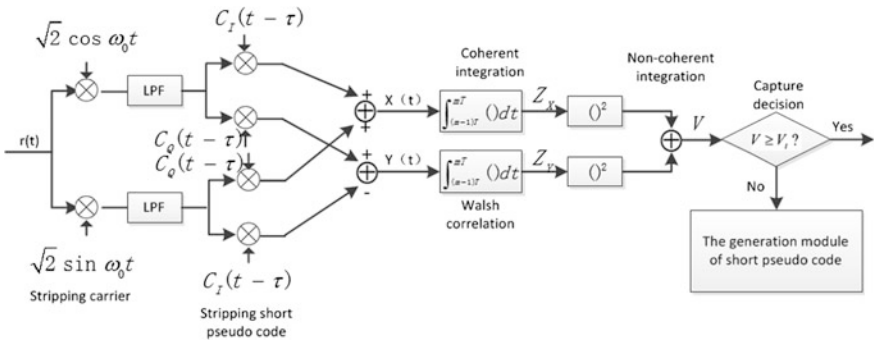

Fig. 1 Existing CDMA signal capture block diagram

$$X(t) = \sqrt{\frac{E_c}{T_c}}[C_I(t)C_I(t-\tau) + C_Q(t)C_Q(t-\tau)]\cos\psi_\omega + n_{II}(t) + n_{QQ}(t) \quad (2)$$

$$Y(t) = \sqrt{\frac{E_c}{T_c}}[C_I(t)C_I(t-\tau) + C_Q(t)C_Q(t-\tau)]\sin\psi_\omega + n_{IQ}(t) - n_{QI}(t) \quad (3)$$

where $n_{ii}(t)$ contains noise, interference between channels and orthogonal interference; Z_X, Z_Y are the results of the coherent integration; $V = Z_X^2 + Z_Y^2$ is a non-coherent integral value.

Because only when the CDMA communication system in the transmission of traffic signals,the phone or the base station will send a continuous reverse or F-Pilot channel, the indoor passive location system is a passive location of the mobile phone in the silent state, so the existing CDMA signal acquisition method can not meet the needs of indoor passive location.

2.2 The Analysis of RACH

Mobile phone captures one of 512 kinds of short PN code (short PN code, cycle length is $2^{15} - 1$) through the F-Pilot to do short PN code synchronous and demodulate the F-SYNC (Forward-Synchronous Channel), changing the state of the local short PN code generator, from the F-SYNC to obtain the long PN code state of base station (long PN code, the cycle length is $2^{42} - 1$) in order to update the local PN code length generator, and finally obtain the long PN code synchronization. To update the status of local long PN code generator, the long PN code synchronization with the base station can be obtained. Different users can be distinguished by the Mask which is 42 points long [6]. Figure 2 shows that the format of the mask. access channel number (ACN) is five points long, the default is '0'; paging channel number (PCN) is 3 points long, the default is '1'. The access can be attained by listening to the forward paging channel matching with the long PN code, and then send the RACH sequence on the appropriate time. Fifteen detection sequences is sent in each

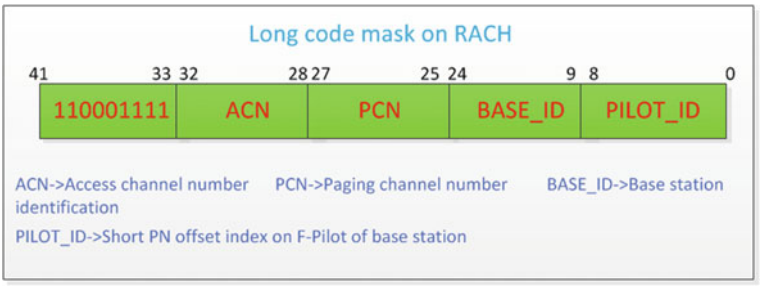

Fig. 2 The mask format of PN long code in access channel

access trying, one detection sequence contains 16 accesses, each access sends the same information, however, the pseudo code is different. There are two types of information in the RACH, which are response information and request information. The response information is the response to the base station, and the request information is about the mobile phone location updating request, registration, paging, etc. Each RACH contains an access preamble and an access channel message body. The characteristics of RACH are the relatively high energy, breaking out suddenly, the access preamble frame consisting of all zero. The access preamble frame continues for about 1+PAM_SZs, it is about 1–16 frames, each frame is 20 ms [6]. Then, the receiver can realize the coherent integration for more or equal to 20 ms. And the message body contains the user's information behind the access preamble, it is easy for the passive location to acquire the user identification. Above all, RACH signal is very suitable for capturing the signal in indoor environment.

RACH composition:

In order to facilitate the analysis, it can be assumed that the detection station only receives a signal from a mobile phone user. According to the Walsh spread spectrum, pseudo code scrambling and carrier modulation process of RACH signal, the formula of RACH is:

$$\begin{aligned} r(t) &= \sqrt{\frac{2E_c}{T_c}} m(t)[C_L(t)C_{SI}(t)\cos(\omega_0 t + \psi_0) + C_L(t)C_{SQ}(t)\sin(\omega_0 t + \psi_0)] + n(t) \\ &= \sqrt{\frac{2E_c}{T_c}} m(t)[C'_{LI}(t)\cos\omega_0 t + C'_{LQ}(t)\sin\omega_0 t] + n(t) \end{aligned} \tag{4}$$

where $C'_{LI}(t) \triangleq C_L(t)C_{SI}(t)\cos\psi_0$; $C'_{LQ}(t) \triangleq C_L(t)C_{SQ}(t)\sin\psi_0$; $C_L(t)$ is the long PN code, $C_{SI}(t)$, $C_{SQ}(t)$ are the same phase, orthogonal short PN code; m(t) is the data sent by RACH.

2.3 Improved RACH Signal Acquisition Method

As can be seen from the RACH signal modulation process, the difference between the pilot signal and RACH signal is mainly about different composition of the local code. The local code of pilot signal mainly contains cophase short PN code C_I and orthogonal short PN code C_Q, while RACH signal not only contains cophase short PN code C_I and orthogonal short PN code C_Q, but also superimposed with a longer period of PN long code in the cophase and orthogonal branches. If the pilot signal capture method is used to capture RACH signal, then the coherent integration of cross-PN long code chips will seriously affect the coherent gain and capture success rate. In this paper, the local PN code I and Q were designed as $C_L(n)C_{SI}(k)$ and

$C_L(n)C_{SQ}(k)$, in order to reduce coherent integral gain loss caused by longer period of PN long code, so as to improve the success rate of capture.

2.3.1 Algorithm Block Diagram and Steps

According to the RACH signal, through the RF front-end conversion and low-pass filtering in detection station, the signal that baseband processor of detection station receives is as follows:

$$r_{IF}(t) = A_{IF}s(t-\tau)\exp\{j[2\pi(f_{IF}+f_d)(t-\tau)+\psi_0]\}+n(t) \tag{5}$$

where A_{IF} is the intermediate frequency signal amplitude; τ is a signal from the mobile phone to the receiver of the propagation delay; f_{IF} is the intermediate frequency. If zero IF receiver, f_{IF} is expected to be 0; f_D is caused by Doppler frequency shift and frequency oscillator frequency offset error; ψ_0 is the IF initial phase; $n(t)$ is the noise signal.

This paper redesigns the signal capture model for the RACH of the CDMA communication system, as shown in Fig. 3, the specific steps can be described as follows:

(1) The received baseband signal, first, enters the carrier stripping module, mainly in the various communication frequency point for the search, a search point down to zero if the signal, that is, signal carrier stripping.
(2) The receiver obtains long code state LC state from the cell base station, and updates the local PN long code generator, by the user to generate a mask the paging slot in a fixed length code, then and now produces short PN code are XOR superposed to form a local code, then the (1) input signal for on line shift related.
(3) The relevant value from the (2) input to the 20 ms is obtained by the coherent integration of the to improve the coherence gain, and the sum of the square sum of the obtained results is $V = I^2 + Q^2$.

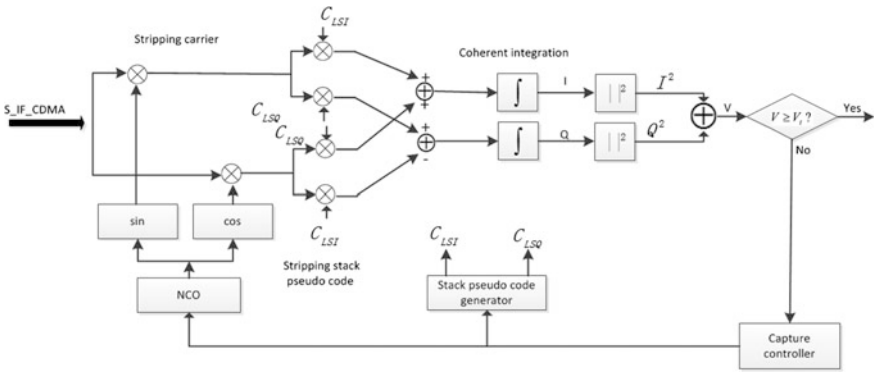

Fig. 3 Capture method block diagram of this paper

(4) Comparing V obtained from (3) and the local threshold to make the decision, if satisfied, that is the success of the capture, conversely, changes the local search strategy, and reenters (1) to capture the next mobile phone user.

3 Experiment Simulation

In order to verify the validity of the proposed indoor passive location RACH weak signal acquisition method, using the data parameters in Table 1, RACH signal acquisition performance was simulated, respectively, using the existing CDMA capture method while SNR = 0 dB, and using the improved local code auto correlation property and the improved acquisition method while SNR = 0 dB/−15 dB/−30 dB (Fig. 4).

Table 1 Data parameters used in simulation

Parameter	Value
ACN (access channel number)	0
PCN (paging channel number)	1
Base station ID	12
Pilot frequency offset	0
Lc_state (long PN code original state)	1
Coherent integration time	20 ms

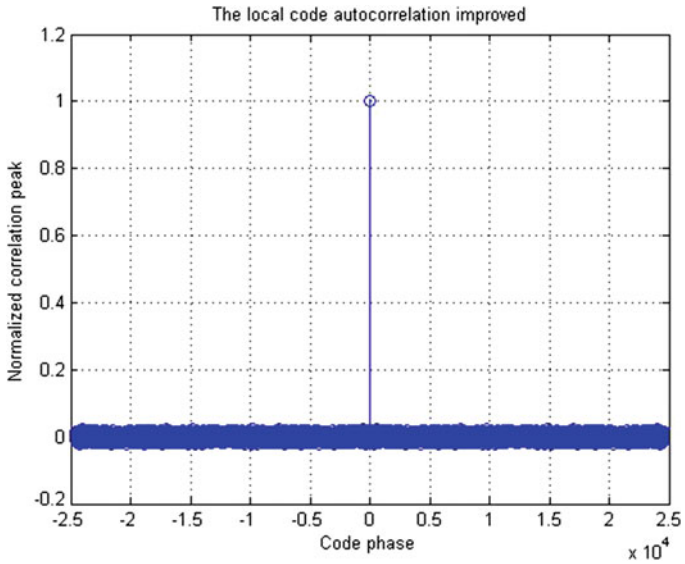

Fig. 4 Improved local code auto correlation property

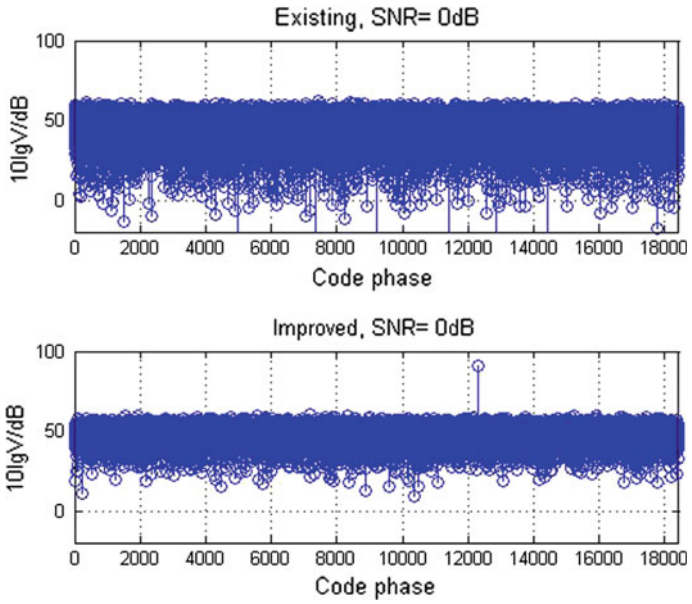

Fig. 5 Existing CDMA capture method and RACH signal acquisition method in this paper, SNR = 0 dB

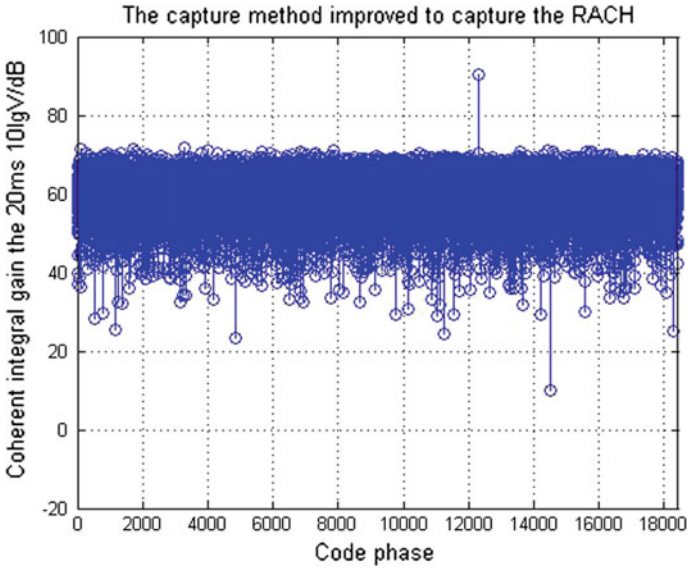

Fig. 6 RACH signal acquisition method, SNR = −15 dB

In view of the above simulation graphics analysis, when the signal to noise ratio, SNR = 0 dB, the compared with existing CDMA capture method, the maximum peak of RACH signal acquisition method in this paper (Fig. 5) is nearly 30 dB above. SNR = −15 dB, the maximum peak of RACH signal acquisition method in this paper (Fig. 6) is 20 dB more than the second peak, SNR = −30 dB (Fig. 7), the maximum peak is still higher than the second peak by 7 dB.

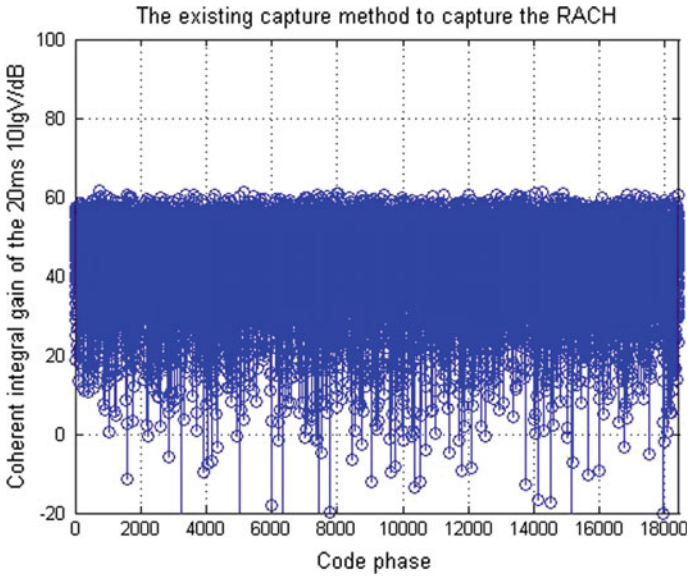

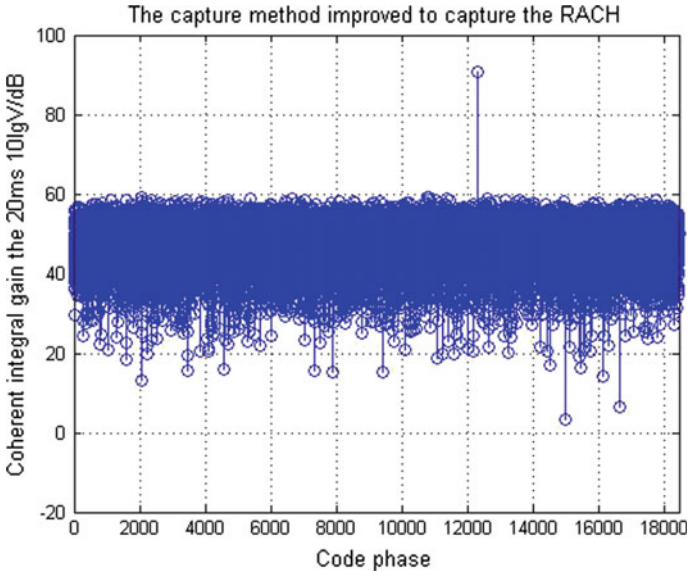

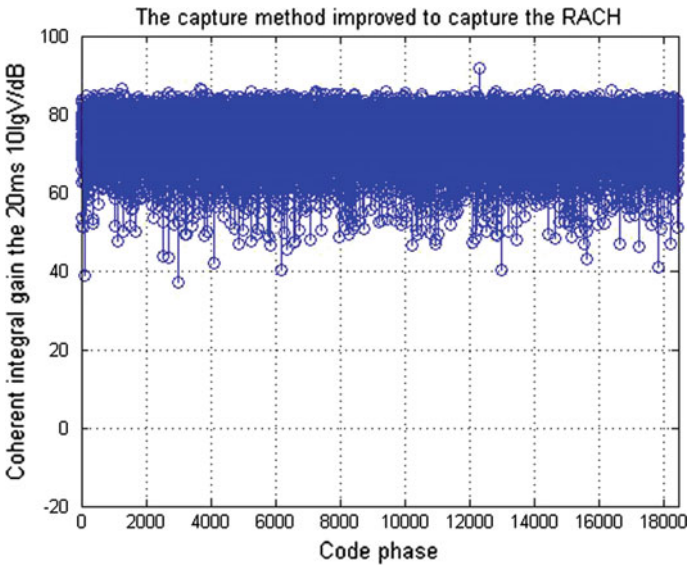

Fig. 7 RACH signal acquisition method, SNR = −30 dB

4 Conclusions

In this paper, the indoor passive positioning system based on CDMA communications, on the basis of the existing CDMA signal capture method, by improving the local code generator design, achieved acquisition for RACH signal under complex indoor environment. This method belongs to the category of passive localization, that is to say, the detection station only receives the signal sent by the mobile phone, without sending any signal back to the phone, and hence it will not affect other functions of the existing communication system. Of course, in view of the weak signal acquisition of indoor passive location system, there are still deficiencies. For example, although the CDMA phone access channel number is 0, and the paging channel number is 1 by default, there is still possibility of using other access channel numbers or that much more users accessed will most likely cause higher capture leakage rate. In view of this issue, multi-user parallel access methods can be used to reduce users' capture leakage rate.

References

1. Feng W, Wang Y-W (2013) Indoor passive location based on location fingerprint. Commun Technol 12. doi10.3969/j.issn.1002-0802.2013.12.011
2. Deng Z, Yu Y (2013) The research on status and development trend of indoor position. China Commun 03

3. Li S, Yi Q, Chen Q (2012) Weak signal acquisition method for GPS software receiver. Comput Appl 32(03):816–818
4. Xie G (2009) Principles of GPS and receiver design. Publishing House of Electronics Industry, Beijing, 376–384
5. Xu B (2011) Research on key technology of non cooperative positioning in CDMA 2000 mobile station. National University of Defense Technology, Changsha
6. Lee JS, Miller LE (2001) CDMA system engineering manual. People's Posts and Telecommunications Press

Review of Timing and Positioning with OFDM

Xin Zhao, Yong Wang, Yonghu Zhang, Yingxue Su, Xiangwei Zhu and Guangfu Sun

Abstract OFDM signal systems have been widely used in mobile communications, digital satellite TV, and have provided higher transmission rate and positioning information service. It has the potential in timing and ranging. Because of limitation of GNSS signal strength, indoors, underground and in the other scenes, CDMA-based GNSS signal receiver sensitivity cannot meet the requirements, or serious in multipath influence, and poor in positioning accuracy. Satellite navigation positioning system based on ranging and transmission with OFDM is still a hot issue in the future. Satellite navigation and positioning is also facing new opportunities and challenges. Methods based on existing OFDM timing and ranging technology are analyzed, which point out that synchronization algorithm and channel estimation is the key to enhance accuracy. Therefore, this paper proposes three aspects of OFDM to enhance the accuracy: ① Combination of a variety of signal system; ② improving 2π limitation of TOA phase measurements in the frequency domain; ③ Accurate channel estimation utilizing OFDM signal.

Keywords OFDM · Signal system · Ranging · Synchronization · Channel estimation

1 Introduction

With OFDM technology developing, the technology has been applied in the video broadcast and communication systems [1, 2], the main applications include wireless LAN, ETSI standard for digital audio broadcasting, HDTV, digital video radio, etc.

X. Zhao (✉) · Y. Wang · Y. Zhang · Y. Su · X. Zhu · G. Sun
National University of Defense Technology, Deya road 109, 410073 Changsha, China
e-mail: zhao101180163@163.com; 1204601443@qq.com

J. Sun et al. (eds.), *China Satellite Navigation Conference (CSNC) 2016 Proceedings: Volume II*, Lecture Notes in Electrical Engineering 389,
DOI 10.1007/978-981-10-0937-2_35

[3]. Given the advantages of OFDM, the mobile communication system currently used has formulated communication standards in the core of OFDM.

With the evolution of mobile communications, satellite navigation and communications also will face new opportunities and progress. With the development of satellite navigation systems, satellite navigation system provides good service on not only timing and positioning, but also on communications and data services. Common mature communications satellites include Intelsat-9,10 series of satellites [4], Inmarsat-4 satellite [5], etc. In the interior, woods, and underground scene, navigation signal based on the CDMA is very serious in multipath influence and poor in positioning accuracy. But the OFDM signal system has good anti-multipath performance. We can overcome these problems to some extent, and it is also simpler to be achieved and costs less. And OFDM signal system has high bandwidth efficiency and data capacity. Therefore many high-volume data transmission services adopt this way. It shows that satellite navigation positioning system based on OFDM ranging and data transmission is still a hot issue in the future [6].

Currently, ranging and positioning signal system based on OFDM is not common, including the famous OFDM positioning system—Xihe systems [7], positioning accuracy of 3 m, which signals use CDMA and OFDM a coupling method of CDMA and OFDM, called the TC-OFDM signal system. Xihe system is excellent indoor and outdoor in positioning, and outdoor up to 1 m accuracy, indoor up to 3 m accuracy. Using CDMA as the synchronous head, OFDM assists in positioning and data transmission. Consequently, it brings the high positioning accuracy and high data transmission capacity. But, positioning indoor needs Xihe's special equipments, and also within the boundary of Xihe's base station.

Mobile LTE downlink signal systems make use of OFDM and chu sequence for synchronization, which is essentially an MC-CDMA signal system, playing a significant role in cell search and positioning, up to synchronization accuracy of 50–100 ns and location accuracy of 30 m.

We found that CDMA and OFDM cooperative positioning is more precise than only using CDMA positioning. With the analysis of Xihe localization systems and mobile communication LTE signals, we will pay close attention to joint positioning of different signals in timing and ranging in the future, for example combination of CDMA and OFDM methods.

This article focuses on analyzing timing and ranging for OFDM signal system and summarizing, and explores novel technological ways to enhance the OFDM system ranging and positioning accuracy. In Sect. 2, principle of the OFDM is introduced. Section 3 describes common synchronization algorithm. In the part of Sect. 4, we mainly focus on representing channel estimation algorithm. Finally, in Sect. 5 the prospects are presented.

2 OFDM Signals System Ranging Principle

2.1 OFDM Signal System Principle

Modulating the data stream on orthogonal subcarriers in the frequency domain is the nature of OFDM technology [8]. Assume that data $x(m)$ is transformed, then the transmitted signal is as follows:

$$s(t) = \sum_{n=0}^{N-1} Re\{A_n x(n) \exp(j2\pi f_n t)\} \tag{1}$$

where f_n is the frequency of subcarriers.

Multi-carrier modulation and demodulation based on FFT are used under the condition of the mutually orthogonal subcarriers according to the generated principle of OFDM signal, and do not need the traditional band-pass filter to match OFDM carrier frequency.

According to the principle of OFDM signal system, the correspondence in frequency domain and time domain is the following [9]:

$$X_k[m] = \frac{1}{\sqrt{N}} \sum_{n=0}^{N-1} x_k[n] \exp\left[-2j\pi m \frac{n}{N}\right] \tag{2}$$

Particularly, the length of CP (cyclic prefix) depends on the channel multipath delay generally.

2.2 OFDM Signals System Ranging Principle

The key in OFDM timing and ranging is the measurement of arrival of time (TOA). Assume that the receiving signal synchronization time is tr. There is deviation between the ideal value and the real value [10], as follows:

$$Tr = tr_o + \Delta tr \tag{3}$$

The transmit time corresponding to the transmitter is the following:

$$T_s = ts_o + \Delta ts \tag{4}$$

where Δt is the deviation between the ideal and real time.

The equation can be obtained from the above as follows:

$$\rho = c(tr_o - ts_o) + c(\Delta tr - \Delta ts) + \varepsilon \tag{5}$$

where, ε is the observation error. The expression is the OFDM timing ranging pseudo-range equation.

Due to propagation delay, the excess phase is introduced after FFT of the signal. The formula is as follows:

$$Y[k] = X[k] \exp[-2j\pi k\vartheta/N] + n[k] \tag{6}$$

where θ is the ratio of the delay and the sampling interval.

According to the principle of OFDM signal system, there are some characteristics in ranging with OFDM signal system as follows:

① anti-multipath effect
Due to the CP (Cyclic Prefix) in OFDM signal system, OFDM signal is not sensitive to time synchronization error as long as the multipath delay is less than the CP length. This maintains the orthogonality between carriers, demodulates the data in OFDM signal correctly, and completes accurate timing ranging.

② anti-frequency selective fading
Since the OFDM signals system modulated data on different subcarriers, the frequency range in each subcarrier is small. It belongs to the flat fading channel. It will not cause distortion in entire OFDM signals, which reduce the impact on the communication link.

③ stringent synchronization requirements
Each carrier in OFDM signal system keeps strict orthogonality. It is sensitive to synchronous timing error, carrier frequency error, and sampling period error and is easy to produce ISI and ICI.

④ high transmission capacity
Since the orthogonal subcarriers were adopted in OFDM signals in frequency domain, the data traffic quantity has been further improved compared with conventional frequency-division multiplexing system.

2.3 Summary

Timing synchronization accuracy limited the improvement of OFDM positioning accuracy. Actually, channel estimation is needed to obtain channel information to compensate and balance the OFDM synchronization time error. Moreover, the positioning accuracy is limited because of the existence of the barriers; the problem of non-line-of-sight is presented. Due to the good frequency-domain features, the OFDM can be used in channel estimation to find the line-of-sight delay. Actually, timing ranging is equal to the channel estimation, and we just get general information channel delay. Channel estimation is the natural means of the problem to solve the non-line-of-sight.

So to upgrade the OFDM timing ranging accuracy, the main methods are as follows:

① finding the start location of the received signal data with proper OFDM synchronization algorithm, including time domain and frequency domain synchronization algorithm.
② channel estimation, get line-of-sight TOA. Moreover, in the OFDM symbol synchronization, channel estimation and equalization of the received signal is beneficial to eliminate ISI and ICI.

Next, the OFDM timing synchronization and channel estimation method is described in detail.

3 Synchronization Algorithm

OFDM synchronization consists of symbol timing synchronization, carrier frequency synchronization, and sampling clock synchronization [11]. For positioning, it is more concerned about the symbol timing synchronization. Symbol timing synchronization refers to accurately find data start time in the modulation of the signal which is crucial to the correct demodulation. If symbol synchronization is error, it will appear the ISI (inter-signal interference), demodulation performance degradation [12].

OFDM ranging is sensitive to synchronization error. Synchronous timing algorithm is mainly divided into two categories: CP (cyclic prefix) and pilot timing synchronization The following are analyzed and summarized.

3.1 Timing Synchronization Based on CP [13, 14]

CP is same as end part of symbol, which urges the possibility of using relevance to synchronization. It assumes that the CP and tail same data of the OFDM symbols are the distance at N sampling points, and the CP is length of L sampling points. One set (I) starts with theta, L points; the other set starts with theta + N, L points in Fig. 1. Using correlation one can deduce start position of the symbol data modulation. Common methods include maximum likelihood estimation, correlation, the improved correlation and difference, the detailed description is in Table 1 (Fig. 1).

In general, synchronization methods based on CP are appreciated for the quantity consecutive OFDM signals, but owing to fewer sampling points, the synchronization accuracy is not enough and is usually used to transmit data in the communications field.

Table 1 Comparison of synchronization methods based on CP

	Algorithm description	Advantages and disadvantages
Maximum likelihood [15]	$\Lambda(\theta,\varepsilon) = \lvert r(\theta)\rvert \cos(2\pi\varepsilon) - \rho\phi(\theta)$ The receiving signal observed is represented by the maximum likelihood probability, the most likely timing error and carrier frequency error value	Considering the received signal energy, high estimation precision, high operation complexity
Correlation method	$\Lambda(\theta,\varepsilon) = \left\lvert \sum_{n=\theta}^{\theta+L-1} r(\theta)r^*(n+N) \right\rvert^2$ Due to the structure of the CP, at the beginning of time L data and $N + L$ OFDM data have similarity, using the correlation method is the most direct method	Ignores the influence of the signal energy item, the accuracy is better than ML algorithm, but reduces the computing complexity
Improved symbols correlation method [16]	$\rho(k) = \frac{\left\lvert \sum_{m=0}^{M-1} r(k+m(N+L))r(k+m(N+L)+N) \right\rvert}{\sqrt{\sum_{m=0}^{M-1} \lvert r(k+m(N+L))\rvert^2} \sqrt{\sum_{m=0}^{M-1} \lvert r(k+m(N+L)+N)\rvert^2}}$ Using multiple consecutive OFDM symbols into the Correlation calculation, nature is still Correlation method	Considering the influence of the energy items, uses more than one symbol on average to improve accuracy, high computational complexity
Differential method [17]	$\Lambda_{th}(k) = \sum_{i=0}^{N_{th}-1} \lvert r(k+i) - r(k+i+N)\rvert^2$ $N_{th} = N_g - t_d$ Using same characteristic of the CP and part OFDM data to carry on estimating timing offset	Serious multipath effect, poor accuracy, the simplest algorithm

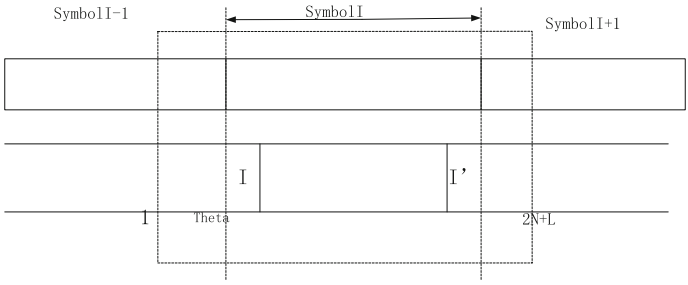

Fig. 1 CP synchronization method

3.2 *Timing Synchronization Method Based on Pilot*

Schmidl and Cox [18] proposed a pseudo-random code as the pilot sequence, only in even-carrier modulation data. After IFFT, in the time domain the form of OFDM symbol ($P = \{\mathrm{CP}A(N/2)A(N/2)\}$) is shown in Fig. 2.

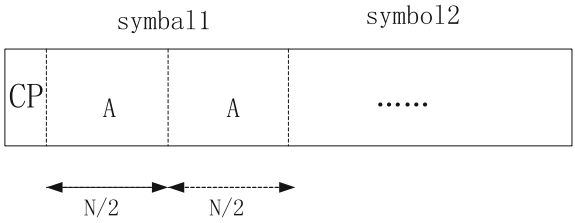

Fig. 2 Form of OFDM symbol

Expressions are as follows:

$$M = \frac{\text{abs}(P(d))2}{\text{abs}(R(d))2} \tag{7}$$

$$\begin{aligned} P(d) &= \sum_{m=0}^{N/2-1} \bar{r}(d+m) * r(d+m+N/2) \\ R(d) &= \sum_{m=0}^{N/2-1} |r(d+m+N/2)|^2 \end{aligned} \tag{8}$$

Due to the presence of CP, M is flat in a certain extreme area. In order to reduce the flat area, many researchers proposed to improve this method, as shown in Table 2.

Table 2 Comparison of improved pilot timing synchronization method

	Improvement	Characteristic
Minn method [19]	Temporal form is divided into four identical portions, $P = \{\text{CP}A(N/4)A(N/4) - A(N/4) - A(N/4)\}$	Obvious changes in Extreme neighborhood, but high root mean square error, which could lead to false positives
[3]'s method	Temporal Sequence into the same size, the two parts conjugate symmetric, $P = \{\text{CP}A(N/2)B(N/2)\}$	Extreme neighborhood is small, root mean square error is relatively small
[20, 21]'s method	Time-domain sequence is divided into four parts, $P = \{\text{CP}ABA * B*\}$, A and B are different	Extreme neighborhood is small, the mean square error is smaller
[22]'s method	Using chu sequence, the time-domain design $P = \{\text{CP}A(N/2)A(N/2)\}$	Better than MINN method, mean square error is relatively small
Joint OFDM method [23]	The first symbol adopted Sch and Cox method, the second symbol transmission pseudo-random code for timing synchronization and carrier frequency synchronization	Improves the timing synchronization accuracy, eases original method Extreme flat problems

For OFDM timing and ranging problems, we can find the key that is how to synchronize OFDM symbol. Synchronization accuracy is higher, more accurately distance is measured. Since there is a one-to-one relationship between data and the carriers, true synchronization must be completed in the frequency domain. For unexpected circumstances, by pilot synchronization method through specific OFDM symbol, all sampling points across the time domain will be used to complete the synchronization with high precision. But it will reduce the data capacity and data transfer rate, which is applied as a data frame header typically.

4 Channel Estimation

The channel estimation can be divided into the blind, non-blind estimation and semi-blind estimation. The blind estimation is different from non-blind estimation, comparison of the characteristics is shown in Table 3.

In view of advantages and disadvantages of the blind and the non-blind estimation, scholars put forward semi-blind estimation, which reach balance of both efficiency and convergence speed of data transmission, and use a less-known sequence. Next three methods were summarized.

Table 3 Comparison of the blind estimation and the blind estimation

	Blind estimation	Non-blind estimation
Connotation and definition	Don't transfer known sequence, the use of statistical information, dealing directly with a large number of received signals for channel information	Transferring known sequence, using the channel information of the known sequence to obtain the whole channel information
The key estimation algorithm	Cyclic prefix cycle stability or zero padding suffix data redundancy and information features	Inserting known sequences, estimating channel state information of known sequence, restoring channel state information every moment
Common methods	Second-order cyclic statistics, signal subspace separation and characteristic finite character set and data information	Decision directed, separation filter, domain transformation, polynomial fitting and interpolation method
Advantages	Only useful data, high communication efficiency	Fast convergence, low complexity, simple implementation
Disadvantages	Slow convergence, higher complexity, the limit of actual application	Due to the known sequence, reduces the communication data capacity

4.1 Non-blind Estimation [24, 25]

Non-blind estimating main process is mainly divided into inserting pilot sequence (known), pilot channel estimation, the full channel state information estimation, and then detailed description is as follows.

1. Pilot insertion
   According to the structure of pilot symbols, pilot can be divided into block pilot [26], comb pilot, and rectangular pilot [27].

   (1) Block pilot signal is inserted to a specific OFDM symbol in a certain period of time. When the channel state changes severely, it is suitable.
   (2) Comb pilot is at a certain interval evenly distributed in OFDM symbol in frequency domain. When the channel state changes severely, it is suitable for the pilot.
   (3) Rectangular pilot is inserted at a certain interval to OFDM symbol in frequency domain and time domain, which has higher spectrum efficiency, but needs to employ interpolation filter in the frequency domain and time domain with high complexity in practice.

2. Pilot channel estimation
   For channel state information matrix H of pilot, the option and complexity should be considered. MMSE criterion can ensure H optimal, but needs inversion of matrix which is complex, so we generally use LS (least square) and the improvement of MMSE (minimum mean square error) method [28]. According to LS criterion, after FFT, $Y = HX + W$, (W noise frequency domain matrix), the estimation $H\hat{} = Y/X$. Under the improved MMSE criterion, when the multipath channel can be simplified as small multipath, the matrix inversion can reduce the dimension, reduce calculation [29], or the pilot sequences design [30] makes the state matrix into a diagonal matrix H to simplify inversion.
3. Complete channel estimation
   Complete channel estimation methods are divided into known channel information matrix channel estimation and unknown channel correlation matrix information channel estimation, the next is analyzed and summarized.
   Known information channel matrix channel estimation mainly includes the two-dimensional Wiener filter, separation filter [24] and singular value decomposition channel estimation [31]. But it is only a theoretical analysis, because the channel autocorrelation matrix is not generally given in practical engineering. Consequently, the channel estimation of unknown channel correlation matrix method is used, the more carries on the detailed introduction.

   (1) Unknown channel information channel estimation
   Methods usually used mainly are decision directed, polynomial fitting, interpolation, DFT, etc. With the development of technology, it also derives some new methods: compression sensing and channel linear. In Table 4 they are analyzed and summarized.

Table 4 Comparison of the traditional channel estimation method

The traditional methods	Description	Characteristics	Improvement
DFT channel estimation [32–35]	The channel response of H^ after IFFT to time domain, zero padding operation, FFT to the frequency domain for CFR (channel frequency response)	Meeting channel delay is integer times of sampling interval	Adding window in IFFT transformation process to reduce the spread of the CFR, or join in MMSE weighted process [36]
Polynomial fitting [37]	Establishing polynomial model to fit characteristics of the channel, Calculating polynomial coefficients specifically referring to the use of H^	Just asking little polynomial coefficients, simple to implement, polynomial order is the key to its complexity	When the moving speed becomes high, higher order polynomial fitting requires for better performance [38], which is the problem to be improved
Interpolation	Given the correlation between subcarriers, fitting after obtaining pilot channel state information. Common interpolation: Lagrange polynomial method, which is divided into first-order linear interpolation, second-order parabolic interpolation and third-order cubic interpolation [38]	Pilot signal is usually evenly distributed, simple implementation, but it brings the noise	The paper [39] made low-pass filter to reduce the noise threshold
Decision directed [40]	After obtaining the pilot the channel state, using the decision method to update the channel coefficients to obtain complete estimation of the channel state information	In the decision process, the error will be delivered, reducing the estimated performance if the channel changes faster than the OFDM cycle, performance decline further	Continuous multi-symbol weighted average alleviates degradation of performance

Table 4 shows that the traditional methods have good adaptability with slowly changing channel, but for increasingly complex channel environment, obviously cannot show good performance. Then it derives a number of new methods, mainly as compressive sensing and channel linearization method.

① compressed sensing channel estimation [41, 42].
Compressed sensing technique is very common in signal reconstruction, which utilizes observed signal and linear expressions to recover original signal in high probability. The general principles can be expressed as follows:

$$\min\|X\|_0, s.t.y = \Phi X + W \tag{9}$$

where y is the observed signal, w is noise, Φ is a matrix transformation.
We can find that the reception signal obtained through the FFT $Y = HX + W$, in the OFDM signal system where H is the channel information and X is a known transmitted signal data, by compressing sensing to estimate channel information H. In [42], the authors improved the traditional compressing sensing technology for OFDM system, and the effect is closer to the ideal least square method. In poor channel environment, we can still get good results.

② channel linearization estimation method [43].
Channel linearization mainly is that time-varying amplitude channel response can be expanded to Taylor series and second order and higher can be ignored to simplify time-varying channel estimation. Actually, such method is an iterative process, since the channel information changes over time. The channel estimation after linearization is taken into the traditional non-blind channel estimation, and we utilize channel information of consecutive OFDM pilot symbols to iterate the channel status of every moment. Channel linear method is proper for dynamic channel, but the decline of traditional methods is very obvious, which is no longer applicable. Apparently dynamic channel estimation for OFDM signal system will be important in future.

4.2 Semi-blind Channel Estimation

Expectation maximization algorithm (EM algorithm) is a kind of common semi-blind estimation in OFDM signal system [44, 45]. EM algorithm is an effective channel estimation method when the available data is incomplete. If the log-likelihood function of received signal is obtained, ML method cannot directly get the maximum likelihood estimation. While the EM algorithm adopts iterative method to calculate expectation and maximum to get the satisfied likelihood estimation. It will be described as follows:.

(1) Calculating the expectation: where Y and H_p are given, calculate expectations of likelihood function of channel matrix H regarding X.

$$Q(H|H_p) = Ex\{f(Y, X|H)|Y, H_p\} \tag{10}$$

(2) Calculating Maximum: After getting the expectation in the last step, the maximum is obtained by derivation. The expression is following:

$$H_{p+1} = \arg\max Q(H|H_p) \tag{11}$$

Repeating the above two steps in algorithmic process, finally the satisfied channel estimation is gained. The results of the EM algorithm are weighted LS results by using the received and transmitted signal cross-correlation function and autocorrelation function. Since the EM algorithm has good adaptability for incomplete data, EM algorithm can improve the edge signal quality for users at the edge of cell receiving superposition of two base stations signals. However, EM algorithm complexity will increase exponentially with the number of data in OFDM symbols increasing, and EM algorithm is not adaptive with the time-varying signal.

4.3 Blind Channel Estimation

Blind channel estimation usually needs to get more signal, and extracts statistical characteristics. Generally, the effect is not as good as using non-blind pilot estimation. So in OFDM signal systems it is not often adopted. Particularly, the subspace separation is a common and effective blind channel estimation method. The received signal can be separated into signal subspace and noise subspace [46], and the two are mutually orthogonal. Normal processing based on orthogonal and second-order statistical properties of the received signal can estimate complete the channel state information. However, it is extremely complex to decompose matrix eigenvalue and separate signal and noise subspaces for the received signal.

5 Conclusion

OFDM signal system is a powerful support for prospective communications and navigation services. But now, OFDM signal positioning accuracy is not high enough which limits the development of OFDM. Based on the current development concerned, I think OFDM signal system can be improved mainly from the following aspects to enhance the positioning accuracy:

(1) Combination of a variety of signal system. Integration of a variety of signals utilizing complementary advantages can reduce multipath effects to improve positioning accuracy such as TC-OFDM, MC-CDMA, etc.
(2) Improving 2π limit of measurements of phase in the frequency domain. In synchronization algorithm, there is a phase ambiguity in delay measurement in the frequency domain. Considering difference resolves phase ambiguity problem, or considering combination of the phase difference expands measurement range.
(3) Accurate channel estimation. OFDM signal system can improve range accuracy by looking LOS of TOA in complete channel estimation.

References

1. Nee RV (2000) OFDM wireless multimedia communications. Artech House
2. Song TC (2001) Next-generation mobile communication systems OFDM mobile communication technology. ll:20–23
3. Zhou Y (2004) Synchronous and ranging technology research OFDM modulated signal time. Nanjing University of Aeronautics and Astronautics, Nanjing
4. Yang Q (1995) Digital mobile communication systems. People's Posts and Telecommunications Press, Beijing
5. Cao Z (1992) Modern communication theory. Tsinghua University Press, Beijing
6. Linglong D, Zhaocheng W, Jun W, Zhixing Y (2010) Positioning with OFDM signals for the next-generation GNSS. In: IEEE Transactions on Consumer Electronics, vol 56, no 2, May 2010, pp 374–379
7. Deng Z (2014) CDMA and orthogonal frequency-division multiple access signal coupling ranging method, apparatus and system, China: 201310611421.3 [P].2014.03.19
8. Lie-Liang Y, Zhang Y (2010) Multicarrier communication. Electronic Industry Press, Beijing
9. Stefania S, Ma N (2012) LTE/LTE-advanced UMTS long term evolution theory and practice. Beijing: People's Posts and Telecommunications Press
10. He F, Wu L (2007) OFDM ranging error analysis—the first part. J Sensing 20(1):154–159
11. He F, Wu L (2007) OFDM ranging error analysis—part II. J Sensing 20(4):835–841
12. Roberts RD (1996) Qualitative analysis of the impact of clock timing error and/or frequency offsets on an OFDM waveform demodulator. In: Southcon/ 96 Conference Record, pp 80–85
13. Speth M, Classen F Meyr II (1997) Frame synchronization of OFDM systems in frequency selective fading channels. In Proceedings of VTC'97, pp 1807–1811
14. Clagen F, Meyr H (1994) Frequency synchronization algorithms for OFDM Systems suitable for communication over frequency-selective fading channels. In Proceedings of VW'94, pp 1655–1659
15. Van de Beek JJ, Sandell M, Borjesson P (1997) ML estimation of time and frequency offset in OFDM systems. IEEE Trans Signal Process 45(7):1800–1805
16. Ramasubramanian K, Baum K(2001) An OFDM timing recovery scheme with inherent delay-spread estimation. In: IEEE GLOBECOM, pp 3111–3115
17. Son SH, Kim J (2008) A robust coarse symbol timing synchronization for OFDM systems in multi-path fading channel. In: IEEE international symposium on consumer electronics, ISCE 2008. IEEE, pp 1–3
18. Schmidl TM, Cox DC (1997) Robust frequency and timing synchronization for OFDM. IEEE Trans Commun 45(12):613–1621
19. Minn H, Bhargava VK, Letaief KB (2003) A robust timing and frequency synchronization for OFDM systems. IEEE Trans Wireless Commun 2(4):822–838
20. Yang G (2008) Research based on passive location for OFDM signals. Xi'an Jiaotong University, Xi'an
21. Ziwen Z (2009) Study of satellite communication systems based on OFDM synchronization technology. Shanghai Jiaotong University, Shanghai
22. Zheng J (2008) broadband wireless OFDM system synchronization algorithm. Beijing University of Posts and Telecommunications, Beijing
23. Ye T (2007) Research based on OFDM training symbol synchronization technology. Beijing Jiaotong University, Beijing
24. Le Y (2000) Pilot-symbol-aided channel estimation for OFDM in wireless systems. IEEE Veh Technol Trans 49(4):1207–1215
25. Yang BG, Letaief KB, Cheng RS(2000) Windowed DFT based pilot-symbol-aided channel estimation for OFDM systems in multipath fading channels. In: Proceedings of IEEE VTC'2000, vol 2. Spring, Tokyo, pp 1480–1484
26. Yeh SC, Lin YY (1999) Channel estimation using pilot tones in OFDM system. IEEE Trans Broadcast 45(4):400–408

27. Yeh CS, Lin YY, Wu YY (2000) OFDM system channel estimation using time-domain training sequence for mobile reception of digital terrestrial broadcasting. IEEE Trans Broadcast 46(3):215–220
28. Wang H, Zhong W (2014) OFDM-based mobile satellite channel estimation algorithms. Comput Technol Dev 24(9):37–42
29. Li Y, Seshadri N, Ariyavisitakul S (1999) Channel estimation for OFDM systems with transmitter diversity in mobile wireless channels. IEEE J Sel Areas Commun 17(3):461–470
30. Li Y (2002) Simplified channel estimation for OFDM systems with multiple transmit antennas. IEEE Trans Wireless Commun 1(1):67–75
31. Ove E, Sandell M, Jaap J (1998) OFDM channel estimation by singular value decomposition. IEEE Trans Commun 46(7):931–939
32. Edfors O, Sandell M, Van DB (2000) Analysis of DFT-based channel estimators for OFDM. Wireless Pers Commun 12(1):55–70
33. Khan LU, Mahmud SA, Khan GM, Zafar MH, Shafiq Z (2015) Improved joint pilot allocation and channel estimation algorithm for OFDM system. In: ICST, pp 8–12
34. Wang X, Wang J, Wang Z (2010) Improved DFT-based channel estimation for OFDM systems over multipath channels, ACM, pp 585–590
35. Song BW (2005) OFDM broadband wireless mobile communication system of the channel and equalization technology research. Zhejiang University, Zhejiang
36. Yang BG, Cao ZG, Letaief KB (2001) Analysis of low-complexity windowed DFT-based MMSE channel estimator for OFDM system. IEEE Trans Commun 49(11):1977–1987
37. Wang XW, Liu KJ (2001) OFDM channel estimation based on time-frequency polynomial model of fading multipath channels. In: IEEE GLOBECOM'01, pp 212–216
38. Huang P, Hu R (2002) Estimate based on the pilot channel and polynomial model. Acta Electronica 30(4):584–586
39. Moon JK, Choi SI (2000) Performance of channel estimation methods for OFDM systems in a multipath fading channels. IEEE Trans Consum Electron 46(1):161–170
40. Yong SC et al (2010) MIMO-OFDM wireless communication technology and matlab achieve. Electronic Industry Press, Beijing Huang Wei, translation
41. Meng J, Li Y, Nguyen N, Yin W, Han Z (2011) High resolution OFDM channel estimation with low speed ADC using compressive sensing. IEEE ICC 57(4):1–6
42. Ye X (2015) OFDM system doubly selective slow fading channel compression sensing estimation. Electron Inf Technol 37(1):169–174
43. Groh I, Gentner C, Sand S (2012) Iterative intercarrier interference mitigation for pilot-aided OFDM channel estimation based on channel linearizations. IEEE Veh Technol Conf 13(1):1–5
44. Nam S-H, Lee S-J, Yoon J-S, Song H-K (2008) EM-based reduced complexity channel estimation for OFDM in mobile wireless system. In: ACM, pp 166–169
45. El-Hamid ZA, El-Henawy A, El-samie FA, El-Shenawy H (2012) FFT/DWT/DCT OFDM Channel estimation using EM algorithm in the presence of chaotic interleaving. In: IEEE, pp 54–60
46. Xiufu H (2009) OFDM channel estimation method. Xi'an: Xi'an University of Electronic Science and Technology

Performance Evaluation of Vehicle-Based POS by Hybrid Use of Total Station and Laser Tracker System

Yanglin Zhou, Guangyun Li, Shuaifeng Zhou, Jingyang Fu and Fengyang Li

Abstract Position and Orientation System (POS) is one of the most important parts of mobile mapping system, whose position and orientation accuracy has raised lots of attention. Many researches have been carried on improving the accuracy of POS, but less have been carried on testing the accuracy of POS, whose tests depend greatly on manufacturer and lack public and systematic method. According to this situation this paper analyzes the calibration techniques for testing the dynamic position accuracy of POS. The methods of counting the time of single measurement and curve fitting have been used for eliminating gross error from the raw observation data. The algorithm of ICP (Iterative Closest Point) is used for modifying the trajectory of total station system, which is realized by the comparison between high-accuracy trajectory of laser tracking system and that of total station system, to enhance the accuracy of dynamic surveying. Overall trajectory comparison and real-time comparison are used for testing the dynamic position accuracy of POS. Outdoor experiments have been carried out to verify the feasibility that this calibration method can be used for testing the dynamic position accuracy of POS.

Keywords POS · Dynamic accuracy inspection · ICP algorithm · Track correction · Error analysis

Y. Zhou (✉) · G. Li · J. Fu · F. Li
School of Navigation and Aerospace Engineering, Information Engineering University, Zhengzhou, China
e-mail: zhouyanglin@126.com

G. Li
e-mail: guangyun_li@sina.com

J. Fu
e-mail: fjynoob@sina.com

F. Li
e-mail: freyr_li@outlook.com

S. Zhou
61206 Troops Beijing, China
e-mail: 448059190@qq.com

J. Sun et al. (eds.), *China Satellite Navigation Conference (CSNC) 2016 Proceedings: Volume II*, Lecture Notes in Electrical Engineering 389,
DOI 10.1007/978-981-10-0937-2_36

1 Introduction

POS plays an important role in mobile mapping system by providing continuous and accurate carrier position and orientation information. With POS's realization of quick and real-time direct georeferencing and multi-sensor orientation, the point cloud and image data of mobile mapping system can have an efficient access to corresponding geographic coordinates [1]. So, POS provides a robust positioning and orientating solution for both vehicle navigation and mobile data collection and many researches have been carried out on improving and evaluating its position and orientation accuracy. However, the center of POS is invisible for direct measurement, so quality analysis of mobile mapping system (e.g., point clouds and image data) [2–4], as well as performance evaluation of component system (e.g., IMU, GNSS, or DMI) becomes most researchers' choice for evaluating the dynamic accuracy of POS [5–7]. But these methods have both advantages and disadvantages at the same time.

Quality analysis can be affected by measurement error, mounting parameters error and sensors' time synchronization error. Besides, this method requires special environment with lots of control points, feature points and feature lines, and the complex data processing procedure making this method less efficient.

The dynamic accuracy evaluation of GNSS receiver, which is a component system of POS, has been chosen for evaluating the positioning performance of POS. Standard track (e.g., railway [8]), together with sensors (e.g., high-speed cameras, photoelectric sensors, and total station [9–11]). This method depends greatly on testing ground has a special request on motion state and cannot reflect the real working state of POS.

In this paper, cooperative target has been used for tracking the motion state of POS, whose relative position to POS was determined before. In order to evaluate the dynamic performance of POS, synthetic measurement scheme has been proposed to make full of total station and laser tracker system. POS LV220 has been used in this paper, whose post-processing accuracy could be found in Table 1.

Outdoor experiment has been carried out. Overall trajectory comparison and real-time comparison were used for testing the dynamic position accuracy of POS.

Table 1 POS LV 220 specification

POS LV 220	Post-processing	IARTK	DGPS
X, Y position (m)	0.020	0.035	0.300
Z position (m)	0.050	0.050	0.500
Roll and pitch (°)	0.020	0.020	0.020
Heading (°)	0.025	0.050	0.050

2 Design of Accuracy Evaluation Scheme

With the integrated use of total station, laser tracker, and GNSS timed device, this paper designed a compound dynamic accuracy testing system to meet the requirement of testing POS's post-processing data, which is 2 cm in horizontal direction and 4 cm in vertical direction (Table 1). This design will compensate deficiencies in each of devices and highlight advantages (laser tracker's surveying accuracy is submillimeter, but it only works within a limited range of 160 m. Besides, without a steady base which has precise coordinates, laser tracker cannot be used for geography referential directly; total station can be used for geography reference with the help of centring device and its tracking range can be expended to 2000 m, while it will also accumulate errors to centimeter.). The synthetic measurement system works more efficiently and effectively than a single component system: total station helps the laser tracker to realize geography reference, while laser provides precise surveying information as reference data for correcting total station's measurement data. Both surveying range and surveying accuracy has been improved by this hybrid scheme.

At present, there are two main methods of evaluating dynamic accuracy: a. evaluate the variable's instantaneous value and its change along with time; b. evaluate the whole change generated from the comparative procedure [12]. After gross error elimination and trajectory correction, overall trajectory comparison and real-time point comparison has been applied to evaluating the dynamic positioning accuracy of POS in this paper.

2.1 Overall Trajectory Comparison

Curve function $f(x)$ is used to fit the reference trajectory Q. After the comparison between $f(x)$ and P_i, the whole track comparison is finished (Fig. 1). But there exists some problems if this method is used directly. Errors would generate from the fitting procedure. Besides, the closest points chosen from $f(x)$ are not the real corresponding points to Q, causing inevitable error on the motion direction. Therefore, piecewise fitting, as well as cross-tracks comparison should be used to evaluate the position accuracy of POS.

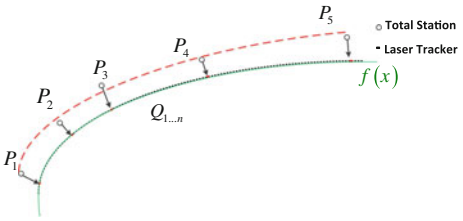

Fig. 1 The comparison of tracking trajectory between total station and laser tracker system

2.2 Real-Time Point Comparison

Both total station and POS achieve same time reference after time synchronization device. However, these systems have different output rate with about 17 and 200 Hz respectively, so the surveying information should be modified before real-time point comparison. In this paper, we use interpolation method to make sure both POS data and total station data have the same time tag.

Experiments have been carried on comparatively low-speed motion state, and both linear interpolation and parabolic interpolation are applied for fitting the motion state of vehicle.

(1) linear interpolation
On the condition of low-velocity motion state, this paper assumes that vehicle does linear motion during each time interval when the vehicle travels along linear street. The linear function can be expressed as: During each time interval, the linear function $f(x)$ can be used to fit the motion state. Two points are chosen, at the beginning and the end of time interval and their two-dimensional coordinates can be expressed as $(x_1,f(x_1))$, $(x_2,f(x_2))$. We use a first-order function $g(x) = ax + b$ to realize the linear fitting procedure. It can be expressed as formula

$$\mathrm{g}(x) = \frac{x - x_2}{x_1 - x_2} \cdot f(x_1) + \frac{x - x_1}{x_2 - x_1} \cdot f(x_2) \tag{1}$$

(2) parabolic interpolation
When the vehicle comes across a big corner, this paper assumes that the vehicle does parabolic motion during each time interval. The parabolic function can be expressed as: During each time interval, the parabolic function $\varphi(x)$ can be used to fit the motion state. Three points are chosen at the beginning, the middle, and the end of time interval. Their two-dimensional coordinates can be expressed as $(x_1, \varphi(x_1))$, $(x_2, \varphi(x_2))(x_2, \varphi(x_3))$. We use a second-order function to realize the linear fitting procedure. It can be expressed as formula 2.

$$h(x) = \varphi(x) = a_2x^2 + a_1x + a_0 \tag{2}$$

3 Error Analysis and Correction

The error source in this synthetic measurement scheme can be divided into two categories: (a) dynamic measurement error (e.g., laser ranging and angular measurement error from total station and laser tracker system, timing error from GNSS);

Table 2 Modules of the dynamic measurement system

Component system	Name	Accuracy
GNSS	OEMV-1(Receiver)	±20 ns
	Trimble ZephyrII(a)	
Total station	Leica	±0.5″ ±(5 mm + 2 ppm)
	TDA 5005 (tracking mode)	
Laser tracker system	Leica	±(15 μm + 6 μm/m)
	AT 901-B	

(b) data processing error, such as coordinate's unification error, time synchronization error and curve fitting error.

The laser tracker system has a dynamic position accuracy of a few submillimeters (Table 2). So, laser tracker system's measurement data is used as reference data in this paper. Coordinates unification error and timing error has little influence on proposed synthetic measurement scheme, with only about 0.36 mm detected in outdoor experiment.

So, in this paper, we mainly analyze and eliminate the dynamic measurement error of total station, which has an angular accuracy of 0.5 arcsecond and a distance measurement accuracy of a few millimeters (Table 2). What's more, a trajectory correction method is proposed, based on ICP algorithm, to decrease the influence of measurement error.

3.1 Elimination of Gross Error Based on the Time of Single Measurement

On the process of tracking measurement, the internal and external light path conversion is not stable, which would cause the periodic gross error of measurement results of total station. Based on the consumed time of total station's single measurement, this paper filters unstable measurement points and excludes part of gross error from the measurement.

The statistics of single surveying data shows that, in the experiment, the average surveying time of the total station is about 0.17 s and some singular points can be found periodically, as shown in Fig. 2.

What can be seen in Fig. 2 is that, in the measurement, the points whose measuring time increase a lot will appear in the interval of about 20 s, which cause larger error in dynamic measurement. Therefore, in data processing, this kind of points should be removed based on the limitation of time, which is consumed by the measurement.

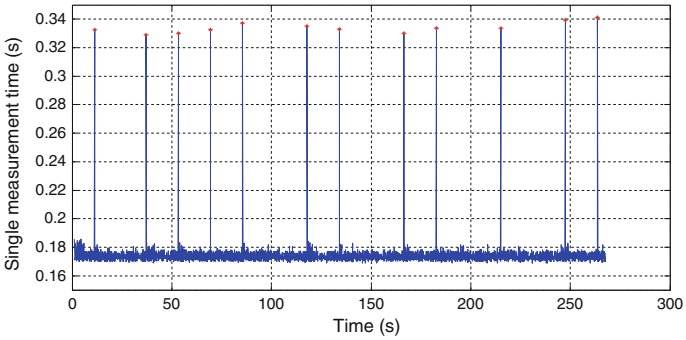

Fig. 2 Statistics on the measurement time of total station

3.2 Elimination of Gross Error Based on Smooth Trajectory

While the vehicle is in motion state, there exists no obvious line vibration or angular vibration, making the trajectory relatively smooth. Therefore, we can filter the measurement data based on the condition of smooth trajectory to remove part of surveying error in the measurement system.

In the experiment, the output rate of laser tracker is 3000 Hz and the output rate of POS system is 200 Hz. Total station's output rate is about 17 Hz, and contains relatively more noise points. Using the method of trajectory contrast, the error of total station measurement based on the measurement data measured by the laser tracker has been shown in Figs. 3 and 4. As is shown in statistical chart, there still exists some error in the data measured by total station.

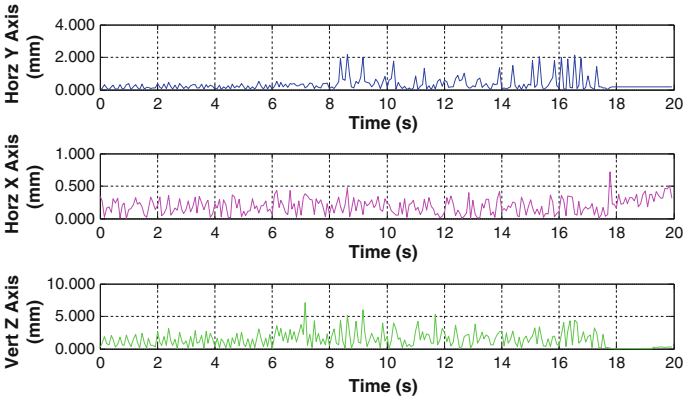

Fig. 3 The error statistics on lateral motion trajectory

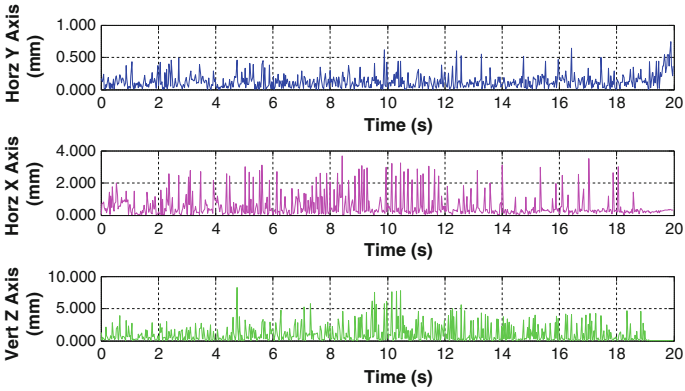

Fig. 4 The error statistics on longitudinal motion trajectory

So, after eliminating the unstable measurement points, we use curve fitting method for the detection of more gross error. Take Z axis for example, specific formula is as follows:

$$z = a_0 + a_1 x + a_2 x^2 + a_3 x^3 \tag{3}$$

Specifically, five-point parabolic fitting method has been used and the formula is expressed as formula 4.

$$\begin{aligned}
\bar{z}_{i-2} &= \frac{1}{70}(69z_{i-2} + 4z_{i-1} - 6z_i + 4z_{i+1} - z_{i+2}) \\
\bar{z}_{i-1} &= \frac{1}{35}(2z_{i-2} + 27z_{i-1} + 12z_i - 8z_{i+1} + 2z_{i+2}) \\
\bar{z}_i &= \frac{1}{35}(-3z_{i-2} + 12z_{i-1} + 17z_i + 12z_{i+1} - 3z_{i+2}) \\
\bar{z}_{i+1} &= \frac{1}{35}(2z_{i-2} - 8z_{i-1} + 12z_i + 27z_{i+1} + 2z_{i+2}) \\
\bar{z}_{i+2} &= \frac{1}{70}(-z_{i-2} + 4z_{i-1} - 6z_i + 4z_{i+1} + 69z_{i+2})
\end{aligned} \tag{4}$$

Fitted value $\bar{z}_i$ equals the coordinate estimate of observed value z_i, set up the threshold δ_1. If the interpolation of fitting values and measured values $d_i = |\bar{z}_i - z_i|$ is bigger than δ_1, there exist gross errors in the measuring results, which should be removed. We set the threshold as 5 mm in this paper.

This method is used to eliminate the gross error and purify the surveying data. Taking vertical experimental observation data as example, the effect of gross error detection is shown in Fig. 5.

Those points with comparative bigger gross error, which should be removed, have been found by curve fitting method and they are marked red in Fig. 5.

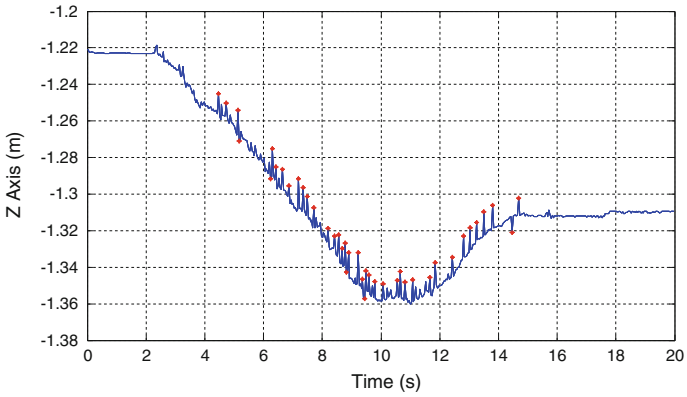

Fig. 5 The error detection on Z axis

3.3 Overall Trajectory Correction Based on ICP Algorithm

After the elimination of gross error, the method of trajectory correction is used for improving total station's dynamic measurement performance. In this method, high-rate and high-accuracy data from laser tracker system is treated as reference data. Improved ICP algorithm [13] has been used to correct total station's final tracking trajectory, ameliorate the performance of synthetic measurement system.

The trajectory of laser tracker system, POS and total station can be found in Figs. 6 and 7.

The proposed trajectory correction algorithm is expressed as followed:

(1) Choose total station's trajectory as uncorrected point cloud P. Laser tracker system is set with 1000 Hz output rate, whose data is used as reference point cloud Q. For each point in P, find the closest point in Q.

$$ds = |p_i - q_i|_{\min} \tag{5}$$

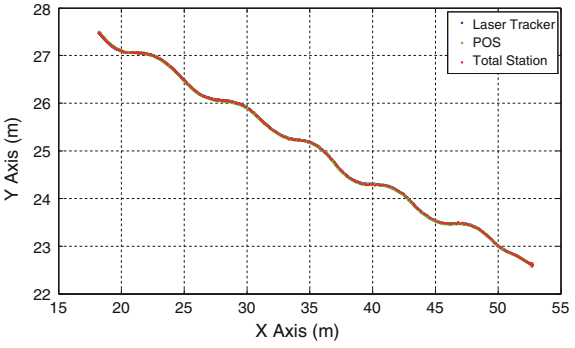

Fig. 6 The comparison of tracking trajectory from different sensors

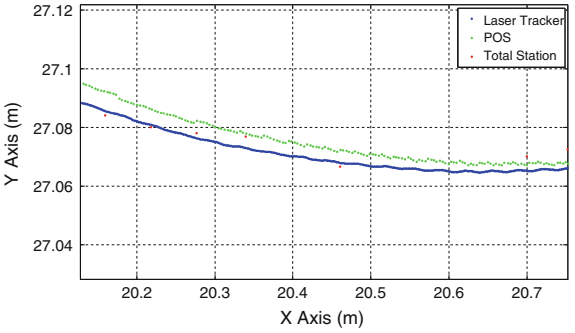

Fig. 7 The comparison of the specific tracking trajectory from different sensors

(2) According to the first four pairs of closest points, the rotation matrix $\boldsymbol{R}_1$ and translation matrix $\boldsymbol{T}_1$ can be calculated with a Coordinates conversion model.

$$P = \boldsymbol{R}_1 Q_0 + \boldsymbol{T}_1 \tag{6}$$

(3) Convert Q with matrix $\boldsymbol{R}_1$ and matrix $\boldsymbol{T}_1$.

$$Q_1 = \boldsymbol{R}_1 Q_0 + \boldsymbol{T}_1 \tag{7}$$

(4) Use the next pair of closest points for calculating new rotation and translation parameters and modify the uncorrected points. New parameters R_n and T_n are used to modify the exit points Q_n.

$$P = \boldsymbol{R}_{n+1} Q_n + \boldsymbol{T}_{n+1} \tag{8}$$

$$Q_{n+1} = \boldsymbol{R}_{n+1} Q_n + \boldsymbol{T}_{n+1} \tag{9}$$

(5) Set a threshold $\delta > 0$, and iterate the procedure, re-associate the uncorrected points and the reference points. Until the change of distance between the closest points is smaller than the threshold $d_n - d_{n+1} < \delta$, stop the iteration.

4 Performance Evaluation and Analysis

As shown in Fig. 8, the experiment area was in Zhengzhou. The red line shows the road with good condition which can be access by car driving, and the total length is 1.5 km. The yellow sign is the control point of GNSS with stable base and the precise coordinates, whose positioning precision is only a few millimeters. The main sections of our experiment was in the green box, it's including 120 m east–west direction straight road and 200 m south–north direction straight road, Point A and Point B are treated as known points for experiment test system.

Fig. 8 The outdoor experiment field

Experimental data processing is shown below:

(1) Gross error elimination
After using statistic method, based on measurement time and the curve fitting method to detect and eliminate gross error from the total station measurement, the comparison of total station and POS output data has been shown in Table 3.
The statistical data shows: through the gross error elimination, we use the overall trajectory for contrast, it detects that the POS systems positioning accuracy in the horizontal direction is 14.4 mm, and vertical positioning accuracy is 26.9 mm.

(2) Overall trajectory correction
Improved ICP algorithm is used for trajectory correction, and the threshold is set as 5 mm. After trajectory correction, the comparison of total station and POS output data has been shown in Table 4.
The statistical data shows that: if we use trajectory correction method and then by calculation, the horizontal error is: 20.7 mm, the vertical error is: 42.9 mm.

Table 3 Comparison between total station and POS (mm)

	Motion state	Longitude	Latitude	Vertical
Experiment 1	East–West	17.1	1.7	26.8
	North–South	1.3	10.7	27.2
Experiment 2	East–West	16.8	1.6	30.3
	North–South	1.4	15.2	30.8
Experiment 3	East–West	11.8	2.3	20.8
	North–South	2.0	14.3	25.7

Table 4 Position accuracy after the trajectory correction (mm)

	Motion state	Longitude	Latitude	Vertical
Experiment 1	East–West	20.9	2.4	43.6
	North–South	2.3	16.9	41.3
Experiment 2	East–West	21.1	2.5	43.8
	North–South	2.4	21.2	40.6
Experiment 3	East–West	20.6	3.4	43.3
	North–South	3.8	22.3	44.7

Table 5 Accuracy of real-time position (mm)

	Motion state	Longitude	Latitude	Vertical
Experiment 1	East–West	19.3	17.6	21.2
	North–South	23.1	14.3	25.1
Experiment 2	East–West	16.5	16.1	33.2
	North–South	18.9	16.7	29.6
Experiment 3	East–West	12.8	12.6	31.2
	North–South	32.8	14.7	26.0

(3) Real-time point comparison
By using the interpolation algorithm mentioned above, the comparison result after interpolation precision has been shown in Table 5.

By the statistics of the data above, it can be found that with the method of time synchronization, the horizontal error is 25.9 mm, and that of the vertical direction is 31.8 mm. Compared with the that in Table 4, according to the coordinate calculate way, time delay can be obtained with an average of 0.0147 s. This kind of inevitable error results from the procedure of total station's unstable data transmission. If we want to use real-time point comparison method for dynamic evaluation, we should adjust the car to relatively low speed to weaken the effect of unstable data transmission.

The experimental results show that: with the method of trajectory contrast. Using dynamic testing system to evaluate POS, the horizontal positioning accuracy is 20.7 mm and the vertical positioning accuracy is 42.9 mm; by comparison with real-time point, the horizontal positioning accuracy is 25.9 mm, the vertical positioning accuracy is 27.7 mm.

5 Conclusion

(1) In this paper methods such as counting the time of single measurement and curve fitting have been used for eliminating gross error from the raw observation data.

(2) The results of outdoor experiments have proved the feasibility and efficiency of the hybrid measurement scheme proposed in this paper. This synthetic measurement depends little on experiment environment, providing users a reliable and robust choice for evaluating the dynamic performance of POS.
(3) The evaluating methods proposed in this paper have some deficiencies. Restricted to laser ranging technology, automatic target recognition technology, and tracking technology, this method could not be applied to testing the POS when it is in high dynamic motion state. Besides, the time synchronization accuracy between different sensors (e.g., total station, laser tracker system and GNSS antenna) should be enhanced to fulfill the needs of high dynamic motion tests.

Acknowledgments This work was supported by the Foundation of He' nan Scientific Committee (152102210007) and the National Science Foundation of China (41501491).

References

1. Cramer M, Stallmann D, Haala N (2000) Direct geo-referencing using GPS/inertial exterior orientations for photogrammetric applications. J Int Arch Photogrammetry Remote Sens 33 (B3):198–205
2. Habib A, Kersting AP, Bang K (2010) Comparative analysis of different approaches for the incorporation of position and orientation information in integrated sensor orientation procedures In: C//Proceedings of Canadian geomatics conference 2010 and ISPRS Commission I Symposium
3. Pinto L, Forlani G (2002) A single step calibration procedure for IMU/GPS in aerial photogrammetry. J Int Arch Photogrammetry Remote Sens 34(B3):210–213
4. Xiuxiao Y (2008) A new method applied for compensating the orientation error of POS. J Progr Nat Sci 2008(08):925–934
5. Zhi Q (2011) Research and experimental analysis on calibration of the airborne POS. Shandong University of Science and Technology, Shandong
6. Chan TO (2011) Feature-based boresight self-calibration of a mobile mapping system[EB/OL] http://www.ucalgary. ca/engo bdocs/MJC/11.20348_TingOnChan.pdf. Cited 15 Mar 2014
7. Jianhong F, Xiuxiao Y (2007) Influence of GPS base station on accuracy of positioning by airborne position and orientation system J. Geomatics Inf Sci Wuhan Univ 05:398–401
8. Talor RK (2003) Dynamic testing of GPS receivers C ASAE Annual meeting, Kansas
9. Fanyu M (2002) The foundation of comprehensive inspection places with GPS receiver and the realization of dynamic evaluation. D Zhengzhou, Information Engineering University
10. Junzheng L (2004) The method of precision evaluation in dynamic GNSS and error analysis. D Zhengzhou, Information Engineering University
11. Feng H (2007) A study of precise inspection technology for dynamic surveying precision. D Zhengzhou, Information Engineering University
12. Zhenyin X (2004) Research on theory and method of error tracing and accuracy-loss diagnosis of dynamic measurement system. D HeFei, HeFei University of Technology
13. Besl PJ, McKay ND (1992) A method for registration of 3-D shapes. IEEE Trans Pattern Anal Mach Intell (Los Alamitos, CA, USA: IEEE Computer Society) 14(2):239–256. doi:10.1109/34.121791

The Experimental Study of MIMU/BeiDou Integrated Navigation System for Land Vehicle Applications in Highly Poor Weather Conditions

Dingjie Wang, Hanfeng Lv and Jie Wu

Abstract The introduction of Micro-Electro–Mechanical-System based IMU (MIMU) is a bold and meaningful conception for small unmanned aerial vehicle (UAV) autonomous approaching and landing. The adoption of a low-cost MIMU with high noise, which is suitable for UAV applications with advantages in cost-effectiveness, lightweight, miniature design, low power consumption, and survivability. However, complicated flight dynamics and MIMU noise pose a great challenge for precise navigation of UAV autonomous landing. In this paper, a precise GNSS/MIMU integrated navigation scheme is derived to achieve autonomous landing, based on STIM-300 MIMU and BeiDou/GPS multi-frequency multi-mode precise relative positioning. The precise MIMU error model is established based on Allan variance analysis to resist the influence of noise uncertainty of MIMU. A real-time improvement is introduced in the conventional data fusion algorithm considering the delayed observations and time synchronization. Moreover, a novel in-flight coarse alignment of MIMU is adopted to guarantee accurate and reliable fine alignment afterward. The land vehicle test results indicate the proposed algorithm can complete accurate and reliable navigation (CatIIIc precision requirements) even in GNSS outages (≤12 s). As a cost-effective scheme, it has significant application potential for small UAV autonomous approaching and landing in highly poor weather conditions such as heavy fog and snow.

Keywords Low-cost MEMS-based IMU (MIMU) · Real-time kinematic positioning (RTK) · Extended Kalman filtering (EKF) · Real-time

D. Wang (✉) · H. Lv · J. Wu (✉)
National University of Defense Technology, 109 Deya Avenue, Changsha 410073, China
e-mail: wangdingjie11@nudt.edu.cn; wdj9003@163.com

J. Wu
e-mail: wujie_nudt@sina.com

H. Lv
e-mail: hanfeng_lv@nudt.edu.cn

J. Sun et al. (eds.), *China Satellite Navigation Conference (CSNC) 2016 Proceedings: Volume II*, Lecture Notes in Electrical Engineering 389,
DOI 10.1007/978-981-10-0937-2_37

1 Introduction

Small UAVs, which achieve sustained aerodynamic flight without airborne human pilots, have important applications in aviation mapping, disaster monitoring, and public security maintenance [1]. Currently, small UAV's landing mainly depends on ground operators by wireless remote control. However, autonomous landing imposes higher requirements upon UAV's independent navigation capability [2]. This means small UAV should still fulfill planned landing automatically even when the wireless remote control is lost for a long time. So it is of critical significance to equip small UAVs with a precise and reliable navigation system.

The accurate determination of the aircraft position, velocity, and attitude relative to the runway is the key to UAV landing. Navigation-grade INS of high quality cannot be applied to small UAVs due to large size, heavy weight and high cost, while low-cost MIMU cannot meet the independent navigation owing to the high and time-varying noise characteristics [3, 4]. The high cost and technical complexity hinder the widespread utilization of radar system (e.g., tracking radar system, instrument landing system, and microwave landing system). It is risky to directly adopt GNSS as the only navigation system due to low data rate and inability to provide 3 dimensional attitudes with single GNSS antenna configuration [5]. Although GNSS can offer high-precision position and velocity information chronically, it is the real-time and integrity problem that suffers [6]. The visual navigation is heavily influenced by weather conditions with restricted real-time performance. So GNSS/MIMU integration seems to be the most promising solution [7, 8]. However, complicated MIMU noise and flight dynamics pose a great challenge for precise navigation of UAV autonomous landing. On the one hand, it is still challenging to achieve in-flight initial alignment without aiding [9]. The large misalignments caused by conventional static alignment methods lead to large linearization errors, deteriorating or destroying the performance of the filter [10–13]. On the other hand, complicated flight dynamics makes the techniques such as Non-holonomic Constraints (NHC) and Zero Velocity Updates (ZUPTs) invalid in UAV [14, 15]. This will cause a sharp drop in MEMS-based inertial navigation accuracy when external aiding is lost. Moreover, the MIMU noise characteristics are influenced by factors such as external temperature and carrier dynamics. As a result, the filter may fall into local optimum or even diverge if the MIMU error modeling is inaccurate [16]. These practical problems still need to be studied and solved in airborne navigation fields.

Motivated by Joint Precision Approach and Landing System (JPALS), this paper designs a GNSS/MIMU integration scheme for small UAV autonomous landing navigation. In order to maintain high precision during short GNSS interruption, the precise MIMU error modeling is established based on Allan variance analysis [17–19]. A novel in-flight coarse alignment aided by GNSS is proposed to guarantee the fine alignment afterward [9]. The alignment and data fusion Kalman filter are enhanced with the real-time performance with the consideration of delayed observations and time synchronization [20–23]. Based on the model, a BeiDou/MIMU

prototype system is established to conduct a series of land vehicle field tests. The results satisfy the CatIIIc precision requirements raised by International Civil Aviation Organization (ICAO). Therefore, the proposed model is suitable for small autonomous vehicles (e.g., UAV). The proposed method has a cost-effective advantage and significant potential in real-time navigation applications, especially in bad weather conditions such as heavy fog and snow.

The contents are organized as follows. Section 2 presents the MIMU/GNSS integration model. Section 3 proposes a new real-time enhanced information fusion algorithm. Vehicle test and conclusions are given in Sect. 4 and 5. The contribution of this paper is to provide a preliminary scheme to solve the MEMS-based navigation for UAV automatic landing application.

2 System Mathematical Modeling

2.1 System Error Dynamics

MIMU navigation error state differential equations are shown in [14]:

$$\begin{cases} \delta \dot{\boldsymbol{r}}^n = \boldsymbol{D}^{-1} \delta \boldsymbol{v}^n \\ \delta \dot{\boldsymbol{v}}^n = \mathbf{C}_b^n \boldsymbol{f}^b \times \delta \boldsymbol{\theta} - (2\boldsymbol{\omega}_{ie}^n + \boldsymbol{\omega}_{en}^n) \times \delta \boldsymbol{v}^n - (2\delta\boldsymbol{\omega}_{ie}^n + \delta\boldsymbol{\omega}_{en}^n) \times \boldsymbol{v}^n + \delta \boldsymbol{g}^n + \mathbf{C}_b^n \delta \boldsymbol{f}^b \\ \delta \dot{\boldsymbol{\theta}} = -\boldsymbol{\omega}_{in}^n \times \delta \boldsymbol{\theta} + \delta \boldsymbol{\omega}_{in}^n - \mathbf{C}_b^n \cdot \delta \boldsymbol{\omega}_{ib}^b \end{cases} \tag{1}$$

where $\delta \boldsymbol{r}, \delta \boldsymbol{v}, \delta \boldsymbol{\theta}$ represents the position, velocity and attitude error; $\delta \boldsymbol{\omega}_{ib}^b, \delta \boldsymbol{f}^b$ represents gyro and accelerometer sensor errors; $\mathbf{C}_A^B$ depicts the transformation from A frame to B frame; $\boldsymbol{\omega}$ is the angular rate; the matrix $\boldsymbol{D}^{-1}$ represents the transformation from navigation frame (North-East-Down) to geodetic frame (Latitude-Longitude-Altitude) $\boldsymbol{D}^{-1} = \mathrm{diag}\{\frac{1}{R_M + h}, \frac{1}{(R_M + h)\cos\varphi}, -1\}$, R_M and R_N are the radius of curvature in prime vertical and meridian, φ is the latitude, h is the altitude. Considering the UAV three-dimensional flight, the sensor error is mainly modeled as 1st Gauss–Markov process of the bias instability and scale factor:

$$\begin{cases} \dot{\boldsymbol{b}}_g = -\frac{1}{T_{gb}} \boldsymbol{b}_g + \boldsymbol{w}_{gb} \\ \dot{\boldsymbol{b}}_a = -\frac{1}{T_{ga}} \boldsymbol{b}_a + \boldsymbol{w}_{ab} \\ \dot{\boldsymbol{s}}_g = -\frac{1}{T_{gs}} \boldsymbol{s}_g + \boldsymbol{w}_{gs} \\ \dot{\boldsymbol{s}}_a = -\frac{1}{T_{as}} \boldsymbol{s}_a + \boldsymbol{w}_{as} \end{cases} \tag{2}$$

where T is the correlation time of gyro/accelerometer 1st Gauss–Markov process; $\mathbf{w}$ is corresponding driven noise, which is determined by Allan variance analysis.

Thus, the state equation in the discrete form is derived as follows:

$$\boldsymbol{x}_k = \boldsymbol{\Phi}_{k,k-1}\boldsymbol{x}_{k-1} + \boldsymbol{\Gamma}_{k-1}\mathbf{W}_{k-1} \tag{3}$$

where $\boldsymbol{x}$ is error state vector, $\boldsymbol{x} = \left[\delta \boldsymbol{r}_{1\times3}\delta \boldsymbol{v}_{1\times3}\delta\boldsymbol{\theta}_{1\times3}\boldsymbol{b}_{g1\times3}\boldsymbol{b}_{a1\times3}\boldsymbol{s}_{g1\times3}\boldsymbol{s}_{a1\times3}\right]^T$; $\boldsymbol{\Phi}_{k,k-1}$ is the discretized state transition matrix; $\boldsymbol{\Phi}_{k,k-1} = \exp(\mathbf{F}(t_k)\Delta t_k) \approx \boldsymbol{I} + \mathbf{F}(t_k)\Delta t_k$; $\boldsymbol{\Gamma}_{k-1}$ is the driven matrix of system noise; $\mathbf{W}_{k-1}$ is the system state noise vector, whose covariance matrix is $E[\mathbf{w}_i\mathbf{w}_k^T] = \mathbf{Q}_k\delta_{ik}$ and $\mathbf{Q}_k$ can be determined by Allan variance analysis; $\mathbf{G}(t)$ is the driven matrix of system noise, i.e., [24]

$$\mathbf{Q}_k \approx \frac{1}{2}[\boldsymbol{\Phi}_{k,k-1}\mathbf{G}(t_{k-1})\mathbf{Q}(t_{k-1})\mathbf{G}^T(t_{k-1})\boldsymbol{\Phi}_{k,k-1}^T + \mathbf{G}(t_k)\mathbf{Q}(t_k)\mathbf{G}^T(t_k)]\Delta t_k \tag{4}$$

2.2 System Measurement Equation

Assume the phase center of GNSS antenna in the n-frame is denoted as $\boldsymbol{r}_{\text{GNSS}}^n$, and MIMU center in the n-frame is denoted as $\boldsymbol{r}_{\text{IMU}}^n$, the vector ℓ_{GNSS}^b from IMU center to GNSS center satisfies the following equation (as shown in Fig. 1):

$$\boldsymbol{r}_{\text{GNSS}}^n = \boldsymbol{r}_{\text{IMU}}^n + \boldsymbol{D}^{-1}\mathbf{C}_b^n\ell_{\text{GNSS}}^b \tag{5}$$

The system measurement equation is obtained as follows:

$$Z_{\boldsymbol{r}} = \delta\,\mathbf{r}_{\text{IMU}}^n + \left(\boldsymbol{C}_b^n\ell_{\text{GPS}}^b\times\right)\delta\boldsymbol{\theta} - \boldsymbol{e}_r \tag{6}$$

where $\boldsymbol{e}_r$ represents the position error and its covariance matrix is $E[\boldsymbol{e}_k\boldsymbol{e}_i^T] = \boldsymbol{R}_k\delta_{ik}$.

Here GNSS adopts the real-time kinematic positioning (RTK) mode with dual-system (BeiDou/GPS) five-frequency (B1/B2/B3/L1/L2) observations, which can reach the magnitude of centimeter in kinematic positioning accuracy.

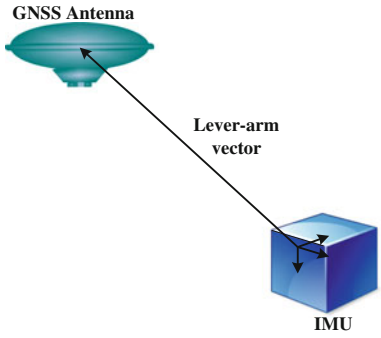

Fig. 1 The lever arm from IMU to GNSS

3 Real-Time Enhanced Data Fusion Algorithm Design

Based on (3)–(4) and (6), the EKF is used to realize the data fusion. The structure is shown in Fig. 2. The conventional KF is composed of time update (7) and measurement update (8).

$$\begin{aligned} \hat{\boldsymbol{x}}_{k,k-1} &= \boldsymbol{\Phi}_{k,k-1}\hat{\boldsymbol{x}}_{k-1} \\ \boldsymbol{Q}_{k-1} &= \frac{1}{2}\left[\boldsymbol{\Phi}_{k,k-1}\bar{\boldsymbol{Q}} + \bar{\boldsymbol{Q}}\boldsymbol{\Phi}_{k,k-1}^{T}\right]\Delta t_k, \bar{\boldsymbol{Q}} = \boldsymbol{G}\boldsymbol{Q}\boldsymbol{G}^{T} \\ \boldsymbol{P}_{k,k-1} &= \boldsymbol{\Phi}_{k,k-1}\boldsymbol{P}_{k-1}\boldsymbol{\Phi}_{k,k-1}^{T} + \boldsymbol{Q}_{k-1} \end{aligned} \tag{7}$$

$$\begin{aligned} \boldsymbol{K}_k &= \boldsymbol{P}_{k,k-1}\boldsymbol{H}_k^{T}\left(\boldsymbol{H}_k\boldsymbol{P}_{k,k-1}\boldsymbol{H}_k^{T} + \boldsymbol{R}_k\right)^{-1} \\ \hat{\boldsymbol{x}}_k &= \hat{\boldsymbol{x}}_{k,k-1} + \boldsymbol{K}_k(\boldsymbol{Z}_k - \boldsymbol{H}_k\hat{\boldsymbol{x}}_{k,k-1}) \\ \boldsymbol{P}_k &= (\boldsymbol{I} - \boldsymbol{K}_k\boldsymbol{H}_k)\boldsymbol{P}_{k,k-1}(\boldsymbol{I} - \boldsymbol{K}_k\boldsymbol{H}_k)^{T} + \boldsymbol{K}_k\boldsymbol{R}_k\boldsymbol{K}_k^{T} \end{aligned} \tag{8}$$

However, some improvements of real-time and accuracy should be put on the conventional EKF implementation, due to the problems such as delayed observation, time-asynchronization and initial alignment for MIMU [23].

3.1 Time Synchronization

The measurement of GNSS and MIMU happens at different time due to their different time/frequency references, as shown in Fig. 3. Synchronization can be

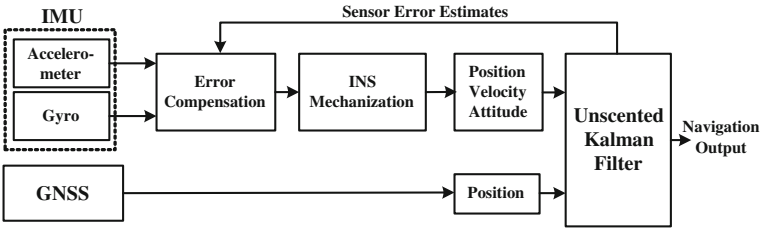

Fig. 2 The algorithm structure for GNSS/MIMU integration

Fig. 3 Measurement time of GNSS and MIMU

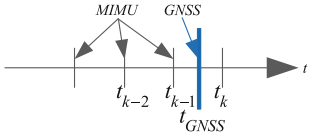

accomplished by interpolation of MIMU position and velocity at the GNSS measurement time. High dynamics applications needs higher order interpolation [15].

$$\begin{aligned}\mathbf{r}^n(t_{\mathrm{GNSS}}) &= \frac{t_k - t_{\mathrm{GNSS}}}{t_k - t_{k-1}}\mathbf{r}^n(t_{k-1}) + \frac{t_{\mathrm{GNSS}} - t_{k-1}}{t_k - t_{k-1}}\mathbf{r}^n(t_k) \\ \boldsymbol{v}^n(t_{\mathrm{GNSS}}) &= \frac{t_k - t_{\mathrm{GNSS}}}{t_k - t_{k-1}}\boldsymbol{v}^n(t_{k-1}) + \frac{t_{\mathrm{GNSS}} - t_{k-1}}{t_k - t_{k-1}}\boldsymbol{v}^n(t_k)\end{aligned} \tag{9}$$

3.2 Kalman Filtering with Delayed Observations

The distributed architecture of RTK requests the base station to broadcast its position and observation to the neighboring rovers through data link. However, this inevitably leads to delayed observation [20–22], as shown in Fig. 4.

To eliminate the adverse influence of delayed measurements on accuracy, we proposed an improved EKF-based real-time data fusion algorithm based on the retrodiction technique [23]. The structure is shown in Fig. 5. The basic idea is presented briefly here: when RTK information at the time t_0 arrives, the MIMU navigation data (including state, error state and error covariance matrix) at the corresponding time t_0 are found from the historical data by retrodiction. The measurement update could be realized with the synchronous historical data at time t_0. Then the navigation information at current time ($t_0 + \Delta t$) can be predicted with the updated data at time t_0. The algorithm implementation can be found in [23].

3.3 MIMU In-Flight Coarse Alignment

KF-based fine alignment heavily relies on coarse alignment to obtain a sound initial attitude; otherwise the subsequent fine alignment cannot achieve a satisfying result. The adoption of low-cost MIMU makes in-flight alignment a challenge. To meet small misalignment condition for fine alignment, a novel in-flight coarse alignment aided by GNSS is derived to obtain the initial attitude based on quaternion. Velocity and its differential information from GNSS and specific forces from MIMU are compared to obtain an analytical solution for the initial angles. This method is demonstrated by flight experiments with sound accuracy and rapid response capability. The algorithm implementation can be found in [9].

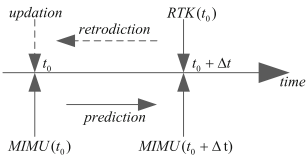

Fig. 4 Delayed measurements due to communication delay

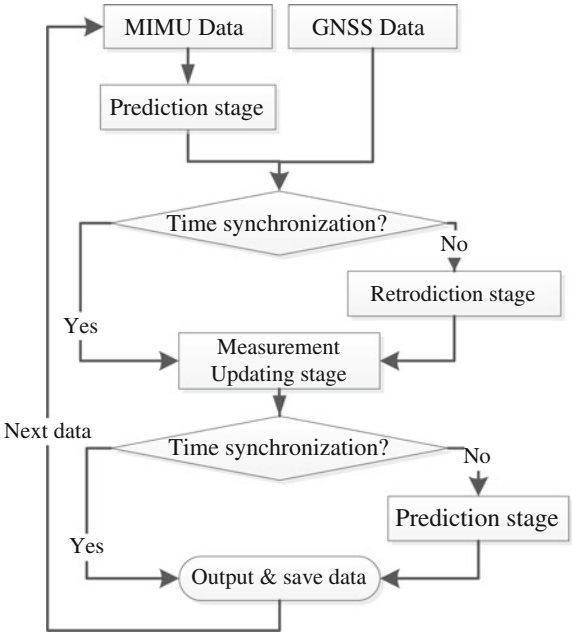

Fig. 5 Algorithm flowchart of real-time information fusion with GNSS delayed measurement

4 Field Test

Land vehicle tests such as accuracy evaluation test and "blind pilot" experiment) are conducted to verify the proposed model. In field test, a STIM-300 collects inertial data and its noise characteristics are listed in Table 1. RTK is adopted as position observation. Two prototype receivers based on OEMV-5 (NovAtel), with GNSS antennas (HX-BS581A Harxon) and Data Transfer Radio (DTR), act as the base and rover. The vehicle equipped with the prototype system runs in relatively high dynamics as the rover. GNSS rate is 1 Hz, while MIMU is 125 Hz.

Accuracy evaluation test adopts POS830 (Wuhan MAP Space Time Navigation Technology co., LTD, performance characteristics are listed in Table 2) as the reference system to evaluate the proposed model. In addition, a "blind pilot" experiment which simulates UAV landing process is designed. The test is carried out in Xiangjiang North Road, Changsha. "0"-like movements are chosen as the main maneuvers to enhance the observability and accelerate the alignment.

Table 1 STIM300 IMU noise parameters

	Gyro	Accelerometer
Bias instability	0.5°/h	0.05 mg
Random walk	0.15°/$\sqrt{\text{h}}$	0.07 m/s/$\sqrt{\text{h}}$
Scale factor (ppm)	±500	±300

Table 2 POS830 accuracy

Positioning	≤0.05 m(1σ)
Yaw	0.005°(1σ)
Leveling	0.002°(1σ)
Bias (Gyro)	0.01°/h(1σ)
Bias instability (Gyro)	0.005°/h(1σ)

The measurement data during the test are recorded for aftermath analysis. The "blind pilot" experiment is mainly used to verify the algorithm in real-time application.

In the following part, the first step is to determine the stochastic modeling parameters of STIM300 via Allan variance analysis. Then the precision evaluation is analyzed based on test data. The feasibility of the GNSS/MIMU integration are demonstrated by "blind pilot" experiment.

4.1 Allan Variance Analysis

The stochastic modeling parameters of STIM-300 are determined based on Allan variance analysis of 12-h MIMU static measurement data. The bias instability and white noise coefficients can be determined according to Figs. 6 and 7, which are listed in Table 3. It can be seen from Tables 1 and 3 that, the axial white noise and bias instability determined by Allan variance analysis are basically consistent with the product datasheet.

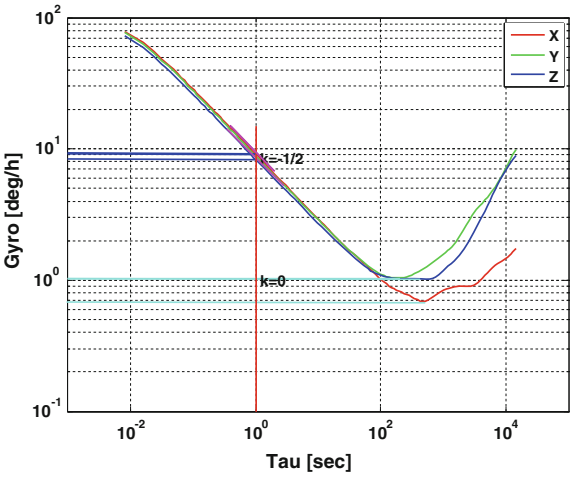

Fig. 6 Gyro Allan variance

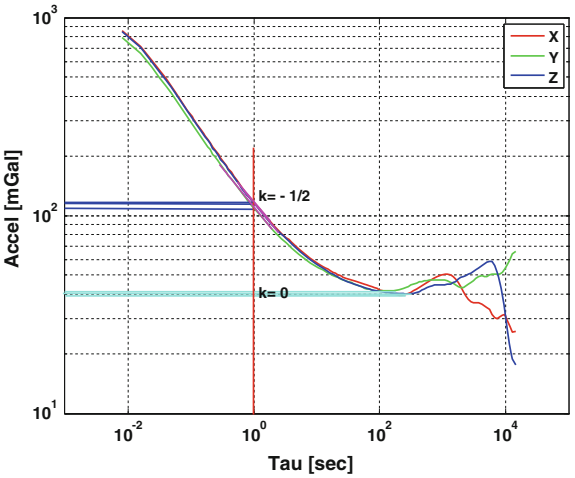

Fig. 7 Accelerometer Allan variance

Table 3 Gyro and accelerometer noise coefficients

	GX	GY	GZ	AX	AY	AZ
White noise(deg/√h or m/s/√h)	0.162	0.157	0.151	0.0985	0.0765	0.0930
Instability(°/h or mg)	0.68	1.04	1.01	0.0414	0.0432	0.0418

4.2 Accuracy Evaluation Test

The accuracy evaluation test was conducted on March 11, 2015 without GNSS outages, in which POS830 and prototype system are both equipped in the vehicle. Taking the RTS smoothing results of GNSS/POS830 IMU as the reference, the results of GNSS/STIM300 are evaluated. The accuracy of GNSS/MIMU model with continuous GNSS aiding relative to the POS830 reference is shown in Table 4 and Fig. 7. Table 4 shows that with continuous GNSS aiding, the accuracy could reach 0.02 m (1σ), 0.01 m/s (1σ) and 0.1° (1σ). The accuracy requirements of CATIIIc precision approach and landing can be met.

Table 4 The statistics of navigation errors with continuous GNSS aiding

Position (m)	Mean	RMS	Velocity (m/s)	Mean	RMS	Attitude (°)	Mean	RMS
North	0.0087	0.0138	North	0.0049	0.0066	Roll	0.0098	0.0134
East	0.0064	0.0097	East	0.0047	0.0064	Pitch	0.0095	0.0131
Down	0.0108	0.0189	Down	0.0078	0.0110	Yaw	0.0791	0.1009

4.3 *"Blind Pilot" Experiment Design*

In order to verify the algorithm effectiveness, this paper designs a "blind pilot" experiment. It means the pilot operates the vehicle according to the navigation visual output during the experiment. The experiment scene is shown in Fig. 8. During the whole test, the front window is covered with curtain and it is impossible for drivers to observe the outside. The driver only relies on the computer visual output to complete the driving.

In the analysis, RTK is intended to interrupt for nine times and each lasts for 12 s. The accuracy evaluation is obtained in this way. The continuous GNSS and STIM300 data are used as reference. The accuracy of GNSS/MIMU integration model with 12 s GNSS outages is obtained. The reference result and the navigation result with 12 s GNSS outages are plotted in Fig. 9. The navigation error is shown in Fig. 10.

Table 5 shows that with 12 s GNSS outages, the integration accuracy could reach 0.43 m (1σ), 0.06 m/s (1σ) and 0.07° (1σ), compared with continuous GNSS aiding. The accuracy requirements of CATIIIc precision landing can still be met with the land vehicle test data.

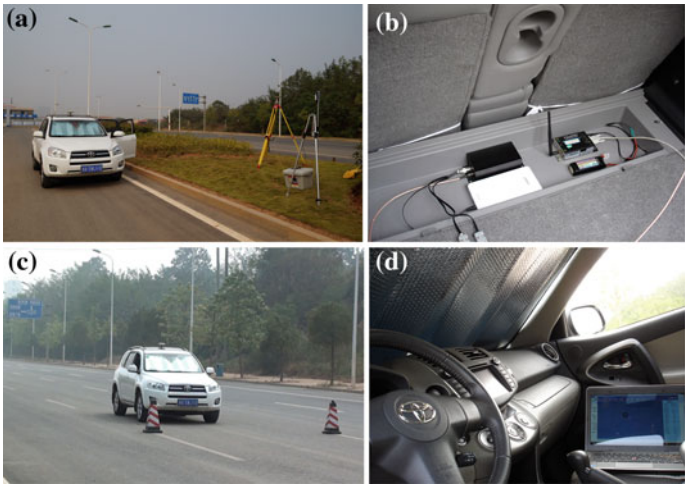

Fig. 8 The equipment and scenario of the automotive autopilot experiment. **a** Equipment. **b** Rover station. **c** Experiment scene. **d** Navigation visualization

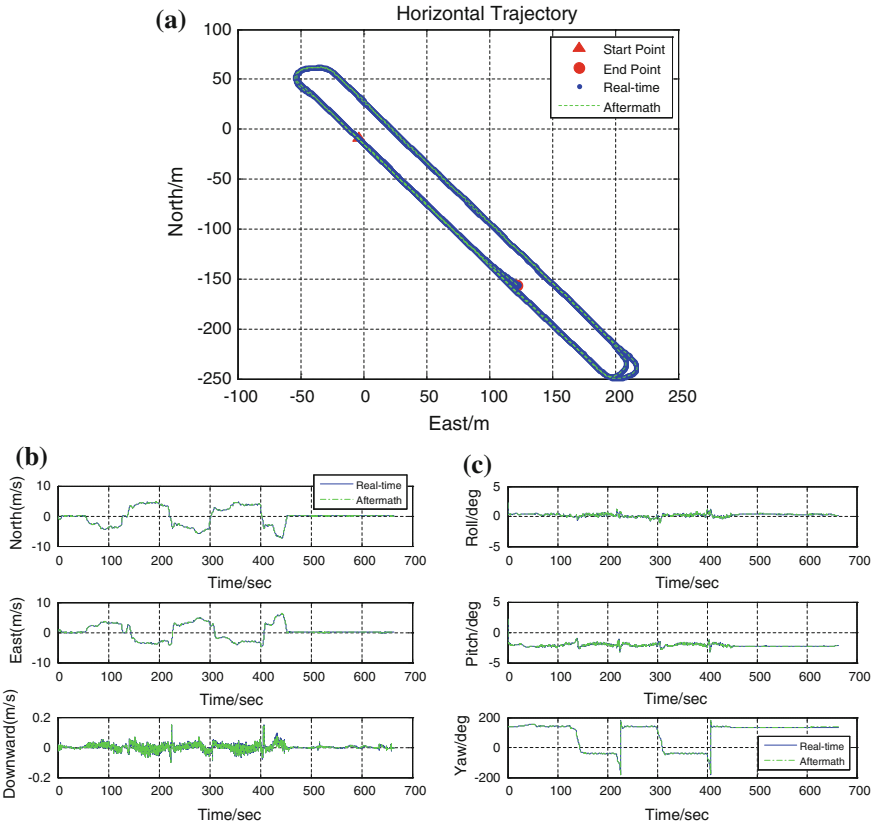

Fig. 9 Comparison of STIM300 IMU with and without 12 s GNSS outages. **a** Comparison of horizontal position. **b** Comparison of velocity. **c** Comparison of attitude

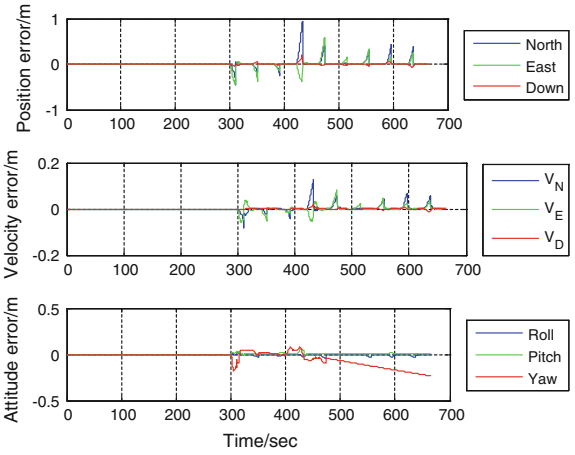

Fig. 10 The navigation error of STIM300 IMU with 12 s GNSS outages

Table 5 The statistics of navigation errors with 12 s GNSS outages

		Mean	RMS
Position (m)	North	0.1723	0.4314
	East	0.0128	0.3646
	Down	0.0060	0.0890
Velocity (m/s)	North	0.0225	0.0649
	East	0.0096	0.0438
	Down	0.0005	0.0010
Attitude (°)	Roll	−0.0277	0.0124
	Pitch	0.0164	0.0152
	Yaw	−0.0956	0.0705

5 Conclusions

A GNSS/MIMU integration scheme is proposed, which can be used for landing navigation of small UAVs. Based on the algorithm, a BeiDou/MIMU prototype system is established to conduct a series of land vehicle field tests. The results show that the proposed model can satisfy the CatIIIc precision requirements raised by ICAO. Therefore, the proposed model is suitable for precise navigation of small UAVs.

The characteristics of MIMU temperature compensation would be studied in the next step. In addition, flight safety is the most critical for these users. So the MIMU-enhanced GNSS integrity is a key problem for the future research.

Acknowledgments The first author is grateful to Prof. NIU Xiaoji and Dr. CHEN Qijin (Wuhan University) for their instructive help in MIMU precise modeling. The authors appreciate Mr. MENG Liangsheng, senior engineer of Flight Dynamics and Control Group (NUDT), for his valuable work in system integration and this makes the results of this paper stand the test of practice.

References

1. Bento MDF (2008) Unmanned aerial vehicles: an overview. InsideGNSS 1:54–61
2. Kurnaz S, Cetin O (2010) Autonomous navigation and landing tasks for fixed wing small unmanned aerial vehicles. Acta Polytech Hung 7(1):87–102
3. Groves PD (2008) Principle of GNSS, inertial, and multisensor integrated navigation system. Artech House, London, pp 407–418
4. Wendel J, Meister O, Schlaile C, Trommer GF (2006) An integrated GPS/MEMS-IMU navigation system for an autonomous helicopter. Aerosp Sci Technol 10(6):527–533
5. Kornfeld RP et al (2001) Applications of global positioning system velocity-based attitude information. J Guid Control Dyn 24(5):998–1008
6. Blomenhofer H (1996–1997) Accuracy, integrity, and availability of GPS-based autopilot-coupled aircraft landings. Navig J Inst Navig 43(4):419–435
7. de La Parra S, Angel J (2005) Low cost navigation system for UAV's. Aerosp Sci Technol 9(6):504–516

8. Kelly RJ, Dalis JM (1994) Required navigation performance for precision approach and landing. Navig J Inst Navig 41(1):1–30
9. Wang D, Chen L, Wu J (2016) Novel in-flight coarse alignment of low-cost strapdown inertial navigation system for unmanned aerial vehicle applications. Trans JSASS 59(1):10–17
10. Kong X (2004) INS algorithm using quaternion model for low cost IMU. Robot Auton Syst 46 (4):221–246
11. Han S, Wang J (2010) A novel initial alignment scheme for low-cost INS aided by GPS for land vehicle applications. J Navig 63(4):663–680
12. Rogers RM (1997) IMU in-motion alignment without benefit of attitude initialization. Navig J Inst Navig 44(3):301–311
13. Shin E, El-Sheimy N (2004) An unscented Kalman filter for in-motion alignment of low-cost IMUs. In: Position location and navigation symposium, pp 273–279
14. Shin E-H (2005) Estimation techniques for low-cost inertial navigation. Doctoral dissertation UCGE reports number 20219. University of Calgary, Canada, pp 45–56
15. Shin E-H (2001) Accuracy improvement of low cost INS/GPS for land applications. Master degree thesis, UCGE reports number 20156. University of Calgary, Canada, pp 35–46
16. Yang Y, He H, Xu G (2001) Adaptively robust filtering for kinematic geodetic positioning. J Geodesy 75(2–3):109–116
17. Niu X, Chen Q, Zhang Q, Zhang H, Niu J, Chen K, Shi C, Liu J (2014) Using Allan variance to analyze the error characteristics of GNSS positioning. GPS Solutions 18(2):231–242
18. Chen Q, Niu X, Zhang Q, Cheng Y (2015) Railway track irregularity measuring by GNSS/INS integration. Navig J Inst Navig 62(1):83–93
19. Zhang Q, Niu X, Chen Q, Zhang H, Shi C (2013) Using Allan variance to evaluate the relative accuracy on different time scales of GNSS/INS systems. Meas Sci Technol 24(8):1659–1666
20. Bar-Shalom Y (2002) Update with out-of–sequence measurements in tracking: exact solution. IEEE Trans Aerosp Electron Syst 38(3):769–778
21. Thomopoulos S, Zhang L (1994) Decentralized filtering with random sampling and delay. Inf Sci 81:117–131
22. Thomopoulos S (1994) Decentralized filtering and control in the presence of delays: discrete-time and continuous-time case. Inf Sci 81:133–153
23. Wang D (2014) Research on the real-time information fusion algorithm for GNSS/MIMU integrated navigation system. In: Proceedings of 2014 IEEE Chinese guidance, navigation and control conference, pp 2028–2033
24. Maybeck PS (1979) Stochastic models, estimation, and control, vol I. Academic Press Inc, New York, p 185

Reliability and Separability Analysis of Multiple-Fault Detection in Visual Navigation Using Reality-Based 3D Maps

Zeyu Li and Jinling Wang

Abstract Vision-based navigation has been widely accepted as a promising approach to obtain position and orientation information in GNSS-denied environments. However, due to the complexity of such environment, a number of factors such as keypoint mismatch may pose faults for the navigation solution, deteriorating navigation performance. Hence fault detection and isolation is essential for the integrity of the navigation solution. Further, multiple faults assumption is more realistic and general than single-fault assumption. However, the system's ability to detect and separate potential faults is one critical aspect. In this paper, reliability and separability in both single-fault and multiple-fault case of visual navigation using reality-based 3D maps is comprehensively analyzed through real data from indoor environment. The analysis demonstrates that geometry has an important impact on reliability and separability in both single-fault and multiple-fault scenarios. The better geometry will enhance reliability and separability of such visual navigation system.

Keywords Visual navigation · Reliability · Separability · MDB · Correlation · MSB · DoP

1 Introduction

Vision-based navigation has been widely applied to obtain position and orientation information for robot, location-based service, augmented reality and autonomous driving. Vision-only navigation can be divided into three categories according to whether the map exists or not: mapless navigation, map-based navigation and simultaneously mapping and navigation [1]. Among them, map-based navigation using a single camera receives much interest from researchers, as the single camera

Z. Li (✉) · J. Wang
School of Civil and Environmental Engineering, UNSW Australia, Sydney 2052, Australia
e-mail: zeyu.li@student.unsw.edu.au; lizeyu.strive@gmail.com

J. Sun et al. (eds.), *China Satellite Navigation Conference (CSNC) 2016 Proceedings: Volume II*, Lecture Notes in Electrical Engineering 389,
DOI 10.1007/978-981-10-0937-2_38

has advantages such as high accuracy, low cost, and noninvasiveness [2]. Moreover, since the map can provide the appropriate spatial information of the surrounding environment, the ambiguity and uncertainty on navigation solution can be reduced.

As a typical map-based navigation methodology using the principle of digital photogrammetry, visual navigation using reality-based 3D map [3] provides a single camera-based approach for obtaining camera's position and orientation. It employs keypoints with known image coordinates and world coordinates, which are defined as pseudo-GCP (PGCP), as the input for navigation solution. With these PGCPs, the calibrated camera's position and orientation can be acquired with regarding to the defined coordinate frame.

Non-faults or single-fault assumption may not be realistic for navigation due to a number of reasons. For example, keypoint mismatch can happen as its performance is related to keypoint algorithm design and environment. These potential faults will degrade the overall integrity of the navigation system. However, one important performance measure is the ability to detect and identify these faults, which can be indicated by reliability and separability. The analysis provides the reference or alert for users whether the navigation system is available for high reliability and separability.

From the perspective of data processing, these faults can be regarded as outliers as they are likely to be different from the bulk of the data in a sense. To exclude these outliers, data snooping under single-outlier assumption originally proposed by Baarda [4] has been widely accepted as a stand module in navigation system [5–7]. It is a local statistic test for each measurement to make decision between null hypothesis and alternative hypothesis with the predetermined level of significance. Another aspect related to outlier detection is internal reliability, which reflects the minimum magnitude of outlier to be detected by outlier statistic tests. According to the predefined Type I and Type II errors, the offset between the null hypothesis and alternative hypothesis (e.g., the noncentrality parameter) can be determined, and then the minimum detectable bias (MDB) can be deduced to evaluate the navigation system's sensitivity for detecting outliers. Traditionally, MDBs are based on non-correlation assumption, which means that each practically outlier statistic is considered to be uncorrelated with others. However, practically outlier statistic can be correlated with each other to varying degrees, which means that this measurement's outlier statistic will affect those of others. In extreme cases, if the correlation between one measurement and another equals to 1, they will have the same outlier statistic if one of them is contaminated by a single outlier, causing type III error [8, 9]. That is, the null hypothesis is correctly rejected but a normal measurement is wrongly judged as an outlier. When the correlation is small enough, MDB can reflect the navigation system's sensitivity to outlier detection precisely. However, if the correlation is large (e.g., larger than 0.8) [8, 9], MDB will no longer be an appropriate indicator to show the navigation system's internal reliability. This introduces minimum separable bias (MSB) [9]. MSB originates from JN test that statistically measures the correlation difference between two outlier statistics. With the predefined Type I and II errors, MSB measures the mean shift between the null hypothesis and alternative hypothesis, which indicates the navigation system's separability.

When multiple outliers exist, the behavior of outlier statistic becomes more complicated. The magnitude of outliers and the number of contaminated measurement will affect generated outlier statistics. Besides, their correlations indicate that one combination's outlier statistic will affects others. But, the behavior of correlated outlier statistic is more complicated. Even two measurements are fully correlated, their outlier statistic is not exactly the same as the relationship can be nonlinear [10].

Reliability and separability are closely related to the geometry strength. In other words, reliability and separability will be improved due to the better geometry, while they will deteriorate if the geometry becomes worse. Vision-based navigation is not an exception. In vision-based navigation, geometry can be defined as the geometric relationship between the surrounding environment and camera. More specifically, it is associated with the number and distribution of PGCPs, as well as the geometric relationship between the camera and PGCPs.

The analysis on the effects of multiple faults has been carried out to further explore reliability and separability in navigation system. Almagbile et al. [11] investigated the influence of correlation on outlier statistic and internal reliability in GPS/INS, and multiple-fault detection can be more effective in measurement model than the state model due to the weak geometry. Wang et al. [10] analyzed the correlation under GNSS only and GNSS/INS scenario, and demonstrated that the integration of INS sensor can reduce the correlation and improve separability.

All the above mentioned reliability and separability analysis are based on GNSS/INS navigation system. Vision-only navigation still lacks a comprehensive analysis to evaluate its reliability and separability. Therefore in this paper, a detailed analysis on the reliability and separability is performed based on the real vision-based indoor navigation data, and the geometry's influence on reliability and separability in the field of vision-only navigation is illustrated in the analysis.

2 Functional Model for Vision-Based Navigation

After the preprocessing including camera calibration, map generation and keypoint matching, keypoints' image coordinates and world coordinates, as well as the camera calibration parameter are known. The next step is to obtain the position and orientation of the camera through collinearity equation shown in Eq. 1. This procedure is also named as space resection in digital photogrammetry.

$$F_x = x - x_0 = -f\frac{a_1(X - X_c) + b_1(Y - Y_c) + c_1(Z - Z_c)}{a_3(X - X_c) + b_3(Y - Y_c) + c_3(Z - Z_c)} \tag{1}$$

$$F_y = y - y_0 = -f\frac{a_2(X - X_c) + b_2(Y - Y_c) + c_2(Z - Z_c)}{a_3(X - X_c) + b_3(Y - Y_c) + c_3(Z - Z_c)} \tag{2}$$

where F_x and F_y are image coordinates on camera's X and Y axis adjusted by the principle point (x_0, y_0), respectively, and X, Y, and Z are the corresponding world coordinates. x_0, y_0 and f are the interior parameters. X_c, Y_c and Z_c are the position of camera. a_i, b_i and c_i $(i = 1, 2, 3)$ are the factors in the rotation matrix generated from rotation angles ω, φ and κ [12].

3 Outlier Statistics for Single-outlier and Multiple-outlier Scenarios

The function model and stochastic model are given, respectively, by:

$$v + l = Ax \tag{3}$$

$$\sum = \sigma_o^2 \mathrm{Q} = \sigma_o^2 \mathrm{P}^{-1} \tag{4}$$

Assuming that there are n observations and t unknowns to be estimated, then for the functional model, A is the $n \times t$ design matrix, x is unknowns to be estimated, v is the $n \times 1$ residuals vector, and l is the $n \times 1$ vector of observations. For the stochastic model, σ_o^2 is the a priori variance factor. Q is the $n \times n$ cofactor matrix, and $\mathbf{P}$ is the $n \times n$ weight matrix.

According to error propagation, dilution of precision (DoP) values are the indicator of estimated accuracy for unknowns and geometric strength, which can be expressed by the square root of the trace operation for the cofactor matrix of unknowns $(A^T PA)^{-1}$:

$$Q_{xx} = (A^T PA)^{-1} \tag{5}$$

$$\mathrm{DoP} = \sqrt{\mathrm{Trace}(Q_{xx})} \tag{6}$$

For the single outlier, the data snooping (w test) method can be employed to detect the corresponding measurement, which is [4]:

$$w_i = \frac{e_i^T Pv}{\sigma_o \sqrt{e_i^T P Q_v P e_i}} \sim N(0, 1) \tag{7}$$

If the number of outliers θ does not exceed $n - t$, the outlier test can be formulated as:

$$v = (A \quad H) \begin{pmatrix} x \\ z \end{pmatrix} - l \tag{8}$$

where z is the vector for the outliers' magnitude, H is a $n \times \theta$ matrix with rank θ. Each column contains zeros, and one in the corresponding position for one outlier, then z can be estimated by using partitioned matrix. With its corresponding variance-covariance matrix through error propagation, the outlier statistic can be constructed as:

$$T^2 = \hat{z}^T \sum_{\hat{z}}^{-1} \hat{z} = \frac{l^T PQ_v PH(H^T PQvPH)^{-1} H^T PQ_v Pl}{\sigma_0^2} \sim \chi^2_{1-\alpha_{w^2},\theta} \tag{9}$$

w and T^2 are the outlier statistics for single outlier and multiple outliers, respectively, If they are larger than the critical value determined by the confidence level, the corresponding measurements are detected as outliers.

4 Reliability for Single-Outlier and Multiple-Outlier Scenarios

When it is assumed that there is one outlier in all the measurements, MDB can be deduced as follow [4]:

$$\mathrm{MDB}_i = \frac{\delta_o \sigma_o}{\sqrt{e_i^T PQ_v Pe_i}} \tag{10}$$

where δ_o equals to $N_{1-\alpha/2}(0,1) - N_\beta(0,1)$, which is the corresponding mean shift in the outlier statistic determined by Type I and Type II errors, α and β, respectively. Under the scenario of multiple outliers, the internal reliability can be given as [13–15]:

$$\nabla_0 S = \nabla S_s \nabla S_u = \sqrt{\frac{\delta_o \sigma_o^2}{\nabla S_u^T H^T PQ_v PH \nabla S_u}} \nabla S_u \tag{11}$$

5 Correlation for Single-Outlier and Multiple-Outlier Scenario

Under the scenario of single outlier, the correlation coefficient between the ith and jth outlier statistic w can be formulated as:

$$\rho_{ij} = \rho_{ji} = \frac{e_i^T PQ_v Pe_j}{\sqrt{e_i^T PQ_v Pe_i}\sqrt{e_j^T PQ_v Pe_j}} \tag{12}$$

With the correlation and JN test, MSB can be derived by [9]:

$$\mathrm{MSB}_{ij} = \frac{\delta_s \sigma \sqrt{2}}{\sqrt{e_i^T P Q_v P (1 - |\rho_{ij}|)}} \tag{13}$$

When multiple outliers exist, there will also be related outlier statistic T^2 linked with two groups of measurements. For example, if the assumed number of outliers are two, which does not exceed $n - t$. T_i^2 is corresponding to the first and second measurement, while T_j^2 is corresponding to the third and fourth one. The correlation between T_i^2 and T_j^2 can be calculated according to approach derived from Li [16]:

$$p_{ij} = H_i^{\theta} P Q_v P H_j^{\theta} \tag{14}$$

$$M_{ij} = (p_{ij})^{-1}(p_{ij})(p_{jj})^{-1}(p_{ji}) \tag{15}$$

$$(Q_{ij})_{\mathrm{Global}} = \frac{tr(M_{ij})}{\sqrt{r_i r_j}} \tag{16}$$

where r_i and r_j are the degrees of freedom for T_i^2 and T_j^2, respectively. Generally the higher correlation means that the outlier statistic (e.g., w_i or T_i^2) will be more affected by the other corresponding one.

6 Experiments

The data were collected from Civil Engineering Building on UNSW campus, which contained 135 query images (epochs) and a number of related reference images. The camera's position and orientation are obtained on an epoch-by-epoch basis. The ground truth of navigation solutions are generated by using GCPs that are set manually. With the world coordinates and image coordinates of these GCPs, the ground truth position and orientation for the corresponding query image can be calculated by space resection.

The majority of the position error lies in 0.05 m, and the largest error in one direction does not exceed 0.1 m. For orientation error, the orientation error on X axis ω has the minimum error range within 0.05°, while φ and K of the cameras are larger than ω, varying from −5° to 5°. However, the majority of orientation error lies between −0.5° and 0.5°. The navigation result is considered to be accurate, which means that the navigation solution is only subjected to random errors.

For MDB, the noncentral parameter is set as 4.13. MSB follows the same configuration. Figure 1 shows the variation of PGCPs' number, DoP, MDB, correlation, and MSB for the 135 epochs. As observed the first subfigure, the number of PGCPs is only one aspect of geometric strength; therefore the higher number of

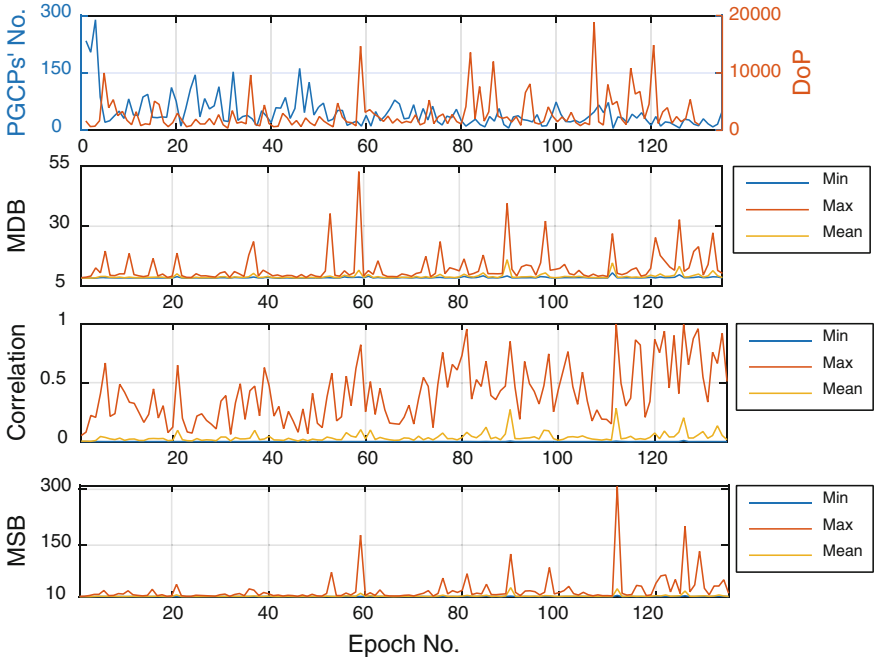

Fig. 1 Variation of PGCPs' number, DoP, MDB, correlation, and MSB for all the epochs in single-fault case

PGCPs does not necessarily lead to stronger geometric strength. However, if the number of PGCPs is lower, there will be more chances for DoP to be higher.

The majority of MDB values wavers around 10 pixels. As the noise level is set as 2 pixels, theoretically it is difficult to detect the bias on the observation if it lies between 2 pixels and 10 pixels. In generally, if the number of PGCPs is less than 15, MDB will have more chances to be larger than others. For example, in epoch 59 and 126, the numbers of PGCPs are 11 and 6, respectively, and they have higher mean MDB values than others. This is because the number of unknowns for navigation solution is constantly equal to 6, and each PGCP will contribute two measurements. Hence, more PGCPs will contribute more to the total redundancy. Due to the higher redundancy number, the overall MDB values become lower.

The correlation between every two outlier statistics and their MDBs affects MSB directly. A higher correlation will produce a higher MSB value. Besides, All the MSBs are numerical higher than MDBs as the separability multiplying factor is always larger than 1 if the predetermined Type I and II errors in MDB and MSB are the same [9]. Therefore, larger MDBs will contribute to larger MSBs. For example, MSB of Epoch 59 is 176.872 pixels, which is significantly higher than most of others, because it has the maximum MDB among all the epochs, and the maximum correlation is equal to 0.822. The maximum correlation of Epoch 112 and 126 are

0.996 and 0.993, respectively, hence their MSBs are 307.711 and 201.124 pixels, respectively, which are the two largest MSBs among all the epochs.

To conduct further analysis, Epoch 112 is analyzed in detail as it has the highest correlation and the minimum number of PGCPs. From the observation for the spatial relationship between the PGCPs and camera, PGCP 3 and 4, as well as PGCP 1 and 2 are close to each other in terms of both image coordinate and world coordinate.

The high correlations (e.g., larger than 0.9) between outlier statistics are shown in Table 1, It should be noted that according to collinearity equation, one PGCP contributes two measurements. For example, the measurement from PGCP 1 is measurement 1 and 2. It is interesting to note that though the coverage area of PGCPs is not small, there still exists high correlations between PGCPs whose image coordinates and world coordinates are similar. Apart from the listed high correlation in Table 1, the other correlations are small.

To further explore the influence of PGCPs' geometry on correlation, a simulation environment which is close to a wall in indoor environment is created. The noise level added on PGCPs' image coordinates is 0.5 pixel, and 0.005 m for the PGCPs' world coordinates. It should be noted that "step" on x axis means the PGCPs' degree of dispersion on the wall. If the step is larger, it means that the PGCP is disperser.

As Figs. 2 and 3 show, when there are four PGCPs, the maximum correlation coefficient is larger than 0.9 even when the distribution of PGCPs is very disperse. The maximum correlation coefficient does not change significantly with the better distribution of PGCPs. However, when the number of PGCPs increases to eight, their correlation coefficients decrease dramatically. The highest correlation coefficient is

Table 1 Correlation coefficients of highly correlated outlier statistics in single-fault case

Corresponding PGCP no.	(1,2)		(3,4)	
Measurement pairs no.	(1,3)	(2,4)	(5,7)	(6,8)
Correlation coefficient	−0.982	−0.997	−0.973	−0.939

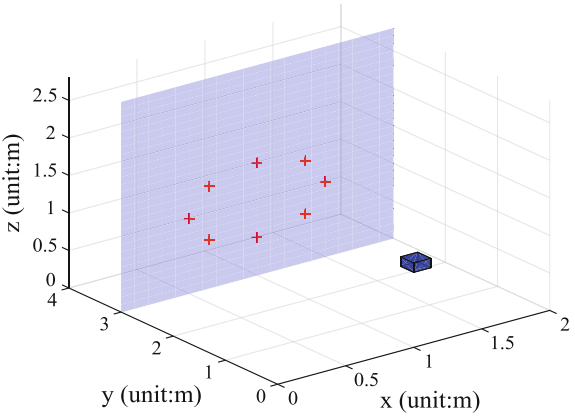

Fig. 2 The spatial relationship between PGCPs and camera

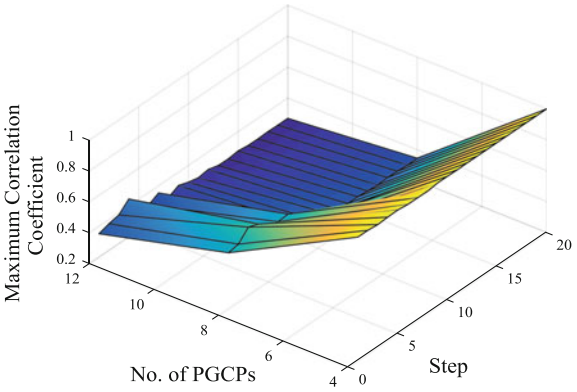

Fig. 3 Variation of maximum correlation coefficient with regarding to PGCPs' number and distribution

0.620. Similarly, when there are 12 PGCPs, the largest correlation coefficient decreases to 0.434 even when the distribution of PGCPs is centralized. When the numbers of PGCPs are 8 and 12, respectively, if their distribution becomes disperser, the correlation among PGCPs will generally decrease if the effects of random noise are removed.

For multiple-outlier case, Epoch 112 is analyzed in detail for the two faults case. There also exist correlations between the outlier statistics according to the Eq. 16. From the observation of the generated correlation coefficient, due to the existence of the high correlation in the single-outlier case, the overall correlation in the multiple-outlier case is high. Moreover, apart from the self-correlations of measurement combinations, which are the diagonal elements of the correlation coefficient matrix, the correlation between measurement combinations can be categorized into two categories according to Wang et al. [10]:

- The measurement combinations that share one or more same measurements (Type A).
- The measurement combinations that do not have any common measurements.

The latter one can be further divided into two subclasses:

- The one that contains highly correlated measurements (Type B).
- The one that does not contain highly correlated measurements (Type C).

Type A generally has high correlation as it contains one or more common measurements. For example, The correlation coefficient between (1,2) and (1,3), as well as (1,2) and (2,3) are 0.974 and 0.999, respectively. Type B also generally has the high correlation as the internal outlier statistic in the combination already has the high correlation with each other. For example, in Table 1, outlier statistics for (1,3) and (2,4) already have high correlations with each other, respectively. The correlation can affect that in the multiple-outlier case. Therefore, the correlation coefficient between (1,2) and (3,4) is 0.998. The correlation of Type C is lower than other two types since the internal outlier statistic in the combination is not significantly

Table 2 PGCPs' number, MDB and correlation coefficient of Epoch 112 and 37 in multiple fault case

Epoch no.	PGCPs' no.	Minimum MDB	Maximum MDB	Mean MDB	Minimum correlation coefficient	Maximum correlation coefficient	Mean correlation coefficient
112	5	10.489	159.175	21.753	0.037	1	0.685
37	12	8.736	25.697	10.389	0.003	0.880	0.259

correlated. For example, the correlation coefficient between (1,2) and (9,10), as well as (1,2) and (7,8) is 0.740 and 0.236, respectively.

Another epoch 37, which contains 12 PGCPs, is chosen to be compared with epoch 112 in reliability and separability. As shown in Table 2, the majority of the correlation coefficient lies from 0 to 0.6. With the increase from 5 to 12 for PGCPs' number, the overall correlations, as well as the overall MDB value under the multiple outliers decrease dramatically.

7 Concluding Remarks

Through the above analysis, the epochs' different performances in reliability and separability in single-outlier and multiple-outlier scenarios closely related to geometry, which contains number and distribution of PGCPs, as well as the spatial relationship between PGCPs and the camera. With the better geometry, vision-based navigation system's ability to detect and separate the faults will be improved significantly.

The selection and design for keypoint extraction and matching algorithm will have a direct impact on the geometry, and then affect reliability and separability. How to select and design the appropriate keypoint algorithm for better geometry is still a problem to be explored.

References

1. Desouza GN, Kak AC (2002) Vision for mobile robot navigation: a survey. IEEE Trans Pattern Anal Mach Intell 24:237–267
2. Davison AJ, Reid ID, Molton ND, Stasse O (2007) MonoSLAM: real-time single camera SLAM. IEEE Trans Pattern Anal Mach Intell 29:1052–1067
3. Li X (2013) Vision-based navigation with reality-based 3D maps. PhD thesis, University of New South Wales, Sydney, Australia
4. Baarda W (1967) Statistical concepts in geodesy, Rijkscommissie voor Geodesie
5. Li X, Wang J, Knight N, Ding W (2011) Vision-based positioning with a single camera and 3D maps: accuracy and reliability analysis. J Global Positioning Syst 10:19–29
6. Alqurashi M, Wang J (2015) Performance analysis of fault detection and identification for multiple faults in GNSS and GNSS/INS integration. J Appl Geodesy 9:35–48

7. Wang J, Wu Y, Alqurashi M (2013) Separability analysis for multiple faults in GNSS/INS integration. In: Proceedings of the international GNSS society symposium
8. Yang L, Wang J, Knight N, Shen Y (2013) Outlier separability analysis with a multiple alternative hypotheses test. J Geodesy 87:591–604
9. Wang J, Knight NL (2012) New outlier separability test and its application in GNSS positioning. J Global Positioning Syst 11:46–57
10. Wang J, Almagbile A, Wu Y, Tsujii T (2012) Correlation analysis for fault detection statistics in integrated GNSS/INS systems. J Global Positioning Syst 11:89–99
11. Almagbile A, Wang J, Ding W, Knight N (2011) Sensitivity analysis of multiple fault test and reliability measures in integrated GPS/INS systems. Arch Photogrammetry, Cartography Remote Sens 22:25–37
12. Atkinson KB (2001) Close range photogrammetry and machine vision. Whittles Publishing, UK
13. Knight NL, Wang J, Rizos C (2010) Generalised measures of reliability for multiple outliers. J Geodesy 84:625–635
14. Förstner W (1983) Reliability and discernibility of extended Gauss-Markov models. Deutsche Geodätische Kommission (DGK), Report A
15. Wang J, Chen Y (1999) Outlier detection and reliability measures for singular adjustment models. Geomatics Res Australas 71:57–72
16. Li D (1986) Trennbarkeit und Zuverlässigkeit bei zwei verschiedenen Alternativhypothesen im Gauß-Markov-Mödell. Z.f.Verm. Wesen 111:114–128

Partial State Feedback Correction for Smoothing Navigational Parameters

Zhenbo Liu, Naser El-Sheimy, Yongyuan Qin, Chunyang Yu and Jinliang Zhang

Abstract When an inertial navigation system regains a valid aiding navigation signal after a long-term outage, normal state feedback correction in the Kalman filter (KF) will cause a large instantaneous jump in the navigation parameters which may severely affect flight control stability. In this paper, we present a partial state feedback correction method in the KF to smooth the navigation parameters to solve this problem. The idea is to partially correct the navigation state in several steps according to the requirement of the guidance and control system. The simplicity of this method lies in the fact that no additional changes of the filter parameters are needed in the algorithm. The capability of residual monitoring and fault detection is the same with normal state feedback correction in the KF. Comparative simulation results show the effectiveness of the proposed method.

Keywords Kalman filter · Inertial navigation system · Smoothing · Fault detection · Feedback control

1 Introduction

Vehicles, like aircrafts, ships, and spacecrafts, have increasing levels of autonomy in recent decades. Typically, the guidance, navigation, and control (GNC) system plays an essential role in providing the autonomy for both manned and unmanned vehicles. The GNC system gives the vehicle the ability to execute flight over a predefined path generated by a path planner [1]. The navigation system in a GNC structure is a key component that outputs the vehicle's current navigation state, which usually includes position, velocity, and attitude. Based on current navigation state and knowledge of the desired objectives, the planning and guidance systems

Z. Liu (✉) · Y. Qin · J. Zhang
School of Automation, Northwestern Polytechnical University, Xi'an, China
e-mail: lzbqqq@126.com

Z. Liu · N. El-Sheimy · C. Yu
Department of Geomatics Engineering, University of Calgary, Calgary, Canada

J. Sun et al. (eds.), *China Satellite Navigation Conference (CSNC) 2016 Proceedings: Volume II*, Lecture Notes in Electrical Engineering 389,
DOI 10.1007/978-981-10-0937-2_39

determine and output a trajectory in an appropriate coordinate system for input to the control system [2].

Among different navigation systems, the inertial navigation system (INS) is the only one that has the capability to produce a complete and continuous set of navigation state data with high precision during a short time span [3]. As inertial navigation is accomplished by integrating the rotational velocity and linear acceleration signals provided by an inertial measurement unit (IMU), sensor noise and bias will cause accumulated errors in navigation states. To maintain long-term navigation accuracy, a so-called aiding sensor is required, such as BeiDou, GPS, camera imagery, or star trackers, to form an integrated navigation system [2].

Sometimes the unexpected loss of aiding signal may occur and last for a certain period. For example, when a spacecraft such as the Space Shuttle reenters the atmosphere, it will experience a 'reentry blackout' which prevents any radio communications with a total outage of less than 20 min [4]. In visual-inertial navigation for a micro aerial vehicle (MAV), strong smog or smoke appearing on the site will block the camera-based visual system. Depending on the accuracy of inertial sensors and mission scenario, INS navigation errors will grow to a relatively large degree until the regaining of aiding information. At the moment of 're-integration', the navigation state is corrected instantaneously, which is a desired result for the estimation problem. However, from the view of the vehicle control, the control system is not expected to have an impulsive large change in position and velocity since a sharp variation outside the normal range in control parameters will occur which may cause instability.

To handle this large jump problem, one can think of the method of adding robust abilities to the trajectory control system (also referred to as guidance system). To simplify the implementation and consider the possibility that the control algorithm may be hard to modify, here we present another approach to perform the navigation state correction in a smooth manner. In classical INS-based integrated navigation systems, the error state space (indirect) Kalman filter (KF) is utilized to estimate the errors in navigation information (position, velocity, and attitude). The estimated error state is used to correct erroneous navigation information. There are two types of correction implementations, feedforward and feedback. Here we focus on the feedback correction procedure, since the basic assumption of the linear dynamic model may be invalid in the case of feedforward correction [5]. So, we call the correction method a 'partial state feedback correction' (shortened as partial feedback) in this paper. The effect of such a method on residual monitoring in the navigation system is also investigated.

2 Partial State Feedback Correction

For generality, the extended Kalman filter (EKF) is present here to show the validity of the method in the case of nonlinear model (system or measurement model). First, we portray the equivalence between the standard indirect feedback correction KF and the EKF in Sect. 2.1.

2.1 KF with Indirect Feedback Correction and EKF

2.1.1 EKF Formulations

In this section, the discrete EKF algorithm is presented as a basis for the partial feedback correction KF equations. The mathematical model of stochastic nonlinear system is described as

$$\dot{X}(t) = f(X(t), t) + B(t)u(t) + G(t)w(t) \tag{1}$$

$$Z(t) = h(X(t), t) + v(t) \tag{2}$$

where $X(t)$ is the system state, $Z(t)$ is the measurement, $u(t)$ is the control signal, $f(\cdot)$ is a nonlinear function describing the time evolution of state, $h(\cdot)$ is also a nonlinear function mapping state to the measurement, $w(t)$, and $v(t)$ are uncorrelated zero-mean white noise.

To linearize the above system model and measurement model, a Taylor series expansion of Eqs. (1) and (2) should be performed. When the most recent estimate of the state vector is chosen to be the linearization point (nominal trajectory), one will have the filter form called EKF. The difference between true trajectory X_k (full state, like position, velocity, and attitude) and nominal trajectory $\widehat{X}_k^n$ is error state δX_k,

$$\delta X_k = X_k - \widehat{X}_k^n \tag{3}$$

where the subscript k denotes the time epoch t_k.

The full state can be estimated by summing the calculated nominal trajectory and error state estimation. Discrete EKF formulations [6] are given as follows.

Time update equations:

$$\widehat{X}_{k/k-1} = \widehat{X}_{k-1} + \int_{t_{k-1}}^{t_k} \left[f\left(\widehat{X}_{k-1}, t\right) + B(t)u(t) \right] \mathrm{d}t \tag{4}$$

$$\delta\widehat{X}_{k/k-1} = \Phi_{k,k-1}\delta\widehat{X}_{k-1} \tag{5}$$

$$P_{k/k-1} = \Phi_{k,k-1}P_{k-1}\Phi_{k,k-1}^T + Q_{k-1} \tag{6}$$

where $\widehat{X}_{k/k-1}$ and $\delta\widehat{X}_{k/k-1}$ are the prediction of full state and error state, respectively, $\Phi_{k,k-1}$ is the transition matrix, $P_{k/k-1}$ is the predicted state covariance matrix, and Q_k is the process noise matrix.

Measurement update equations:

$$K_k = P_{k/k-1}H_k^{\mathrm{T}}\left(H_k P_{k/k-1}H_k^{\mathrm{T}} + R_k\right)^{-1} \tag{7}$$

$$\delta\widehat{X}_k = \delta\widehat{X}_{k/k-1} + K_k\left(\delta Z_k - H_k\delta\widehat{X}_{k/k-1}\right) \tag{8}$$

$$\widehat{X}_k = \widehat{X}_{k/k-1} + \delta\widehat{X}_k \tag{9}$$

$$P_k = (I - K_k H_k)P_{k/k-1}(I - K_k H_k)^{\mathrm{T}} + K_k R_k K_k^{\mathrm{T}} \tag{10}$$

where K_k is the Kalman gain matrix, H_k is the design matrix, R_k is the measurement noise matrix, P_k is the state covariance matrix and δZ_k is the misclosure vector, given by

$$\delta Z_k = Z_k - h\left(\widehat{X}_{k/k-1}, k\right) \tag{11}$$

After state correction in Eq. (9) at time t_k^+ and before next measurement update, full state estimate and nominal state will be the same. From the definition of EKF, the error state estimation should be zero. So, another equation should be added at the end of the measurement update,

$$\delta\widehat{X}_k = 0 \tag{12}$$

The whole EKF algorithm can be seen from Eqs. (4)–(12). Actually, with the knowledge of Eq. (1.12), whole equations can be described in a simplified version which will not be presented here.

2.1.2 Error State-Based KF with Feedback Correction

In the classical inertial-based integrated navigation, the indirect (error state) feedback conventional KF is utilized. Here we will describe the error state KF with feedback correction which is equivalent to EKF.

The navigation parameters are propagated by using INS mechanization equations where the IMU output acts as the control signal just like Eq. (4) in EKF. In local-level frame (n-frame, East-North-up)-based navigation, differential equations of position P (composed of latitude L, longitude λ and height h), velocity V^n, and attitude matrix C_b^n are given by

$$\dot{P} = \begin{bmatrix} 0 & \frac{1}{R_{\mathrm{M}}+h} & 0 \\ \frac{1}{(R_{\mathrm{N}}+h)\cos L} & 0 & 0 \\ 0 & 0 & 1 \end{bmatrix} V^n \tag{13}$$

$$\dot{V}^n = f^n - \left(2\omega_{ie}^n + \omega_{en}^n\right) \times V^n + g^n \tag{14}$$

$$\dot{C}_b^n = C_b^n \left[\omega_{ib}^b \times\right] - \left[\left(\omega_{ie}^n + \omega_{en}^n\right) \times\right] C_b^n \tag{15}$$

where R_{M} and R_{N} are meridian radius of curvature and prime vertical radius, respectively, f^n is the specific force in n-frame, ω_{ie}^n is the earth rotation angular rate vector, ω_{en}^n is the angular rate of navigation frame with respect to (w.r.t.) ECEF frame, and ω_{ib}^b is the angular rate of body frame (b) w.r.t. inertial frame (i).

INS Error equations [7] are obtained by performing Taylor series expansion to Eqs. (13)–(15). The KF state usually consists of navigation error states (position error, velocity error, and attitude error), and sensor error states (biases of gyroscopes and accelerometers). This can be explained by noticing that control signal in Eq. (4) is erroneous, so a sensor error state augmentation is applied in this condition.

When measurement update is finished, feedback correction of the state should be done just as shown in Eq. (9). Then the navigation error state will be assigned zeros (see Eq. (12)). Note that the sensor error states should not set to be zeros, and they can be used to correct the sensors' output.

2.2 Partial Feedback Kalman Filter

In this section, we will present a partial feedback method in standard KF, i.e., error state-based KF, for smoothing navigation parameters. A smoothing procedure is also illustrated.

Here we call normal feedback described in Sect. 2.1 as 'total' feedback or 'complete' feedback and the error state as the 'real' state (not the true state). It is obvious that when partial feedback is taken, the real state ($\delta\widehat{X}_k^r$) will be divided by the correction state ($\delta\widehat{X}_k^c$) and the remaining state ($\delta\widehat{X}_k^l$), that is,

$$\delta\widehat{X}_k^r = \delta\widehat{X}_k \tag{16}$$

$$\delta\widehat{X}_k^r = \delta\widehat{X}_k^c + \delta\widehat{X}_k^l \tag{17}$$

The correction state can be written as a function of the real state,

$$\delta\widehat{X}_k^c = D_k \delta\widehat{X}_k^r \tag{18}$$

where D_k is the diagonal correction matrix which can be determined by the threshold of correction at each time epoch. The relevant elements in D_k will be zeros if some states should not be corrected, such as sensor error state. For the total

feedback states, the corresponding elements will be ones. Suppose partial feedback of ith navigation state is needed, we have

$$\delta\widehat{X}_k^c(i) = \text{sign}\left(\delta\widehat{X}_k^r(i)\right) \cdot T(i)$$

where $\text{sign}(\cdot)$ is to get the sign of a variable, and $T(i)$ is the threshold of ith state.

In this case, the correction in Eq. (9) should be modified to be

$$\widehat{X}_k = \widehat{X}_{k/k-1} + D_k\delta\widehat{X}_k^r \tag{19}$$

Eq. (12) is replaced by

$$\delta\widehat{X}_k = (I - D_k)\delta\widehat{X}_k^r \tag{20}$$

The other parts of filter algorithm remain the same. The reason will be explained in Sect. 3. So, Eqs. (4)–(8), (19), and (20) compose the partial feedback KF algorithm.

In real applications, the correction should be performed in each navigation update cycle to get the smoothest result. Figure 1 portrays the partial feedback procedure. Note that there are multiple correction flags depending on how many states should be partially corrected. Each correction flag has three options: not started, in progress and completed. The partial feedback correction continues until the state is less than the corresponding threshold.

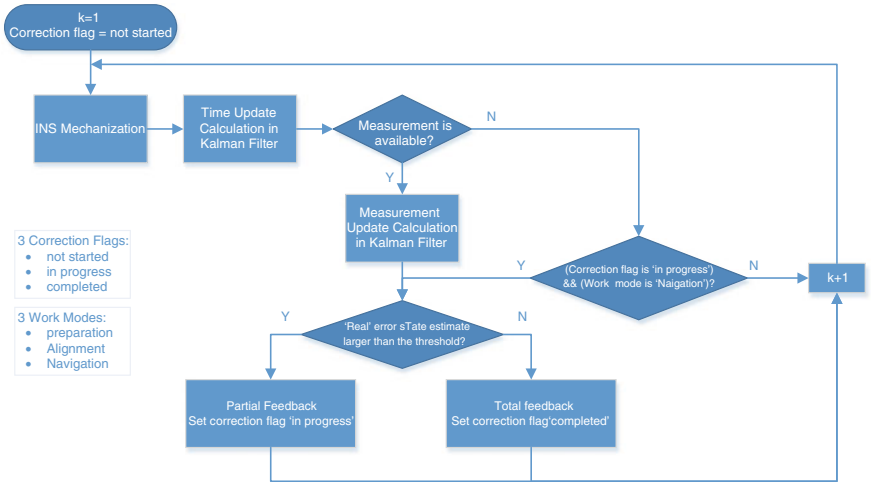

Fig. 1 Partial feedback correction procedure

2.3 Other Issues About Filtering Parameters

Here we will investigate how partial feedback correction in KF will affect the filter parameters, what should be adjusted, and so on.

First, we want to check the residual (innovation sequence), because residual plays an important role in sensor failure detection or reasonableness checking of measurement data [5]. From Eqs. (8) and (11), there are two kinds of expressions of residual in EKF,

$$r_{1,k} = \delta Z_k - H_k \delta \widehat{X}_{k/k-1} \tag{21}$$

$$r_{2,k} = \delta Z_k = Z_k - h\left(\widehat{X}_{k/k-1}, k\right) \tag{22}$$

In the case of normal feedback correction, $\delta \widehat{X}_{k/k-1}$ will be zero, so $r_{1,k}$ and $r_{2,k}$ are identical. However, when partial feedback correction is conducted, $r_{1,k}$ and $r_{2,k}$ are different. It is hoped that the residual value will not be affected by partial feedback correction. Here a residual comparison is made between partial feedback and total feedback mechanism. It is obvious that $r_{2,k}$ of partial feedback is different from that of total feedback since their $\widehat{X}_{k/k-1}$ is different, so we will focus on $r_{1,k}$. Rewrite Eq. (21) using Eqs. (2) and (11) as

$$r_{1,k} = h(X_k, k) - h\left(\widehat{X}_{k/k-1}, k\right) - H_k \delta \widehat{X}_{k/k-1} + v$$

Linearize $h(x_k, k)$ around $\widehat{X}_{k/k-1}$, we get

$$\begin{aligned} r_{1,k} &\approx h\left(\widehat{X}_{k/k-1}, k\right) + H_k\left(X_k - \widehat{X}_{k/k-1}\right) - h\left(\widehat{X}_{k/k-1}, k\right) - H_k \delta \widehat{X}_{k/k-1} + v \\ &= H_k\left(X_k - \left(\widehat{X}_{k/k-1} + \delta \widehat{X}_{k/k-1}\right)\right) + v \end{aligned} \tag{23}$$

In Appendix, we prove that $(\widehat{X}_{k/k-1} + \delta \widehat{X}_{k/k-1})$ in partial feedback and total feedback is the same, so that residual calculated by Eq. (21) in partial feedback remains unchanged compared with total feedback.

Actually, at each measurement update, 'real' error state can be estimated fully, so there is no change in the corresponding 'real' state covariance matrix as well as predicted state covariance matrix. As a consequence, the residual's covariance matrix is unchanged, i.e.,

$$C_r = H_k P_{k/k-1} H_k^T + R_k$$

Therefore, the ability of residual monitoring and fault detection remains the same with the case of total feedback.

If an indicator of precision of correction state $\delta\widehat{X}_k^c$ is required, a 'fake' state covariance matrix P_k^f is introduced here. Here we give the calculation method. Detailed derivation can be found in Appendix. Note that, this P_k^f should not be involved in the state covariance propagation.

$$P_k^f = (I - D_k K_k H_k) P_{k/k-1} (I - D_k K_k H_k)^{\mathrm{T}} + (I - D_k)\left(\widehat{X}_{k/k-1}\widehat{X}_{k/k-1}^{\mathrm{T}}\right)(I - D_k)^{\mathrm{T}} + D_k K_k R_k K_k^{\mathrm{T}} D_k^{\mathrm{T}}$$

3 Simulation and Result Analysis

In this section, we present a mathematical simulation to verify the proposed partial feedback correction KF method.

The trajectory lasts 1800 s, containing straight and level flight and several coordinated turns. There is no aiding signal in first 900 s (just INS mechanization). After that, position and velocity information from a GPS receiver are obtained. GPS accuracy is 5 m in position and 0.5 m/s in velocity. A blunder (an error of 500 m in two horizontal axes) exists at time 905 s. The IMU contains gyroscopes with the bias of $0.02^\circ/\sqrt{h}$ and the angle random walk of $0.002^\circ/\sqrt{h}$) and accelerometers with the bias of 100 μg and the velocity random walk of 100 $\mu g/\sqrt{Hz}$. Initial attitude error, velocity error, and position error are 5′, 0.05 m/s and 5 m on each axis, respectively. Only position should be smoothed, and in 1 s the maximum correction is 100 m.

Here 15 × 1 error states are involved in the estimation, namely, position error, velocity error, attitude error, drift of gyroscopes, and biases of accelerometers. Correction matrix will be

$$D_k = \mathrm{diag}(d_1, d_2, d_3, 1, 1, 1, 1, 1, 1, 0, 0, 0, 0, 0, 0)$$

where d_1, d_2 and d_3 are correction parameters that should be applied to position error state estimation.

For a comparison, the position error, longitude residual (innovations) (here it is multiplied by the Earth's radius to get equivalent distance with unit of meter) and measurement blunder χ^2 test statistic [6] of both partial feedback and total feedback correction are illustrated in Figs. 2 and 3 for a single simulation. Compared with the case of total feedback, partial feedback has the smoother result. The two cases have almost the same result of residuals and blunder test statistic value. As we can see here the blunder at 905 s can be detected and rejected. It is reasonable that

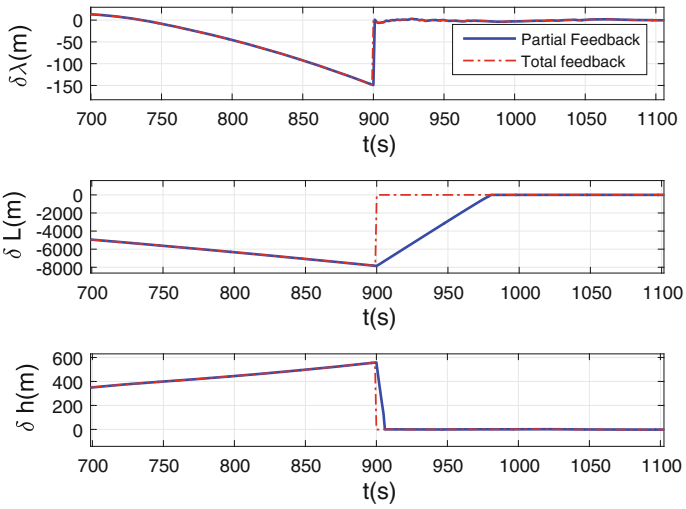

Fig. 2 Position error

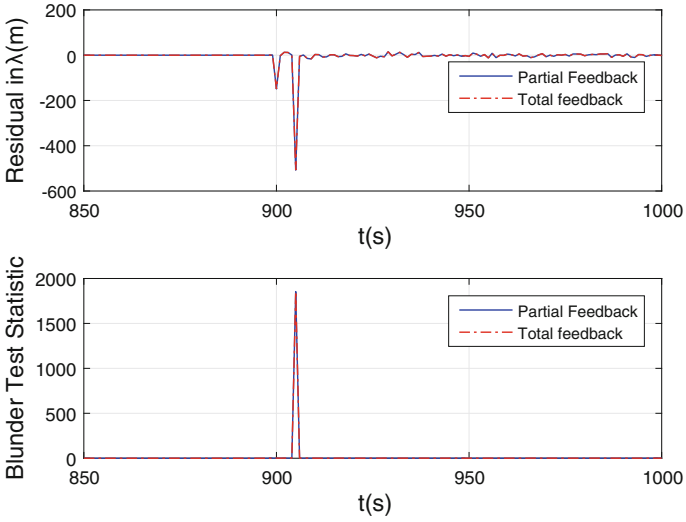

Fig. 3 Residual and blunder test statistic

longitude residual has a large value at 900 s, because at the very beginning of measurement update calculation, the state has not been corrected.

Figure 4 portrays latitude error and upper and lower bound obtained from 'real' and 'fake' state covariance matrix (denoted by 'real' P and 'fake' P) as described in

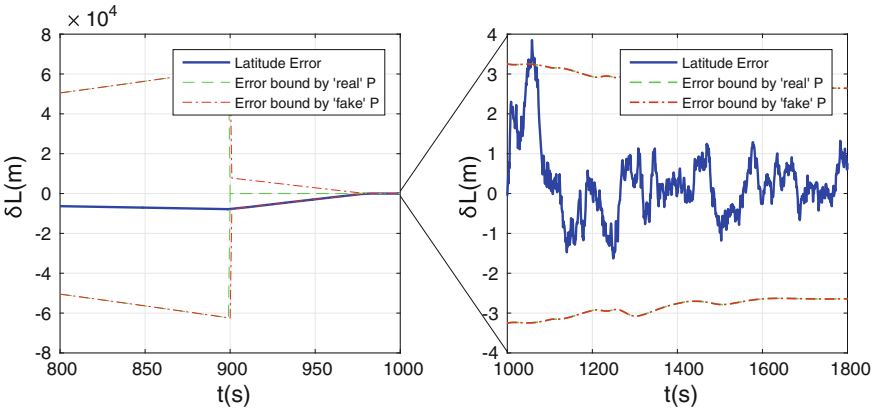

Fig. 4 Latitude error and standard deviation of state covariance

Sect. 2.3. We observe that 'real' P is a precision indicator of 'real' error state estimation, while the 'fake' P is that of correction error state estimation.

4 Conclusion

In this paper, we have presented a partial state correction Kalman filtering method to smooth navigation parameters for a vehicle's GNC system. The main idea of the method is to divide the navigation error state estimation into multiple parts and correct them in the following time steps rather than in a single step. The approach is quite simple to understand and easy to be implemented. The simplicity is proved in detail in this paper. The relevant considerations of proposed method are discussed, especially the calculation of residual and its covariance and two kinds of error state covariance: one is used in the filter propagation and the other is a precision indicator of correction error state.

Appendix

1. $\widehat{X}_{k/k-1} + \delta\widehat{X}_{k/k-1}$ in partial feedback and total feedback is equal.

Proof Equation (4) can be simplified as

$$\widehat{X}_{k/k-1} = \widehat{X}_{k-1} + \left(f\left(\widehat{X}_{k-1}\right) + B_k u_k\right)\Delta T$$

Since $f(x)$ can be linearized as

$$f(X) = f\left(\widehat{X}\right) + F\delta X$$

where F is a Jacobian matrix. Φ in Eq. (5) can be simplified by

$$\Phi = (I + F\Delta T)$$

Case 1: Partial feedback (PF),

$$\begin{aligned}
\widehat{X}_{k-1} &= \widehat{X}^{\mathrm{PF}}_{k-1/k-2} + D_k\delta\widehat{X}^{r}_{k-1} \\
\widehat{X}_{k/k-1} + \delta\widehat{X}_{k/k-1} &= \widehat{X}_{k-1} + f\left(\widehat{X}_{k-1} + B_k u_k\right)\Delta T + (I + F\Delta T)(I - D_k)\delta\widehat{X}^{r}_{k-1} \\
&= \widehat{X}^{\mathrm{PF}}_{k-1/k-2} + D_k\delta\widehat{X}^{r}_{k-1} + \left[f(\widehat{X}^{\mathrm{PF}}_{k-1/k-2}) + B_k u_k + FD_k\delta\widehat{X}^{r}_{k-1}\right]\Delta T \\
&\quad + (I + F\Delta T)(I - D_k)\delta\widehat{X}^{r}_{k-1} \\
&= \widehat{X}^{\mathrm{PF}}_{k-1/k-2} + \delta\widehat{X}^{r,\mathrm{PF}}_{k-1} + \left[f(\widehat{X}^{PF}_{k-1/k-2}) + B_k u_k\right]\Delta T
\end{aligned} \tag{A.1}$$

Case 2: Total feedback (TF),

$$\begin{aligned}
\widehat{X}_{k/k-1} + \delta\widehat{X}_{k/k-1} &= \widehat{X}_{k-1} + f\left(\widehat{X}_{k-1} + B_k u_k\right)\Delta T \\
&= \widehat{X}^{\mathrm{TF}}_{k-1/k-2} + \delta\widehat{X}^{r,\mathrm{TF}}_{k-1} + \left[f(\widehat{X}^{\mathrm{TF}}_{k-1/k-2} + \delta\widehat{X}^{r,\mathrm{TF}}_{k-1}) + B_k u_k\right]\Delta T
\end{aligned} \tag{A.2}$$

The sum of first two components in (A.1) and (A.2) is equal which are estimated as best as possible in the KF measurement update. Very little difference exists in the third part, since very short time interval is multiplied here. So, (A.1) and (A.2) can be thought as equal.

2. 'fake' state covariance matrix P^{f}_{k} Calculation

Proof Here we define 'fake' error of error state estimation $\delta\widetilde{X}_k$. Based on result of Eq. (23),

$$\begin{aligned}
\delta\widehat{X}_k &= \delta X_k - D_k\delta\widehat{X}_k = \delta X_k - D_k\left[\delta\widehat{X}_{k/k-1} + K_k(H_k\delta\widetilde{X}_{k/k-1} + v_k)\right] \\
&= (I - D_k K_k H_k)\delta\widetilde{X}_{k/k-1} + (I - D_k)\delta\widehat{X}_{k/k-1} - D_k K_k v_k
\end{aligned}$$

We know $\delta\widehat{X}_{k/k-1}$ is the estimate based on the measurement at and before time $k-1$, and v_k is the measurement noise at time k. So v_k is uncorrelated with $\delta\widetilde{X}_{k/k-1}$ which equals to $\delta X_k - \delta\widehat{X}_{k/k-1}$. Therefore, we have

$$\begin{aligned} P_k^f &= E\left[\delta\widetilde{X}_k \delta\widetilde{X}_k^{\mathrm{T}}\right] \\ &= (I - D_k K_k H_k) P_{k/k-1} (I - D_k K_k H_k)^{\mathrm{T}} \\ &\quad + (I - D_k)\left(\widehat{X}_{k/k-1}\widehat{X}_{k/k-1}^{T}\right)(I - D_k)^{\mathrm{T}} + D_k K_k R_k K_k^{\mathrm{T}} D_k^{\mathrm{T}} \end{aligned}$$

References

1. Zolghadri A, Henry D, Cieslak J, Efimov D, Goupil P (2013) Fault diagnosis and fault-tolerant control and guidance for aerospace vehicles: from theory to application. Springer, London
2. Farrell J (2008) Aided navigation: GPS with high rate sensors. McGraw-Hill, Inc., New York
3. Quan W, Li J, Gong X, Fang J (2015) INS/CNS/GNSS integrated navigation technology. Springer, Berlin
4. Spacecraft Reentry Communications Blackout. http://www.spaceacademy.net.au/spacelink/blackout.htm. Accessed 15 Dec 2015
5. Maybeck PS (1979) Stochastic models, estimation, and control, vol 1. Academic press, New York
6. Qin Y, Zhang H, Wang S (2012) Theory of Kalman filtering and integrated navigation. Northwestern Polytechnical University Press
7. Qin Y (2006) Inertial navigation. Press of Science, Beijing

Simplified Ellipsoid Fitting-Based Magnetometer Calibration for Pedestrian Dead Reckoning

Donghui Liu, Ling Pei, Jiuchao Qian, Lin Wang, Chengxuan Liu, Peilin Liu and Wenxian Yu

Abstract Pedestrian dead reckoning (PDR) is a relative positioning technique, which determines the relative location of a pedestrian by using step detection, step length estimation, and heading estimation. Since step can be accurately detected and step length can be well modelled, the heading estimation is the dominant element affecting the positioning accuracy. However, heading estimation using magnetometer is seriously influenced by diversity of indoor electromagnetic environment. In order to calibrate the magnetometer measurement, we introduce an ellipsoid equation to represent the error model of magnetometer measurement, and utilize the Singular Value Decomposition and the Cholesky Decomposition for solving the equation in this paper. To achieve an accurate error model, the state-of-the-art magnetometer calibration methods need to obtain massive samples of magnetic field. To collect the data from magnetometer more efficiently, we propose a simplified method to rotate smartphone two circles around arbitrary two of three axes in a 3D space. This data collection method can provide adequate samples to determine the ellipsoid equation within a short period. The experimental results shows that the variance of data applied with proposed method is reduced by 94.08 % on an average, while data collected by six-direction method is reduced by 91.73 % and ∞ shape method by 49.83 % averagely. The calibration process takes just 2–4 s, while the conventional methods need at least 10 s. Compared to 4.59 m of the 95th percentile error without calibration, the PDR field tests show a 1.62 m error with proposed method.

Keywords Magnetometer · Calibration · PDR · Smartphone

D. Liu · L. Pei (✉) · J. Qian · L. Wang · C. Liu · P. Liu · W. Yu
Shanghai Key Laboratory of Navigation and Location-Based Services,
School of Electronic Information and Electrical Engineering,
Shanghai Jiao Tong University, Shanghai 200240, China
e-mail: ling.pei@sjtu.edu.cn; lames@sjtu.edu.cn

J. Sun et al. (eds.), *China Satellite Navigation Conference (CSNC) 2016 Proceedings: Volume II*, Lecture Notes in Electrical Engineering 389,
DOI 10.1007/978-981-10-0937-2_40

1 Introduction

With widespread applications of Global Navigation Satellite System (GNSS), Location-Based Services (LBS) have been widely applied outdoors. However, GNSS signals are degraded or denied in indoor environments. Therefore, it has been one of the most important research hotspots to achieve reliable and accurate indoor navigation and positioning [1, 2].

Increasing computational and sensing capabilities of commercial off-the-shelf (COTS) smartphones boost emerging technologies applied in personal LBS applications [3]. Pedestrian Dead Reckoning (PDR) is an algorithm which uses sensors such as accelerometer, gyroscope and magnetometer to propagate user locations. Since these sensors are integrated into smartphones, smartphone-based PDR system becomes an alternative of indoor positioning methods [4, 5].

PDR system estimates the heading and step length from gait information of a pedestrian to calculate the current position of the pedestrian from the previous position [6]. Since PDR is a relative method, the positioning error will be accumulated over time. The heading estimation dominates the positioning accuracy and stability because step length can be well modelled [7]. However, heading estimation using magnetometer is seriously influenced by diversity of indoor electromagnetic environment. The widely used method of magnetometer calibration is to rotate a smartphone along ∞ figure trajectory for several times, which takes time and outputs are unreliable occasionally. We aim to improve the efficiency of the magnetometer calibration in this paper.

This paper is structured as follows. The analysis of ellipsoid fitting-based error model of magnetometer is given in Sect. 2; the magnetometer calibration-assisted PDR is presented in Sect. 3; the evaluation is illustrated in Sect. 4; and finally the conclusion is drawn in Sect. 5.

2 Ellipsoid Fitting-Based Magnetometer Calibration

To obtain an accurate heading of a pedestrian is one of the major problems in the PDR system. On the one hand, geomagnetic field is influenced by metal objects indoors and other electromagnetic interferences. On the other hand, the accumulated heading drift is unavoidable if we apply gyroscope to calculate the heading. In this paper, we analyze the interference factor of indoor magnetic field and build a mathematical model to calibrate the magnetometer in an indoor environment, which develops the accuracy of an indoor positioning of the system.

2.1 Error Analysis

The sources of the error of the magnetic compass measuring system can be classified into two categories: one is the effect of ferromagnetic materials in the measurement environment on the local magnetic field sensed by magnetometer; the other is the error of the measurement system itself, that is, the instrument error. If we take these factors into consideration, we can gain the accurate measurement model of the magnetometer [8].

Instrument error, caused by the manufacturing process, is mainly divided into non-orthogonal error, sensitivity error and zero variation. The detailed introduction is as follows:

1. Non-orthogonal error: a kind of heading measurement error caused by non-orthogonality of the coordinate axes of magnetometer, which is a kind of nonlinear error.
2. Sensitivity error: a kind of nonlinear error caused by the difference of the sensitivity of the sensor and the amplifier circuit.
3. Zero variation: a kind of linear error resulting from that the zero position of the sensor, analogue circuit and A/D converter circuit is not actually equal to zero.

As for magnetic interference, it can be divided into hard-iron effect and soft-iron effect [9].

1. Hard-iron effect: hard-iron effect is produced by materials in the surrounding environment of the magnetometer that exhibit an additional constant field to the geomagnetic field, thereby generating a constant additive value to the output of each of the magnetometer axes. A permanent magnet, for example, will produce a hard-iron effect.
2. Soft-iron effect: soft-iron material is a magnetic material with low coercivity and high magnetic conductivity. It does not produce magnetic field itself, but influences, or distorts, the magnetic field nearby, and is therefore multiplicative rather than additive. Iron and nickel, for example, will generate a soft-iron effect.

2.2 Error Modelling

According to the introduction and analysis of the error, we can obtain the error model equations of the magnetometer measurement system as follows [10]:

$$\widetilde{\boldsymbol{B}} = \boldsymbol{\varepsilon}_{ni}(\boldsymbol{\varepsilon}_{nm}\boldsymbol{B} + \boldsymbol{\varepsilon}_{lm}) + \boldsymbol{\varepsilon}_{li} + \boldsymbol{\varepsilon}_{w} \tag{1}$$

where $\widetilde{\boldsymbol{B}}$ is a vector consisting of three values measured from magnetic field, which can be expressed as Eq. (2). $\boldsymbol{B}$ represents real magnetic field vector; $\boldsymbol{\varepsilon}_{ni}$ is a 3-by-3

matrix representing nonlinear system errors including sensitivity error and non-orthogonal error; ε_{nm} is also a 3-by-3 matrix representing nonlinear error caused by magnetic interference, namely soft-iron effect; ε_{lm} is a vector representing linear error caused by magnetic perturbation, namely hard-iron effect; ε_{li} and ε_w represent zero variation and sensor noise.

After merger of similar items, we can get Eq. (2).

$$\widetilde{\boldsymbol{B}} = \varepsilon_{ni}\varepsilon_{nm}\boldsymbol{B}_c + \varepsilon_{ni}\varepsilon_{lm} + \varepsilon_{li} + \varepsilon_w = \boldsymbol{A}\boldsymbol{B}_c + \boldsymbol{b} + \varepsilon_w \tag{2}$$

in which $\boldsymbol{A}$ is a matrix representing multiplicative error and $\boldsymbol{b}$ represents linear errors.

As for sensor noise ε_w, on the one hand we can apply the filter to reduce noise to some extents, on the other hand noise cannot be eliminated, which is also not the focus of this paper. With further simplification, we can get Eq. (3).

$$\widetilde{\boldsymbol{B}} = \boldsymbol{A}\boldsymbol{B}_c + \boldsymbol{b} \tag{3}$$

Equation (3) is the error model of magnetometer in this paper.

After magnetometer calibration, magnetic field vector we get should be equal to local geomagnetic vector. At this time, we rotate the smartphone randomly in the three-dimensional space to collect magnetic field data. The modulus of the data should be constant, and equal to the value of local geomagnetic field strength B [11]

$$(\boldsymbol{B}_c)^T\boldsymbol{B}_c = B^2 \tag{4}$$

Combined with Eq. (3), we can get:

$$\left(\widetilde{\boldsymbol{B}} - \boldsymbol{b}\right)^T \left(\boldsymbol{A}^{-1}\right)^T \boldsymbol{A}^{-1}\left(\widetilde{\boldsymbol{B}} - \boldsymbol{b}\right) = B^2 \tag{5}$$

We can find that the form of Eq. (5) is almost equivalent to the ellipsoid equation. Therefore, the errors of magnetometer results in end points of the magnetic field vector are distributed on the surface of an ellipsoid. The centre of this ellipsoid depends on hard-iron effect $\boldsymbol{b}$, and the shape depends on the symmetric matrix $\left(\boldsymbol{A}^{-1}\right)^T\boldsymbol{A}^{-1}$ [12]. The difference is shown in Fig. 1.

If we collect several sets of magnetic field data and figure out the ellipsoid equation of the distribution of magnetic vector, we can calculate $\boldsymbol{A}$ and $\boldsymbol{b}$ by matrix operation.

First, in order to simplify the calculation, we normalize Eq. (5) and get

$$(\boldsymbol{x} - \boldsymbol{o})^T \boldsymbol{A}_e(\boldsymbol{x} - \boldsymbol{o}) = 1 \tag{6}$$

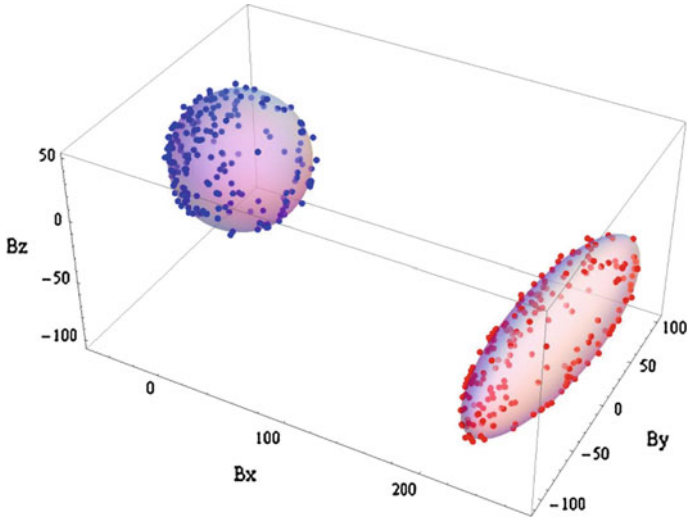

Fig. 1 The comparison of magnetic field data before calibration and data after calibration [13]

Also, we can rewrite it into polynomial form [14]:

$$\boldsymbol{d}(\boldsymbol{x})^{\boldsymbol{T}}\boldsymbol{p} = 0 \tag{7}$$

$$\boldsymbol{A_e} = \begin{pmatrix} p_1 & \frac{p_4}{2} & \frac{p_5}{2} \\ \frac{p_4}{2} & p_2 & \frac{p_6}{2} \\ \frac{p_5}{2} & \frac{p_6}{2} & p_3 \end{pmatrix}, \boldsymbol{o} = -\frac{1}{2}\boldsymbol{A}_e^{-1}\begin{pmatrix} p_7 \\ p_8 \\ p_9 \end{pmatrix}, p_{10} = \boldsymbol{o}^{\boldsymbol{T}}\boldsymbol{A_e}\boldsymbol{o} - 1$$

$$\boldsymbol{d}(\boldsymbol{x}) = [x_1^2, x_2^2, x_3^2, x_1x_2, x_1x_3, x_2x_3, x_1, x_2, x_3, 1]^T$$

Assuming that there are N sets of data of magnetic field strength, the ellipsoid fitting problem can be expressed as:

$$\begin{aligned} \boldsymbol{Dp} &= 0_{N\times 1} \\ \boldsymbol{D} &= [\boldsymbol{d}(\boldsymbol{x}_1), \boldsymbol{d}(\boldsymbol{x}_2), \ldots, \boldsymbol{d}(\boldsymbol{x}_N)]^T \end{aligned} \tag{8}$$

We can apply Singular Value Decomposition (SVD) for matrix $\boldsymbol{D}$ to solve the ellipsoid fitting problem based on least square method, and we get $\boldsymbol{p}$ from the right singular vector. Next, we use Cholesky Decomposition to obtain the matrix $\boldsymbol{A}$ from $\boldsymbol{A_e}$.

2.3 Simplified Calibration Process

To solve the ellipsoid problem, we should collect several sets of magnetic field vectors representing almost all directions in three-dimensional space. In theory, to use SVD solving the ellipsoid equation, we need at least ten vectors to determine the coefficient in ellipsoid equation. Of course, if we get more data for fitting, the model would be more precise and accurate. But typically, the more data we collect, the more time we spend on the collection as well as calculation. Therefore, to collect data needed in calibration, we can design an efficient way to rotate magnetometer on a smartphone to collect a small quantity of magnetic field data but weight more in the calibration process.

In this paper, we design a specific method to rotate smartphone in space in order to collect magnetic field data more valuable to ellipsoid equation. We select two of the three axes of the magnetometer on the smartphone as the rotational axes. Then, we rotate smartphone around these two axes to collect data (Fig. 2).

In principle, after we rotate the smartphone around one axis, we can roughly sketch the shape of the ellipsoid. However, just one circle of rotation cannot determine the equation as shown in Fig. 3. We can create various ellipsoids that pass through the circle unless we can ensure the plane containing the trace of rotation is the symmetric plane which is difficult for us. Therefore, we need to rotate the smartphone around another axis to get another trace on the surface of the ellipsoid. After we get two circles in two mutually perpendicular planes, we can

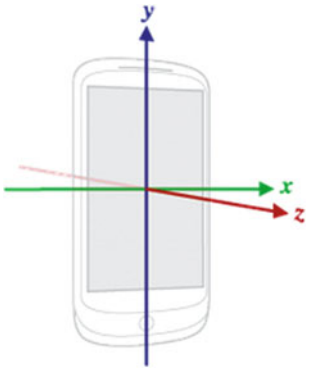

Fig. 2 The body coordinates of a smartphone [15]

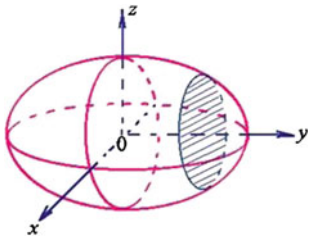

Fig. 3 The shape of an ellipsoid

determine the unique ellipsoid equation. Compared with other methods like six-directional stewing method and ∞ shape method, this method needs fewer data and costs less time with the same effect of calibration.

With a more efficient way to collect magnetic field data, the process of calibration costs less time on solving the ellipsoid equation. Users can also know how to calibrate their own smartphone. So, in this paper, we have specifically made a series of experiments and explored the effect of different rotation modes on the calibration of the smartphone. After comparison, we can find out the most efficient and most effective way to collect data for magnetometer calibration.

3 Magnetometer Calibration-Assisted Pedestrian Dead Reckoning

3.1 The Principle of PDR

The main workflow of PDR algorithm is [16, 17]

1. Use accelerometer to measure the acceleration when a pedestrian walks, and detect whether the pedestrian has taken a step.
2. If the pedestrian does, the acceleration during this step will be used to calculate the step length of this step which will be used in following position update.
3. Magnetometer and gyroscope will be used to estimate the heading of the pedestrian during this step.
4. As the heading and step length is calculated, the next position of the pedestrian can be calculated by iteration of the previous position.

Therefore, the core formula of iteration calculating the pedestrian position is [18–20]

$$\begin{cases} x_{k+1} = x_k + l_k \times \cos\ \theta_k \\ y_{k+1} = y_k + l_k \times \sin\ \theta_k \end{cases} \tag{9}$$

where (x_k, y_k) is the position of the pedestrian at time k, l_k and θ_k are the step length and heading, respectively. (x_{k+1}, y_{k+1}) is the coordinate of the pedestrian at time $k + 1$ after one step.

3.2 Magnetometer Calibration Assist

Anomalies in magnetic fields in an indoor environment are usually irregular. It is difficult and time-consuming for us to figure out the pattern of the trend of magnetic

anomalies [21–23]. So the most appropriate way to obtain accurate heading is to make a magnetometer calibration when the anomalies is quite obvious. However, we still require calibration at the beginning of positioning.

This method can also judge whether there is anomaly by the modulus of magnetic field, which means if the modulus of local magnetic field strength is out of the range of normal geomagnetic field strength. There should be obvious magnetic anomalies. Once the anomaly is detected, the calibration will be activated and the user needs to rotate a phone along a certain path. And after a few seconds, the user can continue indoor positioning.

4 Evaluation

This section first compares the distribution of magnetic field data before and after calibration as well as the result of heading estimation. Then, a series of experiments about simplification of calibration process are shown to compare the performance of different methods of data acquisition. At last, a pedestrian trajectory using PDR applied with magnetometer calibration is shown to demonstrate that PDR with magnetometer calibration assistance can perform better.

In addition, all experiments were conducted in a typical office building. The sensors we used were embedded in a smartphone is AK8963 Magnetometer from Manufacturer AKM with resolution of 0.15 and its sample rate is 100 Hz. The whole calibration process can be achieved both by online and offline.

4.1 Magnetometer Calibration

First, magnetic field data were collected by rotating the smartphone around X and Z axis of its coordinate system. After a few seconds, the data after calibration were obtained. We select a set of representative data from the experiments which is shown in Figs. 4 and 5.

The data used in Figs. 4 and 5 is collected in a typical indoor environment. As shown in Fig. 4, the trace after calibration is much closer to the light green sphere skeleton, which is equivalent to lower variance. From Fig. 5, we can the variance of the data after calibration is greatly reduced from 134.19° to 0.09° (Fig. 6).

Compared with the results of heading estimation with and without calibration, we found that the heading after calibration is closer to the ground truth. The standard deviation of error is quite reduced from 19.50° to 8.80°.

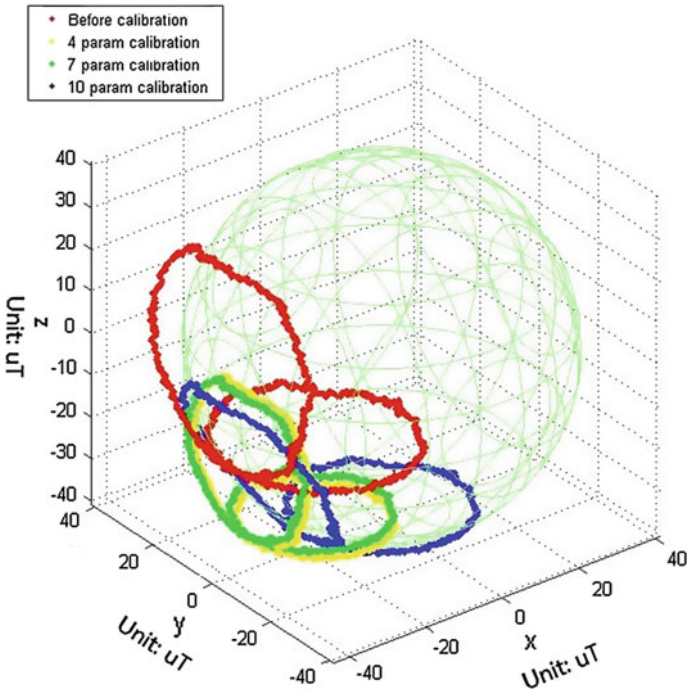

Fig. 4 The distribution of magnetic field data before/after calibration. The *red* trace represents the data without calibration. The others are the data using different form of calibration matrix. The *yellow* one result from the assumption that the calibration matrix is an identity matrix; the *green* one corresponds to diagonal calibration matrix; the *blue* one is using symmetric calibration matrix which is applied with the method proposed in this paper

4.2 Calibration Process Simplification

In this part, experiments were carried to compare the time and performance of different methods of smartphone rotation. We selected several representative methods to make comparison. The results are shown as follows.

As shown in Figs. 7 and 8, rotating cellphone around axes of coordinate system of the phone shows the best performance. The variance of data applied with calibration using this method is reduced by 94.08 % on average, while data collected by six-direction method is reduced by 91.73 % and ∞ shape method by 49.83 % averagely. Unlike six-direction method, the whole process of rotating phone around two axes of the phone takes just 2–4 s, while the former method needs at least 10 s to accomplish.

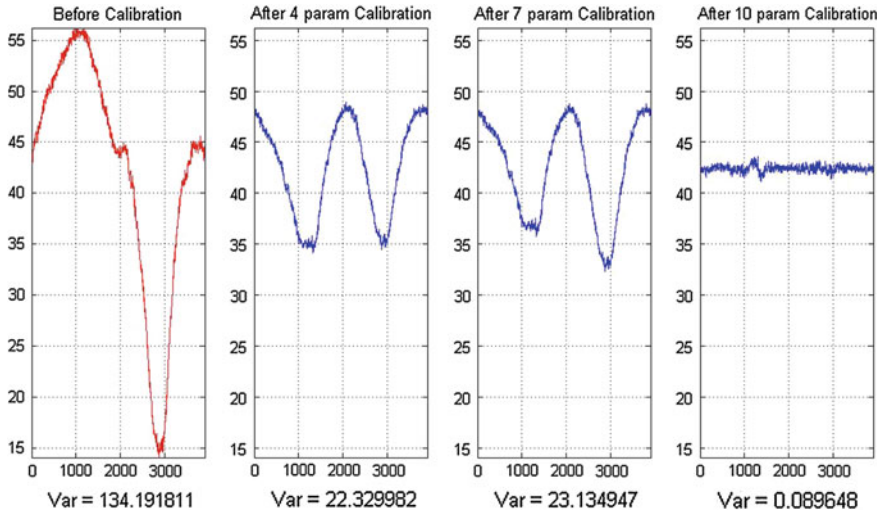

Fig. 5 The modulus of the magnetic field data. The data shown here is the same one as shown in Fig. 4. The *red wave* is the data without calibration. The three *blue curves* from left to right are the results using identity calibration matrix, using diagonal matrix and symmetric matrix, respectively

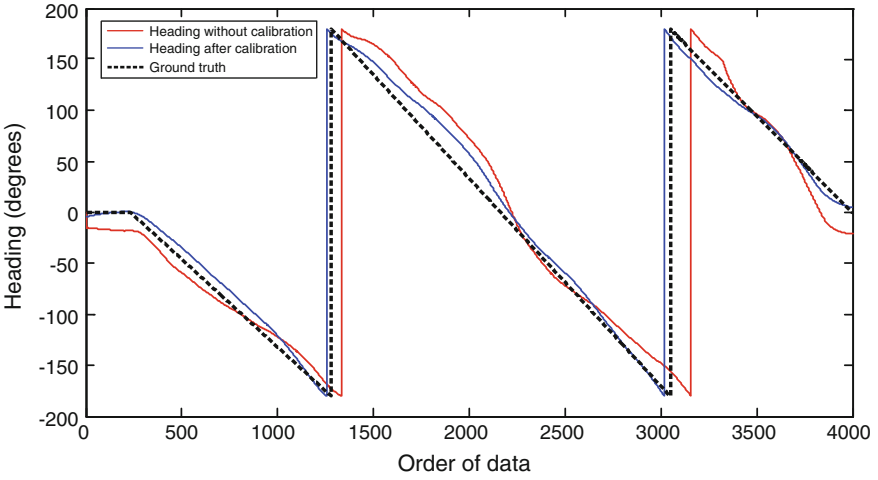

Fig. 6 The heading estimation results without and after calibration. This experiment was conducted by rotating two same smartphones in horizontal plane for 360°

4.3 Indoor Pedestrian Positioning

The magnetometer calibration is an improved function of heading estimation which is a part of PDR system. In order to evaluate the localization performance of our proposed method, we made a comprehensive experiment. In this experiment,

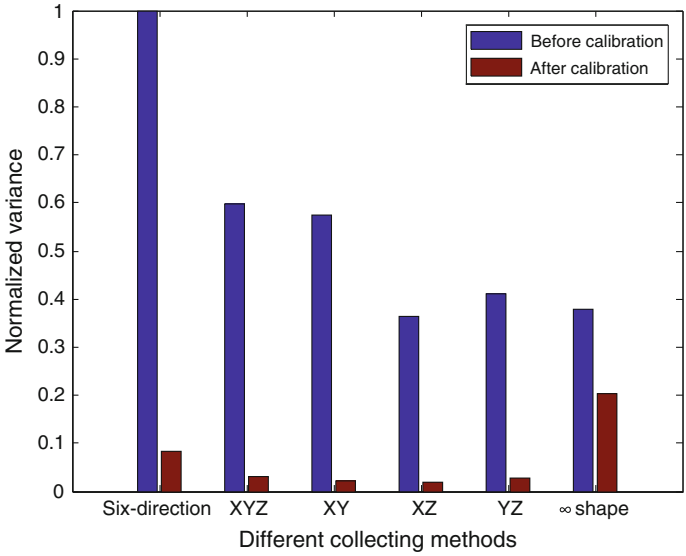

Fig. 7 Variance of different methods of data collected indoors. Six-direction means taking the phone stewing in six different directions (usually direction of coordinate system). XYZ means rotating smartphone around X, Y and Z axis of the smartphone coordinate system, respectively. XY means rotating phone around X and Y axis and so on. The experiments were taken both indoors and outdoors

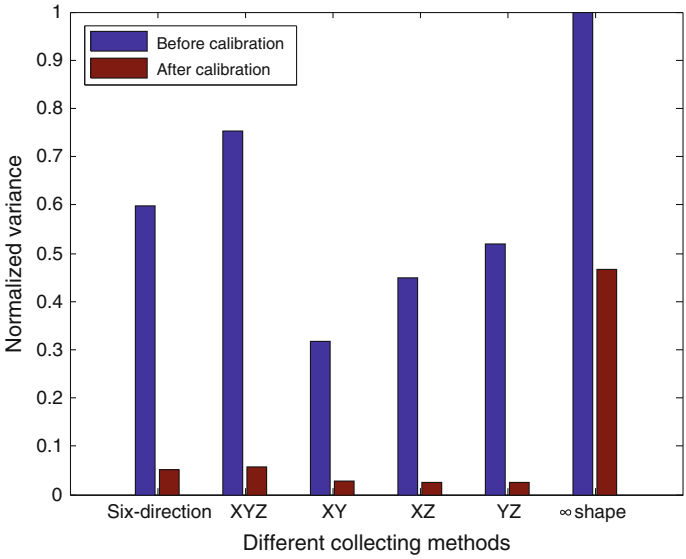

Fig. 8 Variance of different methods of data collected outdoors. The legend is the same as the one in Fig. 7

a pedestrian just walked one circle in an office, we can use the trajectory of the pedestrian to make comparison between conventional PDR and PDR with magnetometer calibration.

From Fig. 9, we can see that PDR made a much better performance after magnetometer calibration. However, the valid range of the calibration is limited. Just calibrating at the beginning cannot ensure the validity of heading in the whole process of positioning. Also the main reason for the low accuracy of the heading when turning around is that the gait is different from that of the straight line. If the personal model of step length is applied, the heading estimation will be improved. The error of two trajectories in the office is listed in Table 1.

As shown in Table 1, the localization errors are significantly reduced using magnetometer calibration assisted PDR because heading drift introduced by uncalibrated magnetometer is mitigated.

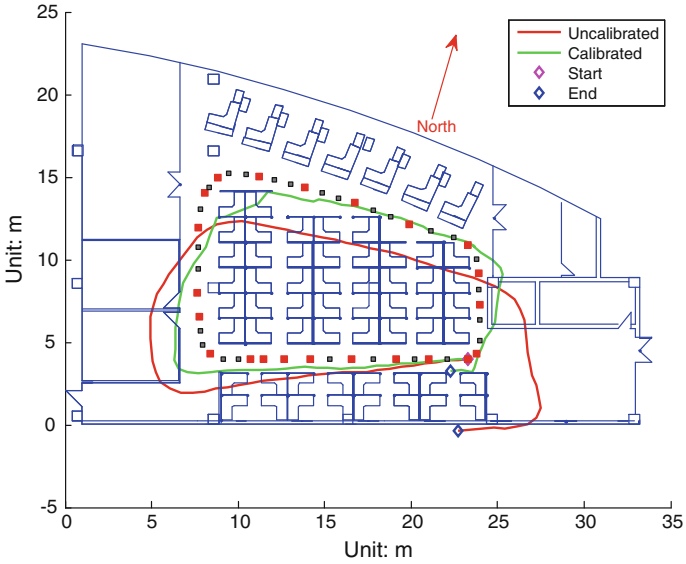

Fig. 9 The field test trajectory of the pedestrian in an office. The *red line* is the trajectory using conventional PDR without calibration. The *green line* is the one using PDR with magnetometer calibration, which is calibrated at the beginning. The *red* and *black solid squares* are the ground truth of localization. Two trajectories both started and ended at the same coordinate in real environment

Table 1 The localization error of PDR in an office

Situation	Mean error (m)	50th percentile error (m)	95th percentile error (m)
Uncalibrated	2.11	2.05	4.59
Calibrated	0.66	0.59	1.62

5 Conclusion

This paper first introduces the ellipsoid fitting-based magnetometer calibration, then proposes a simplified method of calibration, and at last applies the calibration solution in the PDR system. Experiment results demonstrate this method of calibration works better than the mainstream methods. And the simplified process also improves the efficiency of calibration. The PDR assisted with magnetometer calibration makes a better performance than the conventional PDR.

Acknowledgment This work is supported by the National Natural Science Foundation of China under Grant 61573242, in partly by the Shanghai Science and Technology Committee under Grant 14511100300, 15511105100 and partly sponsored by Shanghai Pujiang Program (No.14PJ1405000) and Qingpu Industry-University-Research Project(2015-4).

References

1. Crassidis JL, Lai Kok Lam, Harman RR (2005) Real-time-attitude-independent three-axis magnetometer calibration. J Guid Control Dyn 28(1):115–120
2. Wang JH, Gao Y (2006) A new magnetic compass calibration algorithm using neural networks. Meas Sci Technol 17(1):153–160
3. Li WL, Iltis RA, Win MZ (2013) A smartphone localization algorithm using RSSI and inertial sensor measurement fusion. In: Global communications conference (GLOBECOM), IEEE, pp 3335–3340
4. Woodman O, Harle R (2008) Pedestrian localization for indoor environments. In: International conference on ubiquitous computing. ACM, pp 114–123
5. Rantakokko J, Rydell J, Stromback P et al (2011) Accurate and reliable soldier and first responder indoor positioning: multisensory systems and cooperative localization. IEEE Wirel Commun 18(2):10–18
6. Li F, Zhao C, Ding G et al (2012) A reliable and accurate indoor localization method using phone inertial sensors. In: ACM international conference on ubiquitous computing. ACM, pp 421–430
7. Madgwick, S (2010) An efficient orientation filter for inertial and inertial/magnetic sensor arrays. Report Xio and University of Bristol (UK)
8. Chao M, Jiang D, Wen C (2010) Error analysis and calibration of magnetic compass. Chin. J. Sens. Actuators, 23(4): 56–61
9. Afzal MH, Renaudin V, Lachapelle G (2011) Magnetic field based heading estimation for pedestrian navigation environments. In: International conference on indoor positioning and indoor navigation (IPIN). IEEE, pp 1–10
10. Afzal MH (2011) Use of earth's magnetic field for pedestrian navigation. Dissertation Abstr Int 73(05)
11. Merayo JMG, Brauer P, Primdahl F et al (2000) Scalar calibration of vector magnetometers. Measur Sci Technol 11(2):120–132(13)
12. Fang J, Sun H, Cao J et al (2011) A novel calibration method of magnetic compass based on ellipsoid fitting. IEEE Trans Instrum Measur 60:2053–2061
13. Mark P, Michael S (2014) Magnetic calibration (magnetic.c). Technical note. Freescale, Inc. 2014
14. Bonnet S, Bassompierre C, Godin C et al (2009) Calibration methods for inertial and magnetic sensors. Sens Actuators A 156(2):302–311

15. Sensors Overview | Android. (11 July 2012) Available via android developers https://www.android-dooc.com/guide/topics/sensors/sensors_overview.html. Cited 20 Dec 2015
16. Liu C, Pei L, Qian J, Wang L, Liu P, Yu W (2015) Sequence-based motion recognition assisted pedestrian dead reckoning using a smartphone. In: Proceedings of China satellite navigation conference (CSNC), vol III Chapter 64
17. Chen R, Pei L, Chen Y (2011) A smart phone based PDR solution for indoor navigation. In: Proceedings of the 24th international technical meeting of the satellite division of the institute of navigation (ION GNSS 2011), pp 1404–1408
18. Qian J, Pei L, Ma J, Ying R, Liu P (2015) Vector graph assisted pedestrian dead reckoning using unconstrained smartphone. Sensors 15(3):5032–5057
19. Qian J, Ma J, Ying R, Liu P, Pei L (2013) An improved indoor localization method using smartphone inertial sensors. In: 2013 international conference on indoor positioning and indoor navigation (IPIN), IEEE, pp 1–7
20. Liu Y, Dashti M, Zhang J (2013) Indoor localization on mobile phone platforms using embedded inertial sensors. 10th workshop on positioning navigation and communication (WPNC). IEEE, pp 1–5
21. Wang L, Dong Z, Pei L, Qian J, Liu C, Liu D, Liu P (2015) A robust context-based heading estimation algorithm for pedestrian using a smartphone. In: Proceedings of the 28th international technical meeting of the satellite division of the institute of navigation (ION GNSS 2015). Tampa, FL USA, SEP pp 14–18, 2015
22. Qian J, Pei L, Zou D, Liu P (2015) Optical flow-based gait modeling algorithm for pedestrian navigation using smartphone sensors. Sens J IEEE 15(12):6797–6804. doi:10.1109/JSEN.2015.2464696
23. Renaudin V, Afzal MH, Lachapelle G (2012) Magnetic perturbations detection and heading estimation using magnetometers. J Location Based Serv 6(3): 161–185

Velocity Prediction for Multi-rotor UAVs Based on Machine Learning

Rongzhi Wang, Danping Zou, Ling Pei, Peilin Liu and Changqing Xu

Abstract Currently, multi-rotor UAV's navigation mainly depends on satellite navigation systems. In many environments (e.g., indoor, urban, or canyon), lack of satellite signal will lead UAV navigation to failure. In that case, one backup solution is to use the inertial navigation method. Inertial navigation method integrates measurements from gyroscope and accelerometer to obtain the orientation, speed, and position. Due to the instability of sensor bias, a slight orientation error caused by gyroscopic bias change will lead to enormous position error. Noting that there is a strong correlation between the pose and velocity for a flying multi-rotor UAV, we can search for a solution to calculate velocity directly from UAV's pose. In this work, we propose to use support vector machine (SVM)-based machine learning technique to predict the moving speed of the aircraft. This approach builds a relationship directly between the orientation data and velocity by training. The experiment has two stages. In early stage, we have tested our method in simulation environment; then at later stage, we have tested our method in real-world cases. Experimental results our method can predict the UAV's velocity within the error of 0.3 m/s and the squared correlation coefficient between the predicted velocity and the ground truth is about 0.8. The method can be used as a complementary navigation source to achieve higher localization accuracy and stability.

Keywords Multi-rotor UAV · Machine learning based INS (inertial navigation system) integration · SVM (supported vector machine)

R. Wang · D. Zou (✉) · L. Pei · P. Liu · C. Xu
Shanghai Key Laboratory of Navigation and Location-Based Services,
School of Electronic Information and Electrical Engineering,
Shanghai Jiao Tong University, Shanghai 200240, China
e-mail: dpzou@sjtu.edu.cn

R. Wang
e-mail: wangrongzhi0225@163.com

J. Sun et al. (eds.), *China Satellite Navigation Conference (CSNC) 2016 Proceedings: Volume II*, Lecture Notes in Electrical Engineering 389,
DOI 10.1007/978-981-10-0937-2_41

1 Introduction

Existing multi-rotor UAV's navigation mainly depends on satellite navigation systems, such as GPS, to obtain the position information. But in many scenes, there may be a satellite signal failure, such as around tall buildings, in a deep canyon, and indoor space. Because of loss of satellite signal, GNSS receiver cannot provide the position of UAV, which in consequence cause autonomous navigation to fail.

The classic way remedy of this issue is to use inertial navigation as a backup. An inertial navigation system, INS, consists of gyroscope and accelerometer, which measure the linear acceleration and angular velocity of UAV. The instantaneous velocity and altitude are obtained by integration operation [1]. However, the measurement errors of inertial sensors can be amplified by integration and accumulated over time, and finally lead to a significant error in a short time [2].

Another solution to lack of GNSS signals is to use optical flow sensor [3]. There are many micro-UAVs equipped with optical flow sensors that are used to achieve like obstacle avoidance [4], automatic landing [5], and stable hovering [6]. However, optical flow is influenced by the surface texture and illumination conditions, especially for indoor navigation in the night. Productions from the most advanced UAV companies such as Parrot and DJI have no good solution to the problem of optical flow.

Notice that the special dynamic model of the multi-rotor aircraft, we can build a mathematical relationship between UAV's flying velocity and its attitude and acceleration. But in practice, it is very hard to calibrate all the parameters of dynamic model. So we view this model as a black-box and adopt machine learning technique to train the model, and finally accomplished use the trained parameters to estimate the UAV's velocity.

The proposed method relies on only the IMU readings, without using integration that usually produces a large position error as a typical inertial navigation system does. It also works in any light conditions, not limited only in the daytime, which can be a complementary navigation approach when satellite signal losses and optical flow fails.

2 The Dynamic Model

In this paper, we consider only the altitude-hold control mode that exists in most multi-rotor UAV platforms for clarity. Out method, however, is not limited to this case, and can be also adopted in other modes.

Let $\{A\}$ denote a right-hand inertial frame with unit vectors along the axes denoted by $\{\overrightarrow{\alpha_1}, \overrightarrow{\alpha_2}, \overrightarrow{\alpha_3}\}$; Let $\{B\}$ be a right-hand body fixed frame for the airframe with unit vectors $\{\overrightarrow{b_1}, \overrightarrow{b_2}, \overrightarrow{b_3}\}$. According to Newton's law, we have

$$\mathrm{m}\dot{v} = mg\overrightarrow{a_3} + RF_B \tag{1.1}$$

where F_B combines the principle non-conservative forces applied to the quadrotor's body frame; R is rotation matrix from body frame $\{B\}$ to inertial frame $\{A\}$ transform,

$$R = \begin{bmatrix} c\psi c\theta - s\phi s\psi s\theta & -c\phi s\psi & c\psi s\theta + c\theta s\phi s\psi \\ c\theta s\psi + c\psi s\phi s\theta & c\phi c\psi & s\psi s\theta - c\psi c\theta s\phi \\ -c\phi s\theta & s\phi & c\phi c\theta \end{bmatrix} \tag{2}$$

where ϕ, θ, ψ are the roll, pitch, yaw angle respectively; c and s are abbreviations for cosine and sine.

F_B consists of propeller lift force and induced drag force which can be modeled by

$$F_B = -T_\Sigma \overrightarrow{b_3} - T_\Sigma D v_B \tag{3}$$

where T_Σ, v_B are the propeller lift force and velocity in body frame $\{B\}$; $D \in R^{3\times 3}$ is the coefficient matrix [7] for induced drag.

The reading of accelerometer and the acceleration in inertial frame has the following relationship

$$Ra_{\mathrm{IMU}} + g\overrightarrow{a_3} = \dot{v} \Leftrightarrow a_{\mathrm{IMU}} = R^{\mathrm{T}}\left(\dot{v} - g\overrightarrow{a_3}\right). \tag{4}$$

By formula (1) and (4) we can write

$$ma_{\mathrm{IMU}} = F_B. \tag{5}$$

Recalling (3) we get

$$a_{IMU} = -\frac{T_\Sigma}{m}\overrightarrow{b_3} - \frac{T_\Sigma}{m} DR^{\mathrm{T}} v. \tag{6}$$

Then we gain the velocity which is expresses as

$$v = -\left(DR^{\mathrm{T}}\right)^{-1}\left(\frac{m}{T_\Sigma} a_{\mathrm{IMU}} + \overrightarrow{b_3}\right). \tag{7}$$

When in attitude-hold mode, the vertical direction is in a state of force balance as Eq. (8) expresses.

$$P_v\left(T_\Sigma R\overrightarrow{b_3}\right) = mg \Rightarrow \frac{m}{T_\Sigma} = \frac{P_v R\overrightarrow{b_3}}{g} \tag{8}$$

where P_{h} and P_{v} are defined as the projection matrix onto the x-y plane and z direction.

$$P_h = \begin{bmatrix} 1 & 0 & 0 \\ 0 & 1 & 0 \end{bmatrix}, \quad P_v = [0 \quad 0 \quad 1]. \tag{9}$$

Substituting $\frac{m}{T_\Sigma}$ in (7) using Eq. (8), finally we obtain the horizontal translational velocity

$$v_h = -P_h \left(DR^{\mathrm{T}}\right)^{-1} \left(\frac{P_v R \overrightarrow{b_3}}{g} a_{\mathrm{IMU}} + \overrightarrow{b_3} \right) \tag{10}$$

where $v_{\mathrm{h}} = (v_x, v_y)$ is the horizontal velocity in inertial frame {A}.

Equation (10) tells us that if we get an accurate attitude estimation of R and acceleration estimation of α_{IMU}, the velocity in altitude-hold mode can be theoretically solved without GPS or optical flow. But in practice, parameters in (10) are very hard to be obtained. In this paper, we view dynamic model (10) as a black box, and use machine learning method support vector machine (SVM) to train the model (10). Finally, use the trained model to predict velocity of the flying UAV in altitude-hold mode.

3 SVM Regression

The regression problem is to fit a straight line, a plane, or a super plane to approximate the distribution of given sample points.

For given training dataset

$$T = \{(x_1, y_1), \ldots, (x_l, y_l)\} \in (R^n \times R)^l \tag{11}$$

where $x_i \in R^n, y_i \in R = \{1, -1\}$, $i = 1, \ldots, l$, the regression problem is to find function $g(x)$ which can predict y very well at any input x. A linear regression problem is to find linear function $g(x) = (w \cdot x) + b$ that can fit the samples best. Before detailed introduction of regression, we take a look at SVM linear classification.

SVM linear classification is to deal with following optimization [8]:

$$\begin{aligned} &\min_a \frac{1}{2} \sum_{i=1}^{l} \sum_{j=1}^{l} y_i y_j (x_i \cdot x_j) a_i a_j - \sum_{j=1}^{l} a_j \\ &\text{s.t} \sum_{i=1}^{l} y_i a_i = 0, \quad a_i \geq 0, \quad i = 1, \ldots, l \end{aligned} \tag{12}$$

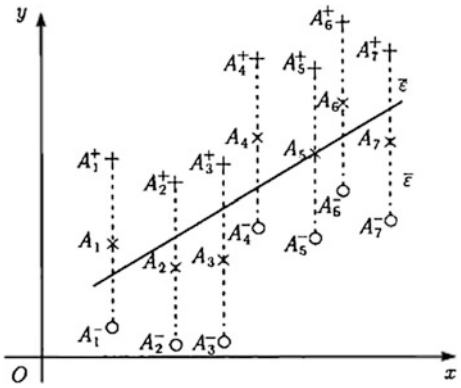

Fig. 1 The method to create two separate parts using training dataset

It can be proved that Eq. (12) has a solution $\alpha^* = \left(a_1^*, \ldots, a_l^*\right)^{\mathrm{T}}$, so the SVM classification problem has solution [9]:

$$w^* = \sum_{i=1}^{l} a_i^* y_i x_i \quad \text{and} \quad b^* = y_i - \sum_{i=1}^{l} a_i^* y_i (x_i x_j) \tag{13}$$

SVM tries to transform linear regression problem to linear classification problem. The basic idea is to create two separate parts by moving each sample in the training set a distance ε along the positive and negative y direction, as shown in Fig. 1.

We denote the two separate parts by $D^+ = \left\{\left(x_i^{\mathrm{T}}, y_i + \varepsilon\right)^{\mathrm{T}}, i = 1, \ldots, l\right.$ and $D^- = \left\{\left(x_i^{\mathrm{T}}, y_i - \varepsilon\right)^{\mathrm{T}}, i = 1, \ldots, l\right.$. Now our goal has been changed to be searching a function to separate the two parts which is exactly the classification problem described as following:

For given classification training set: $\left\{\left(\left(x_1^{\mathrm{T}}, y_1 + \varepsilon\right)^{\mathrm{T}}, 1\right), \ldots, \left(\left(x_l^{\mathrm{T}}, y_l + \varepsilon\right)^{\mathrm{T}}, 1\right),\right.$ $\left(\left(x_1^{\mathrm{T}}, y_1 - \varepsilon\right)^{\mathrm{T}}, -1\right), \ldots, \left(\left(x_l^{\mathrm{T}}, y_l - \varepsilon\right)^{\mathrm{T}}, -1\right)\}$ }, the aim is to solve the following optimization problem [10]:

$$\begin{aligned} &\min_{a^* \in R^{2l}} \frac{1}{2} \sum_{i,j=1}^{l} \left(a_i^* - a_i\right)\left(a_j^* - a_j\right)\left(x_i x_j\right) \\ &\quad + \varepsilon \sum_{i=1}^{l} \left(a_i^* + a_i\right) - \sum_{i=1}^{l} y_i \left(a_i^* - a_i\right), \\ &\text{s.t} \quad \sum_{i=1}^{l} \left(a_i^* - a_i\right) = 0, \quad a_i^* \geq 0, \quad i = 1, \ldots l \end{aligned} \tag{14}$$

which leads to regression problem solution as shown below:

$$w = \sum_{i=1}^{l} \left(a_i^* - a_i\right) x_i, \quad b = y_i - \left(w \cdot x_j\right) + \varepsilon \tag{15}$$

where $\alpha^* = \left(a_1, a_1^*, \ldots, a_l, a_l^*\right)^{\mathrm{T}}$ is the solution of problem (14). Finally, the estimate function $g(x)$ has the form

$$y = (w \cdot x) + b = \sum_{i=1}^{l} (a_i^* - a_i)(x_i \cdot x) + b \tag{16}$$

4 Method

This section describes the method of motion prediction based on machine learning.

4.1 Data Preprocessing

The experiment data includes the gyroscope data, accelerometer data, optical flow data and GPS data. Before training, preprocessing includes flow value filtering, transformation from quaternions to Tait-Bryan angle and rotation matrix, flow velocity conversion between inertial and airframe coordinate need to be done first.

The jittering of UAV when it is flying causes glitch in flow values. We can use a low-pass filter to eliminate it, namely:

$$y(n+1) = w * x(n) + (1 - w) * y(n) \tag{17}$$

where x is the input of filter, y is the output, w is a coefficient to adjust the smoothness of filtering.

As attitude is represented by quaternions in most flight control units, we need to convert it to Tait-Bryan angle roll pitch yaw. The transformation formula shows as below.

$$\begin{aligned} \text{Roll} &= a\tan 2(2 * w * x + 2 * y * z, 1 - 2 * x^2 - 2 * y^2) \\ \text{Pitch} &= a\sin(2 * w * y - 2 * z * x) \\ \text{Yaw} &= a\tan 2(2 * w * z + 2 * x * y, 1 - 2 * y^2 - 2 * z^2) \end{aligned} \tag{18}$$

The conversion between quaternions and rotation matrix is

$$R = \begin{bmatrix} 1-2*(y^2+z^2) & 2*(x*y-w*z) & 2*(x*z+w*y) \\ 2*(x*y+w*z) & 1-2*(x^2+z^2) & 2*(y*z-w*x) \\ 2*(x*z-w*y) & 2*(y*z+w*x) & 1-2*(x^2+y^2) \end{bmatrix}. \quad (19)$$

Now we can use R to get flow velocity in inertial frame $\{A\}$:

$$\text{vel}_A = R*(\text{flow\_}x, \text{flow\_}y, 0)^{\text{T}} \quad (20)$$

4.2 Training Method

The training features are chosen as the sum of roll, pitch, yaw and acceleration from all frames during a short time span t. And the output value is the flow velocity in inertial coordinate. In our experiment, t is 1 s.

In this paper, the SVM regression is implemented by Libsvm tool [11]. The training process includes the following steps: training vector formatting, selection of kernel function, parameter tuning and training dataset choosing.

For training vector formatting, due to the format requirement of Libsvm, the input training vector must meet the format

$$\langle\text{label}\rangle\langle\text{index1}\rangle\langle\text{value1}\rangle\langle\text{index2}\rangle\langle\text{value2}\rangle\ldots$$

where $\langle\text{label}\rangle$ is the output value, $\langle\text{value}\rangle$ is the feature and $\langle\text{index}\rangle$ must start from 1.

Before selection of kernel function, we take a look at formula (10). We know that trigonometric function can be written as Euler formula as shown below.

$$\cos(\theta) = \frac{e^{j\theta} + e^{-j\theta}}{2} \quad (21)$$

Due to the trigonometric function of attitude angel in rotation matrix R, an intuition is that the kernel function may have form like exponential function which leads us to choosing the radial basis function as our kernel.

$$\text{Kernel} = e^{-\text{gamma}*|u-v|^2} \quad (22)$$

Experimental results show that radial basis function has higher estimate accuracy than other kernels, which confirms our previous conjecture. Table 1 lists the four kinds of kernel functions provided by Libsvm tool. We used four kernels alternately

Table 1 The kernel function lists

Kernel 0	Linear: $\mathbf{u}'*\boldsymbol{v}$
Kernel 1	Polynomial: $(\text{gamma} * u' * v + \text{coef0})^{\text{degree}}$
Kernel 2	Radial basis: $\exp(-\text{gamma}*\|u - v\|^2)$
Kernel 3	Sigmoid: $\tanh(\text{gamma}*u' * v + \text{coef0})$

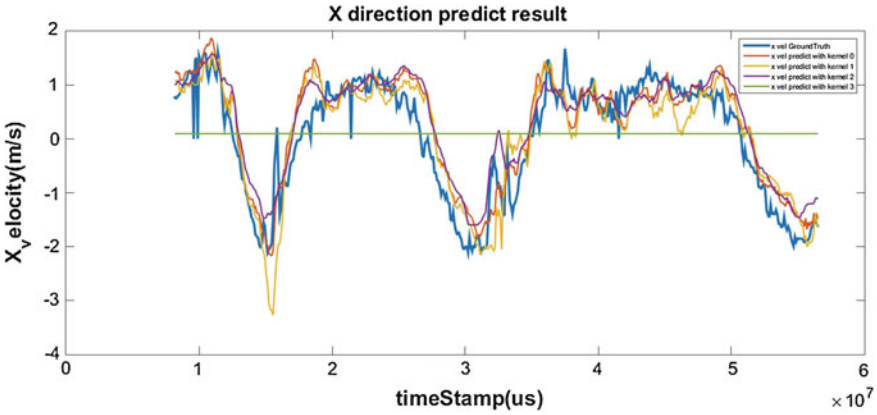

Fig. 2 The comparison of estimation result of four kernels

to train with the same training dataset and obtain corresponding estimation models and use them for prediction with the same test dataset. The result is shown in Fig. 2.

Table 2 also displays the iteration number, STD (standard deviation), SCC (square correlation coefficient) of training result using each kind of kernel.

Considering overall performance of iteration, STD and SCC, we chose the radial basis function as the final kernel.

Parameter tuning is also a very important issue in training process. Table 3 lists the main parameter used in training.

Table 2 The comparison of four kernels predict result

Kernel functions	Iteration	STD (m/s)	SCC
Kernel 0	41,730	0.4811	0.7884
Kernel 1	380,851	1.0782	0.2472
Kernel 2	831	0.4781	0.8211
Kernel 3	424	1.0356	1.1566×10^{-9}

Table 3 The list of main parameters

-c cost	Set cost value, default: 1
-p epsilon	Set ε in loss function, default: 0.1
−e tolerance	Set the termination condition, default: 0.001

Table 4 The process of parameters selecting

参数值	SCC	参数值	SCC	参数值	SCC
-c 0.1	0.77450	*-p* 0.050	0.81640	*-e* 0.0005	0.82103
-c 0.5	0.80054	*-p* 0.100	0.82018	*-e* 0.0010	0.821051
-c 1	–	*-p* 0.150	0.82074	*-e* 0.0015	0.821028
-c 1.5	0.81842	*-p* 0.175	0.821051		
-c 2	0.81962	*-p* 0.2	0.82972		
-c 2.5	0.82018				
-c 3	0.81974				

Tuning parameter is like this. We keep other parameters constant and change the target parameter a little. Step by step, we compare estimation results. Finally, we choose the value that produces the most accurate estimation. Table 4 shows the process of parameter tuning.

Notice that we only use training dataset in parameter tuning.

To choose training dataset, in the experiment, we train the regression models based on each training dataset and use each model to estimate the same test dataset. Finally compare corresponding estimation result and choose the training dataset with the best estimation result.

5 Experiment and Result Analyze

5.1 Hardware Platform

Our experiment is based on a multi-rotor aircraft platform. Figure 3 shows the hardware structure diagram. It mainly consists of pixhawk, odroid, and some other

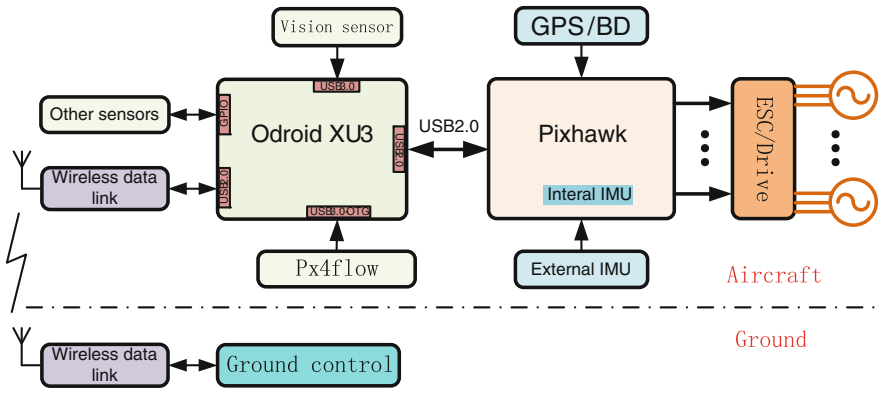

Fig. 3 Hardware structure diagram

Fig. 4 The multi-rotor aircraft used in experiment

sensors. Pixhawk based on Cortex-M4 processor is a high-performance autopilot-on-module for multi-rotors and any other robotic platform. Odroid XU3 is the world's first single-board computer with a heterogeneous multi-Processing (HMP). In our experiment, the odroid is used to collect data from all kinds of sensors including optical flow sensor, GPS, accelerometer, gyroscope, and so on. The p×4flow is an optical flow smart camera which has a native resolution of 752 × 480 pixels and calculates optical flow on a 4× binned and cropped area at 400 Hz. All sensors data can be read into odroid and sent by Wi-Fi to ground control station where the training datasets come from. Figure 4 shows the multi-rotor aircraft used for collecting data.

5.2 Data Collection

Data we need to collect include gyroscope, accelerometer, optical flow, and GPS data. When collecting data, it is required to keep UAV at a constant height, and ensure that the flight action is rich enough. For instance, you can flight along a circle path at a fixed height. We also need to collect datasets in various environments including GPS and optical flow are both available, GPS is available but optical flow is not, optical flow is available while GPS is not.

The first kind of environment needs bright light, rich ground textures and available GPS signal. The dataset collecting in this environment is used to train the estimation model, in which the feature vector contains accelerometer and gyroscope values and the output vector is velocity calculated from GPS or optical flow. The second environment contains dull light that will cause optical flow sensor producing significant error. The data from second environment is used to test the estimation result when optical flow is unavailable based on some specified trained model. The third environment has rich ground texture and bright light while GPS is unavailable.

The data is used to test the estimation result when GPS is unavailable. In order to ensure the sufficient of training and testing dataset, the acquisition time is set to be larger than 3 min in our experiment.

5.3 Training Data Checking

In our training process, the output vector is the optical flow velocity in inertial frame. Because of the sensitivity to environment of optical flow value, there is a high probability that optical flow value has significant error. On the other hand, the attitude angle yaw is influenced by magnetometer fixed on UAV body. If there is a certain intensity of magnetic field in environment which causes a significant effect on magnetometer fixed on UAV, the yaw value will have significant error too.

The way to check training data is to plot the optical flow integration path using flow value and attitude angel yaw, and compare it with path plotted from GPS value, as shown in Fig. 7. If the two paths are consistent, it means optical flow and yaw value have small error, otherwise, it means there is significant error in flow and yaw value and they cannot be used as training dataset. Because the value from optical flow is a two-dimensional vector in body frame, we need to transform it to that in inertial frame using a two-dimensional rotation matrix calculated from angle yaw. Then we integrate the flow value in inertial frame to get the flight path. Finally, we plot the GPS path as the ground-truth path and compare it with optical flow path.

5.4 Result and Analyse

Finally, we use svm-predict function provided by Libsvm to estimate velocity based on estimation model. In our experiment, the ground-truth data is optical flow velocity. We compared it with the estimated velocity to evaluate the performance of our method. In addition, we plotted the ground-truth velocity integration path and estimated velocity integration path, and compared them for more intuitive result.

Figures 5 and 6 show the comparison of ground-truth velocity and estimated velocity using our method.

Table 5 lists the STD and SCC between predicted velocity and ground-truth.

Figure 7 shows the optical flow integration path and GPS path for checking whether optical flow value is available.

Figure 8 shows the flow path and predicted velocity integration path from which we can see the obvious path drift due to the velocity estimation error. But it should be noticed that ground-truth and estimated path have consistent path shape change which tell us our method is reasonable and feasible.

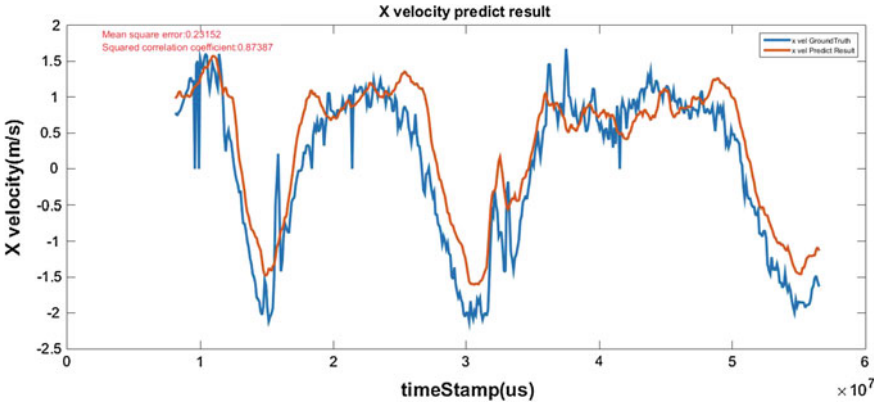

Fig. 5 The *x* direction predicts result (*yellow*) and ground-truth velocity (*blue*)

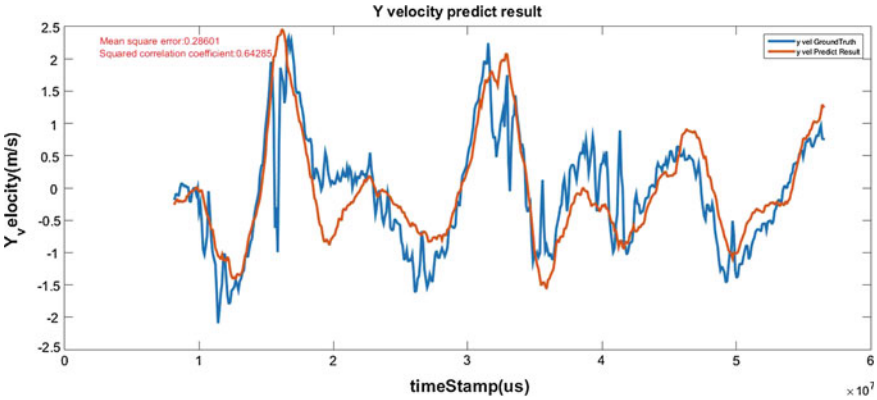

Fig. 6 The *y* direction predicts result (*yellow*) and ground-truth velocity (*blue*)

Table 5 The STD and SCC of X/Y velocity

	STD (standard deviation)	SCC (squared correlation coefficient)
X方向	0.4811 m/s	0.8739
Y方向	0.5348 m/s	0.6429

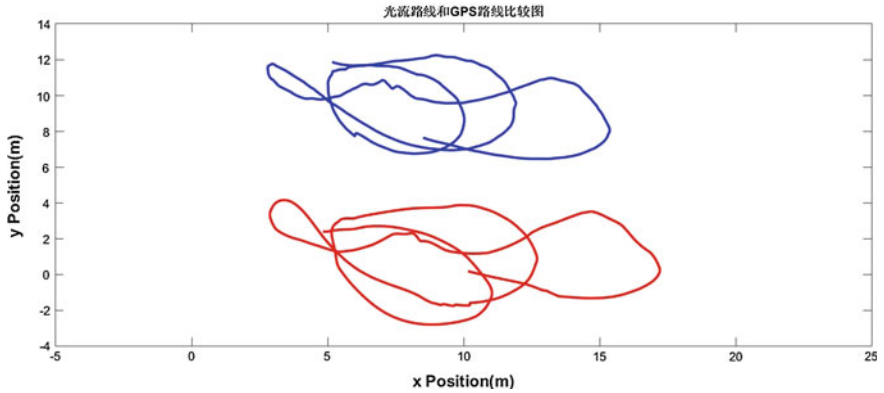

Fig. 7 The p×4flow position (*blue*) and GPS position (*yellow*)

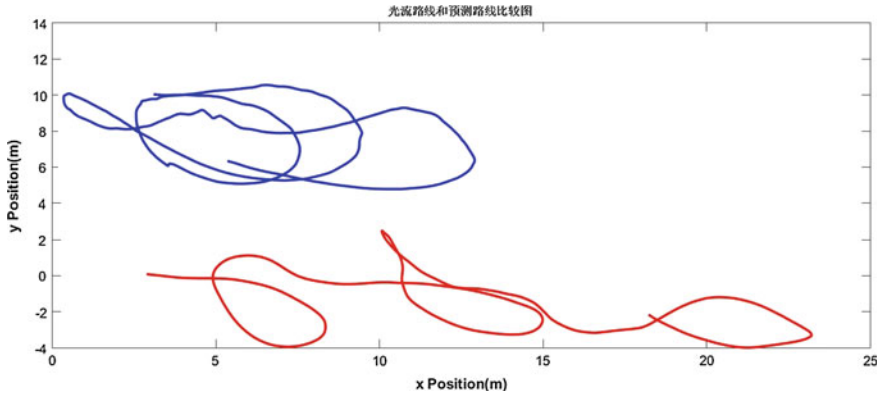

Fig. 8 The p×4flow position (*blue*) and predict position (*yellow*)

6 Conclusion

In this paper, we propose a method based on machine learning to estimate velocity of multi-rotor UAV from inertial measurements without using integration method as in a traditional inertial navigation system. Due to the input feature vector contains only accelerometer and gyroscope readings, our estimation method can work even when GPS and optical flow are both unavailable. This method can be used to assist navigation when the UAV flies into bad environment.

We carried out the experiment in attitude-hold flight mode. We choose optical flow velocity as ground-truth. The result shows that the correlation degree between estimation velocity and Ground-Truth is 0.8739 at X direction and 0.6429 at Y direction. In addition, we plot the estimation path and ground-truth path for comparing intuitively.

In the future research, we will extend our work to free flight mode and wind resisting flight mode, to make our method more flexible to different applications.

Acknowledgment This work is supported by the National Natural Science Foundation of China under Grant 61573242, in partly by the Shanghai Science and Technology Committee under Grant 14511100300, 15511105100 and partly sponsored by Shanghai Pujiang Program (No. 14PJ1405000) and Qingpu Industry-University-Research Project (2015-4).

References

1. Yang M (2010) Research on small strapdown inertial navigation system. Central South University
2. Titterton D, Weston J (2005) Strapdown inertial navigation technology—2nd edition (book review). IEEE Aerosp Electron Syst Mag 20(7):33–34
3. Honegger D, Meier L, Tanskanen P et al (2013) An open source and open hardware embedded metric optical flow CMOS camera for indoor and outdoor applications. In: 2013 IEEE international conference on robotics and automation (ICRA). IEEE, pp 1736–1741
4. Hrabar S, Sukhatme GS, Corke P et al (2005) Combined optic-flow and stereo-based navigation of urban canyons for a UAV. In: 2005 IEEE/RSJ international conference on intelligent robots and systems, (IROS 2005). IEEE, pp 3309–3316
5. Barber DB, Griffiths SR, Mclain TW et al (2007) Autonomous landing of miniature aerial vehicles. J Aerosp Comput Inf Commun 4(5):770–784
6. Romero H, Salazar S, Lozano R (2009) Real-time stabilization of an eight-rotor UAV using optical flow. IEEE Trans Rob 25(4):809–817
7. Mahony R, Kumar V, Corke P (2012) Multirotor aerial vehicles: modeling, estimation, and control of quadrotor. IEEE Robot Amp Amp Autom Mag 19(3):20–32
8. Platt J (1999) Fast training of support vector machines using sequential minimal optimization. Adv Kernel Methods Support Vector Learn 3
9. Cheng X (2012) Study on geometric algorithm of linear optimization problems with equality constraints. Fujian Normal University
10. Deng N, Tian Y (2009) The theory, algorithm and expansion of support vector machine. Science Press, Beijing
11. Chang CC, Lin CJ (2015) LIBSVM—a library for support vector machines. http://www.csie.ntu.edu.tw/～cjlin/libsvm/. Accessed 8 Dec 2015

The Hybrid GNSS-Terrestrial Localization Method Based on the Augmented UKF

Da-peng Li, Bing Liu, Yi Qu, Ting Liu, Ling-chuan Zeng and Ying-kui Gong

Abstract The research progress of the hybrid GNSS-terrestrial localization and its mathematical model are introduced first. The problem of filter divergence applying the augmented unscented Kalman filter to realize the GNSS-terrestrial localization is analyzed. In order to prevent the filter divergence, a cycle reset mechanism for the state estimate variance matrix is adopted during the joint state estimation. The simulation results show that the proposed method could make the filter working steadily meanwhile improve the positioning accuracy.

Keywords Hybrid GNSS-Terrestrial localization · Cycle reset · UKF · Cooperative positioning

1 Introduction

In recent years, with the rapid development of the Internet of things, such as mobile internet, vehicle network etc., the conventional single-user positioning extends to the multi-user one which is called cooperative positioning. The technique of multi-user cooperative localization has more navigation sources (reference points), and better reliability theoretically than the traditional one.

Wymeersch [1] and Costa [2] designed the schemes of Least Squares (LS) and Multidimensional Scaling for wireless networks positioning in the situations of global navigation satellite system (GNSS) unavailable. However, such schemes could not make full use of the prior information and are unsatisfactory in the precision. Peng [3] and Shao [4] propose the cooperative localization methods for vehicular ad hoc networks. These methods only work for the vehicle on the ground.

This work was supported by National Natural Science Foundation of China (91438207).

D. Li (✉) · B. Liu · Y. Qu · T. Liu · L. Zeng · Y. Gong
Academy of Opto-Electronics, Chinese Academy of Sciences, Beijing, China
e-mail: lidapeng@aoe.ac.cn

J. Sun et al. (eds.), *China Satellite Navigation Conference (CSNC) 2016 Proceedings: Volume II*, Lecture Notes in Electrical Engineering 389,
DOI 10.1007/978-981-10-0937-2_42

Richter [5] and Yang [6] use the double difference method of pseudorange to improve the navigation performance. But the inter vehicle distance information is neglected.

As can be seen from the above researches, cooperative positioning is developed from the cooperative localization of WSN, and its application scope extends to the GNSS related fields. However, these researches do not explore the hybrid situation of the space-based navigation sources and the ground users.

Heinrichs [8] and Mensing [9] apply EKF and LS to realize the hybrid cooperative positioning, but without considering the user movement. Caceres [10] provides a method including the user movement. However, it does not work for a long time. The filter got diverged after 10 s, which is demonstrated in the Sect. 3.3.

In this paper, a novel method based on the cycle reset of the state estimate variance matrix is proposed to realize the robust hybrid GNSS-terrestrial cooperative positioning.

2 Problem Formulation

Given the Hybrid GNSS-terrestrial cooperative positioning network with M peers and S satellites depicted in Fig. 1, where the navigation satellites broadcast navigation signals and the users on the ground communicate to each other by a certain communication network (e.g., Ultra Wide-Band (UWB) or WiFi) providing the ability of short/medium distance peer-to-peer ranging.

The problem of localization is formulated as: the state estimation of each node $\tilde{x}_m^t$ and its covariance matrix $\tilde{\mathbf{P}}_m^t$ at each time t, given the vector of pseudorange measurements $\rho_m^t \triangleq \{\rho_{\mathrm{sm}}^t\}$, covariance matrix $\tilde{\mathbf{R}}_{\mathrm{sm}}^t \triangleq \mathrm{diag}\left(\{\sigma_{\mathrm{sm}}^2\}\right)$ and positions $\mathbf{X}_{\mathrm{sm}}^t \triangleq \{x_s^t\}$ for all available satellites $s \in S_m^t$; and terrestrial range measurements

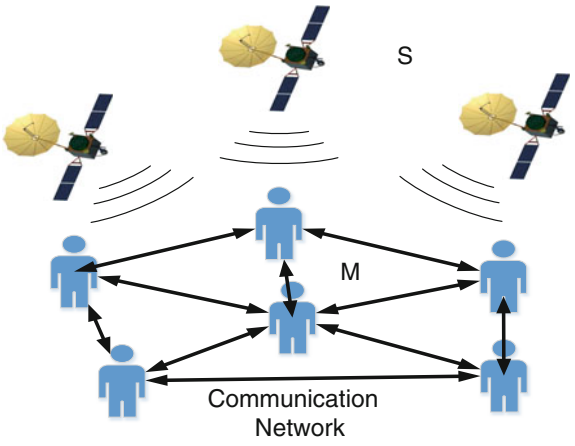

Fig. 1 The hybrid GNSS-terrestrial cooperative positioning network

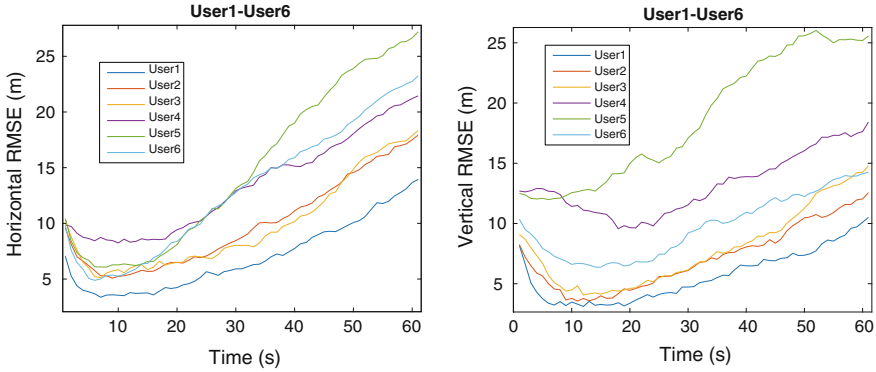

Fig. 2 The mean horizontal/vertical RMSE of user1 to user6 (time from 10 s to 60 s)

$r_m^t \triangleq \{r_{\mathrm{nm}}^t\}$, covariance matrix $\mathbf{R}_{\mathrm{nm}}^t \triangleq \mathrm{diag}\left(\{\sigma_{\mathrm{nm}}^2\}\right)$, and peer position estimates $\hat{X}_{\mathrm{nm}}^t \triangleq \{\hat{x}_n\}$ and $P_{\mathrm{nm}}^t \triangleq \{\hat{P}_n\}$ for all available peers $n \in \mathrm{M}_m^t$, at node m (Fig. 2).

2.1 System Model

The system time evolution is modeled by

$$\begin{aligned} \tilde{x}_m^t &= f\left(\tilde{x}_m^{t-1}, \tilde{\omega}_m^t\right) \\ \tilde{\omega}_m^t &\sim N\left(\mathbf{0}, \tilde{\mathbf{Q}}_m^t\right) \end{aligned} \tag{1}$$

where $f(\cdot)$ is the state transition function, $\tilde{\omega}_m^t$ is the process noise taken as the nonlinearities and perturbations on the system, modeled by a vector of random noise normally distributed with zero mean and covariance matrix $\tilde{\mathbf{Q}}_m^t$.

Since we focus on the positioning of low dynamic users on the ground, the position time (PT) dynamic system in Ref. [10] is chosen. The functions and state vectors are:

$$\begin{aligned} \tilde{x}_m^t = f\left(\tilde{x}_m^{t-1}, \tilde{\omega}_m^t\right) &= \mathbf{F}^t \cdot \tilde{x}_m^{t-1} + \mathbf{W}^t \cdot \tilde{\omega}_m^t \\ &= \mathbf{I} \cdot \tilde{x}_m^{t-1} + \Delta t \cdot \mathbf{I} \cdot \tilde{\omega}_m^t \\ \tilde{\mathbf{Q}}_m^t &= \mathrm{diag}\left(\left[\sigma_{\dot{\mathrm{x}}\mathrm{m}}^2, \sigma_{\dot{\mathrm{y}}\mathrm{m}}^2, \sigma_{\dot{\mathrm{z}}\mathrm{m}}^2, \sigma_{\mathrm{bm}}^2\right]\right) \end{aligned} \tag{2}$$

Where $\tilde{x}_m^t \triangleq [x_m^t, y_m^t, z_m^t, b_m^t]$, (x_m^t, y_m^t, z_m^t) is the mth user position given by Earth Centered Earth Fixed (ECEF) coordinates, b_m^t is the clock bias δt_m with respect to the GNSS time, expressed in meters ($b_m = c \cdot \delta t_m$), $\mathbf{I}$ is the identity matrix of size 4 × 4, and $\Delta t = 1$ s, which is the time elapsed between the previous $t-1$ and current time t.

2.2 Observation Model

The system is observed through pseudorange and terrestrial Peer-to-Peer (P2P) range measurements $z_m^t = \left[\rho_m^t \; r_m^t\right]^{\mathrm{T}}$, having an observation function $h(\cdot)$

$$\begin{aligned} z_m^t &= h\left(\tilde{x}_m^t, \mathbf{X}_{\mathrm{sm}}^t, \mathbf{X}_{\mathrm{nm}}^t, v_m^t\right) \\ &= \begin{bmatrix} h_s(\tilde{x}_m^t, \mathbf{X}_{\mathrm{sm}}^t, v_{\mathrm{sm}}^t) \\ h_n(\tilde{x}_m^t, \mathbf{X}_{\mathrm{nm}}^t, v_{\mathrm{nm}}^t) \end{bmatrix} \\ v_m^t &\sim N\left(\mathbf{0}, \mathbf{R}_m^t\right) \end{aligned} \tag{3}$$

Where $v_m^t = \left[v_{\mathrm{sm}}^t \, v_{\mathrm{nm}}^t\right]^{\mathrm{T}}$ is the observation noise vector, a column vector of random variables, which affects both pseudorange and terrestrial range measurments, normally distributed with zero mean and covariance matrix

$$\mathbf{R}_m^t = \begin{bmatrix} \mathbf{R}_{\mathrm{sm}}^t & \mathbf{0} \\ \mathbf{0} & \mathbf{R}_{\mathrm{nm}}^t \end{bmatrix} \tag{4}$$

(1) Pseudorange measurements observation function is:

$$\begin{aligned} z_s =& h_s(\tilde{x}_m^t, x_s^t) = \left\| x_m^t - x_s^t \right\| + b_m \\ =& \sqrt{\left(\mathrm{x}_m^t - \mathrm{x}_s^t\right)^2 + \left(\mathrm{y}_m^t - \mathrm{y}_s^t\right)^2 + \left(\mathrm{z}_m^t - \mathrm{z}_s^t\right)^2} + \mathrm{b}_m \end{aligned} \tag{5}$$

(2) Terrestrial range measurements observation function in line-of-sight (LoS) condition is:

$$\begin{aligned} z_n =& h_n(\tilde{x}_m^t, x_n^t) = \left\| x_m^t - x_n^t \right\| \\ =& \sqrt{\left(\mathrm{x}_m^t - \mathrm{x}_n^t\right)^2 + \left(\mathrm{y}_m^t - \mathrm{y}_n^t\right)^2 + \left(\mathrm{z}_m^t - \mathrm{z}_n^t\right)^2} \end{aligned} \tag{6}$$

3 Cooperative Positioning Based on the Augmented UKF

With the system and observation model above, a method need to be chosen to estimate the user states (location and their uncertainty). Conventional methods are LS, Kalman filter and particle filter, etc. Considering the balance of computation and accuracy, the UKF [11] is adopted.

3.1 Prediction

The state is augmented with the process noise vector

$$\begin{aligned} x_a^{t-1} &= \left[(\tilde{x}_m^{t-1})^T, (\tilde{\omega}_m^t)^{\mathrm{T}} \right]^{\mathrm{T}} \\ \mathbf{P}_a^{t-1} &= \begin{bmatrix} \tilde{\mathbf{P}}_m^{t-1} & \mathbf{0} \\ \mathbf{0} & \tilde{\mathbf{Q}}_m^t \end{bmatrix} \end{aligned} \tag{7}$$

then the so called sigma points are computed with

$$\begin{aligned} \chi_0^{t-1} &= x_a^{t-1} \\ \chi_i^{t-1} &= x_a^{t-1} + \left(\sqrt{(L+\lambda)\,\mathbf{P}_a^{t-1}} \right)_i, i = 1, \ldots, L \\ \chi_i^{t-1} &= x_a^{t-1} - \left(\sqrt{(L+\lambda)\,\mathbf{P}_a^{t-1}} \right)_{i-L}, i = L+1, \ldots, 2L \end{aligned} \tag{8}$$

where $\left(\sqrt{\cdot}\right)_i$ is the ith column of the Cholesky decomposition, L is the dimension of the augmented state, and Sigma points are propagated through the state transition function

$$\chi_i^{t|t-1} = f(\chi_i^{t-1}),\ i = 0, \ldots, 2L \tag{9}$$

and then used to estimate the predicted a priori state and covariance

$$\begin{aligned} \hat{x}^{t|t-1} &= \sum_{i=0}^{2L} w_i^{\mu}\, \chi_i^{t|t-1} \\ \mathbf{P}^{t|t-1} &= \sum_{i=0}^{2L} w_i^{\mu} \left[\chi_i^{t|t-1} - \hat{x}^{t|t-1} \right] \left[\chi_i^{t|t-1} - \hat{x}^{t|t-1} \right]^{\mathrm{T}} \end{aligned} \tag{10}$$

$$\begin{aligned} w_0^{\mu} &= \frac{\lambda}{L+\lambda} \\ w_0^{\Sigma} &= \frac{\lambda}{L+\lambda} + (1 - \alpha^2 + \beta) \\ w_j^{\mu} &= w_j^{\Sigma} = \frac{1}{2(L+\lambda)} \\ \lambda &= \alpha^2 (L+\kappa) - L \end{aligned} \tag{11}$$

and α, β, and κ are tunable, typically 10^{-3}, 2 and 0, respectively.

3.2 Update

Then the Sigma points propagated are projected through the observation function

$$\varsigma_i^t = h\left(\chi_i^{t|t-1}\right),\ i = 0, \ldots, 2L \tag{12}$$

and recombined to estimate the predicted measurement vector, measurement covariance and state-measurement cross-covariance matrix

$$\begin{aligned}
\hat{z}^t &= \sum_{i=0}^{2L} w_i^{\mu}\, \varsigma_i^t \\
\hat{\mathbf{S}}^t &= \sum_{i=0}^{2L} w_i^{\Sigma} \left[\varsigma_i^t - \hat{z}^t\right] \left[\varsigma_i^t - \hat{z}^t\right]^{\mathrm{T}} + \mathbf{R}^t \\
\hat{\mathbf{P}}_{x|z}^t &= \sum_{i=0}^{2L} w_i^{\Sigma} \left[\chi_i^{t|t-1} - \hat{x}^{t|t-1}\right] \left[\varsigma_i^t - \hat{z}^t\right]^{\mathrm{T}} + \mathbf{R}^t
\end{aligned} \tag{13}$$

Finally, Kalman gain is computed with Eq. 14, while state and covariance estimates are corrected with Eq. 15.

$$\begin{aligned}
\mathbf{P}_{\tilde{x}|z}^t &= \tilde{\mathbf{P}}_m^{t|t-1} (\mathbf{H}^t)^{\mathrm{T}} \\
\mathbf{K}^t &= \mathbf{P}_{\tilde{x}|z}^t (\mathbf{S}^t)^{-1}
\end{aligned} \tag{14}$$

$$\begin{aligned}
\hat{x}^t &= \hat{x}^{t|t-1} + \mathbf{K}^t \Delta z^t \\
\hat{\mathbf{P}}^t &= \hat{\mathbf{P}}^{t|t-1} - \mathbf{K}^t \mathbf{S}^t (\mathbf{K}^t)^{\mathrm{T}}
\end{aligned} \tag{15}$$

3.3 Cooperative Positioning

So far we have described the augmented UKF, but we have not talked about cooperation. The difference between single user positioning and the cooperative one is the information shared among peers and the self-adaption of measure uncertainty. The information shared is composed basically of the distance measurement, the position estimate, and the measure uncertainty in the form of variance.

The measure uncertainty adaption is critical to the performance of the positioning network. If the uncertainty obtained is accurate enough, the filter can correctly adjust the filter gain, which could depress the outliers and make the filter working robust. Otherwise the filter gain will be wrong and the outliers would be amplified, which eventually leads to divergence.

A self-adaption method for the measure uncertainty of peers is proposed by the Ref. [10]. It considers the error of distance measurement and the position estimate receiving from other users. The designed self-adaption method for the measure uncertainty (variance matrix) is as follows:

$$\left(\sigma_{\mathrm{nm}}^{t}\right)_{\mathrm{new}}^{2}=\left(\sigma_{\mathrm{nm}}^{t}\right)_{\mathrm{old}}^{2}+\mathbf{tr}\left(\mathbf{P}_{n\rightarrow m}^{t}\right) \tag{16}$$

Where $\left(\sigma_{\mathrm{nm}}^{t}\right)_{\mathrm{old}}^{2}$ is the original ranging error, $\mathbf{tr}\left(\mathbf{P}_{n\rightarrow m}^{t}\right)$ is the trace of the estimate variance matrix sent from the mth user to the nth user, $\left(\sigma_{\mathrm{nm}}^{t}\right)_{\mathrm{new}}^{2}$ is the ranging error adjusted.

However, this self-adaption method does not work when the $\mathbf{P}_{n\rightarrow m}^{t}$ is not accurate enough. Keeping simulation settings of the Ref. [10] except the simulation time from 10 to 60 s, we do 100 times the Monte Carlo simulation. The results are below:

We can see, as time going on, the horizontal/vertical estimate errors reduce first, and after that increase (close to or more than 20 m). Additionally, the positioning accuracy of the user 1 who receives the most navigation sources, have been pull down by other poorer positioning users, and the filter goes diverging gradually.

Draw the mean trace of user position variance matrix and the mean of measure variance of user 1–6 as follows:

Figure 3 indicates, as time going on, each mean trace of user position variance matrix is decreasing gradually, while the horizontal/vertical position errors are decreasing first and after that increasing as can be seen from Fig. 2. It means the estimate of each user position variance matrix does not agree with the truth and is not accurate enough all the time. That leads the $\left(\sigma_{\mathrm{nm}}^{t}\right)^{2}$ of $\mathbf{R}_{\mathrm{nm}}^{t}$ to decrease when apply the self-adaption method proposed by Ref. [10] (decrease to 5 at 60 s). Therefore, a mismatching filter gain is obtained which leads to divergence eventually. In this paper, we propose a cycle reset mechanism for the user state estimate

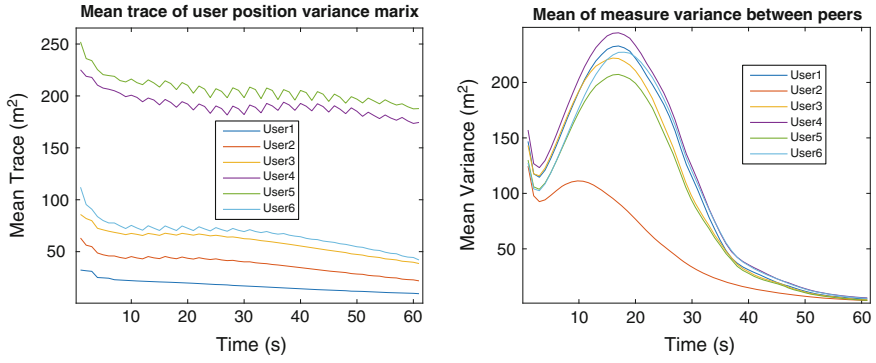

Fig. 3 The mean trace of user position variance matrix and the mean of measure variance

variance matrix to overcome the above problems. Define the reset matrix of the m-th user state estimate variance as follows:

$$\mathbf{P}_m^{\text{reset}} = \begin{pmatrix} \left(\sigma_x^{\text{reset}}\right)^2 \cdot \mathbf{I}_{4\times 4} & \mathbf{0} \\ \mathbf{0} & \left(\sigma_w^{\text{reset}}\right)^2 \cdot \mathbf{I}_{4\times 4} \end{pmatrix} \tag{17}$$

where σ_x^{reset} is the upper limit of the user state standard deviation deteriorated during the location estimation in a short time, σ_w^{reset} is the upper limit of the process noise standard deviation deteriorated during the estimation in a short time.

During the process of filtering, the $\mathbf{P}_m^t$ of mth user is reseted by $\mathbf{P}_m^{\text{reset}}$ every T_{reset} second, described as follows:

$$\left\{\mathbf{P}_m^t = \mathbf{P}_m^{\text{reset}} \middle| \ (t, T_{\text{reset}}) = 0\right\}, m \in M \tag{18}$$

where $(\cdot)$ is the modulo function.

In summary, the pseudo code of the proposed algorithm is:

Initial estimates $\hat{x}_m^0, \hat{\mathbf{P}}_m^0 \ \forall m$
for $t = 1$ **to** T **do**
  Predict $\hat{x}_m^{t|t-1}, \hat{\mathbf{P}}_m^{t|t-1}$ *with Eq.*10
  for $l = 1$ **to** *Niter* **do**
    for all *nodes m* **in parallel do**
      if$(l == 1)$ *Broadcast position predictions* $\hat{x}_m^{t|t-1}$ *and* $\hat{\mathbf{P}}_m^{t|t-1}$
      else *Broadcast position estimations* $\hat{x}_m^t$ *and* $\hat{\mathbf{P}}_m^t$
      end if
      Receive messages from neighbors $\hat{x}_{n\to m}$ *and* $\hat{\mathbf{P}}_{n\to m}$
      *Compute state sigma points with Eq.*8
      Project sigma points $\varsigma_i^t = h(\chi_i^{t|t-1})$ *with Eq.*5 − 6
      Adapt $\left(\sigma_{nm}^t\right)^2$ *with Eq.*16 *and reconstruct* $\mathbf{R}_m^t$
      Compute $\hat{z}^t, \mathbf{S}^t, \hat{\mathbf{P}}_{x|z}^t, \mathbf{K}^t, \hat{x}^t, \hat{\mathbf{P}}^t$ *with Eqs.*13 − 15
      if$(t == T_{reset})$ $\hat{\mathbf{P}}^t = \mathbf{P}^{reset}$ **end if**
    end for in parallel
  end for
end for

Where *Niter* is the maximum number of iterations, $\hat{x}_{n\to m}, \hat{\mathbf{P}}_{n\to m}$ are the estimates of the state and the variance matrix receiving from neighbors. When the first iteration (l = 1), the predictive value $\hat{x}_m^{t|t-1}, \hat{\mathbf{P}}_m^{t|t-1}$ are used to substitute the estimate ones which are unavailable when the filter beginning.

4 Simulations

In this section we compare the hcUKF method [10] with the proposed one in a static 3-D scenario. Satellites' and users' positions and the scenario are the same depicted in Ref. [10].

Initial guesses are set 10 m away of the actual position. The process noise variance matrix $\mathbf{Q}_m^t = 4\,\mathbf{I}$, the Pseudorange and P2P range measurements are corrupted by additive white Gaussian noise with standard deviation $\sigma_{\text{sm}} = 5\,m$ and $\sigma_{\text{nm}} = 0.2\,m$ respectively. The simulation parameters are set as: T = 60 s, Niter = 3, T_{reset} = 5 s, $\sigma_x^{\text{reset}} = 15\,m$, $\sigma_w^{\text{reset}} = 1\,m$ (obtained by experiments). We do 100 times Monte Carlo comparison experiments. Results are as follows:

From the comparison of the error cumulative distribution function, we can see the proposed algorithm raises the proportion of the high accuracy estimation comparing with the hcUKF. The probability of horizontal positioning accuracy within 10 m is enhanced from 0.665 to 0.872. The probability of vertical positioning accuracy within 10 m is enhanced from 0.656 to 0.779.

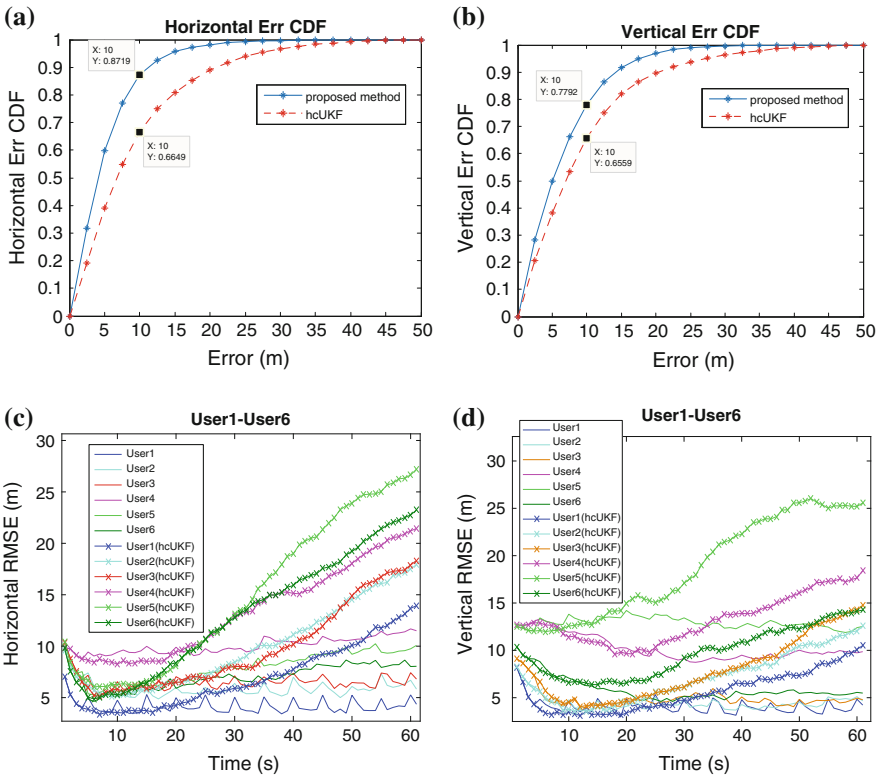

Fig. 4 **a**, **b** The comparison of the error cumulative distribution function. **c**, **d** The mean results of 100 times Monte Carlo experiments

The mean results of 100 times Monte Carlo comparison experiments are shown blow (Fig. 4).

As can be seen, the hcUKF method is diverging and the proposed one avoids the influence of the poor accuracy user to the good one, which keeps the multi-user filtering in a steady way.

5 Conclusion

With the rapid development of the Internet of things, the communication among terminal users is easier than before. The advancing inter-connectivity of users makes the multi-user cooperative positioning possible. Cooperative positioning technology could utilize more navigation information, therefore, has more reliable performance theoretically, and attracts considerable attention. However, the multi-user stable filtering is a big challenge, especially to avoid the bad influence among users. In this paper, a method based on the cycle reset of the state estimate variance matrix is proposed to realize the robust hybrid GNSS-terrestrial positioning. Future work will consider the change of navigation source number and the error characteristics.

References

1. Wymeersch H, Lien J, Win MZ (2009) Cooperative localization in wireless networks. Proc IEEE 97(2):427–450
2. Costa JA, Patwari N, Hero III AO (2006) Distributed weighted multidimensional scaling for node localization in sensor networks. ACM Trans Sens Netw (TOSN) 2
3. Peng X et al. (2013) Cooperative localization for vehicular ad hoc networks. J Comput Res Dev 50(6):1210–1216 (Ch)
4. Shao Z et al (2013) An algorithm based on cooperation and doppler carrier frequency offset for vehicle positioning. J SE Univ 43(6):1135–1140 (Ch)
5. Richter E, Obst M, Schubert R, Wanielik G (2009) Cooperative relative localization using vehicle-to-vehicle communications. In: Information fusion 2009, FUSION '09, 12th international conference on, pp 126–131
6. Yang D, Zhao F, Liu K, Lim HB, Frazzoli E, Rus D (2012) A GPS pseudorange based cooperative vehicular distance measurement technique. In: VTC spring, IEEE, pp 1–5
7. Heinrichs G, Mulassano P, Dovis F (2004) A hybrid positioning algorithm for cellular radio networks by using a common rake receiver. Symp Pers Indoor Mobile Radio 2347–2351
8. Mensing C, Sand S, Dammann A (2009) GNSS positioning in critical scenarios: hybrid data fusion with communications signals. In: Proceedings of the international workshop on synergies in communications and localization (SyCoLo), Dresden

9. Mauricio A, Caceres (2010) Hybrid GNSS-ToA localization and tracking via cooperative unscented kalman filter. In: IEEE 21st international symposium on personal, indoor and mobile radio communications workshops, pp 272–276
10. Julier SJ, Uhlmann JK (1997) New extension of the kalman filter to nonlinear systems. Proc SPIE 3068:P182–P193

Research About Stereo Positioning Using Multi-source Remote Sensing Images

Yingying Li, Hao Wu, Xiaokun Sun and Jie He

Abstract Currently it is very hard to satisfy data source condition of traditional homologous stereo, which means the utilization of existing data is very low. In view of this situation, this paper presents a stereo location process model which can incorporate any number ratio CCD and SAR images with certain overlapping area into a uniform stereo imaging system. A series of algorithm are designed including unified Rational Function Model (RFM) construction, image space stereo adjustment, space forward intersection. A large number of in-orbit tests proved that our method could give full play to complementary advantages of heterologous multi-view images, greatly improve the possibility of stereo location based on existing remote sensing image, while ensuring the final location accuracy. Detail error law analysis under different data combinations is provided for perspective into practical applications.

Keywords Multi-view · Stereo positioning · Rational function model (RFM) · Forward intersection

1 Introduction

With the breakthrough of location, navigation, attitude, time and other key measurement technology on high-resolution satellite platform, stereo location has become an important trend in the field of remote sensing. However, the potential of

Fund Project: the National Natural Science Foundation of China (61501036); National high Resolution Earth Observation Youth Innovation Fund (GFZX04060103-5).

Y. Li (✉) · H. Wu · X. Sun · J. He
Institute of Remote Sensing Information of Beijing, No. 2,
Qinghe Xiaoying East Road, Haidian 100192, Beijing, China
e-mail: 110836315@qq.com

J. Sun et al. (eds.), *China Satellite Navigation Conference (CSNC) 2016 Proceedings: Volume II*, Lecture Notes in Electrical Engineering 389,
DOI 10.1007/978-981-10-0937-2_43

stereo location using different remote sensor data is far from being fully tapped, processing of homologous data is still the main means of producing high-precision DEM [1–3]. But such data acquisition is very harsh and costly, such as three linear array camera, InSAR, etc. Because of the high requirements of satellite design and platform flexibility, homologous location is difficult to be effectively widely applied.

Currently linear CCD and SAR have become the mainstream remote sensors. They have advantages and disadvantages respectively: the SNR of CCD is high, but its stereo visual effect is limited; SAR has the unique advantages of all-weather all-time, especially its side view characteristic make it sensitive for height measurement. With greatly improved image resolution, SAR gradually becomes a good complement for optical remote sensing, and lead to auxiliary location purpose. With the progress of China's space technology, remote sensing images which can be acquired in the type, coverage, resolution and other aspects have been greatly enriched. Then how to use geometric constraints between these heterologous images to perform target area stereo location has become a key issue to be solved, while fully tapping the data availability, abandoning the traditional homologous harsh restrictions on the data source, ensuring the accuracy of stereo location. At present, the research of stereo location with heterologous active and passive remote sensing data is very rare. In literature [4, 5] a large number of control points were independently used to do outside orientation. Under the multi-image input, it means although tight theoretic, but hard control point requirement, many solving parameters, and numerical solver instability. Its verification was carried out based on a small amount of images without in-depth error analysis. The image selection is also some blind and subjective.

Based on this, we propose a stereo approach with multi-source remote sensing images, trying to obtain high-precision data regardless of homologous shackles, and reduce production costs. Our image data can be acquired from different perspective, by different load types, with any number proportion, overlapping each other. Ground points are formed respectively on CCD and SAR images. These two imaging mechanisms are completely different. Their weak correlation is good for the complementarity to construct stereo equations. Compared with the homologous method, the sensors are not integrated on the same satellite platform, and CCD and SAR images are acquired from different height and angle, which lead to a more benign form of observation structure. Especially when the observation beam does not contain each other, the largest intersection angle of its ground point will increase. These factors have provided a good theoretical basis and application advantages for heterologous application. Final we fully verify the feasibility of the scheme through a large number of in-orbit data tests. And detailed analysis of the error law under different data combinations provides a reliable basis for heterologous practical applications.

2 Stereo Positioning Principles Using Heterologous Remote Sensing Images

2.1 RFM Model Construction

It is a premise for heterologous stereo to unify both the totally different CCD and SAR imaging mechanism into equivalent image geometry model. With the generic advantages of rational function model (RFM) [6–8], it is easy to build any homologous or heterologous, two or more location model (Fig. 1). Moreover we can reduce the amount of computation and overcome the iterative non-convergence problem. For any image, the polynomial ratio relationship between image coordinates and geographic coordinates in RFM model is as follows

$$Y = \frac{\mathrm{Num}_l(P, L, H)}{\mathrm{Den}_l(P, L, H)}, \; X = \frac{\mathrm{Num}_s(P, L, H)}{\mathrm{Den}_s(P, L, H)}$$

(X, Y) and (P, L, H) denote the regularization value of image coordinates (*sample, line*) and geographic coordinates (*latitude, longitude, height*). 10 regularization parameters and 80 coefficients for the numerator and denominator polynomial are stored together in RPC file. In this paper, we use a ground independent way to compute RPC. The correspondence between the ground point grid and the image plane is set up as the control points using image strict geometric model. Then the RPC parameters can be solved based on these grid point coordinates. RPC represent the conversion relationship between image coordinates and geographic coordinates.

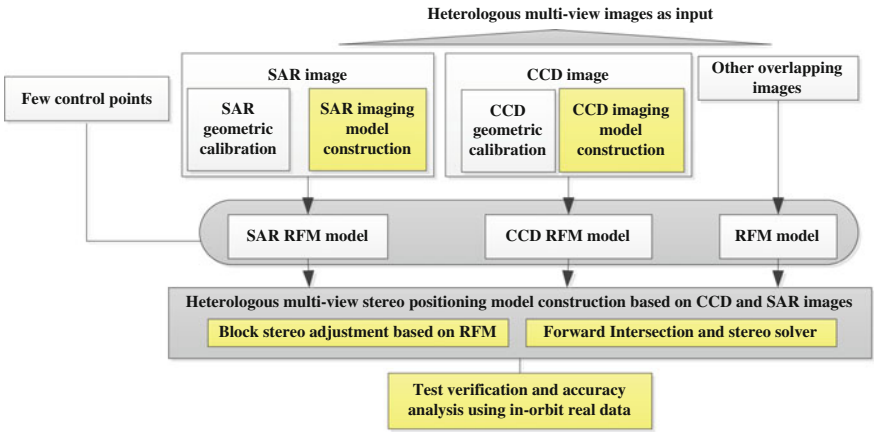

Fig. 1 Flow of heterogeneous multi-view stereo location

Some system error, such as CCD azimuth distortion, can be compensated from the source geometric model by calibration or other means to improve RFM accuracy under uncontrolled condition. In this paper, the Henan scaling field is used to do highly precise CCD image calibration of internal and external orientation elements [9], external calibration devices (such as a corner reflector) are used to conduct the SAR radar systematic delay error [10] calibration.

2.2 Block Stereo Adjustment Based on RFM

Due to some systematic error brought by alternative RFM imaging geometry, stereo adjustment is required to correct the model to fit actual imaging situation better [11–13]. In this paper, RFM stereo adjustment based on image compensation is adopted. Using the connection point constraint and control points, the affine transformation model on the image plane can be established to correct systematic error in row and line direction. RFM location accuracy can be improved further. More accurate 3D model can be set up with little or no control point.

Affine transformation is defined as

$$\begin{cases} F_x = \alpha_0 + \alpha_1 \cdot \text{sample} + \alpha_2 \cdot \text{line} - x = 0 \\ F_y = \beta_0 + \beta_1 \cdot \text{sample} + \beta_2 \cdot \text{line} - y = 0 \end{cases}$$

$\alpha_0, \alpha_1, \alpha_2, \beta_0, \beta_1, \beta_2$ denote affine transformation parameters. x, y denote the measured image coordinates of known points. Error equations for each image are constructed based on a number of connection points and control points to solve the adjustment parameters according to the least squares method. By solving affine transformation model parameters, the translation error due to sensor position and attitude, the rotation and scale error caused by GPS and inertial navigation system can be absorbed.

2.3 Forward Intersection

For heterologous stereo multi-view images, based on the RPC parameters and affine transformation parameters of each image, the ground coordinates can be solved by using space intersection for each stereo tie point obtained through the tie point matching method.

RFM forward intersection means to solve space coordinates of corresponding image point coordinates through RPC parameters of two or more than two images. If the point appears on the n images, 2n equations can be set up. For example, the solver equation of three-view images can be as the following:

$$\begin{cases} \mathrm{Num}_{\mathrm{line},1}(P,L,H) - \mathrm{line}_1 \cdot \mathrm{Den}_{\mathrm{line},1}(P,L,H) = 0 \\ \mathrm{Num}_{\mathrm{sample},1}(P,L,H) - \mathrm{sample}_1 \cdot \mathrm{Den}_{\mathrm{sample},1}(P,L,H) = 0 \end{cases}$$
$$\begin{cases} \mathrm{Num}_{\mathrm{line},2}(P,L,H) - \mathrm{line}_2 \cdot \mathrm{Den}_{\mathrm{line},2}(P,L,H) = 0 \\ \mathrm{Num}_{\mathrm{sample},2}(P,L,H) - \mathrm{sample}_2 \cdot \mathrm{Den}_{\mathrm{sample},2}(P,L,H) = 0 \end{cases}$$
$$\begin{cases} \mathrm{Num}_{\mathrm{line},3}(P,L,H) - \mathrm{line}_3 \cdot \mathrm{Den}_{\mathrm{line},3}(P,L,H) = 0 \\ \mathrm{Num}_{\mathrm{sample},3}(P,L,H) - \mathrm{sample}_3 \cdot \mathrm{Den}_{\mathrm{sample},3}(P,L,H) = 0 \end{cases}$$

Subscript 1, 2, 3 of (*sample, line*) respectively represent the three images. The 3D coordinates of ground tie points can be calculated by the least squares method.

3 Factor Analysis of Error Propagation

3.1 Measurement Error of Tie Points

The nature of eye intersection is the existence of three-dimensional parallax, therefore the measurement accuracy of tie points impact on stereo elevation accuracy greatly, which needs to be considered emphatically. According to the error propagation law deduced in prior study of author [14], the elevation error is

$$m_{Zp}^2 = \left\{ \frac{-f^2H^2x_1\sqrt{(fHtg\theta y_1)^2 + f^2H^2(x_1^2+y_1^2+f^2)}}{(x_1^2+y_1^2+f^2)} - \frac{\left(-fHtg\theta y_1 - \sqrt{(fHtg\theta y_1)^2 + f^2H^2(x_1^2+y_1^2+f^2)}\right)2x_1}{(x_1^2+y_1^2+f^2)^2} \right\}^2 m_{x_1}^2 + \left\{ \frac{\left[-fHtg\theta - \sqrt{(fHtg\theta y_1)^2 + f^2H^2(x_1^2+y_1^2+f^2)}(f^2H^2tg^2\theta y_1 + f^2H^2y_1)\right]}{(x_1^2+y_1^2+f^2)} - \frac{\left(-fHtg\theta y_1 - \sqrt{(fHtg\theta y_1)^2 + f^2H^2(x_1^2+y_1^2+f^2)}\right)2y_1}{(x_1^2+y_1^2+f^2)^2} \right\}^2 m_{y_1}^2$$

In the formula, $m_{x_1}^2$ and $m_{y_1}^2$ denote the measurement variance of tie point in x and y directions; m_{Zp}^2 represents the calculated elevation variance of ground point. Figure 2 draws out the elevation error trends over the rest side while the tie point measurement error fixed in x or y-direction respectively and the intersection angle fixed at 45°. As we can see, the elevation error brought by the measurement error in x-direction is very small compared with the error caused by the y-direction error, that is, the elevation error is mainly decided by the measurement error in vertical orbit direction. Obviously both are proportional to the square increase.

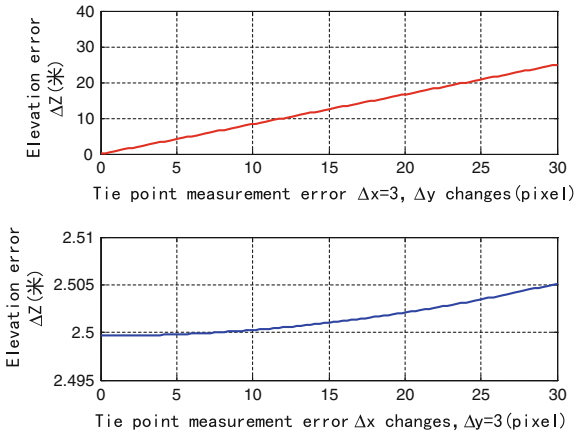

Fig. 2 The curve of elevation error change with the x and y direction measurement error

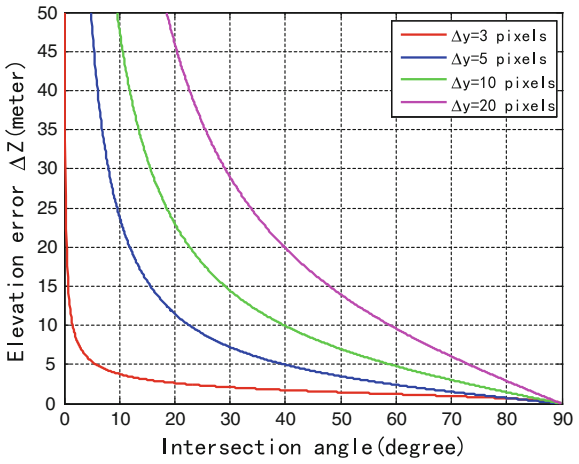

Fig. 3 Curve of elevation error change with intersection angle

Also matching error relates to the image sharpness and texture characteristics. If the resolution is higher, the tie point matching precision means higher. From this point of view, the impact of the resolution and the matching error on the stereo location accuracy are entirely consistent.

3.2 Intersection Angle

Figure 3 draws out the elevation error curve with the intersection angle under different measurement error in the y-direction. As we can see, the greater the intersection angle, elevation error becomes smaller. This is consistent with the traditional homology perspective that location accuracy drops with the intersection

angle increases. However, the intersection angle is not the only consideration for the image choice because different side perspectives will affect single image visual quality, thereby affect the tie point matching accuracy. For example, slant range projection on SAR images will produce image distortion such as foreshortening and top-bottom displacement when the terrain waves. When the nadir angle is smaller, this distortion is more serious, which will cause radar shadows. For CCD images, too large side swing angle will produce cell deformation. All these distortions are extremely unfavorable for automatic or artificial matching tie points, which will finally affect the measurement accuracy.

3.3 Number of Overlay Images

CCD and SAR loads are not integrated on the same aircraft, which means the ground images are obtained from different heights and perspectives. Then the multiple observation of each same ground point can provide more redundant observations. Based on surveying adjustment theory, the greater number of redundant observations can help eliminate gross error, and lead to higher reliability of adjustment results. Especially in the condition of no or sparsely control points, more images involved in the combination can better enhance the final stereo location accuracy.

Further, when the light beams of SAR and CCD do not completely contain each other, the maximum intersection angle of each ground point is higher compared to using a single CCD or SAR image. The resulting image combination will be more stereo and comprehensive with excellent observation structure and adjustment system.

4 Heterologous Stereo Verification and Accuracy Analysis

4.1 Experiment Data

We currently have 1: 10000 and 1: 2000 DOM and DEM precision reference data in Dengfeng region of Henan province. The main area physiognomy category is complete such as mountains, hills, plains, lakes, etc. We have collected multiple CCD and SAR images within the reference range to carry out multi-source stereo tests and to verify the effectiveness of the proposed location model. Accuracy evaluation consists of four values such as coordinate error in X/Y direction, plane error, elevation error. These image parameters are as follows (Table 1).

Table 1 Main parameters of satellite images in experiments

Image	Group	Image time	Resolution (m)	Orbit direction/viewing angle
CCD-A1	Group A	2012-10	0.8	Down orbit/right view angle = 6.7
CCD-A2		2013-03	0.8	Down orbit/right view angle = 2.4
SAR-A		2011-11	3	Up orbit/right view angle = 36.4
CCD-B1	Group B	2014-12	1	Down orbit/right view angle = 6.1
CCD-B2		2015-04	1	Down orbit/right view angle = 28.1
CCD-B3		2015-01	0.8	Down orbit/left view angle = 2.7
SAR-B1		2015-01	3	Up orbit/right view angle = 37.5
SAR-B2		2015-01	3	Down orbit/right view angle = 35.9

4.2 *Comparison Between Homologous and Heterologous Stereo Experiments*

Group A is used to do the comparative experiments of homologous CCD and heterologous stereo scheme. Figure 4 illustrates the relative position of three images, ┼ denotes connection points, △ denotes control points, ○ denotes check points. Test requires a number of these points, in order to compare test results on the same basis, the same batch of points are used. 4 connection points are fixed, the number of control points and checkpoints is total 11. 0-point uncontrolled, 1-point central control and 4-point angle control scheme were tested respectively, the remaining points are considered as check points.

First a traditional two-view CCD stereo experiment is started, its error distribution is given in Fig. 5 (a1, b1, c1) under 0, 1, 4 control points. As we can see, there are obvious regularity systematic error in the absence of control point. In 1-point control scheme, plane accuracy can be greatly improved. But since the CCD image are obtained down the orbit, the angle and the base to high ratio of images acquired at the same target are very limited, such as the angle is only 4.28°, the elevation error

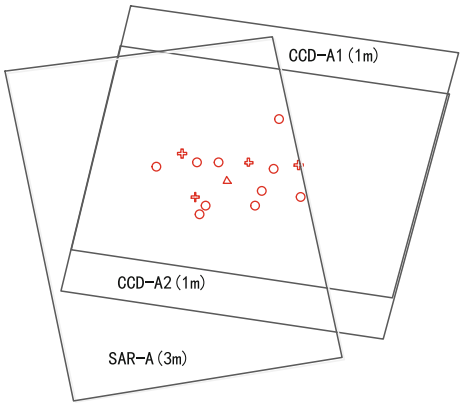

Fig. 4 Relative position of heterogeneous multi-view images

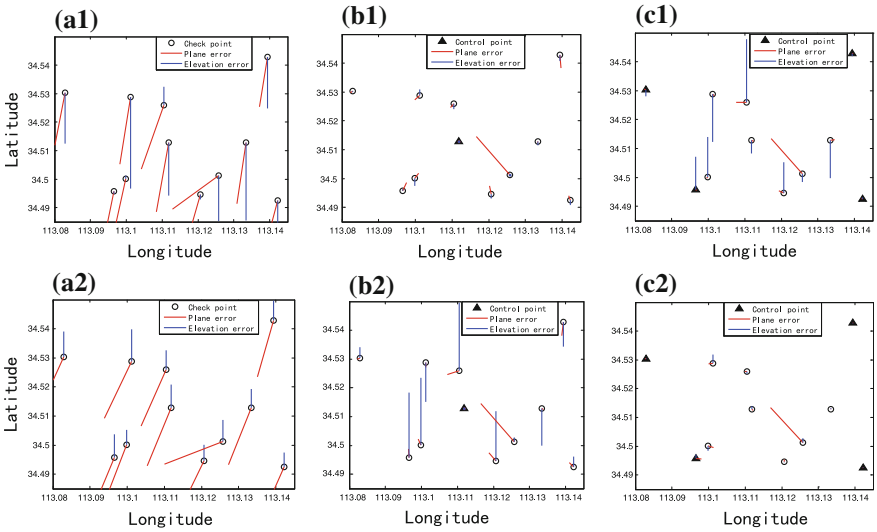

Fig. 5 Error distribution of homology two-view and heterologous three-view images **a1** homologous 0-control **b1** homologous 1-control **c1** homologous 4-control **a2** heterologous 0-control **b2** heterologous 1-control **c2** heterologous 4-control

cannot be better improved. This means that if the stereo condition of images is not good, more control points lead to little elevation accuracy increase. Then we added a SAR image into the test. This up-orbit image and its great viewing angle difference from CCD image provide a good intersection angle for stereo observation. In theory it can lead to higher stereo measurement accuracy. The error distribution map of this heterologous three-view test is also drawn as Fig. 5 (a2, b2, c2).

The statistic of adjustment precision of the above-mentioned two-view homologous and three-view heterologous group is quantified in Table 2. ① The angle increases from 4.28° to 43.16° after SAR image added. The height error control is greatly improved from original 29.017 m down to 3.395 m, more down to 3.039 m under 4-point control. This fully proved a huge contribution of SAR; ② The plane accuracy of three-view group is the highest as 4.888 m under 1 control and 1.802 m under 4-point control. This result is consistent with the prior analysis that the

Table 2 Stereo location accuracy of homology two-CCD images and heterogeneous images

Stereo combination type	Control point number	Error of check points (m)			
		X-direction	Y-direction	Plane	Elevation
CCD two-view	0	8.724	47.558	48.351	34.45
	1	2.856	4.813	5.597	32.594
	4	2.774	0.863	2.906	29.017
Three-view after SAR added	0	13.068	39.244	41.362	14.682
	1	1.573	4.628	4.888	3.395
	4	1.601	0.827	1.802	3.039

adjustment is more reliable while the number of overlap images is higher. The requirement of 1: 50,000 topographic map measurement can be completely satisfied under 1-point control; ③ Although the absolute error of a heterologous combination under uncontrolled condition is 14.682 m, its relative elevation error is less than homologous combination, which means it can be can be used to obtain the relative three-dimensional information.

4.3 *Heterologous Stereo Experiment Using Multi-resolution Complex Combination*

Further the stereo location precision of more complex multi-resolution combinations is validated. We select 5 images including CCD (0.8 m), CCD (1 m), SAR (3 m) as group B of Table 1. Figure 6 shows the relative position of these images. Error contrasts among some typical combinations are shown in Table 3, where "the included angle" means the angle computed directly from satellite side views, "the stereo intersection angle" refers to the true intersection angle computed using the RPC parameters of all involved images after relative orientation. We do this in order to see the law more clearly (Fig. 7).

Seen from the table, the included angle and the stereo intersection angle of homology CCD group is very close, as group 1 and 4. But the intersection angle of every heterologous group is about ten degrees more than its included angle, such as group 8–13. Because SAR is not the central projection constellation, then the equivalent light incident angle calculated using its equivalent RPC parameters is more than the antenna incident angle. This is the advantage of SAR for stereo location. The final location height accuracy is directly related to the intersection angle size. For example, as group 4 and 12, after SAR is added, the intersection angle increased from 32.6° to 53.4°, the elevation error reduces to 2.4 m.

Even with the largest intersection angle unchanged, stereo error is gradually reduced with the increase of the number of images involved. It from another point of view illustrates the necessity for SAR to participate in stereo location.

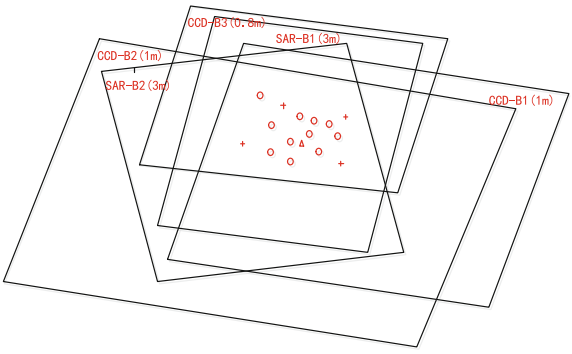

Fig. 6 Relative position of group B

Table 3 Stereo location accuracy of typical image combination under 3-point control

No	Image composite	Group type	Stereo intersection angle	Error of check points (m)			
				X	Y	Plane	Elevation
1	CCD1/CCD2	Opposite side/included angle = 8	7.16	1.533	2.179	2.664	18.227
4	CCD1-3	3-view/included angle = 31	32.6	1.518	2.564	2.979	3.445
8	SAR2/CCD3	Same side/included angle = 7	20.8	5.286	3.020	6.088	5.643
9	SAR2/CCD2	Same side/included angle = 29	46.3	1.866	1.872	2.643	2.933
12	SAR2/CCD1-3	4-view/included angle = 37	53.4	1.595	2.358	2.847	2.416
13	SAR1-2/CCD1-3	5-view/included angle = 72	97.1	1.454	2.565	2.948	4.130

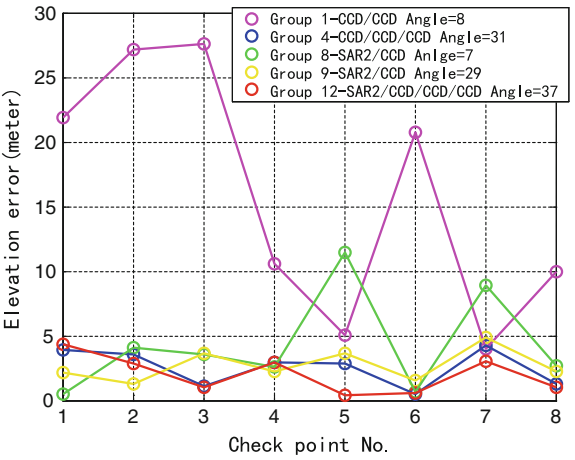

Fig. 7 Elevation error of typical group under 3-control

Moreover, we compare group 12 and 13, and find that after SAR1 is added, the intersection angle becomes beyond 90°, the error grows worse. It shows that if the image radiation difference is too large caused by SAR side view difference, thus the tie point measurement error is too large, which did not help the location accuracy promotion.

5 Conclusion

Aiming at the situation that high domestic satellite data has become increasingly diverse, we propose a complete multi-processing method which expands the conventional homologous stereo to multi-view stereo using heterologous active and passive images. Ground points are formed respectively on CCD and SAR images. These two imaging mechanisms are completely different. Their weak correlation is good for the complementarity to construct stereo equations. The sensors are not integrated on the same satellite platform, CCD and SAR images are acquired from different height and angle, which lead to a more benign form of observation structure. The heterologous multi-view stereo feasibility and accuracy is validated using multi-resolution CCD and SAR image combination. Tests show that this method expands the limitation data source because any overlap, unlimited phase and different type images can be used as an input. It means our method has a strong viability, and the heterologous stereo location can be a good alternative to homologous image while ensuring high precise location. Finally, the error propagation law is analyzed to obtain the dependencies between the affect factors and the heterogeneous accuracy, which will provide a reliable theoretical basis for practical applications.

References

1. Ding H, Yao A (2012) DEM generation and analysis using IKONOS stereo pairs. Sci Surveying Mapp 37(1):179–181
2. Dai J, Song W, Li J (2013) Stereoscopic positioning with multi-source optical high resolution satellite images. Sci Surveying Mapp 38(3):14–16
3. Li R (2012) Joint adjustment using multi-source remote sensing images. Wuhan University, Wuhan
4. Xing S, Xu Q, He J (2009) Combined stereo location among multi-sensor remote sensing images. Geomatics Inf Sci Wuhan Univ 34(5):522–526
5. Xing S, Xu Q, Liu J (2009) Bundle block adjustment with multi-source satellite remote sensing images. Acta Geodaet Cartogr Sin 38(2):125–130
6. Zhang G, Qin X (2013) Spaceborne SAR and InSAR data processing technology based on RPC model. Surveying and Mapping Press, Beijing
7. Fraser CS, Dial G (2006) Sensor orientation via RFMs. ISPRS J Photogrammetry Remote Sens 72(3):182–194
8. Zhang G, Fei W, Li Z (2010) Analysis and test of the substitutability of the RPC model for the rigorous sensor model of spaceborne SAR imagery. Acta Geodaet Cartogr Sin 39(3):264–270
9. Qin X, Jiang Y, Du J (2014) In-orbit geometric calibration and accuracy verification of XX high resolution satellite. In: The 17th China symposium on remote sensing. Xian, pp 120–128
10. Curlander JC (1991) Synthetic aperture rader: system and signal processing. Wiley, New York
11. Fraser CS, Hanley HB (2005) Bias-compensated RFMs for sensor orientation of high-resolution satellite imagery. Photogram Eng Remote Sens 71(8):909–915

12. Zhang L, Zhang J, Chen X (2009) Block adjustment with SPOT imagery and sparse GCPs based on RFM. Acta Geodaet Cartogr Sin 38(4):302–310
13. Li D, Zhang G, Jiang W (2006) SPOT-5 HRS satellite imagery block adjustment without GCPs or with single GCP. Geomatics Inf Sci Wuhan Univ 31(5):377–381
14. Li Y, Wu H, Li X (2015) Study of heterogeneous stereo imaging technology based on active and passive remote sensing data. Geomatics Inf Sci Wuhan Univ 8:1029–1035

Crowdsourced Fingerprint Localization Using Virtual Radio Map

Qiang Chang, Qun Li, Hongtao Hou, Weiping Wang and Wangxun Zhang

Abstract The requirement of indoor localization draws a new challenge to the positioning technique. As the widely availability of WLAN infrastructures, wireless signal fingerprint localization has attracted a lot of attentions. However, it is challenging due to the complexities of the indoor radio propagation characteristics exacerbated by the frequent change of indoor environment and the mobility of the user, the positioning accuracy cannot be guaranteed. Researchers propose crowdsourced fingerprint localization. But designing a sustainable incentive mechanism of crowdsourcing remains a challenge. We propose a virtual radio map based crowdsourcing fingerprint indoor localization algorithm. The basic idea behind our proposed algorithm is simple: we propose Local Gaussian Process to create a virtual database using the training signal database. The virtual database, contains fixed number of reference points, is used for positioning. And the training database, created by user crowdsourcing, is used for updating the virtual database. Simulation results show that our algorithm improves the accuracy for more than 30 %. And the improvement keeps increasing as the change of indoor environment. A small scale experiment proves the efficiency of the algorithm.

Keywords Fingerprint localization · Training database · Virtual database · Gaussian process

Q. Chang (✉) · Q. Li · H. Hou · W. Wang
College of Information System and Management, National University of Defense Technology, Changsha, Hunan, China
e-mail: changqiang@nudt.edu.cn

W. Zhang
Air Force Equipment Research Institute, Beijing, China

J. Sun et al. (eds.), *China Satellite Navigation Conference (CSNC) 2016 Proceedings: Volume II*, Lecture Notes in Electrical Engineering 389,
DOI 10.1007/978-981-10-0937-2_44

1 Introduction

In the era of mobile internet, location-based service (LBS) developed dramatically. Indoor LBS draws new challenges to the traditional navigation and positioning techniques both in coverage and accuracy. All kinds of indoor positioning techniques are developed by researchers. Radio fingerprints [1] outstand over other localization methods because of their accuracy and cost effectiveness in terms of hardware and deployment requirements. Some radio fingerprint-based commercial indoor positioning products are developed, such as Google Maps [2], WiFi Slam [3], and so on. As a result, radio fingerprint indoor location systems have gained more positioning.

Standard fingerprint indoor positioning algorithm consists of two phases: training and localization. During the training phase, a database of location fingerprint mappings is constructed and stored in the location server. The radio signal fingerprint can be GSM [4], FM [5], geomagnetic [6], WiFi [1], and so on. In the localization phase, the users send location queries with the current RSS fingerprints to the location server; the server retrieves the signal database and returns the matched locations using some algorithms, such as k-Nearest Neighbor (KNN) [1], k Weighted Nearest neighbor (KWNN) [7], probabilistic methods [8], neural networks [9], and so on. The positioning accuracy is reported beyond 2 meters. The performance is independent from radio propagation models and cost effectiveness in terms of hardware and deployment requirements. But this technique has some challenges.

First, building a high density of fingerprint database is labor intensive, expensive, and even impossible in some cases. Taking a 100 * 10 m floor as an example, if we want to build a fingerprint database with 1 m samples distance, we have to collect 1000 samples. For each sample, we should measure several times to get reliable result. Sometimes, it is impossible to collect some places' signal fingerprints because of the complex local environments.

Secondly, maintaining a large signal database is expensive. As the environment changes over time due to furniture or signal sources being moved, the fingerprints diverge from those in the database. So, we have to resurvey the entire area to update the database. As indoor environment often changed, we have to update the database frequently, which would be time consuming and expensive.

For these two problems, we propose a virtual radio map-based crowdsourced fingerprint indoor localization algorithm. The basic idea behind our proposed algorithm is simple: we propose local Gaussian process (LGP) to create a virtual database using the training signal database. The virtual database, containing fixed number of reference points (RPs), is used for positioning. The training database, created by user crowdsourcing, is used for updating the virtual database.

2 Related Works

For building the radio fingerprint database with less effort and update the database according to the newly collected data, such that the database reflects the up-to-date radio signal distribution, a lot of work has been done by researchers and some algorithms are proposed, such as Ray tracing [10], simultaneous localization and mapping (SLAM) [11], radio propagation model [12] and other mathematical model [13] based, and crowdsourcing [14]-based algorithm.

Ray tracing needs a very detailed description of the environment such that all the reflections that eventually characterize the received signal can be simulated. This approach is very computationally demanding. Because of these reasons, it is not viable for large-scale setups. In SLAM, the database is populated on the fly, provided that the users are equipped with a receiver and an IMU. In general, the accuracy of positioning with this technique is lower because the database is less accurate. The indoor environments are so complex that no simple mathematical model exists to accurately predict the RSS value. As a result, mathematical model-based radio map creation algorithm does not work well.

Crowdsourcing makes the users contribute themselves to the training phase. The database is updated continuously according to newly collected data, such that the database reflects the up-to-date radio signal distribution. But designing a sustainable incentive mechanism of crowdsourcing remains a challenge. Wu [15] leverages user motions, measured by IMU, to construct a stress-free fingerprint space. The fingerprint space is automatically mapped to the floor plan, so that the calibration effort is not required. But they cannot make full use of ordinary users' contribution. Chintalapudi [16] proposes an algorithm to create the database using user contribution when the users obtain an absolute fixed landmark occasionally. Park [14] merges the training and localization phases into a single state by asking the users' location when needed. But these two algorithms are not practical in real world. In Han's [17] work, users' home or office address is used to tag the locations of collected WiFi signals. Gallagher [18] updates the database by periodically asking the user for its true position. These works mainly focus on the problem of building the radio fingerprint database with less effort. But how to make full use of ordinary user's feedback is still a challenge.

Our study is motivated by these pioneer works but we go further, we propose a virtual radio map-based crowdsourced fingerprint indoor localization algorithm. We propose LGP to create a virtual database using the training signal database, created by user crowdsourcing, for positioning. We can not only update the database according to newly collected data, but also build the radio fingerprint database with less effort.

3 The Algorithm Framework

The desired coverage area is denoted as S. We only concentrate on 2D positioning problem. The coordinate of node i in S is (x_i, y_i). Assuming a user collect fingerprint at a unknown location $p^{(t)}$ at time t. The radio signal is denoted as $F^{(t)} = \{(\mathrm{ID}_j, f_j^{(t)}) | j = 1, 2, \cdots, n^{(t)}\}$, where ID_j is used for distinguishing different signal sources, such as FM, GSM, geomagnetic, and WiFi from different access points. In this paper, we only use WiFi signal as the fingerprint so, ID is the AP's Mac address. The fingerprint database is denoted as DB. The problem in fingerprint localization is estimating the user's current coordinate $p^{(t)}$ based on the measurement $F^{(t)}$ and the database DB.

In crowdsourced fingerprint positioning, DB is created by users. The coordinate uploaded to the database either from other positioning system, such as GNSS, or determined by the user.

For making full use of the user's feed back, we introduce virtual database denoted by DB_v. DB_v contains fixed number of virtual reference point (VRP). The VRP distributed uniformly in the area is determined by training data. The number of the VRP is denoted as N_v. The signal strength of VRPs is estimated using our proposed LGP. LGP employs DB to calculate the signal strength. The user makes use of DB_v for positioning. Figure 1 shows the framework of the proposed algorithm.

After collecting RSS values, if the user gets the current coordinate by other methods. He can upload the fingerprint, containing the coordinate and the RSS values, to the server. The server will add the fingerprint to DB, and update DB_v. If the user wants current location, he can send the positioning requirement, including the RSS, to the server. The server will estimate the coordinate using some algorithm based on DB_v.

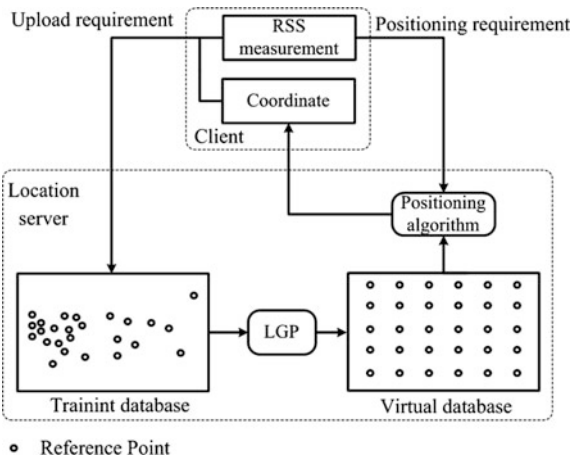

Fig. 1 Framework of the proposed algorithm

Many algorithms can be used to estimate the user's position. In this paper, we adopt the KWNN algorithm. In this algorithm, the k-nearest neighbor RPs are selected based on the RSS signal distance. Then the coordinates are calculated as:

$$p^{(t)} = \left\{ \sum_{i=1}^{K} w_i x_i, \sum_{i=1}^{K} w_i y_i \right\} \tag{1}$$

where (x, y) is the coordinates of RP, and the weight w_i is defined as:

$$w_i = \frac{1/\varepsilon_i}{\sum_{j=1}^{K} 1/\varepsilon_j} \tag{2}$$

ε_i is the difference between the measured RSS and the RSS values available in the database:

$$\varepsilon_i = \left(\sum_{j=1}^{n^{(t)}} |f_j^{(t)} - f_j^i|^q \right)^{1/q} \tag{3}$$

$n^{(t)}$ is the number of AP sensed by the user at time t. f_j^i is the RSS value of AP i at RP j. $f_j^{(t)}$ is the measured RSS value from AP j. q is the parameter.

4 Local Gaussian Process

Gaussian process (GP) is a non-parameter model that estimates Gaussian distribution over functions based on training data. GP is able to approximate an extremely wide range of nonlinear signal propagation models. Additionally, GP also returns the uncertainly of the estimation.

Assuming there are two nodes, denoted as p_i and p_j. $p_i = \{\vec{x}_i, f_i\}$, $p_j = \{\vec{x}_j, f_j\}$. $\vec{x}$ is the coordinate of p, f is the radio strength. The key assumption underlying GP is that the function values at close by points are correlated

$$\mathrm{cov}(f_i, f_j) = k(x_i, x_j) + \sigma_n^2 \delta_{ij} \tag{4}$$

Where σ_n^2 is the variance of a signal strength measurement, δ_{ij} is 1 when $i = j$, other wise 0. $k(x_i, x_j)$ is the Gaussian kernel function:

$$k(x_i, x_j) = \sigma_f^2 \exp(-|\vec{x}_i - \vec{x}_j|^2 / (2l^2)) \tag{5}$$

Where σ_f^2 and l are the signal variance and length scale, respectively. Both parameters determine how strongly the correlation between points drops off.

Given a set of training data

$$(X, F) = \{(\vec{x}_j, f_i) | j = 1, 2, \cdots, n\} \tag{6}$$

we can predict the function value f_* at arbitrary point $\vec{x}_*$:

$$P(f_* | \vec{x}_*, X, F) = N(\mu_{\vec{x}_*}, \sigma^2_{\vec{x}_*}) \tag{7}$$

μ_{x_*} and $\sigma^2_{x_*}$ are defined as:

$$\mu_{\vec{x}_*} = k_*^T (K + \sigma_n^2 I)^{-1} F \tag{8}$$

$$\sigma^2_{\vec{x}_*} = k(\vec{x}_*, \vec{x}_*) k_*^T (K + \sigma_n^2 I)^{-1} F + \sigma_n^2 \tag{9}$$

Here k_* is the $n \times 1$ vector of covariances between x_* and n training inputs X and $K[i, j] = k(x_i, x_j)$, $x_i, x_j \subset X$.

From Eq. (8) and (9), we found that the most computationally part is the inversion of the covariance matrix K. If there are n RPs, it will take time $O(n^3)$. For a large area containing several hundreds of RPs, the matrix would be very large. For the indoor environment, two far away points would be blocked by walls, furniture, and other objects. Their covariance will approximate to 0. So, it is reasonable to assume that the nearest k neighbor nodes are correlated. We call this LGP. Selecting k nearest RPs takes time $O(\text{nk})$. Then we use these k RPs to estimate RSS values, it will cost time $O(k^3)$. The total computational complex for LGP is $O(\text{nk}) + O(k^3)$. Usually we have $k \ll n$, so that $O(\text{nk}) + O(k^3) \ll O(n^3)$.

For evaluating the efficiency of LGP algorithm, we create a radio fingerprint database covering 800 m^2 area using Ray-tracing algorithm. Eight APs are placed in this area. The floor plan of the corridor and the radio map are shown in Fig. 2.

We randomly select 40 RPs from the database to build the training database. Figure 3 shows the radio map created by GP and LGP.

In this simulation, we set $k = 4$. From Fig. 3, we can see that a radio map created by 40 RPs looks very similar to the true radio map. Map created by GP and LGP also look the same. This result proves the efficiency of LGP algorithm.

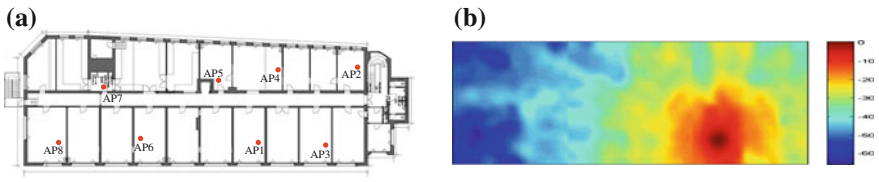

Fig. 2 Floor plan and the radio map

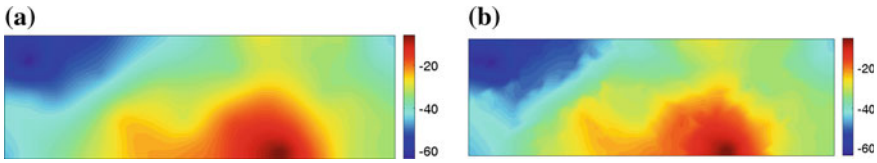

Fig. 3 Radio map created by GP and LGP

5 Performance Evaluation

We first evaluate the performance of the proposed positioning algorithm by simulation using the database created in the previous section. We consider the radio map as the ground truth and use it to generate signal strength measurements by adding 0 mean Gaussian noises with 3 dBm standard deviation.

Figure 4 is the CDF of standard KWNN and new algorithm. In the simulation, the parameters are set as follows: $k = 4$, $K = 3$, $q = 1$. We randomly select 800 nodes for positioning. DB_v contains 100 uniformly distributed VRPs.

From Fig. 4, we can see that the new algorithm performs better than the standard KWNN. The average improvement is 39.5 %. The KWNN average positioning error is 4.77 m, while it is 2.97 m for the new algorithm. The positioning error has been decreased for 37.7 %.

We simulate the crowdsourcing algorithm by adding new RPs to the training database. Figure 5 shows the simulation result.

In this simulation, we compare these two algorithms using root mean square error (RMSE). The number of training data increase from 20 to 100.

From Fig. 5, we can see that the error for both algorithms decrease with the increase of training data number. But the new algorithm performs better; the positioning error is 31.4 % lower than standard KWNN on average. When the training data is 100, which is the same with the virtual database. The new algorithm decreases the error for 26.8 %.

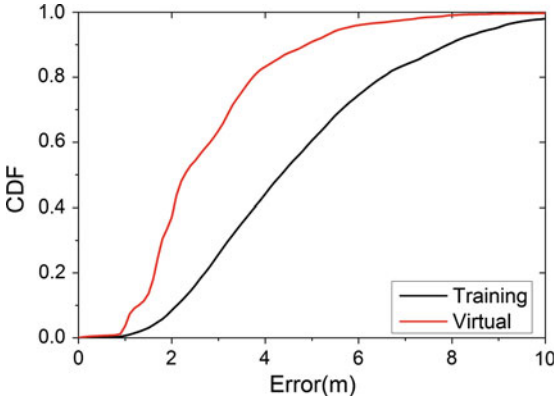

Fig. 4 CDF of different algorithms

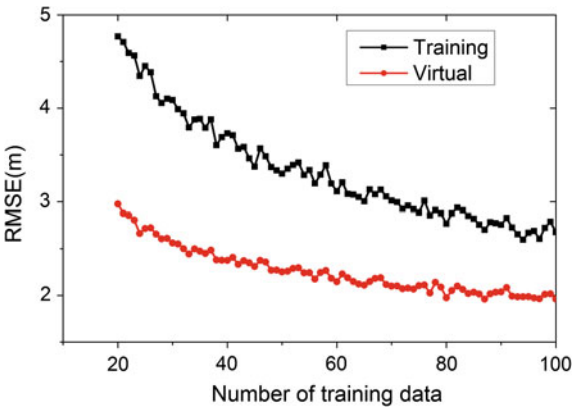

Fig. 5 RMSE varies with the number of training data

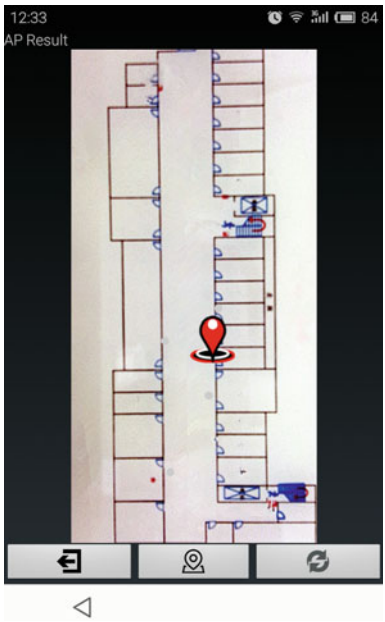

Fig. 6 User interface

For testing the new algorithm in real world, we develop an android APP. Figure 1 is the work flow of the APP. The user can locate themselves using this APP, and they also can upload the fingerprint data to the location server. Figure 6 is the user interface of the APP.

The map is the floor layout of our Laboratory, covering an area of 1440 m^2. Clicking the central button will send positioning requirement. Long pressing the interface will change the map. The right button can send the upload requirement.

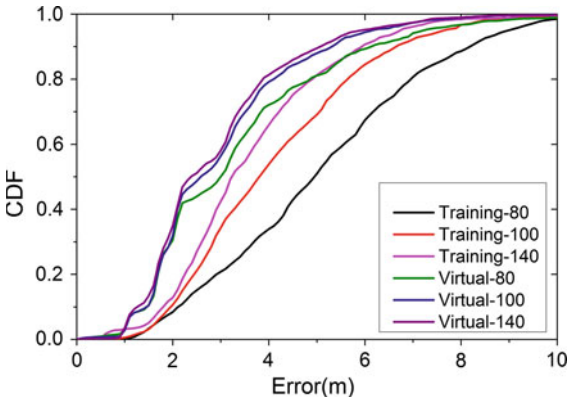

Fig. 7 CDF varies with the number of training data

We apply Meizu MX3 to test the algorithm. During our testing, the training database contains 80 randomly distributed RPs at the beginning. The virtual contains 150 VRPs. Figure 7 is the result.

During the experiment, the user upload new fingerprint to training database while positioning. The training database increases from 80 to 140. From Fig. 7, we can see that the new algorithm performs better than the standard KWNN. When there are 140 training data, the average positioning error is 3.74 m, while the new algorithm is 3.04 m. The new algorithm decreases the error for 18.7 %.

6 Conclusion

For building the radio fingerprint database with less effort, and update the database according to newly collected data, we propose a virtual radio map-based crowdsourced fingerprint indoor localization algorithm. We propose LGP to create a virtual database using the training signal database. The virtual database, containing fixed number of RPs, is used for positioning. The training database, created by user crowdsourcing, is used for updating the virtual database. Simulation and a small-scale experiment prove the efficiency of the algorithm.

References

1. Bahl P, Padmanabhan VN (2000) Radar: an in-building rf-based user location and tracking system. In: 19th annual joint conference of the IEEE computer and communications societies INFOCOM 2000, Proceedings IEEE, vol 2, pp 775–784
2. Google maps (2005) Google maps indoor. http://www.google.cn/maps/about/partners/indoormaps/
3. Ferris B, Fox D, Lawrence ND (2007) Wifi-slam using gaussian process latent variable models. IJCAI 7:2480–2485

4. Varshavsky A, de Lara E, Hightower J, LaMarca A, Otsason V (2007) Gsm indoor localization. Pervasive Mob Comput 3(6):698–720
5. Chen Y, Lymberopoulos D, Liu J, Priyantha B (2012) Fm-based indoor localization. In: Proceedings of the 10th international conference on mobile systems, applications, and services, pp 169–182, ACM 2012
6. Zhang C, Subbu KP, Luo J, Wu J (2015) Groping: geomagnetism and crowdsensing powered indoor navigation. Mob Comput IEEE Trans 14(2):387–400
7. Prasithsangaree P, Krishnamurthy P, Chrysanthis P (2002) On indoor position location with wireless LANs.In: Proceedings of the 13th IEEE international symposium on personal, indoor and mobile radio communications, pp 720–724
8. Castro B, Chiu E, Kremenek T et a1. (2001) A probabilistic room location service for wireless networked environments.In: Proceedings of the international conference on ubiquitous computing, Atlanta Georgia, pp 18–24
9. Nerguizian C, Despins C, Affes S (2004) Indoor geolocation with received signal strength fingerprinting technique and neural networks. In: Proceedings of the ICT, pp 866–875
10. Maher PS, Malaney RA (2009) A novel fingerprint location method using ray-tracing. In: Global telecommunications conference, GLOBECOM 2009, pp 1–5, IEEE 2009
11. Dissanayake M, Newman P, Clark S, Durrant-Whyte HF, Csorba M (2001) A solution to the simultaneous localization and map building (slam) problem. Robot Autom IEEE Trans 17(3):229–241
12. LaMarca A, Hightower J, Smith I, Consolvo S (2005) Self-mapping in 802.11 location systems. UbiComp 2005: Ubiquitous computing, pp 87–104, Springer
13. Koyuncu H, Yang SH (2013) Indoor positioning with virtual fingerprint mapping by using linear and exponential taper functions. In: Systems, man, and cybernetics (SMC) 2013 IEEE international conference on, pp 1052–1057, IEEE 2013
14. Park JG, Charrow B, Curtis D, Battat J, Minkov E, Hicks J, Teller S, Ledlie J (2010) Growing an organic indoor location system. In: Proceedings of the 8th international conference on mobile systems, applications, and services, pp 271–284, ACM 2010
15. Wu C, Yang Z, Liu Y (2015) Smartphones based crowdsourcing for indoor localization. Mob Comput IEEE Trans 14(2):444–457
16. Chintalapudi K, Padmanabha Iyer A, Padmanabhan VN (2010) Indoor localization without the pain. In: Proceedings of the 16th annual international conference on mobile computing and networking, pp 173–184, ACM 2010
17. Han D, Moon B, Yoon G (2014) Address-based crowdsourcing radio map construction for Wi-Fi positioning systems. In: International conference on indoor positioning and indoor navigation, 27–30 Oct 2014
18. Gallagher T, Li B, Dempster AG et al. (2010) Database updating through user feedback in fingerprint based Wi-Fi location systems. In: Ubiquitous positioning indoor navigation and location based service (UPINLBS) 2010, pp 1–8, IEEE 2010

Navigation Source Selection Algorithm of Multisource Navigation System

Zhengfa Shi, Yingkui Gong, Xinlin Zhou and Jiao Wang

Abstract Multisource navigation system consists of GNSS, aerial pseudolite positioning system, and ground pseudolite positioning system. In this paper, the relationship between the elevation, azimuth, and GDOP of multisource navigation system was analyzed, and the error factors of navigation source involved in the multisource navigation system was analyzed; finally, this paper proposed a fast selection algorithm for multisource navigation system. First, the elevation angle of the visible navigation source to the receiver is obtained, and classify them by elevation into low-elevation, medium-elevation and high-elevation areas; second, the azimuth angle of the visible navigation source to the receiver is obtained, and get a set including N (N >7) navigation source based on the fast navigation source selection algorithm; Finally, according to the error factor for each type of navigation source and the erroneous value, combining navigation source selection algorithm-based error, select six group of navigation source from the above set. Simulation shows that multisource navigation system select navigation source using elevation and azimuth with proper calculation, enhancing the positioning solution speed of the receiver.

Keywords Navigation source selection algorithm · Error · Elevation · Azimuth · Multisource navigation

1 Introduction

Global satellite navigation system (GNSS) is not only widely used in various fields of national economy, but also plays an important role in lunar exploration and space information monitoring [1, 2]. At present, people increasingly rely on satellite navigation. However, satellite navigation signal is vulnerable to interference and deception from other signal, only rely on global navigation satellite system has been

Z. Shi · Y. Gong (✉) · X. Zhou · J. Wang
Academy of OPTO-Electronics, CAS, Beijing 100094, China
e-mail: ykgong@aoe.ac.cn; ccut1423@163.com

J. Sun et al. (eds.), *China Satellite Navigation Conference (CSNC) 2016 Proceedings: Volume II*, Lecture Notes in Electrical Engineering 389,
DOI 10.1007/978-981-10-0937-2_45

unable to meet people's needs for the application of high precision, such as intelligent control of automobile, other manned vehicles, aerial refueling of aircraft, attitude control of offshore drilling platform, etc. Aiming at the current shortage of satellite navigation system, we can improve the service performance of the satellite navigation system using variety of enhanced system and pseudolite navigation through information enhancement and signal enhancement.

With the application of multisource navigation system becoming more and more extensive, it is indeed to use the navigation source selection algorithm into multisource navigation system. The navigation source selection algorithm of multisource navigation system is different from the previous selection algorithm. Because the difference noise and error of the different navigation source positioning, it cannot use optimal GDOP algorithm, unit length polyhedron volume method or selection algorithm based on azimuth angle and height angle. Navigation source selection algorithm of multisource navigation system which can provide the priority processing of the navigation information source for receiver [3, 4], also can provide an alternative set of navigation source to user receiver [5], and provide a reference for the following navigation system construction.

In this paper, a fast algorithm is proposed for the navigation system of multisource navigation system. The algorithm reduces the amount of computation in the selected source, while selects the navigation source with the smaller navigation error. It can provide high-accuracy positioning and navigation services for the user receiver.

2 Fast Navigation Source Selection Algorithm

Fast navigation source selection algorithm is a new selection algorithm for multisource navigation system. The algorithm is composed of two parts: the first module is the fast selection of navigation source and the second module is determining the final navigation sources based on the positioning error.

2.1 Model Description of Multisource Navigation System

According to the approximate position of the navigation source, navigation source selection algorithm of multisource navigation system can be described as shown in Fig. 1. The whole system is divided into four layers. The GNSS navigation satellite is considered as the fourth layer, the third layer is the aerial pseudolite, the ground pseudolite is the second layer, and the navigation receiver is the first layer. The data structure of the system is as follows. User receiver set U, element Ui in the set U is the No. i user receiver' number, Navigation satellite set S, set Si is the satellite set that is visible to the No. i user receiver, element Sij in the set Si is the No. j visible satellite to No. i user receiver; aerial pseudolite collection P, set Pi is the aerial

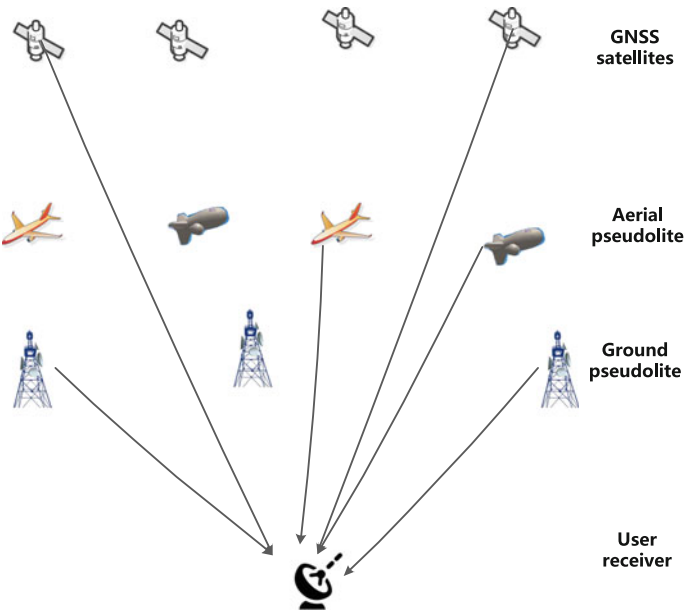

Fig. 1 Model description of multisource navigation system

pseudolite set that visible to No. *i* user receiver, element Pij in the set Pi is the No. *j* visible satellite to No. *i* user receiver, ground pseudolite set *A*, set Ai is the ground pseudolite set that visible to No. *i* user receiver, element Aij in the set Ai is the No. *j* visible ground pseudolite to No. *i* user receiver.

As shown in Fig. 1, the multisource navigation system has four-layer model framework; there are three kinds of navigation sources that provide position information for the receiver, which are position information from satellite, aerial pseudolite, and ground pseudolite. Because these pseudolites can provide positioning services for the receiver, the number of available navigation source will be more than four, and there is a big difference between each kind of navigation source positioning error. Therefore, we can choose the navigation source based on the method of error analysis, which is the cornerstone of the source navigation system.

2.2 Model Description of Multisource Navigation System

In this part, we use elevation angle and azimuth angle to classify the navigation source. The navigation source is divided into three categories: navigation source of zenith region (high elevation), navigation source of non-zenith region (middle elevation), and navigation source of peripheral region (low elevation). As shown in Fig. 2, the user receiver is located at the center of the circle, the blue area represents

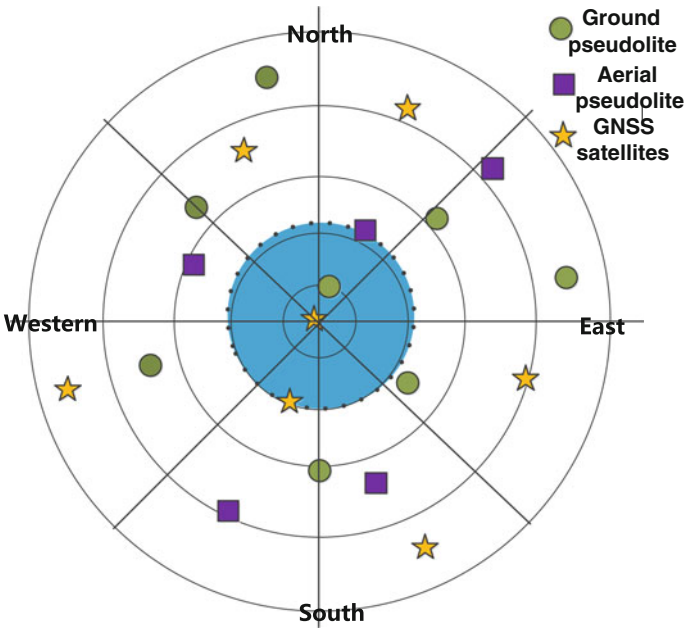

Fig. 2 Schematic diagram of source selection algorithm

zenith region, the elevation of its navigation source relative to user receiver is greater than 70°; the outermost circle is the 15° elevation region line of user receiver, outside this line means the navigation and positioning information is unreliable; other area is the non-zenith region.

Usually, four navigation sources can provide location information for user, but in order to eliminate the time reference error between the navigation sources in multisource navigation system, the system needs at least six navigation sources to provide accurate navigation and positioning services for user.

This paper analyzes the influences caused by the number of navigation source at zenith region to GDOP. Referencing fast satellite selection algorithm [6, 7], we get a table of navigation source number to be selected and located in zenith, as shown in Table 1.

Step One:

Using the relative coordinates between the navigation source and the user receiver, the elevation of the navigation source related to the user receiver is:

$$E = \arctan\left(\frac{z}{\sqrt{x^2 + y^2}}\right) \tag{1}$$

Table 1 Number and location of source selection

Number of navigation source	Number of zenith	Number of non-zenith
8	1	7
9	1	8
10	2	8
11	2	9
12	3	9
13	3	10

Using the relative coordinates between the navigation source and the user receiver, the azimuth of the navigation source related to the user receiver is

$$A = \arctan\left(\frac{x}{y}\right) \tag{2}$$

Step Two:

According to the number required for navigation sources, determine the number of regions in Fig. 2. Such as If we need N ($N \geq 8$) navigation sources, then we divide the circle in Fig. 2 into $\lfloor N/2 \rfloor$ zones. If the navigation source of a certain area is less than two, then select one more navigation source from the adjacent area. If it is not enough to select a sufficient number of navigation sources, expand the search area until sufficient number of navigation sources or traversing 60° azimuth are found. Then the algorithm is complete.

The fast selection of navigation source can quickly select user-desired number of navigation sources in the visible navigation source, and provide a set of navigation sources that are close to the minimum GDOP value. The flow chart of the module is shown in Fig. 3.

2.3 Model Description of Multisource Navigation System

This section describes the error GNSS satellite, aerial pseudolite (aerostat, unmanned aerial vehicle), and ground pseudolite. As shown in Fig. 4, the multipath error means that the direct path 1 is interfered by the reflect path 2 → 2. 2 or 2 → 2.1, which results in difference between transmitted signals and received signals to the navigation information. Near–far effect is the interference between the navigation satellite and the pseudosatellite when a user receiver is located between the far boundary point and the near boundary point. Tropospheric and ionospheric errors

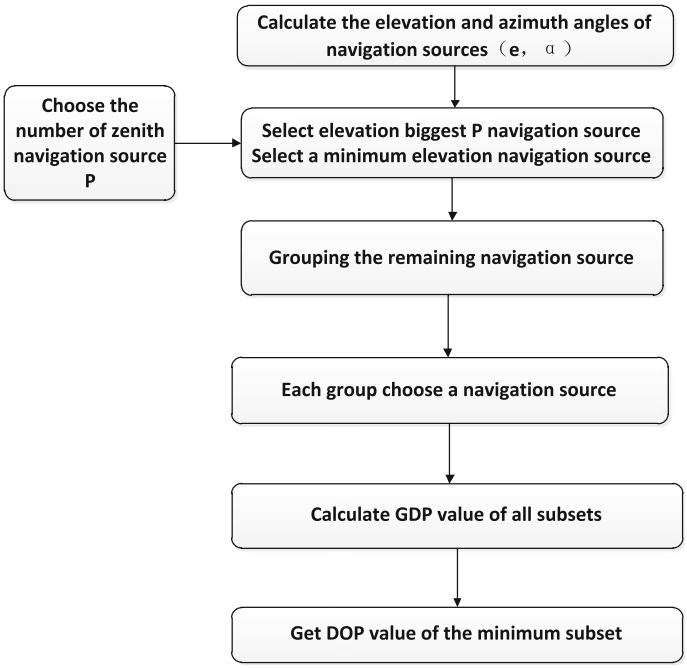

Fig. 3 Flowchart of fast source selection algorithm

are the signal interference in the propagation path disturbed by the troposphere and ionosphere. The position error of the pseudosatellite is shown in the dotted circle in Fig. 4. This error will affect the user's position error. Due to the time difference between the receiver and the navigation source or between the navigation sources, it will produce a large positioning error.

In order to improve the performance of navigation and positioning system, it is required to analyze the error and interference of navigation source in the navigation system. The navigation positioning errors are shown in Table 2.

Above all, we need to analyze the impact of delay and interference on the positioning results in multisource navigation system, and the fusion output can be a model to measure the final positioning accuracy. The model is as follows:

$$\varepsilon = \lambda_1 \varepsilon_1 + \lambda_2 \varepsilon_2 + \cdots + \lambda_{10} \varepsilon_{10} \tag{3}$$

In this formula, ε_1 represents the errors shown in Table 2; λ_1 represents the weight of each error.

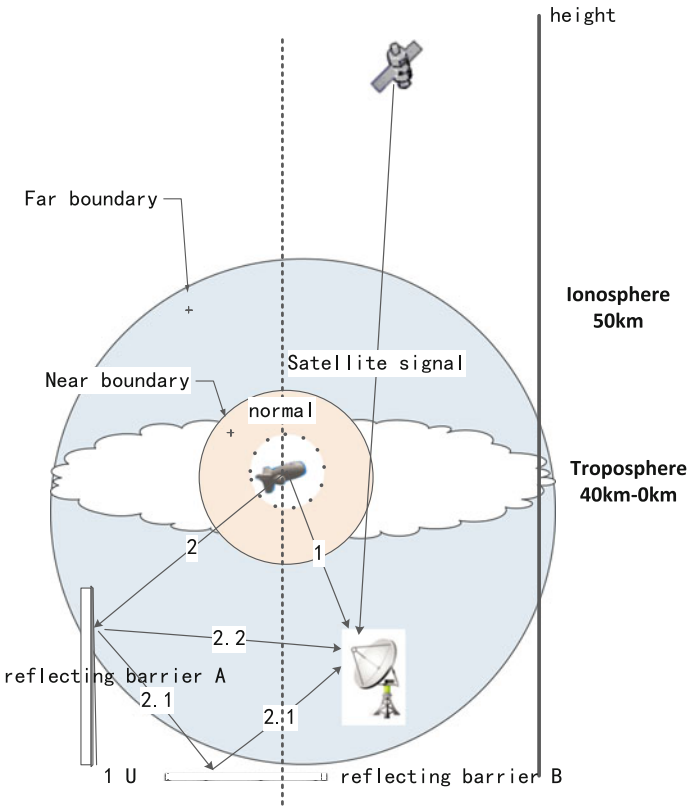

Fig. 4 Error of various navigation sources

Table 2 Error of navigation source

Error		GNSS satellites	Aerial pseudolite	Ground pseudolite
Receiver	Receiver clock error	✓	✓	✓
	Receiver noise	✓	✓	✓
	Receiver delay	✓	✓	✓
Propagation path	Ionospheric delay	✓		
	Tropospheric delay	✓	✓	
	Multipath effect	✓	✓	✓
	Near–far effect	✓	✓	✓
Navigation source	Ephemeris error	✓		
	Position error of aerial pseudolite		✓	
	Position error of ground pseudolite			✓

3 Positioning Principle of Multisource Navigation System

Observation equation for the satellite navigation system is:

$$y = \mathrm{H}x + \varepsilon \tag{4}$$

where y is $m \times 1$-dimensional measurement vector; m is the number of satellites used for navigation; H is geometric observation matrix; ε is the measurement error vector; x is the user state vector (4×1 dimensional vector [8]).

According to observation equation for the satellite navigation system, simultaneous observation equations of GNSS satellite, aerial pseudolite, ground pseudolite is

$$\begin{cases} y_{\text{satellite}} = H_{\text{satellite}} x_{\text{satellite}} + \varepsilon_{\text{satellite}} \\ y_{\text{aerial}} = H_{\text{aerial}} x_{\text{aerial}} + \varepsilon_{\text{aerial}} \\ y_{\text{ground}} = H_{\text{ground}} x_{\text{ground}} + \varepsilon_{\text{ground}} \end{cases} \tag{5}$$

The above equations can be simplified as

$$y_{\text{com}} = H_{\text{com}} x_{\text{com}} + \varepsilon_{\text{com}} \tag{6}$$

where

$$y_{\text{com}} = \begin{Bmatrix} y_{\text{satellite}} \\ y_{\text{aerial}} \\ y_{\text{ground}} \end{Bmatrix} \varepsilon_{\text{com}} = \begin{Bmatrix} \varepsilon_{\text{satellite}} \\ \varepsilon_{\text{aerial}} \\ \varepsilon_{\text{ground}} \end{Bmatrix} H_{\text{com}} = \begin{Bmatrix} H'_{\text{satellite}} & I_{\text{satellite}} & 0 & 0 \\ H'_{\text{aerial}} & 0 & I_{\text{aerial}} & 0 \\ H'_{\text{ground}} & 0 & 0 & I_{\text{ground}} \end{Bmatrix}$$

$$x_{\text{com}} = \begin{bmatrix} x_{\text{user}} & y_{\text{user}} & z_{\text{user}} & \Delta_{\text{satellite}} & \Delta_{\text{aerial}} & \Delta_{\text{ground}} \end{bmatrix}^T$$

Assuming the number of navigation source used in current navigation system is n, $H'_{\text{satellite}}$ is the first three columns of the user observation matrix $H_{\text{satellite}}$, $I_{\text{satellite}}$ is a n-dimensional column vector with the value of the column element is 1, $\varepsilon_{\text{satellite}}$ is a n-dimensional equivalent column vector error, $y_{\text{satellite}}$ is $n \times 1$ dimensional measurement vector, and the other meanings are similar to the satellite navigation system.

x' is the user state vector; x_{user}, y_{user}, z_{user} represents the mobile step at the location of the x, y, z direction; $\Delta_{\text{satellite}}$, Δ_{aerial}, Δ_{ground} is the difference between the three types of navigation source clock and receiver clock; $\varepsilon_{\text{satellite}}$, $\varepsilon_{\text{aerial}}$, $\varepsilon_{\text{ground}}$ indicates the measurement noise error of the three navigation source.

4 Simulation Experiment and Conclusion

As shown in Table 3, the simulation experiments using SimGEN obtain information of GNSS satellites, airborne pseudolite, and ground pseudolite in ECEF coordinate such as three-dimensional position information, elevation, azimuth,

Table 3 Related information of navigation source

	GNSS satellites	Aerial pseudolite	Ground pseudolite
Pos_X	−11718549	−1706779	−1700125
Pos_Y	−11696543	4504966	4487403
Pos_Z	20719068	4204011	4187511
Iono-delay L1	1.64E-08	1.36E-08	0
	6.05E-09	6.19E-09	0
Tropo-delay	2.17E-08	0	0
	2.66E-09	0	0
Elevation	0.0874	0.3248	−0.8048
	0.9248	0.5181	1.1369
Azimuth	0.6452	1.1918	−2.8227
	0.8476	−1.6965	−0.8368

tropospheric delay, and ionospheric delay. Error size, and weight information of other error items in this simulation experiment are not elaborated in this article, please refer to the literature [9] if needed. The receiver is located at 41° north latitude 15, longitude 110° 45 min, from sea level to 0.2 km.

The simulation results are as follows. Figure 5 shows the GDOP value using the minimum GDOP value navigation source selection algorithm and the fast navigation source selection algorithm. Figure 6 shows the difference in the running time of the two navigation source selection algorithm.

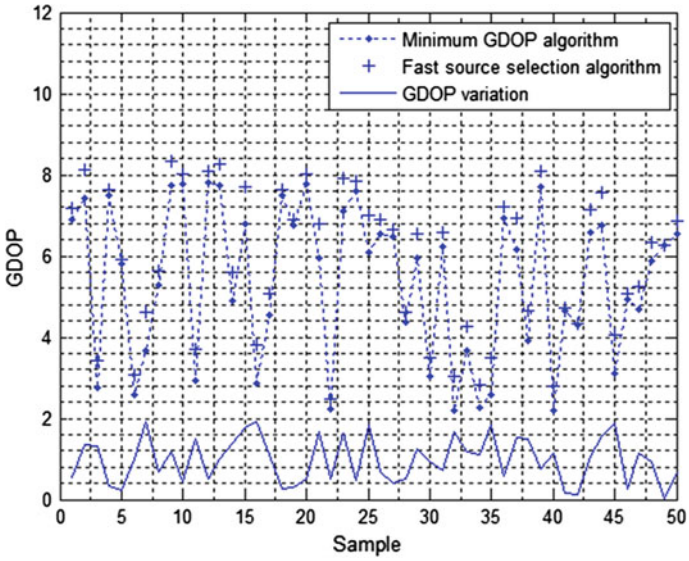

Fig. 5 Simulation result of fast source selection algorithm

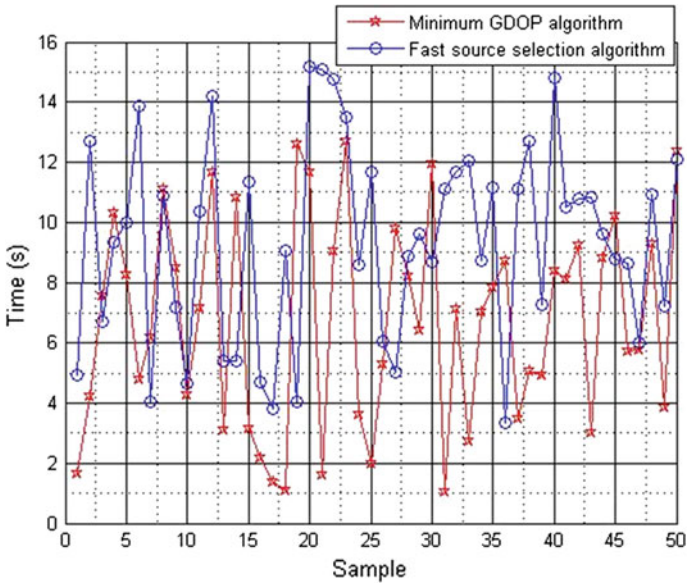

Fig. 6 Running time of two kinds of source selection algorithms

The simulation results show that the fast navigation source selection algorithm proposed in this paper can quickly select the set of navigation source, providing users with high-precision positioning service in the case of few GDOP increasing.

Acknowlegment National Natural Science Fund of the People's Republic of China (Grant No. 91438207).

References

1. Palmerini GB (2014) Assisted GNSS navigation in lunar missions. In: AIAA space and astronautics forum and exposition
2. Force DA, Miller JJ (2013) Combined global navigation satellite systems in the space service volume. In: ION International technical meeting
3. Roongpiboonsopit D, Karimi HA (2009) A multi-constellations satellite selection algorithm for integrated global navigation satellite systems. J of Intell Transp Syst 13(3):127–141
4. Wei M (2012) New satellite selection algorithm for real-time application. In: International conference on systems and informatics (ICSAI 2012), IEEE, pp 2567–2570
5. Roongpiboonsopit D, Karimi HA (2009) A multi-constellations satellite selection algorithm for integrated global navigation satellite systems. J of Intell Transp Syst 13(3):127–141
6. Zhang J (2011) Collaborative space airspace surveillance technology, Aviation Industry Publishing House
7. Roongpiboonsopit D, Karimi HA (2009) A multi-constellations satellite selection algorithm for integrated global navigation satellite systems. J of Intell Transp Syst 13(3):127–141

8. Yin L et al (2013) A satellite selection algorithm for GNSS multi-system based on pseudorange measurement accuracy. In: 5th IEEE International Conference on broadband network & multimedia technology (IC-BNMT 2013), IEEE, pp 165–168
9. Kaplan ED (2005) Understanding GPS: principles and applications. Artech House Mobile Communications

Establishment and Verification of Enhancement Correction Model for Differential Barometric Altimetry

Le Yang

Abstract Indoor location-based service demands precise vertical height information and its degree of distinguishing in the vertical position should be decimeter, so that we can precisely recognize the building floor where the users are, then realize three-dimensional holographic positioning for indoor location-based service. Differential barometric altimetry can realize submeter positioning accuracy for vertical positioning in indoor and outdoor universal environment. But due to the limitation of principle of differential barometric altimetry, this altimetry cannot realize submeter vertical positioning accuracy in local abnormal temperature region. This paper proposes a enhancement correction model for correction to the error of differential barometric altimetry in local abnormal temperature region. The simulation and experiment are also set up to verify the performance of this model. The verification results show that the model realizes the correction for error of the altimetry and keep it having submeter positioning accuracy in local abnormal temperature region. This model enhances the robustness of differential barometric altimetry.

Keywords Vertical positioning · Differential barometric altimetry · Local abnormal temperature region · Enhancement correction model

1 Introductions

Accurate indoor location-based service(LBS) becomes more and more important in recent years especially in the fields of emergency rescue, action against terrorism, special people caring, etc., which has been a great demand of the development strategy of high-tech industry in our country and the international competition of science and technology.

L. Yang (✉)
Communication University of Shanxi, No. 125 Wenhua Road, Jinzhong, China
e-mail: yangle@bupt.edu.cn

J. Sun et al. (eds.), *China Satellite Navigation Conference (CSNC) 2016 Proceedings: Volume II*, Lecture Notes in Electrical Engineering 389,
DOI 10.1007/978-981-10-0937-2_46

Compared with outdoor LBS, indoor LBS need more precise and three-dimensional positioning information, namely the longitude, latitude, and altitude information, so that narrow microspace can be distinguished in crowded buildings. The degree of distinguishing in vertical positioning should be decimeter. At present, differential barometric altimetry can realize submeter positioning accuracy by using simple, cheap, and miniaturized function module [1, 2]. But due to temperature and the inconsistency of change of local pressure [3], differential barometric altimetry cannot realize submeter vertical positioning accuracy in local abnormal temperature region. This paper proposes an enhancement correction model for correction to the error of differential barometric altimetry in local abnormal temperature region. The simulation environment and experiment are also set up to verify the performance of this model. The verification results show the module is feasible and enhances the robustness of differential barometric altimetry.

2 Mechanism of the Model

2.1 Nonlinear Regression Model of Baro Characteristics in Constant Micro-Interval Time Domain Based on Kalman Filter

For the test condition of local abnormal temperature, the atmospheric pressure difference ΔP_{T} of testing in terminal in a period of time is determined by the effect of heat source and human motion. Assuming the pressure difference for the effect of heat source is ΔP_{H} and the difference for the effect of human motion is ΔP_{M}, we have

$$\Delta P_{\mathrm{T}} = \Delta P_{\mathrm{M}} + \Delta P_{\mathrm{H}} \tag{1}$$

Considering the atmospheric pressure changes of testing in terminal, for the effect of human motion and the effect of heat source are ΔP_{T1}, ΔP_{M1} and ΔP_{H1} within microtime segment (t_a, t_b). If $t_b - t_a \to 0$, then $\Delta P_{\mathrm{M1}} \ll \Delta P_{\mathrm{H1}}$, we have

$$\Delta P_{\mathrm{T1}} \cong \Delta P_{\mathrm{H1}} \tag{2}$$

In local abnormal temperature environment with low-speed wind, within microtime segment, the ideal gas state equation is applicable as following:

$$P_{\mathrm{H1}} V_1 = n_1 R_1 T \tag{3}$$

where P_{H1} is atmospheric pressure, V_1 is the gas volume, n_1 is amount of substance, R_1 is the ideal gas constant, and T is gas temperature of thermodynamics within microtime segment (t_a, t_b). As defining $A_1 = n_1 R_1 / V_1$, then $A = A(t, x, z)$. We have

$$\frac{\partial A}{\partial t} \gg \frac{\partial A}{\partial x} \gg \frac{\partial A}{\partial z} \tag{4}$$

so we can get that $A \approx A(t)$ and distribution graph of A, as Fig. 1. ΔP_{H1} can be expressed as:

$$\Delta P_{\mathrm{H1}} = \int_{t_a}^{t_b} A(t)\Delta T(t)dt \tag{5}$$

Within (t_a, t_b), define $\Delta t = (t_b - t_a)/n$, then we have

$$\Delta P_{\mathrm{H1}} = \sum_{i=0}^{n-1} \int_{t_a + i\cdot\Delta t}^{t_a + (i+1)\cdot\Delta t} A(t)\Delta T(t)dt \tag{6}$$

Because $\Delta t \to 0$, the above equation can be rearranged into

$$\Delta P_{\mathrm{H1}} \approx \sum_{i=0}^{n-1} A_i \cdot \{\Delta T[t_a + (i+1)\cdot\Delta t] - \Delta T[t_a + i\cdot\Delta t]\} \tag{7}$$

Define $\Delta T_i = \Delta T[t_a + (i+1)\cdot\Delta t] - \Delta T[t_a + i\cdot\Delta t]$ and $\Delta P_i = A_i \cdot \Delta T_i$, we have

$$\Delta P_{\mathrm{H1}} = \sum_{i=0}^{n-1} \Delta P_i \tag{8}$$

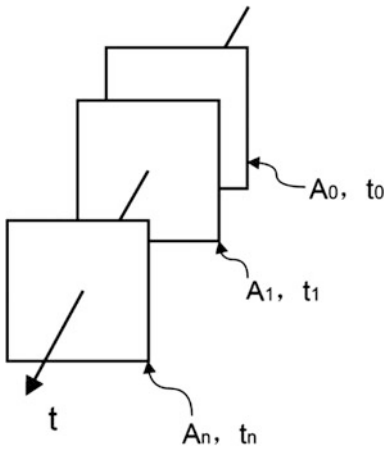

Fig. 1 Atmospheric characteristic parameter A_i

As $\Delta t \to 0$, ΔPi is approximate to the atmospheric pressure difference value of testing in terminal within Δt and ΔT_i is known, so we can compute the $\tilde{A}_i (i = 0, 1, \ldots, n-1)$ of (t_a, t_b). Assuming that the effect of heat source and human motion to atmospheric pressure difference obeys Gaussian distribution, at t_i we can get an equation as follows:

$$\hat{A}_i = \alpha \hat{A}_i - 1 + \varepsilon A_{\text{move}} + \beta \tag{9}$$

where A_{move} is noise caused by motion and β is the noise caused by heat source. By Kalman filter, we can use the optimal estimate $\hat{A}_{i-1}$ at t_{i-1} to get the optimal estimate $\hat{A}_i$ at t_i and $t_i, t_{i-1} \in (t_a, t_b)$. Define $\hat{A}_i$ as follows:

$$\begin{cases} \hat{A}_i = f(\hat{A}_{i-1}, \theta) + e \\ e \sim N(0, \delta^2) \end{cases} \tag{10}$$

where $\theta = (\alpha, \beta, \gamma)$ and $0 < \gamma < 1$. Through hybrid genetic algorithm(HGA) [4], we can obtain nonlinear regression characteristic curve of $\hat{A}_i$ about $\hat{A}_{i-1}$ within (t_a, t_b). The parameters of HGA are shown as Table 1. The above computing is the training process of the model in micro time domain.

Equations (8)–(10) are the parts of the nonlinear regression model of constant baro characteristics in micro-interval time domain based on Kalman filter. Those equations can be also considered as the training of characteristics for indoor atmospheric pressure within micro-interval time domain. Assuming that $\hat{A}_{i+1}$ which is belonged to the computing results in (t_b, t_i) obeys the nonlinear regression model, so we can get ΔP_{Hi} caused by the effect of heat source at arbitrary micro-interval time domain via temperature difference value which is known. Then ΔP_{Mi} can be computed by (1). Again by formula (11), we can obtain the value of height difference due to human motion in any period of time, namely relative vertical positioning information.

$$\Delta H_i = \frac{T_0}{\beta} \left[\left(\frac{P + \Delta P_{\text{Mi}}}{P_0} \right)^{-\frac{\beta R}{g}} - \left(\frac{P}{P_0} \right) \right] \tag{11}$$

where $T_0 = 288.15\,\text{K}$, $\beta = -6.5\,\text{K/km}$, $P_0 = 1013.25\,\text{mPa}$, $R = 287.05287\,\text{m}^2/(\text{s}^2\text{K})$ and P is pressure measurement in terminal when leaving normal area to local

Table 1 Parameters of HGA

Parameter	Value
Population size (the number of time segments of training process, namely n)	25
Hybrid probability P_c	80
Mutation probability P_m	5 %
Maximum evolution generation number G	400

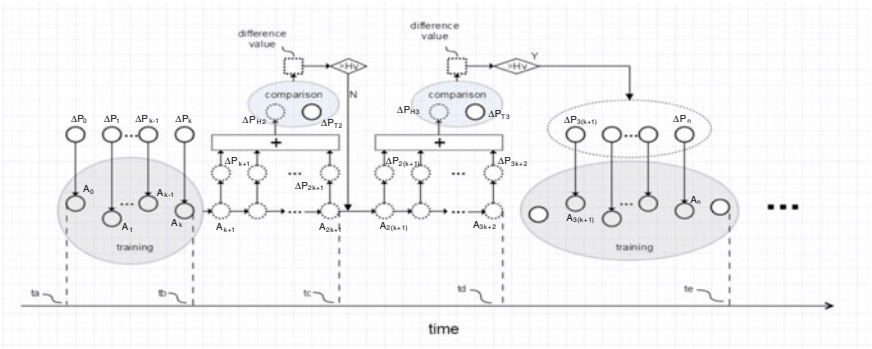

Fig. 2 Principle: enhancement correction model for differential barometric altimetry

abnormal temperature region. Above all the processes, A_i is defined as the atmospheric characteristic parameter.

2.2 Adapt Learning and Correction Algorithm

In the process of model's working, the adapt learning and correction algorithm is used for higher accuracy positioning. The core idea of the algorithm is using the $\hat{A}_i$ which is trained by nonlinear regression model based on Kalman filter to compute the ΔP_{Hi} in microtime period which is caused by the effect of heat source. And ΔP_{Ti} is known by testing in terminal, then we can compute $|\Delta P_{\mathrm{Ti}} - \Delta P_{\mathrm{Hi}}|$. If this value is bigger than threshold value H_{v}, the model will retain the nonlinear regression curve of $\hat{A}_i$, training time domain, and n are amplified appropriately, and the HGA algorithm parameters of population size and maximum evolution generation number also increase accordingly. Finally, the principle of enhancement correction model for differential barometric altimetry is shown as Fig. 2.

3 Verification for Model Performance

Through setting up simulation indoor environment of fire under some constraint conditions and testing experiment of high-power heater, we can verify the performance of model.

3.1 Simulation Indoor Environment of Fire

Similar to tunnel, three kinds of influence on the temperature distribution in indoor fire region are thermal convection, thermal radiation, and heat conduction. As the air's heat transfer coefficient is low and fire source in general is not radioactive material, so we can ignore the thermal radiation and heat conduction, then the temperature distribution model for fire area leeward is as follows [5]:

$$T = T_0 + (T_1 - T_0)\{1 - e^{-K(t-x/\tilde{u})}\}e^{\frac{-aux}{C\rho_0\tilde{u}S}} \tag{12}$$

where T_0 is the initial temperature when the fire did not happen, T_1 is the highest temperature of burning gas, K is fire spread speed, t is burning time, u is the wind speed, $\tilde{u}$ is the conversion of wind speed in standard condition, a is the heat transfer coefficient of the interior wall, C is heat capacity of air, ρ_0 is the density of air in standard condition, and S is longitudinal area of indoor space.

Assuming that basal area and inclination of indoor space are constant, the wind energy equation is shown as follows [6]:

$$\frac{\mathrm{d}}{\mathrm{d}t}\left[c_\mathrm{p}T + gz + \frac{v^2}{2}\right] - \frac{1}{\rho}\cdot\frac{\partial p}{\partial t} = \frac{1}{\rho A}\left[q_\mathrm{p}\delta(s - s_\mathrm{p}) - \alpha P(T - T_r)\right] \tag{13}$$

where t is time, s is the distance along the tunnel axis between observation points and the initial calculation standard point, z is height, ρ is the density of air, v is the air speed, g is acceleration of gravity, p is the atmospheric pressure, T is temperature, c_p is the specific heat capacity of air, q_p is heat release of heat source per unit time, s_p is the initial distance of heat source point along the wheelbase, P is the circumference of indoor space, A is the basal area of indoor space, α is the heat transfer coefficient of wall, and T_r is temperature of wall.

Considering the condition of low wind speed and ignoring the temperature of wall and heat exchange, in microperiod of time, Eq. (13) can be rearranged into

$$\frac{\partial p}{\partial t} = \rho\left(\frac{\alpha P}{\rho A} + c_\mathrm{p}\right)T + \rho g z \tag{14}$$

By Eqs. (11) and (13), we can characterize the indoor temperature distribution and the pressure gradient distribution in the fire region, thus building indoor fire simulation environment is established.

3.2 Simulation and Conclusion

Assuming that the wind flow direction is the positive direction of X axis and the location of the initial calculation standard point is same with the location of fire

source which is at somewhere in negative half of *X* axis. Ignore the friction and heat exchange due to wall in cuboid indoor space. Considering some conditions as follows: the temperature before fire happened is 275 K, the maximum temperature when fire is burning is 1275 K, the wind speed is low and constant that is 0.5 m/s, and the initial atmospheric pressure before fire happened is the standard atmosphere pressure. According to Eqs. (12) and (14), the simulation of indoor region fire can be established.

The simulation: in the cuboid indoor room, we select three points which are A (10, 0, 0), B(0, 0, 0), and C(0, 0, 5) when the fire happened for 5 min. Simulation test trajectory is uniform linear motion of A → B→C → A. The velocity from A

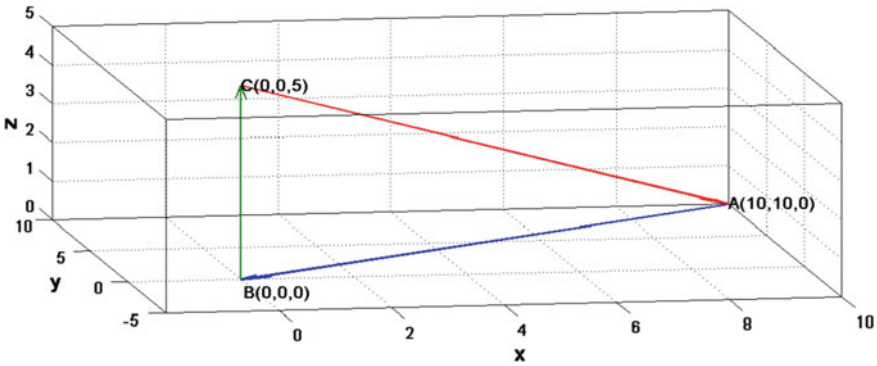

Fig. 3 Simulation: fire region testing

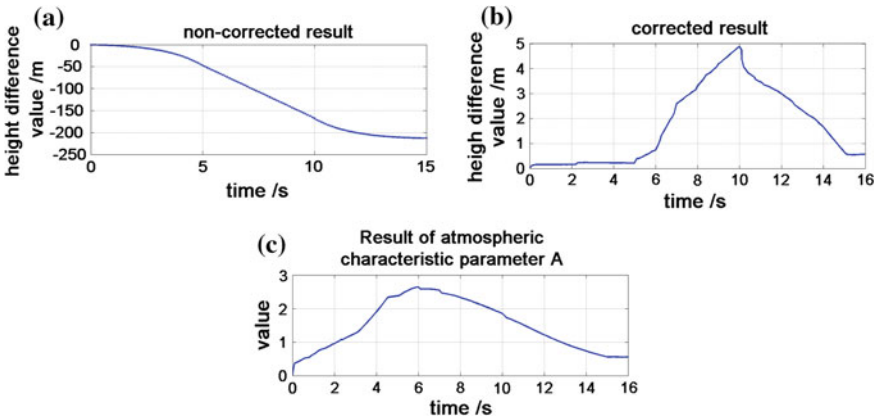

Fig. 4 Curve: testing results of model for simulation of fire region. **a** Testing positioning result without model. **b** Testing positioning result with model. **c** The results of atmospheric characteristic parameter A

Table 2 Testing data of model for simulation of fire region

Observation points	True height difference (m)	Height difference value without model (m)	Height difference value with model (m)	Error of height difference value with model (m)
(8,8,0)	0	−1.760	0.153	0.153
(6,6,0)	0	−5.364	0.156	0.156
(4,4,0)	0	−12.260	0.225	0.225
(2,2,0)	0	−24.900	0.221	0.221
B(0,0,0)	0	−47.420	0.216	0.216
(0,0,1)	1.00	−71.4	0.735	0.265
(0,0,2)	2.00	−95.370	2.580	0.580
(0,0,3)	3.00	−119.311	3.300	0.300
(0,0,4)	4.00	−143.302	4.190	0.190
C(0,0,5)	5.00	−176.300	4.880	0.12
(2,2,4)	4.00	−189.710	3.469	0.531
(4,4,3)	3.00	−201.703	2.996	0.004
(6,6,2)	2.00	−208.104	2.316	0.316
(8,8,1)	1.00	−211.501	1.658	0.658
A(10,10,0)	0	−212.900	0.650	0.650

to B is $V_{ab} = 2.828\,\mathrm{m/s}$, the velocity from B to C is $V_{bc} = 1\,\mathrm{m/s}$ and the velocity from C to A is $V_{ca} = 3\,\mathrm{m/s}$. Complete simulation test process is shown in Fig. 3.

In the above simulation test environment, compute real-time height difference variation on the trajectory and the atmospheric characteristic parameter A which are shown in Fig. 4.

The simulation test results which are obtained at observation points in the trajectory per 1 s are shown in Table 2. Through the results, we can get the conclusion: the model can make differential barometric altimetry realize sub-meter relative positioning accuracy in vertical under local abnormal temperature conditions. If the positioning information in vertical is precise before coming into the fire area, the absolute positioning accuracy can reach the sub-meter.

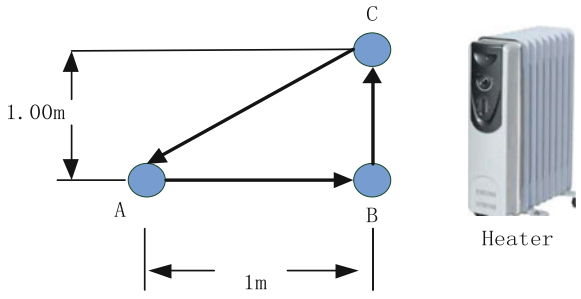

Fig. 5 Schematic diagram: testing experiment

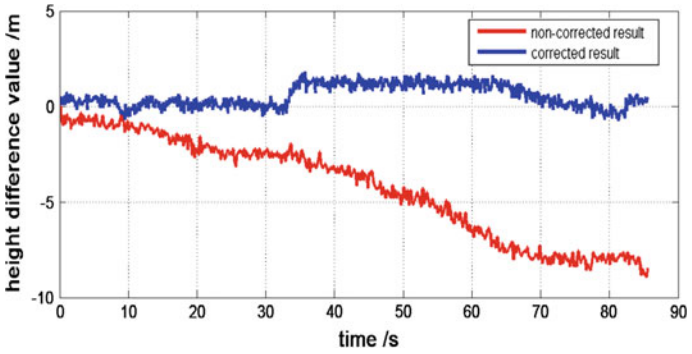

Fig. 6 Curve: results of testing experiment for model

Table 3 Testing data of experiment for model

Observation points	True height difference (m)	The calculating average height difference without model (m)	The calculating average height difference with model (m)	Error of height difference value with model (m)
B	0	−3.626	0.065	0.065
C	1	−7.630	1.198	0.198
A	0	−8.333	0.165	0.165

3.3 Experiment and Conclusion

A high-power heater was placed in a cuboid room under normal environment. The experiment is similar to the simulation of Sect. 3.2. Carry the terminal with constant speed and the movement route is shown as Fig. 5. The testing time of the terminal's movement was: the time from A to B was 10 s and the time of staying at B was 23 s. Then the time from B to C was 5 s and staying at C for 30 s. Finally, the time from C to A was 10 s and staying at A for 10 s. Before the start of the experiment, ensuring that the difference in temperature between point A and B is more than 30 °C. The results are shown in Fig. 6.

Through the results, we can get Table 3 which presents static observation results at A, B, and C points. The results show that the model realizes the vertical positioning accuracy under abnormal temperature testing environment is better than 1 m. The model improves the robustness of differential barometric altimetry.

4 Conclusions

The paper proposed the enhancement correction model and its core idea is: in the microinterval time domain, the atmospheric pressure difference for the effect of human motion can be neglected, thus based on Kalman filter and HGA we can train a nonlinear regression characteristic curve of indoor atmospheric pressure characteristics *A*. By this curve and the testing results of temperature in terminal, the pressure difference caused by heat source can be obtained, so the true height difference due to human motion is known. The testing results show that the model is effective and can be used for universal calibration for differential barometric altimetry in local abnormal temperature environment.

References

1. Deng ZL, Yang L (2014) Research and application of height measurement method in the navigation and positioning system. China Satellite Navigation Conference, 2014
2. Hu ZQ, Zhang LR (2011) Application of differential barometric altimetry in indoor positioning system based on MS5534C. Transducer Microsys. Technol. 30
3. Hu ZQ, Zhang LR (2012) The performance analysis of differential barometric altimeter in indoor positioning system. Chin. J. Sens. Actuators 25:1464–1466
4. Chen JS, Wei G (2001) Hybrid genetic algorithm. China National Knowledge Infrastructure. Available via DIALOG. http://www.rsc.org/dose/title of subordinate document. Cited 2001
5. Dolinski BG (1988) The temperature distribution model for fire area leeward. China National Knowledge Infrastructure. Available via DIALOG. http://www.rsc.org/dose/title of subordinate document
6. Wang SG, Wang RZ (2002) The wind energy equation. China National Knowledge Infrastructure. Available via DIALOG. http://www.rsc.org/dose/title of subordinate document

Part IV
PNT System and Emerging Navigation Technology

Design of the Performance Evaluation Software for X-ray Detectors

Dapeng Zhang, Wei Zheng, Yidi Wang and Lu Zhang

Abstract At present, the X-ray pulsar-based technology is on the step of space verification. It is badly in need of the deep analysis of the craft-carried detector's performance. In addition, the developing departments need the key parameters that influence the performance of the X-ray pulsar-based navigation most. This paper designed a software system which can be used to evaluate the detector's performance. The system can simulate the received photon characteristics with high precision by setting the detector parameters and observed pulsar parameters. Furthermore, it would analyze performance influences to the X-ray pulsar-based navigation by the detector's key parameter, so that the detector performance could be effectively evaluated.

Keywords X-ray pulsar-based navigation system · X-ray detector · Performance evaluation software

1 Introduction

With the rapid development of space technology, the number of on-orbit servicing spacecrafts is increasing. To enhance the ability of autonomous operation, the survival ability of the spacecraft can be improved, and also can reduce the burden of the measurement and control system on ground. Aiming at the problems that the distribution of measurement and control system is concentrated and their geometry is poor in our country, it is particularly important to research X-ray pulsar-based navigation technology to enhance the ability of autonomous operation for the spacecrafts [1–3].

D. Zhang · W. Zheng (✉) · Y. Wang · L. Zhang
College of Aerospace Science and Engineering, National University of Defense Technology, 410073 Changsha, China
e-mail: zhengwei@nudt.edu.cn

J. Sun et al. (eds.), *China Satellite Navigation Conference (CSNC) 2016 Proceedings: Volume II*, Lecture Notes in Electrical Engineering 389,
DOI 10.1007/978-981-10-0937-2_47

X-ray detector is the core sensor device in the X-ray pulsar-based technology application [4–8]. On the basis of the photoelectric effect and Compton Effect produced by the interacting between X-ray photons and detector's sensing material, the device detects the X-ray photons indirectly by measuring the stimulated electrons. According to the difference of the X-ray propagation routes to the sense components, X-ray detector can be divided into collimation-type detectors and focusing-type detector.

At present, the X-ray pulsar-based technology is on the step of space verification. It is badly in need of the deep analysis of the craft-carried detector's performance. In addition, the developing departments need the key parameters that influence the performance of the X-ray pulsar-based navigation most. This paper designed a software system which can be used to evaluate the detector's performance. The system can simulate the received photon characteristics with high precision by setting the detector parameters and observed pulsar parameters. Furthermore, it would analyze performance influences to the X-ray pulsar-based navigation by the detector's key parameter, so that the detector performance could be effectively evaluated.

2 Evaluation Process and Software Framework

The design flow diagram and framework of the software are showed in Fig. 1. According to the research data, establish the background noise database, pulsar database, and detector database, and establish the signal model and detector model accurately. Aiming at the high flux and low flux pulsars, demonstrate the detectors performance and feedback the results to the design departments of the detectors. After the design departments improve the detector, continue to do the performance analysis, until the performance meets requirements.

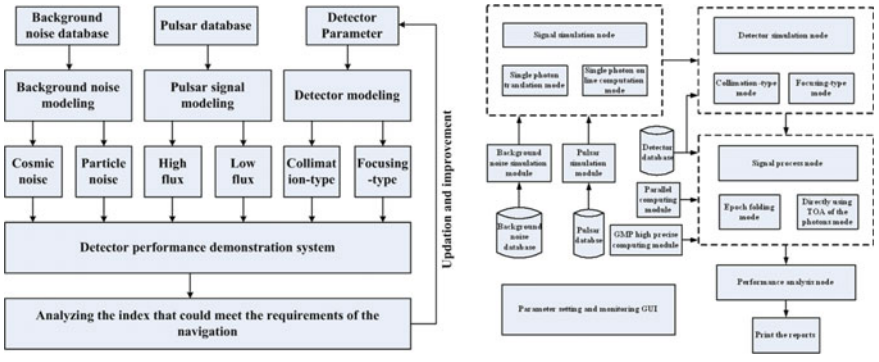

Fig. 1 Design process of the performance evaluation software

3 The Model for the Analysis of the Detector Performance

3.1 The Model for the Pulsar Signal

3.1.1 Models of the Single Photon Time Arrival

To the fixed time t, note the number of the detected photons in $(0, t)$ as N_t. It is random variable of Poisson random process as Eq. (1) shows [9],

$$P(N_t = k) = \frac{\left(\int_0^t \lambda(\xi)\mathrm{d}\xi\right)^k \cdot \mathrm{e}^{-\int_0^t \lambda(\xi)\mathrm{d}\xi}}{k!} \tag{1}$$

The mean value and variance value are,

$$E(N_t) = D(N_t) = \int_0^t \lambda(\xi)\mathrm{d}\xi \tag{2}$$

The detected photons numbers are noted as $N_t - N_s, N_t - N_s$ in arbitrary fixe time interval (s, t). They are also Poisson random process,

$$P(N_t - N_s = k) = \frac{\left(\int_s^t \lambda(\xi)d\xi\right)^k \cdot \mathrm{e}^{-\int_s^t \lambda(\xi)\mathrm{d}\xi}}{k!} \tag{3}$$

Thus, whether photon would be detected in some time interval could be simulated, according to the photon number in this time interval.

3.1.2 Models of the Single Photon Energy

The energy spectrum of pulsar signal's ith phase could be expressed as,

$$F_i(E) = C_i \cdot E^{-\gamma_i} \tag{4}$$

where C_i and γ_i are fitted coefficients. If the number of original data is too low, linear interpolation method could be used to get the energy spectrum function.

If N bins are divided in the pulsar signal's profile, the photon number in ith phase is,

$$N_i = \int_{E_1}^{E_2} F_i(E)\mathrm{d}E \tag{5}$$

where E_1 and E_2 are the upper limit and the lower limit of the detector.

Therefore, the probability density function of the photon energy is *i*th phase which could be expressed as,

$$p_i(E) = k \cdot F_i(E) \tag{6}$$

where k is the uniform coefficient.

According to the phase information in the TOA of the photons, the photons energy could be given by $p_i(E)$.

3.2 The Model for the Space Environments

3.2.1 Models of the Cosmic X-Ray Background

The cosmic X-ray background (CXB) is a kind of cosmic background radiation. This kind of disturbance would be received by the detector. The value of the CXB could be expressed as power-law distribution in 1–20 keV [10] and the unit is keV^{-1} cm^{-2} s^{-1} Sr^{-1},

$$m_{\text{cosmic}}(E) = a \cdot E^{-\lambda}, E < 20 \text{ keV} \tag{7}$$

3.2.2 Models of the Secondary Particle Noise

The secondary particle noise is the noise caused by cosmic primary and secondary proton, electron, and atmospheric photons and neutron; proton radiation is SAA. The amount of the secondary particle is relation to the position, shape, and material of the satellites. The energy spectrum of the secondary particle noise could be expressed as follows, the unit is keV^{-1} cm^{-2} s^{-1}.

$$m_{\text{particle}} = f(E, X, Y, Z, \varepsilon) \tag{8}$$

where X, Y, and Z denotes satellite position in geometric inertial coordination system. ε denotes the coefficient of material and shape of the satellite.

3.3 Model for the Receiving Signal of the Detector

1. Flux of the pulsar signal
   Collimation-type detector:

$$N_p = \int_{E_L}^{E_H} m_p(E)\eta_{\text{detect}}(E)\mathrm{d}E \tag{9}$$

$$\lambda_p = N_p \cdot A_d \cdot r \tag{10}$$

where $m_p(E)$ is the energy spectrum of pulsar signal, $\eta_{\text{detect}}(E)$ is the efficiency curve of the detector, A_d is the physical area of the detector, and r is the duty ratio.

Focusing-type detector:

$$N_p = \int_{E_L}^{E_H} m_p(E)\eta_{\text{detect}}(E)\eta_{\text{reflect}}(E)\mathrm{d}E \tag{11}$$

$$\lambda_p = N_p \cdot A_m \cdot r \tag{12}$$

where $m_p(E)$ is the energy spectrum of pulsar signal, $\eta_{\text{detect}}(E)$ is the efficiency curve of the detector, $\eta_{\text{reflect}}(E)$ is the efficiency curve of the mirror grazing, A_m is the area of the mirror, and r is duty ratio.

2. The time resolution of the photons
   The true time of the ith arrival photon is t_i and T_b is time resolution. If $t'_i - t'_{i-1} < T_b, t'_i$ is abandoned and the next photon is regarded as the ith photon. If not, output t'_i as the measured TOA of the photon.
3. The precision of TOA of the photons
   According to the precision of TOA of the photons, generate Gaussian random number σ_i, and add it to the time mark.

$$t'_i = t_i + \sigma_i \tag{13}$$

4. The time delay distribution simulation

Suppose the delay of the detector obey the distribution of $F(t)$, generate random number and add it the true value.

$$t'_k = t_k + \mathrm{rnd}(F(t)) \tag{14}$$

3.4 Model for the Performance Evaluation

3.4.1 Maximum Likelihood Method

All the detected data is denoted as X, and the signal model could be expressed as,

$$\begin{aligned} R_x &= E\{XX^H\} \quad R_n = E\{nn^H\} \\ X &= p + n \quad R_p(\tau) = E\{pp^H\} \quad R_x(\tau) = R_p(\tau) + R_n \end{aligned} \tag{15}$$

where p and n are effect pulse and noise vectors, $R_p(\tau)$ is the self-correlation matrix of the pulse signal, and R_n is the self-correlation matrix of the noise vector.

The maximum likelihood estimator (MLE) searches the extremum of the likelihood function to estimate the data vector X. Based on the Eq. (15), the likelihood function of X could be expressed as,

$$p(X|\tau) = \frac{1}{\pi^L \det\left(R_n + R_p(\tau)\right)} e^{-X^H\left(R_n + R_p(\tau)\right)^{-1}X} \tag{16}$$

The time of arrival (TOA) is,

$$\hat{\tau} = \arg[\max_\tau \ln p(X|\tau)] \tag{17}$$

3.4.2 The Cross-Correlation Method

Aimed at computing the delay between signal folding wave $p(t)$ and standard profile $s(t)$ (TOA), the method of the cross-correlation could be expressed as,

$$\begin{aligned} \hat{\tau} &= \arg\max_\tau(R(\tau)) \\ R(\tau) &= \frac{1}{N}\sum_{k=1}^{N} p(kT)s(kT-\tau) \end{aligned} \tag{18}$$

where $R(\tau)$ is correlation function, N is the bin number of the profile, and T is the sample period.

4 Implements of the Detector Performance Evaluation Software

1. The working process
   The working process in photon translation mode of the performance evaluation software for X-ray detectors could be described as follows, (Figs. 2 and 3)
   (1) Setting the parameters, e.g., detector's type and select the pulsar;
   (2) Compute the receiving pulse photon number Np during the observation time Tobs;
   (3) Compute the receiving noise photon number Nn during the observation time Tobs;
   (4) Generate the Np and Nn uniform random number from 1 to number of time marks;
   (5) Extract the photon and form a new photon file and generate the photon energy;

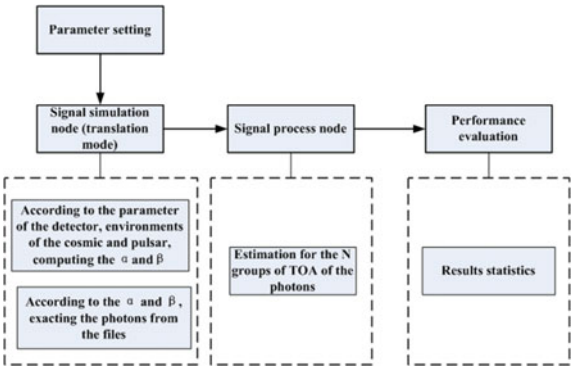

Fig. 2 Working process of the software

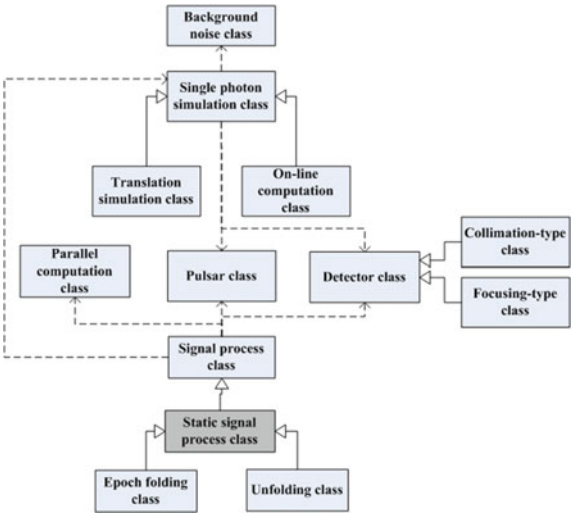

Fig. 3 Relationship of the designed C++ class

(6) Based on the time resolution to judge whether it is necessary to abandon photons;
(7) Based on the precision of the measurement, set the time marks' significand;
(8) Based on the delay distribution, add the detector's random delay;
(9) Use error compensation algorithm to process the data;
(10) Do the TOA estimation to the M groups of photon data;
(11) Based on the TOA estimation results to evaluate the performance.

2. The design of the C++ class
The designed C++ classes are showed as follows,
Background noise class, single photon simulation class, translation simulation class, online computation class, parallel computation class, pulsar class, detector class, collimation-type class, focusing-type class, signal process class, static signal process class, epoch folding class, unfolding class.

5 The Experiments of the Software

The test experiments of the detector performance evaluation software are showed below. The simulation parameter is showed in Table 1.

1. Test for the evaluation of the influence of the sensor area
   Select different sensor area, and do 200 groups of Monte Carlo simulation. The detector performance is showed in Fig. 4 and Table 2.
2. Test for the evaluation of energy resolution of the detector
   Select the secondary noise energy spectrum curve as Fig. 5 shows.
   Take the advantages of the energy resolution, screen out the 1–5 keV photons to do the TOA estimation, the results are showed in Table 3.

Table 1 Parameter setting of the detector

Parameter	Value
Detector physical area	10,000 cm^2
Duty ratio	0.5
View field	0.000239 Sr (nearly 1° × 1°)
Time delay distribution function	Triangular distribution mean value: 30–500 μs
Energy range	1–10 keV
Dark noise	1 ph/s
Time resolution	1 μs
Photon measurement precision	0.1 μs

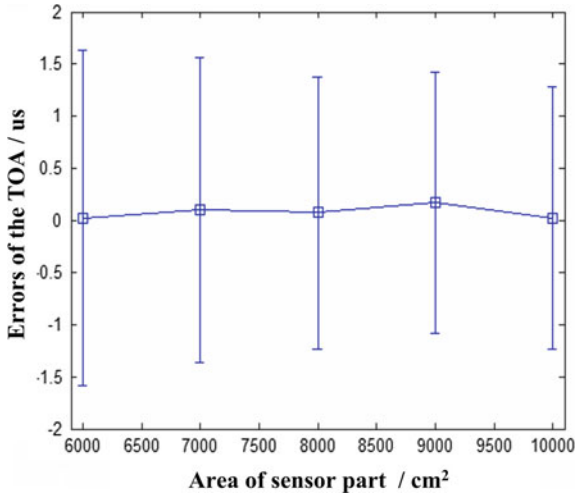

Fig. 4 The influence caused by the area of the sensors

Table 2 Results when observing PSR B0531+21

Sensor area/cm^2	6000	7000	8000	9000	10000
Mean value/μs	0.0210	0.0970	0.0705	0.1730	0.0230
Variance value/μs	1.6089	1.4620	1.3001	1.2508	1.2552

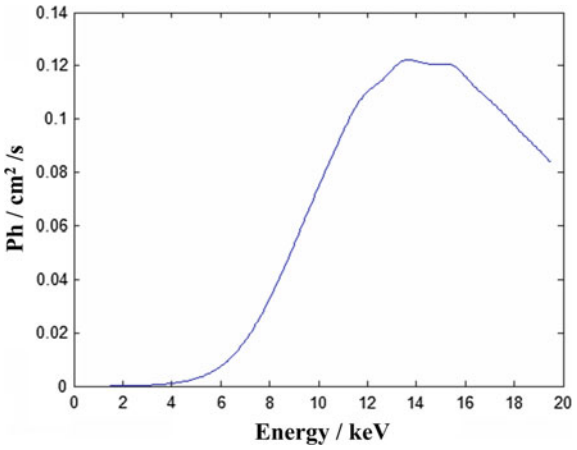

Fig. 5 The curve of particle noise energy spectrum

Table 3 Results when observing PSR B0531+21

Energy range	1–10 keV	1–5 keV	
Energy resolution/eV		200	1000
Mean value (μs)	0.13800	−0.19900	0.20200
Variance value (μs)	1.60158	1.77947	1.62774

6 Conclusions

Nowadays, the X-ray pulsar-based navigation is going to the space technology verification. It is significant to carry out detector performance evaluation. This paper designed a kind of simulation software which is used to evaluate the detector's performance. The software could be used to evaluate both collimation-type and focusing-type detector. The test results show that the function of the software is entire and the performance is reliable. It could be used as reference for detector selection and performance evaluation.

References

1. Shuai P, Ming LI, Chen S, Huang Z (2009) X ray pulse principle and method of satellite navigation system. China Aerospace Press, Beijing
2. Wang Y, Sun S, Li L (2014) Adaptively robust unscented Kalman filter for tracking a maneuvering vehicle. J Guidance Control Dyn 37(5):1696–1701
3. Wang Y, Zheng W, An X (2013) XNAV/CNS integrated navigation based on improved kinematic and static filter. J Navig 66:899–918
4. Lowe BG, Holland AD, Hutchinson IB (2001) The swept charge device, a novel CCD-based EDX detector: first results. Nucl Instr Methods Phys Res A 458:568–579
5. Fedotv MG (2000) CCD detectors for X-ray synchrotron radiation application. Nucl Instr Method Phys Res A 448:192–195
6. Huijun HU (2011) Research for the X ray photon counting detector on pulsar navigation. Chinese Academy of Sciences
7. Ge M (2011) The X-ray emission of pulsars. Chinese Academy of Sciences
8. Xinghua Z, Baosheng Z, Yong'an L (2008) Study of ultraviolet single photon imaging system. J Phys 17(5):715–718
9. Emadzadeh A, Speyer J (2012) X ray pulsar navigation. National Defence Industry Press, Beijing
10. Ge M, Lu F, Qu JL, Zheng S, Chen Y, Han D (2012) X-ray phase-resolved spectroscopy of PSRs B0531+21, B1509-58, and B0540-69 with RXTE. Astrophys J Suppl Ser 199(2):8–10

Research on Gridding Precision Evaluation Method of Geomagnetic Field Model

Yang Chong, Hongzhou Chai, Yifeng Chang, Zongpeng Pan, Huarun Wang and Yuan Liu

Abstract With the in-depth research on geomagnetic field model and geomagnetic navigation, the appropriate method of precision evaluation of the geomagnetic field model is required. WMM model and INTERMAGNET observations data are used to research the precision of the latest WMM2015 model in the world, and analyze the accuracy of different local areas, such as Europe, North America, and China. According to the relationship between truncation order of spherical harmonic coefficients of geomagnetic field model and wavelength of spatial resolution, gridding method is proposed to evaluate the geomagnetic field model. The precision analysis of WMM2015 model in the global and local area is provided for the reference of obtaining the more-refined geomagnetic map in geomagnetic navigation matching.

Keywords Geomagnetic field model · Geomagnetic navigation · Observation · WMM2015 · Truncation order · Gridding

1 Introduction

Geomagnetic field, same as gravity field, is basic physical field of the earth. The earth's magnetic field is a vector quantity varying in time and space. Geomagnetic field model is an approximation of the geomagnetic field using a mathematical

Y. Chong (✉) · H. Chai · Y. Chang · Z. Pan · H. Wang
Institute of Geospatial Information, Information Engineering University, Zhengzhou 450001, China
e-mail: chongyang_geodesy@outlook.com

Y. Chong · Y. Chang
State Key Laboratory of Geo-Information Engineering, Xi'an, China

Y. Chong
Department of Navigation, Naval University of Engineering, Wuhan, China

Y. Liu
72515 Troops, Jinan, China

J. Sun et al. (eds.), *China Satellite Navigation Conference (CSNC) 2016 Proceedings: Volume II*, Lecture Notes in Electrical Engineering 389,
DOI 10.1007/978-981-10-0937-2_48

method. It plays an important role on understanding the earth's interior structure, the activities of ionosphere, geomagnetic navigation and orientation, etc. [1–3]. The World Magnetic Model is internationally recognized as the main field of reference model, which is a joint product of the United States' National Geospatial-Intelligence Agency and the United Kingdom's Defence Geographic Centre, that launches a new model every 5 years. The WMM is the standard model used by the U.S. Department of Defense, the U.K. Ministry of Defence, the North Atlantic Treaty Organization, and the International Hydrographic Organization, for navigation and attitude referencing systems. It is also used widely in civilian navigation and heading systems. Irregular changes in the Earth's core field limit the lifetime of any predictive model such as the WMM. For this reason a revision (WMM2015) was released in December 2014. Effective age for this revision model is as of January 1, 2015 to December 31, 2019 and its data mainly comes from Swarm, *Orested*, and CHAMP magnetic survey satellites. In WMM2015 technical report, the requirement is that the global RMS difference between the WMM and the observed magnetic field at sea level should be within 1° for D and I, within 140 nT for X and Y, within 200 nT for H and Z, and within 280 nT for F for the entire 5-year lifetime of the model [4].

In geomagnetic navigation applications, the geomagnetic field model in the precision of the global and local distribution needs further analysis. A more precise and reasonable method to evaluate the precision of this model on regional is required [5, 6]. Since the geomagnetic field model is under certain truncation order approximate description of the magnetic field, the geomagnetic field model has certain space resolution. The approximation precision of the geomagnetic field in the global or local region will be affected by some big error stations. Therefore, it is necessary to use the spatial resolution which is corresponded with network as basic units and utilize stations of certain grid to get its model accuracy. Moreover, taking the average precision accuracy of all grids in the focus area is a suitable way to evaluate precision accuracy of regional model. Based on this method, this paper analyzed the relationship between observation data released by the INTERMAGNET and WMM2015 model values, also, the global precision of seven geomagnetic elements are given. Meanwhile, traditional precision evaluation results from the latest WMM2015 model in Europe, North America, and China are put forward, then the new gridding method is proposed to evaluate the geomagnetic field model and some beneficial conclusions are gained.

2 The Principle and Method of Geomagnetic Field

Usually, ignoring the external field, the main magnetic field is a potential field and therefore can be written in geocentric spherical coordinates as the negative spatial gradient of a scalar potential. This potential can be expanded in terms of spherical harmonics as below [7].

$$U(r,\theta,\lambda) = R\sum_{n=1}^{N}\sum_{m=0}^{n}\left(\frac{R}{r}\right)^{n+1}(g_n^m\cos m\lambda + h_n^m\sin m\lambda)P_n^m(\cos\theta) \tag{1}$$

where r is the geomagnetic reference radius, θ is the latitude, λ is the longitude, R is the radius in a spherical geocentric reference frame, $P_n^m(\cos\theta)$ are the Schmidt semi-normalized associated Legendre functions, g_n^m, and h_n^m are the time-dependent Gauss coefficients, and N is the degree of the expansion of the WMM.

The field vector components X, Y, and Z in geocentric coordinates are computed as,

$$\begin{cases} X = \sum\limits_{n=1}^{N}\sum\limits_{m=0}^{m=n}\left(\frac{R}{r}\right)^{n+2}(g_n^m\cos m\lambda + h_n^m\sin m\lambda)\frac{\partial P_n^m(\cos\theta)}{\partial\theta} \\ Y = \sum\limits_{n=1}^{N}\sum\limits_{m=0}^{m=n}\left(\frac{R}{r}\right)^{n+2}(g_n^m\cos m\lambda - h_n^m\sin m\lambda)\frac{mP_n^m(\cos\theta)}{\sin\theta} \\ Z = -\sum\limits_{n=1}^{N}\sum\limits_{m=0}^{m=n}(n+1)\left(\frac{R}{r}\right)^{n+2}(g_n^m\cos m\lambda + h_n^m\sin m\lambda)P_n^m(\cos\theta) \end{cases} \tag{2}$$

The magnetic elements H F, D, and I are computed from the orthogonal components.

$$\begin{cases} H = \sqrt{X^2+Y^2} \\ F = \sqrt{X^2+Y^2+Z^2} \\ \sin D = \frac{Y}{H} \\ \sin I = \frac{Z}{F} \end{cases} \tag{3}$$

2.1 Traditional Evaluation Method

Traditional evaluation method is to calculate the difference between observed values from ground stations and the published geomagnetic field model value. The average precision is given in the global or local scope through statistical analysis of the difference.

$$(\Delta B)_i = B_i^{\mathrm{Obv}} - B_i^{\mathrm{Mod}}, \quad i = 1,\ldots,N \tag{4}$$

where B_i^{Obv} is the observatory data, B_i^{Mod} is the model value, $(\Delta B)_i$ is the difference between the observatory data and the model value, i is the number of observatory, N is the total number of observatories.

Maximum, minimum, average, and root mean square error are four indicators to evaluate the model precision as below.

$$\begin{cases} \sigma_1 = \max\{[(\Delta B)_1(\Delta B)_2 \cdots (\Delta B)_i \cdots (\Delta B)_N]\} \\ \sigma_2 = \min\{[(\Delta B)_1(\Delta B)_2 \cdots (\Delta B)_i \cdots (\Delta B)_N]\} \\ \sigma_3 = \sum_{i=1}^{N} (\Delta B)_i \Big/ N \\ \mathrm{RMS} = \sum_{i=1}^{N} [(\Delta B)_i - \sigma_3]^2 \Big/ (N-1) \end{cases} \tag{5}$$

where σ_1 denotes the maximum, σ_2 denotes the minimum, σ_3 denotes the average, and RMS denotes the root mean square error.

However, this is the average precision of the magnetic model in the Earth. In view of the geomagnetic field, model under different truncation order has different characteristics of resolutions. Obviously, it will cover the real situation. Therefore, gridding method is proposed to evaluate the geomagnetic field model.

2.2 Improved Gridding Method

The magnetic field is a potential field satisfying geocentric spherical theory. Using spherical harmonic function model to represent the global distribution of the geomagnetic field is the common way. Model is, however, makes of magnetic dipole, quadrupole, and octupole for an approximate description of the geomagnetic field. The certain error will be introduced by mathematical abstraction and approximate, which is called model error [8].

From Gaussian sphere harmonic theory, it is obviously known that spherical harmonic coefficients need to expand the infinite order to approach the real Earth's magnetic field. In practice, spherical harmonic coefficient of geomagnetic field model is usually spread to a certain order to approximate the magnetic field distribution around the world, which is called truncation error. WMM has truncation order of 12, mainly containing the main magnetic field. Higher order of the Earth's crust and other exogenous field were ignored. Ground observatory, however, contains the full-wavelength geomagnetic field information, so the model value and the observatory data will exist the difference [9, 10].

It is shown that different truncation order has different spatial resolution and wavelength. The relationship between truncation order and the spatial resolution wavelength in geomagnetic field model is shown in the following formula [11]:

$$\lambda = 2\pi R/N \tag{6}$$

where R the radius in a spherical geocentric reference frame, N is the maximum truncation order, and λ is the spatial resolution wavelength.

Therefore, under different truncation order, the main magnetic field and crustal magnetic field have respective spatial resolution wavelength. It needs to be divided into different grid values. As is shown in Table 1.

Table 1 The relationship between truncation order of spherical harmonic and wavelength of spatial resolution

Magnetic field components	Order /N	Wavelength/km	Grid/°	Magnetic field components	Order/N	Wavelength/km	Grid/°
The main magnetic field	10	4003.1	35.9	High order of crust field	70	571.8	5.1
	11	3639.2	32.7		80	500.3	4.4
	12	3336.0	29.9		90	444.7	3.9
	13	3079.3	27.6		100	400.3	3.5
	14	2859.4	25.7		110	363.9	3.2
	15	2668.8	23.9		120	333.5	2.9
Low order of crust field	16	2502.0	22.4		130	307.9	2.7
	17	2354.8	21.1		140	285.9	2.5
	18	2224.0	19.9		150	266.8	2.3
	19	2106.9	18.9	Ultrahigh order	200	200.1	1.7
	20	2001.6	17.9		300	133.4	1.2
	30	1334.4	11.9		400	100.1	0.9
Middle order of crust field	40	1000.8	8.9		500	80.1	0.7
	50	800.6	7.1		600	66.7	0.6
	60	667.2	5.9		720	55.5	0.5

As shown in Table 1, as the increasing of truncation order of spherical harmonic, the wavelength of spatial resolution decreases gradually. According to the relationship between truncation order of spherical harmonic and wavelength of spatial resolution, truncation order of WMM is 12, which is corresponding to the wavelength of the spatial resolution which is 3335 km. The surface of the Earth is divided into regular grid in the length of 3335 km, each grid is paralleled with 30° of latitude and longitude. With series of 30° grid, taking the average value of observatory data in each grid is an effective method to smooth and filter high-order geomagnetic information. As a result, comparing with observatory data, the value of WMM is pretty much the same.

To sum up, the steps of gridding precision evaluation method of geomagnetic field model are shown below.

(1) Based on the geomagnetic field truncation order, the undetermined grid degree can be counted out easily. Then the world is divided into the different grid equally through the obtained degree. According to the latitude and longitude of observatories in the world, observatories are grouped into the different grid. Observatory data in each grid is acquired.
(2) The values of geomagnetic field model is calculated by the center coordinates of each grid, which is regarded as the average values of the geomagnetic field model in respective grid.

(3) Counting the difference between observed values from ground stations and the published geomagnetic field model values in each divisive grid. Simultaneously, RMS in individual grid is summarized.
(4) The RMS of F in each grid is drawn into the global grid. Finally, we can get the final evaluation figure of grid precision.

3 Experiments and Results Analysis

3.1 Data Collection

The experiment model is WMM2015, the observatory data is derived from the website of INTERMAGNET, including 130 observatories in the global scale from 2014.5 to 2015.5. Based on the comparison of component between the model value and the observatory data from the global and regional scale, the estimation of geomagnetic model precision is summarized.

Research areas include Europe, North America, Chinese mainland and its surrounding areas. The observatories in these areas have different intensity. Europe, where is from 30° to 75° in latitude and from −30° to 45° in longitude, contains 42 geomagnetic observatories. North America, where is from 15° to 85° in latitude and from −170° to −50° in longitude, contains 23 geomagnetic observatories. Chinese mainland and its surrounding areas, where is from 0° to 55° in latitude and from 70° to 140° in longitude, contains 19 geomagnetic observatories.

The distribution of geomagnetic stations around the world is shown in Fig. 1.

From Fig. 1, we can find that most geomagnetic stations are distributed in the northern hemisphere, and a few stations are interspersed among the two poles of the

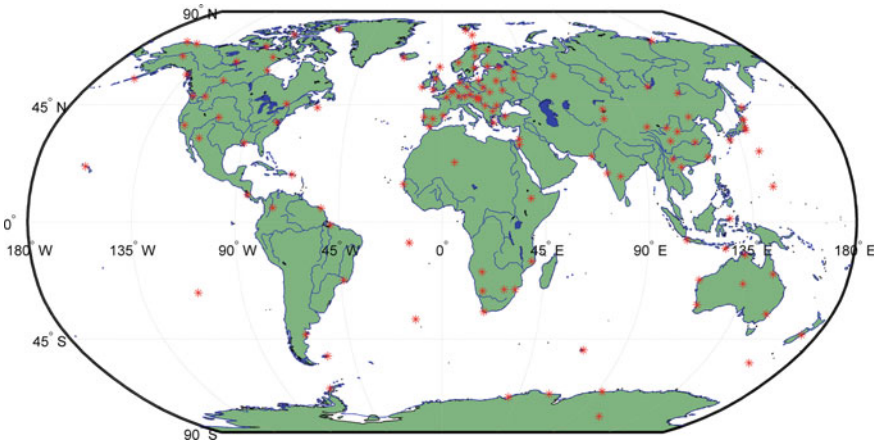

Fig. 1 The distribution of geomagnetic stations around the world

Earth. Locally, number of geomagnetic stations in Europe is numerous, which have intensive distribution and good uniformity, covering most of the land. It is useful for the construction of geomagnetic field model and the evaluation of accuracy, providing a good data base. Number of stations in North America is less than Europe, and larger blank area exists in the central region. The distribution of those stations is well proportioned in geometric construction. Chinese mainland and its surrounding areas have a few and uneven geomagnetic stations. In its western regions, a large blank area is appeared obviously.

On the basis of coordinates of geomagnetic station from the INTERMAGNET, seven elements of geomagnetic model are calculated through the position of observatories. Compared model value with observatory data, the residual error can be probed easily. Through the analysis of the difference in global and regional area, the precision of the geomagnetic field model can be evaluated greatly.

3.2 The Results of Traditional Method

The observatory data is supposed to handle the reduction to a certain moment, including 130 observatories in the global scale. Here the moment is 2015.0. Observatory annual mean values are put forward later. Meanwhile, we should calculate the corresponding observatory values of WMM2015 in 2015.0. According to Gaussian potential theory, seven elements of geomagnetic field can calculated by Gaussian coefficient of WMM2015. These are the northerly intensity X, the easterly intensity Y, and the vertical intensity Z and the following quantities derived from X, Y, and Z: the horizontal intensity H, the declination angle D, the inclination angle I, and the total intensity F.

Table 2 shows geomagnetic field model accuracy of evaluation results which are calculated by the traditional method.

From Table 2, in the global scale, the RMS of D and I is 0.93° and 0.65°, respectively, through WMM2015, the RMS of X, Y, and H is around 170 nT, Z and F is larger, which is below 200 nT. In Europe, the RMS of D and I is 0.79° and 0.12°, respectively, the RMS of X, Y, and H is less than 140 nT, Z and F is around 180 nT. In North America, the RMS of D and I is all less than 1°, the RMS of X and Y is 112.64 and 100.15 nT, respectively, and they are superior to 140 nT, the RMS of H and Z is 175.90 and 108.10 nT, respectively, and they are superior to 200 nT,

Table 2 The traditional method to calculate geomagnetic field model accuracy of evaluation results

Intensity	D/°	H/nT	I/°	X/nT	Y/nT	Z/nT	F/nT
Europe	0.79	122.73	0.12	110.88	138.20	177.24	188.78
North America	0.79	108.10	0.15	112.64	100.15	175.90	162.48
China	0.83	126.06	0.40	115.50	180.76	246.09	182.43
World	0.93	183.96	0.65	168.68	176.41	242.34	194.73

the RMS of F is 182.43 nT, and it is superior to 280 nT. In Chinese mainland and its surrounding areas, the RMS of D and I is 0.83° and 0.40°, respectively. We can clearly see that RMS of the inclination angle I is higher than Europe and North America, but below average of the world. The RMS of X is equivalent to the other area. Not only the RMS of Y and Z are significantly larger than Europe and North America, but also it exceeds the world average, which are reach to 180.76 and 246.09 nT, respectively. The RMS of F is equivalent to the Europe and North America, which is 182.43 nT.

By contrast, traditional precision evaluation method of the geomagnetic field model do not well distinguish from real precision distribution of the geomagnetic field model on different regions.

3.3 The Results of Gridding Method

The grid is selected from the range in 30° × 30°, and it is necessary to count out the difference between model value and observatory data in each grid. The RMS from every grid represents the precision of the geomagnetic field model in the homologous grid. In order to demonstrate the accuracy of seven geomagnetic elements in global and regional scale more clearly, the average RMS of these seven geomagnetic elements in different grids, which are from the four areas, are put forward to stand the average precision of the geomagnetic field model in the corresponding region.

Table 3 shows geomagnetic field model accuracy of evaluation results which are calculated by the gridding method.

From Table 3, from the comparison of the seven geomagnetic elements, we can find that the RMS of D is higher than I, and the RMS of X, Y, and H have the same wave range nearby 100 nT, and the RMS of Z and F is about 150 nT. From the global and regional scale, the RMS of the former is larger than the latter. In Chinese mainland and its surrounding areas, the RMS of Z and F exceeds the world average level. From the regional scale, the RMS of all seven geomagnetic elements in Chinese mainland and its surrounding areas are greater than Europe and North America, of which X, Y, Z, and I have obviously distance.

In order to demonstrate the geomagnetic field model accuracy of evaluation results by the gridding method, the RMS of F from the Europe, North America,

Table 3 The gridding method to calculate geomagnetic field model accuracy of evaluation results

Intensity	D/°	H/nT	I/°	X/nT	Y/nT	Z/nT	F/nT
Europe	0.57	74.31	0.09	71.69	55.64	86.12	85.99
North America	0.53	107.67	0.16	106.74	94.64	178.26	153.67
China	0.59	134.47	0.72	130.59	181.32	295.06	212.90
World	0.78	150.34	0.61	142.07	123.78	191.35	168.09

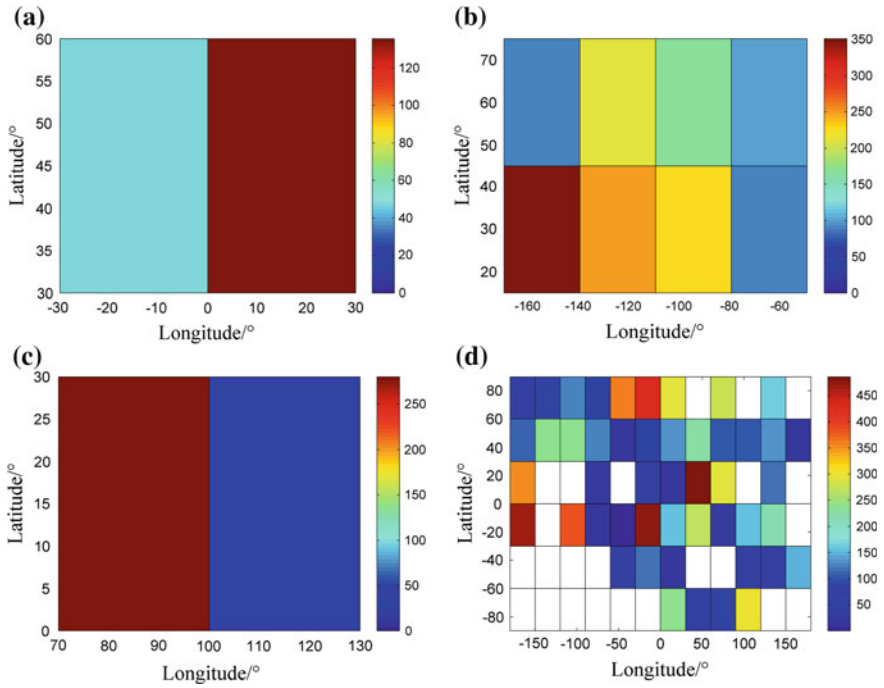

Fig. 2 The distribution of grid precision

China and the global scope of geomagnetic are calculated in turn. Results are shown in the below figures.

From Fig. 2, the distribution of grid precision from the Europe (a), North America (b), China (c) and the world (d) are displayed in turns. The blank area stands that none of observatory is distributed in the relevant grid. Different grid has various precisions of geomagnetic model. As is shown in the figure (a), Europe have many observatories, which are distributed intensively and uniformly. That is the reason why the RMS of the left part of the figure (a) is around 50 nT, and the right one is also about 110 nT. In the figure (b), the RMS of central and southwestern North America is higher than the other part. Owing to the sparse observatory distribution, the RMS of central part is about 200 nT, and the RMS of southwestern part is about 300 nT. In the figure (c), the RMS of western China is higher than the eastern part. Owing to the sparse observatory distribution in western China, its RMS is around 300 nT. As is shown in the figure (d), we can see that the grid density of the southern hemisphere is higher than the northern hemisphere. It is mainly attributed to most stations which are distributed in the northern hemisphere. Meanwhile, Europe has the highest density and continuous grid, second is North America, China and surrounding areas is in the end.

4 Conclusions

To sum up, WMM2015 has good applicability on a global scale, which is a joint product of NGA and DGC. Different geomagnetic elements have different precision in the global or regional area. Compared with the traditional method, gridding precision evaluation method of geomagnetic field model is more intuitive and practical.

(1) From the global scale, comparison precision between WMM2015 and observatory is 0.93° for D, 0.65° for I, 168.68 nT for X, 176.41 nT for Y, 242.34 nT for Z, 183.96 nT for H, and 194.73 nT for F. The precision of model varies from different regional area. The precision of Europe and North America is better than Chinese mainland and its surrounding areas, which is mainly attributed to more observatories and uniform observatory distribution. Meanwhile, the RMS of geomagnetic field model in regional area is less than the world.

(2) According to the relationship between truncation order of spherical harmonic coefficients of geomagnetic field model and wavelength of spatial resolution, gridding method is proposed to evaluate the geomagnetic field model in the global and local area. After a new evaluation method put forward, comparison precision between WMM2015 and observatory is 0.78° for D, 0.61° for I, 142.07 nT for X, 123.78 nT for Y, 191.35 nT for Z, 150.34 nT for H, and 168.09 nT for F. Compared with the traditional method, gridding precision evaluation method of geomagnetic field model can better reflect its precision distribution.

(3) Analysis of the precision of the geomagnetic field model in local areas is conducive to make better use of geomagnetic field model data. WMM2015 cannot calculate the geomagnetic field in China accurately, mainly due to the time and spatial resolution which cannot meet the requirements. Based on WMM2015 model, there is a recommendation that combined with the satellite magnetic survey, aviation magnetic survey, ground magnetic survey, and marine magnetic survey data in China, it is necessary to build high-precision geomagnetic model in China, and provide for the reference to obtain the more-refined geomagnetic map in geomagnetic navigation matching.

Acknowledgments Thanks to the INTERMAGNET for providing worldwide observatory data. This work was supported by National Natural Science Foundation of China (41574010, 41476087, 41274045) and State Key Laboratory of Geo-information Engineering (SKLGIE 2014-M-1-1).

References

1. Wang D (2003) Analysis of the international geomagnetic reference field error in the China continent. Chin J Geophys 46(2):171–174
2. Psiaki ML (1995) Autonomous orbit and magnetic field determination using magnetometer and star sensor data. J Guid Control Dyn 18(3):584–592
3. Peng FQ (2006) Geomagnetic model and geomagnetic navigation. Hydrogr Surveying Charting 26(2):73–75
4. Chulliat A, Macmillan S, et al (2015) The US/UK world magnetic model for 2015–2020. BGS and NOAA 112 pp
5. Zhou J, Ge ZL, Shi JG et al (2008) Key technique and development for geomagnetic navigation. J Astronaut 29(5):1467–1472
6. Sun Y, Zhang JS, Wang SC et al (2011) Time-variation update for geomagnetic navigation reference map based on secular variation model of main geomagnetic field. J Chin Inertial Technol 19(5):543–548
7. Xu WY (2009) Physics of electromagnetic phenomena of the earth. University of Science and Technology of China Press, Hefei
8. Xu WY, Bai CH, Kang GF (2008) The world magnetic model of the globe magnetic anomaly. Chin J Geophys 23(3):641–651
9. Li ZL, Bian SF (2011) World magnetic model (WMM) 2010 and its application. Ship Electron Eng 31(2):58–61
10. Xu RG, Li ZJ, Zhang WJ et al (2014) Accuracy and application of EMM2010 in Chinese mainland. J Jilin Univ (earth science edition) (03):1018–1030
11. Macmillan S (2010) Earth's magnetic field. Geophys Geochem

Analysis on the Influence Factors to Atmospheric Polarization Navigation

Yawen Ou, Pengfei Wu, Chaoli Tang and Heli Wei

Abstract With the increasing demand for navigation, and the establishment of the PNT (positing navigation time) system, the autonomous navigation method based on the atmospheric polarization properties has been one of the hot topics. As atmospheric scattering is dominated by Rayleigh scattering under clear-sky condition, atmospheric radiation polarization picture is stable. Thus, the atmospheric polarization navigation can be effectively under clear sky. However, for turbid atmosphere containing aerosol particles, polarization picture's stability is seriously affected, especially in tropospheric low visibility condition. Under these conditions, the effectiveness of navigation by atmospheric polarization significantly reduces, which becomes the important factor limiting the application of atmospheric polarization navigation in near-surface haze condition. Therefore, analyzing the factors of atmospheric polarization properties and the feasibility of navigation by atmospheric polarization in different atmospheric conditions is significant for the study of complex atmospheric conditions polarized radiation and the development of new application fields of atmospheric polarization navigation. This paper describes the research advances about atmospheric polarization properties and its navigation method, and analyzes the influence factors to atmospheric radiation polarization properties, including the optical parameters of aerosol particles (such as the complex refractive index and scale spectrum of aerosol particles), atmospheric turbidity, and sun-observation geometry orientation. The feasibility of navigation using atmospheric polarization in troposphere and stratosphere above is further investigated.

Y. Ou · P. Wu (✉) · C. Tang · H. Wei
Key Laboratory of Atmospheric Composition and Optical Radiation, Anhui Institute of Optics and Fine Mechanics, Chinese Academy of Sciences, Hefei, China
e-mail: wupengfei@aiofm.ac.cn

Y. Ou
e-mail: ouyawen@mail.ustc.edu.cn

Y. Ou · H. Wei
Department of Environmental Science and Optoelectronic Technology, University of Science and Technology of China, Hefei, China

J. Sun et al. (eds.), *China Satellite Navigation Conference (CSNC) 2016 Proceedings: Volume II*, Lecture Notes in Electrical Engineering 389,
DOI 10.1007/978-981-10-0937-2_49

Keywords Atmospheric polarization navigation · Atmospheric polarization characteristics · Rayleigh scattering · Turbid atmosphere

1 Introduction

The solar light is natural light, which has same vibration in all directions. After scattering by atmospheric molecules and aerosol particles, the vibration intensities show differences in different directions, and the scattering light becomes partially polarized light or the linearly polarized light. The polarized light in the sky presents a regular pattern, which presents the polarization information including the degree and direction of polarization. This is called the atmospheric polarization mode [1].

After Arago first discovered the phenomenon of light polarization in the sky in 1809, Rayleigh [2] and Mie [3] founded Rayleigh scattering theory and Mie scattering theory by studying the scattering of gas molecules and aerosol particles in the atmosphere, respectively. These theories were used to explain the polarization of scattering sky light. Since, the atmospheric polarization theory system has been mature, the measurement technology of the sky polarized light was gradually developed. At present, some sky polarized light detection systems have been developed by researchers, such as a point-source sky polarized light detection system [4], an imaging all-sky polarized light detection system [5], a spectral polarization radiometer [6], and so on. During the studying process of atmospheric polarization properties, Wehner [7] found that sand ants can determine its own position by using the direction information of the ultraviolet polarized light. Since then, the bionic scientists discovered that the butterfly, spider, and other creatures can also navigate using the sky-polarized light in succession. Inspired by this, bionic polarization sensitive neuron model [8, 9] was designed, and the bionic polarization sensor was realized based on the bionic model. The experiments to robot with the polarized detecting sensor [10, 11] were carried out successfully, which verified the feasibility of using polarized light to locate and navigate. A combinatorial method [12] providing the attitude information of aircraft using polarized light, and a high-precision polarized light navigating instrument for vehicles real-time navigation [13] are gradually emerging.

In summary, the present researches on polarization navigation of atmospheric scattering light are mostly carried out in the near surface. However, the atmospheric polarization information can be seriously affected by the scattering of atmospheric aerosol under the condition of low visibility, which becomes one of the important factors limiting the application of atmospheric polarization navigation in near-surface haze or fog conditions. Therefore, analyzing the influencing factors of atmospheric polarization properties and the feasibility of navigation using atmospheric polarization in different atmospheric conditions is significant for the study of

polarization properties under complex atmospheric conditions and the development of new application fields of atmospheric polarization navigation.

This paper first introduced the research progress about the atmospheric polarization properties and its navigation method. Then the influencing factors on atmospheric polarization properties were analyzed, including the optical parameters of aerosol particles (such as the complex refractive index and size distribution of aerosol particles), atmospheric turbidity, and sun-observation geometry orientation. At last, the feasibility of navigation using atmospheric polarization in troposphere, stratosphere, and higher altitude atmosphere was further investigated simply.

2 Analysis of the Influence Factors to Atmospheric Polarization Properties

2.1 Distribution of Atmospheric Polarization of Molecular Scattering

In a clear sky or in the middle to upper atmosphere with Rayleigh scattering, natural incoming solar light will be scattered by molecules in the atmosphere and becomes polarized light. The polarization properties are relatively simple. Considering the case of a natural light incoming and single scattering, if the intensity of natural light is I_0, the intensity of vertical and horizontal components is I_{0r} and I_{0l}, respectively, $I_{0r} = I_{0l} = I_0/2$, the intensity of the scattering light by gas molecules is

$$I = I_r + I_l = I_{0r}\frac{k^4\alpha^2}{r^2} + I_{0l}\frac{k^4\alpha^2\cos^2\Theta}{r^2} = \frac{I_0\alpha^2}{r^2}\left(\frac{2\pi}{\lambda}\right)^4\frac{1+\cos^2\Theta}{2} \tag{1}$$

where $k = 2\pi/\lambda$, α is polarizability, Θ is the scattering angle, r is the distance from the observer to the particle, and λ is wavelength.

After scattered by atmospheric molecule, which obeys the Rayleigh scattering theory, the scatting light is mainly linearly polarized light, and the linear degree of polarization (DOP) is defined as

$$P(\Theta) = \frac{I_r - I_l}{I_r + I_l}P_{\max} = \frac{\sin^2\Theta}{1+\cos^2\Theta}P_{\max} \tag{2}$$

where $P_{\max}$ represents the maximum degree of polarization under ideal condition, and the value is generally 1.

In Fig. 1, the relationship between the degree of polarization and the scattering angle for Rayleigh scattering light of single isotropic atmospheric molecule is shown.

From Fig. 1, it can be seen that the degree of polarization of forward and backward scattering light is 0, which indicates that the scattering light is totally

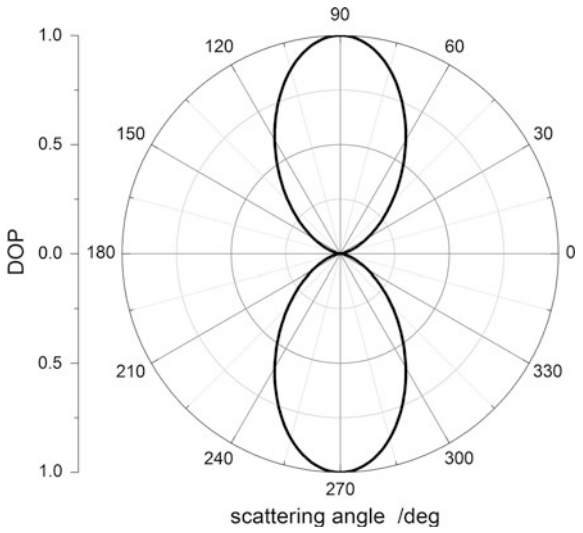

Fig. 1 The relationship between the degree of polarization and the scattering angle for Rayleigh scattered light

nonpolarized. When the scattering angle is 90° or 270°, the degree of polarization is 1, which indicates that the scattering light is fully polarized, i.e., it is the linearly polarized light. For other scattering angles, the scattering light is partially polarized light. According to Rayleigh scattering theory, the degree of polarization is symmetric with the scattering angle, and is only related to the scattering angle. This calculation mode of degree of polarization can describe atmospheric polarization pattern in clear-sky well. However, when considering the molecular aggregation, we need to correct the calculation mode due to multiple scattering effects, because the mode mentioned above is used only for a single molecule.

2.2 *Effects of Optical Properties of Aerosol Particles on Polarization Distribution*

The Mie scattering theory can be used to describe the light scattering by aerosol particles. For the basic theory of light scattering problems, Mie scattering theory is applied to deal with uniform spherical particles with any size and complex refractive index. The bulk degree of polarization of the scattering light can be obtained if the size distribution of the multi-particles system is known

$$LP_{\mathrm{M}}^{V} = \frac{\int_{r_1}^{r_2} [i_2(r) - i_1(r)]n(r)dr}{\int_{r_1}^{r_2} [i_2(r) + i_1(r)]n(r)dr} \tag{3}$$

where $n(r)$ is the size distribution of aerosol particles, which represents the number of the particles in unit volume within radius $r \sim r + dr$, r_1 and r_2 are the lower and

upper limits of the particle radius, respectively. i_1 and i_2 are the scattering intensity function.

Assuming that the size distribution of aerosol particles is in accordance with the Junge's distribution. Junge's distribution is widely used to describe the size distribution of atmospheric aerosols. The actual experimental results show that most of aerosol distributions in the near-surface layer are consistent with the Junge's distribution to some extent. Junge's distribution is as follows:

$$n(r) = \frac{dN(r)}{dr} = Kr^{-(\upsilon+1)} \tag{4}$$

where K is a constant related to the particle concentration, υ is Junge index, and represents the distribution shape characteristic. It reflects the proportion of aerosol particles with different sizes, i.e., a large value of υ indicates a larger proportion of small particles, and smaller value of υ indicates a greater proportion of large particles.

For aerosol particles, the degree of polarization of the scattered light is related not only with the scattering angle, but also with the incident light wavelength, scattering particle properties (such as particle size parameters and complex refractive index, etc.). Firstly, the map of relationship between the degree of polarization and the scattering angle under different Junge indices υ is shown in Fig. 2. Where, we assume that the complex refractive index of aerosol is $m = 1.45 - i0.004$, the wavelength is $\lambda = 550$ nm, and the particle radius is $0.01 - 1$ μm in the calculations.

From the Fig. 2, we can see that under different particle size distributions, the relationships between the degree of polarization and scattering angle show apparent differences. For larger Junge index, i.e., small particles are dominant, the degree of polarization at the scattering angle of about 90° is largest. With the Junge index decreases, the proportion of large particles gradually increases, and the maximum degree of polarization gradually shifts to the back direction. It can also be seen that

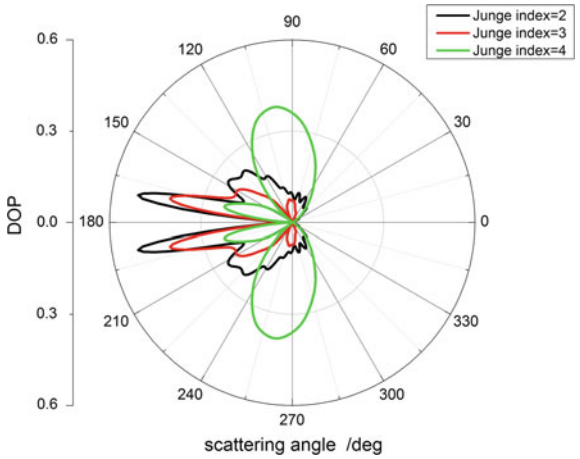

Fig. 2 The relationship between the degree of polarization and the scattering angle under different Junge index

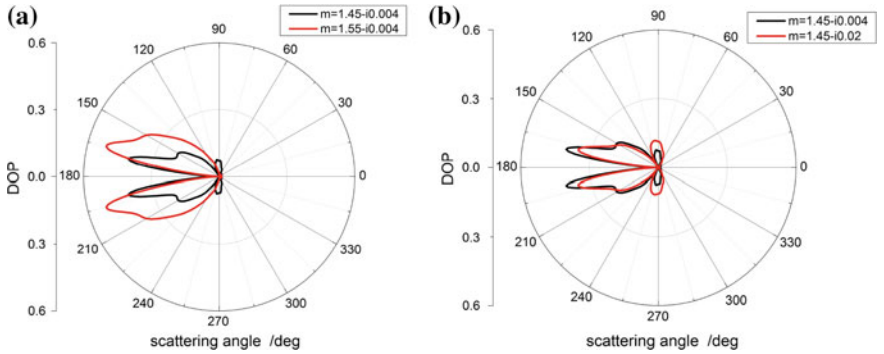

Fig. 3 The relationship between the degree of polarization and the scattering angle under different real (**a**) and imaginary (**b**) parts of complex refractive index

the degree of polarization of Mie scattering is smaller compared with Rayleigh scattering.

Then, the relationship curves between the degree of polarization and the scattering angle are given under different real and imaginary parts of complex refractive index of aerosol particles, as shown in Fig. 3, where we assume that the size distribution of aerosol is Junge's distribution with the Junge index of 3, the wavelength is $\lambda = 550\,\text{nm}$, and the radius is $0.01 - 1\,\mu\text{m}$.

From Fig. 3, we can see that the relationship between the degree of polarization and scattering angle is obviously different under different real parts of complex refractive index. It indicates that the particle scattering is important to the degree of atmospheric polarization. However, the change trends of the degree of polarization and scattering angle under different imaginary parts of complex refractive index are approximately the same. It indicates that the influence of the imaginary part on atmospheric polarization is less compared with the real part, and the effect of particle absorption on the degree of atmospheric polarization can be ignored to a certain extent.

2.3 *Effects of Atmospheric Turbidity on the Polarization Distribution of the Whole Sky*

For the actual turbid atmosphere with the molecules and aerosol particles, the degree of polarization of scattered light is related not only with the scattering angle and optical properties of scattering particles, but also with the atmospheric turbidity, solar position, and other factors. Therefore, the influences of various factors are needed to be considered in the calculation model of the polarization degree of sky scattering light. In this paper, we analyze the influences of the above factors on the degree of atmospheric polarization through an empirical model of Wilkie [14]. The Wilkie model was firstly proposed in 2004, which first determined the main impact

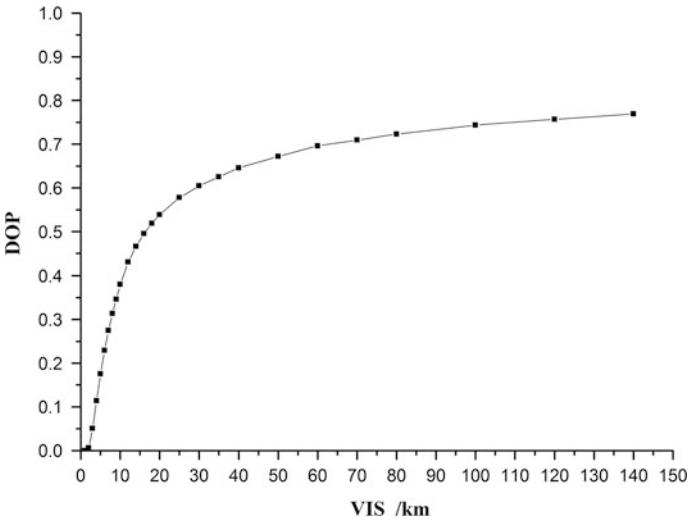

Fig. 4 The relationship between degree of polarization and atmospheric visibility

factors of the atmospheric polarization, and then combined these factors together to obtain an empirical computational expression. In the model, we computed all-sky scattering intensity distribution using the MODerate resolution TRANsmittance (MODTRAN) atmospheric radiative transfer mode.

Figure 4 shows the relationship between the degree of polarization and atmospheric visibility. Where, we assume that the solar zenith angle is 45°, the azimuth angle is 180°, the observer zenith angle is 30°, and the azimuth angle is 60°.

It can be seen from Fig. 4, the degree of polarization increases and tends to be flat with the increase of the atmospheric visibility. When the visibility is less than 20 km, the degree of polarization is closely related to visibility, and decreases

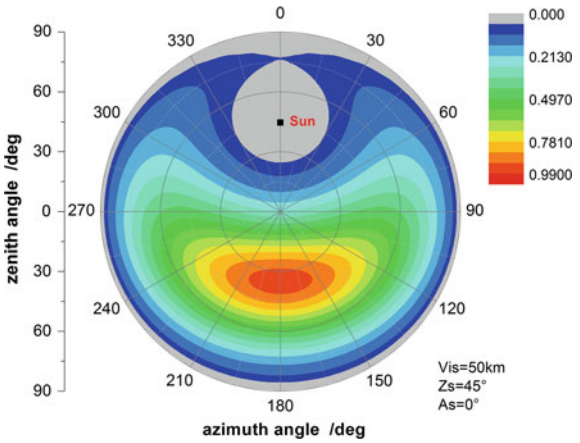

Fig. 5 The whole sky degree of polarization distribution under the visibility of 50 km

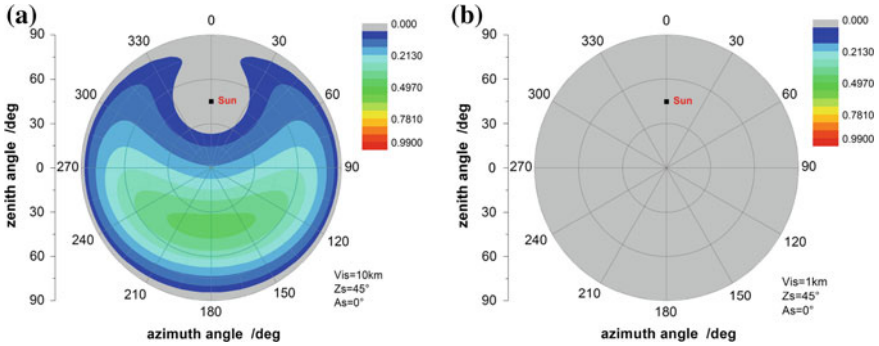

Fig. 6 The whole sky degree of polarization distribution under the visibility of 10 km (**a**) and 1 km (**b**)

sharply with the decrease of visibility. Thus, the effect of the turbid atmosphere to the degree of polarization under low visibility is quite obvious.

The following diagrams in Figs. 5 and 6 are the whole sky degree of polarization distribution under different visibilities. We assume that the solar zenith angle is 45° and the solar azimuth angle is 0°.

It can be seen from the above figures, when the incoming angle of sun is fixed, the whole sky degree of polarization increases with the increase of visibility. When the visibility is reduced to 1 km, we can see that the whole sky degree of polarization is decreased to almost zero.

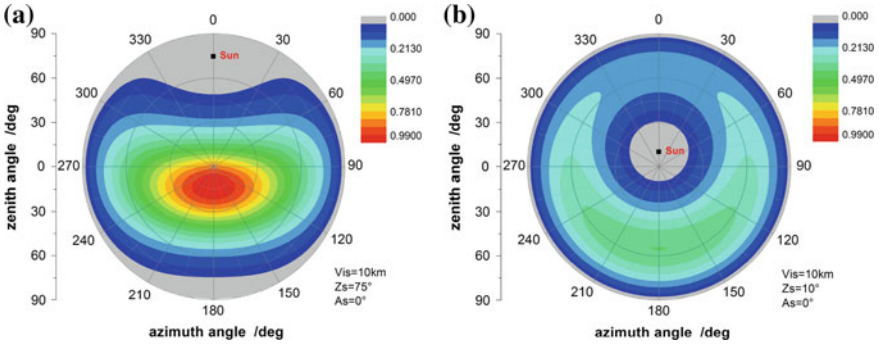

Fig. 7 The whole sky degree of polarization distribution under the solar zenith angle of 75° (**a**) and 10° (**b**)

2.4 *Effects of the Sun Position on the Polarization Distribution of the Whole Sky*

The following are the whole sky degree of polarization distribution under different solar zenith angles with visibility of 10 km, as shown in Fig. 7.

It can be seen from Fig. 7 that the degree of polarization is very small in the area near the sun, and the degree of polarization in the opposite area is larger. For a fixed visibility, the degree of polarization of the whole sky is related with the zenith angle. The larger solar zenith angle (approaching ground level) is corresponding to the bigger degree of polarization. With the solar zenith angle decreasing (approaching the zenith), the overall degree of polarization of the whole sky is reduced.

3 Feasibility Analysis of Polarization Navigation in Middle and Upper Atmosphere

At present, the Dead Reckoning (DR) method is widely used in mostly polarization navigation on the ground. The focus of DR navigation is to obtain the heading angle in real time. The heading angle is divided into relative heading angle (the angle between the current carrier move direction and the solar meridian) and absolute heading angle (the angle between the carrier move direction and the geographical north direction). Due to the whole sky atmospheric polarization pattern is symmetric with the solar meridian, the solar meridian can be extracted according to the stable polarization diagram, and subsequently the relative heading angle can be obtained [15]. Through referring astronomical calendar, we can get the angle between the geographical north direction and the solar meridian. According to the angle and relative heading angle, the absolute heading angle can be obtained further. The errors of the above polarization navigation method do not accumulate over time. It is high precision, relative simple, and independent.

In order to solve the problem that the carrier longitude and latitude information cannot be obtained through atmospheric polarization navigation, Cheng et al. [16]. developed an experimental platform which consists of a three-camera skylight polarization angle measuring module, an OCTANS inertial navigation module and an ephemeris inquiring module. Using the platform, they obtained the information of platform latitude and longitude. The experimental result is consistent with the actual value. However, the algorithm needs two measurements and the device needs to maintain a constant heading angle during the two observation periods. That results in these devices can only obtain the information of latitude and longitude of static carrier. Thus, it is not suitable for real-time location of dynamic vehicle.

In addition, for three-dimensional spatial navigation, researches mostly concentrated on the combinational navigation of polarized light and GPS, the geomagnetic or inertial navigation method. In the combinational navigation method,

the polarized light is used to measure the aircraft attitude angle. It can greatly improve the measurement accuracy of attitude angle.

According to the above description, it can be seen that the atmospheric polarization navigation is a developing and exploratory technique and there are many problems needing to be solved in the future. We are going to put forward a kind of novel polarization navigation scheme applying in middle to upper atmosphere. Based on the analysis in the paper, under weather conditions of haze, fog, or cloud in the low troposphere, especially in the surface boundary layer, the atmospheric polarization information is affected seriously by the turbid atmosphere, and the atmospheric polarization pattern is unstable, thus the accuracy of the atmospheric polarization navigation is limited. As for the middle to upper atmosphere above the stratosphere, the weather is clear and sunny, and there are less aerosol particles. The scattering by atmospheric gas molecules is dominated by Rayleigh scattering in the atmosphere layer, so the atmospheric scattering polarization information is stable, and the accuracy of polarization navigation will be higher than the troposphere. It is easy to use atmospheric polarization information for locating of flight vehicle. So, for the aircraft flying in the stratosphere or in the upper atmosphere, it is easy to obtain a stable and accurate real-time polarization information, and not subject to the influence of turbid atmosphere, the polarization navigation will be more effective. We will verify the algorithm accuracy of our polarization navigation scheme by actual experiments and apply the scheme to polarization navigation program further. According to our calculation and analysis, the specific effective height can be initially determined at different latitude regions: Effective navigation height is above 20 km in the low latitude area (the tropopause height is about 16–17 km); effective navigation height is above 20 km in summer and 15 km in winter for mid-latitude area (the tropopause height is 16–17 km in summer, and about 10 km in winter); for high latitude area (the tropopause height is about 8 km), the effective navigation altitude is above 10 km.

In summary, atmospheric polarization navigation will be an effective method for the aircraft in high altitude atmosphere; and it can be used as an independent navigation technology or in the form of integrated navigation technology with other navigation methods.

References

1. Coulson KL (1988) Polarization and intensity of light in the atmosphere. A. Deepak Pub., Hampton, VA
2. Rayleigh L (1871) On the light from the sky, its polarization and color. Phil Mag, 107–127
3. Mie G (1908) Contributions to the optics of turbid media, particularly of colloidal metal solutions. Ann Phys (Leipzig) 25(3):337–445
4. Brines ML, Gould JL (1982) Skylight polarization patterns and orientation. J Exp Biol 96 (1):69–91
5. Miyazaki D, Ammar M, Kawakami R et al (2009) Estimating sunlight polarization using a fish-eye lens. IPSJ Trans Comput Vis Appl 1(288–300):1–2

6. Sun X, Hong J, Qiao Y (2005) Investigation of Polarized Properties of Atmospheric Scattering Radiation. Chin J Quant Electron 22(1):111–115
7. Wehner R, Srimivasan MV (1981) Searching behavior of desert ants, genus cataglyphis. J Comp Physiol 142:315–338
8. Labhart T (1999) How polarization-sensitive interneuron-ones of crickets see the polarization pattern of the sky: A field study with an optoelectronic model neuron. J Exp Biol 202:757–770
9. Fan Z, Gao J (2008) Investigation of atmospheric polarization information measurement method imitating POL-neurons of cataglyphis. Chin J Sci Instrum 29(4):745–749
10. Lambrinos D, Moller R, Labhart T et al (2000) A mobile robot employing insect strategies for navigation. Robot Auton Syst 30(1):39–64
11. Chu J, Chen W, Wang H et al (2011) Mobile robot navigation tests with polarization sensors. Opt Precis Eng 19(10):2419–2426
12. Lu H, Yin H, Huang X (2007) Polarized-light/geomagnetism/GPS/SINS integrated navigation. J Astronaut 28(4):897–902
13. Li D, Wang X, Huang X (2005) High-precision polarized skylight navigation system
14. Wilkie A, Robert FT, Ulbricht C et al (2004) An analytical model for skylight polarisation. In: Eurographics symposium on rendering
15. Tian L, Gao J, Fan Z et al (2012) The method of the navigation direction angle calculation with the distribution of the atmospheric polarization pattern. Acta Electron Sin 1(40):141–146
16. Cheng Z, Mei T, Liang H, Wang D (2015) Analysis and implementation of the skylight polarization autonomous positioning method. Opto-Electron Eng 42(6):33–38

A CFAR Detection Algorithm for X-ray Pulsar Signal Based on Time-Frequency Entropy

Lu Wang and Xizheng Ke

Abstract Focusing on the X-ray pulsar signal detection in high background noise, a class of CFAR detection algorithms is proposed based on time-frequency entropy (TFE). Firstly, the definition of the pulsar signal TFE is given, moreover, the TFE difference of signal and noise is verified by theoretical derivation from the view of energy distribution. Then the distribution characteristic of TFE of pulsar signal is analyzed theoretically. The theoretical analysis result is further verified by Monte Carlo method. We detect the observation signal based on CFAR with the test statistic designed by TFE. We have also verified the effectiveness of this method by simulation experiment. The simulation results show that the time-frequency Rényi entropy detection algorithm based on ST generates the optimal detection performance.

Keywords X-ray pulsar · Signal detection · Shannon entropy · Rényi entropy

1 Introduction

Pulsars are highly magnetized, rapidly rotating neutron stars which emit uniquely identifiable signals that are periodical to a high level of accuracy. For some pulsars, the stability of their rotation period over long timescales is comparable with terrestrial atomic clocks [1]. Pulsars have pulse radiation performance at multiple wavelengths, most of the pulsar radiation energy is concentrated in the X-ray band of the electromagnetic spectrum. For detector miniaturization, X-ray pulsar-based navigation has been suggested as an attractive approach for autonomous deep space navigation [2] in recent years. Because of the long distance from the earth and X-ray noise interference from the space background, most of the received X-ray

L. Wang (✉) · X. Ke
School of Automation and Information Engineering, Xi'an University of Technology, Xi'an 710048, China
e-mail: wanglu_xidian@163.com; luw@xaut.edu.cn

X. Ke
e-mail: xzke@263.net

J. Sun et al. (eds.), *China Satellite Navigation Conference (CSNC) 2016 Proceedings: Volume II*, Lecture Notes in Electrical Engineering 389,
DOI 10.1007/978-981-10-0937-2_50

pulsar signals are neglected [3]. Therefore, the detection of X-ray pulsar signal plays an important role in pulsar deep space autonomous navigation system.

At present, the frequency domain algorithm based on FFT is widely used for the detection of pulsar signal [4], which require calculating the power spectrum of uncumulative observed data that needs considerably longer computational time; Furthermore, harmonic interference may cause the detection error under the condition of low SNR. In order to solve the problems above, a detection algorithm based on time-frequency entropy (TFE) for X-ray pulsar is proposed in this paper, the detected signal in the new method is the cumulative pulse profile rather than the uncumulative observed data.

Under the gaussian white noise, the optimal algorithm based on time-frequency match filtering [5] is commonly used, which needs a prior knowledge. The energy accumulation detection algorithm based on time-frequency domain filtering is often used [6, 7] while the prior knowledge is unknown, however, different kinds of time-frequency transform require different kinds of denoise algorithm, this kind of algorithm do not have universality; Moreover, the detection performance will be influenced by noise energy accumulation under the condition of low SNR.

TFE [8] is a metric for measuring the average degree of dispersion of random variable, which has both time and frequency shift invariance. Inspired by this, a constant false alarm (CFAR) detection algorithm based on TFE for X-ray pulsar signal is proposed. This algorithm is based on the fact that TFE of a signal plus noise is always less than the entropy of the noise itself. The test statistic is designed by the TFE of observed signal in this algorithm, and the test statistic's distribution characteristics will be proved. Meanwhile, the effectiveness of this method is verified by simulation.

2 Time-Frequency Entropy

A probability distribution is required for calculating the uncertainty of a random variable by entropy, therefore the time-frequency power spectrum is analogous to probability density function, and TFE is calculated by the time-frequency power spectrum in this paper. Time-frequency analysis method can be classified into linear and bilinear time-frequency representation by time-frequency joint function [9]. The linear time-frequency representation has two typical forms, including short time Fourier transform (STFT) and *S*-transform (ST), if $X(t, f)$ is the linear time-frequency representation of signal $x(t)$, the time-frequency power spectrum $\boldsymbol{P}_1$ of $x(t)$ is shown as a formula (1), where $\circ$ represents Hadamard product of two matrices; Cohen class time-frequency distribution is one typical form of the bilinear time-frequency representation. Wigner–Ville distribution (WVD) is the most basic one in Cohen class time-frequency distribution, we define $X(t, f)$ as the linear time-frequency representation of signal $x(t)$, if $X(t, f)$ is the bilinear time-frequency

representation of signal $x(t)$, the time-frequency power spectrum $\boldsymbol{P}_2$ of $x(t)$ is shown as formula (2).

$$\boldsymbol{P}_1 = \mathbf{X} \circ \mathbf{X}^* \tag{1}$$

$$\boldsymbol{P}_2 = \mathbf{X} \tag{2}$$

$$P^i_{\text{nor}}(t,f) = \frac{P_i(t,f)}{\int\int P_i(t,f)\mathrm{d}t\mathrm{d}f}, \quad i = 1,2. \tag{3}$$

$$\begin{cases} \int\int P^i_{\text{nor}}(t,f)\mathrm{d}\tau\mathrm{d}f = 1 \\ P^i_{\text{nor}}(t,f) \in [0,1], \quad \forall\tau,f \end{cases} \quad i = 1,2. \tag{4}$$

$$H(\boldsymbol{P}^1_{\text{nor}}) = -\int\int P^1_{\text{nor}}(t,f)\log_2 P^1_{\text{nor}}(t,f)\mathrm{d}t\mathrm{d}f \tag{5}$$

From formula (3), the normalized joint energy probability density $\boldsymbol{P}^i_{\text{nor}}$ is calculated by $\boldsymbol{P}_1$ or $\boldsymbol{P}_2$. The average degree of dispersion of $\boldsymbol{P}^1_{\text{nor}}$ can be calculated according to formula (5) by Shannon entropy since formula (4) condition is satisfied; $\boldsymbol{P}^2_{\text{nor}}$ does not meet the nonnegative condition in formula (4), and finite entropy cannot be obtained with formula (5), therefore the average degree of dispersion of $\boldsymbol{P}^2_{\text{nor}}$ is figured out by Rényi entropy; In addition, the average degree of dispersion of $\boldsymbol{P}^1_{\text{nor}}$ can be calculated by Rényi entropy too; The formula of a-order time-frequency Rényi entropy is shown as follows [8]:

$$H_\alpha(\boldsymbol{P}^i_{\text{nor}}) = \frac{1}{1-\alpha}\log_2\int\int (P^i_{\text{nor}}(t,f))^\alpha \mathrm{d}t\mathrm{d}f \quad a > 0, a \neq 1, \quad i = 1,2. \tag{6}$$

Where both $H(\boldsymbol{P}^1_{\text{nor}})$ and $H_a(\boldsymbol{P}^1_{\text{nor}})$ have time and frequency shift invariance, and here a equals 3 [8].

3 A CFAR Detection Algorithm Based on TFE for X-ray Pulsar Signal

3.1 Theory Analysis of TFE Detection Algorithm

The detection of cumulative sequences is a binary detection, the hypothesis test is shown as follows [10]:

$$\begin{aligned} H_0 &: y(m) = u(m), \quad m = 0,1,2,\ldots,M-1 \\ H_1 &: y(m) = s(m) + u(m), \quad m = 0,1,2,\ldots,M-1. \end{aligned} \tag{7}$$

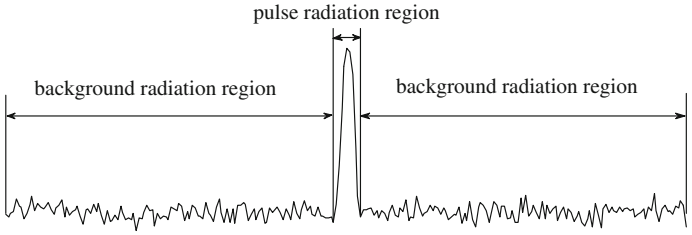

Fig. 1 Structure of the average pulse profiles for PSR B0818-13 (SNR = 10 dB)

Where $y(m)$ and $s(m)$ represent a cumulative profile and a standard profile of pulsar, respectively, and $u(m)$ is a white Gaussian noise [11] with zero mean and variance σ^2, $s(m)$ and $u(m)$ are uncorrelated.

Energy distribution of background noise is flatter than that of pulsar cumulative profile's, hence the value of TFE for background noise is bigger than that of pulsar cumulative profile's, so TFE is used in this article as the metric for measuring the average degree of dispersion of signal power spectrum. The difference between TFE of noise and TFE of pulsar signal may seem obvious in some condition of SNR. For this reason, the theory behind this paper is that TFE of signal plus noise is always less than that of noise's, this difference can be used to distinguish X-ray pulsar signal from noise. This theory basis will be proved by derivations of formulas in the following.

Pulsar cumulative profile is composed of pulse radiation region and background radiation region, they are the equal of signal and noise, respectively. A cumulative profile of PSR B0818-31 is shown in Fig. 1, it can be seen that pulse radiation region in one signal cycle is very thin, and the other part is noise. Normalized power spectral of S-transform domain for pulsar cumulative profile and background noise are shown in Fig. 2a, b, respectively. It can be seen that the distribution of pulsar signal is concentrated and signal power spectral is varied great ranges. Noise power spectral is just the opposite.

Let $\boldsymbol{C_y}$ be the normalized time-frequency power spectrum matrix of $y(m)$, the size of $\boldsymbol{C_y}$ is $M \times M$, elements of $\boldsymbol{C_y}$ will be sorted in descending order, from which we get an array $A = \{q_m\}_{m=1}^{L}$, $L = M \times M$, and this array meets the following three conditions:

$$\sum_{m=1}^{L} q_m = 1, \quad q_1 \geq q_2 \geq \cdots \geq q_L, \quad q_m \in [0,1], \quad m = 1, 2, \ldots, L \tag{8}$$

Two arrays for average pulse profile and noise in Fig. 2a, b can be obtained by the approach above, the corresponding arrays are $A_y = \{e_m\}_{m=1}^{L}$ and $A_n = \{p_m\}_{m=1}^{L}$, respectively. From Fig. 2a, we know that the amplitude of power spectrum between noise and average pulse profile are significantly different, therefore an array index K exists under certain SNR, which divide $\boldsymbol{A}_y$ into two parts,

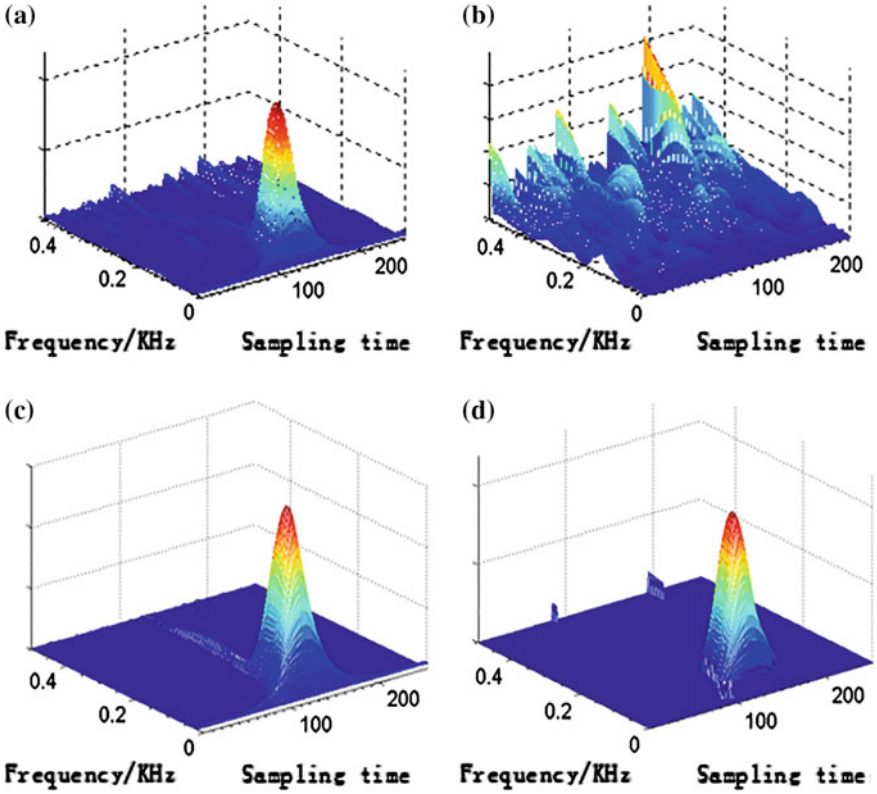

Fig. 2 Normalized power spectral of *S*-transform domain for average pulse profiles of PSR B0818-13, background noise of the corresponding, pulsar standard profiles of PSR B0818-13, and the power spectral in **a** after threshold filter. **a** Average pulse profiles. **b** Background noise. **c** Standard profiles for PSR B0818-13. **d** After threshold filter for PSR B0818-13

$A_{y1} = \{e_i\}_{i=1}^{K}$ represents a set of power spectrum of pulsar signal and $A_{y2} = \{e_j\}_{j=K+1}^{L}$ represents a set of power spectrum of noise. We will determine index K next.

Figure 3 shows two curves of $\boldsymbol{A}_y$ and $\boldsymbol{A}_n$, area1 denotes mutual area under the two curves, area2 signifies the area, which is determined by subtracting area1 from the total area under the curve $\boldsymbol{A}_y$, area3 is the area, which is determined by subtracting area1 from the total area under the curve $\boldsymbol{A}_n$. Combining with formula (8), we get some conclusions as follows:

$$\begin{cases} \text{area1} + \text{area2} = 1 \\ \text{area1} + \text{area3} = 1 \\ \text{area2} = \text{area3} \end{cases} \tag{9}$$

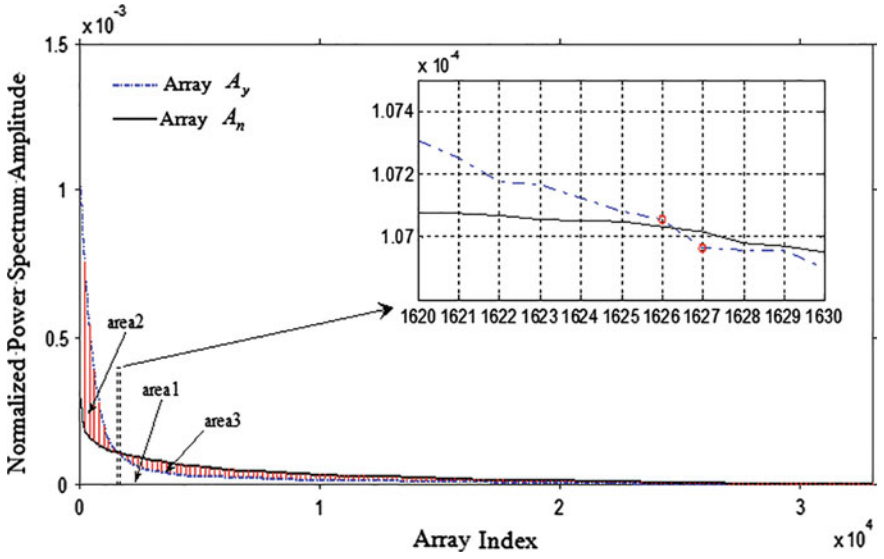

Fig. 3 Array $\boldsymbol{A}$y and $\boldsymbol{A}n$

In addition, it also can be seen from Fig. 3, when $1 \le m \le 1626$, then $e_m > p_m$. When $1627 \le m \le L$, then $e_m < p_m$. Here's 1626 is the index of the element nearest to the intersection point of the two curves. e_{1626} is regarded as a threshold, $\boldsymbol{C_y}$ in Fig. 2a is smoothed with threshold filter, the corresponding result is shown in Fig. 2d; The normalized power spectral of standard profile for PSR B0818-13 is shown in Fig. 2c, by comparison, noise and signal in $\boldsymbol{A}_y$ can be distinguished well by e_{1626}. In conclusion, the element in $\boldsymbol{A}_y$, which is nearest to the intersection point between $\boldsymbol{A}_y$ and $\boldsymbol{A}_n$, can distinguish pulsar signal from noise, the index of this element is the value of K.

$\boldsymbol{A}_y$ is divided into two parts by index K, $A_{y1} = \{e_i\}_{i=1}^{K}$ and $A_{y2} = \{e_j\}_{j=K+1}^{L}$. Similarly, $\boldsymbol{A}_n$ is divided into two parts, $A_{n1} = \{p_i\}_{i=1}^{K}$ and $A_{n2} = \{p_j\}_{j=K+1}^{L}$; Combining formula (8) with formula (9), we can get:

$$\sum_{i=1}^{K}(e_i - p_i) = \sum_{j=K+1}^{L}(p_j - e_j) \tag{10}$$

We set the total energy as 1 in this paper, in formula (10), the left of the equals sign represents the formula for calculating area2; The right of the equals sign represents the formula for calculating area3, that is the sum of energy for $\boldsymbol{A}_{n2}$ higher than $\boldsymbol{A}_{y2}$; For $\boldsymbol{A}_{n2}$ and $\boldsymbol{A}_{y2}$, supposing $\Delta = \{\Delta_j = p_j - e_j\}_{j=K+1}^{L}$. Each element value in $\boldsymbol{A}_y$ and $\boldsymbol{A}_n$ is the ratio of the point energy to total energy, so for array $\boldsymbol{A}_n$ of

noise, we can move the rich part of $\boldsymbol{A}_{n2}$ relative to $\boldsymbol{A}_{y2}$, that is Δ, from $\boldsymbol{A}_{n2}$ to $\boldsymbol{A}_{n1}$, to get an array the same as array $\boldsymbol{A}_y$ of pulsar cumulative profile. Hence, we can demonstrate that TFE of a signal plus noise is always less than the TFE of the noise itself by analyzing the energy is shifting from $\boldsymbol{A}_{n2}$ to $\boldsymbol{A}_{n1}$. We will discuss time-frequency Shannon entropy (TFSE) and time-frequency Rényi entropy (TFRE) separately.

1. **Time-Frequency Shannon Entropy**

Assuming $p_i \in \boldsymbol{A}_{n1}$, $p_j \in \boldsymbol{A}_{n2}$, $q \in (0, p_j]$, we move $((q/p_j) \times 100)\%$ energy from p_j to p_i and get a new array $\boldsymbol{A}'_n = \{p_1, p_2, \ldots, p_i q, \ldots, p_j q, \ldots, p_L\}$.

When using Shannon entropy, H and H' denote TFSE for $\boldsymbol{A}_n$ and $\boldsymbol{A}'_n$ separately, the corresponding formula is shown as formula (11a) and (11b). Supposing the difference between H and H' is ΔH, the corresponding formula is shown as formula (12).

$$H = -\sum_{m=1}^{L} p_m \log_2 p_m \tag{11a}$$

$$H' = -\sum_{\substack{m=1 \\ m \neq i,j}}^{L} p_m \log_2 p_m - (p_i + q)\log_2(p_i + q) - (p_j - q)\log_2(p_j - q) \tag{11b}$$

$$\begin{aligned} \Delta H &= H - H' \\ &= (p_i + q)\log_2(p_i + q) + (p_j - q)\log_2(p_j - q) - p_i \log_2 p_i - p_j \log_2 p_j \end{aligned} \tag{12}$$

The first-order and second-order derivative of function $f(x) = x \log_2 x, x \in (0, 1]$ are as follows:

$$f'(x) = \log_2 x + \frac{1}{\ln 2} \tag{13a}$$

$$f''(x) = \frac{1}{x \ln 2} \tag{13b}$$

$$\begin{cases} p_i \geq p_j \\ p_i + q > p_j - q \end{cases} \tag{14}$$

The formula (14) is deduced by formula (8), then, we can deduce formula (15) by using the Lagrange mean value theorem [12] for *f*(x).

$$\begin{cases} f(p_i + q) - f(p_i) = f'(\varepsilon_1)q & \varepsilon_1 \in (p_i, p_i + q) \\ f(p_j) - f(p_j - q) = f'(\varepsilon_2)q & \varepsilon_2 \in (p_j - q, p_j) \end{cases} \tag{15}$$

Since the second-order derivatives of f(x) is greater than zero, $f'(x)$ must be a monotone increasing function, then inequality, $f'(\varepsilon_1) > f'(\varepsilon_2)$, is true, hence, there is a inequality as follows:

$$(p_i + q)\log_2(p_i + q) + (p_j - q)\log_2(p_j - q) > p_i \log_2 p_i + p_j \log_2 p_j \tag{16}$$

Finally inequality, $f'(\varepsilon_1) > f'(\varepsilon_2)$, is proved. With moving the energy of array $\boldsymbol{A}_{n2}$ to that of array $\boldsymbol{A}_{n1}$, the value of Shannon entropy for new array decreases. We reach a conclusion that the theoretic fundamental, on which the algorithm depends, is true for time-frequency Shannon entropy.

2. **Time-Frequency Rényi Entropy**

When using Rényi entropy, H_a and $H_a^{'}$ denote TFRE for $\boldsymbol{A}_n$ and $\boldsymbol{A}_n'$ separately, the corresponding formula is shown as formula (17a) and (17b). Supposing the difference between H_a and H_a' is ΔH_a, the corresponding formula is shown as formula (18). We set a equal to 3, here.

$$H_a = -\frac{1}{2}\log_2\left(\sum_{m=1}^{L} p_m^3\right) \tag{17a}$$

$$H_a' = -\frac{1}{2}\log_2\left(\sum_{\substack{m=1 \\ m \neq i,j}}^{L} p_m^3 + (p_i + q)^3 + (p_j - q)^3\right) \tag{17b}$$

$$\Delta H_a = H_a - H_a' \tag{18}$$

The uniform expression for formula (17a) and (17b) is shown as follows:

$$f(X) = -\frac{1}{2}\log_2 X \tag{19}$$

where X is the sum of probability density to the third power, and the probability density meets formula (8). Combining formula (8) with formula (20), we can deduce that $X \in (0, 1]$. In addition, f(x) is a monotonic decreasing function in the definitional domain. For the monotone decreasing function f(x),

$$\left(\sum_{m=1}^{L} p_m^3\right) \geq \sum_{m=1}^{L} p_m^3 \tag{20}$$

Supposing $X = \sum_{m=1}^{L} p_m^3$, $X' = \sum_{\substack{m=1 \\ m \neq i,j}}^{L} p_m^3 + (p_i + q)^3 + (p_j - q)^3$ and $\Delta X = X - X'$. The problem of comparing H_a and H_a' can be converted to a problem of comparing the value of X and X', that is:

$$\Delta X = X - X' = p_i^3 + p_j^3 - (p_i + q)^3 - (p_j - q)^3 \tag{21}$$

The first- and second-order derivative of function $g(t) = t^3$, $t \in (0,1]$are given in formula (22a). Taking formula (14) as a reference, then formula (23) is deduced from the Lagrange mean value theorem [12].

$$g'(t) = 3t^2 \tag{22a}$$

$$g''(t) = 6t \tag{22b}$$

$$\begin{cases} g(p_i + q) - g(p_i) = g'(\varepsilon_1)q & \varepsilon_1 \in (p_i, p_i + q) \\ g(p_j) - g(p_j - q) = g'(\varepsilon_2)q & \varepsilon_2 \in (p_j - q, p_j) \end{cases} \tag{23}$$

Since $g''(x)$ is greater than zero, $g'(x)$ must be a monotone increasing function, then inequality, $g'(\varepsilon_1) > g'(\varepsilon_2)$, is true, hence there is a inequality as follows:

$$g(p_i + q) + g(p_j - q) > g(p_i) + g(p_j) \tag{24}$$

Finally, $X < X'$ is proved, then $H_a > H_a'$ is true also. With moving the energy of array $\boldsymbol{A}_{n2}$ to that of array $\boldsymbol{A}_{n1}$, the value of Rényi entropy for new array decreases. We reach a conclusion that the theoretic fundamental, on which the algorithm depends, is true for time-frequency Rényi entropy.

The theory basis in this paper has been verified by Monte Carlo simulation in article [13], hence, we would not retest again here. The experiment shows that the average value of noise samples' TFE is independent of SNR, but the average value of cumulative profiles of pulsar signal's TFE reduces as the SNR increases. Under the same condition, the average TFE of noise is greater than the average TFE of cumulative sequence containing pulsar signal, which can be applied to detecting X-ray pulsar signal and the algorithm has certain robustness. Thus, the theory basis that TFE of a signal plus noise is always less than the entropy of the noise itself in the detection algorithm is considered viable.

3.2 CFAR Detection Algorithm Based on TFE

Based on the above conclusion, we will use TFE to design the detection statistic, the distribution character of detection statistic will be analyzed in theory and the corresponding analysis results will be verified by the Monte Carlo. On this basis, the detection statistic will be detected by CFAR algorithm.

Let $\boldsymbol{C_y}$ is the normalized time-frequency power spectrum matrix of observed signal $y(m)$, In line with the conclusion in Sect. 3.1, the decision rule of the detection algorithm is given as:

$$H_i(\boldsymbol{C}_{\mathrm{y}}) \underset{H_1}{\overset{H_0}{\gtrless}} \gamma, \quad i = 1, 2. \tag{25}$$

where γ is the decision threshold; $H_1(\boldsymbol{C}_{\mathrm{y}})$, in formula (26a), is discrete TFSE; $H_2(\boldsymbol{C}_{\mathrm{y}})$, in formula (26b), is discrete TFRE; the size of $\boldsymbol{C}_{\mathbf{y}}$ is $M \times M$.

$$H_1(\boldsymbol{C}_{\mathrm{y}}) = -\underbrace{\sum_{m=0}^{M-1}\sum_{n=0}^{M-1} C_{\mathrm{y}}(m,n)\log_2 C_{\mathrm{y}}(m,n)}_{X_1} \tag{26a}$$

$$H_2(\boldsymbol{C}_{\mathrm{y}}) = \frac{1}{1-\alpha}\log_2\left[\underbrace{\sum_{m=0}^{M-1}\sum_{n=0}^{M-1} C_y^{\alpha}(m,n)}_{X_2}\right] \tag{26b}$$

Here, we will use CFAR detection algorithm to detecting the observed signal, the expression of false alarm probability is shown as follows:

$$P_{\mathrm{f}}^i = \mathrm{P}_i(D_1|H_0) = \mathrm{P}_i(H_i(\boldsymbol{C}_{\mathrm{u}}) < \gamma), \quad i = 1, 2. \tag{27}$$

where P_{f}^i denotes the false alarm probability, D_1 denotes the true hypothesis H_1, $H_i(\boldsymbol{C}_{\mathrm{u}})$ is the TFE of noise. According to formula (27), P_{f}^i has something to do with the probability distribution of $H_i(\boldsymbol{C}_{\mathrm{u}})$.

Both X_1 and X_2 in formula (26) are the sum of multiple independent random variables, based on the central limit theorem, we know that both X_1 and X_2 obey an approximate Gaussian distribution (the corresponding verification experiment is shown in Sect. 4.1), Therefore, both $H_1(\boldsymbol{C}_{\mathrm{y}})$ and $H_2(\boldsymbol{C}_{\mathrm{y}})$ are functions that depend on the Gaussian variables X, the corresponding formulas are shown as follows:

$$H_1(\mathbf{C}_{\mathrm{y}}) = Y_1 = -X, \quad X \in [-2\log_2 \mathrm{M}, 0] \tag{28a}$$

$$H_2(\mathbf{C}_{\mathrm{y}}) = Y_2 = \frac{1}{1-\alpha}\log_2 X, \quad X \in (0, 1] \tag{28b}$$

Based on the derivability of function Y_1 and Y_2, the probability density function of $H_1(\boldsymbol{C}_y)$ and $H_2(\boldsymbol{C}_y)$ can be derived out by Eq. (29), they are shown in formula (30a) and (30b), respectively.

$$f_Y(y) = f_X[h(y)] \cdot |h'(y)| \tag{29}$$

$$f_Y^1(y) = f_X(x) \tag{30a}$$

$$f_Y^2(y) = f_X\left(2^{(1-\alpha)y}\right) \cdot (\alpha - 1)\ln 2 \cdot 2^{(1-\alpha)y} \tag{30b}$$

When $\boldsymbol{C}_y = \boldsymbol{C}_u$, let $X_i \sim N(m_{i0}, \sigma_{i0}^2)$, then the relationship between γ with P_f^i is shown below:

$$P_f^1 = \int_{-\infty}^{\gamma} f_Y^1(y)\mathrm{d}y = \int_{-\infty}^{\gamma} \frac{1}{\sqrt{2\pi}\sigma_{10}} \mathrm{e}^{-\frac{(y-m_{10})^2}{2\sigma_{10}^2}} \mathrm{d}y = \Phi\left(\frac{\gamma - m_{10}}{\sigma_{10}}\right) \tag{31a}$$

$$P_f^2 = \int_{-\infty}^{\gamma} f_X(2^{(1-\alpha)y}) \cdot (\alpha - 1)\ln 2 \cdot 2^{(1-\alpha)y}\mathrm{d}y = 1 - \Phi\left(\frac{2^{(1-\alpha)\gamma} - m_{20}}{\sigma_{20}}\right) \tag{31b}$$

where $\Phi(x) = (2\pi)^{-\frac{1}{2}} \int_{-\infty}^{x} \mathrm{e}^{-\frac{t^2}{2}}\mathrm{d}t$; With a certain false alarm probability, CFAR detection can be realized by figuring out the value of γ with formula (31a) and (31b).

We will deduce the expression of detection probability P_d^i, the expression of P_d^i can be expressed as shown in formula (32) by using formula (25), where $H_i(\boldsymbol{C}_{s+u})$ is the TFE of pulsar average profile.

$$P_d^i = \mathrm{P}_i(D_1|H_1) = \mathrm{P}_i(H_i(\mathbf{C}_{s+u}) < \gamma), \quad i = 1, 2. \tag{32}$$

When $\boldsymbol{C}_y = \boldsymbol{C}_{s+u}$, let $X_i \sim N(m_{i1}, \sigma_{i1}^2)$, substituting formula (30a) and (30b) into formula (32), respectively, then the expression of P_d^i is shown as follows:

$$P_d^1 = \int_{-\infty}^{\gamma} f_Y^1(y)\mathrm{d}y = \int_{-\infty}^{\gamma} \frac{1}{\sqrt{2\pi}\sigma_{11}} \mathrm{e}^{-\frac{(y-m_{11})^2}{2\sigma_{11}^2}} \mathrm{d}y = \Phi(\frac{\gamma - m_{11}}{\sigma_{11}}) \tag{33a}$$

$$P_d^2 = \int_{-\infty}^{\gamma} f_X(2^{(1-\alpha)y}) \cdot (\alpha - 1)\ln 2 \cdot 2^{(1-\alpha)y}\mathrm{d}y = 1 - \Phi\left(\frac{2^{(1-\alpha)\gamma} - m_{21}}{\sigma_{21}}\right) \tag{33b}$$

4 Experiment and Analysis

4.1 Verifying Gaussian Distribution Characteristics of Statistics X_i

In this section, taking pulsar B0531+21 for example, the deduction that the statistics X_1 and X_2 in formula (26a) and (26b), respectively, are subject to Gaussian distribution will be verified by Monte Carlo Simulation, and the statistics X_1 will be verified based on TFSE of STFT and ST separately, the statistics X_2 will be verified based on TFRE of STFT, ST and WVD separately also.

The sampling point number is 256, and SNR is 2 dB in this experiment, taking 100 white Gaussian noises and pulsar average profile, respectively, as samples to estimate the theory parameters of gaussian distribution for $X_{i,\mathrm{u}}$ and $X_{i,\mathrm{s+u}}$, the corresponding theory parameters are (m_{i0}, σ_{i0}^2) and (m_{i1}, σ_{i1}^2), respectively, and $i = 1, 2$. The corresponding theory Gaussian probability density curves are shown in Figs. 4 and 5 with dash lines; In Fig. 4, $X_{i,\mathrm{u}}$ and $X_{i,\mathrm{s+u}}$ denote the detection statistics of the TFSE for noise and pulsar average profile, respectively. In Fig. 5,

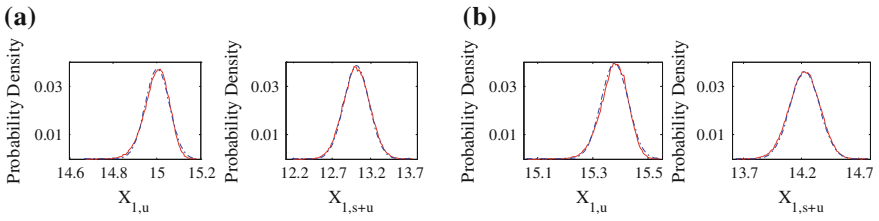

Fig. 4 Verifying Gaussian distribution characteristics of statistics X_1 **a** ST-TFSE, **b** STFT-TFSE

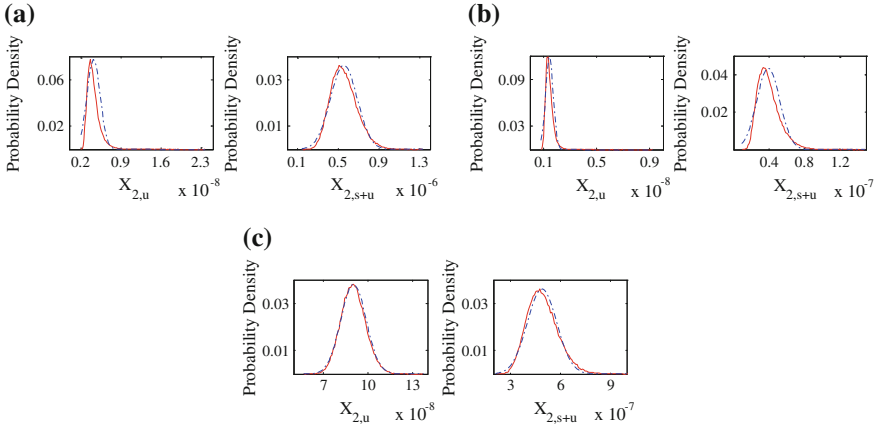

Fig. 5 Verifying Gaussian distribution characteristics of statistics X_2 **a** ST-TFRE, **b** STFT-TFRE, **c** WVD-TFRE

$X_{2,\mathrm{u}}$ and $X_{2,s+\mathrm{u}}$ denote the detection statistics of the TFRE for noise and pulsar average profile, respectively. Under the same SNR, taking 100,000 white Gaussian noises and pulsar average profile, respectively, to calculate the detection statistics for each sample, then getting two sets of the detection statistics $\left\{X_{i,\mathrm{u}}^{j}\right\}_{j=1}^{K}$ and $\left\{X_{i,\mathrm{s}+\mathrm{u}}^{j}\right\}_{j=1}^{K}$, $i=1,2$. The probability density of $X_{i,\mathrm{u}}$ and $X_{i,\mathrm{s}+\mathrm{u}}$ can be estimated by the frequency distribution histogram of the two sets. The corresponding curve is the full lines in Figs. 4 and 5; We can get a conclusion that both the statistics X_1 and X_2 obey an approximate Gaussian distribution from some comparison with the dash line and full line in Figs. 4 and 5. In addition, we can get that the value of TFE for noise is greater than that of pulsar average pulse profile's from Figs. 4 and 5.

4.2 Experimental Analysis of the Detection Algorithm

4.2.1 Detection Performance of the Algorithm

In this section, taking pulsar B0531+21and B1706-44 for example, five TFE in Sect. 4.1 are used to verify the detection performance of this algorithm. Taking 100 white Gaussian noises and pulsar average profile, respectively, as training sample sets, the sampling point number is 256. Let false alarm probability equal to 0.001, the theory detection probability under different SNRs is calculated by formula (33a) and (33b), and the simulation detection probability is obtained by 100000 times the Monte Carlo simulations; both theory and simulation curves of detection probability for five methods are shown in Fig. 6. It can be known from Fig. 6 that the theory curves of detection probability is agreed well with that of the simulation result; For detection algorithm based on TFSE, the performance of ST-TFSE is much better; For detection algorithm based on TFRE, the performance of ST-TFSE is the best; Besides, ST-TFRE is the best of the five algorithms, and ST-TFSE is the next, this is because that the aggregation of ST is better than that of STFT's, in addition, with respect to WVD, ST do not have the interference terms.

4.2.2 Performance Comparison of Different Algorithms

In this section, taking pulsar B0531+21 for example, and keeping the false alarm probability is 0.001, comparing two detection algorithm separately based on ST-TFSE and based on ST-TFRE with two CFAR detection algorithm, respectively, based on FFT power spectrum entropy and based on bispectrum entropy. Their detection probability curves are shown in Fig. 7, as shown in this figure, four detection algorithms represent as FFT-RE, FFT-SE, BIS-RE and BIS-SE, and the theory curves of detection probability of the four methods are agreed well with that

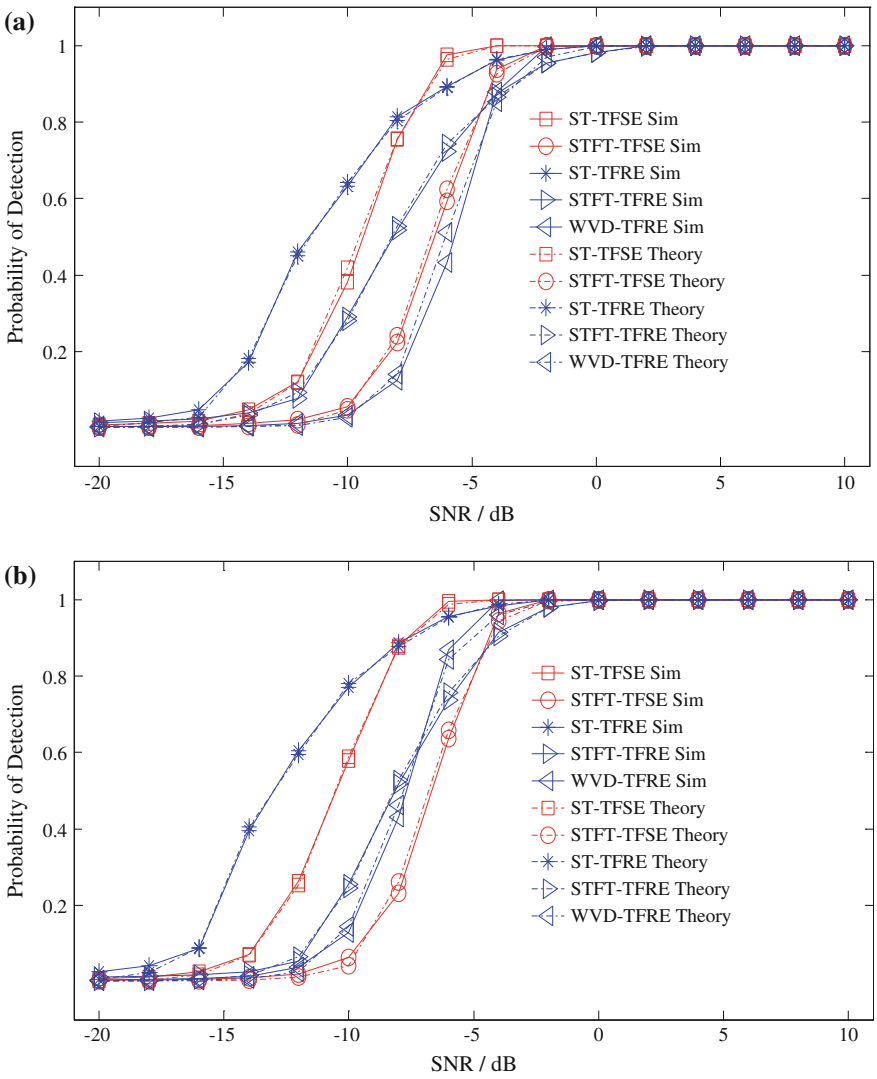

Fig. 6 Theory and simulation curves of detection probability **a** PSR B0531 + 21, **b** PSR B1706 - 44

of the simulation result; From Fig. 7, it can be seen that ST-TFSE has the best detection performance in these methods based on Shannon entropy, and ST-TFRE has the best detection performance in these methods based on Rényi entropy. Besides, when the value of SNR is low, Rényi entropy detection algorithm is better than that of Shannon entropy in whole with the same power spectrum.

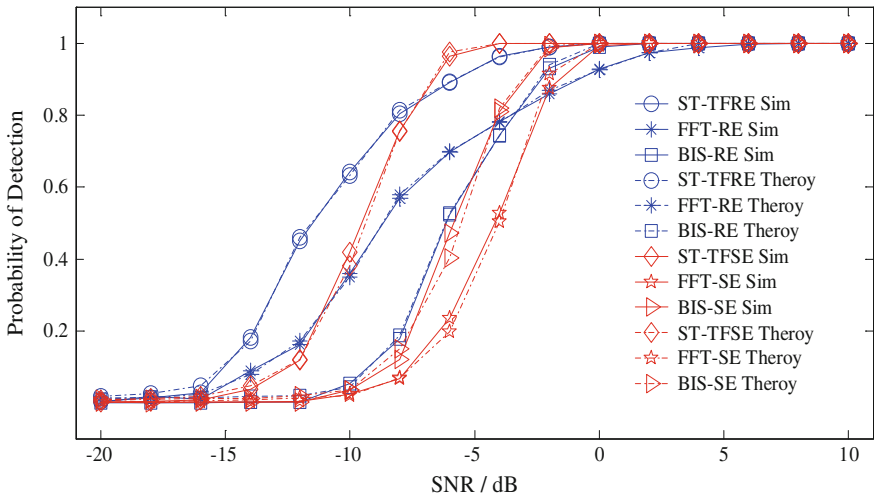

Fig. 7 Comparison the detection performance of different algorithm

Table 1 Comparing the complexity of algorithms

Name	Real multiplication	Real addition	Logarithm
FFT	$(2ML)\log_2(ML)+4ML$	$(2ML)\log_2(ML)+2ML$	0
ST-TFSE	$(2M)\log_2 M+12M^2$	$(2M)\log_2 M+6M^2-2$	M^2
ST-TFRE	$(2M)\log_2 M+(10+\alpha)M^2+1$	$(2M)\log_2 M+6M^2-2$	1

4.3 Complexity Analysis of Algorithm

In this section, the time complexity of the TFE detection algorithm based on ST and the detection algorithm based on FFT power spectrum are compared. Both the new detection algorithm and the FFT power spectrum detection algorithm are based on power spectrum. Hence, we only compare the complexity of power spectrum computation. The complexity of three algorithms are shown in Table 1, where M is the sampling point number in one cycle, K is the total number of cycles, K always is a big number. We can see from Table 1 that the calculation of detection algorithm based on ST-TFRE is the least, and the calculation of detection algorithm based on FFT is the largest.

5 Conclusion

In this paper, a class of CFAR detection algorithms is proposed based on TFE, which use the difference of TFE between signal and noise, and design the detection statistic by the TFE of observed sequence. This method does not need to know prior information, such as the period of pulsar, duty cycle, flux intensity, etc. The algorithm also has a low computational complexity and a good detective performance. We have verified the effectiveness of this method by simulation experiment. The simulation results show that the time-frequency Rényi entropy detection algorithm based on ST generates the optimal detection performance. However, the true space environment is extremely complex, this algorithm has some limitations under the true complex noise environment that may restrict the engineering realization. Therefore, the future work should be studying and improving the performance of this algorithm before being in practical application.

Acknowledgment This work is supported by National Science Foundation of China (61377080).

References

1. Smith FG (1997) Pulsars, 1st edn. Cambridge University, Cambridge
2. Sheikh SI (2005) The use of variable celestial X-ray sources for spacecraft navigation. Dissertation. University of Maryland, Maryland
3. Shrauner JA (1997) Phase coherent observations and millisecond pulsar searches. Physics Department, Princeton University, New Jersey
4. Seward FD, Harnden FR, Helfand DJ (1984) Discovery of a 50 millisecond pulsar in the Large Magellanic Cloud. ApJL 287:19–22
5. Flandrin PA et al (1988) Time-frequency formulation of optimum detection. IEEE Trans Acoust Speech Sig Process 36(9):1377–1384
6. Shang H, Shui P, Zhang S et al (2007) Energy integration detection via time-frequency distribution and morphological filtering. J Electron Inf Technol 29(6):1416–1420
7. Wang L, Xu L, Zhang H et al (2013) Pulsar signal detection based on S-transform. Acta Phys Sin 62(13):139702-1–139702-10
8. Baraniuk RG, Flandrin P, Jansen AJ et al (2001) Measuring time-frequency information content using the Renyi entropies. IEEE Trans Inf Theory 47:1391–1409
9. Zou H, Zhou X, Li Y et al (2009) Which time-frequency analysis—a survey. Chin J Electron 28(9):78–84
10. Taylor JH (1992) Pulsar timing and relativistic gravity. Class Q Grav 341:117–134
11. Hanson J, Sheikh SI, Graven P (2008) Noise analysis for X-ray navigation systems. IEEE/ION PLNS 704–713
12. Ganchang W (1999) Advanced mathematics, vol 1. Higher Education Press, Beijing
13. Wang L, Xu L, Zhang H et al (2014) A constant false alarm rate detection algorithm for X-ray pulsar signal based on time-frequency entropy. J Huazhong Univ Sci Technol 42(7):113–117

Research on Pulse Profile Stability of the X-ray Pulsar PSR B1509-58

Lirong Shen, Xiaoping Li, Haifeng Sun, Haiyan Fang, Mengfan Xue and Jinpeng Zhu

Abstract Pulse profiles of X-ray pulsars play an important role in X-ray pulsar-based navigation (XPNAV) and studying the rotation and emission characteristics of the pulsars. In this paper, we present an X-ray timing analysis of the young Crab-like pulsar PSR B1509-58 by using archival Rossi X-ray Timing Explorer (RXTE) data. We have investigated the stability of the PSR B1509-58 pulse profile in the energy band of 2–60 keV. The analysis results show that in the energy band of 2–30 keV, the flux is the largest than that of the 30–45, 45–60 keV, the 2–30 keV energy band possess the most photon series in 2–60 keV. As the energy range increases, the Pearson's correlation, between the standard pulse profile and the integrated pulse profiles of 2–30, 30–45, 45–60 keV, varies small, all the Pearson's correlations in different energy ranges are above 0.99, meanwhile, in the energy ranges of 2–30 keV, there is no obvious phase delay between the integrated pulse profile and the standard pulse profile, which means that the pulse profile is stable.

Keywords X-ray pulsar · Pulse profile · The stability of pulse profile

1 Introduction

Pulsars are rotating neutron stars which have been observed in radio, visible, X-ray, and gamma-ray ranges of the electromagnetic spectrum and are regarded as the ideal clock in the universe because of their high and steady rotation rate [1–3, 13]. Especially the millisecond pulsars, which rotate even more stable and their stabilities are comparable with those of the atomic clocks [6]. In recent years, these pulsars have been considered to be a new approach for assisting deep space navigation. Among them, the small X-ray detector placed on the spacecraft can realize

L. Shen (✉) · X. Li · H. Sun · H. Fang · M. Xue · J. Zhu
School of Aerospace Science and Technology, Xidian University, Xi'an 710071, China
e-mail: slr_xidian@163.com; lili_19870622@163.com

J. Sun et al. (eds.), *China Satellite Navigation Conference (CSNC) 2016 Proceedings: Volume II*, Lecture Notes in Electrical Engineering 389,
DOI 10.1007/978-981-10-0937-2_51

the X-ray signals receiving and the good geometric dispersion of X-ray pulsars make the X-ray pulsar become the good candidate for deep space exploration [10].

The basic observation of X-ray pulsar-based navigation (XPNAV) is the time of arrival (TOA) of X-ray photons [11]. Folding the light curve of the pulsars by using their respective pulse period, an average pulse profile can be obtained. These pulse profiles can help to study the connection between the timing characteristic and the X-ray emission characteristic for the pulsars. In addition, these pulse profiles can also help us to obtain the pulse TOA by comparing the integrated pulse profile at the spacecraft with the standard pulse profile at the Solar System Barycenter (SSB). Then the pulse TOA can be used to determine the distance between the spacecraft and the SSB. Thus, the stability of the pulse profile is very important for XPNAV and studying more physical characteristics of the X-ray pulsars.

PSR B1509-58 is a young energetic rotation-powered pulsar which was discovered within the supernova remnants MSH 15-52 characterized by a complex structure with thermal and nonthermal components [4]. It was initially discovered in soft x-ray band of the electromagnetic spectrum by the Einstein satellite [1]. Subsequently, it was discovered in radio, hard x-ray, and γ-ray ranges of the electromagnetic spectrum [7–9]. Its position is in full agreement with the radio coordinates of pulsar with $\alpha = 15$ h13 m55 s.617 and $\delta = -59°08'08''0.87$ (J2000.0). PSR B1509-58 is extremely stable with a period of about 150 ms and has the largest pulse period derivative of 1.5×10^{-12}ss^{-1} [5]. By using the pulsar's spin parameters, the characteristic age of PSR B1509-58 is inferred about 1700 years [4], which is the second smallest characteristic age after Crab pulsar [1]. It also has spin-down luminosity $\dot{E} = 1.8 \times 10^{37}$ergs s^{-1} and a surface magnetic field $B_p = 1.5 \times 10^{13}$G [4], which makes it become one of the most energetic and highest field pulsars known. In addition, the timing and the spectrum of PSR B1509-58 with Rossi X-ray Timing Explorer (RXTE) have been studied by many researchers. Margaret measured the 2–50 keV pulsed flux for 14.7 year of X-ray observations and found that it is consistent with being constant on all relevant timescales. He also searched for variability in the pulse profile and found that it is consistent with being stable on timescales of days to decades [14]. Litzinger presents an analysis of the X-ray spectra of PSR B1509-58 observed by RXTE over 14 years [15]. Ge mingyu used two Gaussian functions to fit and analyze the pulse profile of the PSRB1509-58 in the energy range of 2–60 keV for the data observed in 13 years, he found that the spectrum of PSR B1509-58 is significantly hard in the center of the pulse [16]. Pradhan used the Fourier decomposition technique to investigate the harmonics of the pulse profile of the PSR B1509-58 in the energy range of 2–24 keV for the data observed from the year of 1996 to 2011 [17], he did not find any significant variation of the harmonic components of the pulse profile in comparison to the fundamental.

As a candidate pulsar of XPNAV, the pulsar profile stability of the PSR B1509-58 determines the precision of the position and velocity measurement in deep space exploration. Thus, in this paper, we studied the X-ray pulse profile of

PSR B1509-58 in details in the energy of 2–60 keV using the data observed by RXTE over 16 years from January 6, 1996 to January 1, 2012. The energy range will be divided into 2–30, 30–45 and 45–60 keV for studying the pulse profile stability.

2 Observations and Data Reduction

RXTE satellite was launched into low-Earth orbit On December 30, 1995 to observe the fast-moving, high-energy worlds of black holes, neutron stars, X-ray pulsars, and bursts of X-rays, and was decommissioned on January 5, 2012. Proportional Counter Array (PCA), High-Energy X-ray Timing Experiment (HEXTE), and All-Sky Monitor (ASM) are the main observation instruments. Researchers can propose observations with two of XTE's instruments: PCA and HEXTE. PCA covers the energy range of 2–60 keV and the HEXTE covers the higher energy range of 15–250 keV. Thus, this two instruments are coaligned and can complement each other. Data from the All-Sky Monitor (ASM) are not proprietary [18].

The proportional counters of PCA cover the 2–60 keV energy range with large effective area of about 6500 cm^2. Thus, a large number of observation data of PSR B1509-58 are collected by PCA. The PCA data have two basic formats: Science array (SA) and Science event (SE). In this paper, the Science event format data of PSR B1509-58 is analyzed, which is recorded in Good Xenon mode with 1 μs time resolution.

We adopt 276 observations from January 6, 1996 to January 1, 2012 for the pulse profile stability analysis. The duration of all these observations is of the order of kilo seconds, which is enough for us to perform detailed pulse profile stability analysis. Before performing the pulse profile analysis, we use the HEAsoft software to preprocess the pulsar data.

First, standard procedures and selection criteria are applied to the observation data to avoid the earth occultation, point unstable, significant electron contamination as well as the contamination from South Atlantic Anomaly (SAA), solar, bright Earth, and particle. Here, we set that the elevation angle of observation instrument and horizontal plane of the earth is greater than 10, the offset of observation instrument from the source is lower than 0.02 and the NUM_PCU_ON equals 5, ELECTRON2 (electron contamination) is lower than 0.1 [16].

Then, For GoodXenon event data, the events are split between two EA's and telemetered in two separate files: GoodXenon1 and GoodXenon2. These two files must be combined to form the FITS event list using the script MAKE_SE. Then the XTEFILT is adopted to create the filter file for each observation and the MAKETIME is adopted to generate the Good Time Interval (GTI) file. Finally, the resulted new events data will be used in the pulse profile analysis [10].

3 Pulse Profile Stability Analysis

Before generating the pulse profile, it is necessary to conduct the barycentric corrections, which help that the arrival times of all selected events are converted to the Solar System Barycenter. In order to generate a pulse profile, in this paper, the best periods are searched through folding the observed photon series using different candidate periods to reach the maximum χ^2 with a resolution of 10^{-8} s.

Firstly, it is needed to calculate the absolute phase Φ_i of photon series t_i in [0, 1] using a candidate period T as the Eq. (1), where t_0 is the first photon received. Then calculate the remainder of the absolute phase using mod which refers to a module of a number.

$$\Phi_i = \frac{t_i - t_0}{T} \bmod 1.0 \tag{1}$$

Then, divided the [0, 1] with m phase bins, calculate the number of the photons in n_i bins, the total photons $N = \sum n_i$. The χ^2 can be calculated by

$$\chi^2 = \sum_{i=1}^{m} \frac{(n_i - N/m)^2}{N/m}, \tag{2}$$

where the best period is the candidate period which makes the χ^2 reach maximum. Fig. 1 shows the frequencies of the observations and the residuals of a quadratic

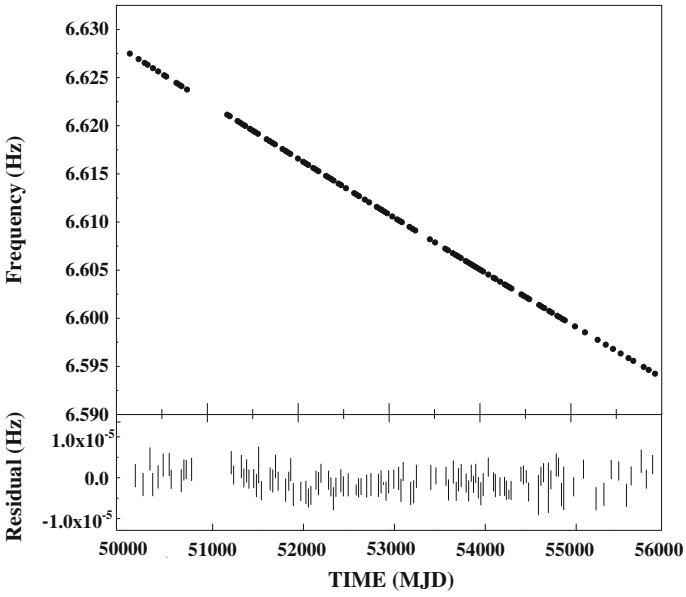

Fig. 1 Frequencies of the observations and the residuals of a quadratic polynomial fit

polynomial fit, which verified that the rotation frequency of the pulsar gradually slows down as the time increases.

Figure 2 shows the period search result of the real data packet 70701-01-03-00 of PSR B1509-58, Fig. 3 shows the integrated pulse profile of this observation with the high-precision period.

From Fig. 3 we can see that the X-ray pulse profile of PSR B1509-58 is a broad asymmetric single peak with the leading side much steeper than the trailing one, and the pulse profile is consistent with the shape measured by Rots et al. [12].

After summing up the aligned and normalized pulse profiles of each observation, we obtain a standard pulse profile. We compared the normalized individual profile with the standard pulse profile, no evident variability was found between them, which verifies the pulse profile stability of the PSR B1509-58.

Then, in order to research the variation of pulse profile versus energy ranges, in each Epoch, pulse profiles with 128 phase bins were created by using the data of three different energy ranges (2–30, 30–45, 45–60 keV). Because that as the time

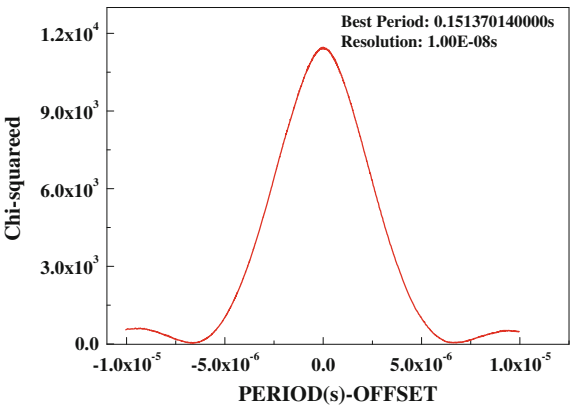

Fig. 2 The χ^2 in the pulse profile for different candidate pulse periods

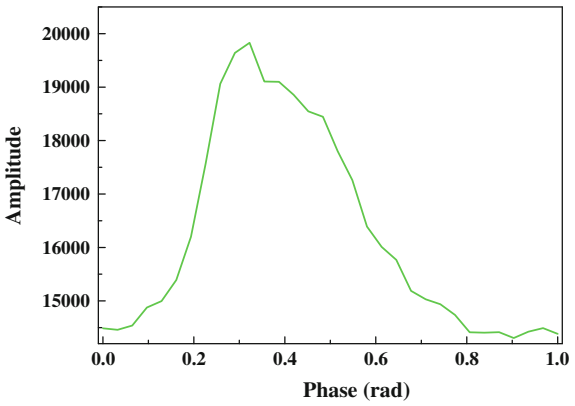

Fig. 3 The integrated pulse profile of PSRB1509-58 with 32 phase bins

Table 1 Energy-channel conversion of each Epoch

Epoch Channel E_MAX (keV)	Epoch1 (launch–96.3.21	Epoch2 (96.3.21–96.4.15)	Epoch3 (96.4.15–99.3.22)	Epoch4 (99.3.22–00.5.12)	Epoch5_PCU0 (00.5.13–present)	Epoch5_PCU1-4 (00.5.13–present)
30	110–111	92–93	80–81	68–69	66–67	70–71
45	160–162	136–138	118–119	102–103	98–99	106–107
60	208–210	178–180	154–156	134–135	130–131	136–138

goes on, the corresponding relationship between PCA channels and energy ranges has changed, so in this paper we selected the channels corresponding to the required energy ranges which are shown in Table 1. It is quite useful for the research of the variation of pulse profile versus energy ranges, even though the information in this table should be considered only approximate. In Epochs 1–4, the data were generated for the full PCA with all detectors and layers added. For calibration Epoch 5, due to the leakage loss of the propane layer gas in PCU 0, the data were generated separately for PCU0 and for PCUs 1–4.

In each energy range, firstly, it is needed to sum up the aligned pulse profiles which is integrated using the photons received in this energy range. Then, the mean pulse profiles are obtained by dividing the summed pulse profiles by the total number of observations. Then, the mean pulse profiles are fitted using the Gaussian fitting. The final pulse profiles are shown in Fig. 4.

Then, we compared the pulse profile of different energy ranges after subtracting a DC offset from each pulse profile using the mean flux of phase range of 0.8–1.0. The results are shown in Fig. 5.

Figures 4 and 5 depicted that the pulse profiles of PSR B1509-58 consist of a single asymmetrical peak below the energy range of 60 keV. In the energy ranges of 2–30 keV, the flux is the largest than the others, and the 2–30 keV energy ranges possess the most photon series in 2–60 keV. In the energy range 30–45 and 45–60 keV, the fluxes are very small.

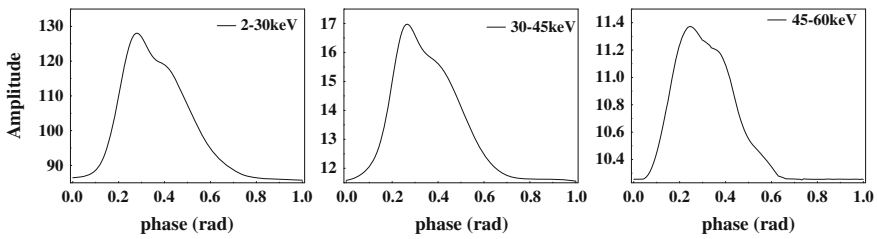

Fig. 4 The fitted pulse profiles with 128 phase bins for the data of three different energy ranges of PSR B1509-58

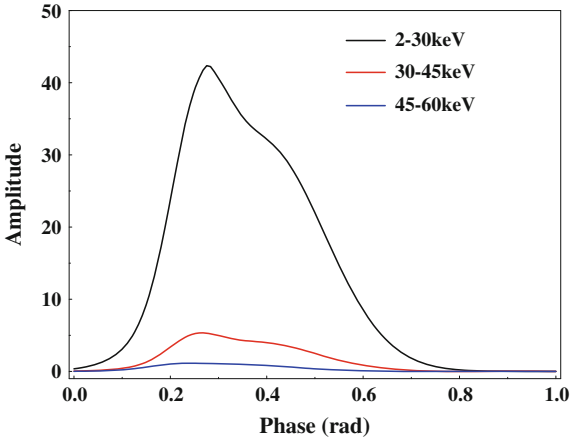

Fig. 5 Comparison of pulse profiles of different energy ranges after subtracting a DC offset from each pulse profile using the mean flux of phase range of 0.8–1.0

Table 2 Comparison of the integrated pulse profiles of each energy ranges and the standard pulse profile

Energy ranges	2–30 keV	30–45 keV	45–60 keV
Pearson's correlation coefficient	1	0.9995	0.9965
FW20	0.0680	0.0668	0.0645
FW30	0.0598	0.0574	0.0573
Phase delay	0	0.002	0.005

After peak normalized, we calculated the Pearson's correlation, the phase delay of these pulse profiles with the standard pulse profile as well as calculated the full width 20 % maximum (FW20) and full width 30 % maximum (FW30) of the pulse profiles. The results are shown in Table 2.

From Table 2, we can see that as energy ranges increase, the Pearson's correlation in different energy ranges varies small, all the Pearson's correlations in different energy ranges are above 0.99, which indicate the stability of the pulse profile in different energies.

The FW20 as well as FW30 of the pulse profiles in Table 2 also depicted the detail difference of the pulse profile in different energy ranges. As energy ranges increase, the FW20 as well as FW30 of the pulse profiles become smaller even though this changes are very small, it indicates that the pulse width of different energy ranges is becoming narrowed as the energy range increases. In addition, in the energy range of 2–30 keV there is no obvious phase delay between the integrated pulse profile and the standard pulse profile, which means that the pulse profile is stable. However, from Table 2, we can see that there are some phase delays between the integrated pulse profiles in the energy ranges of 30–45 keV as well as 45–60 keV and the standard pulse profile, which is because that the fluxes in high-energy ranges are small, the signal-to-noise ratio of pulse profile is low, the pulse profile is easily affected by the noise, so it leads to phase delays in 30–60 keV.

4 Conclusions

In this paper, we present an X-ray timing analysis of the young, Crab-like pulsar PSR B1509-58 by using archival Rossi X-ray Timing Explorer (RXTE) data. We have investigated the stability of the PSR B1509-58 pulse profile in the energy range of 2–60 keV. The analysis results show that in the energy range of 2–30 keV, the flux is the largest than the others, and the 2–30 keV energy ranges possess the most photon series in 2–60 keV. As the energy range increases, the Pearson's correlation in different energy ranges varies small, all the Pearson's correlations in different energy ranges are above 0.99, meanwhile, there is no obvious phase delay between the pulse profile in the energy range of 2–30 keV and the standard pulse profile, which means that the pulse profile is stable.

Acknowledgments This paper is supported by the National Program on Key Basic Research Project of China (973) (No.2014CB340205) and National Natural Science Foundation of China (Nos. 61301173 and 61473228).

References

1. Kaspi VM, Manchester RN et al. (1994) On the spin-down of PSR B1509-58. The Astrophys J 422:83–86
2. Blandford RD (1994) On the timing history of PSR B1509-58. Mon Not R Astron Soc 267:7–8
3. Marsden D, Blanco PR et al (1997) The X-ray spectrum of the plerionic system psr b1509-58/msh 15-52. Astrophys J 491:39–42
4. Gaensler BM, Arons J et al (2002) Chandra imaging of the X-ray nebula powered by pulsar b1509-58. Astrophys J 569:878–893
5. Cusumano G, Mineo T et al (2001) The curved X-ray spectrum of PSR B1509-58observed with BeppoSAX. Astron Astrophys 375:397–404
6. Zhang CH, Wang N, Yuan JP et al (2012) Timing noise study of four pulsars. Sci China Phys Mech Astron 55(2):333–338. doi:10.1007/s11433-011-4620-6
7. Seward FD, Harnden FR (1982) A new, fast X-ray pulsar in the supernova remnant MSH 15–52. Astrophys J 256:45–47
8. Manchester RN, Tuohy IR et al (1982) Discovery of radio puldations from the X-ray pulsar in the supernova remnant G320.4-1.2. Astrophys J 262:31–33
9. Ulmer MP, Matz SM et al (1993) Gamma-ray and radio observations of PSR B1509-58. Astrophys J 417:738–741
10. Shen LR, Li XP et al (2015) A novel period estimation method for X-ray pulsars based on frequency subdivision. Front Inf Technol Electron Eng 16(10):858–870. doi:10.1631/FITEE.1500052
11. Sheikh, S.I. (2005). The use of variable celestial X-Ray sources for spacecraft navigation. PhD Thesis, University of Maryland, USA
12. Rots AH (2003) 2800 Days of monitoring the timing of PSR B1509-58 with RXTE, heasarc.gsfc.nasa.gov
13. Livingstone MA, Kaspi VM et al (2005) 21 years of timing PSR B1509 − 58. Astrophys J 619(2):1046–1053
14. Livingstone MA, Kaspi VM (2011) Long-term X-ray monitoring of the young pulsar PSR B1509-58. Astrophys J 742:31(7 pp) doi:10.1088/0004-637X/742/1/31

15. Litzinger E, Pottschmidt K et al (2011) Monitoring PSR B1509–58 with RXTE: spectral analysis 1996–2010. Acta Polytechnica 51(6):38–41
16. Ge M. Y., Lu F. J., et al (2012). X-ray phase-resolved spectroscopy of PSRs B0531 + 21, B1509-58, and B0540-69 with RXTE. Astrophys J Suppl Ser 199(2):20 pp. doi:10.1088/0067-0049/199/2/32
17. Pradhan P, Paul B et al (2015) Variations of the harmonic components of the X-ray Pulse Profile of PSR B1509-58. 15(1)28–36. doi:10.1088/1674-4527/15/1/003
18. Jahoda K, Swank J H et al (1996) EUV, X-ray, and Gamma-ray instrumentation for astronomy VII. In: Sigmund OHV, Gumm M (eds) SPIE proceeding 2808, vol 59. SPIE, Bellingham, 1996

Discovery and Theory of the Shadow Reference Points

Xingang Feng and Dong Liu

Abstract The triangulation location is the same mathematical principles of the Global Navigation Satellite Systems (GNSSs) and the double-star positioning system, and the range between the navigation satellite and the user has to be measured. The three-dimensional position and clock offset can be solved by GNSS, while only the three-dimensional position can be gotten by the double-star positioning system. The position error is advanced by increasing the navigation satellite number generally. In this paper, the range calculation model of relay navigation is given. Based on the model, we present a theory on how the points with the known distance to the user are discovered in space, and the points are called the shadow reference points. Moreover, the error function of the relay range is analyzed. The shadow reference points can be applied as navigation satellite in order to improve the position error. Especially, the relay distance between the shadow reference points and the user is not needed to be measured, it can be obtained by calculation.

Keywords Relay range · Shadow reference points · Vector

1 Introduction

The deep space exploration is one of the important branches in aerospace fields. The moon is the only nature satellite for the earth, and the average distance between them is 384,000 km. When the human being explores and applies the deep space, the moon is the idealist transfer base. Exploring the moon has been the hotter issue in the international aerospace industry. In 2013, the Chang'e 3 had been launched successfully by China in order to explore the moon scientifically for the human being. Spacecraft lands the moon, even mankind appear on the moon, which have been an important kind of moon probes. One of the basic needs is to present the navigation service for the moon vehicle in order to get the exact position and

X. Feng (✉) · D. Liu
China Academy of Space Technology, Xi'an, China
e-mail: fengxg338@163.com

J. Sun et al. (eds.), *China Satellite Navigation Conference (CSNC) 2016 Proceedings: Volume II*, Lecture Notes in Electrical Engineering 389,
DOI 10.1007/978-981-10-0937-2_52

establish the router plane. Currently, the main navigation technologies include astronomical navigation, autonomous navigation, inertial navigation, optical guidance, etc. Global Navigation Satellite Systems (GNSSs) such as GPS, GLONASS, Galileo, and BeiDou have been researched and applied to various space applications in LEO, GEO, HEO orbits, and even lunar mission [1, 2]. Over the past several decades, the range between the navigation satellites and the users are measured in the GNSSs and the double-star positioning system.

However, it is an idea that GNSS would be applied for the moon navigation. One of the main difficulties is the value of dilution of precision (DOP) is rather larger, varied from 1000 to 10,000. If the range error is 1 m, the position error is about from 1 to 10 km [3] A nature method is that if one satellite is launched to the region A in Fig. 1, then the DOP value can be reduced largely. Here, we present a question: are there some reference points which can be served as navigation satellite if the satellite is not launched to the region A. By other words, if the moon would be removed, the user will be a free spacecraft, then the satellite can still be launched to the region A? In fact, there are numerous inartificial navigation satellites with the known distance to the user in the region A, and these satellites are called the shadow reference points in this paper. On the condition of no user clock offset, the mathematical proof is founded that why there are countless shadow reference points in the region A. It is very interesting that the distance between the shadow reference points and the user is obtained by mathematical calculation, not by measurement.

2 Model of the Relay Navigation

The shadow reference points are discovered which begins by the model of relay navigation in Fig. 1. Here, several terms are described as follows:

In XYZ coordinate system User: $U = (x, y, z)$
Vector measurement satellite: $S_m^{(1)} = \begin{bmatrix} x_m^{(1)} & y_m^{(1)} & z_m^{(1)} \end{bmatrix}$
Relay navigation satellite: $S_e^{(i)} = \begin{bmatrix} x_e^{(i)} & y_e^{(i)} & z_e^{(i)} \end{bmatrix}$, $i = 1, 2, 3$

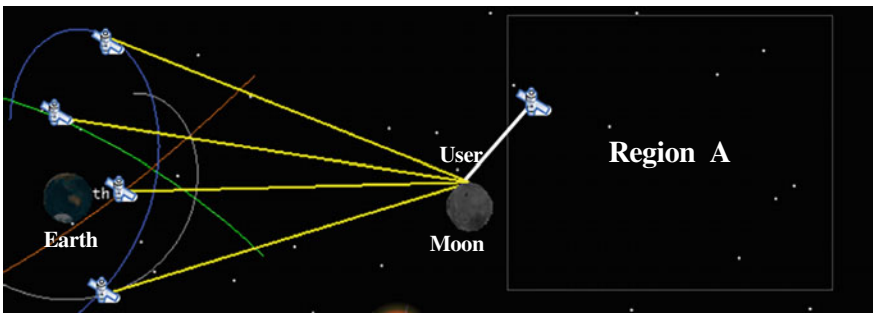

Fig. 1 Model of the relay range measurement

The vector of $\overrightarrow{S_m^{(1)}U}$ is measured by $S_m^{(1)}$, the range, azimuth angle, elevation angle, are R_e, α_e, θ_e, respectively.

$$R_e = R + dR, \alpha_e = \alpha + d\alpha, \theta_e = \theta + d\theta$$

The true user and false user are, respectively, denoted as U and U_e

$$U = R \cdot [\cos\theta\cos\alpha \quad \cos\theta\sin\alpha \quad \sin\theta] + S_m^{(1)}$$
$$U_e = R_e \cdot [\cos\theta_e\cos\alpha_e \quad \cos\theta_e\sin\alpha_e \quad \sin\theta_e] + S_m^{(1)}$$

Vector $\overrightarrow{S^{(i1)}} = S_e^{(i)} - S_m^{(1)}, \left\|\overrightarrow{S^{(i1)}}\right\| = R_{i1}$

Vector $\overrightarrow{S^{(i1)}}$ is the same in coordinate system *XYZ*. Suppose

$$\overrightarrow{S^{(i1)}} = R_{i1} \cdot [\cos\theta_1\cos\alpha_1 \quad \cos\theta_1\sin\alpha_1 \quad \sin\theta_1]$$

The cosine value between $\overrightarrow{S^{(i1)}}$ and $\overrightarrow{S_m^{(1)}U}$ is calculated as:

$$\cos\gamma = \frac{\left(\overrightarrow{S^{(i1)}}, \overrightarrow{S_m^{(1)}U}\right)}{\sqrt{\left(\overrightarrow{S^{(i1)}}, \overrightarrow{S^{(i1)}}\right)} \times \sqrt{\left(\overrightarrow{S_m^{(1)}U}, \overrightarrow{S_m^{(1)}U}\right)}}$$

The relay range between U and $S_e^{(i)}$, is expressed as:

$$\rho^{(i)} = \sqrt{R^2 + R_{i1}^2 - 2\cos\gamma \cdot R \cdot R_{i1}} \tag{1}$$

3 Existence of the Shadow Reference Points

Suppose, the ephemeris error of $S_m^{(1)}$ is $\Delta S_m^{(1)} = \left[\mathrm{d}x_m^{(1)} \quad \mathrm{d}y_m^{(1)} \quad \mathrm{d}z_m^{(1)}\right]$, The ephemeris error of $S_e^{(i)}, i = 1,2,3$ is $\Delta S_e^{(i)} = \left[dx_e^{(i)} \quad dy_e^{(i)} \quad dz_e^{(i)}\right]$, the error of R_{i1} is dR_{i1}.

$d\rho^{(i)}$ is obtained by total differential of function (1). $d\rho^{(i)}$ is composed of three parts, the first part is the error caused by $\Delta S_m^{(1)}, \Delta S_e^{(i)}$, the second part is the error caused by $d\alpha, d\theta$, and the third part is the error caused by dR, dR_{i1}.

The error function caused by $\Delta S_m^{(1)}, \Delta S_e^{(i)}$ is expressed as:

$$\begin{aligned}&\frac{\partial \rho^{(i)}}{\partial x_m^{(1)}} \mathrm{d}x_m^{(1)} + \frac{\partial \rho^{(i)}}{\partial y_m^{(1)}} \mathrm{d}y_m^{(1)} + \frac{\partial \rho^{(i)}}{\partial z_m^{(1)}} \mathrm{d}z_m^{(1)} + \frac{\partial \rho^{(i)}}{\partial x_e^{(i)}} \mathrm{d}x_e^{(i)} + \frac{\partial \rho^{(i)}}{\partial y_e^{(i)}} \mathrm{d}y_e^{(i)} + \frac{\partial \rho^{(i)}}{\partial z_e^{(i)}} \mathrm{d}z_e^{(i)} \\ &= \frac{\partial \rho^{(i)}}{\partial x_e^{(i)}} \left(\mathrm{d}x_e^{(i)} - \mathrm{d}x_m^{(1)} \right) + \frac{\partial \rho^{(i)}}{\partial y_e^{(i)}} \left(\mathrm{d}y_e^{(i)} - \mathrm{d}y_m^{(1)} \right) + \frac{\partial \rho^{(i)}}{\partial z_e^{(i)}} \left(\mathrm{d}z_e^{(i)} - \mathrm{d}z_m^{(1)} \right)\end{aligned} \tag{2}$$

Generally, $\mathrm{d}x_e^{(i)} \neq \mathrm{d}x_m^{(1)}, \mathrm{d}y_e^{(i)} \neq \mathrm{d}y_m^{(1)}, \mathrm{d}z_e^{(i)} \neq \mathrm{d}z_m^{(1)}$, Eq. (2) is no zero. If one sphere is constructed with the center $S_m^{(1)}$ and the radius $k \times R(k > 0)$, and the sphere is called the shaded sphere. Any point P on the sphere and the $S_m^{(1)}$ have the same error, then the Eq. (2) is zero. An interesting and amazing result is appeared from the viewpoint of mathematical, the point P and $S_e^{(i)}$ have no difference, so the point P can be served as the relay navigation satellite.

Suppose $\|PU_e\| - \|PU\| = \Delta r$. Whether there are some points P' on the sphere can meet the $\mathrm{d}\rho^{(i)} = 0$

In order to analyze the Δr conveniently, the coordinate shift and rotate transform is applied to get the new coordinate $X'Y'Z'$, the origin of $X'Y'Z'$ coordinate system coincide with the $S_m^{(1)}$, the axis of Z' coincide with the vector $\overrightarrow{S_e^{(1)}U_e}$ The rotate matrix is denoted as $C_e(\theta_e, \alpha_e)$

$$C_e(\theta_e, \alpha_e) = \begin{bmatrix} -\sin\alpha_e & \cos\alpha_e & 0 \\ -\sin\theta_e \cos\alpha_e & -\sin\theta_e \sin\alpha_e & \cos\theta_e \\ \cos\theta'_e \cos\alpha_e & \cos\theta_e \sin\alpha_e & \sin\theta_e \end{bmatrix}$$

Here, three cases are given.

1. when $\mathrm{d}R = \mathrm{d}R_{i1} = 0\,, \quad \mathrm{d}\alpha \neq 0,\ \mathrm{d}\theta \neq 0$
   In the coordinate system $X'Y'Z'$, any elevation angle $\theta' \neq 90^\circ$ there are two points P'_{a1}, P'_{a2} corresponding azimuth angle α'_1, α'_2, it will meet $d\rho^{(i)} = 0$

$$\alpha'_1 = \arctan(-\mathrm{d}\alpha \cdot \cos\theta / \mathrm{d}\theta), \alpha'_2 = \alpha'_1 + 180^\circ$$

   When $\alpha'_3 = \alpha'_1 \mp 90^\circ$, Δr would be the maximum value and the minimum value.
2. when $\mathrm{d}R \neq 0, \mathrm{d}\alpha = \mathrm{d}\theta = 0$
   In the coordinate system $X'Y'Z'$, $\cos\gamma = \sin\theta'_1$, $\mathrm{d}R_{i1} = k \times \mathrm{d}R$

$$\frac{\partial \rho^{(i)}}{\partial R} \times \mathrm{d}R + \frac{\partial \rho^{(i)}}{\partial R_{i1}} \times \mathrm{d}R_{i1} = \mathrm{d}R\sqrt{1 + k^2 - 2k\sin\theta'_1}$$

3. when $\mathrm{d}R \neq 0, \mathrm{d}\alpha \neq 0, \mathrm{d}\theta \neq 0$

$$
\begin{aligned}
d\rho^{(i)} &= \frac{\partial \rho^{(i)}}{\partial \alpha} + \frac{\partial \rho^{(i)}}{\partial \theta} + \frac{\partial \rho^{(i)}}{\partial R} \\
&= \frac{kR\cos\theta_1'}{\sqrt{1+k^2-2k\sin\theta_1'}} \cdot \sqrt{(\cos\theta \cdot \mathrm{d}\alpha)^2 + (\mathrm{d}\theta)^2} \\
&\quad \times \sin(\alpha' + \phi) + dR\sqrt{1+k^2-2k\sin\theta_1'} \\
&= A \cdot \sqrt{(\cos\theta \cdot \mathrm{d}\alpha)^2 + (\mathrm{d}\theta)^2} + D
\end{aligned}
$$

Here, $\phi = \arcsin\left(\frac{\mathrm{d}\alpha\cdot\cos\theta}{\sqrt{(\mathrm{d}\theta)^2 + (\mathrm{d}\alpha\cdot\cos\theta)^2}}\right)$

The total range error $d\rho^{(i)}$ is composed of AC variable and DC variable. When A > |D|, $d\rho^{(i)} = 0$ could be meet always, and there are two points. In the coordinate system $X'Y'Z'$, the azimuth angle which could be meet the $\mathrm{d}\rho^{(i)} = 0$ is expressed as β_1', β_2', the corresponding points are $P'_{\beta 1}, P'_{\beta 2}$. $P'_{\beta 1}, P'_{\beta 2}$ is transformed to $P_{\beta 1}, P_{\beta 2}$ of coordinate system XYZ

$$
\begin{aligned}
P_{\beta 1} &= (C_e)^{-1} P'_{\beta 1} + S_m^{(1)} \\
P_{\beta 2} &= (C_e)^{-1} P'_{\beta 2} + S_m^{(1)}
\end{aligned}
$$

The points $P_{\beta 1}, P_{\beta 2}$ are called the shadow reference points.

When θ' vary from $-90°$ to $90°$, all the shadow reference points formed a ring of shadow reference points.

4 Simulation

4.1 Simulation of Range Error

Suppose $S_m^{(1)} = [0 \quad 0 \quad 0]$ in the coordinate system XYZ. The true vector value and its error of vector $\vec{S_m^{(1)}U}$ are written in Table 1.

The rotate matrix is $C_e(45° + 30\,\mathrm{urad}, 60° - 40\,\mathrm{urad})$.

In the coordinate system $X'Y'Z'$, $k = 2, \theta' = 60°, \alpha' = [-180°, 180°]$

The simulation result $d\rho^{(i)}$ is Fig. 2.

Total: the range error $\mathrm{d}\rho^{(i)}$ in case of $\mathrm{d}R \neq 0, \mathrm{d}\alpha \neq 0, \mathrm{d}\theta \neq 0$
dR: the range error $\mathrm{d}\rho^{(i)}$ in case of $\mathrm{d}R \neq 0, \mathrm{d}\alpha = 0, \mathrm{d}\theta = 0$
dFW: the range error $\mathrm{d}\rho^{(i)}$ in case of $\mathrm{d}R = 0, \mathrm{d}\alpha \neq 0, \mathrm{d}\theta = 0$
dYJ: the range error $\mathrm{d}\rho^{(i)}$ in case of $\mathrm{d}R = 0, \mathrm{d}\alpha = 0, \mathrm{d}\theta \neq 0$

Table 1 Measurement value of vector

	True value	Error
Distance (m)	1,000,000	20
Elevation angle	45°	30 urad
Azimuth angle	60°	−40 urad

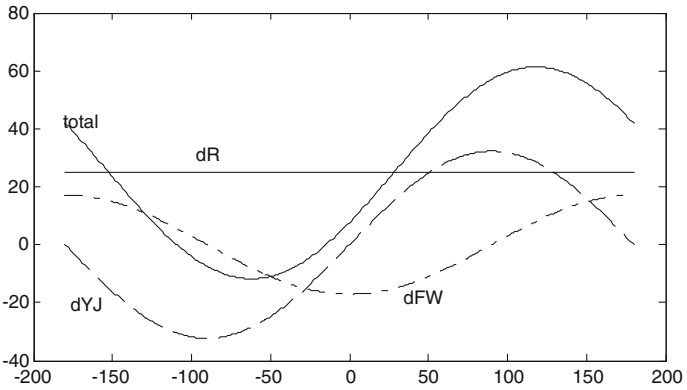

Fig. 2 The simulation result of range error

The simulation result of range error illustrates that the theoretical analysis is correct completely. In fact, when the $d\alpha, d\theta$ are larger, the shadow reference points exist still.

4.2 Applying Simulation of Shadow Reference Points

The coordinate value of $S_m^{(1)}, S_e^{(1)}, S_e^{(2)}, U$ is in Table 2, the unit is the meter.

The steps of applying the shadow reference points to calculating the user position are as follows:

Step1: selecting one vector measurement satellite $S_m^{(1)}$ to measure the vector between the $S_m^{(1)}$ and the user U, we can get the result $\overrightarrow{S_m^{(1)}U}$, $\left\|\overrightarrow{S_m^{(1)}U}\right\| = R_e$

Table 2 The coordinate value of satellite and user

	x	y	z
$S_m^{(1)}$	9501375.163	11323297.439	7506092.134
$S_e^{(1)}$	−8171561.854	14067339.668	3189068.500
$S_e^{(2)}$	6394037.333	−3284195.351	14938707.236
U	223635318.842	266518194.661	200868699.999

Step2: selecting one vector measurement satellite $S_e^{(i)}$ to measure the range between the $S_e^{(i)}$ and the user U, we can get the result $R^{(i)}$.

Step3: to get the new coordinate $X'Y'Z'$, the origin of $X'Y'Z'$ coordinate system coincides with $S_m^{(1)}$, the axis of Z' coincides with the vector $\overrightarrow{S_m^{(1)}U_e}$

Step4: in $X'Y'Z'$, the constant θ_1' is confirmed

Step5: in $X'Y'Z'$, azimuth angle α' rotate from $-180°$ to $180°$, the point P' which meets the $\mathrm{d}\rho^{(i)} = 0$ exists certainly.

Step6: $P = (C_e)^{-1}P' + S_m^{(1)}$, where the point P is in XYZ coordinate system

Step7: suppose k = 2

Step8: the range between P and the user is

$$\rho = R_e\sqrt{1 + k^2 - 2k\sin\theta_1'}$$

Step9: the distance between the user and $S_m^{(1)}, S_e^{(i)}$, P are $\left\|S_m^{(1)}U\right\| = R_e$, $\left\|S_e^{(i)}U\right\| = R^{(i)}$, $\|PU\| = \rho$, respectively

Step10: the least square method is used to solved the user position by satellites $S_m^{(1)}, S_e^{(1)}, P$ and ranges $\left\|S_m^{(1)}U\right\| = R_e, \left\|S_e^{(i)}U\right\| = R^{(i)}, \|PU\| = \rho$. The position results are a sequence which is a line in the 3D space.

The vector result measured by $S_m^{(1)}, S_e^{(1)}, S_e^{(2)}$ is illustrated from Tables 3, 4 and 5 in XYZ coordinate system.

The traditional least square method is denoted as method 1. The method by applying the shadow reference points is denoted as method 2. The simulation result is in Table 6 by two methods and is displayed in Fig. 3.

The three lines corresponding satellites groups $S_m^{(1)}, S_e^{(1)}, P$, $S_m^{(1)}, S_e^{(2)}, P$, and $S_e^{(1)}, S_e^{(2)}, P$ in Fig. 3 are position error by method 2. The point * in Fig. 3 is the U_e error measured by $S_m^{(1)}$. The unit of axis is meter.

Table 3 Vector result1

	$\overrightarrow{S_m^{(1)}U}$	
	True value	Error
Distance (m)	385184209.688	−5
Elevation angle	30.1332°	−4.7446 urad
Azimuth angle	50.0012°	21.2985 urad

Table 4 Vector result2

	$\overrightarrow{S_e^{(1)}U}$	
	True value	Error
Distance (m)	395655289.307	9
Elevation angle	29.9753°	0.7607 urad
Azimuth angle	47.4417°	10.6543 urad

Table 5 Vector result3

	$\vec{S_e^{(2)}U}$	
	True value	Error
Distance (m)	393137457.835	−7
Elevation angle	28.2267°	25.9757 urad
Azimuth angle	61.161°	27.9363 urad

Table 6 The position result and DOP of two methods

	Method 1	Method 2
Δx (m)	310.4089	290.6613
Δy (m)	−181.0064	−197.8724
Δz (m)	−114.8266	−122.6607
PDOP	63.43	25.96
XDOP	39.78	20.33
YDOP	16.50	15.98
ZDOP	46.57	2.21

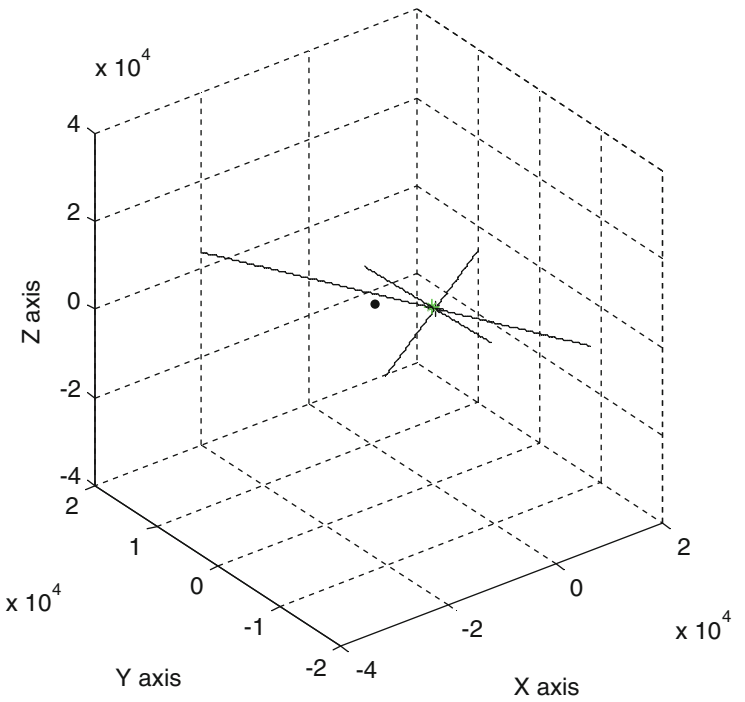

Fig. 3 Three lines in 3D space by method 2

5 Conclusion

The range calculation model of relay navigation is established in this paper. The shadow reference points are discovered and confirmed by analyzing the model, and the error function of the range between the shadow reference points and the user is proposed.

The simulation results prove the existence and validity of the shadow reference points completely. According to the result of Fig. 3, method 2 can partly improve the result of method 1. A lot of simulation results indicate that result of method 2 is better or worse because of the randomness of measurement error. Compared to the unique result of method 1, the method 2 provides a possibility to improve the position result at least. The shadow reference points can be used not only for lunar navigation but also for the similar navigation case.

References

1. Bamford W, Heckler G, Holt G, Moreau M (2008) A GPS receiver for lunar missions. In: Proceedings of Instrumental Navigation. Technical Meeting, San Diego, CA
2. Winternitz LMB, Bamford WA, Heckler GW (2009) A GPS receiver for high-altitude satellite navigation. IEEE J Sel Top Sign Process 3(4):541
3. Xie G (2011) Principles of GPS and receiver design. Publishing House of Electronics Industry, 7

A New Multichannel Acquisition Method for Navigation Signal Based on Compound Carrier

Ruidan Luo, Ying Xu and Hong Yuan

Abstract Navigation signal based on compound carrier (NSCC), the novel modulation scheme for navigation augmentation, has the special multi-carrier (MC) structure and flexible structure parameters, which enables it possess significant efficiency of navigation augmentation in terms of integrated communication and navigation service. However, due to its special structure, the conventional acquisition methods cannot be applied on the NSCC. The paper, based on the characteristics of NSCC, proposed a kind of multichannel acquisition method for multi-carrier system. The proposed method combines multichannels to realize energy accumulation of NSCC subcarriers by utilizing NSCC knowledge. This method is easy to implement with slight modification of current receivers. Both the theoretical analysis and simulation results illustrate that the proposed method achieves desirable acquisitio777n performance, reduces computation load and speeds up the acquisition with the restricted hardware in comparison of the conventional single-carrier acquisition methods.

Keywords NSCC · Multichannel · Acquisition · FFT

1 Introduction

Global Navigation Satellite Systems (GNSSs) and its augmentation systems are undergoing a process of enhancement and diversification. The ever-increasing user requirement in terms of accuracy, robustness, integrity and reliability, is stimulating the evolution for future advanced GNSSs [1–3]. Based on the ubiquitous terrestrial

R. Luo (✉)
University of Chinese Academy of Sciences, Beijing 100049, China
e-mail: luoruidan@aoe.ac.cn

R. Luo · Y. Xu (✉) · H. Yuan
Academy of Opto-Electronics Chinese Academy of Science, Dengzhuang South Road No. 9, Beijing 100094, Haidian District, China
e-mail: nadinexy@aoe.ac.cn

J. Sun et al. (eds.), *China Satellite Navigation Conference (CSNC) 2016 Proceedings: Volume II*, Lecture Notes in Electrical Engineering 389,
DOI 10.1007/978-981-10-0937-2_53

communication infrastructures, the integration of navigation and communication becomes a significant orientation, providing no gap coverage service and enhanced performance.

One promising solution to realize the integration is to optimize signal modulation scheme [4–9]. The new signal design must aim at improving the overall navigation performance, as well as enabling integrated communication and navigation service. For the specific purpose, we proposed an integrated signal, called Navigation Signal based on Compound Carrier (NSCC). NSCC, as a kind of multi-carrier (MC) signal, is generated by superposition and multiparameter adjustment of subcarriers, allowing for great degree of freedom in signal design. The preliminary exploration has been conducted to confirm the feasibility [10–12]. The comprehensive performance evaluation demonstrates its structure characteristics and superiority in spectrum efficiency, multipath mitigation, and antijamming capability.

NSCC, however, has an obvious drawback in the synchronization algorithm design due to its multi-carrier modulation scheme. The conventional acquisition methods are designed to process single-carrier signal with single channel. Since its subcarriers adopt the Binary Phase Shift Keying (BPSK) modulation, NSCC can be directly processed by conventional algorithms with each channel for each subcarriers method. There is no doubt that the method will inevitably multiply the computation load and resource occupation.

The acquisition is the most computationally intensive process, and thus its improvement focuses on reducing the time consumption, computation load, and resource occupation. The FFT-based algorithm allows a simultaneous search of all Pseudo Random Noise (PRN) code phases, reducing considerably acquisition time consumption for each signal channel [13–15]. The follow-up improved algorithms mostly adopt joint acquisition and collective detection to realize multi-satellite signals acquisition with no obvious increment of complexity and consumption [16–19].

It is noteworthy that the composite code method is employed by the joint acquisition. Beach firstly proposed the composite code method [20, 21]. He generated a composite Gold code sequence by a specific algorithm as the local replica code to acquire four satellite PRN code simultaneously. Then, Lin and Jan proposed multi-C/A code acquisition, employing the sum of two or more PRNs as local replica code [22]. The algorithm is easier to implement and less complexity, but there is a tradeoff between the number of the summed PRNs and the algorithm performance.

Accordingly, the paper proposes an acquisition method for NSCC which takes advantage of its mutually orthogonal subcarriers. This method sums the baseband of subcarriers to acquire the received NSCC signal, and then we only have to determine the summed peak in the search space. Thus, we call this proposed method the "multichannel acquisition method," just as its name implying that we combine all the NSCC subcarriers to process the acquisition.

The proposed method will speeds up the acquisition process and decrease the hardware resource occupation with this collective process. In addition, It only

modifies the conventional FFT-based correlator acquisition slightly, therefore, it is easy to implement with existing receivers. Its multichannel processing mean can also be applied to multifrequency and multi-satellite signal joint acquisition and combined with other enhanced algorithms for weak signals.

The rest of the paper is organized as follows: Sect. 2 gives a background on NSCC modulation scheme and its basic structural characteristic. Section 3 discusses the concept and the algorithm of the multichannel acquisition method. The complete acquisition framework and procedures are given combined with the comprehensive theoretical analysis. Section 4 employs comparative simulations to validate the proposed method and evaluate its acquisition performance. Finally, the conclusion is addressed in the Sect. 5.

2 NSCC Signal and Its Properties

An NSCC signal transmits an integrated information data stream over M complex parallel subcarriers. Figure 1 describes the NSCC modulation. It possesses an OFDM-like structure, but its function distinguishes itself from OFDM. NSCC is targeting to provide integrated communication and navigation service and improve the service quality in challenging environments, demanding for adjustable and malleable structure forms.

According to the *i*-th transmitter, the time-domain representation of the baseband NSCC modulation is given by:

$$S^i(t) = \sum_{m=1}^{M} A_m^i C_m^i(t) D_m^i(t) \cos(2\pi(f_0 + \Delta f_m)t + \varphi_m) \tag{1}$$

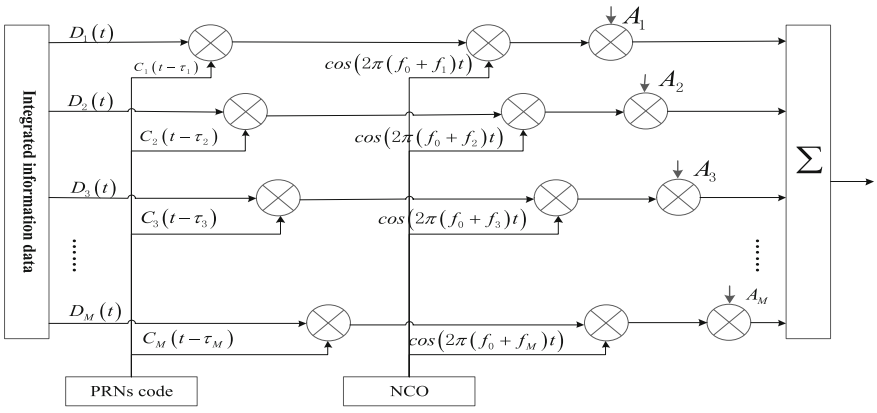

Fig. 1 NSCC modulation schematic block diagram

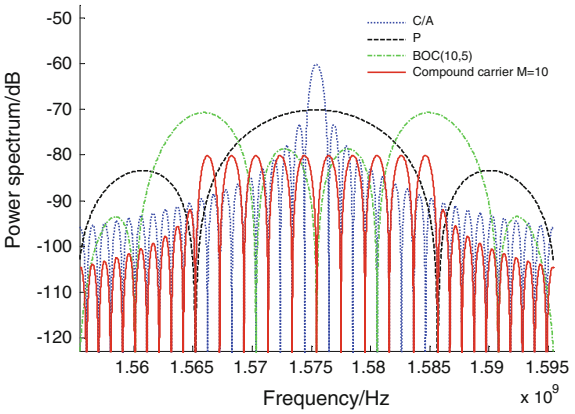

Fig. 2 Comparison of PSDs for NSCC(10), C/A, P, BOC (10, 5)

Where, the index i and m refer to the i-th transmitter and m-th subcarrier respectively, M is the number of subcarriers, A_m is the amplitude of the m-th subcarrier, C_m is the PRNs code modulating the m-th subcarrier, D_m is the integrated information transmitted at the m-th subcarrier, f_0 is the initial frequency of NSCC, Δf_m is the frequency interval between the initial subcarrier and the m-th subcarrier, φ_m is the initial phase of the m-th subcarrier. The transmitters are identified with the PRNs sets. The PRNs and frequency orthogonality among the subcarriers can be utilized to suppress the inter-channel interference (ICI).

The representative spectral profile of NSCC with flat power distribution, along with C/A code, BOC(10, 5), P code at L1 frequency band, are illustrated in Fig. 2. Obviously, NSCC has compact PSD profile, implying superior spectrum efficiency and its side lobes magnitude decreases with greater rapidity, compared with other legacy navigation signals. Therefore, it is less vulnerable to adjacent channel interference (ACI) in the frequency domain.

3 Multichannel Acquisition Algorithm

3.1 The Framework of Multichannel Acquisition Algorithm

The acquisition is based on the evaluation and processing of the Cross Ambiguity Function (CAF), which presents a sharp peak corresponding to the values of code phase delay and Doppler frequency shift. The conventional algorithm implementing the CAF consists mainly of correlator, matched filter and FFT-based correlator. The correlator and the matched filter, straightforward calculations of the CAF, both require a large number of operations, which is proportional to PRNs code length, the number of samples per chip and integration time. The process will cost much computing time and resource occupation. The FFT-based correlator utilizes

FFT/IFFT operation to allow a simultaneous search of all possible code phase. Thus, this approach for GNSS software receiver application will save considerably mean acquisition time.

However, the above conventional algorithms are generally utilized to process single-carrier signal in the single channel. NSCC modulation, in essence, is a special case of multi-carrier direct-sequence code division multiple access (MC-DS-CDMA). Each NSCC subcarriers can be processed with the conventional algorithms separately in a bank of sub-channels, which will inevitably multiple hardware occupation and computation load. Therefore, a judicious design for NSCC is necessary.

The multichannel acquisition provides a solution to the problem by taking advantage of mutually orthogonality among subcarriers. The method first generates the desired NSCC subcarriers signal respectively and then sums them as the NSCC replica for correlation. The FFT-based correlator is adopted with the consideration for time consumption. Thus, only a slightly modification of the conventional acquisition algorithm needs to be done. The mutually orthogonal subcarriers can largely mitigate the ICI of NSCC signal. The search space created by the proposed method will emerge an obvious peak which concentrates all subcarriers power. We then estimate the coarse information in terms of the code delay time and Doppler shift based on the peak. If the high dynamic receiver causes great Doppler shift, we also can adjust the code phase and Doppler shift of subcarriers of the NSCC replica in accordance with linear relation between them. The framework of multichannel acquisition method is showed in the Fig. 3.

The proposed method implements the NSCC acquisition with no addition of time consumption and resource occupation compared with the conventional acquisition methods. This method can also be utilized to realize the multifrequency joint acquisition and multi-satellite joint acquisition. However, the disadvantage of the proposed method is that the combination of subcarriers will bring in

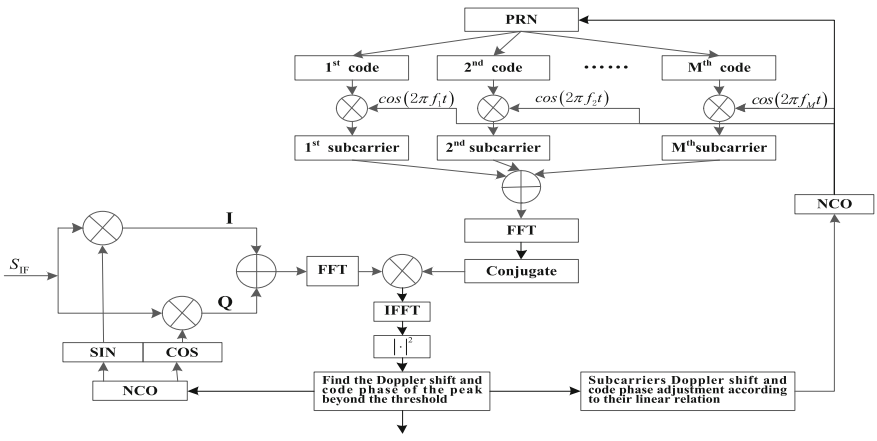

Fig. 3 Framework of acquisition for NSCC based on MCM

cross-correlation terms resulting in the noise floor increase, and the number of the cross-correlation terms is proportional to the number of NSCC subcarriers. In the following analysis, the mathematical model of the proposed method is presented and the signal terms at the output are calculated by formula derivation, which demonstrates the feasibility of the proposed method and evaluates the cross-correlation terms.

3.2 Mathematical Model

The received NSCC signal is filtered by the front-end filter, downconverted from radio frequency (RF) to intermediate frequency (IF). The NSCC IF signal can be written as,

$$S_{IF}(\tau, \Delta f_d) = \sum_{m=1}^{M} A_m C_m(t-\tau) D_m(t-\tau) \cos\left(2\pi\left(f_{IF} + \Delta f_m + \Delta f_{d,m}\right)(t-\tau) + \varphi_m\right) + n(t) \tag{2}$$

where, τ is the time delay due to propagation of the signal, Δf_d is the difference between the frequency of the local carrier and the incoming signal, $\Delta f_{d,m}$ is the Doppler frequency shift of the m-th subcarrier, $n(t)$ is the stationary additive white Gaussian noise (AWGN).

The NSCC IF signal is mixed with the local carrier, and then down converted to baseband in-phase (I) and quadrature-phase (Q) signals. Its corresponding composite form can be expressed as,

$$\begin{aligned} S_{\mathrm{IF},1}(\tau, \Delta f_d) = {} & S_{IF} \cos\left(2\pi\left(f_{\mathrm{IF}} + \Delta f_1 + \Delta \hat{f}_{d,1}\right)t\right) \\ & + jS_{\mathrm{IF}} \sin\left(2\pi\left(f_{\mathrm{IF}} + \Delta f_1 + \Delta \hat{f}_{d,1}\right)t\right) \end{aligned} \tag{3}$$

where, $\Delta \hat{f}_{d,1}$ is the estimated Doppler frequency shift of the first subcarrier.

The high frequency components in the Eq. (3) will be filtered in the coherent integration process. For simplicity and without loss of generality, we neglect the impact of the high frequency components and navigation data D_m. The in-phase components can be expressed as,

$$\begin{aligned} S_{\mathrm{IF},1,I}(\tau, \Delta f_d) &= S_{\mathrm{IF}} \cos\left(2\pi\left(f_{\mathrm{IF}} + \Delta f_1 + \Delta \hat{f}_{d,1}\right)t\right) \\ &= \frac{1}{2}\sum_{m=1}^{M} A_m C_m(t-\tau) \cos\left(2\pi\left(\Delta f_m - \Delta f_1 + \Delta f_{d,m} - \Delta \hat{f}_{d,1}\right)t - \varphi_{m,1}\right) + n_{1,I}(t) \end{aligned} \tag{4}$$

Similarly, the quadrature-phase component can be expressed as,

$$\begin{aligned} S_{\mathrm{IF},1,Q}(\tau,\Delta f_d) &= S_{\mathrm{IF}}\sin\left(2\pi\left(f_{\mathrm{IF}}+\Delta f_1+\Delta\hat{f}_{d,1}\right)t\right) \\ &= -\frac{1}{2}\sum_{m=1}^{M}A_m C_m(t-\tau)\sin\left(2\pi\left(\Delta f_m-\Delta f_1+\Delta f_{d,m}-\Delta\hat{f}_{d,1}\right)t-\varphi_{m,1}\right)+n_{1,Q}(t) \end{aligned} \tag{5}$$

Substituting Eqs. (4) and (5) into Eq. (3), the composite form can be rewritten as,

$$\begin{aligned} S_{\mathrm{IF},1}(\tau,\Delta f_d) &= S_{\mathrm{IF},1,I}(\tau,\Delta f_d)+jS_{\mathrm{IF},1,Q}(\tau,\Delta f_d) \\ &= \frac{1}{2}\sum_{m=1}^{M}A_m C_m(t-\tau)\mathrm{e}^{-j\left(2\pi\left(\Delta f_m-\Delta f_1+\Delta f_{d,m}-\Delta\hat{f}_{d,1}\right)t-\varphi_{m,1}\right)}+n_1(t) \end{aligned} \tag{6}$$

where, $n_{1,I}(t)$ and $n_{1,Q}(t)$ are the in-phase and quadrature-phase of AWGN $n(t)$, respectively. $n_1(t)$ is their composite form after quadrature demodulation.

After the FFT operation, the frequency domain representation of $S_{\mathrm{IF},2}(\tau,\Delta f_d)$ can be showed as,

$$\begin{aligned} S_{\mathrm{IF},2}(\tau,\Delta f_d) &= \int_T S_{\mathrm{IF},1}\left(\tau,\Delta f_{d,m}\right)\mathrm{e}^{j2\pi f\tau}\mathrm{d}t \\ &= \int_T \frac{1}{2}\sum_{m=1}^{M}A_m C_m(t-\tau)\mathrm{e}^{-j\left(2\pi\left(\Delta f_m-\Delta f_1+\Delta f_{d,m}-\Delta\hat{f}_{d,1}\right)t-\varphi_{m,1}\right)}\cdot\mathrm{e}^{-j2\pi ft}\mathrm{d}t+n_1(f) \end{aligned} \tag{7}$$

where, T is the coherent integration time, $n_1(f)$ is the expression of $n_1(t)$ in frequency domain.

The local NSCC replica can be expressed as,

$$C_L=\sum_{m=1}^{M}C_m(t)\cos\left(2\pi\left(\Delta f_m-\Delta f_1+\Delta\hat{f}_{d,m}-\Delta\hat{f}_{d,1}\right)t\right) \tag{8}$$

where, $\Delta\hat{f}_{d,m}$ is the estimated Doppler shift of the m-th subcarrier.

After the FFT and then conjugation operation, the expression can be showed as,

$$conj(fft(C_L))=conj\left(\int_T\sum_{m=1}^{M}C_m(t)\cos\left(2\pi\left(\Delta f_m-\Delta f_1+\Delta\hat{f}_{d,m}-\Delta\hat{f}_{d,1}\right)t\right)\cdot\mathrm{e}^{-j2\pi ft}\mathrm{d}t\right) \tag{9}$$

Then, multiple the Eqs. (8) and (9), the result can be shown as follows,

$$
\begin{aligned}
&S_{IF,3}(\tau,\Delta f_d) = S_{IF,2}(\tau,\Delta f_d)\cdot conj(fft(C_L))\\
&= \int_T \frac{1}{2}\sum_{m=1}^{M} A_m C_m(t-\tau)\mathrm{e}^{-j\left(2\pi\left(\Delta f_m-\Delta f_1+\Delta\hat{f}_{d,m}-\Delta\hat{f}_{d,1}\right)t-\varphi_{m,1}\right)}\cdot \mathrm{e}^{-j2\pi f(t-\tau)}\mathrm{d}(t-\tau)\\
&\quad\cdot\int_T \sum_{n=1}^{M} C_n(t)\cos\left(2\pi\left(\Delta f_n-\Delta f_1+\Delta\hat{f}_{d,n}-\Delta\hat{f}_{d,1}\right)t\right)\cdot \mathrm{e}^{j2\pi ft}\mathrm{d}t\\
&= \frac{1}{4}\cdot\left[\begin{array}{l}
\displaystyle\int_T\int_T \sum_{\substack{m=1\\ m=n}}^{M} A_m C_m(t-\tau)C_n(t)\mathrm{e}^{-j2\pi\left(\Delta f_{d,m}-\Delta\hat{f}_{d,n}\right)t}\cdot \mathrm{e}^{-j2\pi f(t-\tau)}\cdot \mathrm{e}^{j2\pi ft}\cdot \mathrm{e}^{j\varphi_{m,1}}\mathrm{d}(t-\tau)\mathrm{d}t\\
\quad+\displaystyle\int_T\int_T \sum_{\substack{m=1\\ n=1\\ m\neq n}}^{M} A_m C_m(t-\tau)C_n(t)\mathrm{e}^{-j2\pi\left(\Delta f_{d,m}-\Delta\hat{f}_{d,n}\right)t}\cdot \mathrm{e}^{-j2\pi f(t-\tau)}\cdot \mathrm{e}^{j2\pi ft}\cdot \mathrm{e}^{j\varphi_{m,1}}\mathrm{d}(t-\tau)\mathrm{d}t
\end{array}\right]\\
&= \frac{1}{4}\cdot\left[\begin{array}{l}
\displaystyle\int_T\int_T \sum_{\substack{m=1\\ m=n}}^{M} A_m C_m(t-\tau)C_n(t)\mathrm{e}^{-j2\pi\left(\Delta f_{d,m}-\Delta\hat{f}_{d,n}\right)t}\cdot \mathrm{e}^{j2\pi f\tau}\cdot \mathrm{e}^{j\varphi_{m,1}}\mathrm{d}t\mathrm{d}\tau\\
\quad+\displaystyle\int_T\int_T \sum_{\substack{m=1\\ n=1\\ m\neq n}}^{M} A_m C_m(t-\tau)C_n(t+\tau)\mathrm{e}^{-j2\pi\left(\Delta f_{d,m}-\Delta\hat{f}_{d,n}\right)t}\cdot \mathrm{e}^{j2\pi f\tau}\cdot \mathrm{e}^{j\varphi_{m,1}}\mathrm{d}t\mathrm{d}\tau
\end{array}\right]\\
&= \frac{1}{4}\cdot\left[\begin{array}{l}
\displaystyle\sum_{\substack{m=1\\ m=n}}^{M} A_m C_m^*(f)C_n(f)\cdot TSa\left(\pi\left(\Delta f_{d,m}-\Delta\hat{f}_{d,n}\right)T\right)\cdot \mathrm{e}^{j\varphi_{m,2}}\\
\quad+\displaystyle\sum_{\substack{m=1\\ n=1\\ m\neq n}}^{M} A_m C_m^*(f)C_n(f)\cdot TSa\left(\pi\left(\Delta f_{d,m}-\Delta\hat{f}_{d,n}\right)T\right)\cdot \mathrm{e}^{j\varphi_{m,2}}
\end{array}\right]
\end{aligned}
\tag{10}
$$

After IFFT algorithm, the expression can be given as,

$$
\begin{aligned}
&S_{IF,4}(\tau,\Delta f_d) = \int S_{IF,3}(\tau,\Delta f_d)\cdot e^{j2\pi ft}\mathrm{d}f\\
&= \frac{1}{4}\cdot\left[\begin{array}{l}
\displaystyle\sum_{\substack{m=1\\ m=n}}^{M} A_m C_m^*(f)C_n(f)\cdot TSa\left(\pi\left(\Delta f_{d,m}-\Delta\hat{f}_{d,n}\right)T\right)\cdot \mathrm{e}^{j\varphi_{m,2}}\\
\quad+\displaystyle\sum_{\substack{m=1\\ n=1\\ m\neq n}}^{M} A_m C_m^*(f)C_n(f)\cdot TSa\left(\pi\left(\Delta f_{d,m}-\Delta\hat{f}_{d,n}\right)T\right)\cdot \mathrm{e}^{j\varphi_{m,2}}
\end{array}\right]
\end{aligned}
\tag{11}
$$

Thus, the final decision random variable can be expressed as,

$$
R(\tau,\Delta f_d) = \left|S_{IF,4}(\tau,\Delta f_d)\right|^2 \tag{12}
$$

When the received NSCC signal is correctly aligned with the local NSCC replica aligns, there will be an obvious correlation peak in the two-dimensional search space. The correlation peak refers to a cell corresponding to the estimated code

delay and Doppler frequency shift. As shown in Eq. (11), the multichannel method realizes the energy accumulation NSCC subcarriers. The cross-correlation terms can be ignored according to cross-correlation property of C/A code. However, if NSCC adapts one C/A code to modulate its subcarriers for simplification, the cross-correlation terms will strengthen the background noise. The more the number of NSCC subcarriers, the higher the noise floor will be. There is a tradeoff between the number of subcarriers and algorithm performance.

3.3 Procedures of Multichannel Acquisition Method

In order to further investigate the multichannel method for NSCC acquisition application, the procedures are depicted in Fig. 4 and are expressed as follows:

- Step 1: Generate the C/A set of the desired NSCC signal, and then multiply the C/A set with subcarriers whose frequency intervals are allocated according to the desired NSCC, respectively.
- Step 2: Sum up the modulated subcarriers as the local NSCC replica.
- Step 3: Perform FFT to transform the local NSCC replica into frequency domain and then take its complex conjugate.
- Step 4: Mix the received NSCC signal with local carrier which contains the estimated Doppler frequency shift, and obtain the composite baseband signal.
- Step 5: Perform FFT to transform the composite baseband signal into frequency domain, then multiply it with the product of Step 3.
- Step 6: Perform IFFT to transform the product of Step 5 into time domain and take absolution.
- Step 7: Adjust the estimated Doppler frequency shift in Step 4, and re-execute Step 5-Step 6 to produce the correlation output for the other Doppler frequency shift bins until a complete two-dimensional search space is created.

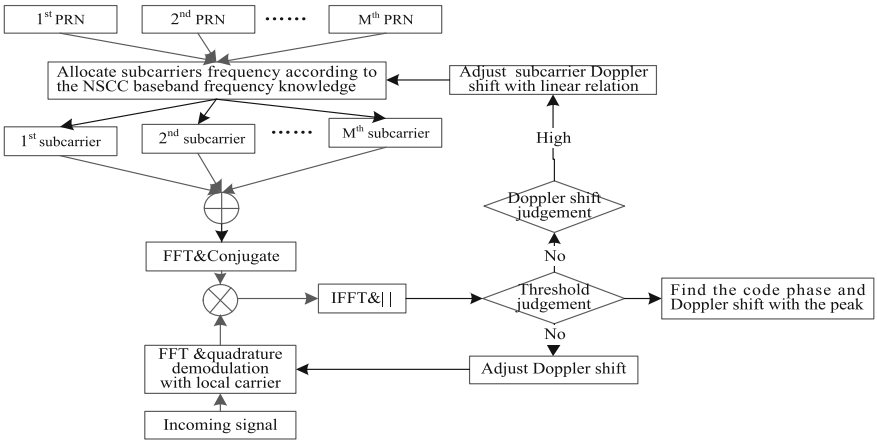

Fig. 4 The complete procedure of the multichannel acquisition method

– Step 8: Search the correlation peak with threshold judgment in the space created by Step 7, to obtain the code delay and Doppler shift of the peak.
– Step 9: If the detectible Doppler shift is very high, the code delay and Doppler shift of each NSCC subcarriers need compensate according to the linear relationship among subcarriers at Step 1, then, repeat the Step 2-Step 6 to verify the suspected peak.

3.4 Statistical Model

The residual code-phase offset and residual Doppler shift will result in the diminution of the peak. In order to estimate the diminution, the statistical model is analyzed.

The multichannel method conducts a search in the two-dimensional space, which is divided into cells according to the continuous time–frequency uncertainty region. We obtain the code phase and Doppler shift of the cell closest to the true peak. For each NSCC subcarriers, the power attenuation factors can be modeled by η_τ and η_d, as defined in Eqs. (13) and (14), respectively.

Assume that the residual code-phase offset is ε_τ and the residual Doppler shift is ε_d. The peak attenuation caused by ε_τ can be given as,

$$\eta_\tau = 20 \cdot \lg(1 - |\varepsilon_\tau / T_c|), \quad \varepsilon_\tau \in (-T_c, T_c) \tag{13}$$

The peak attenuation caused by ε_d can be given as [23],

$$\eta_d = 20 \cdot \lg\left(\left|\frac{\sin(\pi \cdot \varepsilon_d \cdot N \cdot T_c)}{N \cdot \sin(\pi \cdot \varepsilon_d \cdot T_c)}\right|\right), \quad \varepsilon_\tau \in (-T_c, T_c) \tag{14}$$

where, T_c is the symbol duration of the PRNs code. The corresponding plots are illustrated in Fig. 5.

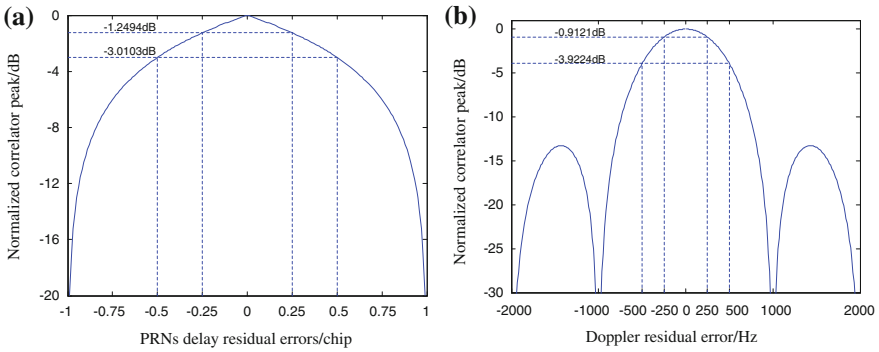

Fig. 5 The impact of code delay and Doppler shift to correlation peak. **a** The impact of code delay to correlation peak. **b** The impact of Doppler shift to correlation peak

As is shown is Fig. 5, the diminution of the peak is 1.25 dB with 0.25 chip residual code-phase offset, and 3.01 dB with 0.5 chip residual code-phase offset. The diminution of the peak is approximately 0.91 dB with $1/(2 \cdot N \cdot T_c)$ residual Doppler shift, and 3.92 dB with $1/(N \cdot T_c)$ residual Doppler shift.

The acquisition is a combined detection/estimation problem. The estimated problem is considered in the above analysis, then, we investigate the process in the view of detection.

The principle of signal detection is based on the binary hypothesis test. The null hypothesis denoted H_0, is verified when the NSCC signal is absent or incorrectly aligned with the local replica. The decision random variables lead to a central χ^2 distribution with two degree of freedom. Thus, the probability density function (PDF) under H_0 is given by [24],

$$p(z|H_0) = \frac{1}{2\sigma^2}\exp\left(-\frac{z}{2\sigma^2}\right), \quad z \geq 0 \tag{15}$$

The alternative hypothesis denoted H_1, implies perfect code and Doppler shift alignment of the NSCC signal and the local replica. The decision random variables lead to a noncentral χ^2 distribution with two degree of freedom. Thus, the PDF under H_1 is given by [25],

$$p(z|H_1) = \frac{1}{2\sigma^2}\exp\left[-\left(\frac{z+\lambda}{2\sigma^2}\right)\right] I_0\left(\frac{\sqrt{z\lambda}}{\sigma^2}\right), \quad z \geq 0 \tag{16}$$

where, λ refers to the signal power terms in the Eq. (11), σ^2 refers to the noise power terms and the cross-correlation terms in the Eq. (11), $I_v(\cdot)$ is the v^{th} order modified Bessel function of the first kind defined by [26],

$$I_v(x) = \sum_{k=0}^{\infty} \frac{\left(\frac{x}{2}\right)^{v+2k}}{k!\Gamma(k+v+1)} \tag{17}$$

Where $\Gamma(\cdot)$ is the gamma function, defined by,

$$\Gamma(x) = \int_0^{\infty} \mathrm{e}^{-t} t^{x-1} \mathrm{d}t \tag{18}$$

According to the Eqs. (15) and (16), if the decision valuables exceed a pre-assigned threshold β, the single-trial cell false alarm probability is expressed as,

$$P_{fa} = \int_{\beta}^{+\infty} p(z|H_0)\mathrm{d}z = \exp\left(-\frac{\beta}{2\sigma^2}\right) \tag{19}$$

The cell decision probability is expressed as,

$$P_d = \int_{\beta}^{+\infty} p(z|H_1)\mathrm{d}v = Q_1\left(\sqrt{\frac{\lambda}{\sigma^2}}, \sqrt{\frac{\beta}{\sigma^2}}\right) \tag{20}$$

where, $Q_1(a, b)$ is the first order generalized Marcum Q-function. For simplification, The figure corresponding to Eqs. (19) and (20) will be given in the next section combined with detection performance simulation.

4 Simulation

The mathematic model and statistical model of the multichannel method were analyzed in the previous sections. Note that, the cross-product terms caused by ICI, in some extent, will degrade the efficiency and performance of the MCM method. In this section, the comparative simulations were conducted to validate and evaluate the proposed method. The impact, caused by the cross-correlation terms in Eq. (11), will be evaluated quantitatively with constant false alarm rate (CFAR).

4.1 The Validity of the Multichannel Method

The search spaces are created by the multichannel method for NSCCs are showed in Fig. 6. In order to observe the apparent peak, the high carrier-to-noise ratio (C/N_0) was selected. For all simulations the parameters are showed in Table 1.

As illustrated in Fig. 6, the search spaces created by the proposed method for NSCC with 5 subcarriers and the conventional acquisition for C/A code both

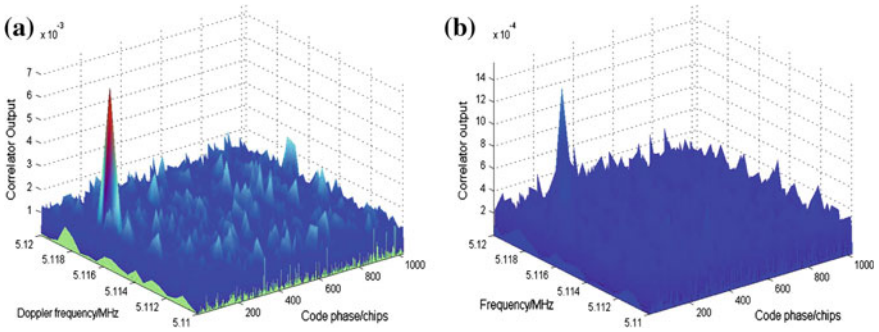

Fig. 6 The search space comparison between C/A and NSCC. **a** The search space created by multichannel method for NSCC. **b** The search space created by conventional method for C/A

Table 1 The simulation parameters

Parameter	Value
C/N_0	45 dB/Hz
Number of subcarriers M	4, 5, 6, 7
Sampling frequency	30.325 MHz
Pre-detection integration time	1 ms
Subcarrier interval	2.046 MHz
Code frequency	1.023 MHz
Doppler shift	1500 Hz
Code phase	70 chip
PRN code set	PRN 1

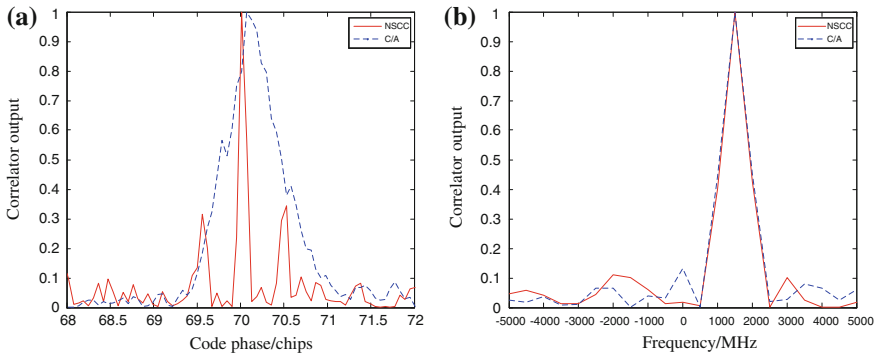

Fig. 7 The peak attenuation caused by code delay and Doppler shift. **a** The peak attenuation caused by code delay. **b** The peak attenuation caused by Doppler shift

present an obvious correlation peak. The detailed profiles of the both peaks are shown in the Fig. 7. The code phase and Doppler shift of the peak align with the true value, implying that the two acquisition methods both acquire the desired signal. Note that, the search space created by the proposed method for NSCC is noisier than that of the traditional method for C/A. This is because the NSCC adopts the same PRNs code with equal code delay, thus, there is no code orthogonality among its subcarriers. This kind of configuration brings in cross-correlation terms, which raises the noise floor. Furthermore, the Fig. 7 shows that the NSCC presents superior tracking performance with narrower autocorrelation function (ACF) profile due to the inclusion of frequency information in the NSCC baseband.

Figure 8 shows the search space created by the proposed method for NSCCs without code orthogonality to illustration the impact of cross-correlation terms. Obviously, as the number of NSCC subcarriers increase, the search space becomes nosier. The reason is that more number of subcarriers will bring in more cross-correlation terms.

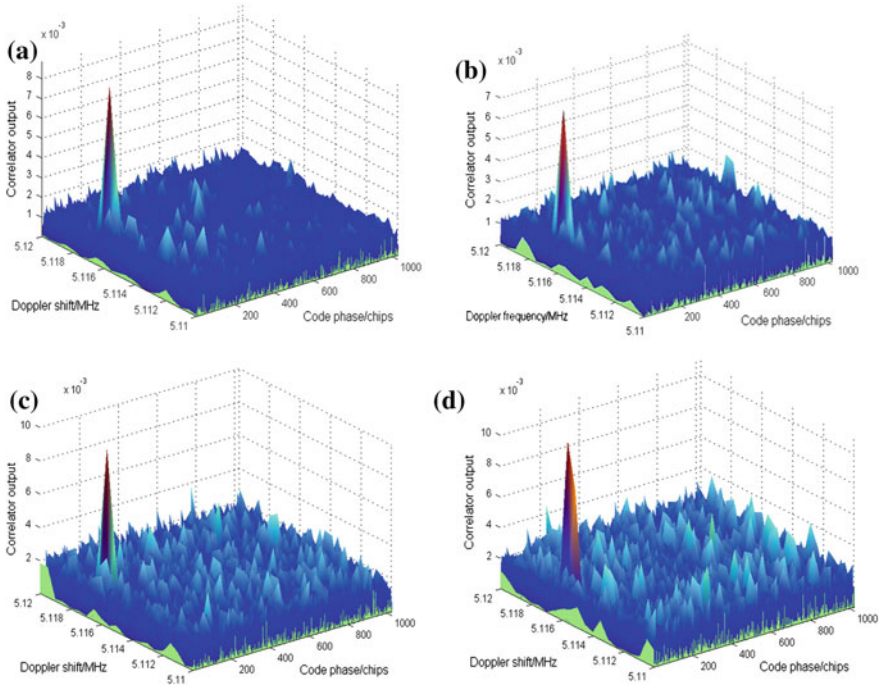

Fig. 8 The search space created by the proposed method for NSCCs. **a** The search space for NSCC(4). **b** The search space for NSCC(5). **c** The search space for NSCC(6). **d** The search space for NSCC(7)

4.2 The Performance of the Multichannel Method

The CFAR approach is very useful for evaluating the performance of acquisition method. In this section, particular signal-to-noise rate (SNR) and detection probabilities for the NSCCs with different number of subcarriers were evaluated by the means of Monte Carlo simulations under CFAR. Its ICI impact is quantified with the comparative analysis, and an optimization with adjusting the NSCC subcarriers PRNs configuration is verified.

The additional simulation parameters are listed in the Table 2. The threshold can be obtained according to Eq. (19).

Table 2 Additional simulation parameters

Parameter	Value
CFAR	10^{-3}
Number of Monte Carlo	10,000
PRNs delay of adjacent subcarrier	70 chip
PRN code set	PRN 1,2,3,4,5,6,7

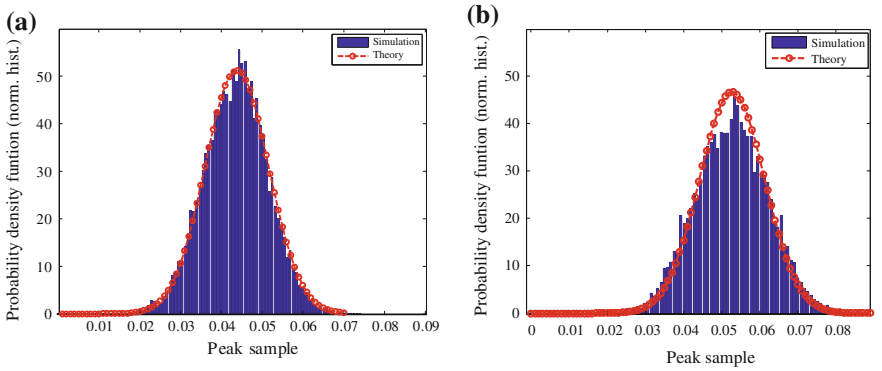

Fig. 9 The comparison of probability density function of NSCCs without code orthogonality. **a** NSCC with 4 subcarriers. **b** NSCC with 6 subcarriers

Figure 9 presents the probability density functions and histograms of NSCCs without code orthogonality. The signal to noise ratio is set as high as −30 dB for clear observation. As can be seen from Fig. 9a, for the NSCC with 4 subcarriers, the theoretical PDF curve and the histogram based on the Mont Carlo simulated peak data, are almost matched. The fact validates the theoretical analysis with the assumption of the statistical model. However, as the NSCC subcarriers increase, the histogram deviates from the theoretical PDF curve, as shown in Fig. 9b. The ICI caused by the cross-correlation terms affect the PDF and lead to the deviation.

Figure 10 shows the detection performance for NSCCs without code orthogonality. The simulation curves diverge from the red line denoting the theoretical data. The detection performance degrades slightly as the number of the NSCC subcarriers increases. This result agrees with the previous studies that the number of the cross-correlation terms grows with the number of the NSCC subcarriers. The more the cross-correlation terms grow in number, the stronger the background noise becomes. Therefore, in order to get the optimization of the separation among the

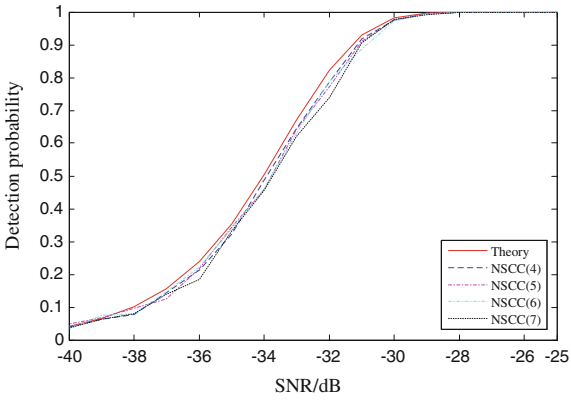

Fig. 10 Comparison of detection performance for NSCCs without code orthogonality

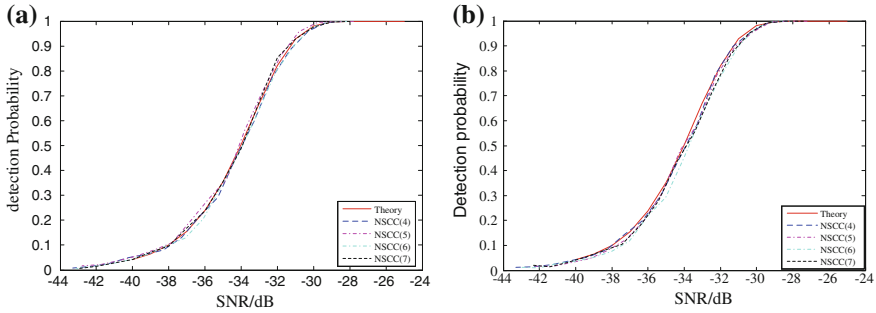

Fig. 11 Comparison of detection performance for NSCCs with code orthogonality. **a** Different PRNs modulate subcarriers. **b** Different code phase modulated subcarriers

subcarriers for detection, a judicious choice of parameters, especially about the PRNs, is needed.

In order to suppress the ICI, the separation among the subcarriers needs to be strengthened. That is, the different PRNs or same PRN with different code phases modulates the NSCC subcarriers. This measure, in fact, utilizes the code orthogonality to eliminate the ICI. The corresponding simulation was conducted to validate the code separation.

As illustrated in the Fig. 11, the simulation curves nearly overlap with the theoretical curve (red line). The detection performance does not deteriorate as the number of the NSCC subcarriers increases, which highlights the validity of the code orthogonality.

5 Conclusion

The NSCC modulation, as the potential future signal modulation scheme for integration of navigation and communication, has drawbacks in acquisition algorithm design due to its MC nature. The multichannel acquisition method is proposed to implement the acquisition of the NSCC signal with low computation load and restricted hardware. The method employs the MC signal as the NSCC replica and installs it by exploiting the mutually orthogonality among subcarriers, which achieve the accumulation of NSCC subcarriers power, and finally realizes the NSCC subcarriers acquisition synchronously. The proposed method is easy to implement with slight modification of FFT-based correlator method.

The acquisition performance is affected by the number of subcarriers of the desired NSCC without code orthogonality. Therefore, the consideration for the tradeoff between the number of the NSCC subcarriers and acquisition performance is needed. The optimization of the NSCC configuration will mitigate the ICI and thus improve acquisition performance.

The researches on the NSCC acquisition provide advisable proposal and theoretical basis for further signal modulation scheme research.

Acknowledgments This work was supported by the National Natural Science Foundation of China (Grant No. 61102130), the National Science and Technology Major Project (Grant No. 2016ZX03001022-005) and the National High Technology Research and Development Program ("863" Program) of China (Grant No. 2015AA124101 and Grant No. 2015AA124002).

References

1. Hofmann-Wellenhof B, Lichtenegger H, Wasle E (2007) GNSS–global navigation satellite systems: GPS, GLONASS, Galileo, and more. Springer Science & Business Media, Heidelberg
2. Tang Z, Zhou H, Hu X et al (2010) Performance evaluation research of compass navigation signal. Sci China Ser G 5:592–602
3. Ai GX, Shi HL, Wu HT et al (2008) A positioning system based on communication satellites and the Chinese Area Positioning System (CAPS). Chin J Astron Astrophys 8(6):611–630
4. Garcia-Pena A, Julien O, Macabiau C et al (2012) FMT signal options and associated receiver architectures for GNSS. In: Position location and navigation symposium (PLANS), 2012 IEEE/ION, pp 898–912
5. Emmanuele A, Luise M, Won JH et al (2011) Evaluation of filtered multitone (FMT) technology for future satellite navigation use. In: Proceedings of the 24th international technical meeting of the satellite division of the institute of navigation (ION GNSS 2011), pp 3743–3755
6. Dai L, Wang Z, Wang J et al (2010) Positioning with OFDM signals for the next-generation GNSS. IEEE Trans Consum Electron 56(2):374–379
7. Liu X, Liang M, Morton Y et al (2014) Performance evaluation of MSK and OFDM modulations for future GNSS signals. GPS Solutions 18(2):163–175
8. Zhongliang D, Yanpei Y, Xie Y et al (2013) Situation and development tendency of indoor positioning. Commun China 10(3):42–55
9. Betz JW (2013) Signal structures for satellite-based navigation: past, present, and future. In: Proceedings of ION-Pacific PNT-2013, Institute of Navigation, Honolulu, pp 131–137
10. Xu Y, Yuan H (2011) Navigation signal structure based on complex carrier modulation. Sci China Phys Mech Astron 54(6):1035–1045
11. Luo R, Xu Y, Yuan H (2015) A joint acquisition method for navigation signal based on compound carrier with CAFR. Acta Aeronautica et Astronautica Sinica 36(7):2381–2391 (in Chinese)
12. Luo R, Xu Y, Yuan H (2015) Acquisition for navigation signal with complex carrier modulation based on co-herent superposition. J Astronnautics 36(8):961–968 (in Chinese)
13. Spangenberg SM, Scott I, McLaughlin S et al (2000) An FFT-based approach for fast acquisition in spread spectrum communication systems. Wirel Pers Commun 13(1–2):27–55
14. Molino A, Girau G, Nicola M et al (2008) Evaluation of a FFT-based acquisition in real time hardware and software GNSS receivers. In: Proceedings of the 10th international symposium on spread spectrum techniques and applications. Bologna, Italy, pp 25–28
15. Borio D, O'Driscoll C, Lachapelle G (2010) Composite GNSS signal acquisition over multiple code periods. IEEE Trans Aerosp Electron Syst 46(1):193–206
16. Closas P, Fernandez-Prades C, Fernandez-Rubio JA (2009) Cramer-Rao bound analysis of positioning approaches in the GNSS receivers. IEEE Trans Signal Process 57(10):3775–3786
17. Closas P, Fernandez-Prades C, Fernandez-Rubio JA (2007) Maximum likelihood estimation of position in GNSS. IEEE Signal Process Lett 14(5):359–362

18. Axelrad P, Bradley BK (2012) Collective detection and direct positioning using multiple GNSS satellites. Navig J Inst Navig 58(4):305–321
19. Tong HB, Zhu XW, Zhang GZ et al (2013) Detection performance analysis of joint acquisition for multi-satellite signals. J Electron Inf Technol 36(5):1069–1074 (in Chinese)
20. Beach MA (1990) A novel acquisition technique for NAVSTAR GPS. In: Fifth international conference on radio receivers and associated systems, IET, pp 177–181
21. Hsu LT, Sun CC, Jan SS (2008) Performance analysis of composite PRN code acquisition methods for GNSS signal. In: Proceedings of international symposium on GPS/GNSS 2008, vol 2. Tokyo, Japan
22. Jan SS, Lin YC (2009) A new multi-C/A code acquisition method for GPS. GPS Solutions 13 (4):293–303
23. Ta TH, Pini M, Presti L (2014) Combined GPS L1C/A and L2C signal acquisition architectures leveraging differential combination. IEEE Trans Aerosp Electron Syst 50 (4):3212–3229
24. Omura JK (1994) Spread spectrum communications handbook. McGraw-Hill, New York
25. Sourour EA, Gupta SC (1990) Direct-sequence spread-spectrum parallel acquisition in a fading mobile channel. IEEE Trans Commun 38(7):992–998
26. O'Mahony NM (2010) Variable dwell time verification strategies for CDMA acquisition with application to GPS signals. Department of Electrical and Electronic Engineering, National University of Ireland

Cycle Duty Design of Pulse Navigation Signal

Maoshu Zeng, Zhili He and Ying Xu

Abstract Pulse navigation signal is usually utilized to carry navigation information instead of continuous signal by pseudolite navigation systems such as LOCATA, whose carrier tracking methods commonly use traditional continuous signal systems'. For pulse signals, traditional carrier tracking models are deficient of parameter of cycle duty. Moreover, pulse positioning navigation (PPN) signal's cycle duty tends to be selected simply in consideration of near-far effect's interferences other than tracking performances. Besides, current coherent integration model ignores impact of high-ordered input signal in its analysis. Aimed at those problems, high-ordered model of coherent integration is built on basis of which cycle duty is introduced in the model to research its tracking performances. Finally, designs of optimal loop characteristic frequency and corresponding optimal cycle duty are derived according to the proposed model followed with simulations. The simulations show the error caused by optimal loop characteristic frequency is the smallest, and so it is with the optimal cycle duty, which verifies the model.

Keywords Pulse navigation · Signal · LOCATA · Cycle duty · Coherent · Integration

1 Introduction

Current pseudolite navigation systems usually use the periodic pulse navigation (PPN) signal rather than continuous signals. LOCATA system, for instance, employs time-division structure, which is equivalent to changing signal's cycle duty, meaning to avoid near-far effects between pseudolite bases [1–3]. Such pseudolite systems have stronger signal power [4], allowing them to realize indoor–outdoor seamless positioning

M. Zeng (✉)
University of Chinese Academy of Sciences, 100086 Beijing, China
e-mail: zengmaoshu@aoe.ac.cn

M. Zeng · Z. He · Y. Xu
Academy of Opto-Electronics, Chinese Academy of Sciences, 100086 Beijing, China

J. Sun et al. (eds.), *China Satellite Navigation Conference (CSNC) 2016 Proceedings: Volume II*, Lecture Notes in Electrical Engineering 389,
DOI 10.1007/978-981-10-0937-2_54

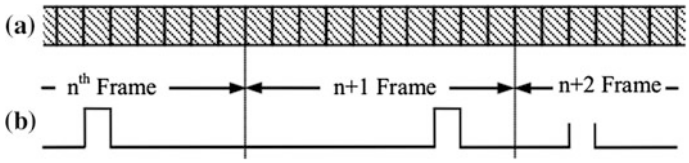

Fig. 1 LOCATA signal. **a** Each frame's structure. **b** Pseudolite pulse signal

[5–7]. Similarly ranged by pseudo-range and carrier phase, LOCATA's ranging methods are the same with GNSS's. The detailed signal structure is shown in Fig. 1 [8]. Each frame is 1 ms long and contains 10 slots of 0.1 ms duration each (in the receiver, once certain slot's coherent value is void, its value is abandoned.), with every frame carries one slot of pseudo-random (PN) code (code period is 200 frames).

One of the key GNSS receiver techniques, carrier tracking loops, which are often phase-lock loops (PLL), plays role of ensuring precise tracking of the received carrier signal. For the continuous signal, once acquired by the receiver, it can be accurately synchronized by the tracking loop. Literature [9] researches pulse signals' acquisition and tracking, and introduces pulse signals' advantages comparing to continuous signals. Literature [10] introduces tracking loop structure of the continuous signal. Literature [1] illustrates pulse signals can also be tracked by continuous signal tracking methods. Literature [11, 12] further formulates PLL design of pulse signal receiver. Though high-ordered inputs are critical dynamics, it is overlooked by most literature in coherent integration and phase discrimination (PD) analysis. And literature [3, 13] shows pulse cycle duty is selected in account of interferences caused by near-far effects other than tracking precision.

Aimed at abovementioned problems, a high-ordered model is built to analyze the relation between cycle duty and coherent integration, followed by discussions of influences of different GNSS signal cycle duties on receivers' tracking performances. Then an optimal loop characteristic frequency and an optimal cycle duty under such conditions are derived with simulation verifications.

2 Common Coherent Integration Model Analyses

After PN codes are striped by correlation, for better synchronization, carrier is sent to the carrier tracking loop, or PLL.

$$\begin{aligned} I_P(n) &= \frac{1}{T_{\text{coh}}} \int_{t_1}^{t_1+T_{\text{coh}}} i_p(t)\mathrm{d}t \approx a\ \sin c(f_e T_{\text{coh}}) \cos\left[\omega_e(t_1 + \frac{T_{\text{coh}}}{2})\right] \\ Q_P(n) &= a\ \sin c(f_e T_{\text{coh}}) \sin\left[\omega_e(t_1 + \frac{T_{\text{coh}}}{2})\right] \end{aligned} \tag{1}$$

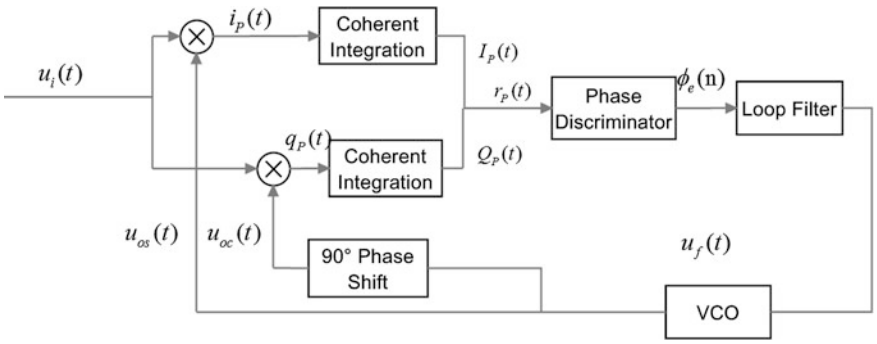

Fig. 2 Common GNSS receiver PLL structure

The math models of common coherent integration are shown as Eq. (1) [14]. Here, $\omega_e = \omega_i - \omega_o$. And common PLL structure is shown in Fig. 2 [14, 15].

Taking in-phase branch for instance, since there must be a high-frequency component in $i_p(t)$, implied by Eq. (1), a low-pass filter is inevitably required. In GNSS receivers, coherent integration acts as the low-pass filter with an extra function of improving signal-to-noise ratio (SNR). In addition, known from Eq. (1), coherent integration values depend not only on integration duration but also on signal duration.

Thus, PD result is shown as follows [14]:

$$r_P(n) = I_p(n) + jQ_p(n) = A_P(n)e^{j\phi_P(n)} \tag{2}$$

$$A_P(n) = a \sin c(f_e T_{\text{coh}}) \tag{3}$$

$$\phi_P(n) = 2\pi f_e \left(t_1 + \frac{T_{\text{coh}}}{2} \right) \tag{4}$$

Equation (3) is the vector amplitude. Equation (4) is the discriminated phase, or the phase difference. Observing Eq. (4), PD results of the coherent integration are just averages of inputs' phase offsets in integration duration.

3 High-Ordered Coherent Integration Model of PPN Signal

As Eq. (1) model is limited to the 1st-ordered component $\omega_e t$ instead of high-ordered component in reality, it may not equal the real discriminated value. Moreover, for periodic pulse signals, the cycle duty is a decisive factor to coherent integration duration. Obviously the formula does not include such variable.

3.1 PPN Signal Model

Based on LOCATA signal model, a new signal model, called periodic pulse navigation (PPN) signal model, is proposed by letting time slot fixed. Spaced by pulse repetition period ΔT with certain cycle duty, the PPN signal is denoted as Eq. (5).

$$u(t) = \sum_{i=0}^{\infty} \delta(t - i\Delta T) * \sum_{n=0}^{N-1} a_n P\left(\frac{t}{T_0} - n\right) \cos(\omega_i t) \tag{5}$$

Here, $P(t)$ denotes rectangular function, representing each bit. a_n is amplitude of each bit, valued by ± 1 arbitrarily. ω_i is carrier frequency. T_0 is the duration of code chip. ΔT is the period of each pulse. N is the number of chips in every pulse.

Let Ω be the cycle duty, T_{coh} be the pulse duration or integration duration, the expression about the cycle duty can be derived as Eq. (6).

$$\text{NT}_0 = T_{\text{coh}} = \Omega \times \Delta T. \tag{6}$$

3.2 High-Ordered Coherent Integration Model

Equation (7) represents the high-ordered input or input phase.

$$\theta_i(t) = \Delta\omega_N \times t^N + \Delta\omega_{N-1} \times t^{N-1} + \cdots + \Delta\omega_1 \times t + \theta_{\text{const}} \tag{7}$$

$\Delta\omega_N$ is the Nth-ordered dynamics coefficient, $\theta_i(t)$ is the Nth-ordered input.

As mentioned in the last chapter, the PD result of the 1st-ordered input is just the average of all input phase offsets in duration of integration, which enlightens us that since coherent integration can be regarded as inner product of all frequency components in the integration duration T_{coh}, the discriminated amplitudes and phases should be the mean correlation offsets and the mean phase offsets, respectively.

Accordingly, for higher-ordered inputs, it can be educed that the discriminated phase should also be the mean phase offset, for the underlying fact that the coherent integration result is still an inner product. Using numerical analysis verification, discriminated results indicate the theory holds in case of inputs with 2nd, 3rd, 4th and 5th order. Besides, results manifest components with different orders are independent. Without loss of generality, it can be elicited that PD result of coherent integration must be sums of mean phase offsets of input with different orders in duration of integration, and each order's result is independent, which can be expressed as Eq. (8), the model with higher-ordered input.

$$\phi_e(t_{\text{coh}}) = F_{\text{dis}}(\theta_i(t_{\text{coh}}))|_{t_{\text{coh}}=T_{\text{coh}}} = \frac{\Delta\omega_N \times T_{\text{coh}}^N}{N+1} + \cdots + \frac{\Delta\omega_1 \times T_{\text{coh}}}{2} + \theta_{\text{const}}. \tag{8}$$

3.3 Introduction of Cycle Duty

When the input's order is less than the GNSS receiver PLL's order, it can be accurately tracked. When they are equal, there will be a stable error. When the input's order is higher, PLL will finally lose lock. Therefore, to assess system performance, more emphasized is the order equal to PLL's, or stable error, as it will give rise to positioning errors if tracked.

For convenience, the following researches are carried out based on the example that a 2nd-ordered tracking loop (3rd-ordered PLL) tracks a 3rd-ordered PPN input signal (ramping frequency signal).

Phase θ_i of a ramping frequency signal in a single pulse period is denoted as Eq. (9). In the formula, ΔT is the pulse period.

$$\theta_i(t) = \Delta\omega t^3 * \delta(t - n\Delta T) * P\left(\frac{t}{T_{\text{coh}}}\right) (n \text{ is an arbitrary integer}) \tag{9}$$

For Eq. (8), the variable is Eq. (10). Here, the time constant t_1 represents the initial moment, and the time variable t_{coh} represents the integrand. Since pulse repetition rate is much slower than carrier frequency, though Doppler Effect causes deformation, for T_{coh}, the effect is minimal. Therefore T_{coh} is taken as a constant.

$$\theta_i(t_{\text{coh}}) = \Delta\omega(t_1 + t_{\text{coh}})^2 \tag{10}$$

Substituting Eqs. (10) and (6) into Eq. (8), Eq. (11) is derived.

$$\begin{aligned} \theta_{\text{dis}} &= F_{\text{dis}}(\Delta\omega t_1^2 + 2\Delta\omega t_1 t_{\text{coh}} + \Delta\omega t_{\text{coh}}^2)\big|_{t_{\text{coh}}=T_{\text{coh}}} \\ &= \Delta\omega t_1^2 + \Omega\Delta\omega t_1 \Delta T + \Omega^2 \frac{\Delta\omega \Delta T^2}{3} \end{aligned} \tag{11}$$

Thus, the formula turns to a function about the cycle duty. Replacing initial moment t_1 with sampled time variable $t_n = t_1 + n \cdot \Delta T$, Eq. (11) becomes Eq. (12).

$$\theta_{\text{dis}} = \Delta\omega\left(t_n + \frac{\Omega\Delta T}{2}\right)^2 + \Omega^2 \frac{\Delta\omega\Delta T^2}{12} \tag{12}$$

The ideal discriminated result should be sampled input phase sequence equally spaced by pulse repetition period ΔT as Eq. (13).

$$\theta_{\text{dis}} = \Delta\omega\left(t_n + \frac{\Omega\Delta T}{2}\right)^2 \tag{13}$$

Observing Eqs. (12) and (13), for a ramping frequency signal, discriminated result of coherent integration can be thought as sum of an ideal discriminated result and a constant. For the higher-ordered input signals the conclusion remains similar that due to coherent integration's 'average', the result is a sum of a sampled input phase sequence and an 'attached' lower-ordered input phase, defined as 'attached input phase'.

$$\Delta\theta_{\text{dis}} = \theta_{\text{dis}} - \theta_{\text{dis}}^{\text{theory}} = \Omega^2 \frac{\Delta\omega \Delta T^2}{12} \tag{14}$$

In this case, attached input phase is denoted by Eq. (14), which is a cycle duty relevant amount, for the larger cycle duty, the farther its value deviates from ideal value.

4 Optimal Loop Characteristic Frequency and Optimal Cycle Duty

4.1 Effects on System Response

As a new variable to system, attached input phase's effect on system performance is discussed below.

1. Effect on system's filter performance.

According to Eq. (3), filter performance of coherent integration can be approximated by Eq. (15).

$$\sigma_{\text{filter}}|_{\max} = \frac{\left|\sin(f_{\text{high}} T_{\text{coh}})\right|\big|_{\max}}{2 f_{\text{IF}} T_{\text{coh}}} \frac{f_e T_{\text{coh}}}{\sin c(f_e T_{\text{coh}})} \approx \frac{1}{2\Omega f_{\text{IF}} \Delta T} \tag{15}$$

$f_{\text{high}} = 2f_{\text{IF}} + f_e \approx 2f_{\text{IF}}$ represents high-frequency component. Due to stochastic property of $f_{\text{high}} T_{\text{coh}}$, only the envelope is considered. Since $f_{\text{IF}} \Delta T \gg 1$, for $0.05 < \Omega < 0.5$, filter performance degradation normally can be overlooked.

2. Effects on system thermal noise

For a 2nd-ordered loop, the thermal noise is evaluated by Eq. (16) [14].

In the case, for $0.05 < \Omega < 0.5$, the thermal noise $\sigma_{t\text{PLL}}$ is bounded within $(2\sigma_{t\text{PLL0}} \sim 1.1\sigma_{t\text{PLL0}})$, where $\sigma_{t\text{PLL0}}$ is the thermal noise when $\Omega = 1$.

$$\sigma_{t\text{PLL}} = \frac{180^\circ}{\pi} \sqrt{\frac{B_L}{C/N_0} \left(1 + \frac{1}{2\Omega \Delta \text{TC}/N_0}\right)} \tag{16}$$

3. Effect on transient error response

A loop response in s domain is denoted by Eq. (17).

$$\theta_e(s) = \theta_i(s)H_e(s) \tag{17}$$

Evidently error response is proportional to input, which indicates transient response is also proportional to the input. Hence longer coherent integration results in larger attached input phase, which inevitably magnifies transient response, that is, without considering other variables, the larger the cycle duty is, the larger the loop response will be, and the more likely the loop tends to lose lock.

4. Effect on stable error response

As mentioned before, the lower-ordered input signal can be tracked without stable error. Lower-ordered signal as the attached input phase is, it still affects stable error, given that it is after all an extra amount that itself becomes an intrinsic error brought in by coherent integration.

The stable error is denoted as Eq. (18) [14]. Here, ω_n means the characteristic frequency. In this example, the value is Eq. (19).

$$\theta_e = \frac{1}{\omega_n}\frac{\mathrm{d}^N R}{\mathrm{d}t^N} \tag{18}$$

$$\theta_e = \frac{\Delta\omega\Delta T^2}{\omega_n^2} \tag{19}$$

To express loop error clearly, the real discriminated phase error is further defined as 'total discriminated error phase', denoted by $\theta_{\text{total\_dis\_error}}$, shown in Eq. (20), which is the absolute value of loop stable error resulting from tracking equal-ordered input minus error brought in by coherent integration, namely, the attached input phase.

$$\theta_{\text{total\_dis\_error}} = |\Delta\theta_{\text{dis}} - \theta_e| \tag{20}$$

In conclusion, cycle duty of PPN signal affects both transient and stable responses. If cycle duty becomes larger, filter performance improves while thermal noise mitigates, at cost of tougher transient response and possible larger total discriminated error.

4.2 Selection of Optimal Characteristic Frequency

GNSS receivers mainly focus on the total phase error which causes positioning errors. As shown in Eq. (20), total discriminated error is a cycle duty dependent variable. Then it is possible to select certain value to minimize the total error.

Combining Eqs. (14) and (19), the total discriminated error can be derived as Eq. (21).

$$\theta_{\text{final\_error}} = \left|\Delta\omega\left(\frac{T_{\text{coh}}^2}{12} - \frac{\Delta T^2}{\omega_n^2}\right)\right| = \left|\Delta\omega\Delta T^2\left(\frac{\Omega^2}{12} - \frac{1}{\omega_n^2}\right)\right| \tag{21}$$

If the cycle duty Ω is assumed fixed, obviously, when $\omega_n\Omega > 2\sqrt{3}$, as ω_n becomes larger, the error becomes larger; when $\omega_n\Omega < 2\sqrt{3}$, as ω_n becomes larger, the error turns otherwise; when $\omega_n\Omega = 2\sqrt{3}$, the error is cancelled out. Based on such law, the error can be adjusted by characteristic frequency ω_n. And for certain value of cycle duty, once Eq. (22) holds, the optimal 2nd-ordered characteristic frequency under minimum error is found.

$$\omega_n = \frac{2\sqrt{3}}{\Omega}. \tag{22}$$

5 Simulations and Analyses

For a 2nd-ordered loop, let $\Omega = 0.1$, $\Delta T = 1$ ms, $\Delta T = 1$ ms, carrier-to-noise ratio (C/N) be 50 dBHz. By calculation, $\omega_n \approx 34$ according to Eq. (22), and $\omega_n \approx 30$ according to the traditional selection method (e.g. [10]). The simulation starts from 400 ms with 30 Hz/s^2 ramping dynamics. The results are shown in Fig. 3.

Through comparison of both methods, it is concluded that when $\omega_n \approx 34$, the error σ_e is roughly 0.17, when $\omega_n \approx 30$, the error σ_e is about 0.23, which indicates the proposed characteristic frequency is better.

Let $\Delta T = 1ms$, C/N equal 50 dBHz, and noise bandwidth be 15 Hz. Then via an empirical function $B_L = 0.53\omega_n$, it is calculated that $\omega_n \approx 34$. Based on Eq. (22), it is calculated that $\Omega \approx 0.1$. Likewise, triggered from 400 ms with 30 Hz/s^2 ramping dynamics, the results of different cycle duty are shown in Fig. 4.

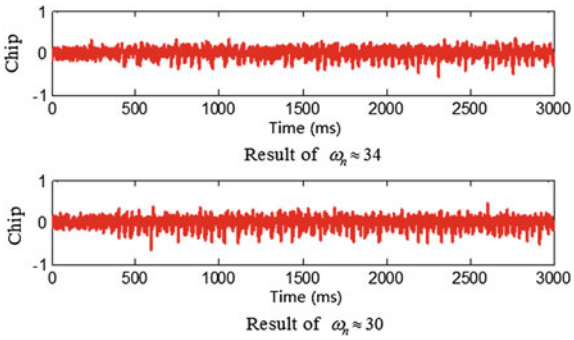

Fig. 3 Comparison of results of the two different methods

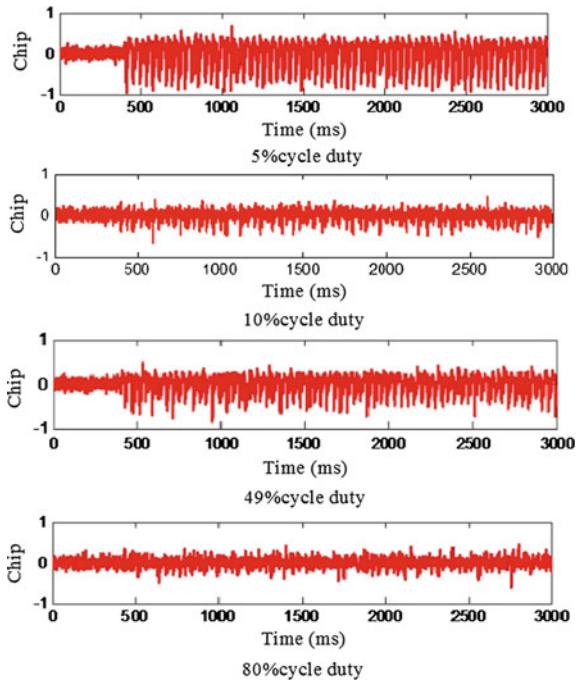

Fig. 4 Tracking results under different cycle duty

Observing Fig. 4, it is easy to find that as cycle duty approaches from 0.05 to 0.1, the optimal value, the error diminishes to the minimum, meaning that the stable error has been roughly cancelled out by the attached error. When cycle duty continues rising, to 0.49 in the case, the result certainly aggravates, which indicates the error suffers from the total discriminated error more severely. But finally when cycle duty ceases rising at 0.8, the error becomes small again due to enormous filter performance and thermal noise performance improvement.

As shown in Fig. 5, when cycle duty $\Omega = 0.1$, if SNR varies within range of ± 10 dB, the loop does not lose lock, which illustrates its viability.

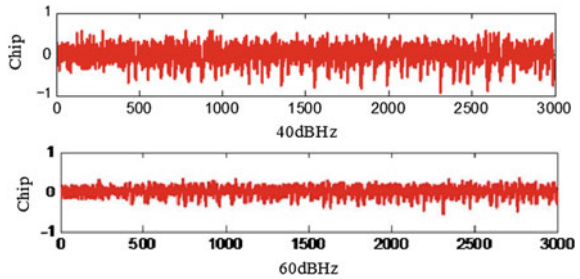

Fig. 5 Tracking results under different C/N

6 Conclusions

For the periodic pulse navigation signal tracking, traditional analyses lack high-ordered coherent integration model and performance-based cycle duty selection method. Thus, a high-ordered coherent integration discriminating model about cycle duty is proposed. The model shows coherent integration introduces some attached lower-ordered input signals by integration's 'averaging', and the cycle duty underlies in the model. Because the attached signal affects the final error by the analysis, therefore, via choosing the optimal characteristic frequency by the proposed method, the loop stable error can be compensated. Similarly through the model, the optimal cycle duty is derived. Finally, simulations are carried out, which shows verification of the proposed method.

References

1. Wu L (2015) Research and simulations of LOCATA signal acquisition mechanism. Sci Technol Vis 15:84–85+104
2. Wei Y (2013) LOCATA—a new positioning constellation. Mod Navig 06:461–465
3. Barnes J, Rizos C, Wang J et al (2003) Locata: the positioning technology of the future. In: Proceedings of the 6th international symposium on satellite navigation technology including mobile positioning & location services, Melbourne, Australia July, 2003
4. Khan FA, Dempster A, Rizos C (2010) Novel algorithms for weak. Low SNIR Signal Acquisition
5. Rizos C, Roberts G, Barnes J et al (2010) Experimental results of locata: a high accuracy indoor positioning system. In: International conference on indoor positioning and indoor navigation (IPIN), 2010. IEEE, pp 1–7
6. Barnes J, Rizos C, Wang J et al (2003) Locata: a new positioning technology for high precision indoor and outdoor positioning. In: Proceedings 2003 international symposium on GPS/GNSS, pp 9–18
7. Li Y, Rizos C (2010) Seamless navigation through a locata-enhanced GPS and INS integrated system. In: International symposium on GPS/GNSS, Taipei, Taiwan, pp 26–28
8. Khan FA, Dempster A, Rizos C (2011) Efficient algorithms for locata navigation receiver sensitivity improvement. J Global Positioning Syst 9(2):131–144
9. Ke S (2010) Research and key module design of digital impulse radio ultra-wideband receiver. Fudan University
10. Rinder P (2004) Design of a single frequency GPS software receiver. Aalborg Universitet. Institute of Electronic Systems
11. Crawford JA (2008) Advanced phase-lock techniques. Artech House
12. Yang Z (2002) Impulse phase-lock technique and its application. Radio Commun Technol 04:47–48+53
13. Scholtz R (1993) Multiple access with time-hopping impulse modulation. Milcom IEEE 93 (1993.2): 447–450
14. Gang X (2012) Principles of GPS and receiver design. Publishing House of Electronics Industry
15. Li C, Yang S, Ji Z (2012) Performance analysis of fast GPS signal acquisition based on PMF and Window FFT. J Beijing Inst Technol 03:291–297